ORNL-4895

C-578

TEST OF 6-INCH-THICK PRESSURE VESSELS. SERIES 1: INTERMEDIATE TEST VESSELS V-1 AND V-2

95,820

R. W. Derby
J. G. Merkle
G. C. Robinson
G. D. Whitman
F. J. Witt

BLANK PAGE

Printed in the United States of America. Available from
National Technical Information Service
U.S. Department of Commerce
5285 Port Royal Road, Springfield, Virginia 22151
Price: Printed Copy $7.60; Microfiche $0.95

ORNL-4895
UC-78 – Light-Water
Reactor Technology

Contract No. W-7405-eng-26

REACTOR DIVISION

HEAVY-SECTION STEEL TECHNOLOGY PROGRAM

TEST OF 6-INCH-THICK PRESSURE VESSELS.
SERIES 1: INTERMEDIATE TEST VESSELS
V-1 AND V-2

R. W. Derby G. C. Robinson
J. G. Merkle G. D. Whitman
F. J. Witt

FEBRUARY 1974

OAK RIDGE NATIONAL LABORATORY
Oak Ridge, Tennessee 37830
operated by
UNION CARBIDE CORPORATION
for the
U.S. ATOMIC ENERGY COMMISSION

CONTENTS

BLANK PAGE

FOREWORD

The work reported herein was performed mostly at Oak Ridge National Laboratory (ORNL) under sponsorship of the USAEC's Heavy-Section Steel Technology (HSST) Program, which is directed by ORNL. The program is conducted as part of the ORNL Pressure Vessel Technology Program, of which G. D. Whitman is director. The cognizant engineer for the USAEC is J. R. Hunter.

This report is designated Heavy-Section Steel Technology Program Technical Report No. 25. Prior reports in this series are:

1. S. Yukawa, *Evaluation of Periodic Proof Testing and Warm Prestressing Procedures for Nuclear Reactor Vessels*, HSSTP-TR-1, General Electric Company, Schenectady, N. Y. (July 1, 1969).
2. L. W. Loechel, *The Effect of Section Size on the Transition Temperature in Steel*, Martin Marietta Company, Denver, Colo. (Nov. 20, 1969).
3. P. N. Randall, *Gross Strain Measure of Fracture Toughness of Steels*, HSSTP-TR-3, TRW Systems Group, Redondo Beach, Calif. (Nov. 1, 1969).
4. C. Visser, S. E. Gebrielse, and W. VanBuren, *A Two-Dimensional Elastic-Plastic Analysis of Fracture Test Specimens*, WCAP-7368, Westinghouse Electric Corporation, PWR Systems Division, Pittsburgh, Pa. (October 1969).
5. T. R. Mager, F. O. Thomas, and W. S. Hazelton, *Evaluation by Linear Elastic Fracture Mechanics of Radiation Damage to Pressure Vessel Steels*, WCAP-7328 (Rev.), Westinghouse Electric Corporation, PWR Systems Division, Pittsburgh, Pa. (October 1969).
6. W. O. Shabbits, W. H. Pryle, and E. T. Wessel, *Heavy Section Fracture Toughness Properties of A 533 Grade B Class 1 Steel Plate and Submerged Arc Weldment*, WCAP-7414, Westinghouse Electric Corporation, PWR Systems Division, Pittsburgh, Pa. (December 1969).
7. F. J. Loss, *Dynamic Tear Test Investigations of the Fracture Toughness of Thick-Section Steel*, NRL-7056, U.S. Naval Research Laboratory, Washington, D.C. (May 14, 1970).
8. P. B. Crosley and E. J. Ripling, *Crack Arrest Fracture Toughness of A 533 Grade B Class 1 Pressure Vessel Steel*, HSSTP-TR-8, Materials Research Laboratory, Inc., Glenwood, Ill. (March 1970).
9. T. R. Mager, *Post-Irradiation Testing of 2 T Compact Tension Specimens*, WCAP-7561, Westinghouse Electric Corporation, PWR Systems Division, Pittsburgh, Pa. (August 1970).
10. T. R. Mager, *Fracture Toughness Characterization Study of A 533, Grade B, Class 1 Steel*, WCAP-7578, Westinghouse Electric Corporation, PWR Systems Division, Pittsburgh, Pa. (October 1970).
11. T. R. Mager, *Notch Preparation in Compact Tension Specimens*, WCAP-7579, Westinghouse Electric Corporation, PWR Systems Division, Pittsburgh, Pa. (November 1970).
12. N. Levy and P. V. Marcal, *Three-Dimensional Elastic-Plastic Stress and Strain Analysis for Fracture Mechanics. Phase I: Simple Flawed Specimens*, HSSTP-TR-12, Brown University, Providence, R. I. (December 1970).
13. W. O. Shabbits, *Dynamic Fracture Toughness Properties of Heavy Section A 533 Grade B, Class 1 Steel Plate*, WCAP-7623, Westinghouse Electric Corporation, PWR Systems Division, Pittsburgh, Pa. (December 1970).
14. P. N. Randall, *Gross Strain Crack Tolerance of A 533-B Steel*, HSSTP-TR-14, TRW Systems Group, Redondo Beach, Calif. (May 1, 1971).

BLANK PAGE

15. H. T. Corten and R. H. Sailors, *Relationship between Material Fracture Toughness Using Fracture Mechanics and Transition Temperature Tests*, T&AM Report No. 346, University of Illinois, Urbana, Ill. (Aug. 1, 1971).

16. T. R Mager and V. J. McLoughlin, *The Effect of an Environment of High Temperature Primary Grade Nuclear Reactor Water on the Fatigue Crack Growth Characteristics of A 533 Grade B Class 1 Plate and Weldment Material*, WCAP-7776, Westinghouse Electric Corporation, PWR Systems Division, Pittsburgh, Pa. (October 1971).

17. N. Levy and P. V. Marcal, *Three-Dimensional Elastic-Plastic Stress and Strain Analysis for Fracture Mechanics, Phase II: Improved Modeling*, HSSTP-TR-17, Brown University, Providence, R. I. (November 1971).

18. S. C. Grigory, *Six-Inch-Thick Flawed Tensile Tests, First Technical Summary Report, Longitudinal Specimens 1 through 7*, HSSTP-TR-18, Southwest Research Institute, San Antonio, Tex. (June 1972).

19. P. N. Randall, *Effects of Strain Gradients on the Gross Strain Crack Tolerance of A 533-B Steel*, HSSTP-TR-19, TRW Systems Group, Redondo Beach, Calif. (May 1, 1972).

20. S. C. Grigory, *Tests of Six-Inch-Thick Flawed Tensile Specimens, Second Technical Summary Report, Transverse Specimens Numbers 8 through 10, Welded Specimens Numbers 11 through 13*, HSSTP-TR-20, Southwest Research Institute, San Antonio, Tex. (June 1972).

21. L. A. James and J. A. Williams, *Heavy Section Steel Technology Program Technical Report No. 21, The Effect of Temperature and Neutron Irradiation upon the Fatigue-Crack Propagation Behavior of ASTM A 533, Grade B, Class 1 Steel*, HEDL-TME-72-132, Hanford Engineering Development Laboratory, Richland, Wash. (September 1972).

22. S. C. Grigory, *Tests of Six-Inch-Thick Flawed Tensile Specimens, Third Technical Summary Report, Longitudinal Specimens Numbers 14 through 16, Unflawed Specimen Number 17*, HSSTP-TR-22, Southwest Research Institute, San Antonio, Tex. (August 1972).

23. S. C. Grigory, *Tests of Six-Inch-Thick Flawed Tensile Specimens, Fourth Technical Summary Report, Tests of One-Inch-Thick Flawed Tensile Specimens for Size Effect Evaluation*, HSSTP-TR-23, Southwest Research Institute, San Antonio, Tex. (June 1973).

24. S. P. Ying and S. C. Grigory, *Tests of Six-Inch-Thick Tensile Specimens, Fifth Technical Summary Report, Acoustic Emission Monitoring of One-Inch and Six-Inch-Thick Tensile Specimens*, HSSTP-TR-24, Southwest Research Institute, San Antonio, Tex. (November 1972).

Copies of these reports may be obtained from Laboratory Records Department, Oak Ridge National Laboratory, P.O. Box X, Oak Ridge, Tenn. 37830.

TEST OF 6-INCH-THICK PRESSURE VESSELS. SERIES 1: INTERMEDIATE TEST VESSELS V-1 AND V-2

R. W. Derby G. C. Robinson
J. G. Merkle G. D. Whitman
F. J. Witt

1. INTRODUCTION

With the emergence of nuclear reactors as one of the major heat resources, the electric power industry in the United States and even throughout the world has been quick to recognize the potential of nuclear reactor systems for power generation. With this recognition has followed the rapid development of two major systems to commercial status – the boiling-water reactor (BWR) system and the pressurized-water reactor (PWR) system. Plants involving these systems are now coming into operation with capacities exceeding 1100 MW(e). Indeed, as the civilian nuclear power industry has grown, so have the sizes of the individual plants. This increase has resulted mainly from scaling up smaller systems with some modification in pressures and operating temperatures. As a consequence, the pressure vessels of the systems have increased in diameter and thickness. The thickness of the plate for fabricating some larger PWR vessels approaches 12 in., with diameters of the vessels from 14 to 16 ft. The standard operating temperature is around 550°F. Pressures range upward to around 2500 psi for the PWR systems, whereas for BWR systems the vessels are designed for about 1250 psi.

The main concern of the Heavy-Section Steel Technology (HSST) Program is the massive pressure vessels used in civilian water reactor systems, with emphasis on the effects of flaws, material inhomogeneities, and discontinuities on the behavior of the vessels under startup, operating, cooldown, and accident conditions. This interest stems from the fact that flaws (discontinuities) inherently exist in vessels, though possibly quite small, and that in-service inspection techniques are still being developed for applicability during the service life of the plants, some being designed to operate 40 years. The objective of the HSST program is to develop the technology necessary to establish a reliable means for estimating a conservative margin of safety against fracture for nuclear pressure vessels during the service life of the plants, particularly fracture that might endanger the public.

Structural integrity of nuclear reactor pressure vessels is insured by designing and fabricating according to the standards set by the code for nuclear pressure vessels, by detecting flaws of significant size that occur during both fabrication and service, and by developing methods capable of producing quantitative estimates of fracture conditions by which safety margins may be determined should flaws of significant size exist or develop. The program is concerned mainly with developing the pertinent fracture technology. It deals with the knowledge of the material used in these thick-walled vessels, the rate of growth of flaws, and the combinations of flaw size and stress (or strain) that would cause fracture and thus limit the allowable loads, temperature, and/or life of a vessel.

The primary objective of the simulated service task of the program, of which pressure vessel testing is a part, is to demonstrate the ability to predict failure, including tough, transitional, and frangible fracture. To predict the fracture conditions in a complex structure, the stresses and strains caused by service loads in the absence of flaws and cracks must be determined, and a fracture criterion specified in terms of obtainable parameters (stress, strain, energy, fracture toughness, etc.) is required, Finally, the value of the fracture criterion for the material as it occurs in the structure in service must be measured by suitable laboratory tests.

Specifically then the original objectives emphasized in the simulated service task were

1. to demonstrate capability to predict the "vessel transition temperature" for a selected crack configuration using the material of interest (ASTM A533, grade B, class 1 plate; ASTM A508, class 2 forging);
2. to demonstrate, for the materials of interest, capability to predict various combinations of load (pressure), temperature, and crack configuration in full-thickness walls (6 in. or more) that will not cause fracture and, finally, a combination that will cause fracture for both frangible and tough fracture conditions.

As originally planned,[1-3] the above objectives were to be attained by means of the generally successive testing of a series of specimens of the following types: 6-in.-thick flawed tensile specimens, nozzle corner simulation specimens, full-thickness (12-in.-thick) tensile specimens, intermediate vessel test specimens (6 in. thick), and full-scale vessel specimens. However, the rapid advancement in fracture technology, feasibility, and costs have combined to alter these plans, so that only the 6-in.-thick tensile specimens[4-8] and the intermediate vessels of the original series are being tested. These tests, however, are supplemented by the testing of large compact tension specimens[9] and model specimens and vessels. The intermediate vessel tests now play a dual role. First, they serve to develop the technology by providing input to sharpen proposed methods for quantitative fracture evaluation; second, the tests must demonstrate that the methods of fracture analysis are quantitative and applicable to reactor pressure vessels.

The intermediate vessel tests have been subdivided into four series:

1. flaws in cylindrical vessels, A508, class 2 forging steel – two vessels;
2. flaws in cylindrical vessels with longitudinal weld seams, A508, class 2 forging steel, submerged-arc welds – three vessels;
3. flaws in cylindrical vessels with longitudinal weld seams, A533, grade B, class 1 plate steel, submerged-arc weld – two vessels;
4. cylindrical vessels with radially attached nozzles, vessels of A508, class 2 forging steel and A533, grade B, class 1 plate steel; nozzle of A508 class 2 forging steel – three vessels.

This report contains a comprehensive description of the pertinent factors considered in the design of the vessels and construction of the test facility and those leading to the tests of series 1, as well as a documentation of test results and fracture predictions. Emphasis is placed on providing the test results in such a manner that they form a resource for any investigators interested in the problem of fracture

Several series of large and small specimens have been tested under the auspices of the HSST program. A common characteristic of all the tests has been that of a size effect (difference in normalized load, strain, energy, etc., between geometrically similar specimens) at a given temperature for all temperatures investigated (up to 550°F). Common also has been a characteristic transition from frangible to tough behavior over a relatively small temperature range well below 200°F. Since laboratory specimens differ widely from vessels, it is necessary to ascertain if vessels exhibit the same characteristic at fracture that laboratory specimens do. The primary objective of the two tests described in this report is to ascertain if pressure vessels exhibit a size effect at all applicable temperatures and, if such a size effect is exhibited, to ascertain if the size effect for the vessel can be determined from compact tension specimens. The secondary objective is to provide a preliminary evaluation for the potential of crack arrest once initiated from critical flaw-size–load–toughness conditions.

References

1. *Program Plan of the Heavy Section Steel Technology Program, a USAEC-Sponsored Program of Oak Ridge National Laboratory,* Apr. 1, 1968, revised Feb. 27, 1970 (unpublished).
2. F. J. Witt, "The Heavy Section Steel Technology Program – an Engineering Investigation of the Structural Behavior of Thick Pressure Vessels," *Nucl. Eng. Des.* 8(1), 22–38 (July 1968).
3. F. J. Witt, J. G. Merkle, and L. F. Kooistra, "Fracture Behavior Investigations under the USAEC-Sponsored Heavy Section Steel Technology Program," *Pressure Vessel Technology:* Part II – *Materials and Fabrication,* proceedings of the First International Conference on Pressure Vessel Technology, The American Society of Mechanical Engineers, New York, pp. 709–721, 1969.
4. S. C. Grigory, *Six-Inch-Thick Flawed Tensile Tests, First Technical Summary Report, Longitudinal Specimens 1 through 7,* HSSTP-TR-18, Southwest Research Institute, San Antonio, Tex. (June 1972).
5. S. C. Grigory, *Tests of Six-Inch-Thick Flawed Tensile Specimens, Second Technical Summary Report, Transverse Specimens Numbers 8 through 10, Welded Specimens Numbers 11 through 13,* HSSTP-TR-20, Southwest Research Institute, San Antonio, Tex. (June 1972).
6. S. C. Grigory, *Tests of Six-Inch-Thick Flawed Tensile Specimens, Third Technical Summary Report, Longitudinal Specimens Numbers 14 through 16, Unflawed Specimen Number 17,* HSSTP-TR-22, Southwest Research Institute, San Antonio, Tex. (August 1972).
7. S. C. Grigory, *Tests of Six-Inch-Thick Flawed Tensile Specimens, Fourth Technical Summary Report, Tests of One-Inch-Thick Flawed Tensile Specimens for Size Effect Evaluation,* HSSTP-TR-23, Southwest Research Institute, San Antonio, Tex. (June 1973).
8. S. P. Ying and S. C. Grigory, *Tests of Six-Inch-Thick Tensile Specimens, Fifth Technical Summary Report, Acoustic Emission Monitoring of One-Inch and Six-Inch-Thick Tensile Specimens,* HSSTP-TR-24, Southwest Research Institute, San Antonio, Tex. (November 1972).
9. F. J. Witt, *HSST Program Semiannu. Progr. Rep. Aug. 31, 1971,* ORNL-4681, pp. 21–23.

2. DESIGN AND FABRICATION OF THE INTERMEDIATE TEST VESSELS

General Design Requirements

The intermediate test vessels occupy the final phase of specimen testing under task K, simulated-service testing, of the HSST program. Prior tests of laboratory-scale specimens have been planned and implemented to provide data for the establishment of test conditions for the intermediate test vessels and to provide an extensive base for the extrapolation of failure hypotheses to full-size vessels for realistic environmental conditions. A quantified characterization of failure under frangible, transitional, and tough loading regimes is the primary goal of this phase of testing. Therefore, a number of parameters, namely, flaw origin in base material, flaw origin in weld metal, weld location, biaxial stress state, complex stress state, flaw size and shape, and temperature, have been selectively varied among the vessels to provide for the various stress and metallurgical states which normally exist in commercial nuclear reactor vessels.

Table 2.1 gives the base material and welding parameters utilized in the vessels to provide metallurgical state variations. Figure 2.1 shows a partially sectioned view of vessels V-1, V-2, V-3, V-4, V-6, V-7, and V-8 and Fig. 2.2 shows a partially sectioned view of vessels V-5, V-9, and V-10. Figure 2.3 shows the orientations of girth and longitudinal welds that are used to contain flaws in the testing of vessels V-3, V-4, V-6, V-7, and V-8.

Vessels V-1 through V-6 were advertised for competitive bidding under ORNL Job Specification JS-120-228 (Rev. 2).[1] Union Carbide Corporation Purchase Order 77Y-36160V for these vessels was awarded to Taylor Forge Division, Gulf and Western Products Company, on December 23, 1969. Under this purchase order an option was obtained for the purchase of spare components comprising the head and access nozzle subassembly shown in Fig. 2.1. This option was exercised for vessels V-7 through V-10, and these vessels were advertised for competitive bidding under ORNL Job Specification JS-120-228 (Rev. 2)

Table 2.1. Vessel base material and welding parameters

A = applicable; NA = not applicable

Vessel designation	Cylindrical shell base material	Nozzle material	Welds located in cylindrical shell		Vessel combinations fabricated from same heat and/or same weld filler metal lot				
			Girth	Longitudinal	Heat			Weld filler metal	
					A[1]	B[2]	C[3]		
V-1	A508, class 2	NA	NA	NA	A			NA	
V-2	A508, class 2	NA	NA	NA	A			NA	
V-3	A508, class 2	NA	NA	A		A			A
V-4	A508, class 2	NA	NA	A		A			A
V-5	A508, class 2	A508, class 2	NA	NA	A			NA	
V-6	A508, class 2	NA	A	A		A			A
V-7	A533-B, class 1	NA	NA	A			A		A
V-8	A533-B, class 1	NA	NA	A			A		A
V-9	A533-B, class 1	A508, class 2	NA	A			A		A
V-10	A533-B, class 1	A508, class 2	NA	A			A		A

[1]Cylindrical shells for vessels V-1, V-2, and V-5 forged from single-piece forging poured from two heats, National Forge 3V913 and 1V3809.

[2]Cylindrical shells for vessels V-3, V-4, and V-6 forged from single piece forging poured from two heats, National Forge 3V928 and 1V3825.

[3]Cylindrical shells for vessels V-7 through V-10 fabricated from plate produced from Lukens heat B52[illegible]

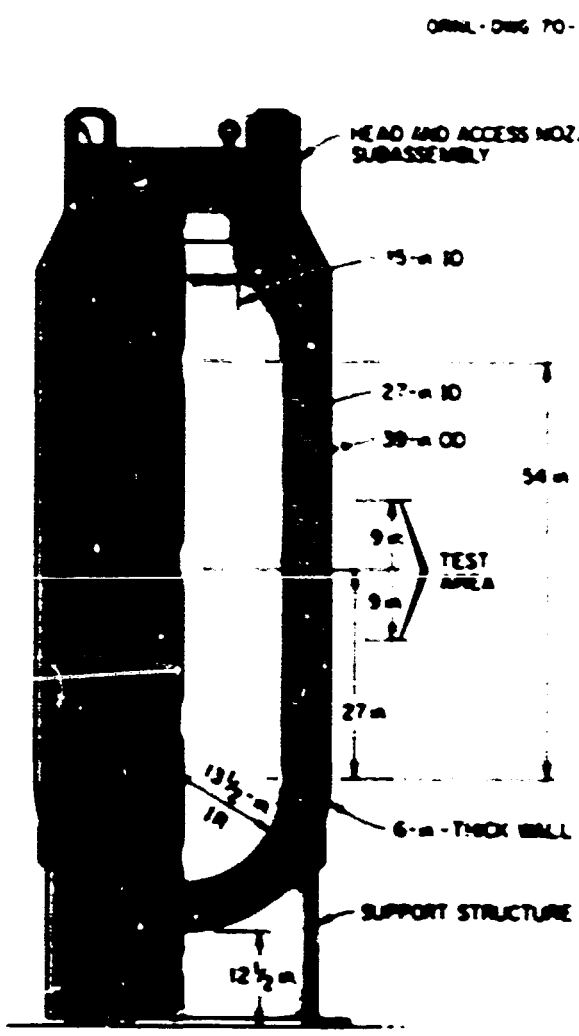

Fig. 2.1. HSST intermediate vessel.

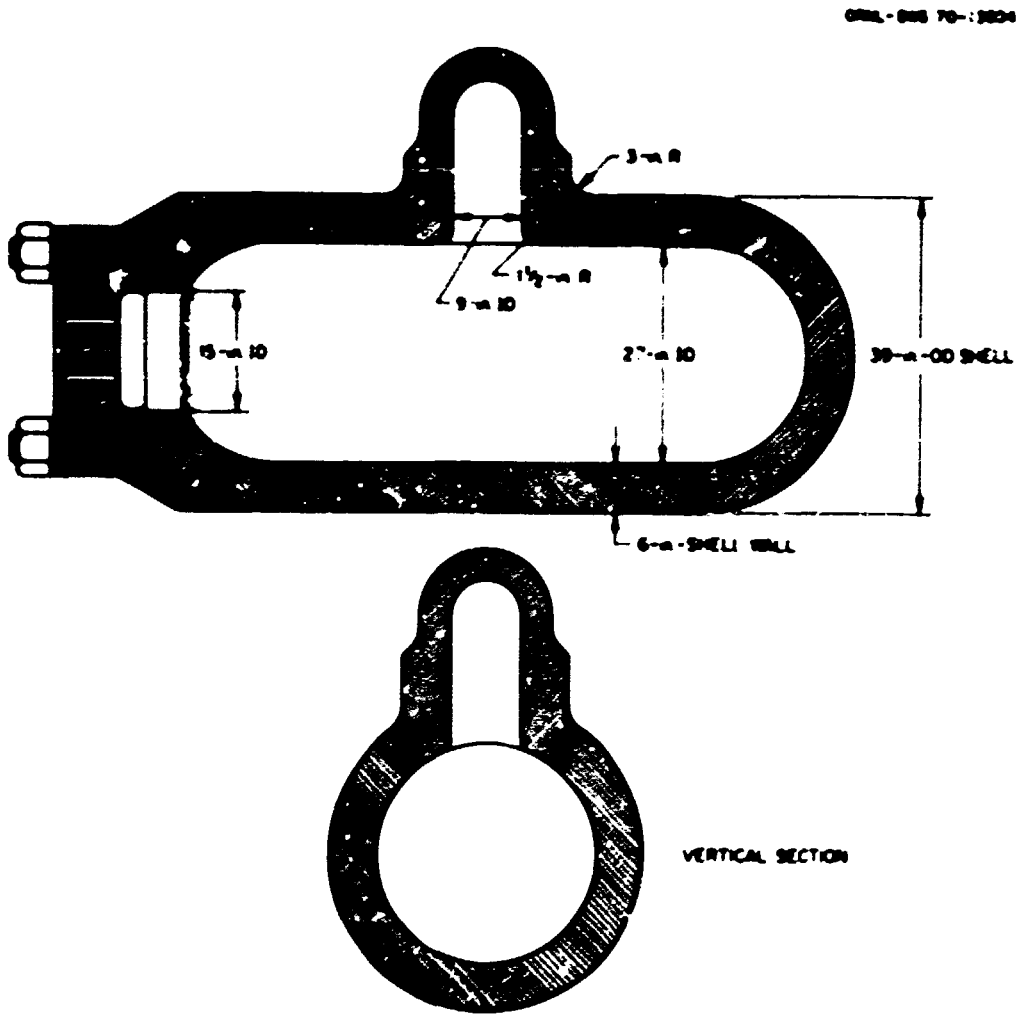

Fig. 2.2. Intermediate test cylindrical vessel with 9-in.-ID test nozzle.

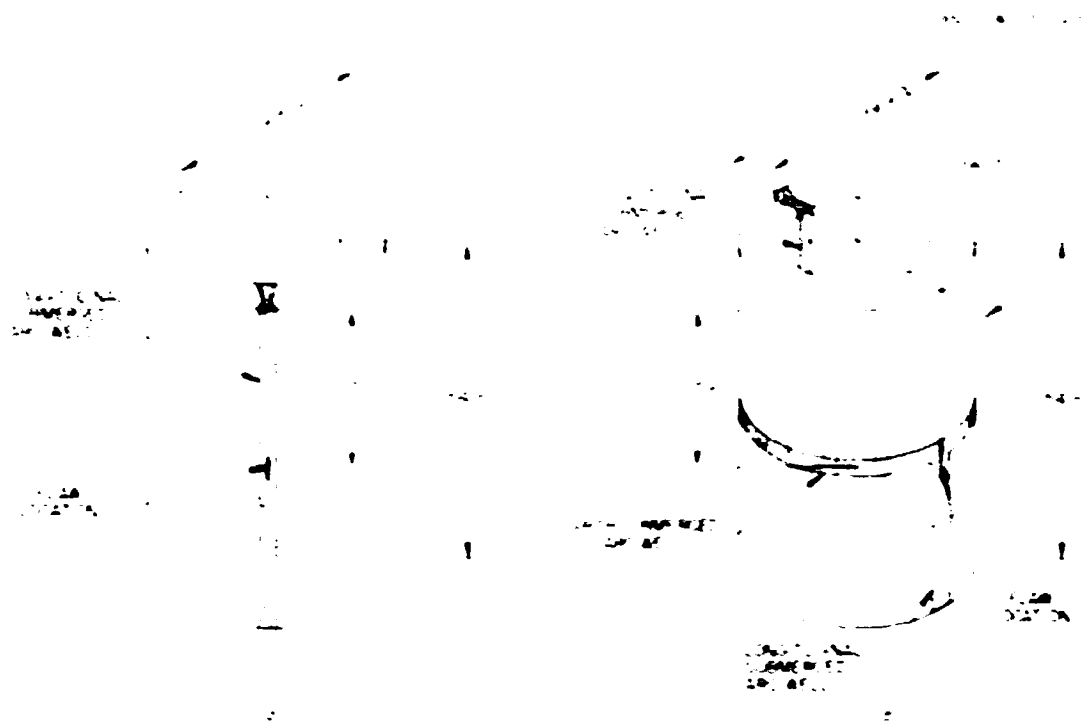

Fig. 2.3. Weld orientation for flaw location. *(a)* Vessels 3, 4, 7, 8, 9, 10; *(b)* vessel 6.

as amended by Union Carbide Corporation Request A-8278-77. An award for fabrication of these vessels was made to Taylor Forge Division, Gulf and Western Products Company, on April 7, 1972, under Union Carbide Corporation Purchase Order 77Y-94290V.

Under the provisions of the initial contract, Taylor Forge was responsible for the design of the head and access nozzle subassembly in accordance with the requirements of Section III of the ASME Pressure Vessel Code. To provide increased assurance that this subassembly would not fail prior to the failure of the flawed cylindrical shell of the test vessel, a design pressure over double the allowable design pressure of the cylindrical shell (20,000 psi) was utilized, and the allowable stress intensity for secondary membrane plus bending was arbitrarily set at 1.1 times the stress intensity that would be experienced by the cylindrical test course, if assumed infinite, at a pressure loading of 20,000 psi. Also under the provisions of the initial contract, the Taylor Forge design was verified by an analysis performed by Teledyne Materials Research Company under subcontract to Union Carbide Corporation.[2]

In addition to strict adherence to the quality assurance provisions of Section III of the ASME Pressure Vessel Code, an additional inspection technique was imposed on all welds: both longitudinal and shear beam ultrasonic testing of all welds was required. Subsequent experience demonstrated that this additional requirement was essential to obtain the high degree of integrity necessary for this test series.

Design Verification of Head and Access Nozzle Subassembly

Teledyne Materials Research (TMR) analyzed the head and access nozzle assembly by using an orthotropic finite-element composite closure technique.[2] This technique was used rather than the conventional compatibility interaction analysis because of the following advantages:

1. An interaction solution requires three unit load case solutions and two member stress solutions for each assembly component. The interaction analysis is then performed by forcing equilibrium and compatibility at assumed points of compatibility. A typical solution for cover, gasket, shell, and bolt entails 3 structural models, 20 sets of analyses, and a compatibility interaction solution. The composite closure analysis method permits a complete solution with only two analyses of one composite model.

2. The cover is idealized with an orthotropic ligament area that closely approximates the true rigidities.

3. Bolt interface load distributions and load transfer at points of compatibility between the cover and shell are inherent in the solution; thus the results are more representative of the actual system behavior.

4. The bolt or stud is coupled to the shell in a manner that accounts for the shear flexibility at the threaded end.

5. For thermal-gradient environments, the composite closure method includes the correct stiffness characteristics (modulus of elasticity vs temperature), whereas influence matrices used in the interaction solution are based on room or average temperature.

6. The composite model can be modified so that the results include the effects of interface gapping or sliding, if these conditions are found to exist.

In general, the closure assembly was structurally idealized as a finite-element model that included and accounted for the effects of bolt preload, pressure interactions, and local interface flexibilities. In addition, the effects of closure interface gaps were included in the final solution.

The work did not include the evaluation of thermal transient conditions. The seal membrane was not evaluated because it was anticipated that yielding would occur during the first operational cycle.

An adaptation of an operational finite-element computer program for the stress analysis of axisymmetric solids (SAAS) was employed for the analysis.[3] The program determines the stress and strain distribution within either homogeneous or heterogeneous thick-walled orthotropic bodies of revolution under axisymmetric mechanical or thermal loading conditions. The program employs an axisymmetric quadrilateral or triangular ring element and utilizes the displacement (stiffness) method of structural analysis. Unlike the usual "shells-of-revolution" type of computer program, which accounts only for middle surface elastic deformation, SAAS takes into account (and determines) elastic deformation throughout the entire body. Thus the effects of local flexibility are an integral part of the solution.

The stud, shell, and cover ligament areas of the subassembly are nonaxisymmetric with respect to the shell center line. Since SAAS handles only bodies of revolution, it was necessary to modify the properties of element rings in order to obtain equivalent rigidities in the respective areas. The geometry and orthotropic property modifications result in an idealized system that has rigidities equivalent to those of the actual closure assembly; thus the displacements and rotations from the SAAS solution will be accurate. To permit detection and accounting for cover gapping or sliding between the cover and the shell, TMR conceived and developed an extremely thin element solely as a device for coupling and decoupling adjacent elements.

The final finite-element solution included 20,000 psi internal pressure, bolt preload, and the aforementioned film elements uncoupling modifications. The distorted geometry of the assembly for this loading is shown in Fig. 2.4 and in Figs. 2.5–2.8, which illustrate radial, axial, circumferential, and shear isostress plots of the assembly. Stud stresses were found to comply with the membrane and bending stress limitations stipulated by Section III of the ASME Code. The results of the stress analysis of the head and access nozzle assembly are summarized below:

Stress category	Maximum bolt stress (psi)	Allowable bolt stress (psi)
P_m	79,500	83,600
$P_m + P_b$	83,500	125,700

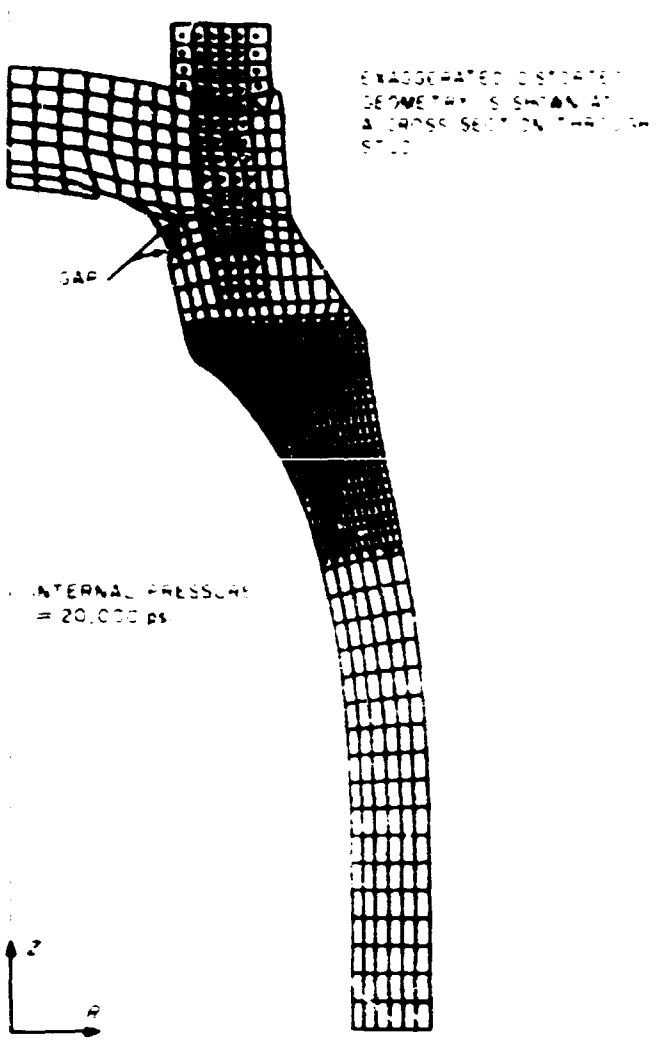

Fig. 2.4. Distorted geometry of HSST intermediate vessel with pressure and preload at 400 F for cover gap case.

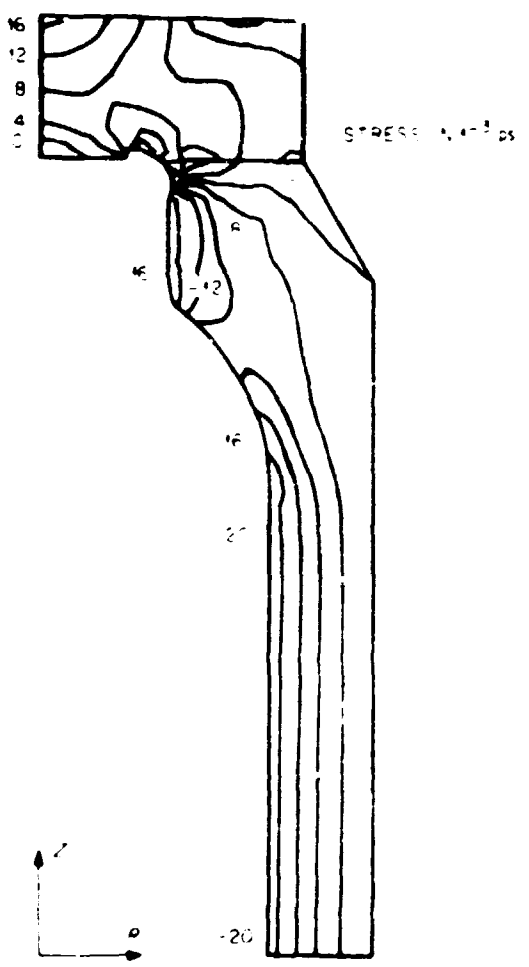

Fig. 2.5. Radial stress isostress lines for HSST intermediate vessel with pressure and preload at 400°F for cover gap case.

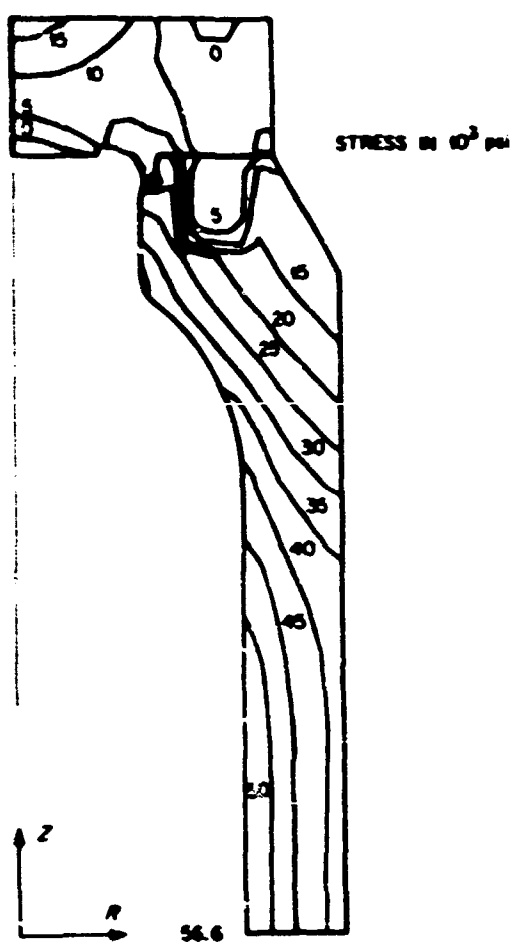

Fig. 2.6. Hoop (axial) stress isostress lines for HSST intermediate vessel with pressure and preload at 400°F for cover gap case.

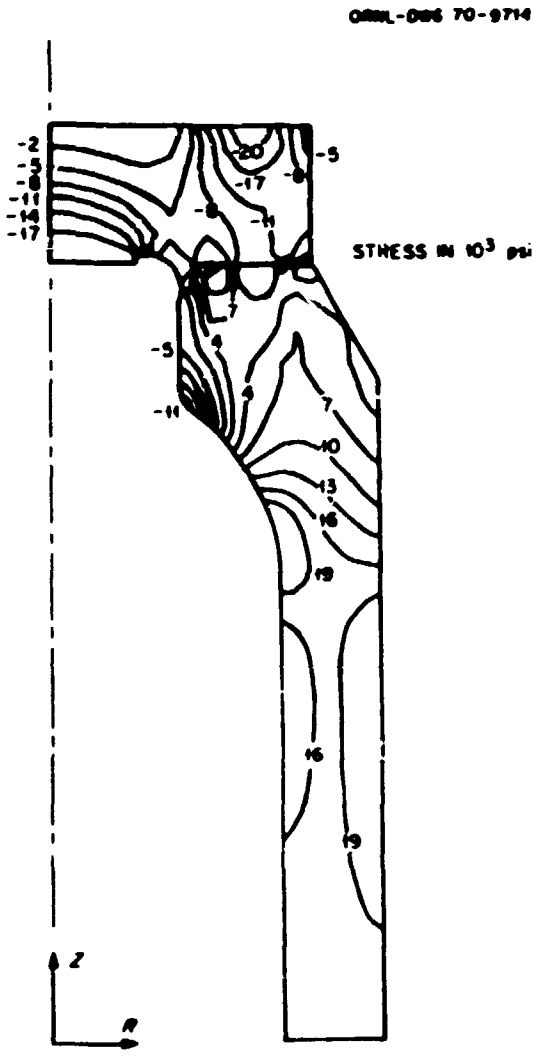

Fig. 2.7. Circumferential stress isostress lines for HSST intermediate vessel with pressure and preload at 400°F for cover gap case.

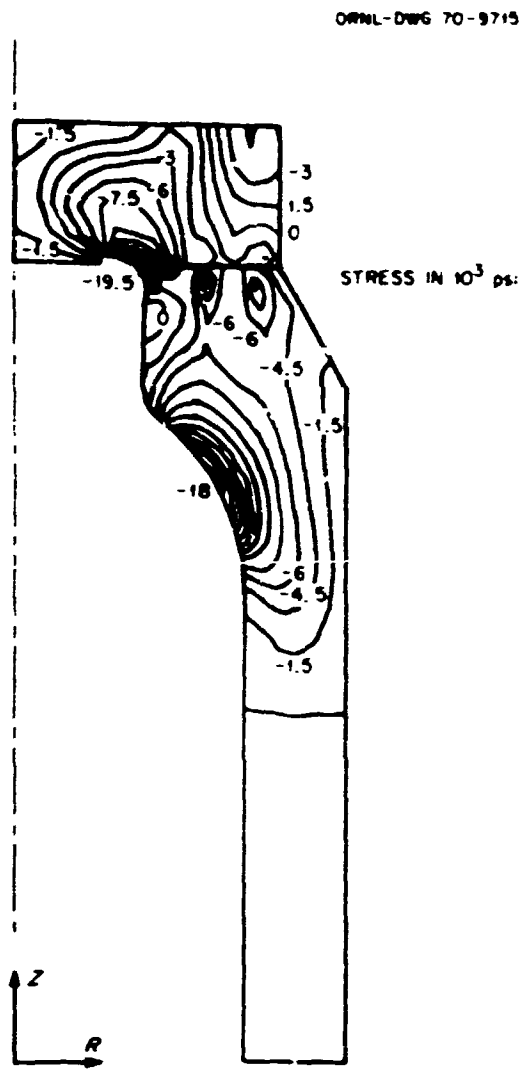

Fig. 2.8. Shear stress isostress lines for HSST intermediate vessel with pressure and preload at 400°F for cover gap case.

Section III of the 1968 ASME Boiler and Pressure Vessel Code and Summer 1968 Addenda, paragraph N-416.1, defines categories and allowable stress. The maximum stress occurred in the shell portion of the closure assembly as follows:

Stress category	Maximum shell stress intensity (psi)	Allowable shell stress intensity (psi)
$P_m + P_b + P_L + Q$	76,600	84,500

Design Verification of the Radially Attached Nozzle

The geometry of the radially attached nozzle on vessels V-5, V-9, and V-10 was chosen somewhat arbitrarily. Existing and planned reactor vessels have D_m/d_i (shell mean diameter to nozzle inside diameter) ratios that vary from about 3 to 6; a value of 4 was selected for the radial nozzles of the intermediate vessels. Designers currently use considerable variations in the choice of nozzle outside fillet and inside corner radii within the latitude permitted by Section III of the ASME Code. An overreinforced configuration was chosen which had a nozzle thickness equal to the shell thickness and fillet and corner radii in the midrange of Section III requirements, similar to the configurations used by designers of reactor vessels. Since it is desired that the stress concentration factor of the intermediate vessel nozzle corner be

equal to that used in reactor vessels, about 2.7 to 2.8, it was anticipated that some slight modification to the chosen geometry might be required. This factor was then investigated analytically and experimentally under the complex-stress-state task of the HSST program.

Classical mathematical methods of stress analysis are not strictly applicable to the complex configuration of the typical heavy-section vessel-nozzle junction. Finite-element methods are the logical choice for such a situation. However, three-dimensional finite-element analyses present certain complexities of their own, both in the idealization and in the computational processes, and have not been as widely applied as the two-dimensional programs. Utilizing the three-dimensional finite-element program SAFE-3D, which was operational at ORNL, Krishnamurthy proceeded with the investigation of the stress analysis of nozzle junction in the following steps.[4]

1. The geometrical relationships necessary to define the idealized configuration of various surfaces on, and points within the wall of, a thick-walled cylindrical-vessel–nozzle junction with a curved transition were formulated.

2. A computer program entitled HST-NODES, to generate the idealized geometry, and a finite-element mesh suitable for a three-dimensional analysis of the junction were developed.

3. The intermediate test vessel radial nozzle junction was analyzed with the three-dimensional elastic finite-element analysis program (SAFE-3D) for pressure loading.

4. The results were evaluated.

The study was limited to the particular vessel-nozzle configuration defined by the following and shown in Fig. 2.9.

1. The vessel and the nozzle are both cylindrical, with straight axes intersecting at right angles; thus the nozzle is radially attached to the vessel.

2. The radius and the wall thickness of both the vessel and the nozzle are constant over the portion of the junction analyzed and, by implication, for a certain distance beyond this portion.

3. Both the inner and outer transitions between the vessel and the nozzle are circular arcs and are not necessarily concentric.

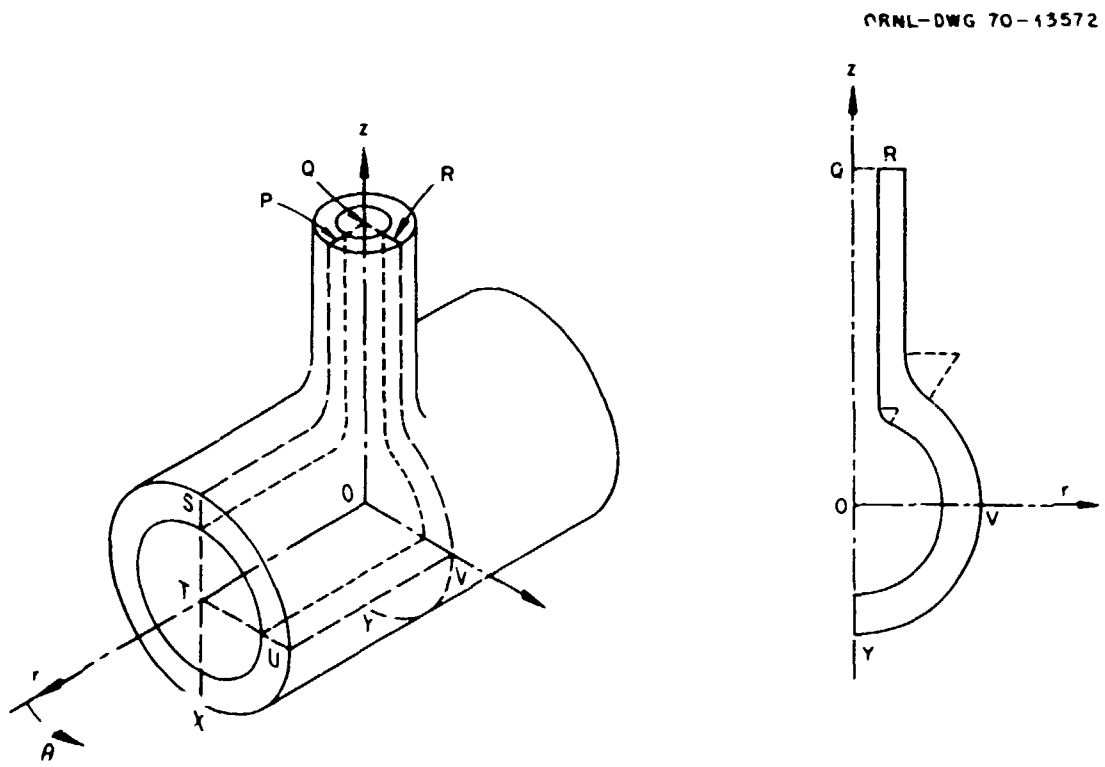

Fig. 2.9. Vessel-nozzle junction.

4. Each transition arc connects tangentially with both the vessel and the nozzle.

The HST-NODES program was developed to provide considerable flexibility in the definitions of the element size to accommodate zones of high stress concentration. Supplied with the inner and outer dimensions of the symmetry sector, the number of slices, angular parts, and trace divisions for the idealization, and certain options, the program will generate all the additional information necessary for the computations on the intermediate layers, compute the cylindrical coordinates, and print and also punch the values out in sequential order. A typical mesh generated (an actual case solved) is shown in Fig. 2.10.

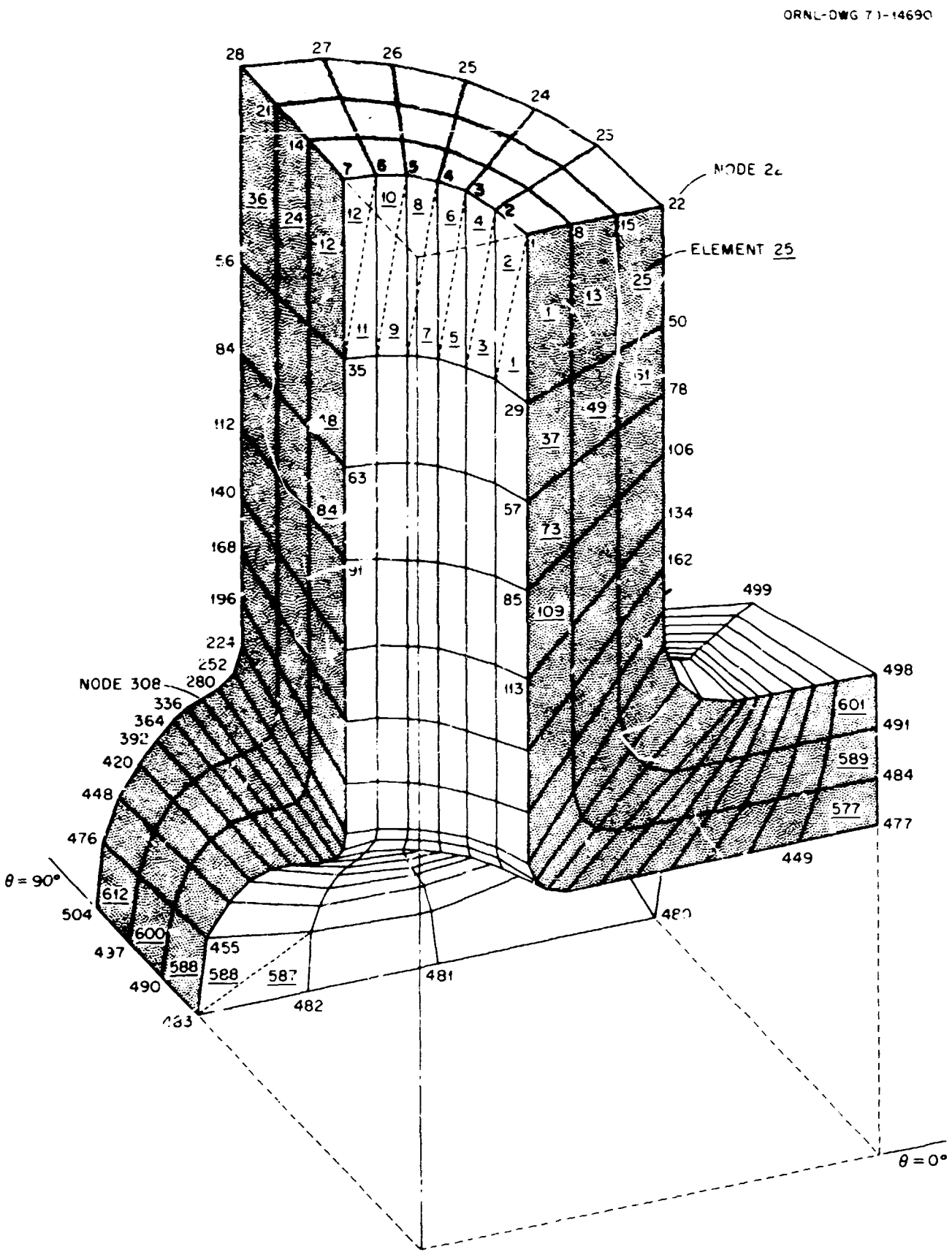

Fig. 2.10. Node and element numbering scheme for 3-D analysis, coarse mesh. Underscored numbers are element indices.

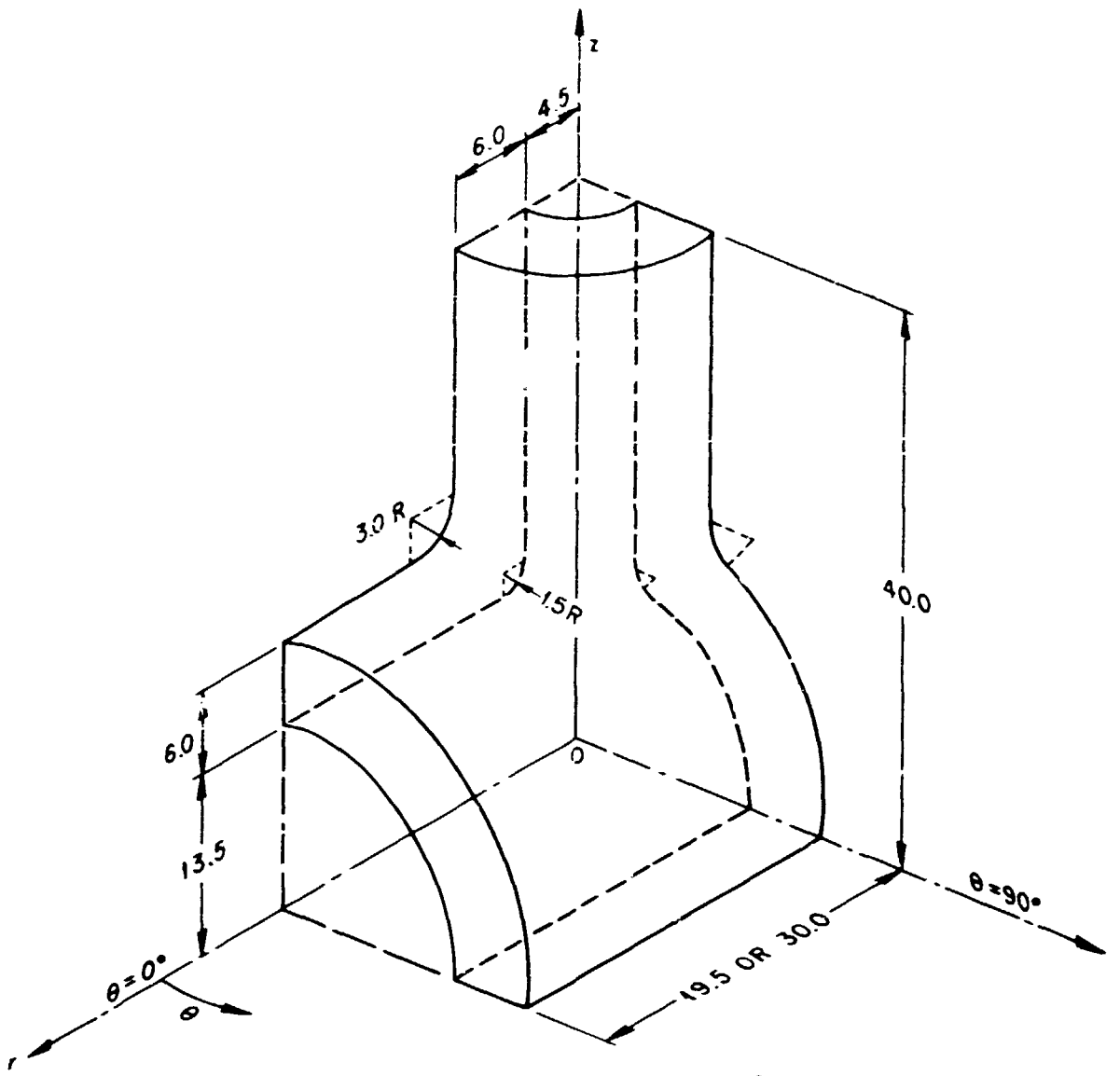

Fig. 2.11. Symmetry sector of the pipe-nozzle junction chosen for analysis.

The pipe-nozzle junction selected for the study was a simplified version of the intermediate test vessel of the HSST program depicted in Fig. 2.2. The vessel internal diameter was 27.0 in., and the nozzle internal diameter was 9.0 in. The internal and external transition radii were 1.5 and 3.0 in. Although the nozzle had a stepped exterior, the wall thickness was assumed uniform at 6.0 in. for both the nozzle and the vessel. The maximum height (Z_m) of the nozzle top above the equatorial plane was taken as 40.0 in.; two values of half pipe lengths (P_l), 19.5 and 30.0 in., were chosen for the analysis to examine the effects, if any, of the length of pipe on the stress distribution in the transition region. A one-eighth symmetry sector was selected. Figure 2.11 illustrates the simplified model along with the principal dimensions and the coordinate axes.

Since the main purpose of the study was to obtain an estimate of the stress concentration in the transition region, the simple situation of internal pressure was considered adequate. An arbitrary value of 1000 psi was chosen for convenience. Further, the stresses at the "cut" ends of the nozzle and the vessel were assumed uniformly distributed over the cross-sectional area of the walls at values which would equilibrate the pressure acting on the areas of the open ends. This assumption would correspond to the situation where the nozzle and the vessel were rigidly capped.

In order to examine the effects of mesh size and pipe length, three cases were analyzed as summarized by Table 2.2.

Table 2.2. Details of the three cases analyzed

Case	Pipe designation	Pipe length (in.)	Mesh designation	Number of nodes	Number of segments
1	Short	19.5	Coarse	504	18
2	Short	19.5	Fine	2112	32
3	Long	30.0	Medium	1170	26

An examination of the stress output revealed the following characteristics:

1. The shear stresses everywhere were generally much smaller than the normal stresses. Further, the regions of high shear stresses and of high normal stresses did not coincide.

2. The radial stresses σ_r were all within the range of ±1000 psi throughout the region analyzed.

3. The circumferential stresses σ_θ were maximum on the inner surface at the longitudinal section, near the transition region. The maximum shear stresses $\tau_{\theta z}$ in this region were of magnitude about 5% of the maximum circumferential stresses.

4. The axial stresses σ_z were maximum on the inner surface near the intersection of the transverse section and the equatorial plane. The maximum shear stresses in this region were between 10 and 20% of the maximum axial stresses.

5. The maximum circumferential stress for any mesh was more than twice the maximum axial stress, and much higher than the maximum radial stress. Further, in the region of maximum circumferential stress, the radial and axial stresses were very low, about 15% of the maximum circumferential stress.

On the basis of the preceding observations, it was considered unlikely that the critical principal stresses would be much different from the critical normal stresses. More detailed evaluation was confined to the normal stresses only.

Figures 2.12–2.18 depict the contour plots of σ_r, σ_θ, and σ_z at 0 and 90° sections for all three meshes and at 45° for the medium mesh only. Figures 2.12 and 2.13 show the three plots of radial stress distributions at 0 and 90°; Figs. 2.14 and 2.15 show circumferential stress distributions at 0 and 90°; Figs. 2.16 and 2.17 show axial stress distributions at 0 and 90°. Figure 2.18 shows σ_r, σ_θ, and σ_z distributions at 45° for the medium mesh. The known boundary conditions used to plot the contours are indicated on the plots in parentheses. A comparison of the plots indicates that the differences in the length of pipe do not significantly affect the stress distribution, especially in the transition region.

The effects of the mesh sizes may also be observed by comparing the plots for the coarse, medium, and fine meshes in Figs. 2.12–2.17. In every case, the stress gradients are seen to change progressively with mesh refinement, the change being generally to increase the gradient, as could be expected.

The technique of fitting the stress values with a least-squares exponential fit was used to obtain an extrapolation to the surface. A technique known as the h^n extrapolation, where h is a parameter for element size and n is the number of nodes, was used to obtain an extrapolation to the continuum. With these techniques a value of 6700 psi was found as the maximum circumferential stress at the junction; dividing this value by the nominal circumferential stress, a stress concentration factor of 3.0 was obtained.

Derby, of ORNL, examined the stress concentration at the nozzle junction by performing an experimental stress analysis of an epoxy model of the intermediate test vessels V-5, V-7, and V-10.[5] A view of the model vessel after strain gaging and ready for assembly is shown in Fig. 2.19. The strain gages were applied to the inside of the vessel before assembly of the components, and then a number of small holes were tapped in the hemispherical end caps. Brass bolts were dipped in epoxy and screwed into these holes.

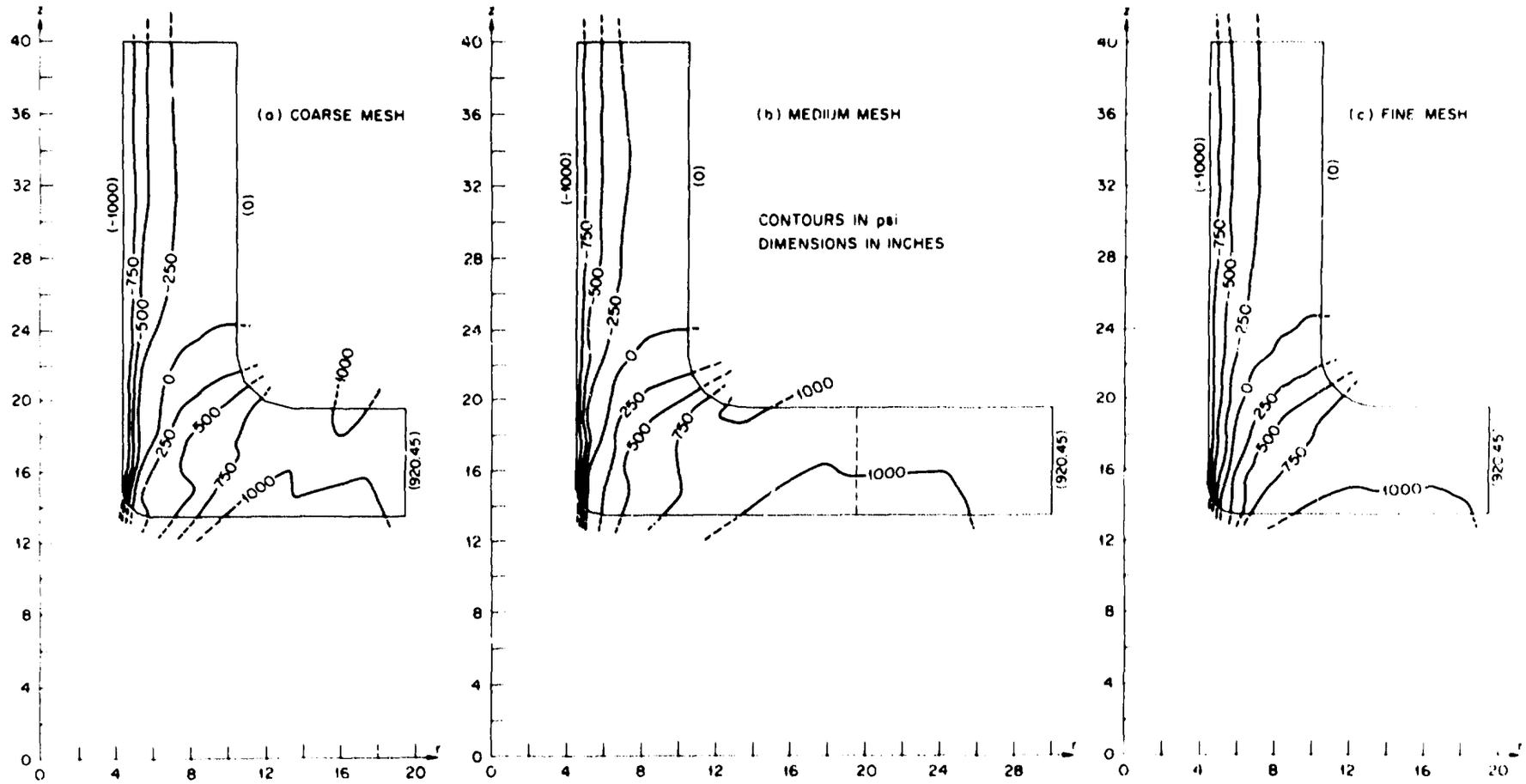

Fig. 2.12. Radial stress contours (σ_r) on longitudinal section ($\theta = 0^\circ$).

ORNL DWG 70-13810R

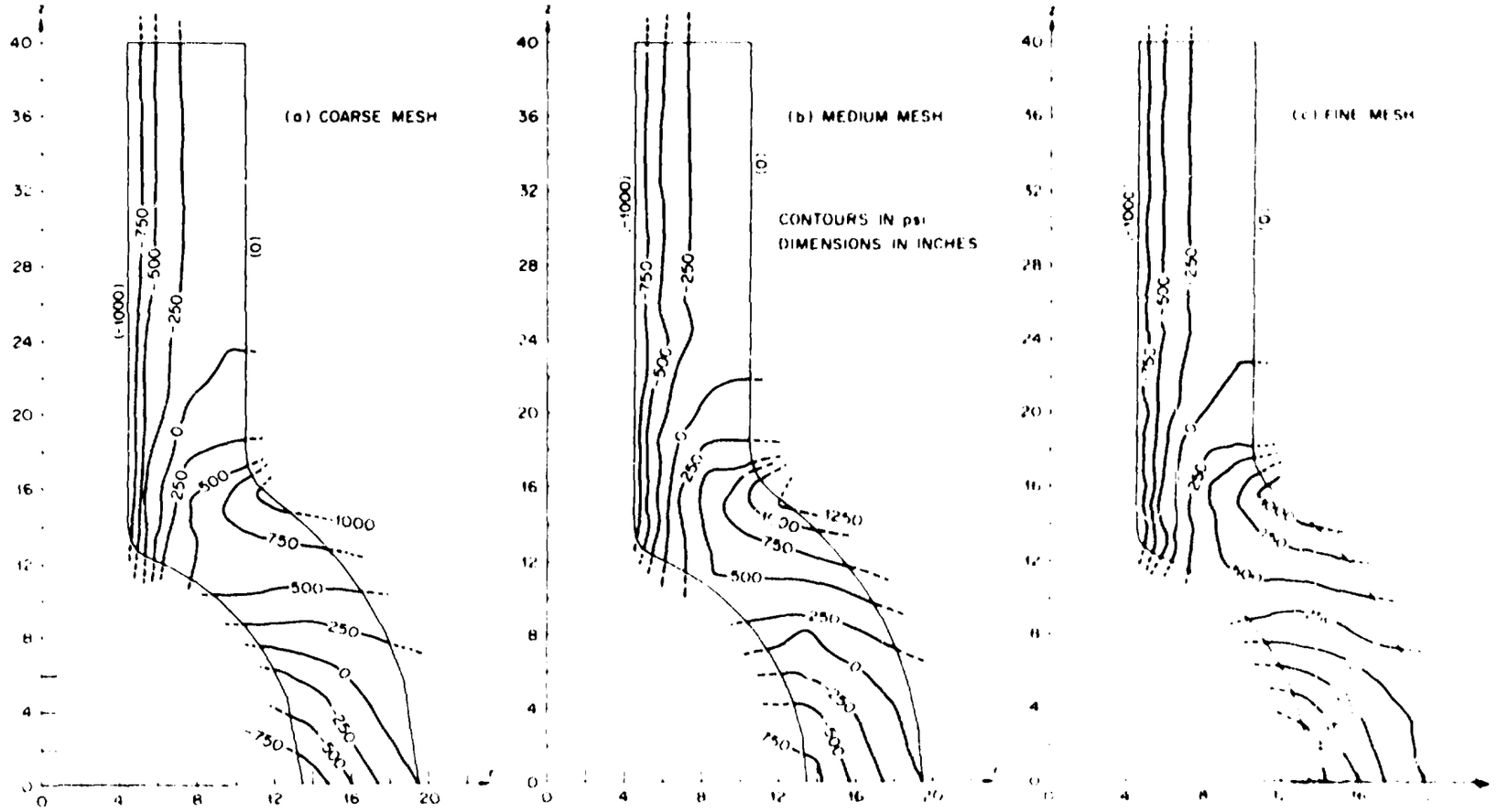

Fig. 2.13. Radial stress contours (σ_r) on transverse section ($\theta = 90^{\circ}$).

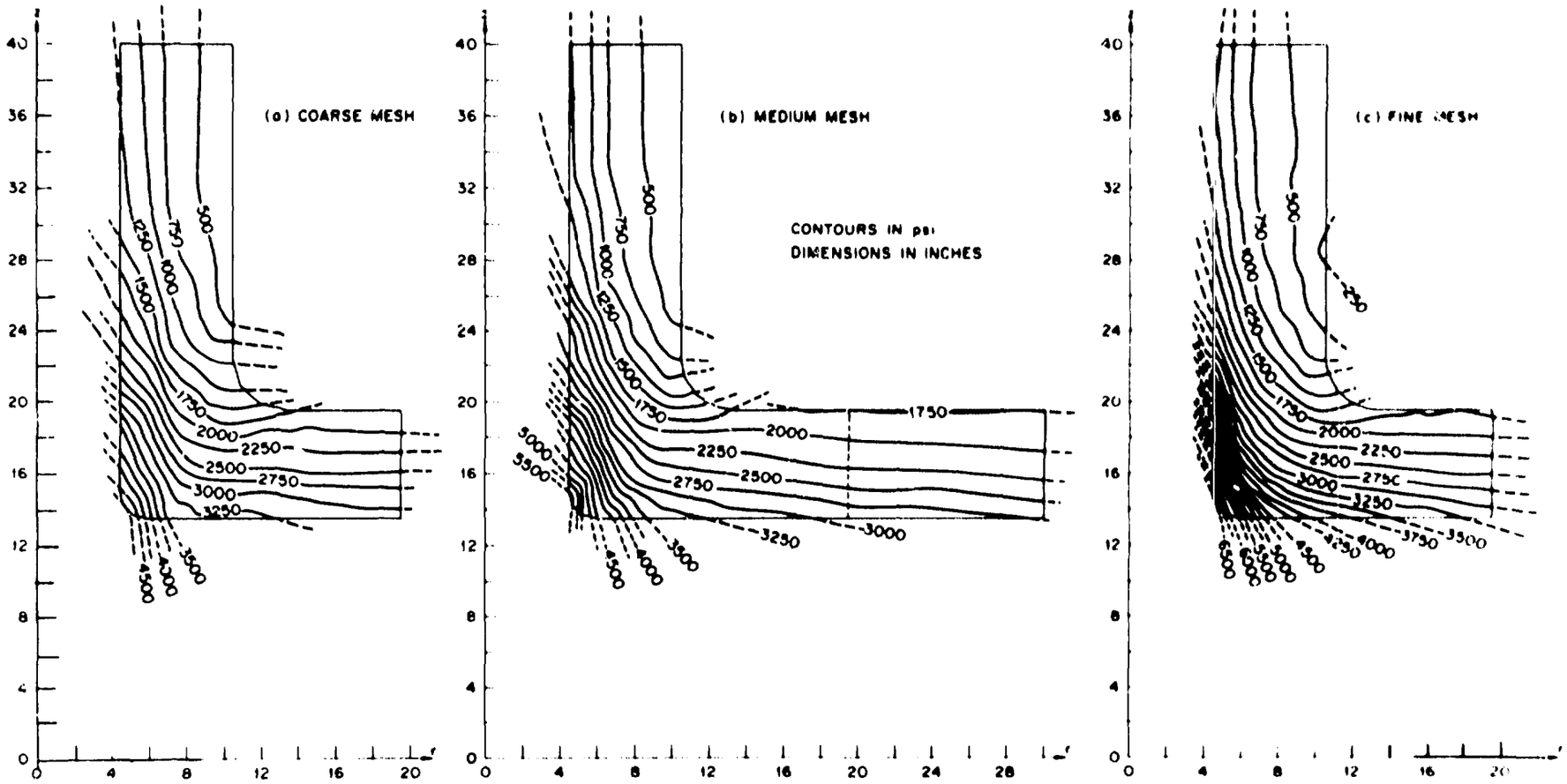

Fig. 2.14. Circumferential stress contours (σ_θ) on longitudinal section ($\theta = 0^\circ$).

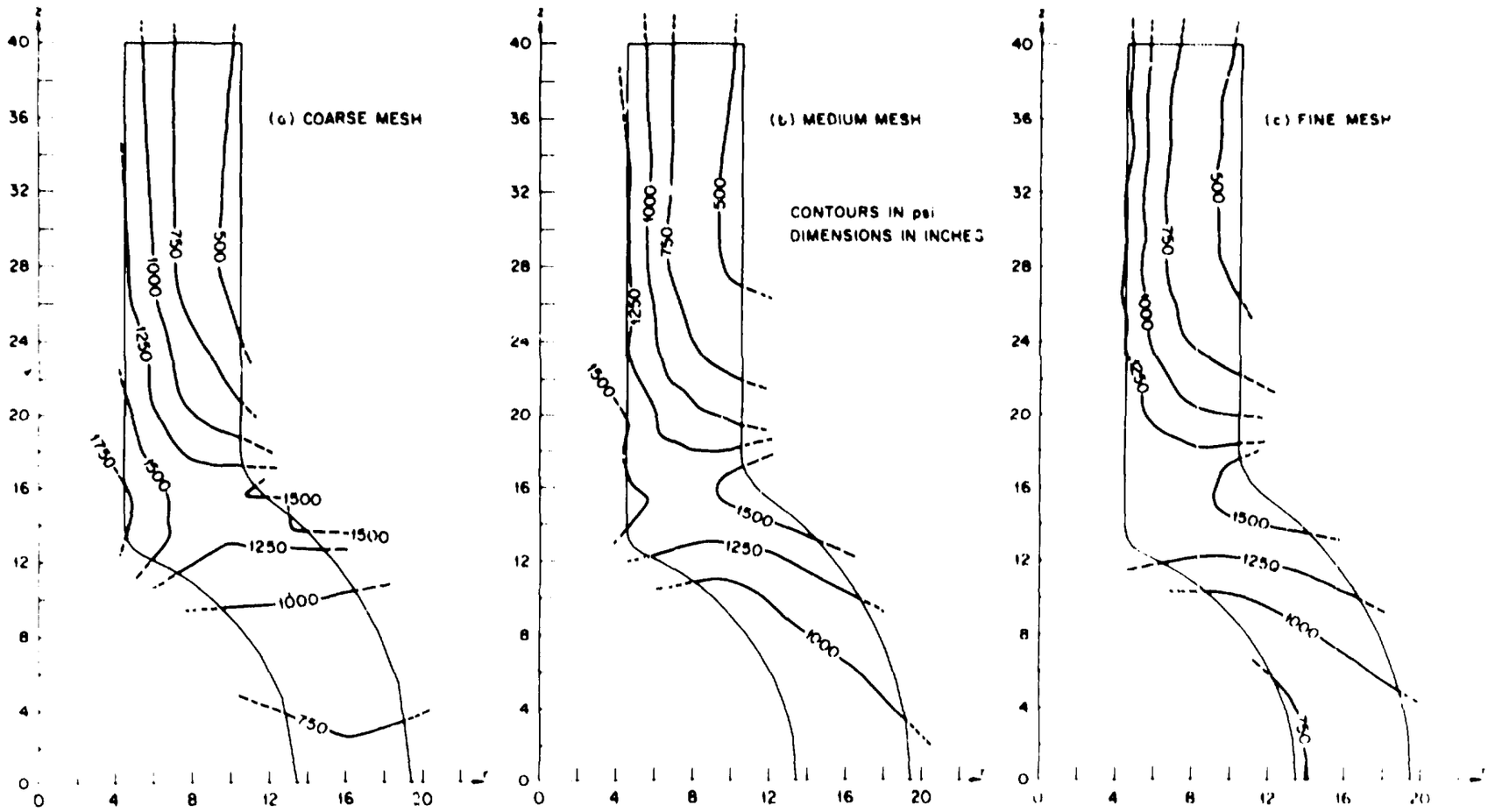

Fig. 2.15. Circumferential stress contours (σ_θ) on transverse section ($\theta = 90^\circ$).

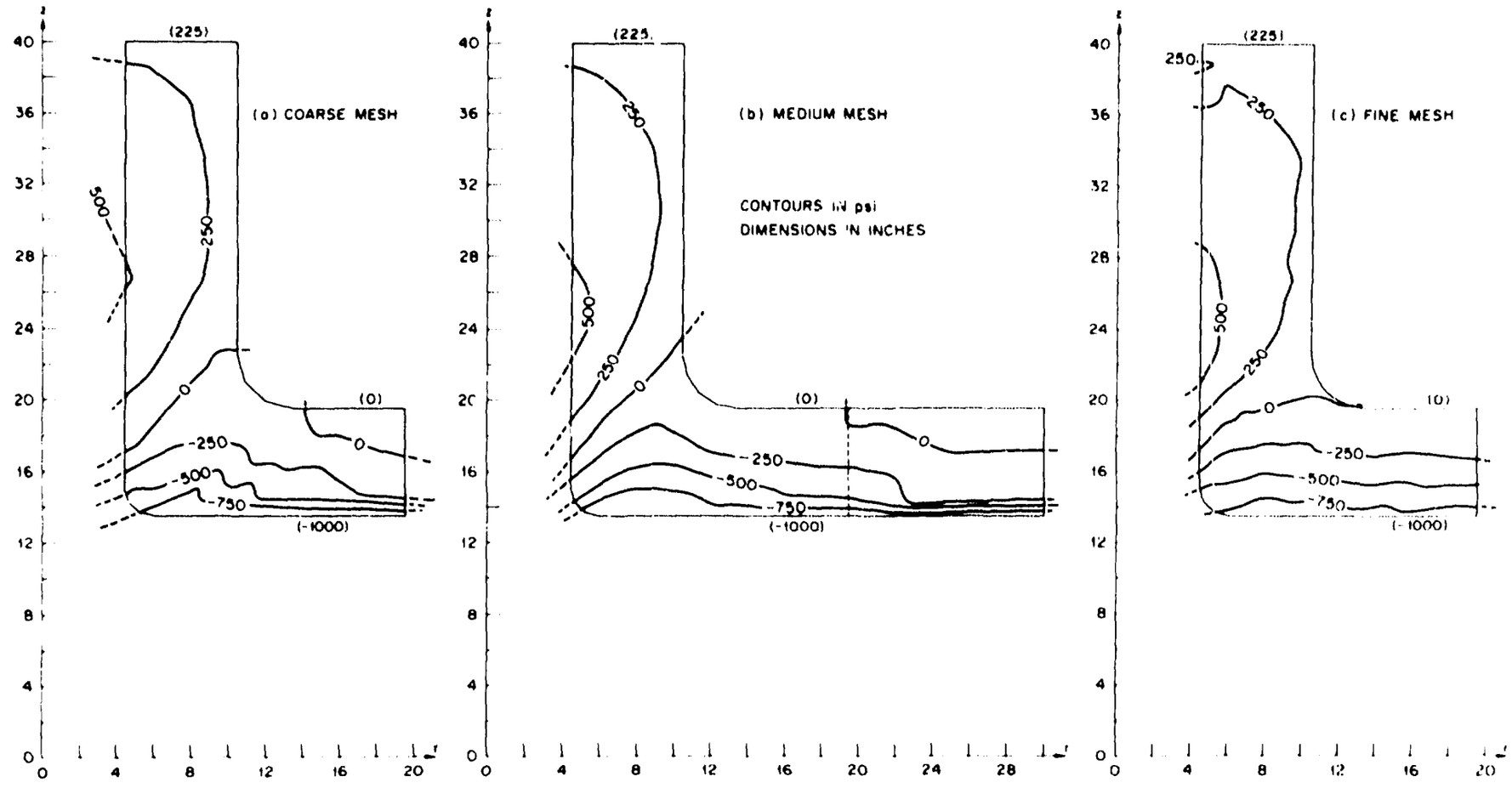

Fig. 2.16. Axial stress contours (σ_z) on longitudinal section ($\theta = 0^\circ$).

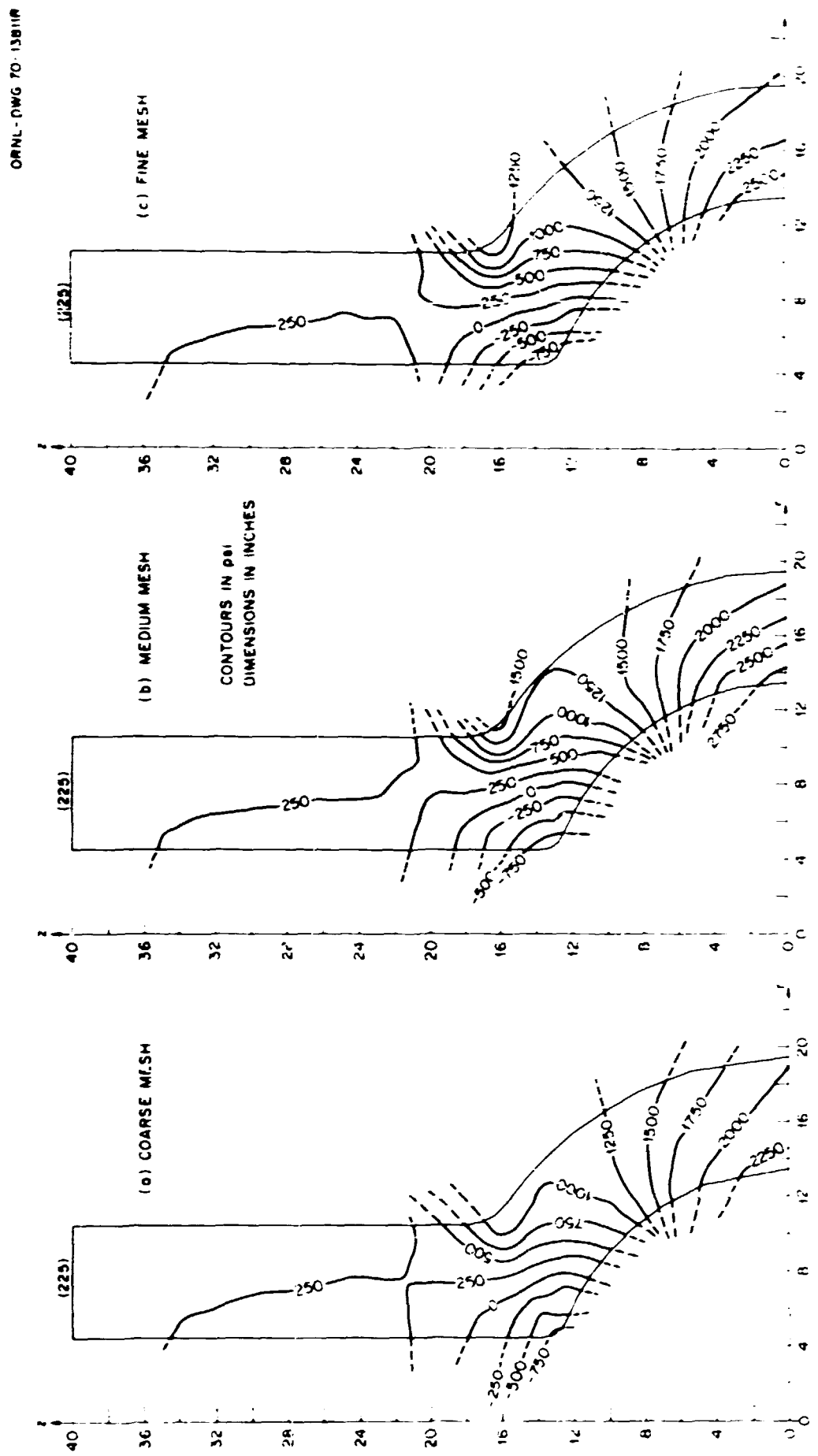

Fig. 2.17. Axial stress contours (σ_z) on transverse section ($\theta = 90^\circ$).

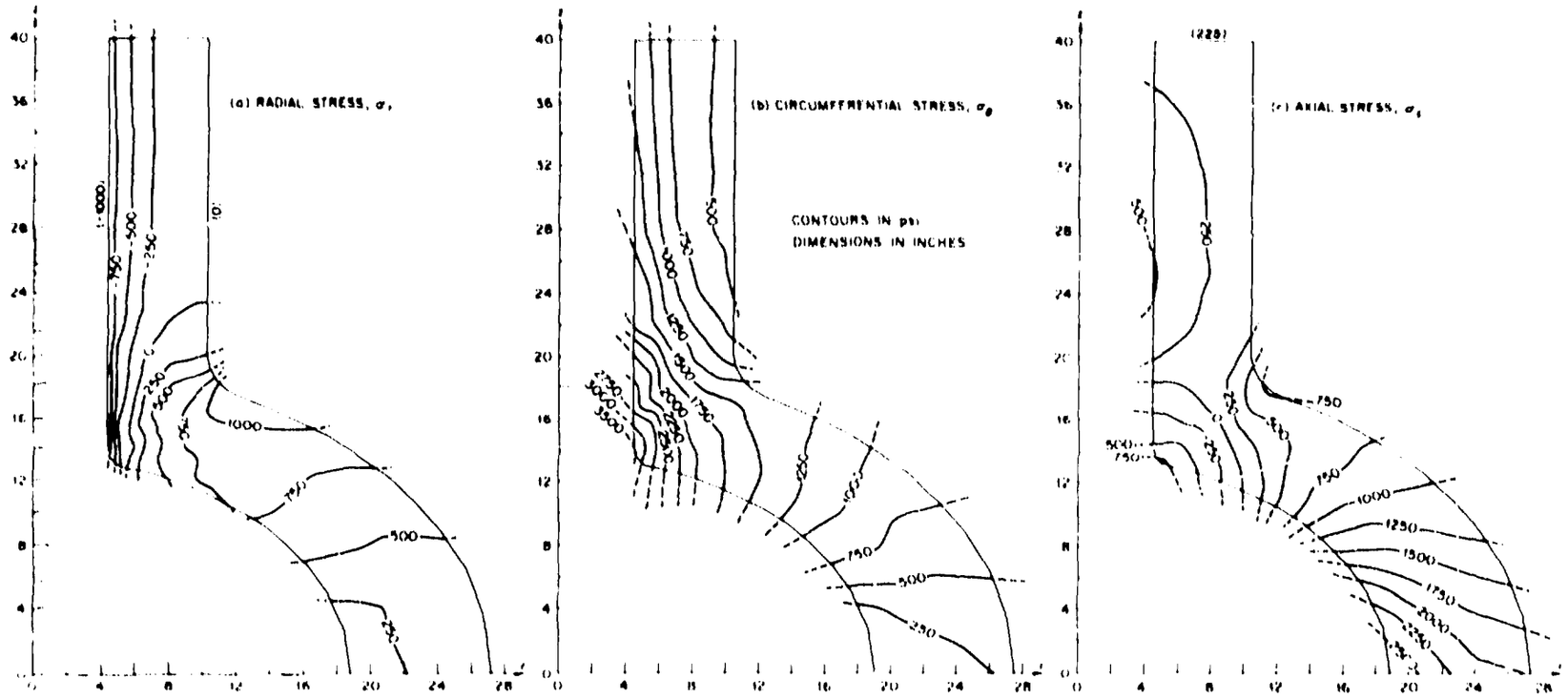

Fig. 2.18. Medium mesh stress distributions on 45° meridional section.

Fig. 2.19. Small epoxy vessel with strain gages in place ready for assembly.

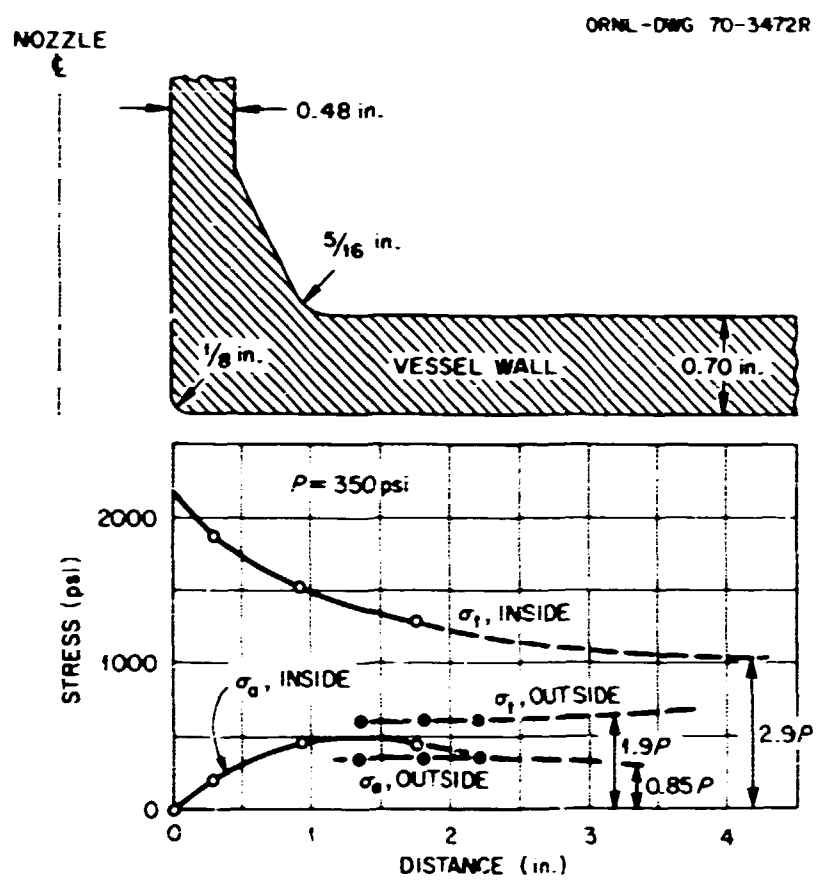

Fig. 2.20. Axial (σ_a) and tangential (σ_t) stresses on the inside and outside of the wall of the epoxy model of the intermediate test vessel by experimental stress analysis.

When the epoxy had set, each bolt made an excellent "lead-through." Wires from the strain gages were soldered to the bolts on the inside. Finally, the vessel was glued together, and lead wires were soldered onto the exterior end of the brass bolts.

Some of the results of the experimental stress analysis are shown in Fig. 2.20. The dashed lines indicate extrapolations to the stresses given by Lame's equation for tangential stress and by "force over area" for the axial stress.

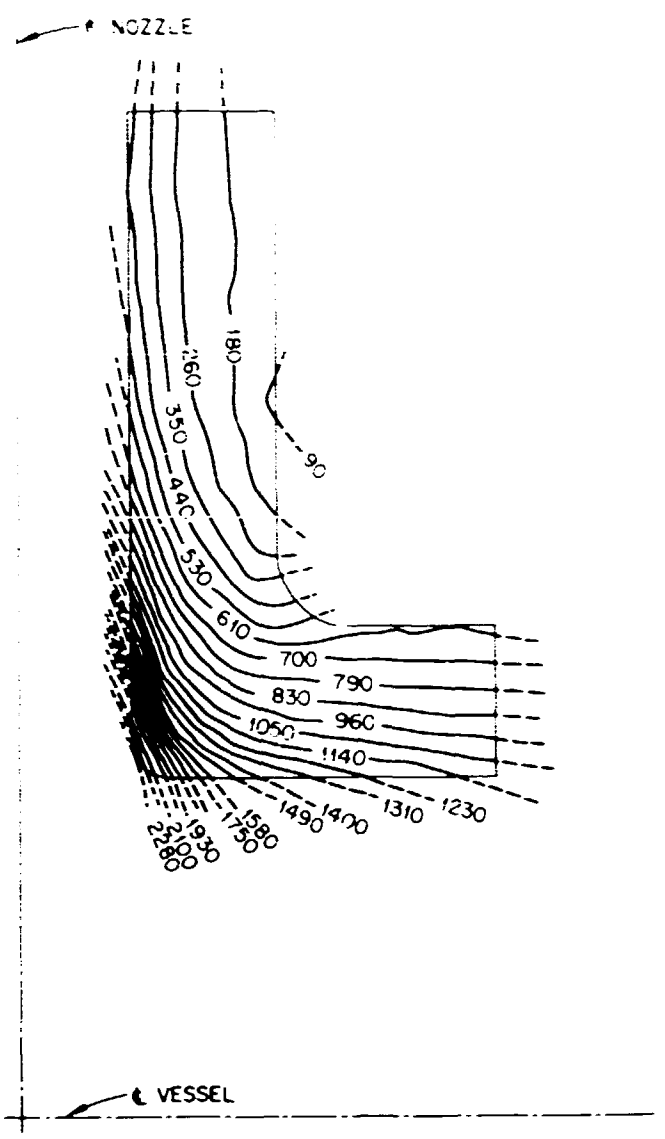

Fig. 2.21. Tangential stresses in the nozzle region of the intermediate test vessel by finite-element analysis.

For comparison, Krishnamurthy's results shown in Fig. 2.14*c* are shown adjusted to a pressure of 350 psi in Fig. 2.21. The agreement is excellent; for example, at the inside nozzle corner the experimental analysis gives 2200 psi, while the finite-element analysis gives 2280 psi. The outside σ_t was measured at 600 psi, whereas the finite-element analysis shows 610 psi.

General Procurement Activities for Vessels V-1 through V-6

The procurement efforts as monitored and reported by Childress, of ORNL,[6] are summarized in this section. Emphasis has been placed on final results, and all of the descriptive material and interim activities have not been included. Childress is currently preparing a report covering all aspects of vessel procurement.

Fabrication of the vessel components for vessels V-1 through V-6 was sublet to two forging manufacturers: National Forge Company and Lenape Forging Company. Lenape made the hemispherical heads and the flat head closure covers, and National Forge made the shell courses, closure flanges, and a weld test plate to be used for qualification of Taylor Forge welders. All components were fabricated from ASTM A508, class 2 materials.

Materials for the hemispherical heads were obtained from a billet with a 32-in.-square cross section, made from a single melt, heat Q2A18. The ladle analysis for heat Q2A18 follows:

	Ladle analysis (wt %)
C	0.19
Mn	0.78
P	0.008
S	0.022
Si	0.23
Cr	0.39
Ni	0.82
Mo	0.63
V	0.003

The billet was cut into six sections that measured 32 X 14 X 45 in. long, and each weighed about 4500 lb. Each piece was heated to 1960°F, formed into a square configuration, temperature dropped to 1740°F, reheated to 2050°F, and pressed into a preheated lubricated die. After completion of the forging operations, each piece was then heat treated as follows: (1) normalized at 1650 ± 25°F and cooled in air, (2) austenitized at 1560 ± 25°F, (3) quenched in agitated water, (4) tempered at 1225°F minimum and cooled in air, and (5) stress relieved at 1125 ± 25°F for 1 hr per inch of metal thickness. Figure 2.22 shows the completed rough forging, test specimen location, and thermocouple attachment for heat-treatment control. The test specimens for determining mechanical properties of the forgings were heat treated by Lenape by using their Data-trak programmed testing procedure.

The 31-in.-diam flat heads were forged from pieces of billet measuring 26 X 26 X 13½ in. long. Each piece was cubed and rounded into a cylindrical configuration on an open-die press and then upset into a 33-in.-OD, 10½-in.-deep die. The upset ratio was 2:1. A rough-finished forging is sketched in Fig. 2.23.

The flat heads were subjected to the same heat-treatment and mechanical testing procedures as the hemispherical heads. Cooling curves for the hemispherical and flat heads are shown in Fig. 2.24.

The chemical analyses for the hemispherical and flat heads are given in Table 2.3, and results of the mechanical testing performed by Lenape on specimens from the flat and hemispherical heads are given in Table 2.4

The flat heads were inspected ultrasonically after all machining was completed. The parts were scanned using a Branson model Z-101-A 1-in.-diam 2.25-MHz transducer and SAE 40W oil. The transducer was placed over a smooth, flat area on the forging, and the back-reflection signal was adjusted to approximately 75% of full screen height. Scanning was performed from the flat side and from the circumference of each head, and each scan path was overlapped 50% to assure complete coverage Lenape's applicable inspection procedure designated as rejectable "any indication accompanied by a complete loss of back reflection not associated with or attributable to geometric configuration." The loss of back reflection was no more than 40% in any instance. The hemispherical heads were also inspected to the same ultrasonic procedure, and each was found to be acceptable. All parts were subjected to liquid penetrant testing.

The National Forge Company made the shell courses, closure flange, and a weld test plate. The ingot used to make the shell courses for vessels V-3, V-4, and V-6 (see Table 2.1) weighed about 200,000 lb and was poured simultaneously from two furnace heats, 3V928 and 1V3828. The configuration of the ingot was essentially a truncated cone, 76 in. in diameter at the top ingot end and 65 in. in diameter at the bottom end by 12 ft long, excluding the hot top.

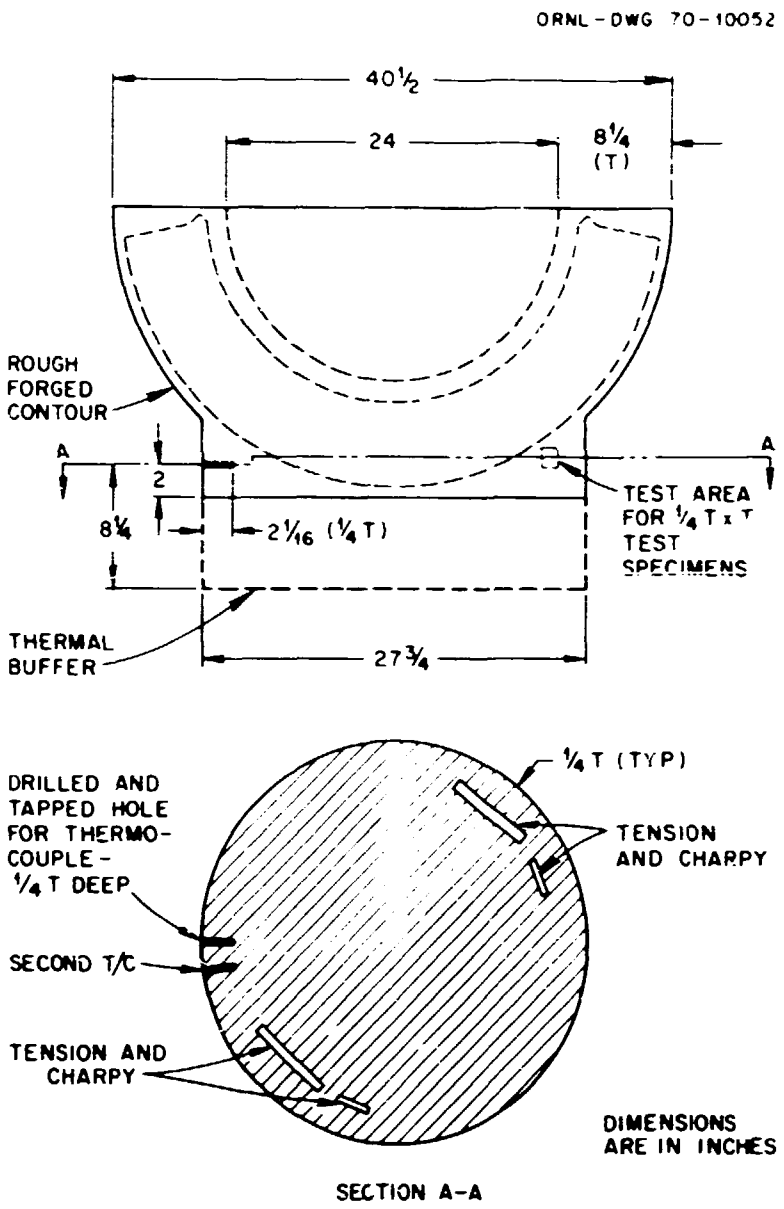

Fig. 2.22. Completed rough forging of a hemispherical head for the intermediate test vessels.

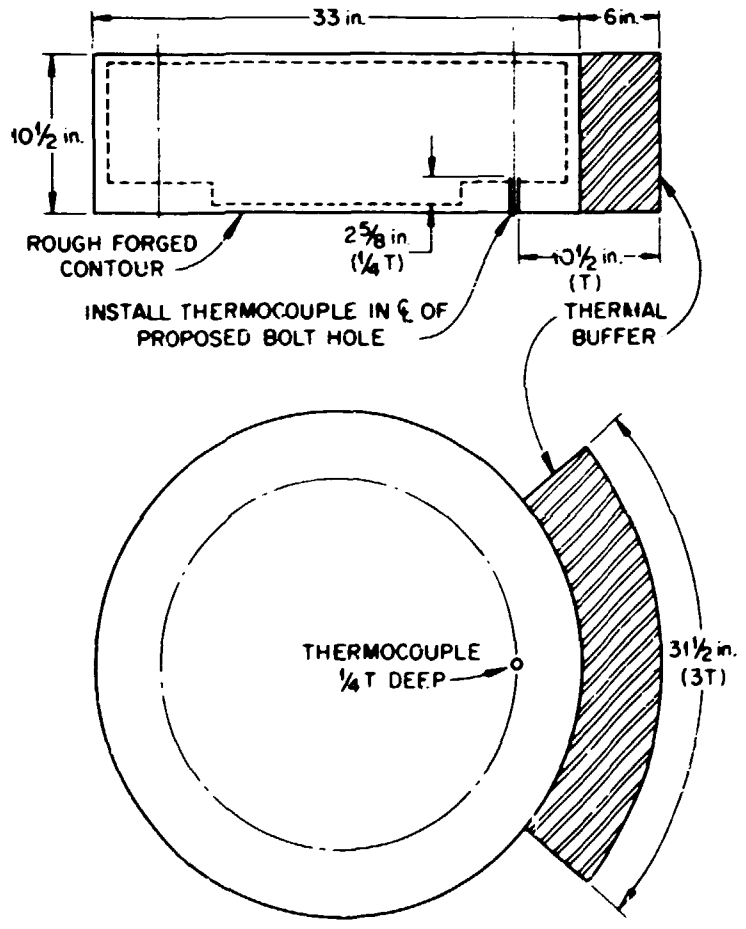

Fig. 2.23. Completed rough forging of a flat head.

Table 2.3. Chemical analyses for the hemispherical and flat heads (wt %)

C	Mn	P	S	Si	Cr	Ni	Mo	V
Hemispherical heads, ladle analysis								
0.19	0.78	0.008	0.022	0.23	0.39	0.82	0.63	0.03
Flat heads, ladle and check								
0.19	0.78	0.008	0.022	0.23	0.39	0.82	0.63	0.03
0.197	0.75	0.019	0.023	0.22	0.41	0.87	0.59	0.01

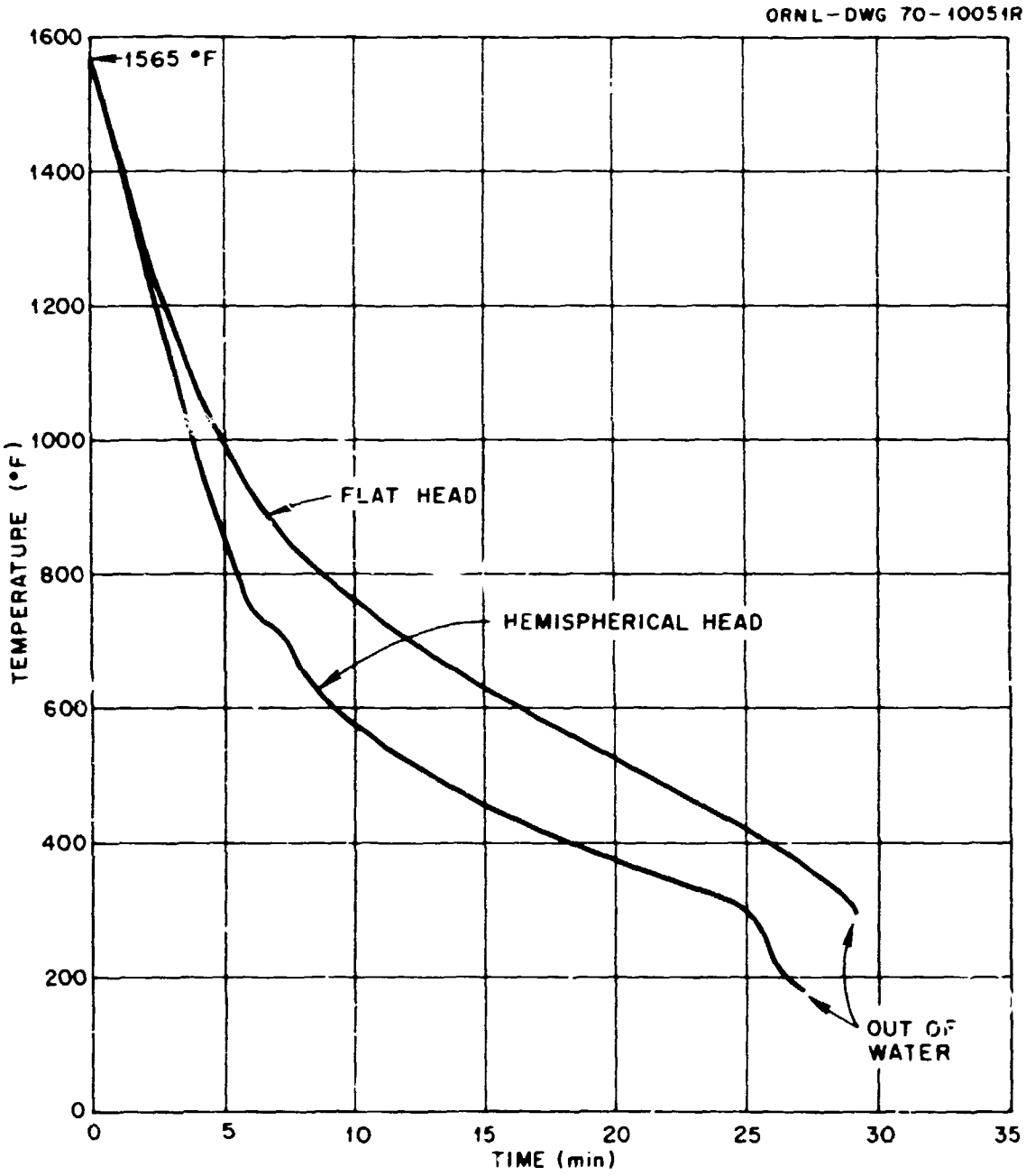

Fig. 2.24. Cooling curves for the hemispherical and flat heads for the intermediate test vessels.

Table 2.4. Mechanical properties obtained on specimens from the flat and hemispherical heads

Lenape ID No.	Temperature (°F)	Ultimate tensile strength (ksi)	Yield strength (ksi)	Reduction in area (%)	Elongation (%) in 2-in gage length	C_v values at +10°F (ft-lb)
			Hemispherical heads			
1	0	87.0	70.0	64.9	23.5	37-43-34
	180	87.7	70.6	59.8	22.0	42-43-39
2	0	87.3	70.6	67.0	24.0	39-31-31
	180	87.5	77.6	64.2	24.3	87-52-71
3	0	99.3	79.8	68	23	60-60-51
	180	96	78.7	68	23	47-51-52
4	0	95	78.7	67	23	74-49-71
	180	96	79.7	64	22.5	47-44-49
5	0	95.5	78	62	22.5	41-46-34
	180	95.6	78.7	62	22.5	28-31-36
6	0	96.5	80.5	67	22.5	28-31-31
	180	95	78	65	22.5	32-25-33
			Flat heads			
1	Room	90.5	70.9	66	23.5	82-78-65
	Room	90	72	67	23.5	81-85-47
2	Room	89	69.3	47.4	21.5	42-44-40
	Room	92.5	74	62.5	23.5	36-31-37
3	Room	91	71	56	24	38-41-39
	Room	90.5	70.6	64	23.5	51-54-50
4	Room	90	69	63	23.5	45-43-51
	Room	90	70.3	65	23.5	39-35-52
5	Room	90.1	73.3	62	22.5	35-22-38
	Room	87.5	74.8	64.9	21.5	39-37-37
6	Room	91.8	72.8	41.8	19	50-48-52
	Room	89.2	70.4	49.3	20.5	53-54-47

The ladle and check chemical analyses (wt %) are given below.

	C	Mn	P	S	Si	Ni	Cr	Mo	V
Ladle	0.27	0.87	0.007	0.012	0.32	0.74	0.34	0.64	0.04
Check	0.24	0.84	0.009	0.011	0.35	0.72	0.35	0.66	0.04
Check	0.25	0.86	0.009	0.012	0.35	0.72	0.34	0.65	0.04

The ingot used to make the shell courses for vessels V-1, V-2, and V-5 was also poured simultaneously from two furnace heats, 3V913 and 1V3809. The ladle and check analyses (wt %) are given below.

	C	Mn	P	S	Si	Ni	Cr	Mo	V
Ladle	0.26	0.75	0.010	0.014	0.26	0.81	0.45	0.61	0.05
Check	0.27	0.77	0.013	0.015	0.32	0.82	0.43	0.58	0.05
Check	0.27	0.77	0.013	0.013	0.33	0.81	0.44	0.59	0.05

The ingots were forged in the temperature interval 2350° down to 1440°F proceeding through an octagonal shaping to a final rough cylindrical shape having a usable length of about 27½ ft and a nominal diameter of 41 in. Following removal of the unusable material from each end, the ingot was heat treated and inspected in conformance with the following National Forge procedure:

> Immediately on removing the two ends, the usable length will be returned to the furnace and "equalized" at 1180°F for 8 hr. On completion of the 8-hr hold, the forging will be allowed to furnace cool to 500°F and held at this temperature for 22 hr. Following this 22-hr hold, the temperature will be raised at a rate of 90°F/hr to 1180°F and held for 8 hr, then raised at 100°F/hr to 1600°F and held at this temperature for 32 hr. Following the 32-hr hold, the forging will be removed from the furnace and air cooled to 700°F, then returned to the furnace and furnace cooled to 500°F. It then will be held at 500°F for 22 hr. After this 22-hr hold, without cooling further, the temperature will be raised at 90°F/hr to 1240°F and held for 30 hr. The forging will then be furnace cooled to below 500°F, thus completing the post forge heat treatment.
>
> On completion of post forge heat treatment, the forging will receive a preliminary ultrasonic inspection, after which it will be sawed into three pieces of equal length (a 2-ft prolongation will be left on each piece). Each piece will then be shipped to the NF plant in Irvine, Pa., for machining, final heat treatment, and final ultrasonic inspection.

The parts were then shipped to National's Irvine plant for trepanning, final heat treatment, final machining, and inspection. Heat treatment provided the shell courses at Irvine essentially consisted of the same procedure applied to the ingot described previously. One shell, National's No. 6, was equipped with six surface-mounted and three imbedded stainless-steel-sheathed Chromel-Alumel thermocouples (prior to normalizing) as shown in Fig. 2.25. The normalizing, austenitizing, cooling, and tempering curves are shown in Figs. 2.26–2.29. Mechanical test results for the various shells obtained at this point are given in Table 2.5.

It will be noted that the tensile properties listed in this table are somewhat atypical of A508, class 2 materials. In fact, the yield values in Table 2.5 were about the expected ultimate tensile strength of the welds to be used in the intermediate test vessels. If the vessels had been used in the condition noted at that point, higher test pressures (to rupture the vessels) than originally anticipated would have been required. In turn, the resultant higher test pressures would have placed an added burden on the test equipment, which

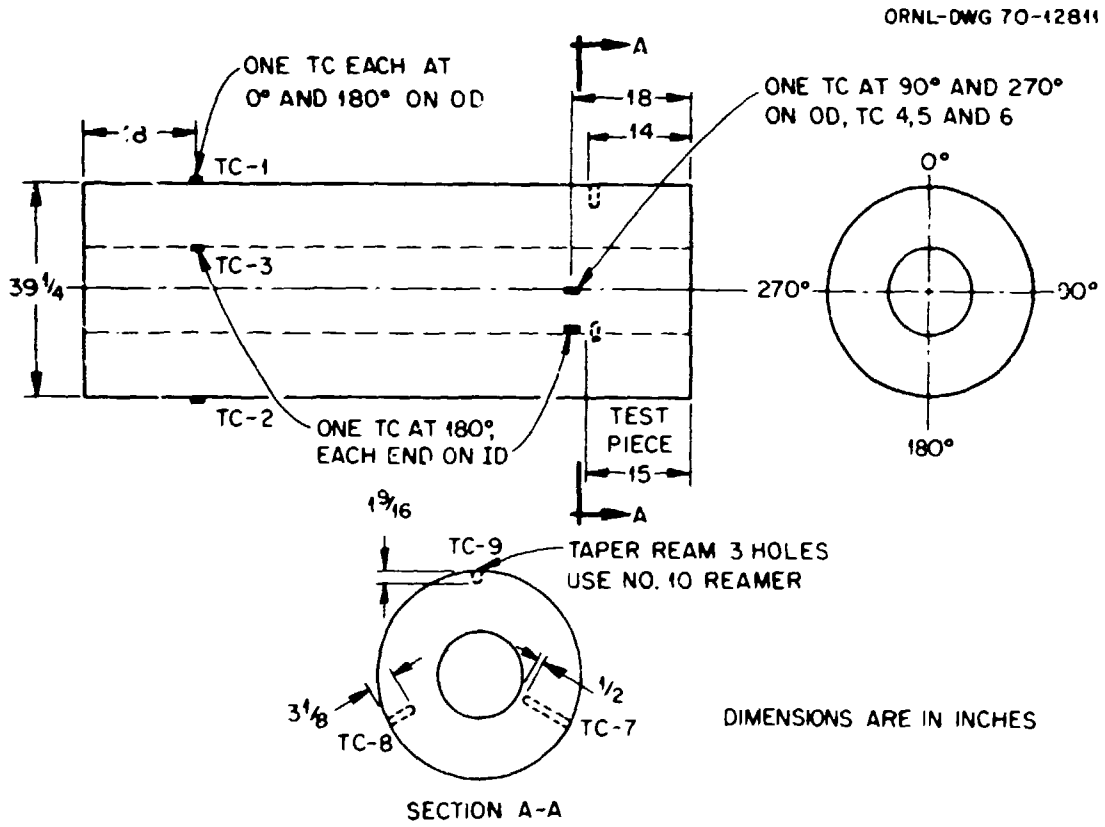

Fig. 2.25. Location of thermocouples on shell 6.

would have required new hazards evaluations. Perhaps more significantly, vessel failure at other than the flaw could have occurred.

Information was developed at ORNL by Berggren, Stelzman, and Canonico[7,8] which indicated that the strength properties of the shells could be downgraded by controlled retempering. It may be noted from Fig. 2.29 that the tempering temperature for the shells was about 1280°F, maximum, Hence in consideration of retempering there was concern for the lower transformation temperature (AR_1), which was thought to be between 1325 and 1350°F. Using materials from shell prolongations and Data-trak testing procedures, the

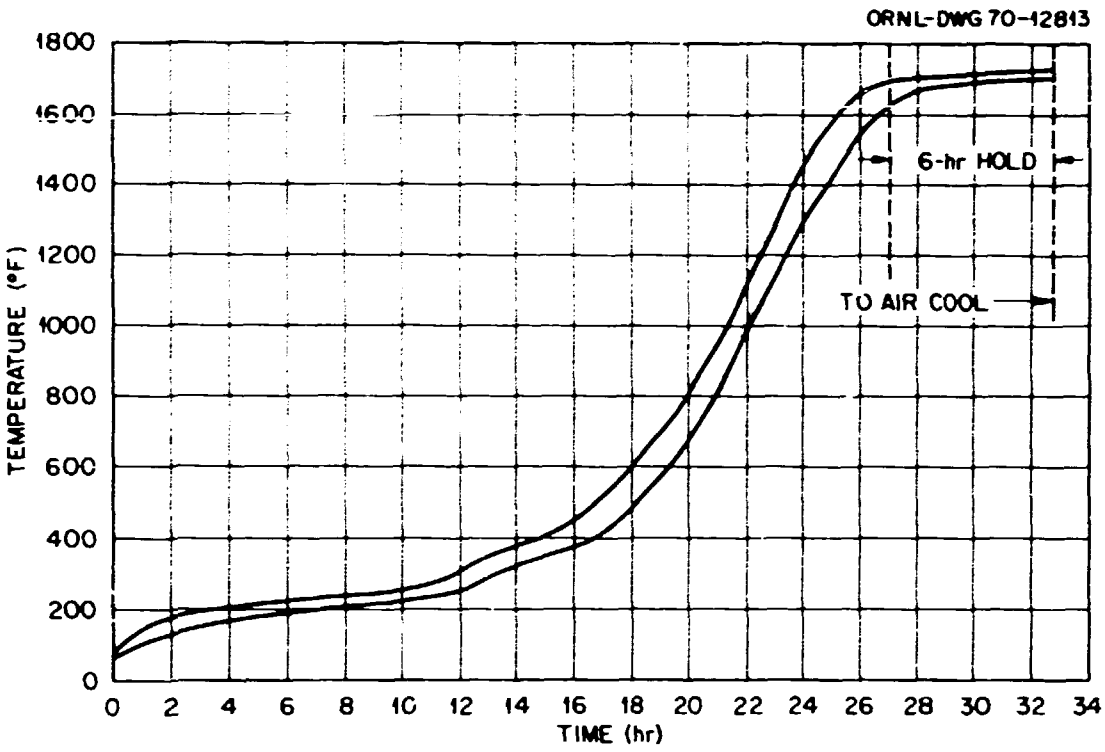

Fig. 2.26. Spread in thermocouple readings during normalizing of shell 6.

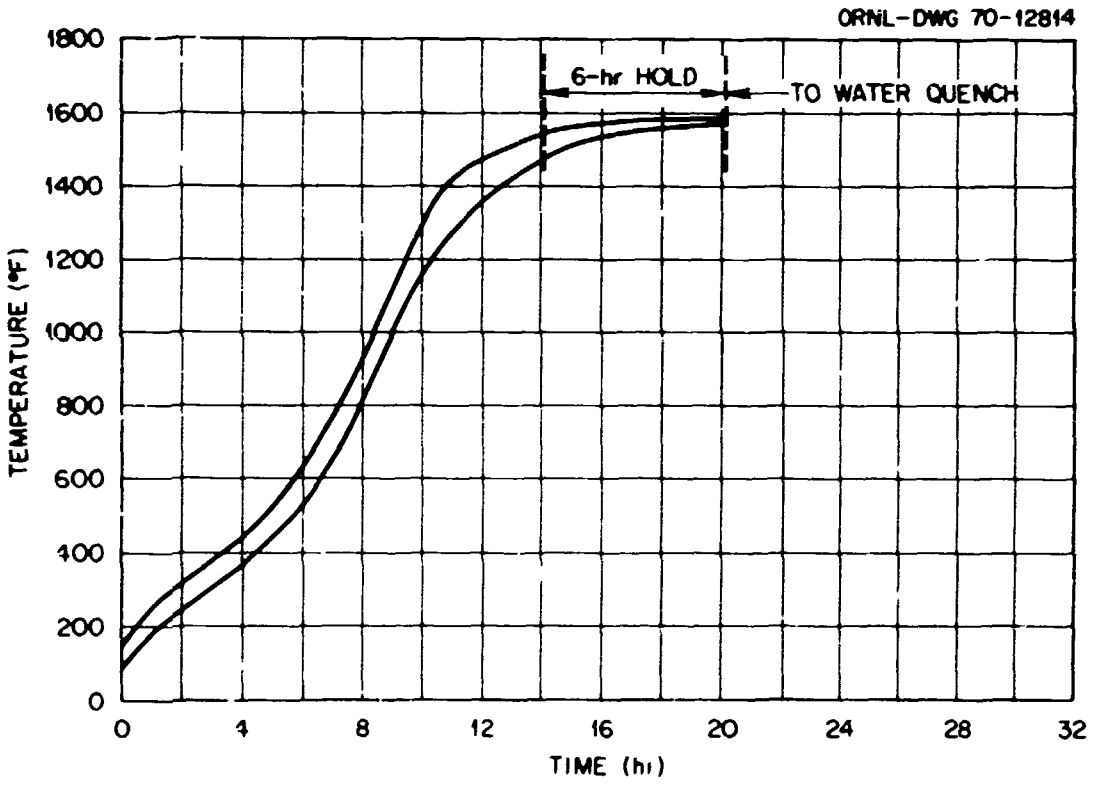

Fig. 2.27. Spread in thermocouple readings during austenitizing of shell 6.

data developed justified retempering a single shell course at about 1320°F, maintaining as little deviation as possible.

Shell 9 was retempered by National Forge on February 2 and 3, 1971. The part was equipped with seven thermocouples as shown in Fig. 2.30. The heatup period comprised some 14 hr, after which couple 4 (located on the inside surface) was reading about 1295°F; the remaining couples were recording in the vicinity of 1310°F. At the end of the 6-hr hold period, each recorded about 1320°F except couple 4, which recorded a temperature of 1310°F.

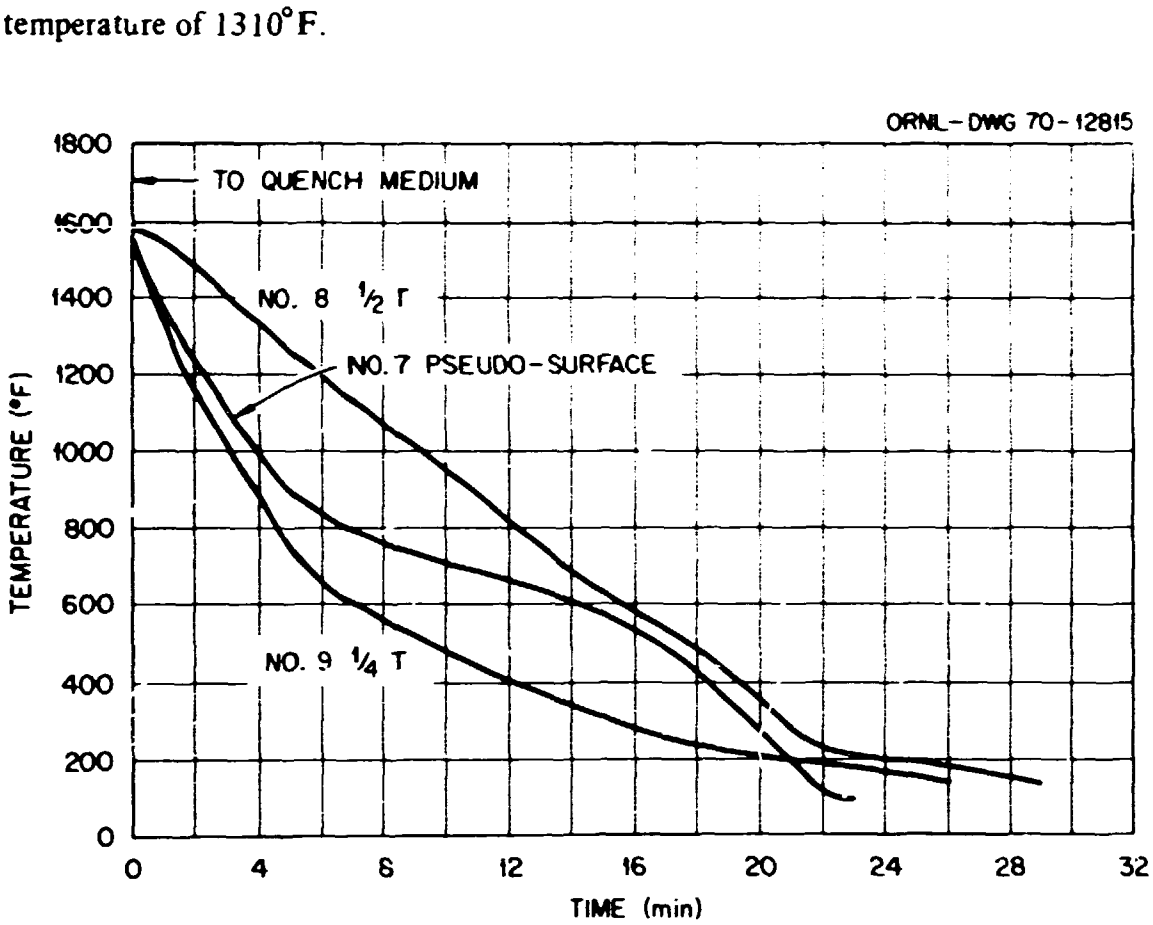

Fig. 2.28. Cooling curves for the imbedded thermocouples in shell 6.

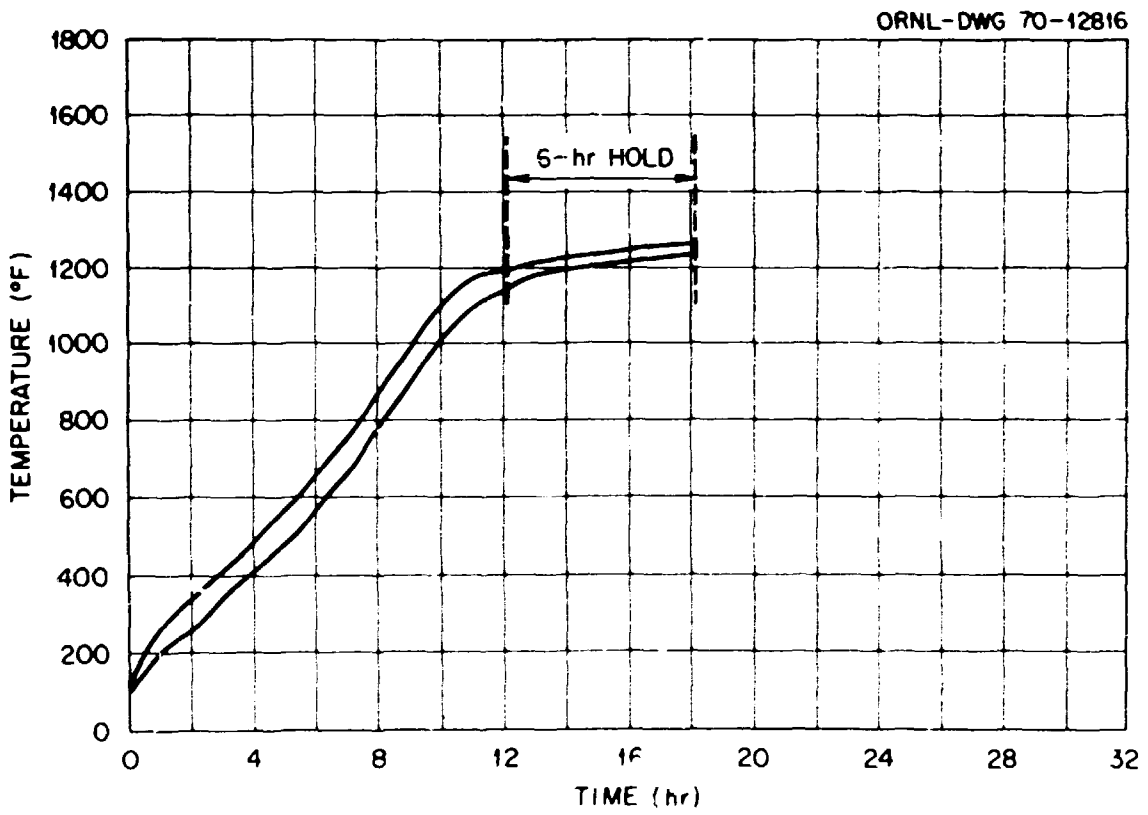

Fig. 2.29. Spread in thermocouple readings during tempering of shell 6.

Table 2.5. Mechanical properties for the shell courses for vessels V-1 to V-6

National ID No. and vessel No.	Ultimate tensile strength (ksi)	Yield strength (ksi)	Reduction of area (%)	Elongation (%) in 2 in. gage length	C_v values at +10°F (ft-lb)	NDTT (°F) P-3 drop weight
4, V-1	105.5	85	65.4	22	66-55-51	−20
	107.3	87	66.1	22.5	45-54-54	
5, V-5	107	86.5	66.3	22.5	44-60-64	−20
	107.5	87	67	22.5	50-55.5-53.5	
6, V-2	109.5	88	65.2	22	57-43.5-51.5	−20
	109.5	88	65.9	22.5	39-63-62.5	
7, V-6	106.25	85	65.9	23	57-40-44.5	−20
	103.5	82.5	66.5	22.5	48.5-50-48	
8, V-4	103	83	68.6	24	78-71-79	−20
	102.75	82	69	24	85-69-67	
9, V-3	107	87.5	67.9	23	62.5-60-55	−20
	107.5	88.5	67.7	23	38.5-72-74	

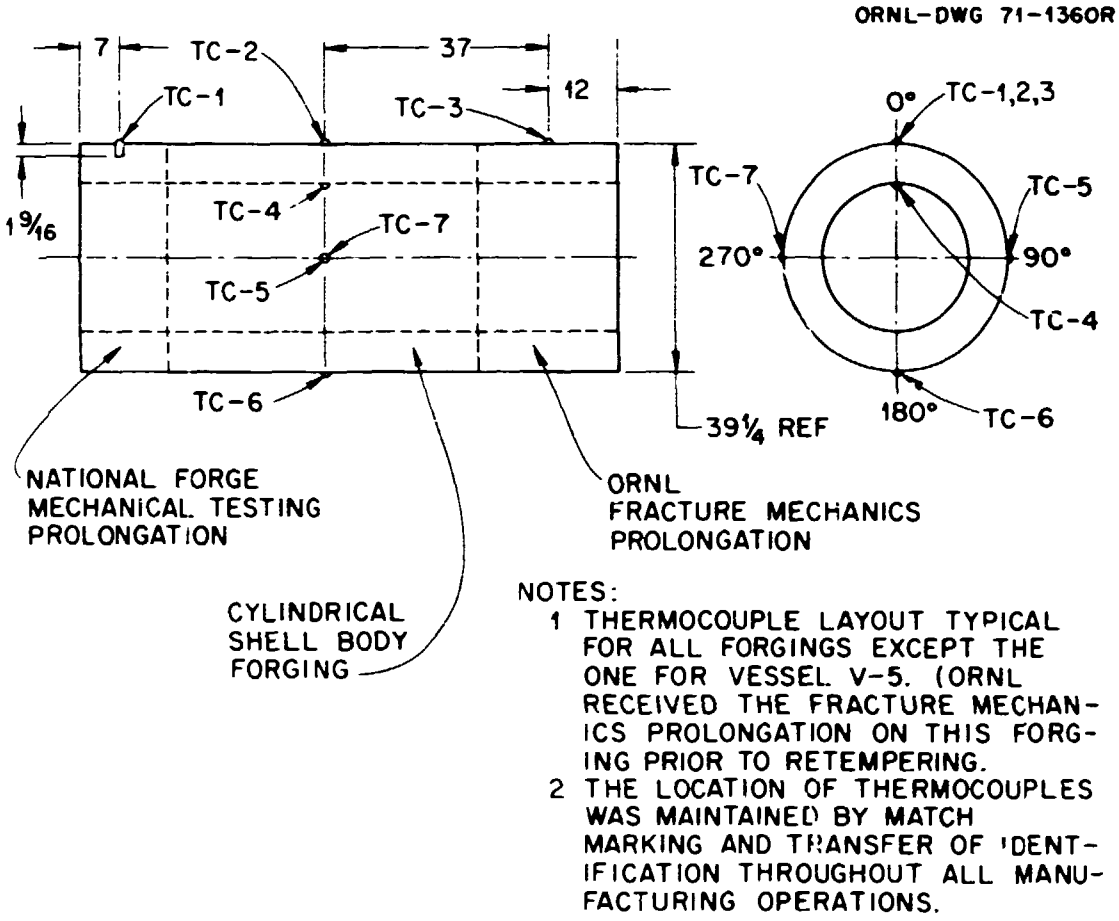

Fig. 2.30. Location of thermocouples on shell 9 (to be retempered).

On completion of the hold period, the part was cooled in the furnace at about 200°F hr to 600°F. Material for the mechanical test specimens was removed from the shell prolongation and stress relieved at 1125 ± 25°F for 24 hr. The mechanical test results for the retempered shell are:

Ultimate tensile strength (psi)	Yield strength (psi)	C_v values at 10°F (ft-lb)
91,500	72,000	66-40-33
92,250	71,500	62.5-79-55.5

Premised on these data and further metallographic studies, the remaining shells were retempered. Test results for the various shells following retempering are given in Table 2.6.

The material for the closure flanges was melted and forged at National's Irvine plant. The reported ladle and check analyses (wt %) for this heat, 9 3584, are given below.

	C	Mn	P	S	Si	Ni	Cr	Mo	V
Ladle	0.22	0.69	0.008	0.008	0.27	0.82	0.34	0.63	0.09
Check 1	0.21	0.70	0.008	0.008	0.27	0.82	0.34	0.62	
Check 2	0.20	0.69	0.008	0.008	0.26	0.80	0.33	0.62	

The ingot from which the closure flanges were made was essentially a truncated cone and weighed 78,000 lb, including the hot top. The ingot was forged in the temperature interval 2450 down to 1580°F into a solid round bar 41½ in. in diameter and 12 ft long. Shortly after forging was completed, the part was charged into a furnace and held at 800°F for 4 hr. The temperature was then raised at 100°F/hr until the part reached 1700°F and held at this temperature for 22 hr. It was then removed from the furnace and air cooled to about 300°F. With a furnace preheated to 650°F, the part was recharged and held at this temperature for 3 hr. It was then heated at a rate of 75°F/hr to 1260°F and held for 44 hr, furnace cooled at 50°F/hr to 1100°F, and then air cooled to ambient temperature. On completion of the postforging heat treatment, the part was subjected to a preliminary ultrasonic inspection.

The rough forging was rough-turned to 39½ in. OD, and a 14½-in.-diam section was trepanned from the center essentially as shown in Fig. 2.31. In this form, the forging was subjected to final heat treatment prior to sectioning. The austenitizing, cooling, and tempering curves are shown in Figs. 2.32–2.34.

Material for mechanical test specimens was secured from the prolongation near the bottom ingot end of the forging (see Fig. 2.30). After tempering, the test material was removed and subjected to a stress-relieving heat treatment of 1125 ± 25°F for 30 hr and cooled per paragraph N-532.3 of Section III of the ASME Code. The results obtained from the mechanical testing are:

Ultimate tensile strength (ksi)	Yield strength (ksi)	Reduction in area (%)	Elongation (%) in 2 in. gage length	C_v values at +10°F (ft-lb)
86	64	69	25	52-59-47
87	66			33.5-35-39

Six closure flanges were made from this forging, and National Forge assigned them numbers 1 through 6, beginning at the bottom ingot end (excluding prolongation). Each piece was identified so that the bottom ingot end could be distinguished from the top end.

Table 2.6. Test results after retempering at 1320°F

Shell and vessel No.	Ultimate tensile strength (ksi)	Yield strength (ksi)	Reduction of area (%)	Elongation (%)	C_v at +10°F (ft-lb)	Percent shear	Lateral expansion
4, V-1	93.75	72	71	27	48	41	0.046
					50.5	37	0.044
					52	40	0.043
	91.5	69.5	67	26	53.5	40	0.046
					61.5	37	0.057
					61	40	0.050
5, V-5	94.75	72.5	68.4	25.5	65	47	0.059
					60	43	0.060
					77.5	40	0.061
	93.75	72.5	69.7	25.5	66	43	0.060
					59	45	0.059
					77	46	0.062
6, V-2	94	72	71.8	27	60.5	41	0.048
					65.5	40	0.055
					70.4	40	0.059
	94.5	74	70.4	27	53.5	39	0.045
					60	40	0.052
					61	37	0.050
7,V-6	92	71.5	71.2	27	71	45	0.060
					53.5	34	0.047
					72	40	0.064
	91.25	67.5	68.8	25	51	40	0.044
					55.5	31	0.046
					57	34	0.049
8, V-4	91.25	71.5	68.4	26	86.5	45	0.073
					61.5	43	0.052
					70.5	41	0.060
	91.75	71.5	70.4	26.5	66.5	41	0.059
					69.5	34	0.054
					58.5	32	0.050
9, V-3	91.5	72	69.9	27	66	43	0.060
					40	35	0.039
					33	33	0.031
	92.25	71.5	71	27	62.5	42	0.055
					79	47	0.061
					55.5	37	0.049

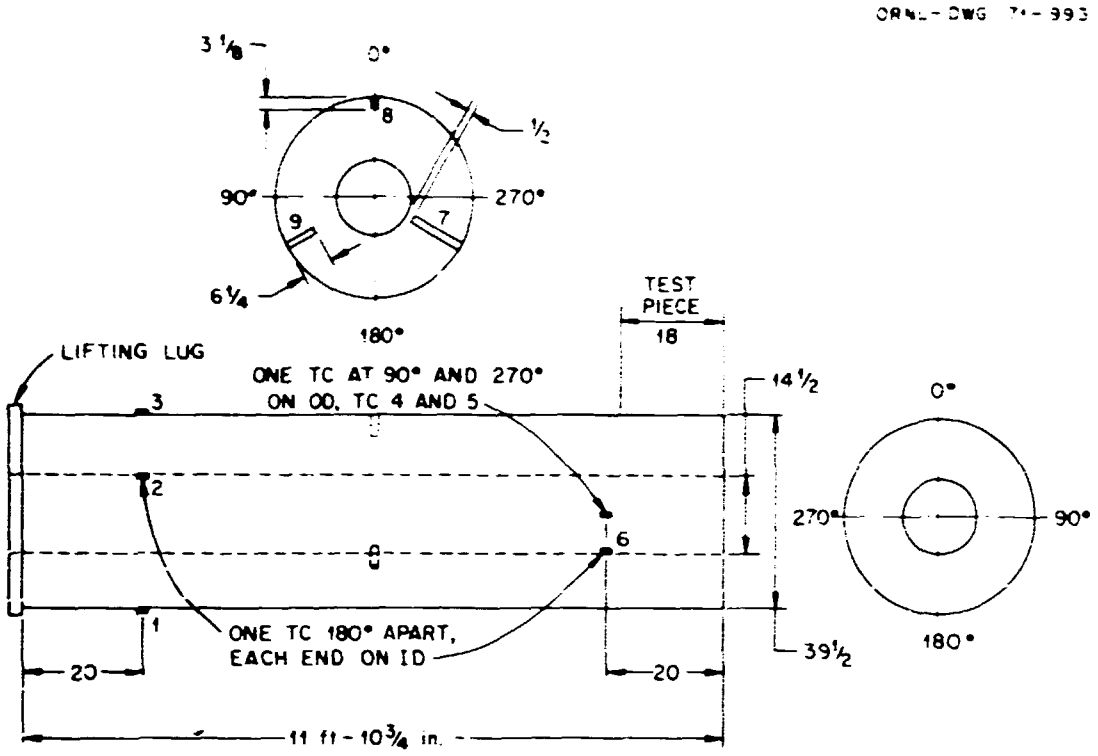

Fig. 2.31. Location of thermocouples in the forging used to make the closure flanges.

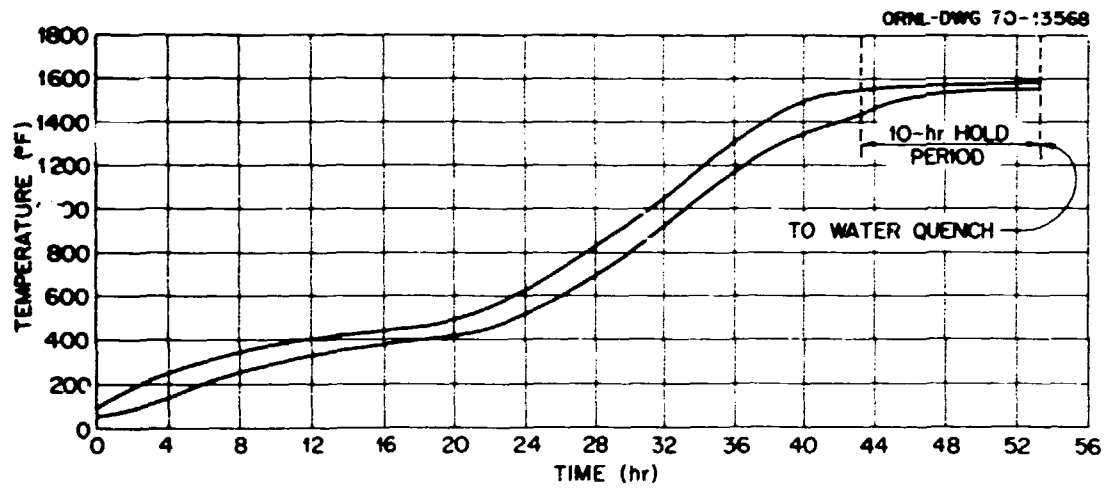

Fig. 2.32. Spread in thermocouple readings during austenitizing of the closure flange forging.

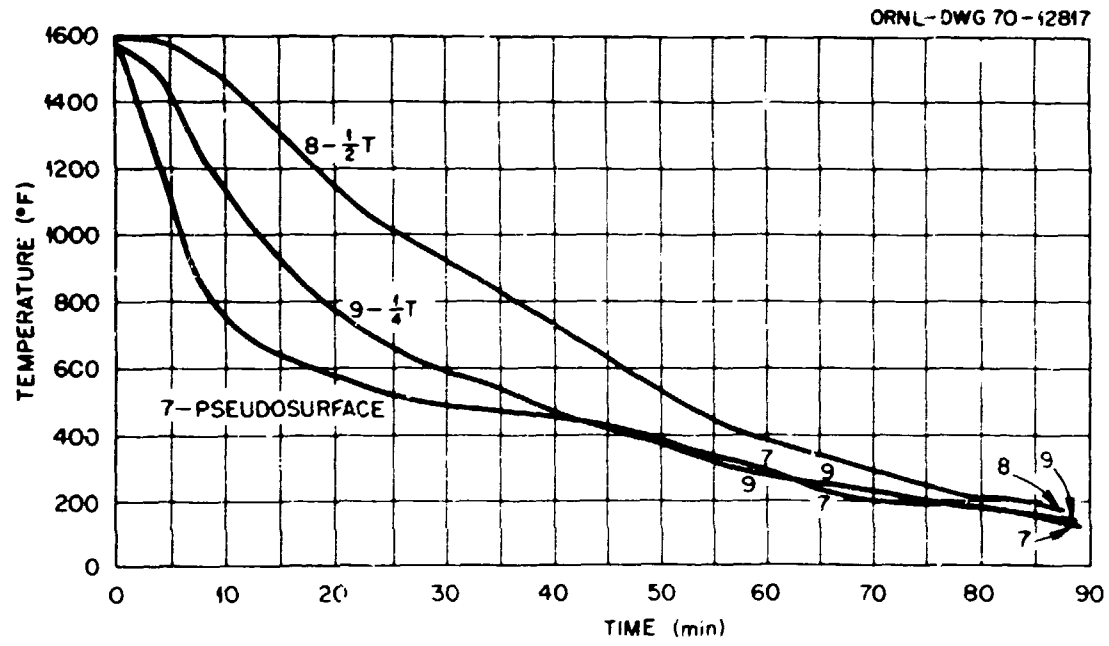

Fig. 2.33. Cooling curves for the imbedded thermocouples in the closure flange forgings.

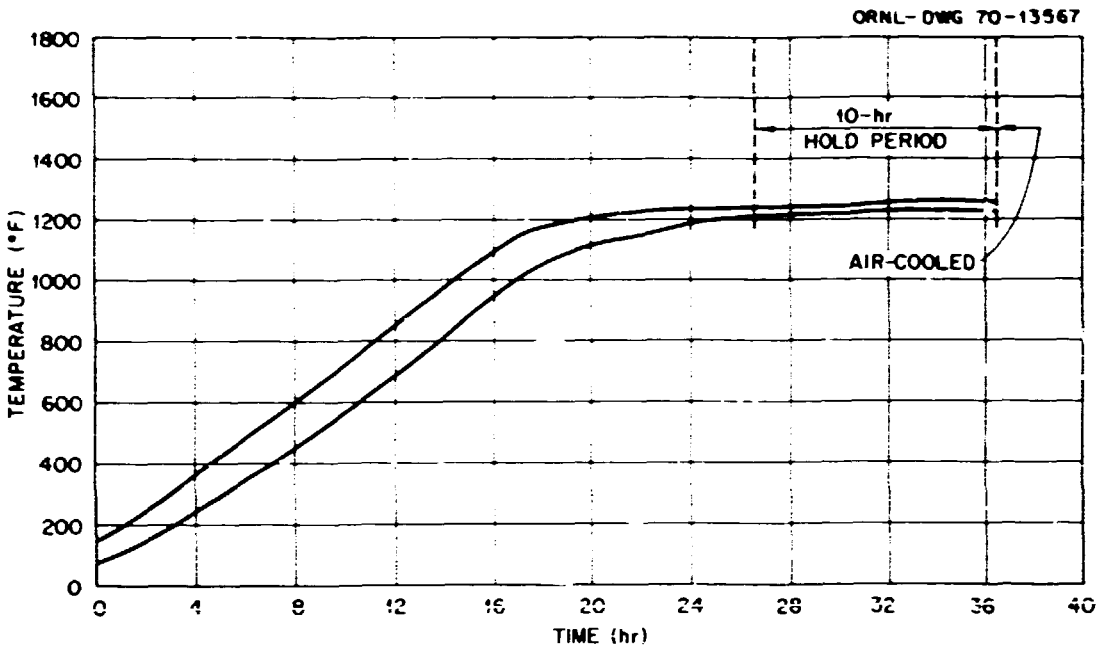

Fig. 2.34. Spread in thermocouple readings during tempering of the closure flange forging.

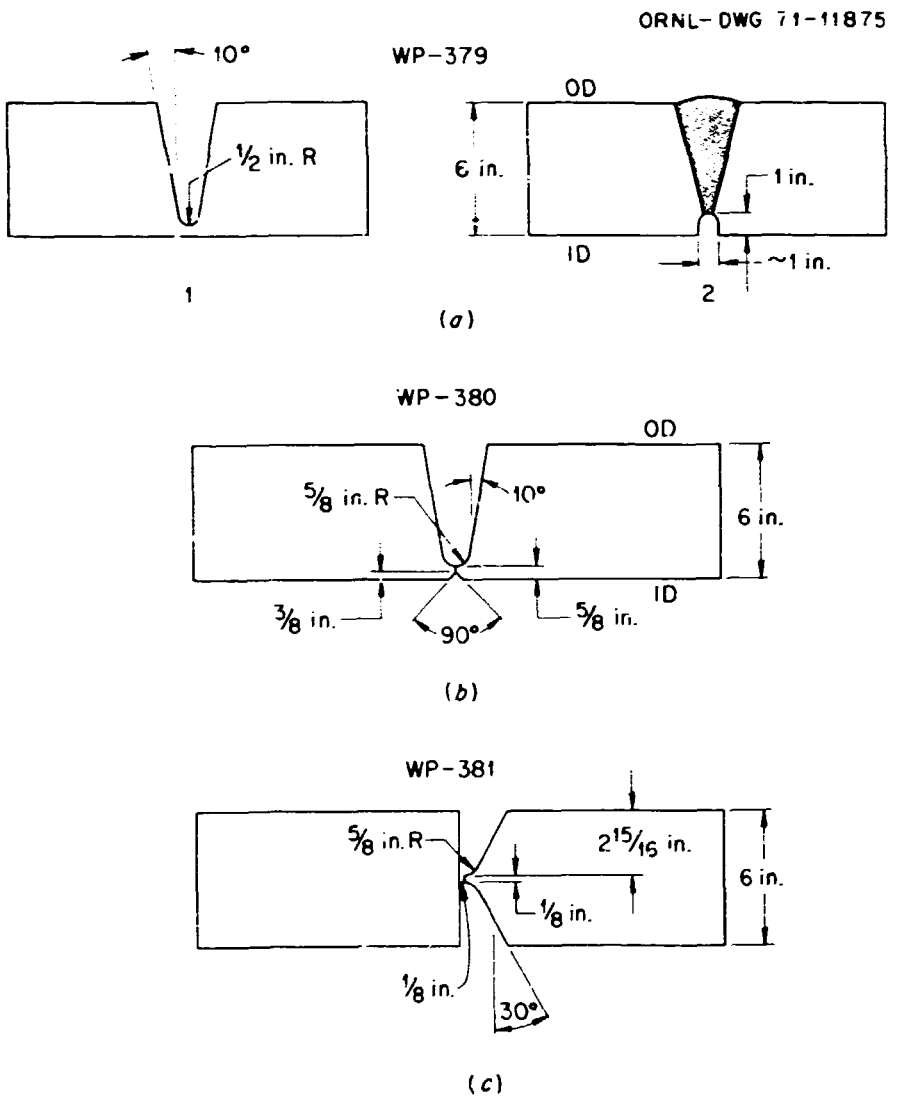

Fig. 2.35. Joint preparations for Taylor Forge welding procedures.

On completion of final inspection, the parts were shipped to the Taylor Forge plant in Paola, Kansas, for assembly. Taylor Forge qualified three welding procedures: two submerged-arc (WP-379 and WP-380) and a shielded-metal-arc procedure (WP-381). All tests were qualified in the flat position; the joint configuration for each is shown in Fig. 2.35.

The joint configuration for procedure WP-379, used in making the longitudinal seams, is shown in Fig 2.35*a*. The outside groove is prepared by machining and is inspected with magnetic particles prior to welding. Essentially, the conditions of the procedure are as follows:

1. preheat 300 to 500°F and maintain until postweld heat treatment (PWHT);
2. filler wire: RACO-127, $^{3}/_{16}$ in. in diameter, single wire feed;
3. interpass temperature: 500°F maximum;
4. flux: Linde type 0091, size 65 X 200;
5. travel speed: approximately 12 in./min;
6. current: ac, 750 A, 30 to 32 V;
7. on completion of the outside, the inside is ground to solid metal and welded in much the same manner as the outside.

The basic parameters noted for procedure WP-379 (for longitudinal seams) are also applicable to procedure WP-380 (circumferential seams), except that the inside portion of the weld is applied with shielded-metal-arc electrodes.

The joint configuration for the shielded-metal-arc procedure is shown in Fig. 2.35*c*. This procedure is used for all repair welding and for attachment of a nozzle to vessel V-5.

A weld deposit chemical analysis from procedure WP-379 (RACO heat 34445, flux lot 3977) showed:

C	Mn	P	S	Si	Cr	Mo	Ni	V
0.10	0.86	0.016	0.021	0.19	0.06	0.49	0.06	Trace

Mechanical properties from an all-weld tensile specimen from the $^{1}/_{4}$-T location are:

UTS (ksi)	YS (ksi)	Elongation (%)	Reduction of area (%)
85	71.5	28	62.5

The results of Charpy V-notch tests made on full-size specimens tested at +10°F are:

Location	C_V (ft-lb)	Mils lateral expansion	Percent ductile fracture
Parent metal $^{1}/_{4}$ T	36-40-45	25-28-34	30-40-40
HAZ $^{1}/_{4}$ T	43-47-49	34-41-38	50-50-50
Weld $^{1}/_{4}$ T, top	90-96-97	66-57-70	80-80-80
Weld $^{1}/_{16}$ in., bottom surface	77-84-74	53-53-52	80-95-80

A deposit analysis (wt %) from procedure WP-380 (RACO heat 34445, flux lot 3977) gave:

C	Mn	P	S	Si	Cr	Mo	Ni	V
0.13	0.77	0.015	0.020	0.19	0.07	0.50	0.08	Trace

Mechanical properties from an all-weld tensile specimen from the ¼-T location are:

UTS (ksi)	YS (ksi)	Elongation (%)	Reduction of area (%)
81.5	69.4	28	64.9

The results of Charpy V-notch tests made on full-size specimens tested at +10°F are:

Location	C_v (ft-lb)	Mils lateral expansion	Percent ductile fracture
Parent metal ¼ T	37-55-60	29-41-46	20-25-25
HAZ ¼ T	48-57-62	40-45-49	40-40-50
Weld ¼ T, bottom	87-92-92	66-63-68	90-80-80
Weld 1/16 in., top surface	84-91-95	66-73-74	80-80-80

A deposit analysis from procedure WP-381 (Alloy Rods heat 01L3333, lot F25827A, and heat CTY538, lot B012A27A) showed (in wt %):

C	Mn	P	S	Si	Cr	Mo	Ni	V
0.09	1.33	0.012	0.012	0.52	0.05	0.52	0.99	0.02

Mechanical properties from an all-weld tensile specimen from the ¼-T location showed:

UT (ksi)	YS (ksi)	Elongation (%)	Reduction of area (%)
95.3	84.8	29	70.8

The values for ultimate tensile strength and yield strength are for the manual metal arc procedure (see Fig. 2.35), which was not used for welding in the test area. The results of Charpy V-notch tests made on full-size specimens tested at +10°F are:

Location	C_v (ft-lb)	Mils lateral expansion	Percent ductile fracture
Parent metal ¼ T	78-78-68	56-56-51	40-40-40
HAZ ¼ T	86-96-128	62-75-64	60-60-90
Weld ¼ T, top	75-73-85	60-57-65	70-70-80
Weld 1/16 in., bottom surface	76-72-70	65-62-61	80-80-80

Welding materials for the circumferential seams of vessels V-1 and V-2 were as follows:

Location	Wire			Flux	
	Type	Size (in.)	Heat	Type	Lot
Inside fill	8018 NM	3/16	CTY538		
Outside fill	RACO 127	3/16	3AE445	Linde 0091	3977

Welding materials for the circumferential and longitudinal seams for vessel V-3 were as follows:

Location	Wire			Flux	
	Type	Size (in.)	Heat	Type	Lot
		Circumferential seams			
Inside fill	8018 NM	5/32	302115		
Outside fill	RACO 127	3/16	34E445	Linde 0091	3977
		Longitudinal seams			
Inside fill	RACO 127	3/16	34E445	Linde 0091	3977
Outside fill	RACO 127	3/16	34E445	Linde 0091	3977

Welding materials for the circumferential and longitudinal seams for vessel V-4 were as follows:

Location	Wire			Flux	
	Type	Size (in.)	Heat	Type	Lot
		Circumferential seams			
Inside fill	8018 NM	5/32	OIL333		
Outside fill	RACO 127	3/16	34E445	Linde 0091	3977
		Longitudinal seams			
Inside fill	RACO 127	3/16	34E445	Linde 0091	3977
Outside fill	RACO 127	3/16	34E445	Linde 0091	3977

Because of the sensitivity of the mechanical properties of the shell courses to the reheat treatment, special care was exercised by National Forge to maintain identity of the shells throughout all operations. Figure 2.36 shows the letter designations used to identify the shell courses, mechanical testing prolongation, and fracture mechanics prolongations. Figure 2.37 identifies the various parts and shows the shell orientation for vessels V-1 through V-6.

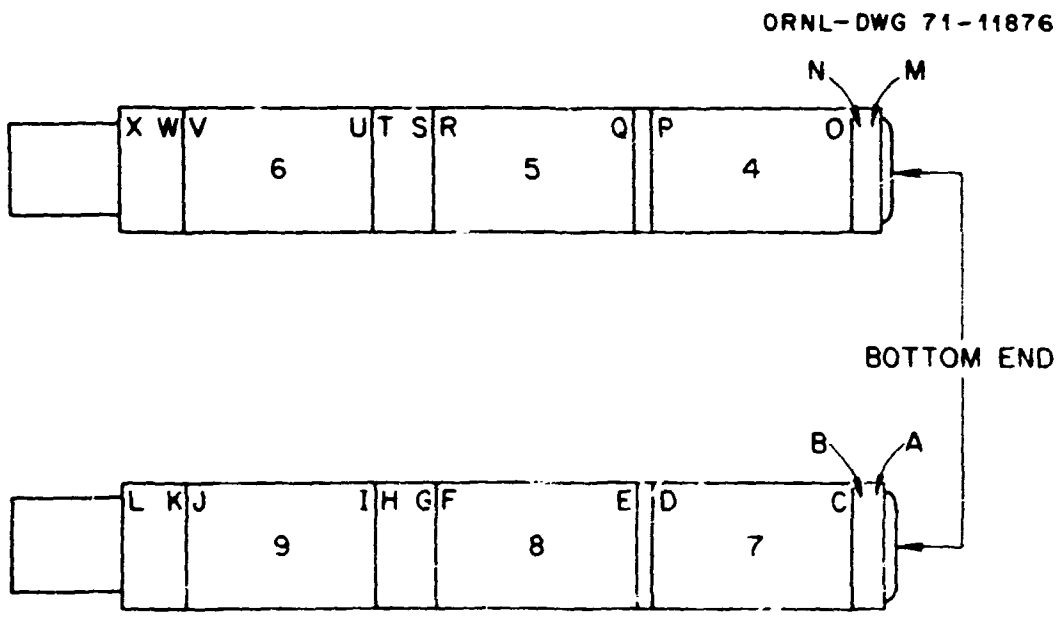

Fig. 2.36. Identification of shell courses by National Forge.

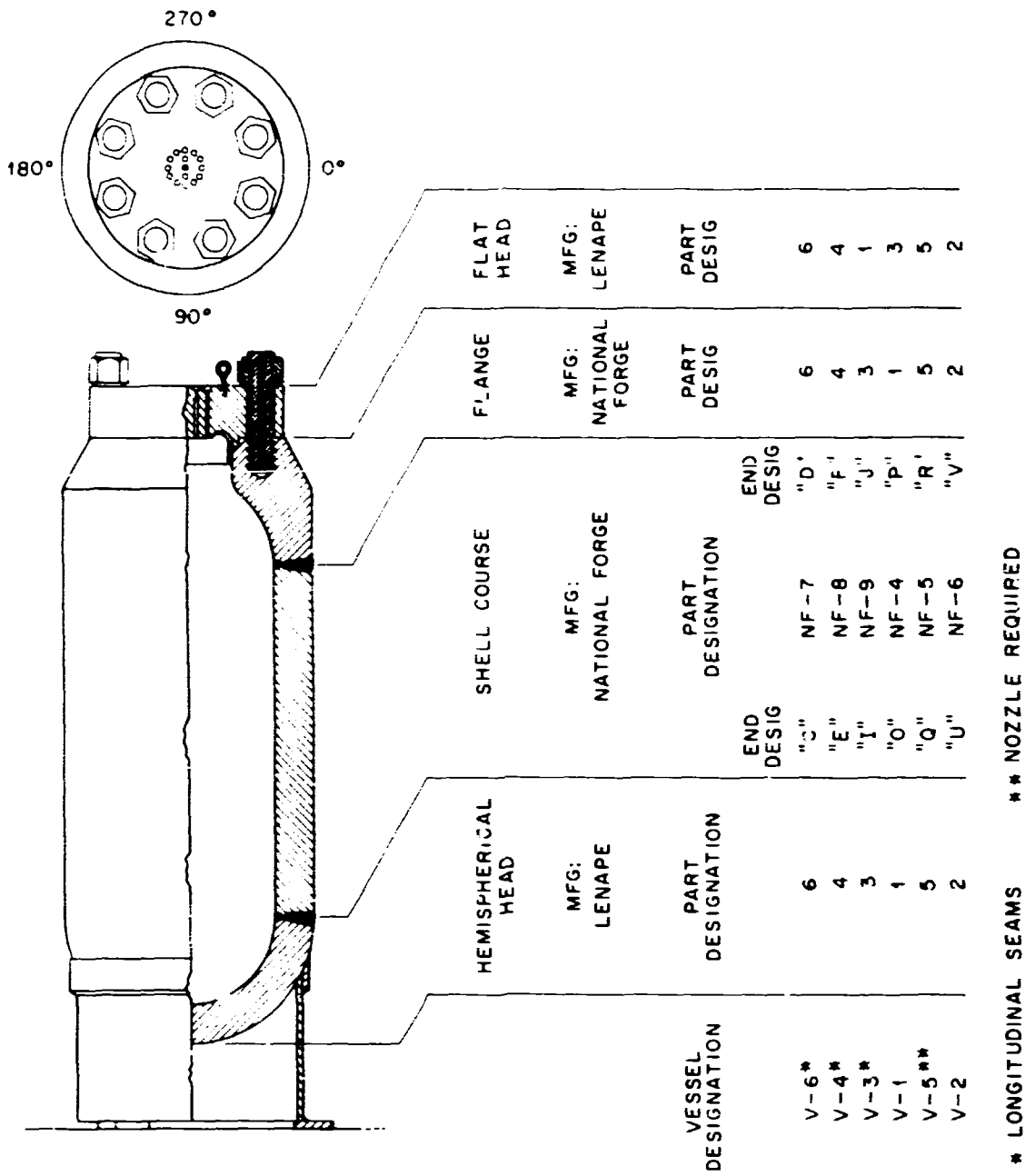

Fig. 2.37. Vessel part identification and shell orientation at assembly.

References

1. Union Carbide Corporation, Nuclear Division, Specification JS-120-228, Revision 2, Intermediate Test Vessels, HSST Program (Sept. 9, 1968).
2. Teledyne Materials Research Company, *HSST Intermediate Vessel Closure Analysis*, Report E-1253(b) (HSST Program Technical Manuscript No. 3) (Mar. 25, 1970).
3. E. L. Wilson and R. M. Jones, *SAAS, Finite Element Stress Analysis of Orthotropic, Temperature-Dependent Axisymmetric Solids of Revolution*, Aerospace Report TR-0158 (S3816-22)-1 (September 1967).
4. N. Krishnamurthy, *Three-Dimensional Finite Element Analysis of Thick-Walled Vessel–Nozzle Junctions with Curved Transitions*, ORNL-TM-3315 (Mar. 24, 1971).
5. F. J. Witt, *HSST Program Semiannu. Progr. Rep. Aug. 31, 1971*, ORNL-4764, pp. 56–62.
6. F. J. Witt, *HSST Program Semiannu. Progr. Reps., Aug. 31, 1971*, ORNL-4764; *Feb. 29, 1972*, ORNL-4816.

7. R. G. Berggren and W. J. Stelzman, "Retempering Study of HSST Intermediate Test Vessels," *HSST Program Semiannu. Progr. Rep. Feb. 28, 1971*, ORNL-4681, pp. 91–93.

8. D. A. Canonico, "The Metallurgical Assessment of Retemper Temperature on the Intermediate Vessel Test Courses," *HSST Program Semiannu. Prog. Rep. Feb. 28, 1971*, ORNL-4681, pp. 94–98.

3. THE TEST FACILITY

Site Selection

A study was made to determine the best available site for the intermediate-vessel tests. A number of local and out-of-state sites were considered, and the old power plant adjacent to the Oak Ridge Gaseous Diffusion Plant (ORGDP) was finally selected because of the following advantages:

1. a well-maintained 60-ton overhead crane,
2. massive concrete piers already in position to serve as barricades,
3. readily available electric power and water,
4. protection from the elements,
5. easy accessibility on paved roads,
6. wide separation from other personnel and equipment,
7. completely unclassified area.

Facility Design Criteria

Design of the facility was premised upon providing capability of failing the intermediate vessels over a complete range of frangible, transitional, and tough failure behavior for various flaw shapes and sizes. These criteria led to the establishment of a nominal pressurization capability of 30,000 psig and heat transfer capability over the temperature range from −50 to 350°F. These limits were set prior to the obtaining of much of the data under the HSST program, so that considerable conservatism was exercised.

Since destructive testing of the intermediate vessels leads to the potential generation of dangerous missiles and uncontrolled release of the pressurization fluid, confinement was necessary to protect personnel and equipment. To avoid complexities in the design and fabrication of the vessels, no provisions, nozzles, or baffles were made for internal fluid circulation for temperature control; therefore all heat transfer had to be accomplished at the vessel exterior surface. Since failure of the vessel could breach the externally located heat exchanger, the pressurization fluid and heat transfer fluid must of necessity be compatible or the same. In addition, their release must not present problems of toxicity, flammability, or excessive energy release. Therefore the pressurization and heat transfer systems were designed to utilize the same fluid having the following characteristics: (1) low flammability, (2) high fluidity at −50°F, (3) low toxicity, (4) noncorrosive, (5) low vapor pressure at 350°F, (6) good heat transfer characteristics, (7) low compressibility, and (8) compatibility with internally located instrumentation. Triethyl phosphate appears to be the only liquid which satisfies all these requirements. An ethylene glycol–water solution also provides an acceptable fluid medium over a more restrictive temperature range.

Facility Design

The massive concrete foundation previously used as the valve pit in the southwest end of the turbine foundation for unit 8 was selected and modified as the test pit for the intermediate vessels. A view of the top of the pit from the turbine room operating floor is shown in Fig. 3.1. A mockup vessel is shown in position in a view of the test pit from the turbine room floor elevation in Fig. 3.2. Figure 3.3 presents a view of the test pit through the access opening from the basement floor elevation, again with the mockup vessel in position prior to modifications of the structure. A section through the test pit is shown in Fig. 3.4. Two new reinforced concrete slabs and a wood shield plug to cap the pit are shown.

Fig. 3.1. View of top of intermediate vessel test pit from turbine room operating floor prior to modifications.

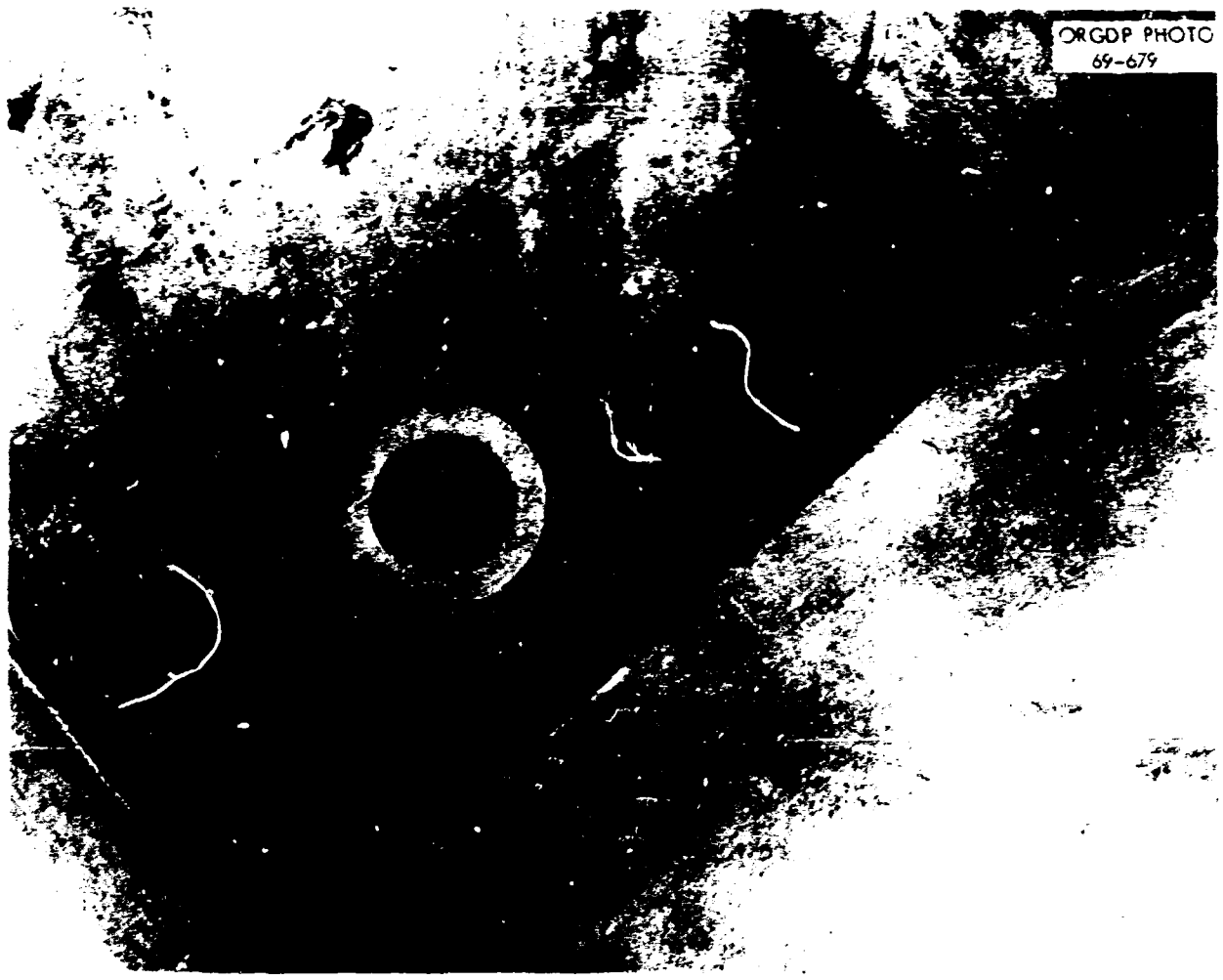

Fig. 3.2. View of the test pit from turbine room floor.

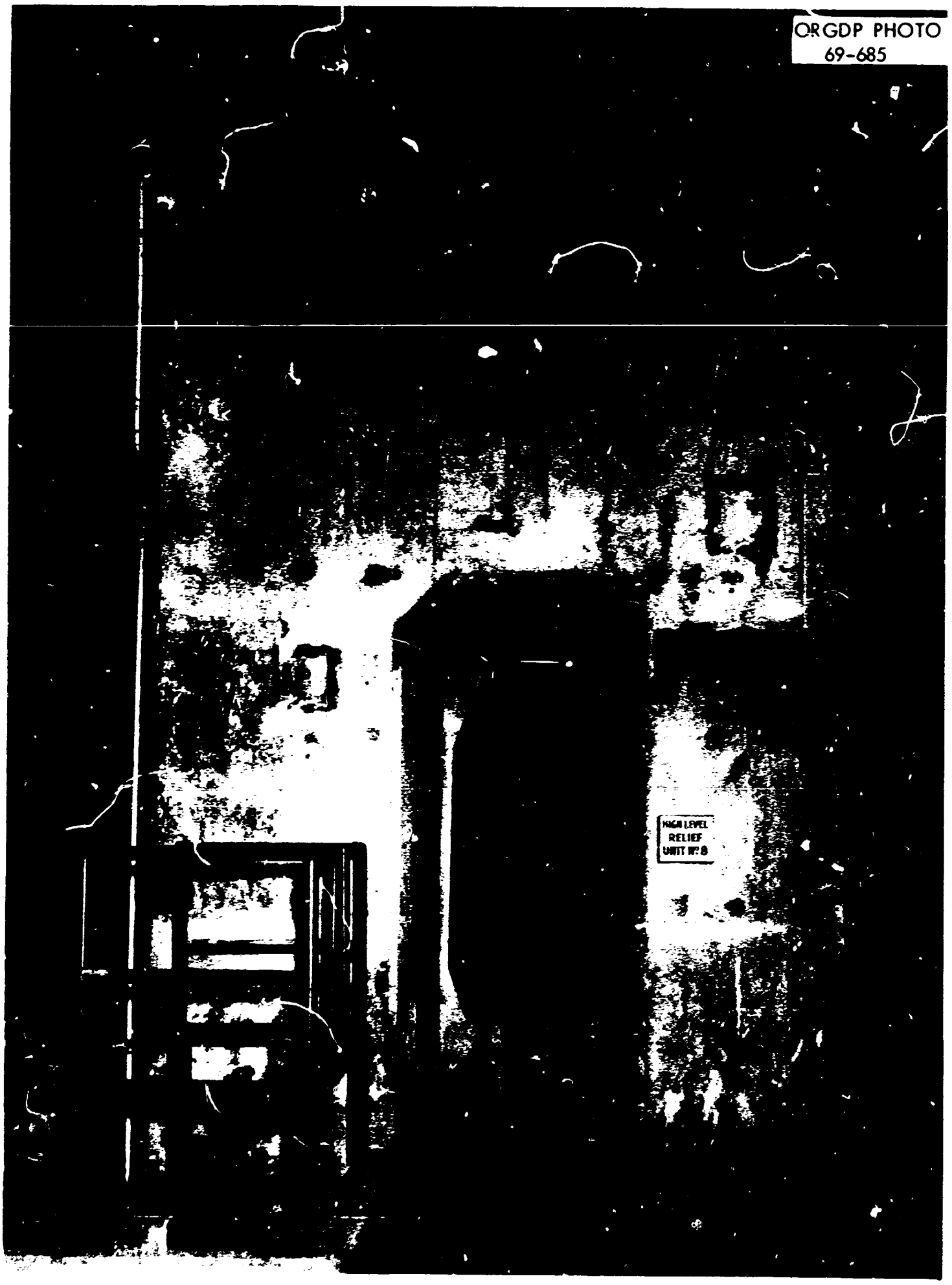

Fig. 3.3. View of mockup of test vessel from basement floor elevation.

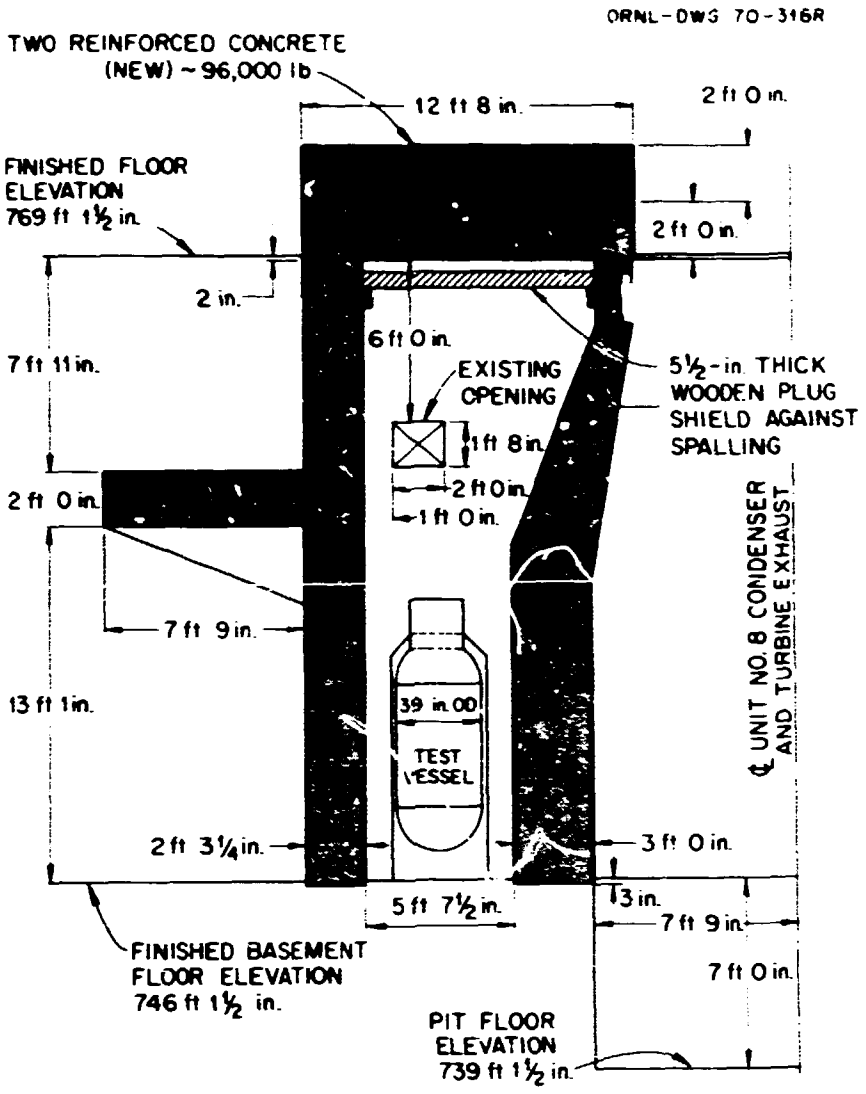

Fig. 3.4. Sectional view of intermediate vessel test pit.

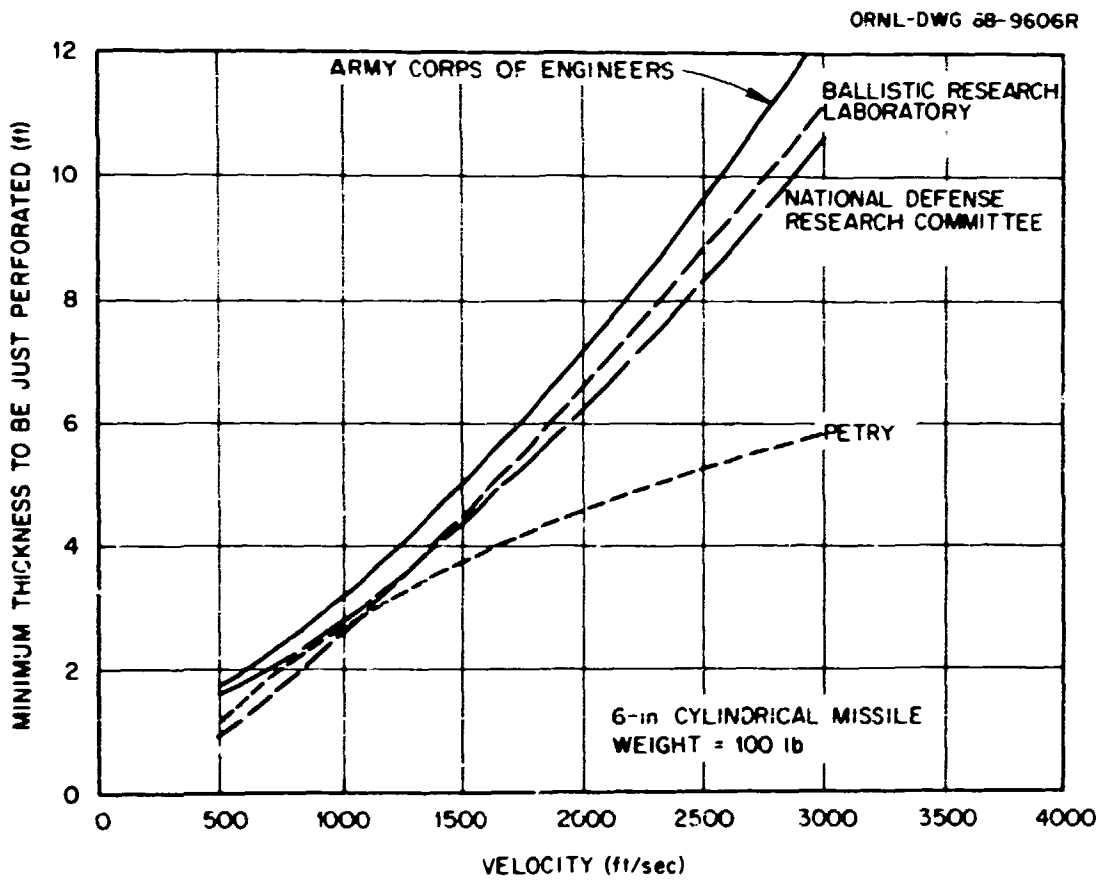

Fig. 3.5. Comparison of results obtained with formulas for calculating perforation of reinforced concrete by a small missile.

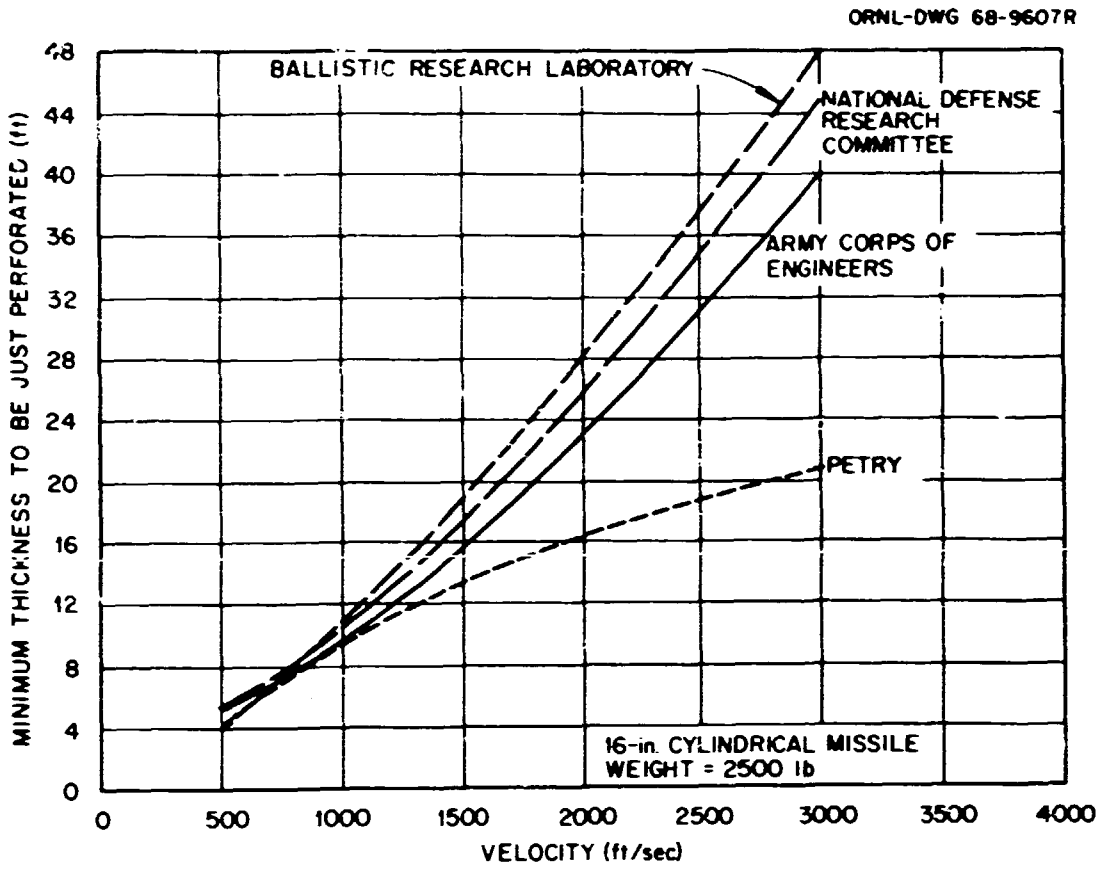

Fig. 3.6. Comparison of results obtained with formulas for calculating perforation of reinforced concrete by a large missile.

The adequacy of the existing reinforced concrete structures and the design of the new were premised upon a very conservatively based hazards analysis by Segaser[1] and complementary calculations by Offhaus[2] and Gamble.[3] Figures 3.5 and 3.6 present perforation vs missile velocity curves for various ballistic formulas and for two different missile sizes. Adequacy of barrier thickness was premised on prevention of perforation assuming the most conservative ballistic formula, the most conservatively based missile velocity, and a full range of missile sizes. Because of inadequate data, Meyerer and Bender[4] experimentally determined the thermodynamic properties of triethyl phosphate at high pressure. These data were used in the energy evaluation.

A jacketed heat exchanger concept was developed for heating and cooling the intermediate vessels. Figure 3.7 shows a conceptual heat exchanger arrangement mounted on a mockup of the intermediate vessel. Figures 3.8 and 3.9 present curves of cooling and heating times based on a jacketed arrangement calculated by means of the TOSS[5] and SIFT[6] transient heat transfer computer programs.

Based on these calculations the pressurization and heat transfer system flow diagrams shown in Fig. 3.10 were developed. To effect anticipated appreciable economies, a considerable portion of these systems was derived from salvaged equipment. One item was the refrigeration system previously used on the Homogeneous Reactor Experiment, HRE-2.[7] The unit was revamped extensively and skid mounted as shown in Fig. 3.11.

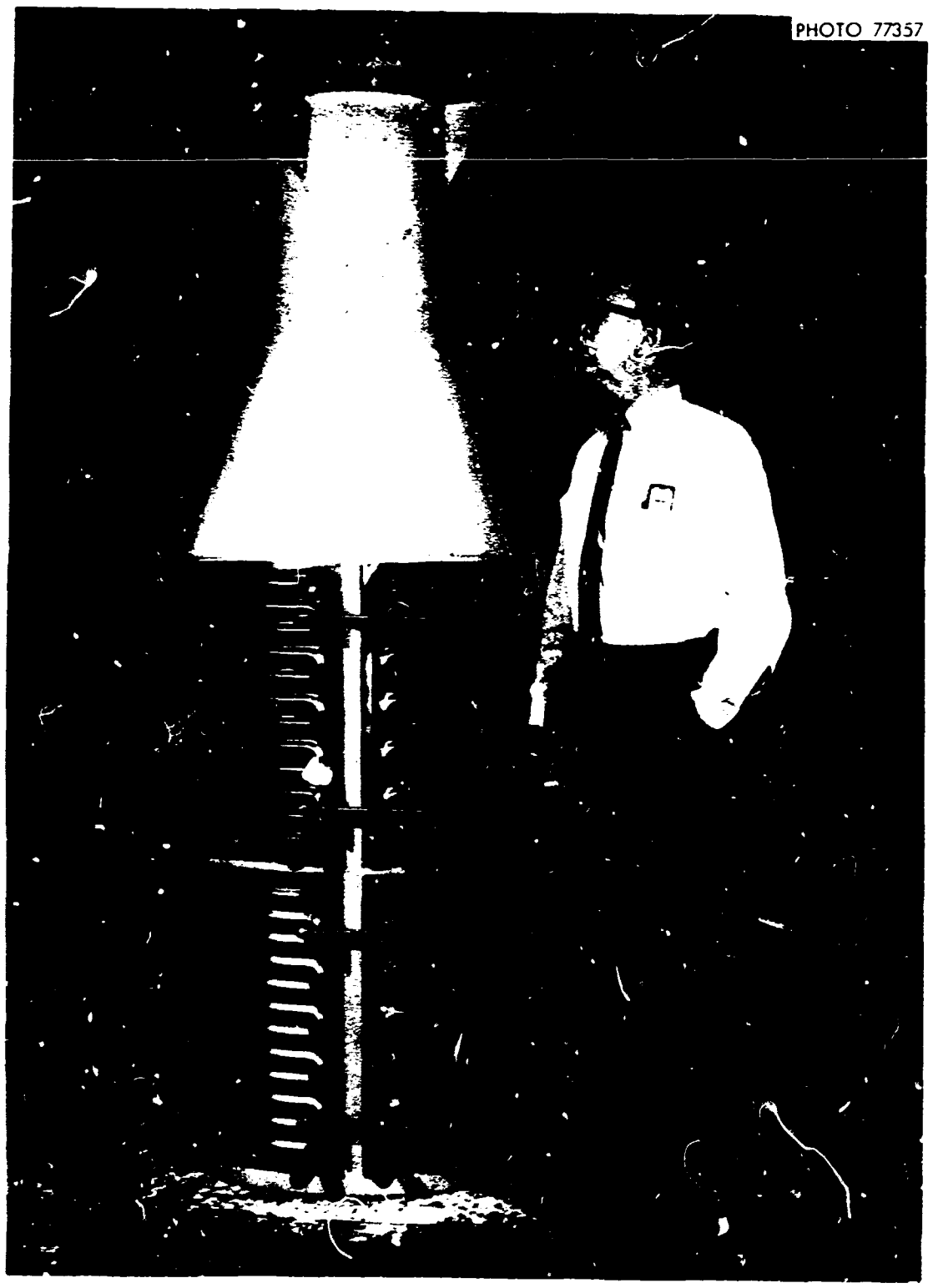

Fig. 3.7. Tranter plate-coil heat transfer unit mounted on mockup of intermediate vessels.

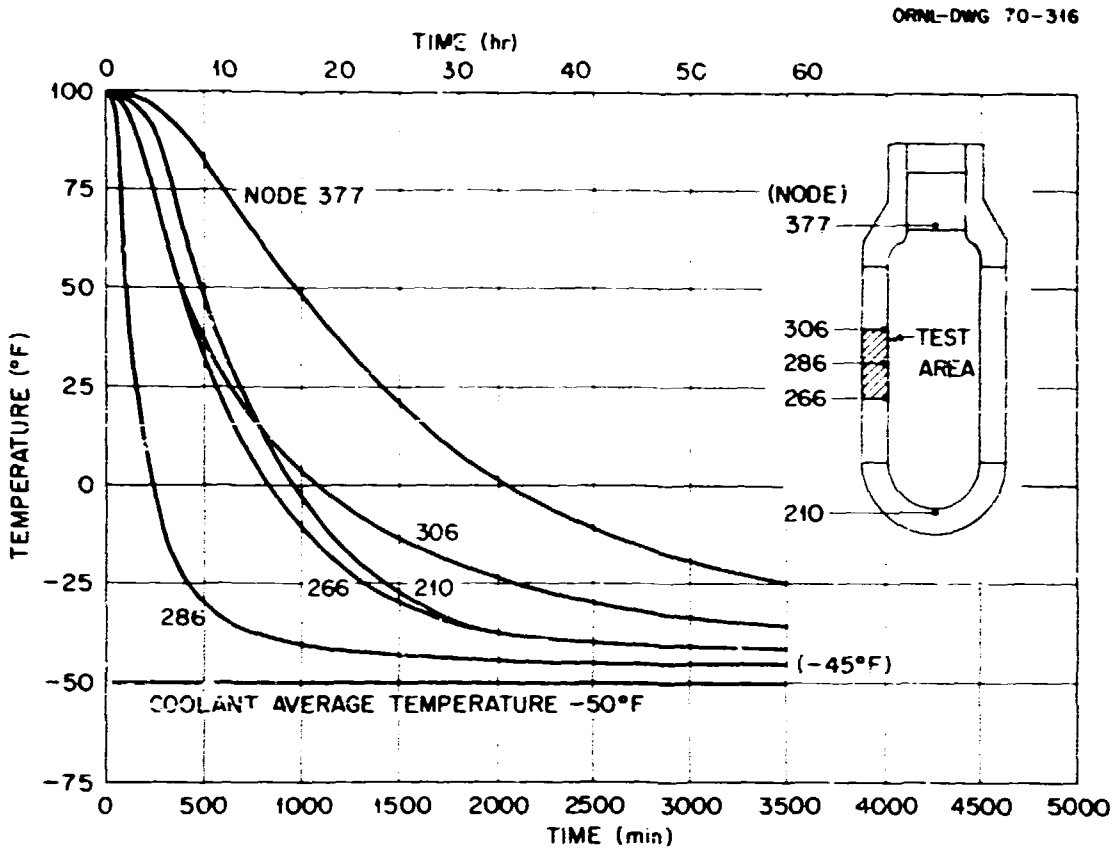

Fig. 3.8. HSST intermediate vessel test. Cooling time.

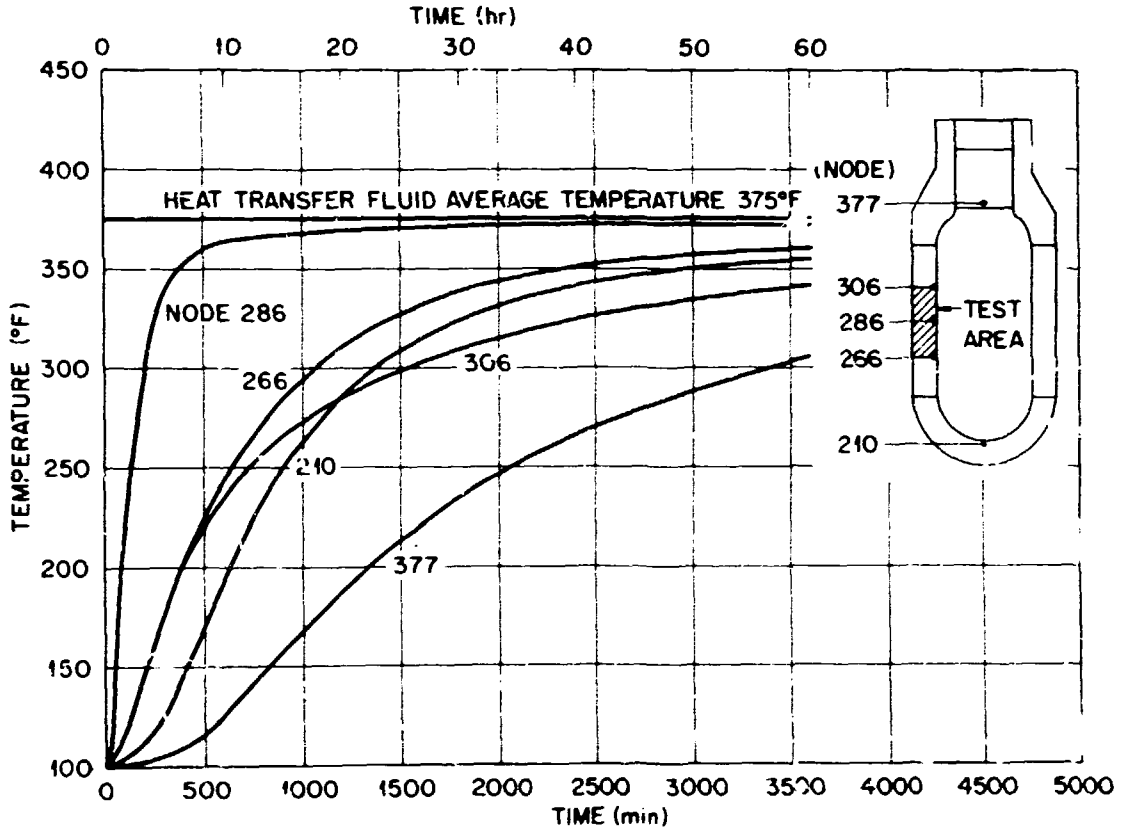

Fig. 3.9. HSST intermediate vessel test. Heating time.

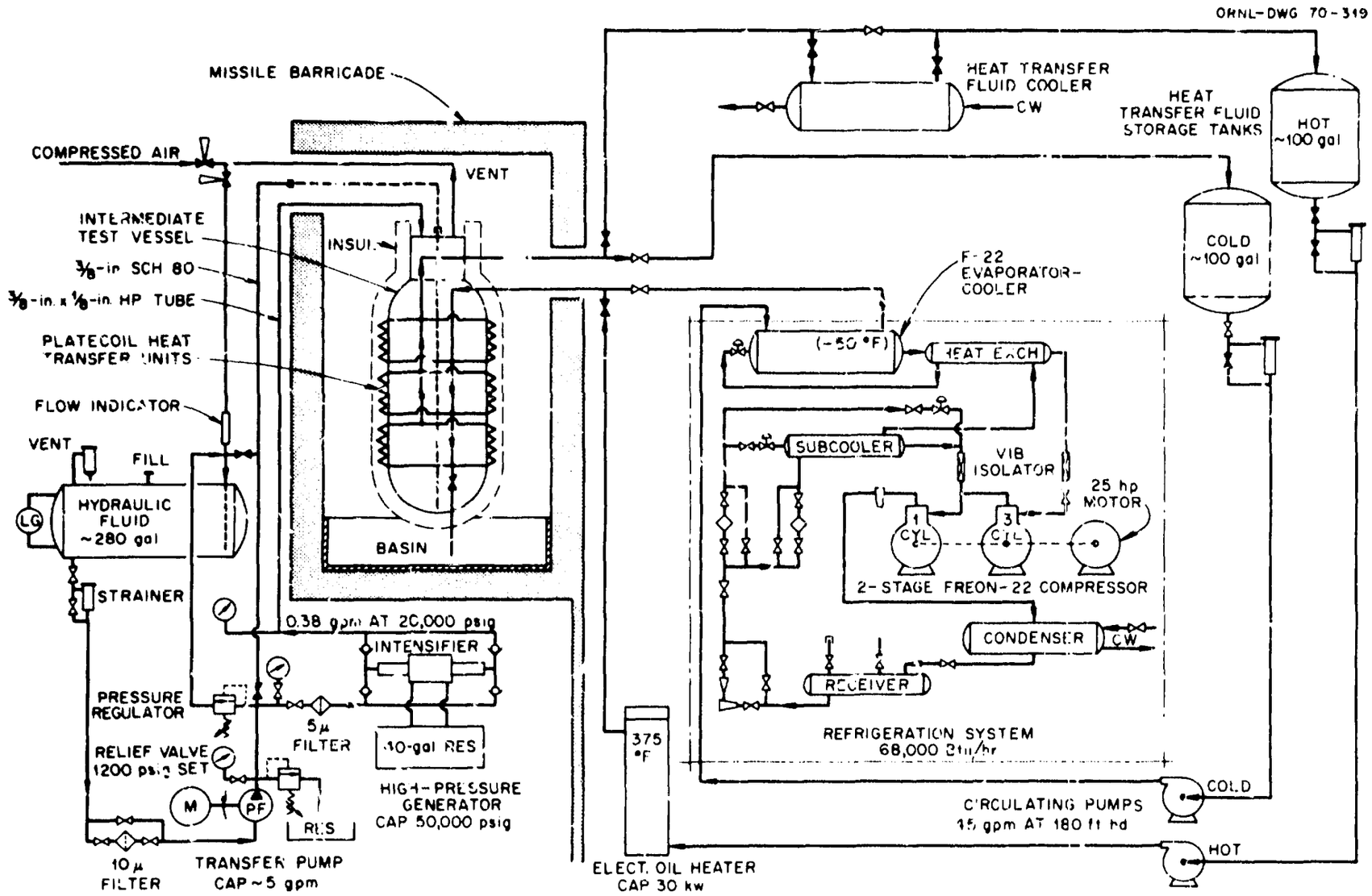

Fig. 3.10. HSST intermediate vessel test. Schematic flow diagram.

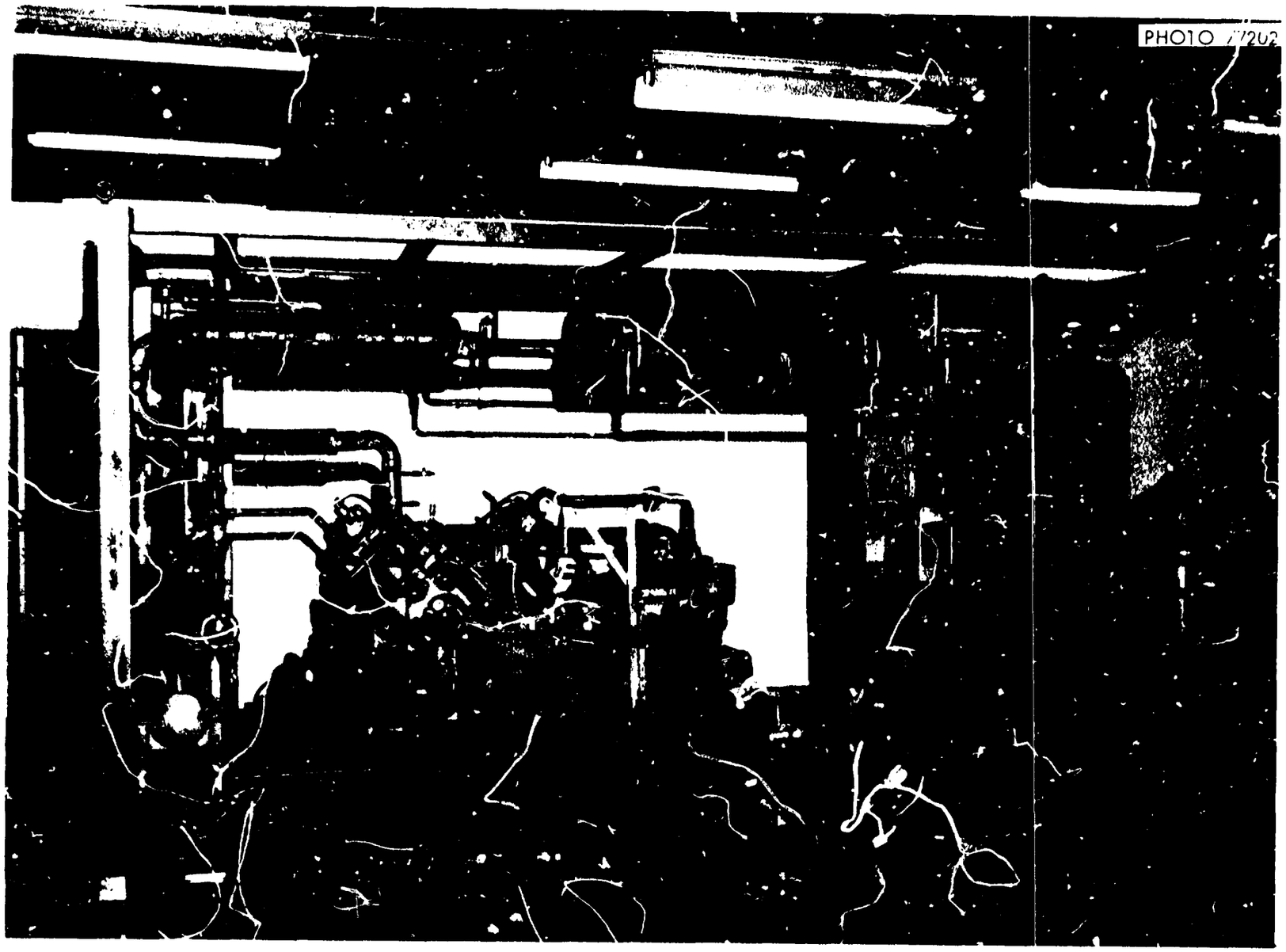

Fig. 3.11. Refrigeration system for low-temperature vessel test.

Detailed design, fabrication, and construction were implemented according to the quality assurance program plan[6] to reflect the usage of second-hand equipment and the need for special precautions because of the potential hazards involved with the testing program. Fabrication and construction of various portions of the systems were accomplished by labor forces at all three of the AEC Oak Ridge plants, by Rust Engineering Company forces, and by purchase orders as funding and scheduling would permit. Figure 3.12 shows a perspective view of a part of the completed systems, and the equipment in the test pit with vessel V-1 in place is shown in Fig. 3.13. Figure 3.14 shows a view of the control room, which houses the control panels (center of photo), the television monitoring systems, and the data acquisition system.

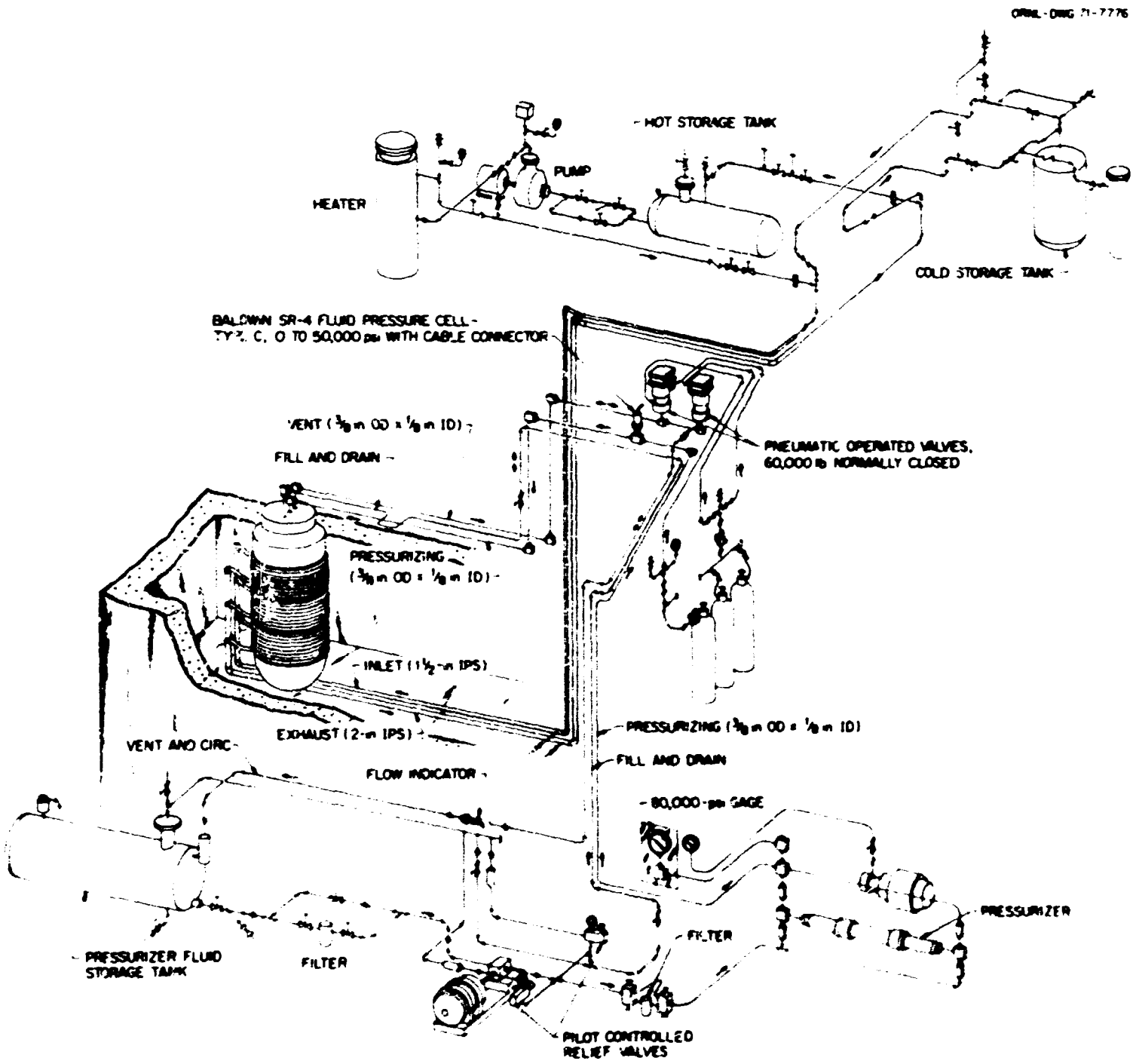

Fig. 3.12. Perspective view of intermediate vessel of part of the pressurization and heat transfer systems.

Fig. 3.13. View of test pit from turbine room floor with vessel V-1 and associated equipment in place.

Fig. 3.14. View of control room.

References

1. C. L. Segaser, *System Design Description of the Intermediate Vessel Tests for the Heavy-Section Steel Technology Program*, ORNL-TM-2849 (June 1970); revised July 1973.

2. Werner Offhaus, "Calculation Check-Barricade Thickness, Oak Ridge Gaseous Diffusion Plant," Mar. 28 1969 (unpublished calculation).

3. W. L. Gamble, "Containment Slabs for Pressure Vessel Tests," May 21, 1969 (unpublished calculation).

4. A. C. Meyerer and D. F. Bender, *Viscosity and P-V-T Relations of Triethyl Phosphate at High Pressures*, Massachusetts Institute of Technology Chemical Engineering Practice School Report CEPS-X-119 (Dec. 16, 1970).

5. D. Bagwell, *TOSS, an IBM-7090 Code for Computing Transient or Steady State Temperature Distribution*, ORGDP K-1494 (July 1962).

6. D. Bagwell, *SIFT, an IBM-7090 Code for Computing Heat Distributions*, ORGDP K-1528 (July 1962).

7. R. H. Chapman, *HRE-2 Design Manual*, ORNL-TM-348 (March 1964).

8. R. W. Derby and C. L. Segaser, *Quality Assurance Program Plan, Intermediate Vessel Test Facility*, ORNL-TM-3373 (May 1971).

4. MATERIALS INVESTIGATIONS

As described previously, the cylindrical course for series 1 vessels is 54 in. long in the test region of interest, with the middle third being designated the test area. A 24-in.-long prolongation was fabricated for each vessel cylinder. After removal from the cylindrical course, the prolongation received all subsequent postweld and repair weld heat treatments to which the cylindrical course was subjected. The orientation and alignment of the cylindrical course was maintained.

Upon receipt at ORNL the prolongations from both vessels were cut as outlined in Fig. 4.1. More specific details of the initial cutting are given in ORNL drawings 10476R-491-C Rev. 0, and 10476R-492-C, Rev. 0, for vessel V-1 and ORNL drawings 10476R-475-C, Rev. 1, and 10476R-476 D, Rev. 0, for vessel V-2. Each investigator received in turn the material for his investigations. The tests scheduled for each prolongation are summarized in Table 4.1, and the results pertinent to the vessel tests are presented below.

Tensile and Impact Test Results

Tensile, Charpy impact, and drop-weight nil ductility transition (NDT) temperature tests were run from the prolongation material of each vessel as a function of through-the-thickness locations. The specimen orientations are shown in Fig. 4.2.

A typical stress-strain diagram for circumferential orientation (C) is shown in Fig. 4.3. The room-temperature yield and ultimate strengths as a function of through-the-thickness location are shown for both prolongations in Fig. 4.4, and the data are given in Table 4.2. The NDT temperature was determined at three locations through the thickness, and results are given in Table 4.3.

Table 4.1. Mechanical property and materials investigations prior to testing each intermediate test vessel[a]

Test and orientation	Location[b]	Maximum number of tests per location	Type of data
Tensile, circumferential	OS, 1/4t, 1/2t, 3/4t, IS	2–4	σ_y, σ_u, σ–ϵ curve
Tensile axial	OS to IS	1	σ_y, σ_u, σ–ϵ curve
Tensile, through thickness	1/4t to 3/4t	2	σ_y, σ_u, σ–ϵ curve
Drop weight nil ductility transition (NDT)	OS, 3/8t, 3/4t	6	NDT temperature
Charpy, circumferential	OS, 1/4t, 3/8t, 1/2t, 5/8t, 3/4t, IS	12–22	Energy, MLE, etc.
Charpy, axial	1/4t	14–22	Energy, MLE, etc.
Charpy, precracked, static circumferential	OS, 1/4t, 1/2t, 3/4t, IS	8–10	K_{IcC_v}, energy, etc.
Charpy, precracked, dynamic circumferential	3/8t, 5/8t	8–12	K_{IdC_v}, energy, etc.
Charpy, precracked, static axial	1/4t	8	K_{IcC_v}, energy, etc.
0.85t CTS, circumferential[c]	1/12t, 1/2t, 11/12t	2–9	K_{Icd}, $d = 0.85$
4t CTS, circumferential[c]	1/2t	6	K_{Ic4}, J_{IC}
0.85-in.-thick pressure vessels	1/12t to 11/12t	6	δ–ϵ curves, COD, etc.

[a]Data obtained as applicable; test temperature to emphasize projected test temperatures of vessel.

[b]Measured from outside surfaces: OS = outside surface, 1/4t = 1 1/2 in., etc.; IS = inside surface.

[c]Tests being performed by Westinghouse Electric Corp. under UCCND Subcontract 3196. All other investigations are being performed at ORNL except the drop-weight NDT tests, which were performed by Naval Research Laboratory.

Table 4.2. Room-temperature tensile properties for material from the prolongations of V-1 and V-2, circumferential (C) orientation

Depth[a]	Vessel V-1				Vessel V-2			
	Lower yield (ksi)	Ultimate strength (ksi)	Total elongation[b] (%)	Reduction in area (%)	Lower yield (ksi)	Ultimate strength (ksi)	Total elongation[b] (%)	Reduction in area (%)
1/16	75.8	95.5	21	66	78.1	99.1	18	64
	75.8	96.8	19	66	77.4	97.6	19	67
1/12	74.2[c]	96.2[c]	23.5[c]	54.5[c]	73.2[c]	92.9[c]	23[c]	60[c]
	74.5[c]	96.6[c]	22.5[c]	54.4[c]		93.0[c]	25[c]	61[c]
1/4	72.1	93.4	19	66	73.2	95.1	16	53
	70.1	91.9	20	64	72.5	95.0	17	66
1/2	69.1	90.0	21	67	71.0	93.4	18	59
	68.5	89.1	22	66	70.4	93.2	18	58
	70.6[c]	91.2[c]	25[c]	58.3[c]	70.9[c]	92.7[c]	25[c]	60[c]
	70.7[c]	91.3[c]	26[c]	60.4[c]	74.6[c]	95.8[c]	21[c]	61[c]
3/4	68.4	89.4	21	67	70.7	92.7	18	54
	68.9	89.6	21	63	71.1	92.7	19	55
	70.4[c]	91.4[c]	25.5[c]	59.9[c]	73.3[c]	95.3[c]	23[c]	57[c]
	70.2[c]	91.8[c]	23.5[c]	64.0[c]	75.0[c]	96.0[c]	21[c]	49[c]
23/24	69.5	91.4	23	62	71.1	93.3	18	65
	71.6	92.6	20	55	71.0	93.0	17	63

[a]Fraction of wall thickness (6 in.) from outside surface.
[b]Length-to-diameter ratio of 7.
[c]Results from standard 0.505-in.-gage-diam specimens; other data from 0.178-in.-diam miniature specimens.

ORNL-DWG 72-3605

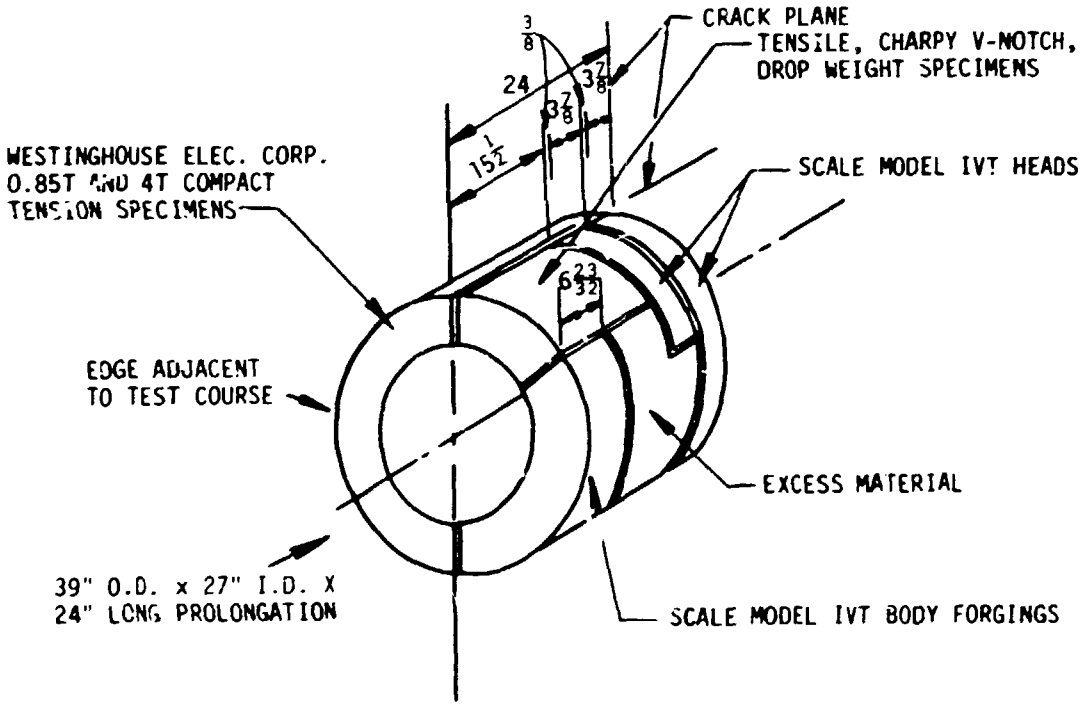

Fig. 4.1. Cutting plan for the prolongations of vessels V-1 and V-2.

Table 4.3. Drop-weight NDT temperature (°F) for vessels V-1 and V-2

	V-1	V-2
Outside surface	0	−10
Center	10	10
Inside surface	10	0

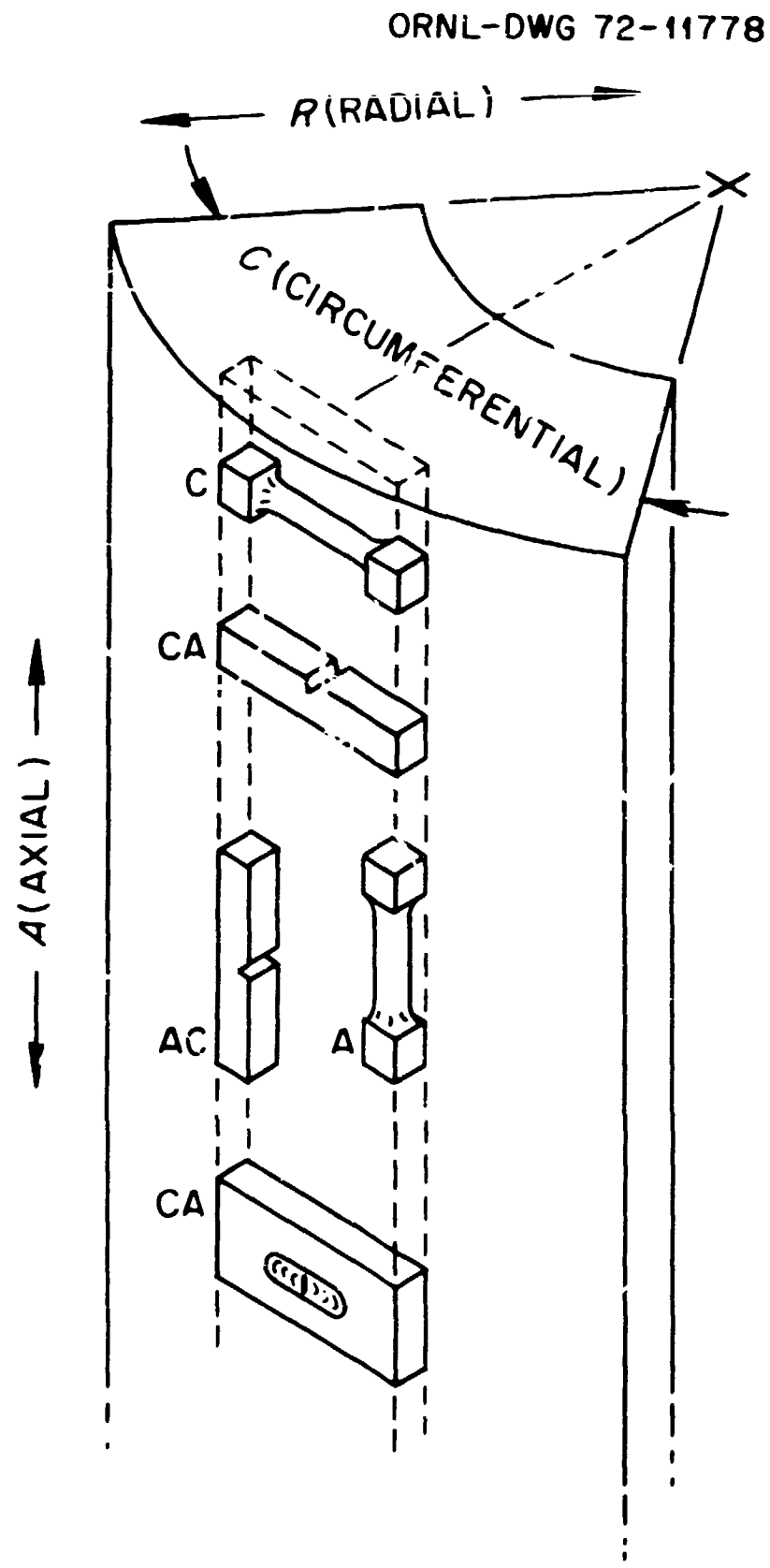

Fig. 4.2. Specimen orientation notation for HSST intermediate vessel materials showing tensile, Charpy V-notch, and drop-weight specimens.

Partial Charpy energy curves were obtained in the circumferential (CA) direction at five locations through the thickness, and full curves were obtained at two nonsurface locations. These data are summarized for vessels V-1 and V-2 in Figs. 4.5 and 4.6 respectively. Axially oriented (AC) Charpy specimens were also tested, and these results are compared with similar circumferential results in Figs. 4.7 and 4.8. Figure 4.9 shows a full curve of circumferential Charpy energy results for the two materials the Charpy data are given in Tables 4.4–4.6. The work reported in this section was performed by W. J. Stelzman of the Metals and Ceramics Division, ORNL.

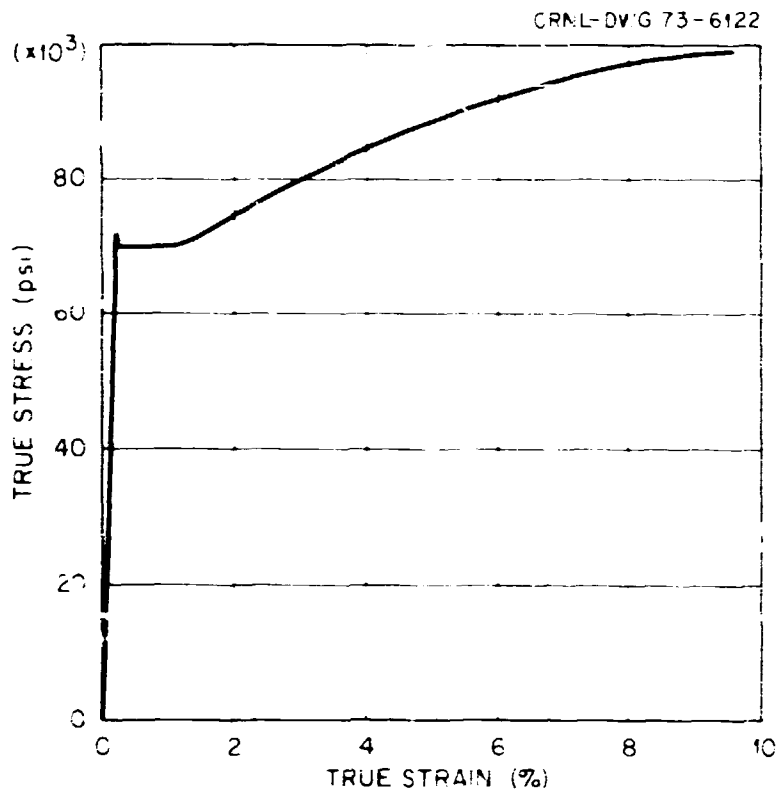

Fig. 4.3. Typical circumferential stress-strain curve at half thickness from intermediate vessel prolongation V-1.

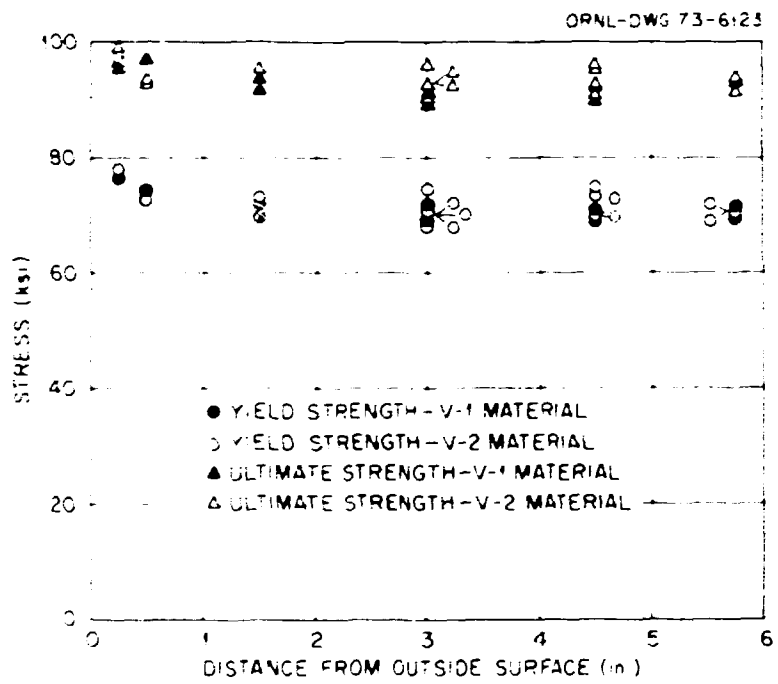

Fig. 4.4. Room-temperature tensile strength properties of prolongations of vessels V-1 and V-2, circumferential (C) orientation.

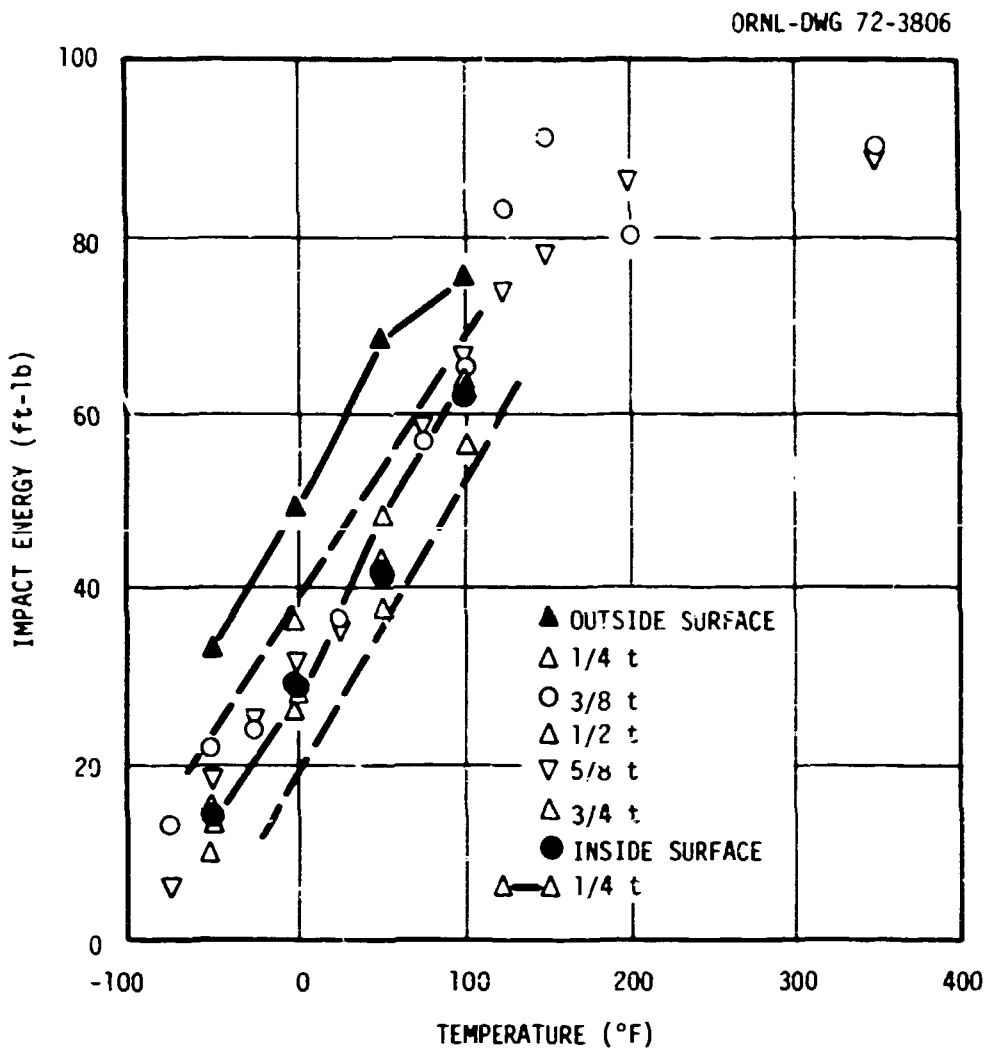

Fig. 4.5. Results from through-the-thickness study of the variation of Charpy impact energy with temperature for vessel V-1, circumferential orientation. The designation $^1/_4t$ means $^1/_4$ thickness measured from the outside surface, etc. Dashed lines indicate scatter band of nonsurface results.

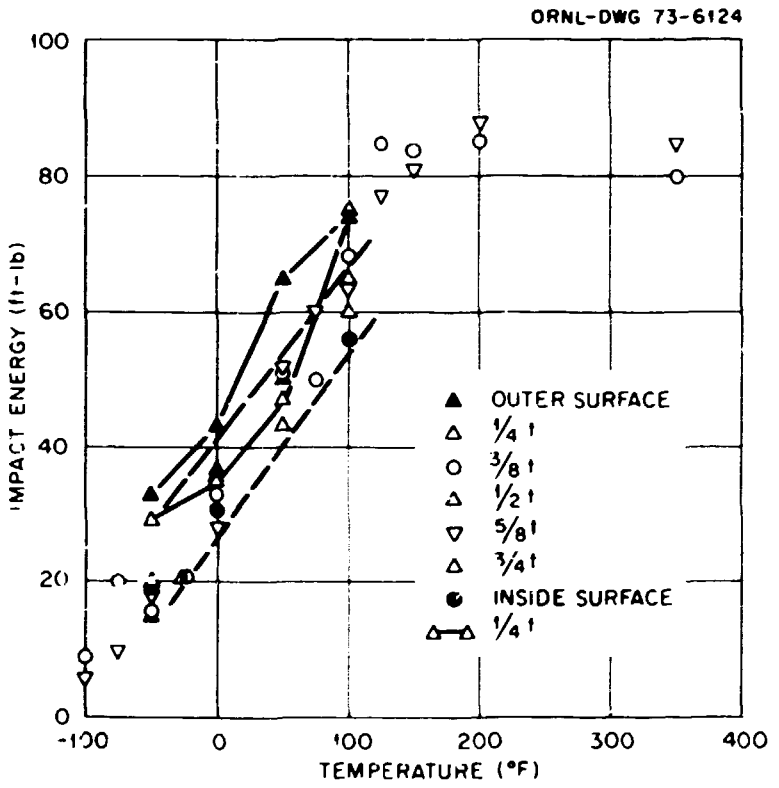

Fig. 4.6. Results from through-the-thickness study of the variation of Charpy impact energy with temperature for vessel V-2, circumferential orientation. The designation $^1/_4t$ means $^1/_4$ thickness measured from the outside surface, etc. Dashed lines indicate scatter band of nonsurface results.

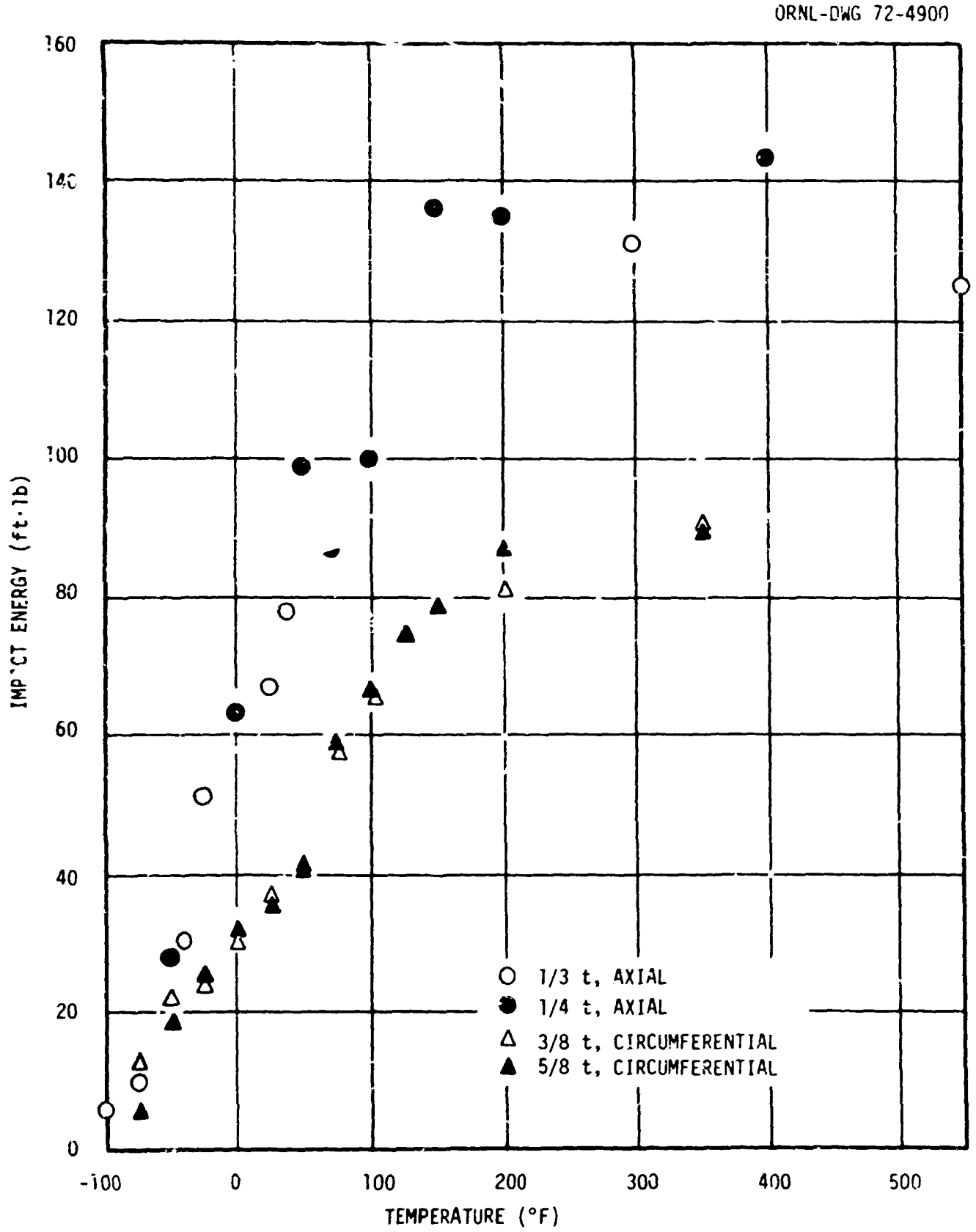

Fig. 4.7. Comparison of Charpy impact energies for axial and circumferential orientation, vessel V-1.

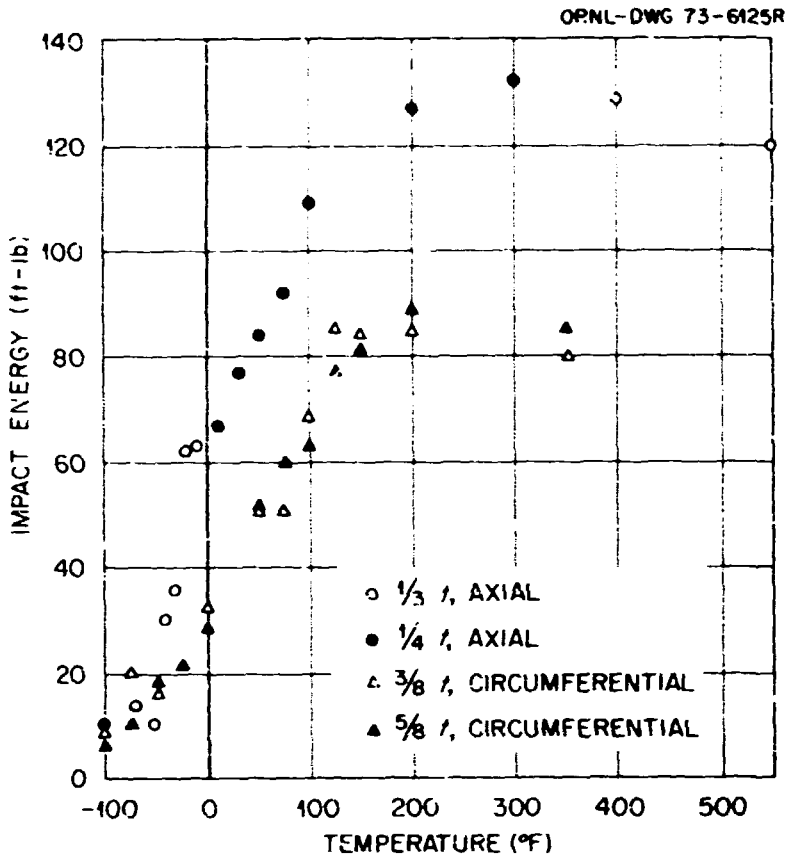

Fig. 4.8. Comparison of Charpy impact energies for axial and circumferential orientation, vessel V-2.

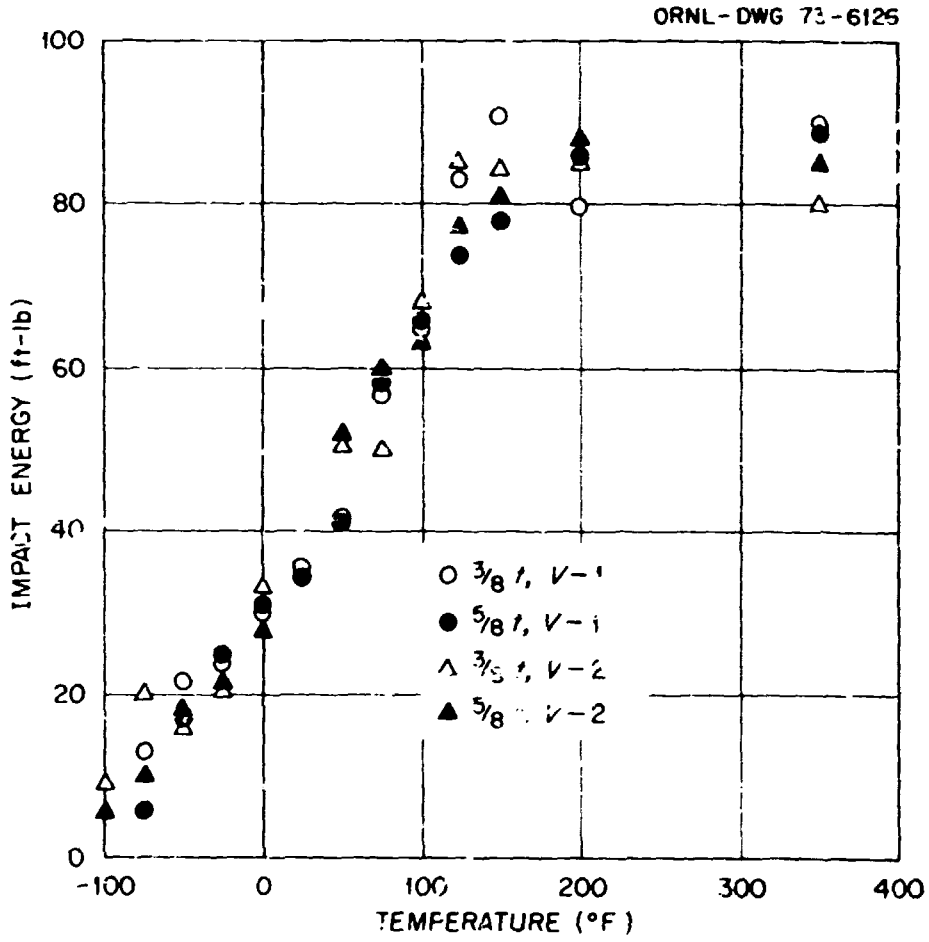

Fig. 4.9. Full Charpy energy data for vessel V-1 and V-2 material, circumferential orientation.

Table 4.4. Charpy impact data from the prolongation of vessel V-1 as a function of temperature and location, circumferential (CA) orientation

Specimen No.	Location[a]	Test temperature (°F)	Energy (ft-lb)	Lateral expansion (mils)
1V1000	0	−50	33	26
1V1012	1/4t	−50	14	9
1V1024	1/2t	−50	14	10
1V1036	3/4t	−50	10	8
1V1048	1t	−50	14	10
1V1001	0	0	49	35
1V1013	1/4t	0	28	23
1V1025	1/2t	0	36	30
1V1037	3/4t	0	26	21
1V1049	1t	0	29	22
1V1002	0	50	68	55
1V1014	1/4t	50	48	38
1V1026	1/2t	50	38	32
1V1038	3/4t	50	43	34
1V1050	1t	50	42	37
1V1003	0	100	75	59
1V1015	1/4t	100	64	49
1V1027	1/2t	100	65	52
1V1039	3/4t	100	56	48
1V1051	1t	100	62	50
1V1070	3/8t	−75	13	10
1V1063	3/8t	−50	22	16
1V1069	3/8t	−25	24	19
1V1062	3/8t	0	30	26
1V1068	3/8t	25	37	30
1V1061	3/8t	50	41	36
1V1067	3/8t	75	57	48
1V1060	3/8t	100	65	57
1V1066	3/8t	125	83	69
1V1065	3/8t	150	91	72
1V1064	3/8t	200	80	67
1V1071	3/8t	350	90	72
1V1092	5/8t	−75	6	2
1V1085	5/8t	−50	19	17
1V1091	5/8t	−25	25	20
1V1084	5/8t	0	32	26
1V1090	5/8t	25	35	26
1V1083	5/8t	50	41	36
1V1089	5/8t	75	59	46
1V1082	5/8t	100	66	52
1V1088	5/8t	125	74	60
1V1087	5/8t	150	78	67
1V1086	5/8t	200	86	70
1V1093	5/8t	350	89	70

[a]Depth of specimen measured from outer surface, t = 6;0 and 1t nominal.

Table 4.5. Charpy impact data from the prolongation of vessel V-2 as a function of temperature and location, circumferential (CA) orientation

Specimen No.	Location[a]	Test temperature (°F)	Energy (ft-lb)	Lateral expansion (mils)
2V1000	0	−50	33	23
2V1018	1/4t	−50	29	23
2V1036	1/2t	−50	20	15
2V1054	3/4t	−50	15	13
2V1072	1t	−50	20	16
2V1001	0	0	43	38
2V1019	1/4t	0	35	26
2V1037	1/2t	0	37	29
2V1055	3/4t	0	35	33
2V1073	1t	0	31	27
2V1002	0	50	65	53
2V1020	1/4t	50	47	40
2V1038	1/2t	50	43	39
2V1056	3/4t	50	51	38
2V1074	1t	50	51	40
2V1003	0	100	74	60
2V1021	1/4t	100	74	60
2V1039	1/2t	100	62	50
2V1057	3/4t	100	65	58
2V1075	1t	100	56	50
2V1094	3/8t	−100	9	5
2V1099	3/8t	−75	20	13
2V1093	3/8t	−50	16	12
2V1098	3/8t	−25	21	14
2V1092	3/8t	0	33	25
2V1091	3/8t	50	51	41
2V1101	3/8t	75	50	45
2V1090	3/8t	100	68	60
2V1097	3/8t	125	85	63
2V1096	3/8t	150	84	67
2V1095	3/8t	200	85	70
2V1100	3/8t	350	80	70
2V1116	5/8t	−100	6	3
2V1121	5/8t	−75	10	7
2V1115	5/8t	-50	18	14
2V1120	5/8t	−25	21	18
2V1114	5/8t	0	28	23
2V1113	5/8t	50	52	42
2V1123	5/8t	75	60	47
2V1112	5/8t	100	63	54
2V1119	5/8t	125	77	64
2V1118	5/8t	150	81	70
2V1117	5/8t	200	88	67
2V1122	5/8t	350	85	72

[a]Depth of specimen measured from outer surface, t = 6; 0 and 1t nominal.

Table 4.6. Charpy impact data from prolongation of V-1 and V-2, axial (AC) orientation

Specimen No.	Location[a]	Test temperature (°F)	Energy (ft-lb)	Lateral expansion (mils)
		Vessel V-1		
1V1110	1/3t	100	6	4
1V1112	1/3t	75	10	7
1V1109	1/4t	50	28	21
1V1127	1/3t	40	30	25
1V1114	1/3t	25	51	38
1V1107	1/4t	0	63	49
1V1115	1/3t	25	67	51
1V1125	1/3t	40	78	58
1V1105	1/4t	50	99	69
1V1104	1/4t	72	87	65
1V1116	1/4t	100	120	86
1V1121	1/4t	150	136	92
1V1118	1/4t	200	135	86
1V1112	1/3t	300	131	89
1V1120	1/4t	400	143	91
1V1123	1/3t	550	125	90
		Vessel V-2		
2V1136	1/4t	100	10	9
2V1145	1/3t	70	14	16
2V1144	1/3t	50	10	12
2V1157	1/3t	40	30	25
2V1142	1/3t	30	36	32
2V1155	1/3t	20	62	49
2V1140	1/3t	10	63	51
2V1139	1/4t	10	67	53
2V1137	1/4t	30	77	59
2V1135	1/4t	50	84	64
2V1134	1/4t	75	92	71
2V1148	1/4t	100	109	80
2V1150	1/4t	200	127	92
2V1151	1/4t	300	132	91
2V1152	1/3t	400	129	91
2V1153	1/3t	550	120	92

[a]Depth of specimen measured from outer surface, t = 6.

Fracture Toughness Results

Series of 0.85t (0.85-in.-thick) and 4t compact tension specimens and precracked Charpy specimens were tested at temperatures up to 200°F. The variations of toughness through the thickness as a function of temperature were determined from the small specimens, while the large (4t) specimen results were used mainly to approximate the full-thickness toughness in combination with the small-specimen results. In all cases the toughness parameters, K_{Icd}, which may be used in both brittle and ductile fracture assessments, were calculated.[1,2] The tests were all performed statically; these results are summarized below.

A total of 44 compact tension specimens including 14 4t specimens were tested. The specimens were selected as shown in Fig. 4.10. Results from these specimens, obtained under subcontract by Westinghouse Electric Corporation, are given in Tables 4.7 and 4.8.

Thirty-five precracked Charpy specimens were tested in slow bend for each vessel. These results are summarized in Tables 4.9 and 4.10. The testing of the precracked Charpy specimens was performed under the direction of W. J. Stelzman of the Metals and Ceramics Division, ORNL.

Various plots of the K_{Icd} data are shown in Figs. 4.11–4.13.

Discussion

In Fig. 4.4 the yield strengths of materials from both prolongations are seen to average slightly above 70 ksi, with the V-2 properties slightly above those of V-1. Ultimate strength properties vary in the same manner. In both cases, strength properties increase near the outside surface due to quenching. Similar behavior is not evident near the inside surface, indicating a less satisfactory heat flow internal to the cylinder than external during quenching. Figure 4.3 shows the typical yield plateau of this grade of steel.

Table 4.7. Fracture toughness results determined from testing 4t and 0.850t compact tension specimens from prolongation of vessel V-1

Specimen No.	Test temperature (°F)	Crack length (in.)	Maximum load (lb)	Energy to maximum load (in.-lb)	P_Q (lb)	Energy to P_Q (in.-lb)	K_{Icd} (ksi $\sqrt{in.}$)
0.850t Compact tension specimens (outside surface)							
V1B-13	100	0.958	8,390	230.2	3,000	17.6	113.0
V1B-12	50	0.883	10,750	266.2	3,100	17.0	112.0
V1B-7	±0	0.888	12,300	1,037.7	4,100	32.4	214.0
V1B-8	+100	0.868	12,090	813.3	4,100	29.6	192.0
V1B-10	+130	0.871	11,800	842.9	4,000	26.7	202.0
V1B-11	+130	0.896	11,100	945.8	3,500	21.4	219.0
V1B-9	+200	0.858	11,850	1,036.9	4,100	30.7	209.0
0.850t Compact tension specimens (center thickness region)							
V1B-19	50	0.880	10,250	209.7	5,000	41.0	163.0
V1B-14	±0	0.888	11,370	410.8	4,000	28.0	142.0
V1B-15	+100	0.881	11,400	1,059.2	4,200	30.9	225.0
V1B-17	+130	0.888	10,950	1,391.6	3,600	29.7	223.0
V1B-18	+130	0.868	11,350	1,312.4	3,100	18.7	237.0
V1B-16	+200	0.880	11,000	1,005.0	4,000	29.5	213.0
0.850t Compact tension specimens (inside surface)							
V1B-20	+130	0.880	11,600	975.7	3,000	15.7	215.0
V1B-21	+130	0.883	11,390	1,100.7	3,600	22.6	230.0
4t Compact tension specimens (center thickness region)							
V1B-6	±0	4.098	149,000	5,264.0	62,000	900.0	136.0
V1B-2	+100	4.123	232,000	27,550.0	80,000	1632.0	292.0
V1B-1	+120	4.328	204,500	22,372.0	60,000	924.0	285.0
V1B-5	+130	4.120	227,500	28,130.0	42,000	450.0	295.0
V1B-4	+130	4.273	213,500	27,172.0	78,000	1584.0	305.0
V1B-3	+200	4.100	228,500	25,134.0	80,000	1584.0	280.0
4t Compact tension specimen (inside surface)							
V1B-22	+130	4.133	232,000	35,520.0	80,000	2464.0	270.6

The Charpy energy curves of Figs. 4.5 and 4.6 exhibit the typical transition behavior of quenched and tempered steels as a function of both location and temperature. No real differences in the energy transition for the two materials are seen. The upper shelf energy is near 90 ft-lb, and the energy near NDT is between 30 and 40 ft-lb. As noted in Figs. 4.7 and 4.8, the axially oriented Charpy data (fracture running circumferentially) definitely indicate a lower transition temperature and higher shelf toughness, as might be expected since the weak direction for toughness is the circumferential (fracture running axially) direction. Figure 4.9 further demonstrates that the Charpy energy curves for the two materials are about the same.

The lower-bound static fracture toughness exhibits a transition with location and temperature; however, the differences between the two materials (nonsurface) are more pronounced than for Charpy data (see Figs. 4.11 and 4.12). At NDT, a toughness well over 100 ksi $\sqrt{in.}$ is seen. The shelf toughness from precracked Charpy tests is seen to be as low as −50°F for outside surface material. For outside surface material, the higher shelf levels determined for the 0.85-in.-thick compact tension specimens are some 80° higher, but part of the increase is due to the thickness of the specimens containing material with sharp toughness gradients.

Table 4.8. Fracture toughness results determined from testing 4t and 0.850t compact tension specimens from prolongation of vessel V-2

Specimen No.	Test temperature (°F)	Crack length (in.)	Maximum load (lb)	Energy to maximum load (in.-lb)	P_Q (lb)	Energy to P_Q (in.-lb)	K_{Icd} (ksi $\sqrt{in.}$)
0.850t Compact tension specimens (outside surface)							
V2B-11	50	0.886	12,200	437.8	4,000	27.6	146.3
V2B-9	+0	0.851	12,200	760.2	4,000	28.9	176.7
V2B-10	+25	0.873	12,250	911.4	4,000	29.9	198.0
V2B-12	+32	0.873	12,440	852.6	4,000	25.8	206.2
V2B-8	+100	0.860	12,450	910.1	4,000	26.2	206.5
V2B-13	+130	0.855	12,300	736.2	4,000	25.0	188.2
V2B-7	+130	0.873	11,550	860.2	4,000	28.8	196.0
0.850t Compact tension specimens (center thickness region)							
V2B-16	+0	0.913	10,500	493.2	4,000	28.6	160.5
V2B-17	+25	0.860	11,800	575.9	4,000	27.5	160.2
V2B-18	+32	0.890	11,260	958.4	4,000	30.0	209.0
V2B-15	+50	0.885	11,500	729.9	4,000	26.3	190.1
V2B-19	+50	0.885	11,200	941.4	4,000	31.2	201.3
V2B-14	+100	0.893	11,400	1,173.0	4,000	28.0	241.2
0.850t Compact tension specimens (inside surface)							
V2B-20	+32	0.876	12,120	911.8	4,000	28.5	204.1
V2B-21	+32	0.886	11,600	697.3	4,000	29.5	178.7
4t Compact tension specimens (center thickness region)							
V2B-4	+0	4.125	164,000	6,768.0	80,000	1564.0	148.0
V2B-6	+25	4.133	184,500	9,344.0	80,000	1512.0	177.1
V2B-2	+32	4.295	186,000	10,772.0	80,000	1516.0	202.4
V2B-5	+50	4.115	236,000	29,584.0	80,000	1532.0	311.3
V2B-1	+75	4.326	210,500	26,992.0	80,000	1724.0	304.7
V2B-3	+100	4.120	237,500	30,420.0	80,000	1620.0	311.4
4t Compact tension specimen (inside surface)							
V2B-22	+32	4.100	180,500	14,260.0	80,000	2576.0	165.7

Table 4.9. Lower-bound static fracture toughness K_{IcC_v} from vessel V-1 prolongation as a function of location and temperature determined from precracked Charpy specimens, circumferential orientation

Specimen No.	Location[a]	Test temperature (°F)	K_{IcC_v} (ksi $\sqrt{in.}$)
1V-1010	0	−50	171
1V-1022	1/4t	−50	109
1V-1034	1/2t	−50	87
1V-1046	3/4t	−50	98
1V-1058	1t	−50	92
1V-1004	0	0	167
1V-1016	1/4t	0	133
1V-1028	1/2t	0	136
1V-1040	3/4t	0	126
1V-1052	1t	0	154
1V-1005	0	50	173
1V-1017	1/4t	50	174
1V-1029	1/2t	50	173
1V-1041	3/4t	50	162
1V-1053	1t	50	184
1V-1006	0	76	151
1V-1018	1/4t	76	152
1V-1030	1/2t	76	167
1V-1042	3/4t	76	173
1V-1054	1t	76	174
1V-1007	0	100	158
1V-1019	1/4t	100	154
1V-1031	1/2t	100	161
1V-1043	3/4t	100	181
1V-1055	1t	100	169
1V-1008	0	130	155
1V-1020	1/4t	130	148
1V-1032	1/2t	130	*b*
1V-1044	3/4t	130	169
1V-1056	1t	130	173
1V-1009	0	200	152
1V-1023	1/4t	200	161
1V-1033	1/2t	200	169
1V-1045	3/4t	200	164
1V-1057	1t	200	174

[a]Depth of specimen measured from outer surface, t = 6;0 and 1t nominal.
[b]Instrument failure.

Table 4.10. Lower-bound static fracture toughness K_{IcC_v} from vessel V-2 prolongation as a function of location and temperature determined from precracked Charpy specimens, circumferential orientation

Specimen No.	Location[a]	Test temperature (°F)	K_{IcC_v} (ksi $\sqrt{in.}$)
2V-1004	0	−100	135
2V-1022	1/4t	−100	92
2V-1040	1/2t	−100	74
2V-1058	3/4t	−100	60
2V-1076	1t	−100	81
2V-1005	0	−50	177
2V-1023	1/4t	−50	127
2V-1041	1/2t	−50	106
2V-1059	3/4t	−50	148
2V-1077	1t	−50	109
2V-1006	0	0	176
2V-1024	1/4t	0	161
2V-1042	1/2t	0	130
2V-1060	3/4t	0	119
2V-1072	1t	0	165
2V-1010	0	32	160
2V-1026	1/4t	32	143
2V-1046	1/2t	32	174
2V-1064	3/4t	32	175
2V-1082	1t	32	186
2V-1007	0	50	161
2V-1025	1/4t	50	171
2V-1043	1/2t	50	166
2V-1061	3/4t	50	192
2V-1079	1t	50	*b*
2V-1008	0	100	182
2V-1026	1/4t	100	168
2V-1044	1/2t	100	174
2V-1062	3/4t	100	165
2V-1080	1t	100	159
2V-1009	0	200	162
2V-1027	1/4t	200	167
2V-1045	1/2t	200	151
2V-1063	3/4t	200	151
2V-1081	1t	200	165

[a]Depth of specimen measured from outer surface, t = 6;0 and 1t nominal.
[b]Instrument failure.

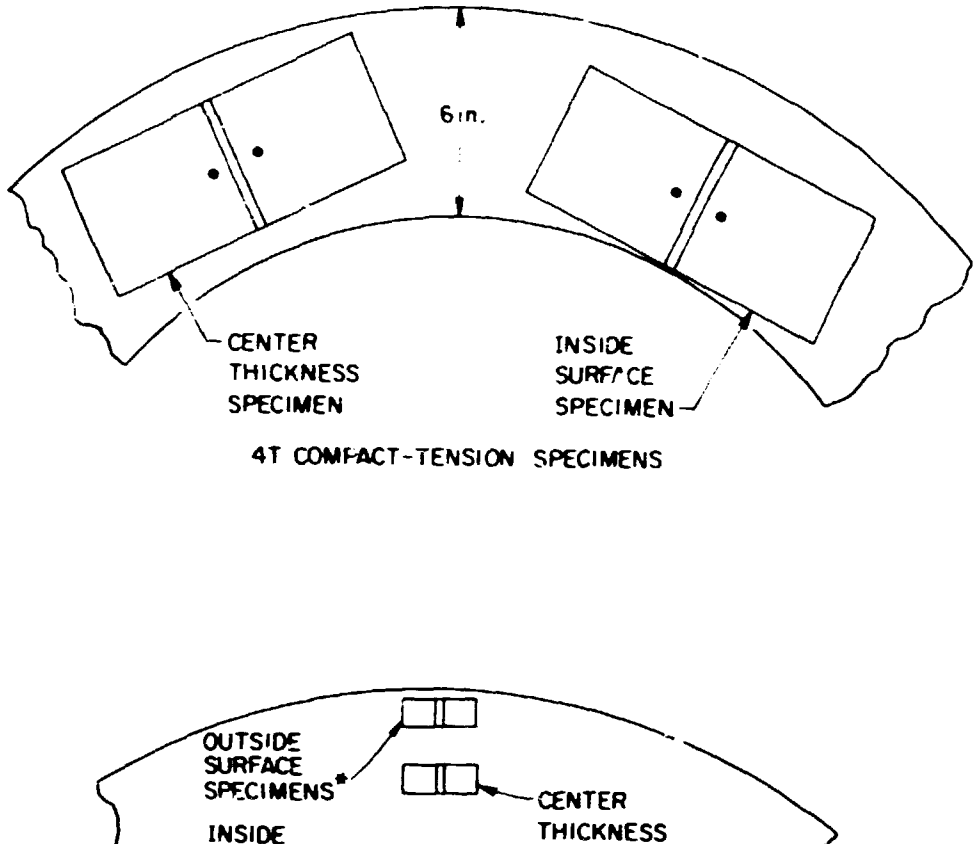

*SURFACE OF SPECIMEN WAS $^{3}/_{16}$-in. FROM SURFACE OF MATERIAL

Fig. 4.10. Location of compact tension specimens from pressure vessel prolongations V-1 and V-2.

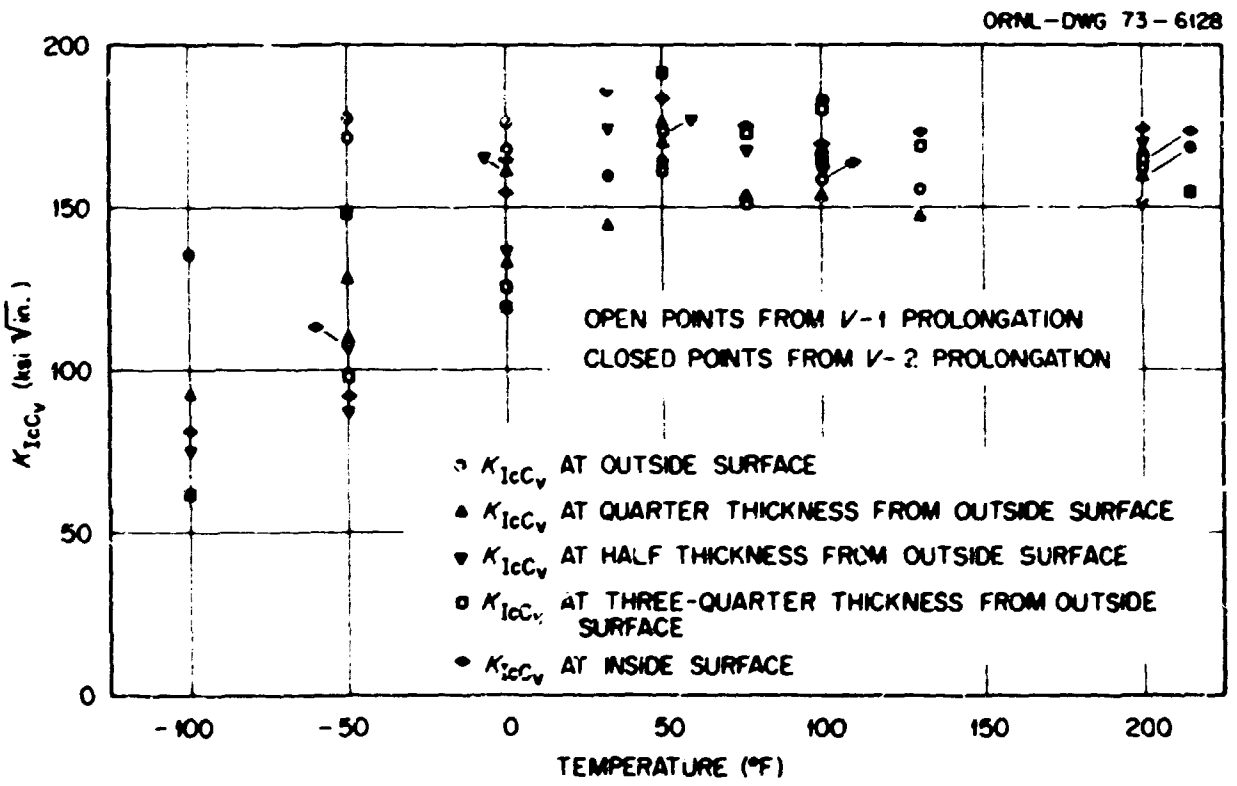

Fig. 4.11. Lower-bound static fracture toughness for vessels V-1 and V-2 from precracked Charpy specimens as a function of location and temperature, circumferential (CA) orientation.

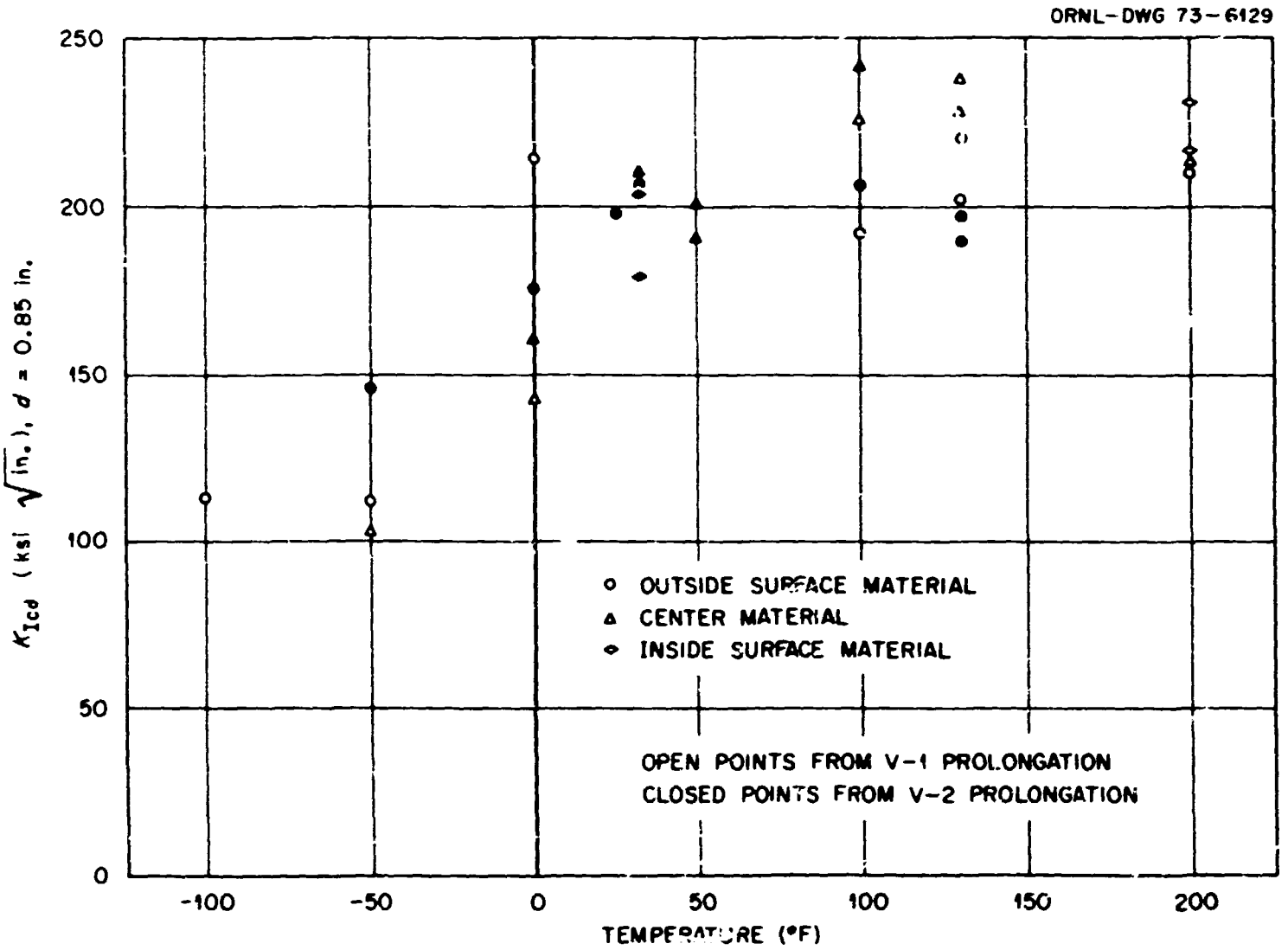

Fig. 4.12. Lower-bound static fracture toughness for vessels V-1 and V-2 from 0.85-in.-thick compact tension specimens, circumferential orientation.

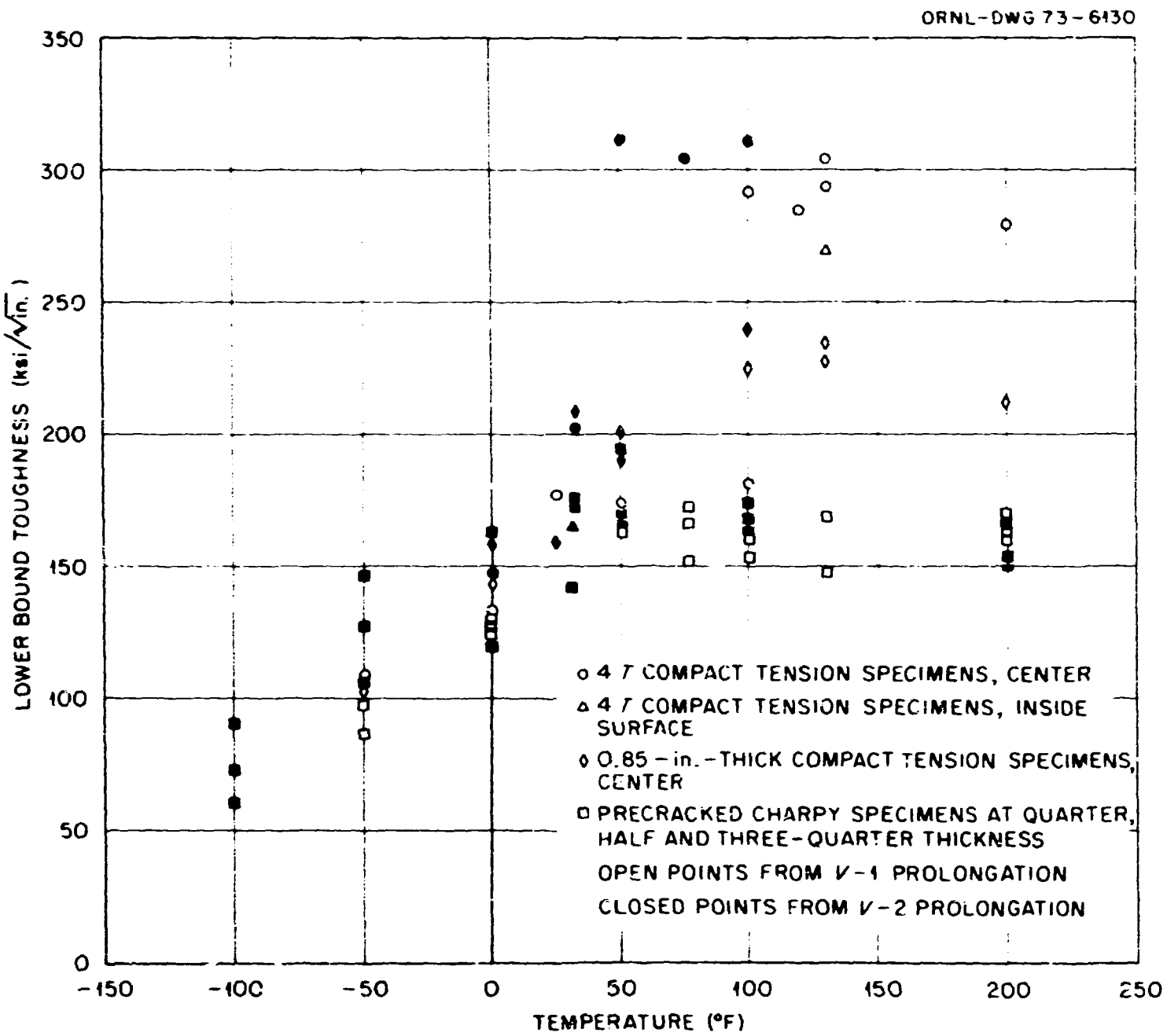

Fig. 4.13. Comparison of lower-bound static fracture toughness for vessels V-1 and V-2 between 4*t* compact tension specimens and smaller nonsurface specimens, circumferential orientation.

In Fig. 4.13 the comparison is seen to demonstrate the fracture toughness bounding property of the smaller specimens. Essentially, the smaller specimen value either equals the value from the larger one or is less. Exceptions occur only occasionally in the frangible and transition region, where the values are expected to be the same. For instance, the variability at the selected test temperature (32°F) of vessel V-2 demonstrates the general behavior in the transition region. Here an actual static fracture toughness of from 160 to 200 ksi $\sqrt{\text{in.}}$ is readily indicated, but the data would not seem to warrant further accuracy. The data are sufficiently indicative to allow reasonable evaluations based on either fracture mechanics or transition-temperature-oriented procedures.

References

1. F. J. Witt and T. R. Mager, *A Procedure for Determining Bounding Values on Fracture Toughness K_{Ic} at Any Temperature*, ORNL-TM-3894 (October 1972).

2. F. J. Witt, *The Equivalent Energy Method for Calculating Elastic-Plastic Fracture* (to be published).

5. MODEL VESSEL TESTS

One of the primary characteristics of research sponsored by the HSST program since its inception has been the testing of large thick specimens in conjunction with geometrically similar smaller ones. The test plan of the intermediate vessel is no exception. Such tests of the model vessels provide a direct comparison of the effect of thickness on fracture behavior between the vessel results and the results from the compact tension specimens described in the previous chapter. More specifically, it allows for a direct comparison of the volumetric energy ratios[1,2] and other parameters between the pressure vessels and the compact tension specimens. This chapter presents both the fabrication history of the vessels and the test results.

Design and Fabrication

A prime criterion for the model vessels was that they be, insofar as possible, both geometrically and metallurgically similar to the prototype vessel. Consequently, the cylinders of the model vessels were to be made from the prolongation with the axis of the model vessel parallel to the axis of the vessel. The limit on the outside diameter was 6 in. Since, however, specimens from the same location in the model vessel wall were planned for testing, an outside diameter of 5.54 in. was chosen for the vessel. This gave a scale factor of 7.06. The wall thickness of the model was 0.85 in. A minor exception to the condition of similarity was the heads or closures of the models, which were not analogous to the manway of the prototype vessel. However, since the heads are far removed from the flawed region, this deviation was considered insignificant. The final design for the models, including the weld design, is shown in Fig. 5.1. The materials from which the model vessels were to be fabricated are identified for both vessels in Fig. 4.1.

Once the vessel components were machined, the heads were welded to the cylinder using a preheat of 400°F. The root pass was made using a TIG weld, and the joint was completed using a medium-strength, low-hydrogen electrode (8010C-3). After the heads were welded on, each vessel was given a postweld heat

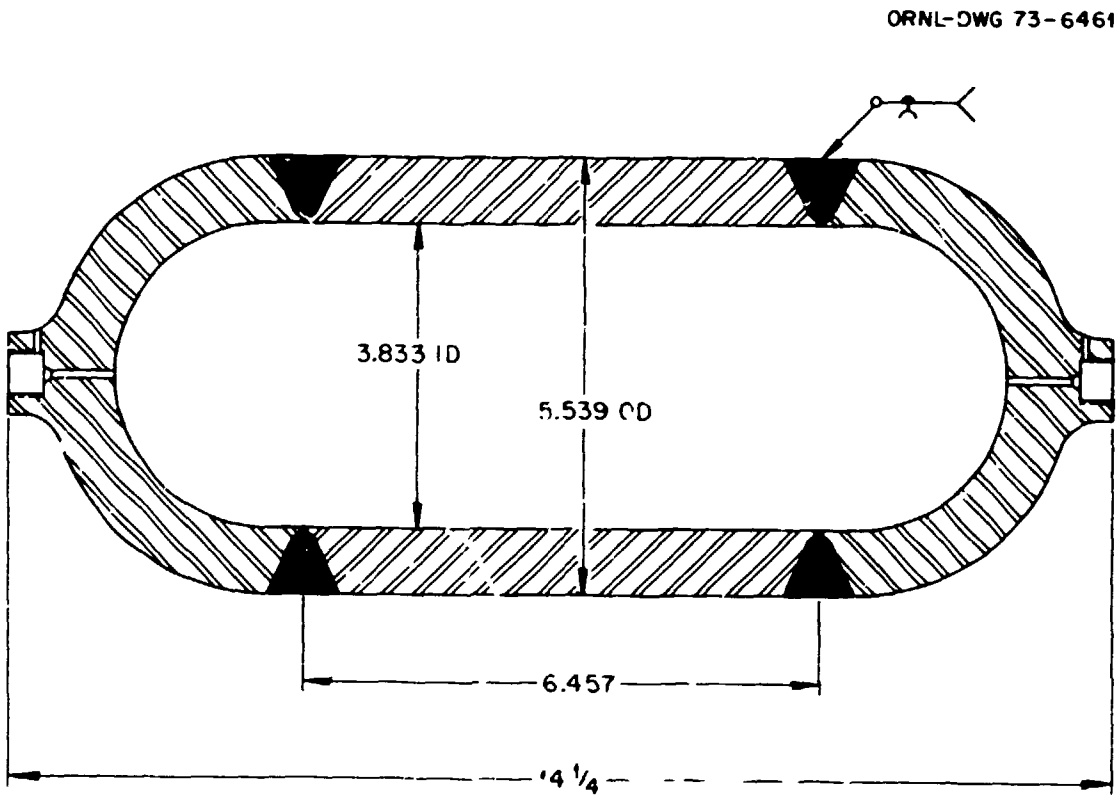

Fig. 5.1. Sketch of the 1/7.06 scale model vessels.

Fig. 5.2. Photograph of some model vessels.

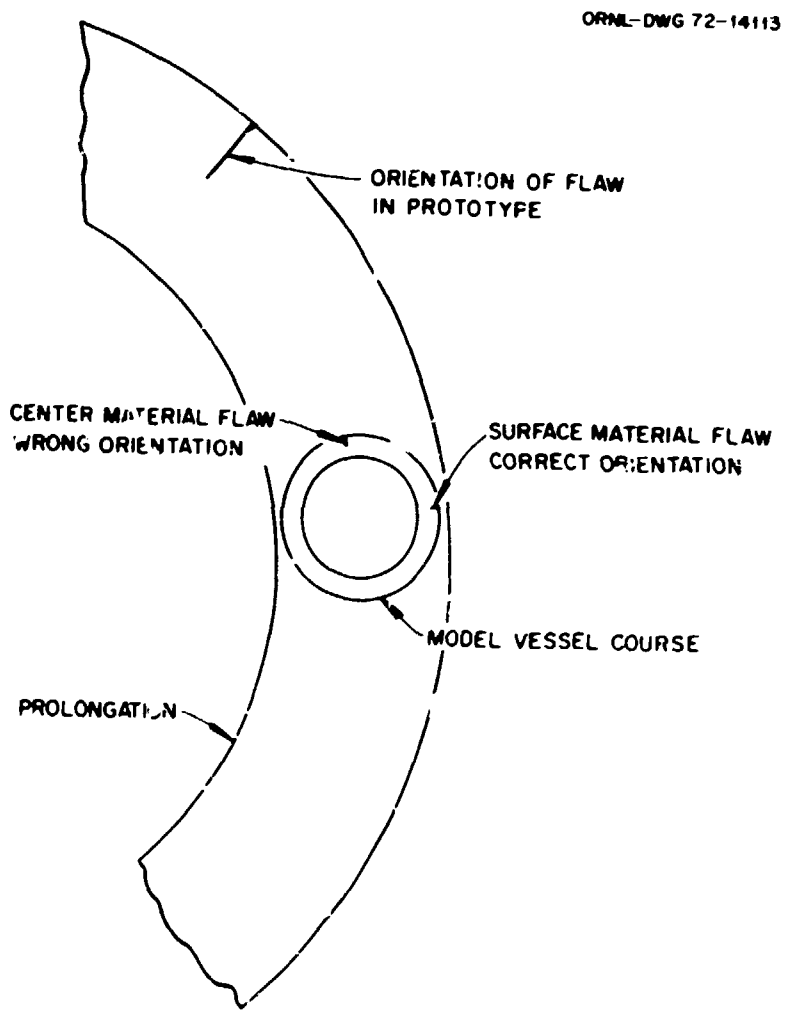

Fig. 5.3. Orientation of the cylindrical positions of the model vessels in the prolongations.

treatment of 2 hr in argon at 1100°F. Six vessels were fabricated from each of the vessel prolongation materials. Some finished vessels are shown in Fig. 5.2.

The model vessels were oriented as shown in Fig. 5.3. It may be observed that the models could not be truly metallurgically similar to the prototype vessel. This problem was minimized by carefully maintaining the identification of the near-surface materials (both outside surface of the prototype vessel and inside surface). This gives the choice of placing the flaws either in the near-surface materials of the prototype vessel or the center material. As shown in Fig. 5.3, a radially oriented axial flaw in the center material, however, would be oriented 90° to a similar flaw in the prototype vessel. A radially oriented axial flaw in near-surface material would be properly oriented with a similar flaw in the prototype vessel but would be well into the tougher near surface of the prototype vessel as compared with the flaw in the prototype vessel. This problem was circumvented, however, by taking specimens from both near-surface and center material (see Chap. 4) so that the fracture behavior of the vessel could be adequately evaluated.

The flaws were placed in the models by using the electron-beam weld procedures developed by Hudson and Canonico.[3] Briefly, a small notch was placed in the vessel, and an electron beam was passed through the notch (thus embrittling this region) with the vessel in a vacuum chamber. The notch region was filled with acid, and voltage was applied. Eventually the hydrogen from the acid and the residual stresses in the embrittled region resulted in the formation of a crack equal to the depth of penetration of the electron beam.

Test Conditions and Experimental Results of the Models from Vessel V-1 Prolongation

Since the model vessels were to be tested sufficiently prior to the prototype vessel to allow for data evaluation, a flaw size had to be selected for the models prior to completion of the investigation of the feasibility of placing a flaw in the prototype vessel. Such a flaw size selection was made, and the model vessels were flawed. The flaw was placed in center material in two of the vessels. Each vessel was instrumented with nine primary strain gages. The strain gage locations are given in Fig. 5.4 for models from V-1 vessel prolongation.

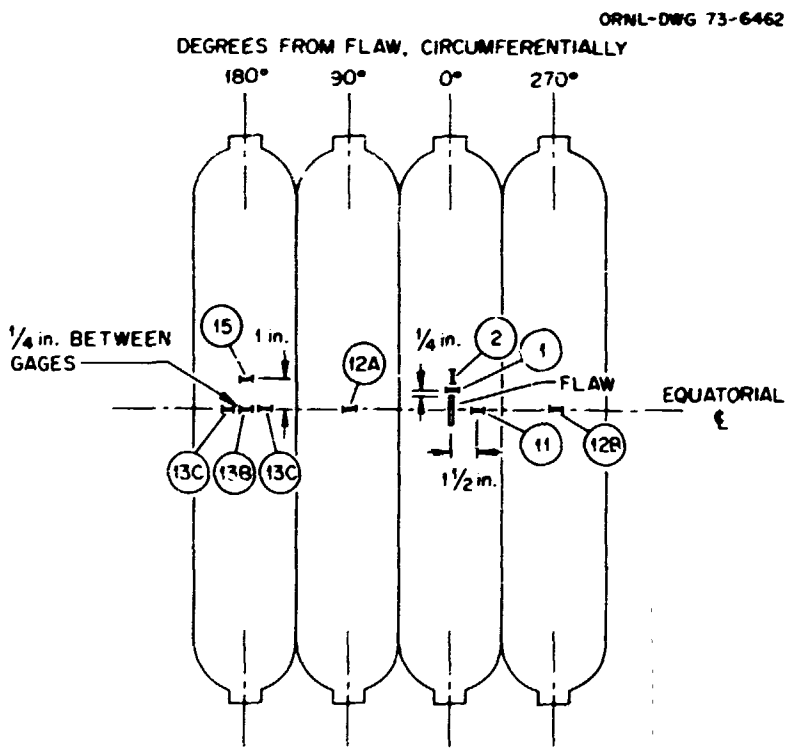

Fig. 5.4. Location of strain gages on model vessels from V-1 material.

Test temperatures for the models ranged between −35 and 130°F. Four vessels were tested at 130°F (the temperature selected for the prototype test), two with flaws in near outside surface material and two with flaws in center material. Plots of representative pressure-strain data for the vessels are given in Figs. 5.5 and 5.6. In Fig. 5.5 the circumferential strain in line with the flaw is quite large at fracture (exceeding 5%), while the axial strain at the same location and the circumferential strain near the unloaded crack surface are much less. Both are less than the circumferential strain 180° from the flaw. In Fig. 5.6 the unwanted metallurgical variability described previously (see Fig. 5.3) is emphasized. The center material has a lower yield pressure. Also, for the same size flaw, its location in surface material is apparently slightly better in terms of strain than for a location in center material for the orientation investigated. The test parameters and pertinent results are given in Table 5.1. The complete set of pressure-strain results are given in Appendix D.

The data most representative of the behavior of the vessel in the region of the flaw but with the flaw not present are those obtained at the same location of the flaw but on the opposite side 180° away. These data for the six vessels are given in Fig. 5.7.

In Fig. 5.7, the nominal outside circumferential yield pressure of the center material was less than that of the near-surface material. For a given pressure the strains after yielding of the center material always exceeded that of the near-surface material. The increase in yield pressure with lowering temperature was expected. The reproducibility of the pressure-strain results is noteworthy.

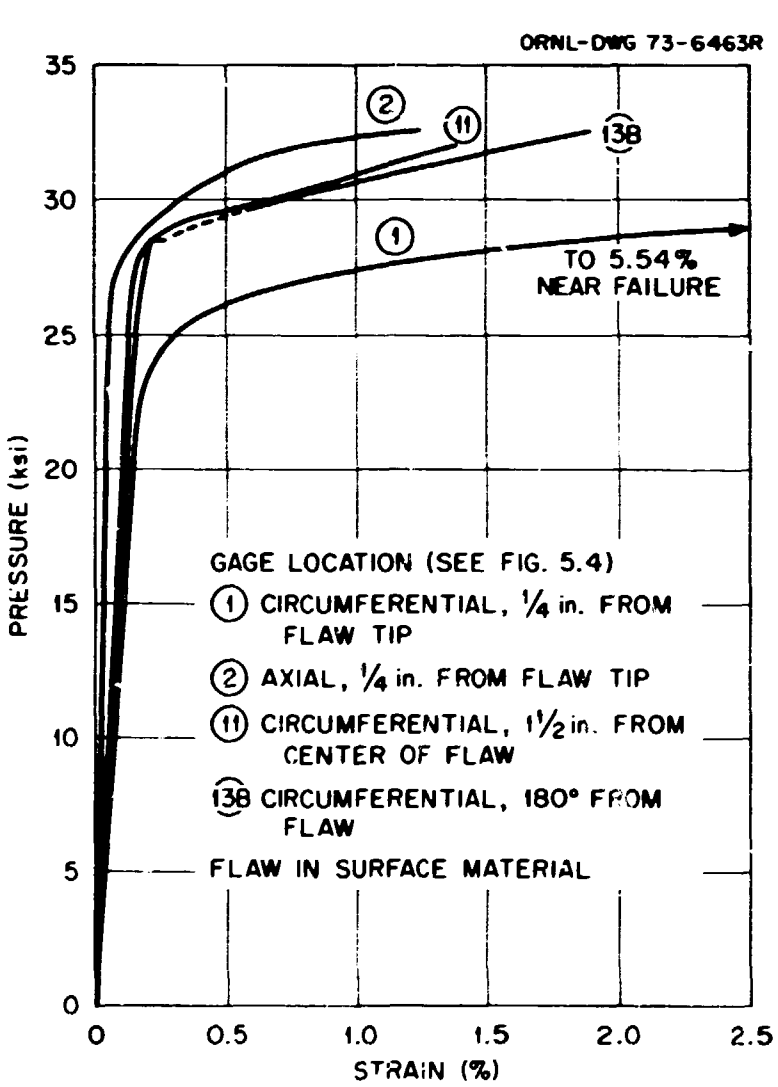

Fig. 5.5. Pressure-strain curves for region near flaw compared with pressure–circumferential-strain curve 180° from flaw. Model vessel VI-Al-F, no attempt made to define yield plateau.

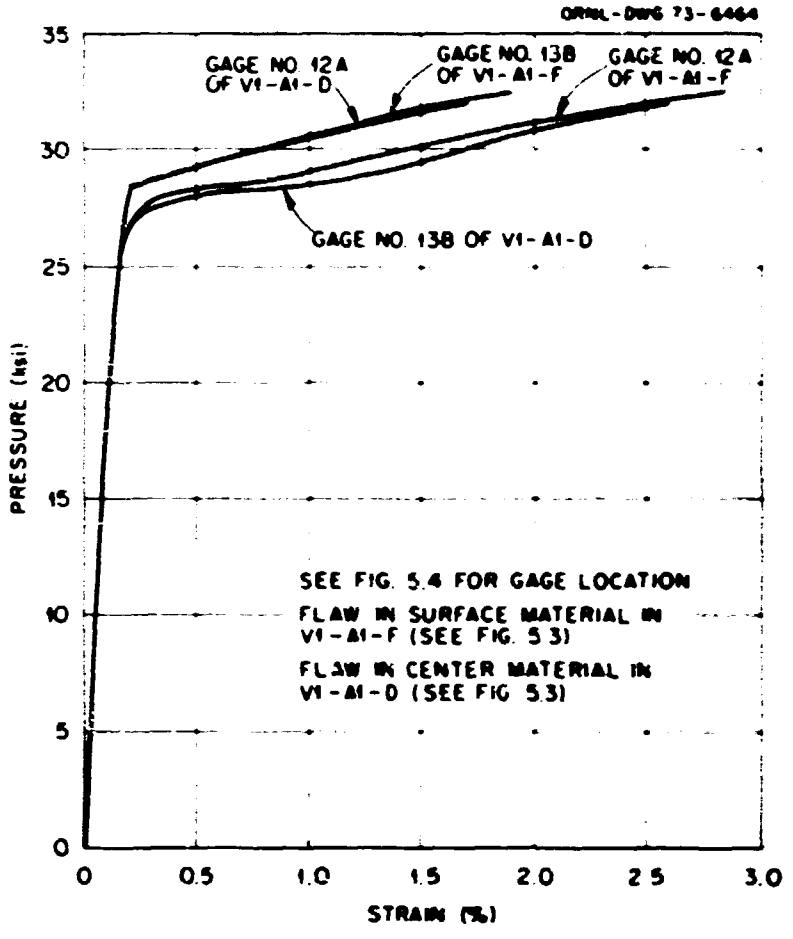

Fig. 5.6. Comparison of pressure-strain behavior in surface and center material of model vessels. See Fig. 5.3.

Table 5.1. Test parameters and pertinent results for model vessels from V-1 prolongations

Model No.	Test temperature (°F)	Flaw depth (in.)	Flaw length (in.)	Flaw location (see Fig. 5.3)	Burst pressure[a] (ksi)	Nominal strain at burst[b] (%)	Fracture mode
V1-A1-A	130	0.32	1.4	Center material	31.5	2.60	Leak
V1-A1-B	0	0.32	1.4	Surface material	35.0	1.86	Split, no fragment
V1-A1-C	130	0.32	1.4	Surface material	32.2	1.66	Leak
V1-A1-D	130	0.33	1.4	Center material	32.3	2.66	Leak
V1-A1-E	−35	0.31	1.4	Surface material	31.0	0.182	Split, no fragment
V1-A1-F	130	0.32	1.4	Surface material	32.5	1.90	Leak

[a]Maximum pressure in vessel.
[b]Circumferential strain 180° from flaw - strain gage 13B (see Fig. 5.4).

The failure of the vessel (V1-A1-E, Table 5.1) tested at −35°F was significant in that it failed at a much lower strain than would be expected based on the corresponding behavior of the compact tension specimens, discussed in Chap. 4. Since some difficulty was experienced in testing this vessel due to the low temperature, additional testing was planned. As seen later, this vessel test was as noteworthy as any performed, although the fact was not appreciated at that time.

The increment in pressure with no increment in strain at the near-failure pressure for vessel V1-A1-F clearly indicates (based on similar behavior from the other tests) that the strain is ready to move across the yield plateau. Actually, at the yield plateau the strain increases to about 0.5% or over with no increment in pressure. To actually define the behavior experimentally is rather time consuming; for example, at initial

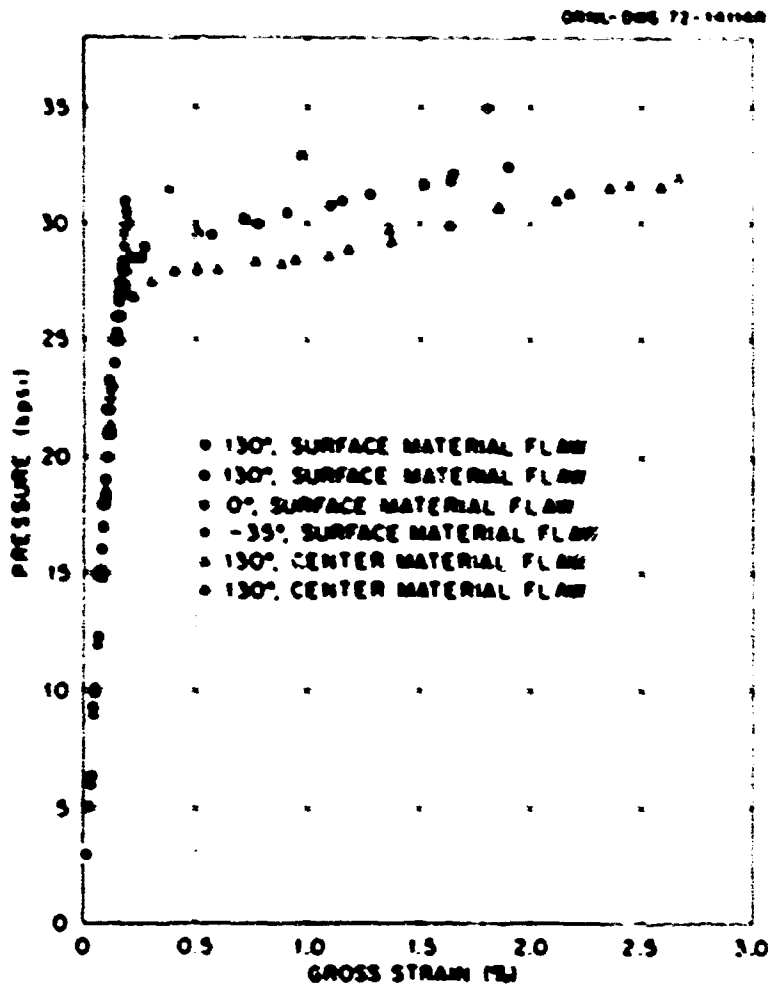

Fig. 5.7. Pressure–circumferential-strain curves 180° from flaw (gage 13B, Fig. 5.4) for the six model vessels from V-1 material.

yielding, the pressure drops, and regaining the exact same pressure yields the vessel further, etc. Finally, regaining the same pressure produces no further straining. A higher pressure is then required to produce additional strain. Without following this procedure the yield plateau in the pressure-strain curve is seldom accurately determined experimentally.

The fracture mode of the model vessels varied. As shown in Table 5.1, the vessels tested at 130°F all exhibited a relatively small leak, while the two tested at 0 and −35°F presented end-to-end fractures which arrested in the heads. Both types of fracture are seen in Fig. 5.8.

The flaw sizes for the model vessels are given in Table 5.1. For a scale factor of 7.06, the flaw size scaled to that for the prototype vessel is about 2.26 in. deep by 9.9 in. long, which contrasted considerably with that which was actually in the vessel, as discussed later.

Test Conditions and Experimental Results of the Models from the Vessel V-2 Prolongation

Only four of the six model vessels from the prolongation of vessel V-2 were tested prior to the test of vessel V-2. Since the actual flaw size in vessel V-1 was available prior to the test of the vessel, such a flaw scaled to the model was placed in this series of vessels. As discussed later, the flaws in vessels V-1 and V-2 were to be the same size and shape. A comparison of the flaw sizes in vessels V-1 and V-2 with the flaws in both series of models is shown in Fig. 5.9. The square corners on the model flaws are due to the procedure of initiating the electron-beam welding. The test parameters for the V-2 model vessels are given in Table 5.2, and strain gage locations are given in Fig. 5.10. The large number of gages indicated in Fig. 5.10 was used only on one vessel. The pressure-strain results from all four tests are given in Appendix D.

PHOTO 4219-73

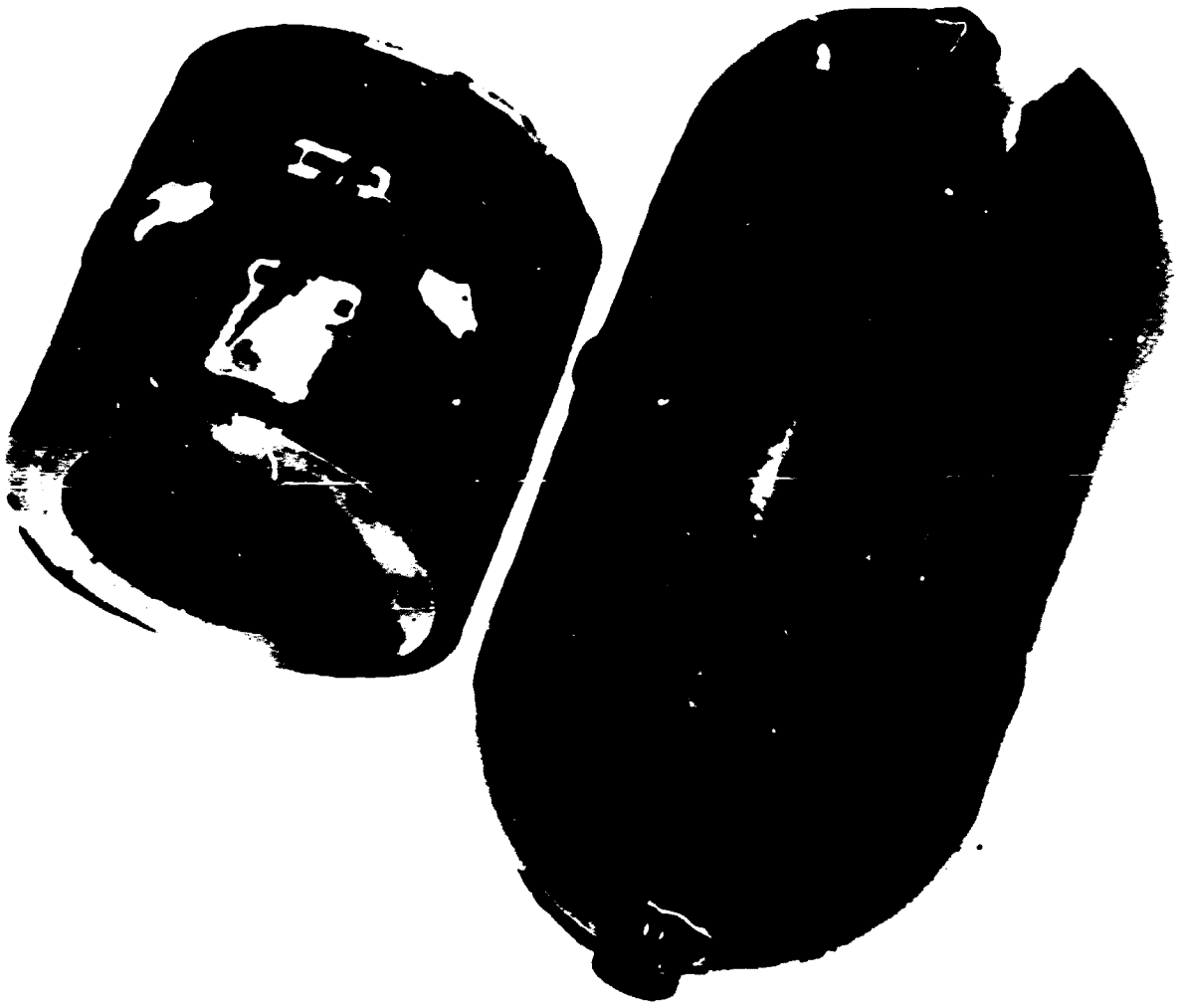

Fig. 5.8. Fracture modes demonstrating both leakage (vessel V1-A1-F, 130°F test, heads removed for reuse) and extensive rupture (vessel V1-A1-E, −35°F test).

ORNL-DWG 73-6465

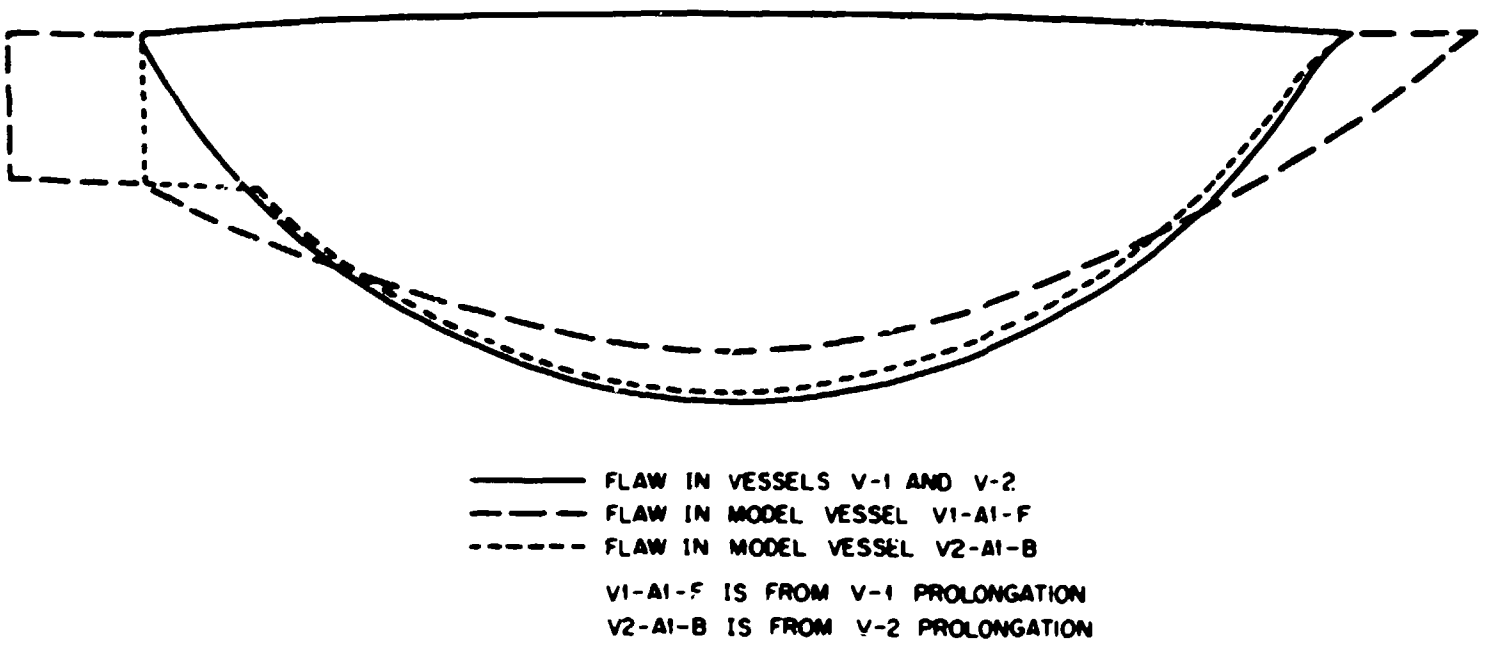

Fig. 5.9. Comparison of flaws in vessels V-1 and V-2 with flaws in two model vessels scaled to vessels 6 in. thick. Vessel V-1 and the models were tested at 130°F.

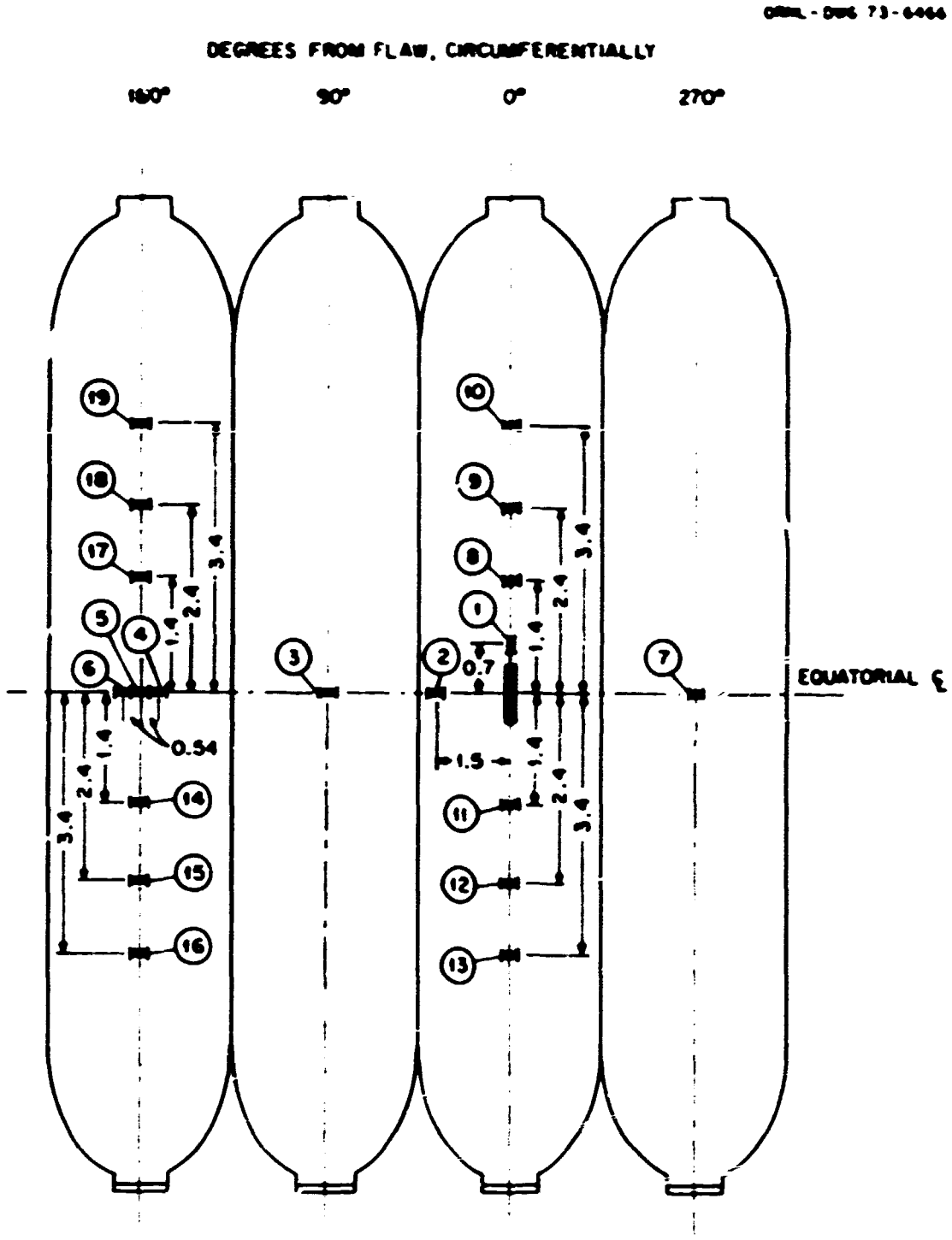

Fig. 5.10. Strain gage locations for the model vessels from vessel V-2 prolongation.

Table 5.2. Test parameters and pertinent results for model vessels from V-2 prolongations

Model No.	Test temperature (°F)	Flaw depth (in.)	Flaw length (in.)	Flaw location (see Fig. 5.3)	Burst pressure[a] (ksi)	Nominal strain at burst[b] (%)	Fracture mode
V2-A1-A	32	0.35	1.15	Center material	35.5	2.79	Split, no fragment
V2-A1-B	130	0.36	1.14	Surface material	34.7	2.39	Leak
V2-A1-D	−55	0.36	1.15	Surface material	34.7	1.43	Three fragments
V2-A1-F	32	0.36	1.14	Surface material	36.5	2.49	Leak

[a]Maximum pressure in vessel.
[b]Circumferential strain 180° from flaw -- strain gage 5 (see Fig. 5.10).

Since the fracture behavior of the model vessels was used by some analysts to predict the behavior of vessel V-1 (see Chap. 9 and Appendix C), the effects of the discrepancy in the flaw size of the models from vessel V-1 prolongation and vessel V-1 were first evaluated by testing a vessel at 130°F. A comparison of the circumferential outside surface pressure-strain curves in the region of the flaw but 180° removed is seen in Fig. 5.11. Apparently the shape and size of the flaw had a significant effect on the failure strain. As seen in Appendix C, this result made a considerable difference in prediction of the behavior of vessel V-1 using the equivalent-energy method.

A comparison of the four models from the V-2 prolongation of the outside surface circumferential pressure strain curves in the region of the flaw but 180° removed is given in Fig. 5.12. While the fracture strain of the vessel tested at −55°F was a surprise if compared with the vessel tested at −35°F in the vessel V-1 series, it will be seen later that the behavior of the −55°F test vessel is consistent with that of compact tension specimens of similar thickness and location.

The vessels tested at 130 and 32°F exhibited leakage (see Fig. 5.13), while the ones tested at 0 and 55°F presented much more severe fractures. As seen in Fig. 5.14, an end-to-end crack was developed in the vessel tested at 32°F (center material), while the vessel (fracture strain was 1.4%) tested at −55°F fragmented into three pieces.

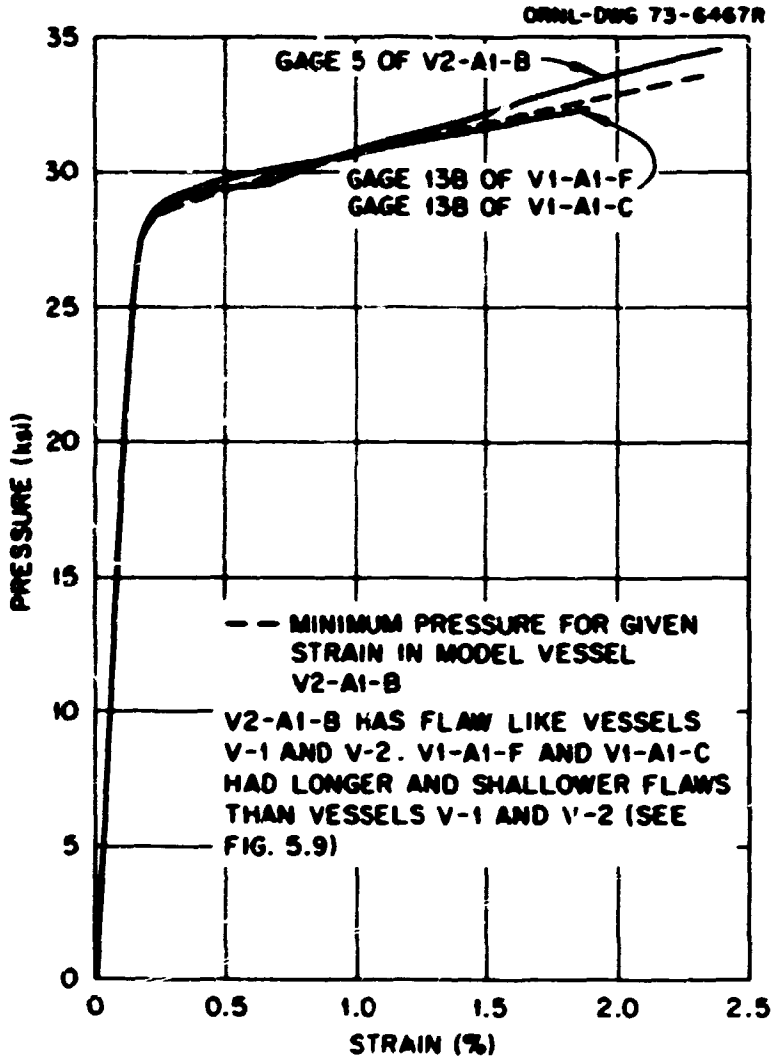

Fig. 5.11. Comparison of pressure-strain curves 180° from flaws in model vessels with different flaw shapes. No attempt made to define yield plateau.

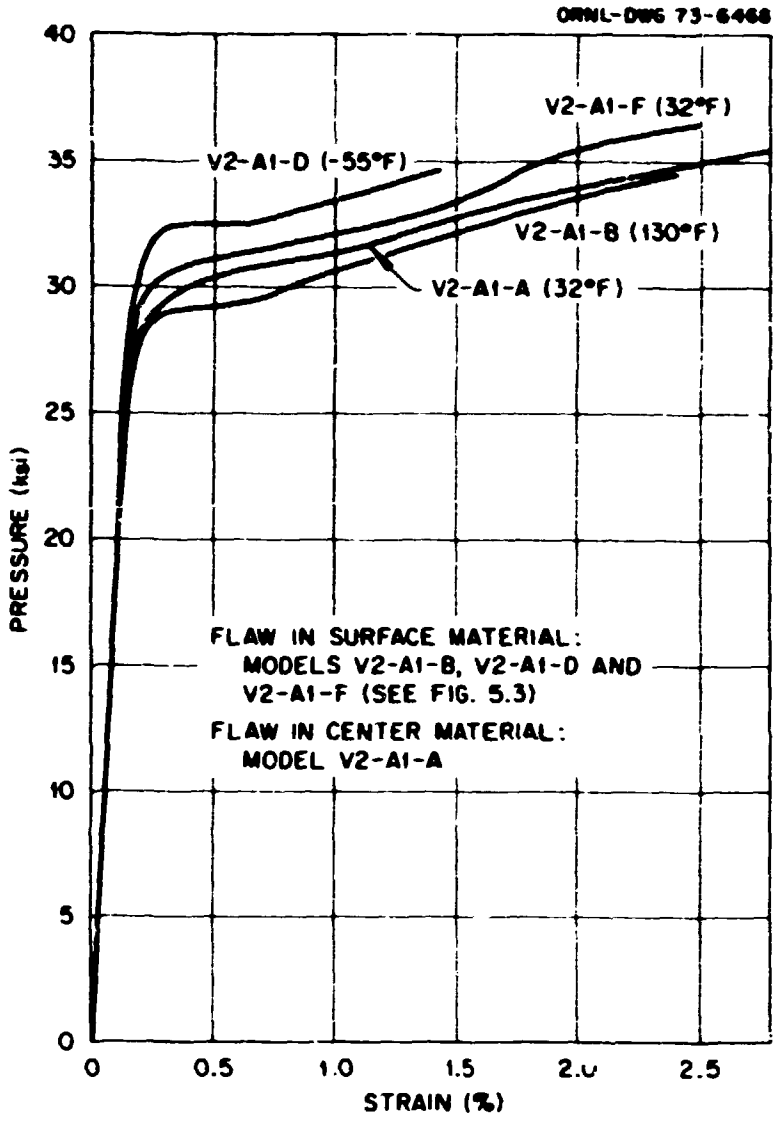

Fig. 5.12. Pressure–circumferential-strain (gage 5, Fig. 5.10) curves 180° from flaw for model vessels from V-2 material. Yield plateau defined in test of model V2-A1-D only.

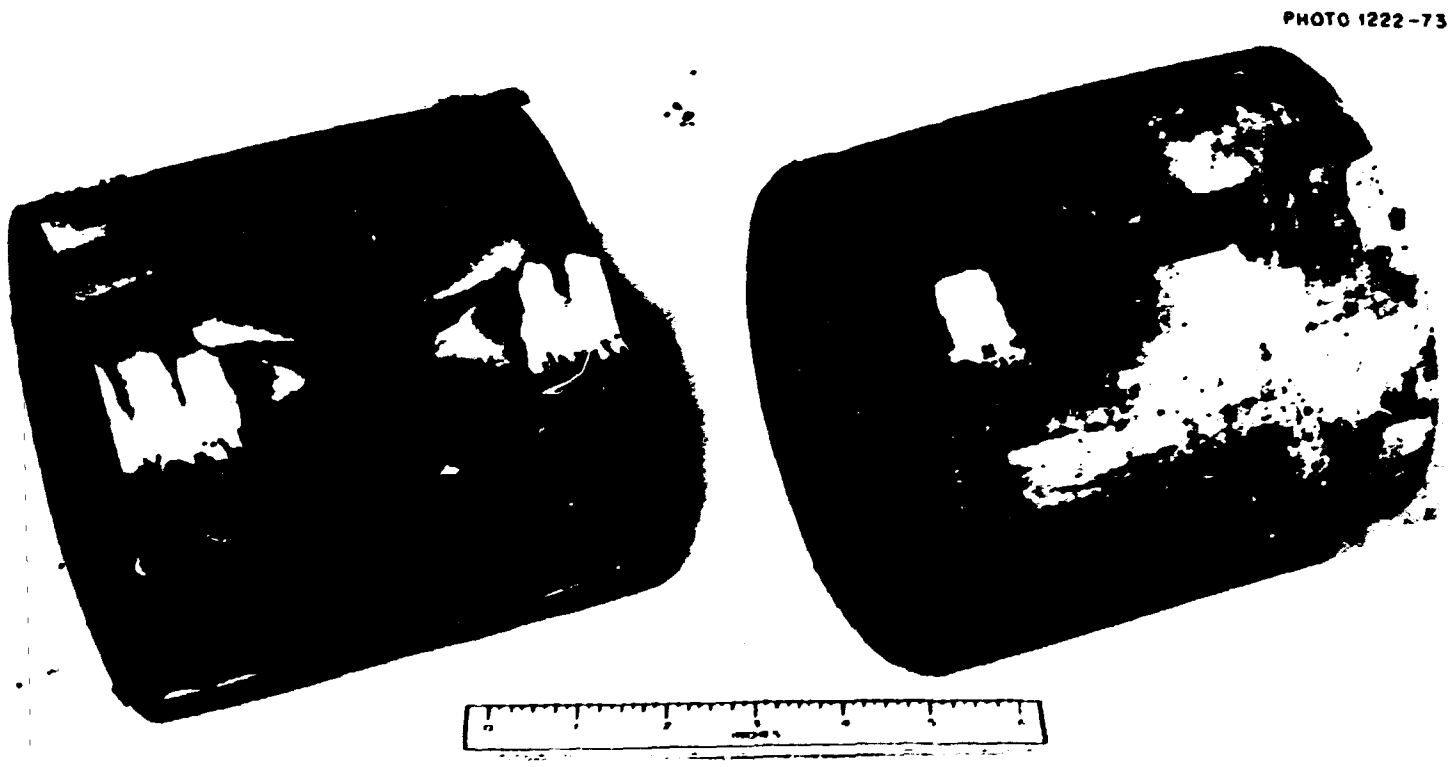

Fig. 5.13. Fracture mode of vessels tested at 130 and 32°F. V-2 material, flaws in surface material, heads removed for reuse.

PHOTO 4221-73

Fig. 5.14. Fracture mode for model vessel tested at 32 and −55°F respectively. V-2 material; flaw in center material for 32°F test; flaw in surface material for −55°F test.

References

1. F. J. Witt, *The Equivalent Energy Method for Calculating Elastic-Plastic Fracture* (to be published).
2. F. J. Witt, "Factors Influencing a Quantitative Safety Assessment of Water Reactor Pressure Vessels," to be published in the *Proceedings of the National Topical Meeting on Water Reactor Safety, American Nuclear Society, May 26–28, 1973, Salt Lake City, Utah (1973).*
3. D. A. Canonico and J. D. Hudson, "Technique for Generating Sharp Cracks in Low Alloy High-Strength Steels," paper 20, 5th Annual Information Meeting, Heavy-Section Steel Technology Program, Oak Ridge National Laboratory, Oak Ridge, Tenn. Mar. 25–26, 1971.

6. BASIS FOR SELECTION OF FLAW SIZE AND TEST TEMPERATURE

The criteria for selecting the flaw size required: (1) a much larger flaw than could be missed by preservice nondestructive testing of a typical nuclear reactor vessel of 6-in. wall thickness or could be grown from an acceptable flaw indication that measured less than half the wall thickness; (2) a flaw small enough that significant plastic strain would occur prior to failure at a temperature of at least 200°F; (3) one that could be sharpened; and (4) one that could be, when scaled by the prototype-model scale factor (7.06, as discussed previously), accurately placed in the complementary model vessel tests. Since these were essentially the same criteria used for selecting the flaw size in the tensile specimen tests containing sharp flaws,[1-5] that flaw size was selected. The machine notch was cut by a circular blade having a 5-in. radius, forming a section of 8 in. surface length and 2 in. depth. The technique for sharpening flaws by local fatigue on the 6-in. flawed tensile specimens was, with some changes, transferable to the vessels (see Chap. 7). A half inch of crack growth at middepth of the machined notch was found necessary to obtain some flaw growth near the surface as desired (the same phenomenon as noted for the flawed tensile specimens). The final configuration selected was a fatigue-sharpened flaw $2\frac{1}{2}$ in. deep and 8 in. long with some flaw growth near the surface.

Specimens, indeed structures, are known to exhibit a rapid increase in toughness over a small temperature range using almost any measure of toughness. Often within this narrow temperature range erratic behavior can occur. Duplicate tests at the same temperature can produce widely varying results. Such variation may be attributed to a combination of the test being performed and the fact that all materials exhibit a more or less marked degree of variability. The pressure vessel offers the best example of test preciseness as far as loading goes, but flaw preparation and material variations still contribute to the variation of results, especially in the transitional region. It seemed logical, then, for a first test, to select a temperature at which tough behavior with a minimum of variation is anticipated. Indeed, higher initiation toughness usually occurs at temperatures below what is considered shelf behavior. As seen previously, the greatest initiation toughness probably occurs slightly above 100°F. However, results from 4-T compact tension specimens indicated a pop-in behavior occurring at 100°F, whereas at 120°F this behavior did not occur (see Figs. 6.1 and 6.2). If pop-in arrest behavior is indicative of near nonarrest behavior, then a test

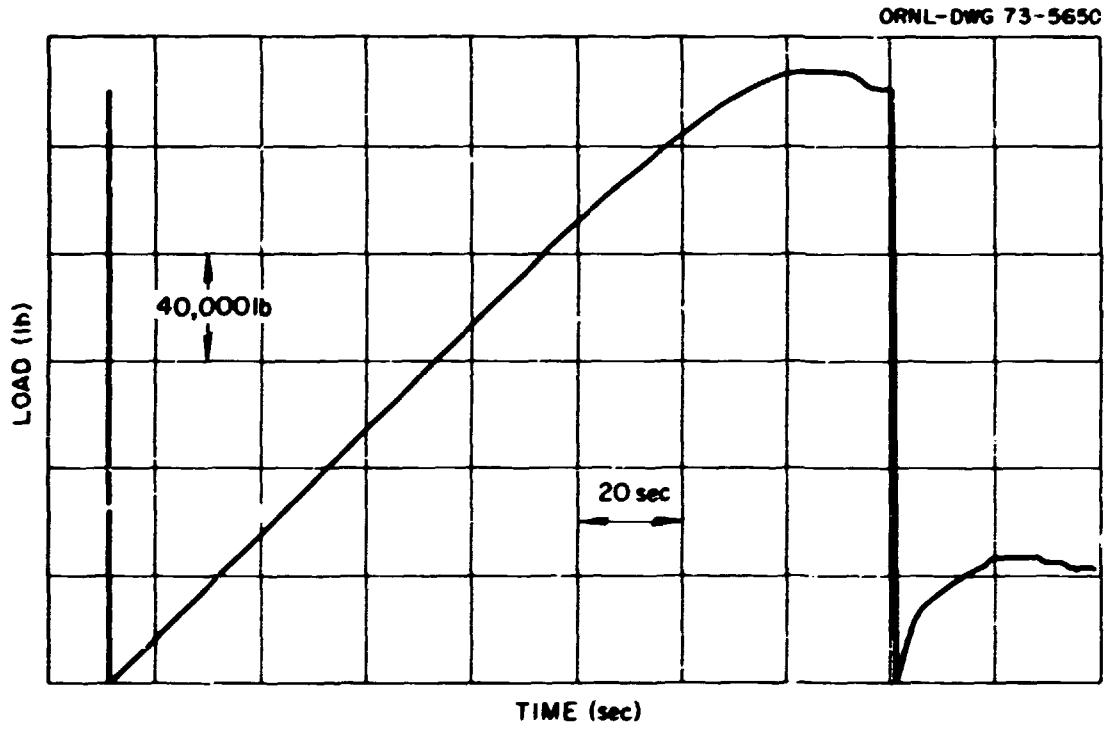

Fig. 6.1. Load-time curve for 4t compact tension specimen V1B-2 tested at 100°F.

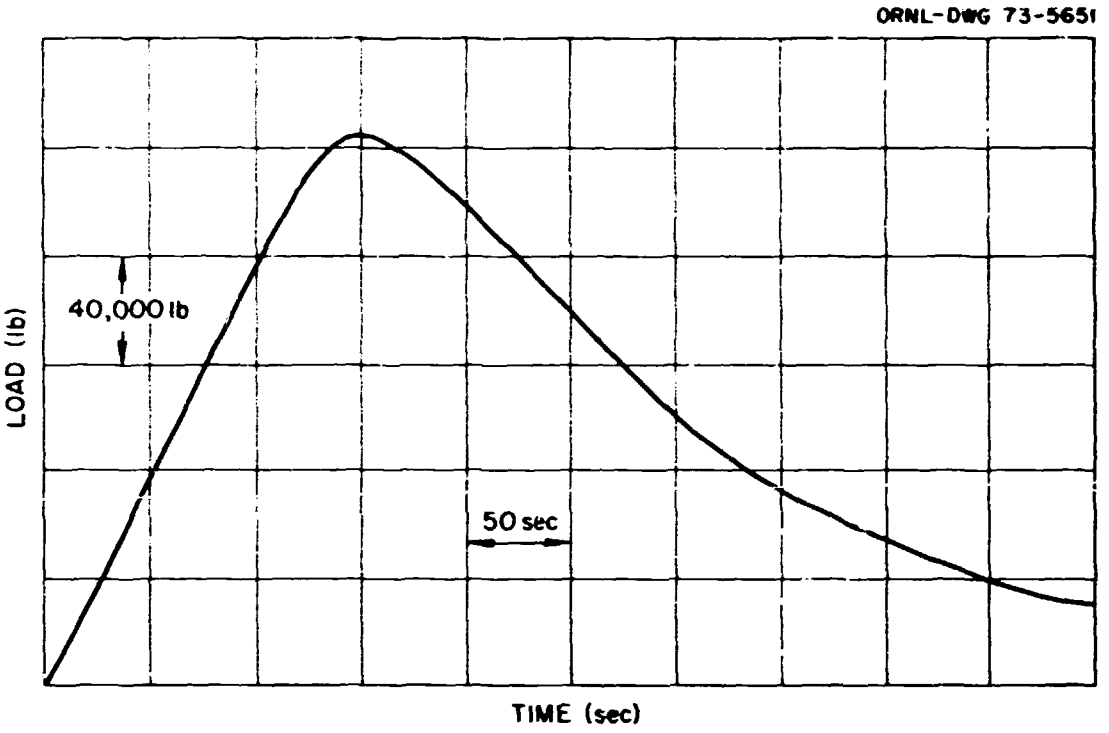

Fig. 6.2. Load-time curve of 4t compact tension specimen V1B-1 tested at 120°F.

below 120°F is not warranted if a leak-type fracture is desired. Since, however, the vessel is 6 in. thick, a 10° margin was selected to account for the increase in thickness. Thus the test temperature for vessel V-1 was selected as the lowest temperature at which tough ductile fracture would occur, but high enough to avoid pop-in initiation. This would indicate that crack arrest would occur if the vessel could dissipate its stored energy quickly enough upon rupture. However, as discussed later, such was not the case.

The temperature selection of vessel V-2 was essentially to be based upon the success in meeting the objectives of vessel V-1. Indeed the objectives were fully met – to wit, a ductile rupture did occur without pop-in; the fracture behavior was successfully calculated (although somewhat in retrospect), and significant data were obtained. The crack did not arrest, but such was not the primary objective of this test.

Since vessel V-2 was, as near as possible, exactly the same as vessel V-1 and with the success noted above, it was decided to test vessel V-2 in the rapidly increasing toughness transition for the vessel but above the temperature at which brittle fracture would apply based on the available specimen data. Again the transition fracture behavior of the vessel was assumed to be that depicted by examining the fracture toughness K_{Icd} data (see Chap. 4). With the limited amount of data available, the test temperature was selected as 32°F.

References

1. S. C. Grigory, *Six-Inch-Thick Flawed Tensile Tests, First Technical Summary Report, Longitudinal Specimens 1 through 7*, HSSTP-TR-18, Southwest Research Institute, San Antonio, Tex. (June 1972).
2. S. C. Grigory, *Tests of Six-Inch-Thick Flawed Tensile Specimens, Second Technical Summary Report, Transverse Specimens Numbers 8 through 10, Welded Specimens Numbers 11 through 13*, HSSTP-TR-20, Southwest Research Institute, San Antonio, Tex. (June 1972).
3. S. C. Grigory, *Tests of Six-Inch-Thick Flawed Tensile Specimens, Third Technical Summary Report, Longitudinal Specimens Numbers 14 through 16, Unflawed Specimen Number 17*, HSSTP-TR-22, Southwest Research Institute, San Antonio, Tex. (August 1972).

4. S. C. Grigory, *Tests of Six-Inch-Thick Flawed Tensile Specimens, Fourth Technical Summary Report, Tests of One-Inch-Thick Flawed Tensile Specimens for Size Effect Evaluation*, HSSTP-TR-23, Southwest Research Institute, San Antonio, Tex. (June 1973).

5. S. P. Ying and S. C. Grigory, *Test of Six-Inch Thick Tensile Specimens, Fifth Technical Summary Report, Acoustic Emission Monitoring of One-Inch and Six-Inch-Thick Tensile Specimens*, HSSTP-TR-24, Southwest Research Institute, San Antonio, Tex. (November 1972).

7. PREPARATION OF VESSELS FOR TESTING

Flaw Sharpening

One of the primary tasks associated with the first intermediate vessel tests was the sharpening of the flaws. The general technique used was the same local fatiguing of a notch as was used in the 6-in. tensile specimens.[1] Essentially, a notch of the approximate shape of the desired crack is carefully sealed and then filled with oil through a small access hole. To grow the crack, the oil in the notch is repeatedly pressurized to about 20,000 psi.

The actual cyclic pressure was determined by the desired cyclic stress intensity factor at the tip of the fatigue growing crack, according to the expression

$$\Delta p = \frac{\Delta K_I}{C\sqrt{\pi a}} ,$$

where C is the fracture mechanics shape factor for uniform stress. For example, with a cyclic pressure of 20,000 psi, a = 2.0 in., and a calculated value of C = 0.9, the value of ΔK_I is 45,000 psi $\sqrt{\text{in.}}$. Details of the procedure for sharpening the flaw are given below.

Since none of the available machine tools had enough capacity to support the vessels (12 tons) while the notch and sealing flat were being machined, some special tools were designed and fabricated for these jobs. The first was a modified version of a commercially available saw used for cutting masonry or heavy timbers. As can be seen in Fig. 7.1 the saw was mounted on a large counterweighted arm, which in turn was mounted on a saddle, held to the vessel with a chain. The depth of cut and the rate at which the blade was fed into the vessel wall were controlled by a lever, which can be seen in the top of Fig. 7.2.

Once the notch had been cut to the desired depth, a flat area about $\frac{1}{32}$ in. deep was ground onto the surface to provide a sealing surface. Again a holder for a commercially available tool was fabricated (see Fig. 7.3). Basically, the device consists of a guide bed and a clamp to hold the surface grinder in the bed. The feed rate is controlled by indexed levers. Following grinding, it was necessary to hand finish the surface with a parallel bar and emery paper.

Sealing the notch presented a more difficult problem on the vessels than on the 6-in. tensile specimens.[1] The rectangular cross section and compact size of the tensile specimens made the fabrication and application of a heavy clamp relatively simple, but with the vessels it was necessary to make a much larger clamping device. Two versions are shown in Figs. 7.4 and 7.5. In the earlier version (Fig. 7.4), 16 turns of cable were made around the vessel and over two mounts on the sealing device, and the cables were then tightened by raising the mounts with jack bolts. Although some difficulty with relaxation was experienced, the technique was made to work by retightening the cables after allowing them to relax overnight, but before a pressure load was applied to the seal. A more effective approach is shown in Fig. 7.5, where the cables have been replaced by 1-in.-thick steel straps. The men in the figure are applying a load to the straps by tightening the jack bolts. In practice, it was found that four men were needed to get the necessary prestress on the straps and hence on the sealing surface. Without the necessary force, the O-ring seal would leak regardless of how carefully the sealing surface had been prepared.

Measuring the crack depth also required new techniques. On the 6-in.-thick tensile specimens, it was possible to follow the growth of the crack by moving an ultrasonic transducer on a face of the specimen that was parallel to the crack. With the vessel geometry, this could not be done, so it became necessary not

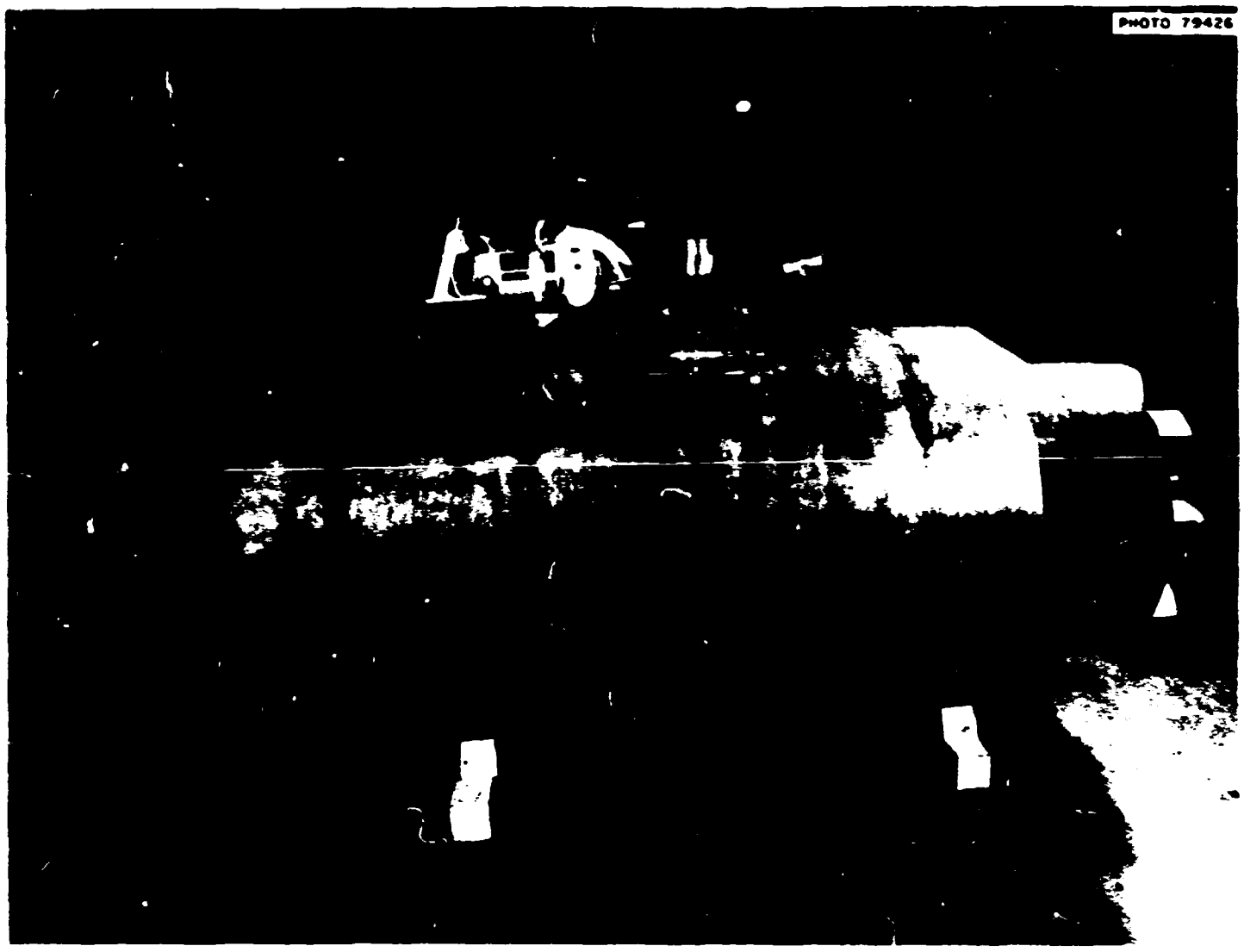

Fig. 7.1. Saw mounted on vessel in preparation for cutting the notch.

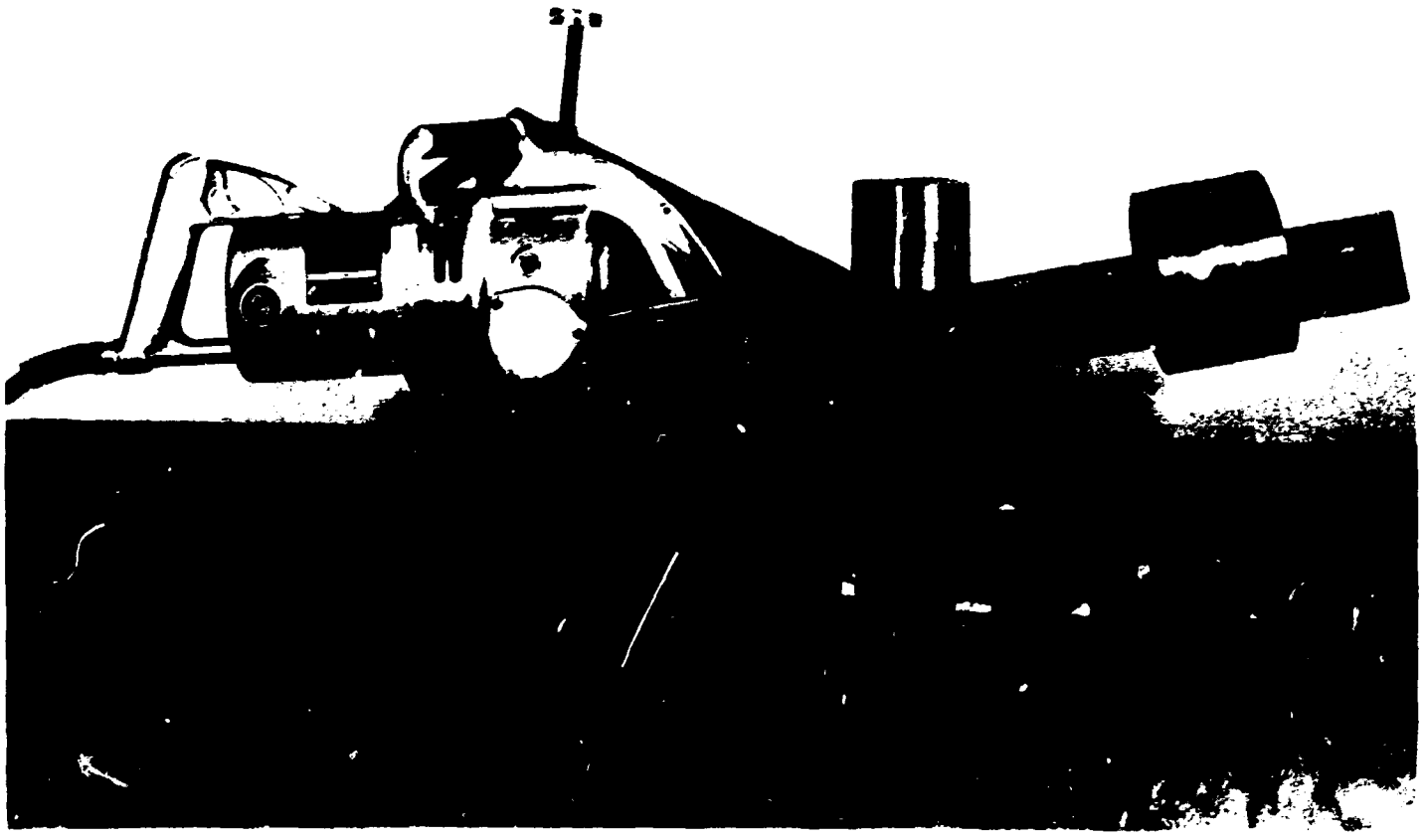

Fig. 7.2. Notch partially cut in vessel.

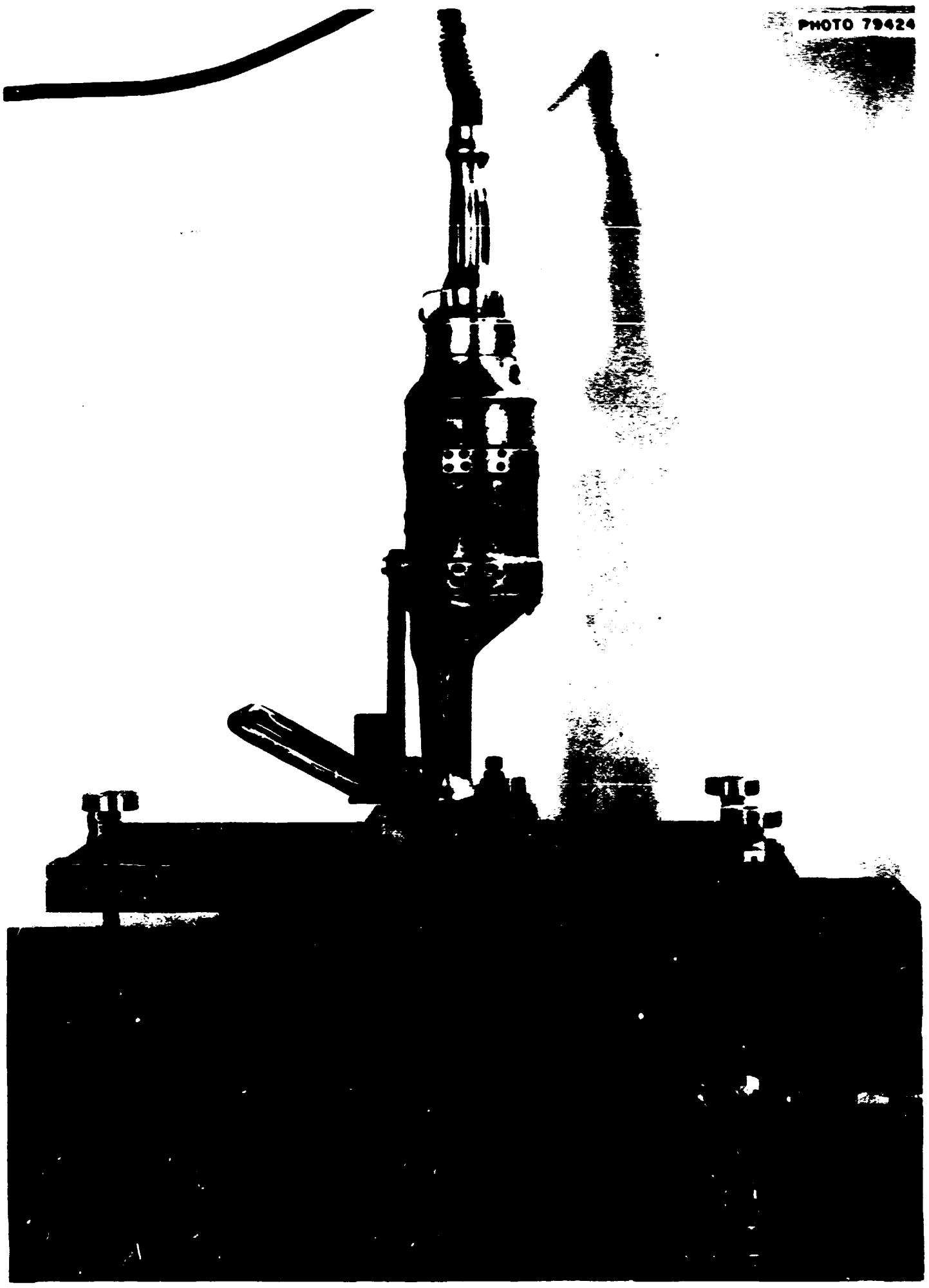

Fig. 7.3. Surface grinder attached to vessel in preparation for grinding a small flat area to provide a sealing surface.

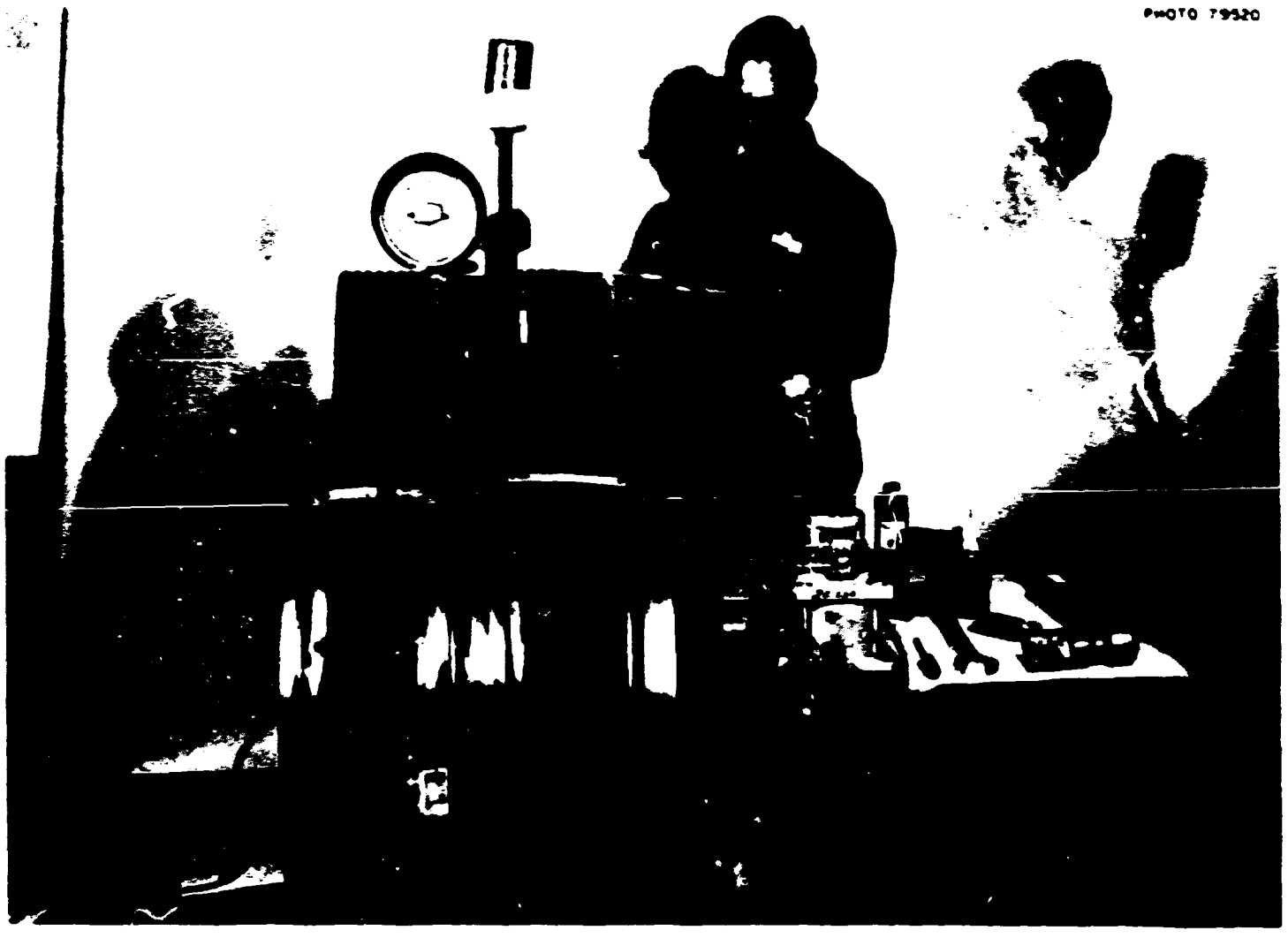

Fig. 7.4. Clamping device using cables for obtaining a seal being evaluated on a vessel prolongation.

Fig. 7.5. Clamping device using metal straps for obtaining a seal shown on vessel V-1.

Fig. 7.6. Setup for monitoring crack growth on a vessel.

only to rely on shear-wave ultrasonics but also to be able to infer the change in the size of the crack with a transducer that was forced to move along a curved path. Such movement was monitored by a guide bar cemented to the side of the vessel, as shown in Fig. 7.6. This bar acted as a guide for the ultrasonic transducer as it was pushed or pulled by an indexing motor and a pinion gear hung on the side of the vessel.

Because of the cylindrical geometry, three practice runs were made on a prolongation from one of the forgings. Such a run in progress is shown in Fig. 7.4. After each run the region around the flaw was burned out, chilled in liquid nitrogen, and then broken open by driving a chisel into the starter notch. After the first practice run, it was found that the flaw was considerably smaller than predicted. On the second run it was slightly larger, and on the third run the size was almost exactly as predicted. The various flaw sizes are shown in Fig. 7.7. As seen later, the flaws turned out to be within 0.10 in. of the desired depth of 2.5 in. The crack growth detection was performed under the direction of K. K. Klindt, Inspection Engineering Department, ORNL.

Both during the practice runs mentioned above and in the actual sharpening of the flaws in the vessels, it was found that more than three times as many cycles were required to grow the same amount of crack in a vessel as in a 6-in. tensile specimen, say 75,000 cycles instead of 20,000. This was true even though the starter notches were the same size and the cyclic pressures were the same. It seems likely that the difference in geometry was more important than the difference in material.

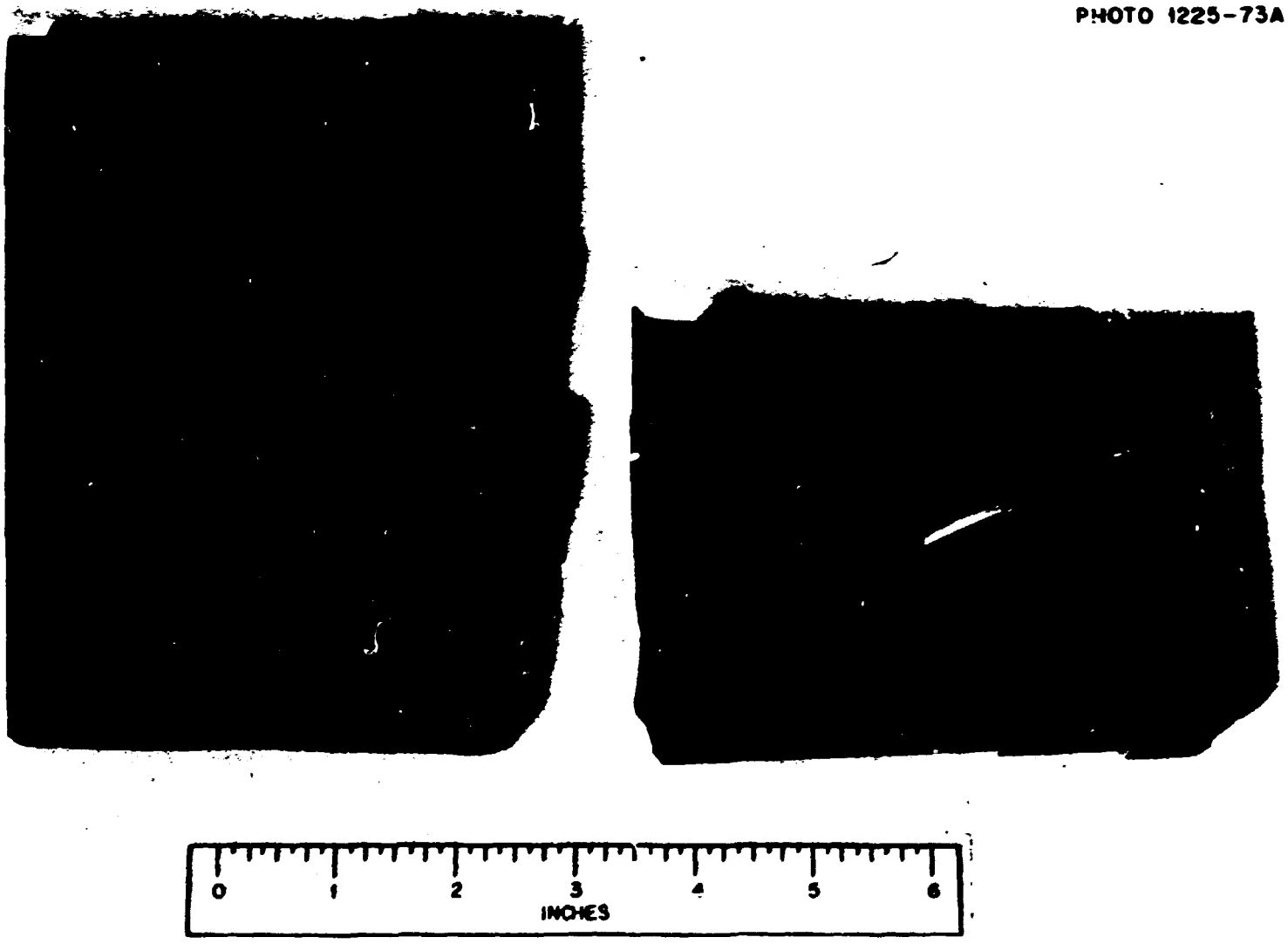

Fig. 7.7. Various flaw sizes obtained in a vessel prolongation during the development of the flaw monitoring procedure for the vessels. Arrows define fatigue growth.

Instrumentation

Strain-gage instrumentation. Approximately 90 quarter-inch-long high-elongation strain gages were cemented to vessel V-1 and a somewhat smaller number to V-2. The details of the cementing procedure are discussed at length in Appendix A. About 30 strain gages were placed on the inside of each vessel and almost twice as many on the outside. (The technique used for sealing the lead wires is also discussed in Appendix A.)

The diagrams in Fig. 7.8 show the general instrumentation plan for vessels V-1 and V-2; specific details are given in Fig. 7.9 and 7.10.

Thermocouple instrumentation. About 12 Chromel-Alumel thermocouples were used to monitor the temperatures of both vessels before and during the tests. See Fig. 7.8 for locations of thermocouples.

Crack-opening displacement measurements. A dial indicator mounted on a short post adjacent to the flaw was positioned to measure the motion of another post on the opposite side of the flaw. Two approaches were used to record the readings on the dial. The camera of a closed-circuit television set was focused on the notch and the dial. As the pressure was increased, personnel in the control room could watch the notch open and at the same time record the readings on the dial indicator. As a backup for the TV camera a solenoid-controlled 35-mm still camera was also focused on the notch and dial. A digital

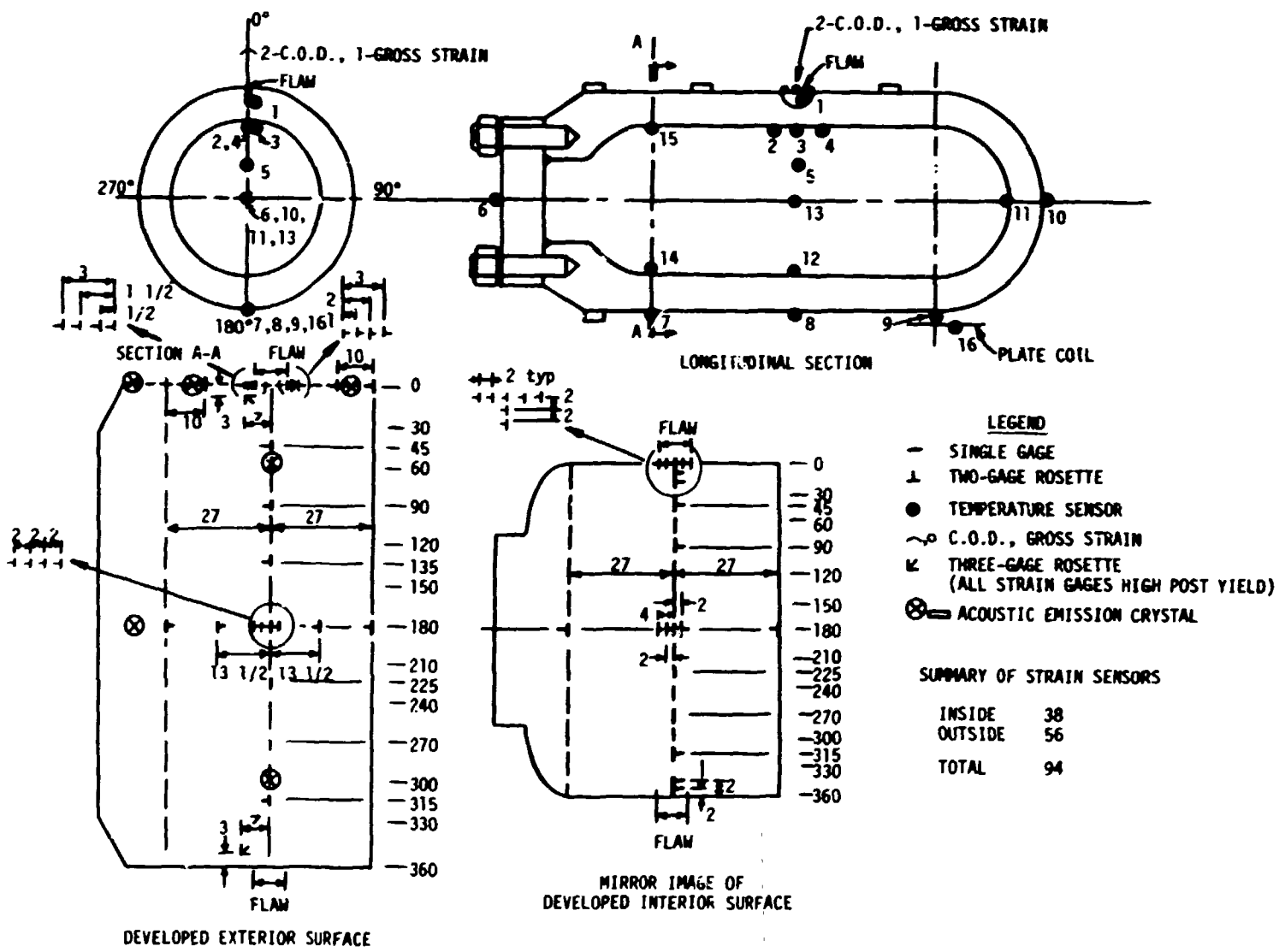

Fig. 7.8. General instrumentation plan for vessels V-1 and V-2.

ORNL - DWG 73-6469

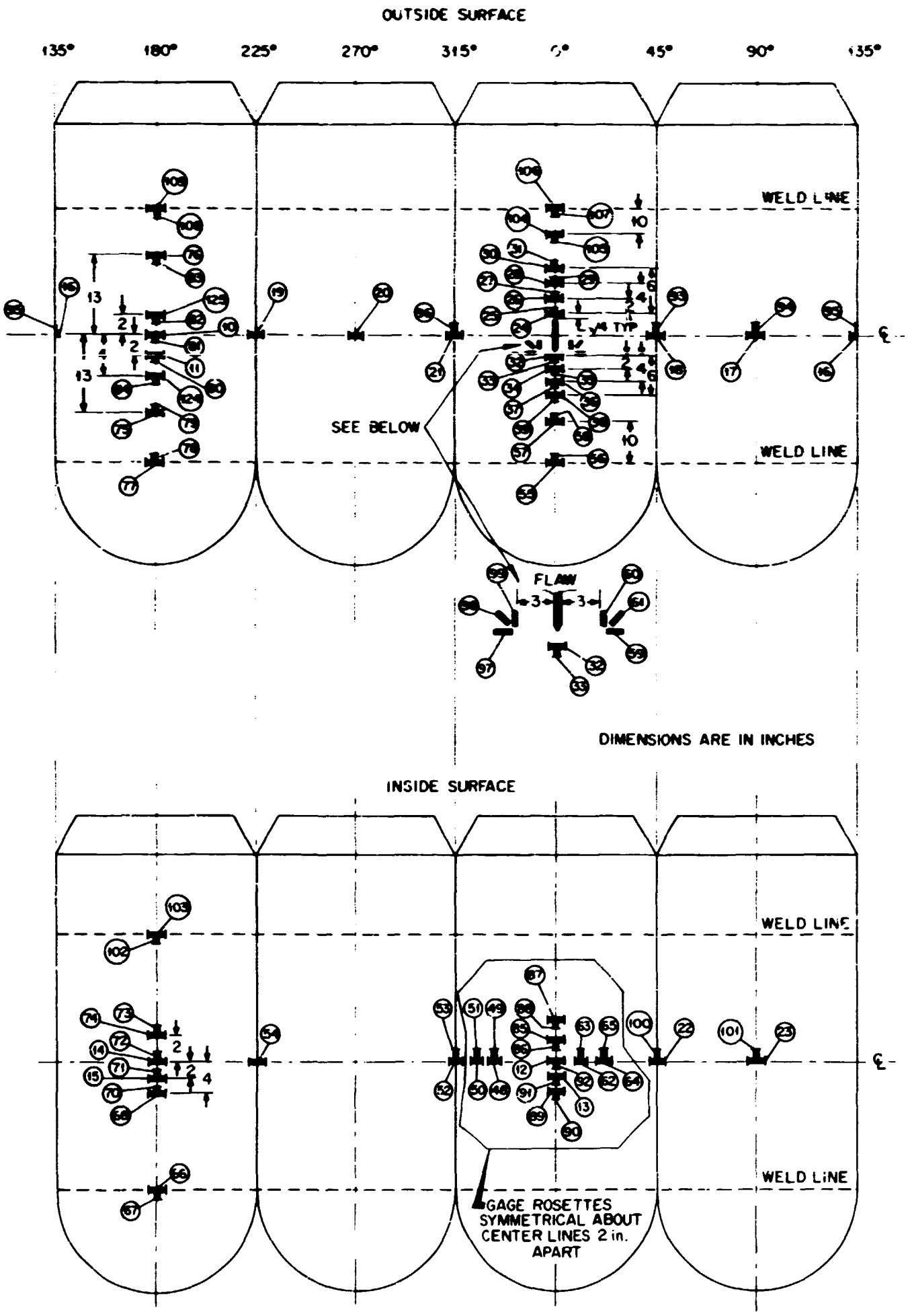

Fig. 7.9. Locations of strain gages for vessel V-1.

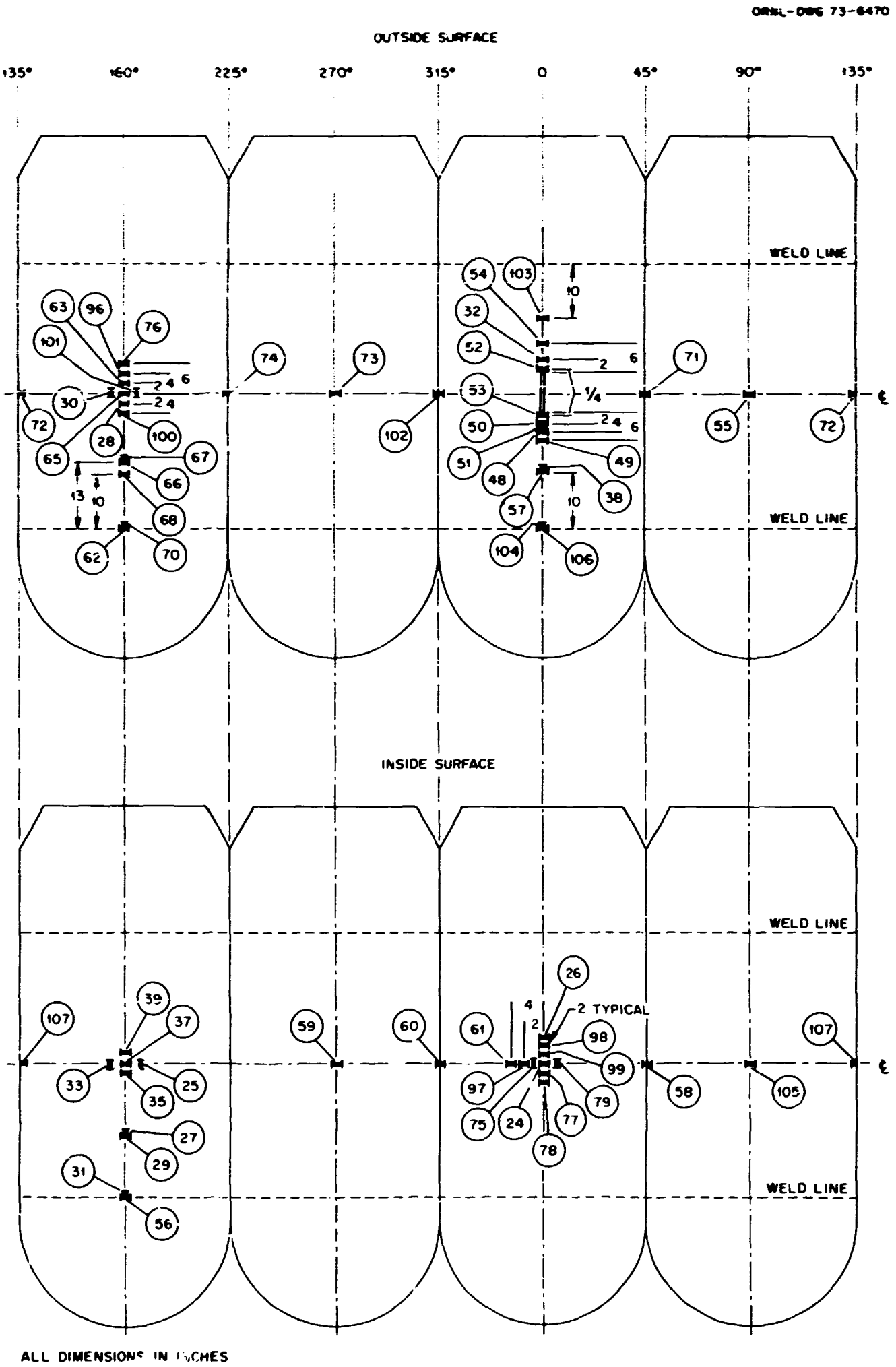

Fig. 7.10. Locations of strain gages for vessel V-2.

counter was mounted near the notch. Whenever a photograph was taken by pushing a button in the control room, the operator also recorded the photograph number and the pressure in the vessel. The crack-opening displacement devices were developed by A. A. Abbatiello, ORNL.

Pressure measurements. Two completely independent systems were used to monitor pressure. The most straightforward method was to use another closed-circuit TV set to follow a conventional Bourdon pressure gage mounted near the high-pressure pump. This approach was basically a redundancy for a more precise system that consisted of a commercially available load cell, a signal conditioning and excitation unit, and an L&N recorder. After having been calibrated at a standards laboratory, this device was accurate to ±250 psi in 30,000 psi.

Acoustic emission devices. Both vessels V-1 and V-2 were monitored by acoustic emission specialists from a commercial laboratory who brought their own equipment to the test site and installed it themselves. Southwest Research Institute monitored the tests of these two vessels. The locations of the acoustic transducers are also indicated in Figs. 7.8 and 7.9.

Reference

1. A. A. Abbatiello and R. W. Derby, *Notch Sharpening in a Large Tensile Specimen by Local Fatigue*, ORNL-TM-3925 (November 1968).

8. TESTING OF VESSELS V-1 AND V-2

Vessel V-1 Test

Final preparations for test of vessel V-1. The test of vessel V-1 was scheduled for June 29, 1972. A top view of the vessel just prior to placing the two 24-ton concrete slabs on the test pit was shown previously in Fig. 3.13. The pressure gage in this figure was monitored by a remote television camera with a zoom lens, which also enabled one to scan the stud and penetration regions of the vessel for malfunctioning or leakage during the test. The flawed region of the vessel prior to placing the crack opening displacement (COD) gage in place is shown in Fig. 8.1. The transducers at top and bottom center are acoustic monitors.

The heating system for the vessel was turned on three days prior to the test date to test the heating system under service conditions and to assure that the whole vessel would be at a uniform temperature. The computerized data acquisition system was activated at the same time. From the printout of the data system, it was possible to monitor both the temperature in the vessel and the temperature-induced apparent strains. It soon became obvious that about 12 strain gages were not responding. Furthermore, several gages which were located under water on the inside of the vessel appeared to be grounded. However, since the layout of gages was highly redundant, the loss of a few gages could be tolerated.

The COD gage and the acoustic monitors were placed on the vessel shortly before pressurization. The fully instrumented vessel in the region of the flaw is shown in Fig. 8.2. Final check-out in the control room prior to pressurization was shown in progress previously in Fig. 3.14. Pressurization was initiated at 10:47 AM on June 29, 1972.

Test of vessel V-1. When pressurization of vessel V-1 began, about 20 gages did not appear to be responding. Twelve of these were located near the flaw and were in the axial direction. The several other gages which were located beneath the plate coils also failed to respond. The remainder were on the inside and had evidently succumbed to the hot water environment.

Proceeding in pressure steps of about 4000 psi (see Fig. 8.3, curve 1), a pressure of about 18,000 psi was obtained. At each step, all the strain gages and thermocouples were read, and continuous monitoring of crack opening displacement, pressure vs strain, pressure vs time, acoustic emission vs time, and acoustic emission vs pressure was also performed. Pertinent results were compared at each pressure interval with those from the model tests (see Chap. 5) and with an analysis based on Lamé equations.[1] At 18,000 psi an Autoclave fitting (one of ten; see Appendix A) in the closure head began to leak, and the test was terminated.

Upon inspection it was found that the O-ring in the fitting had failed. The replacement of the O-ring necessitated that the eight lead wires from either strain gages or thermocouples which passed through the fitting be cut. While inspecting the facility during the O-ring replacement, a leak in the blind flange of the low-pressure side of the intensifier was discovered. This flange was severely cracked and could not be repaired or replaced immediately, so the renewal of the test was scheduled for June 30.

Upon replacing the flange, the cause of the flange failure was first investigated, and it was determined that pressure surges in the intensifier unit caused the fracture. This problem, not evident in the system during check-out with small-volume containers, was minimized by changing the operating procedure recommended for the intensifier unit.

The test was reinitiated the afternoon of June 30. Proceeding as before, a pressure of 19,000 psi was reached, at which time a leak in another Autoclave fitting occurred, this time during pressure hold (see Fig. 8.3, curve 2). Again the leak was repaired with the attendant cutting of lead wires. A third attempt again resulted in leakage at around 19,000 psi (see Fig. 8.3, curve 3). Thus it became apparent that a systematic malfunctioning was occurring. The fittings were rated for 40,000 psi at 400°F and had been checked in an

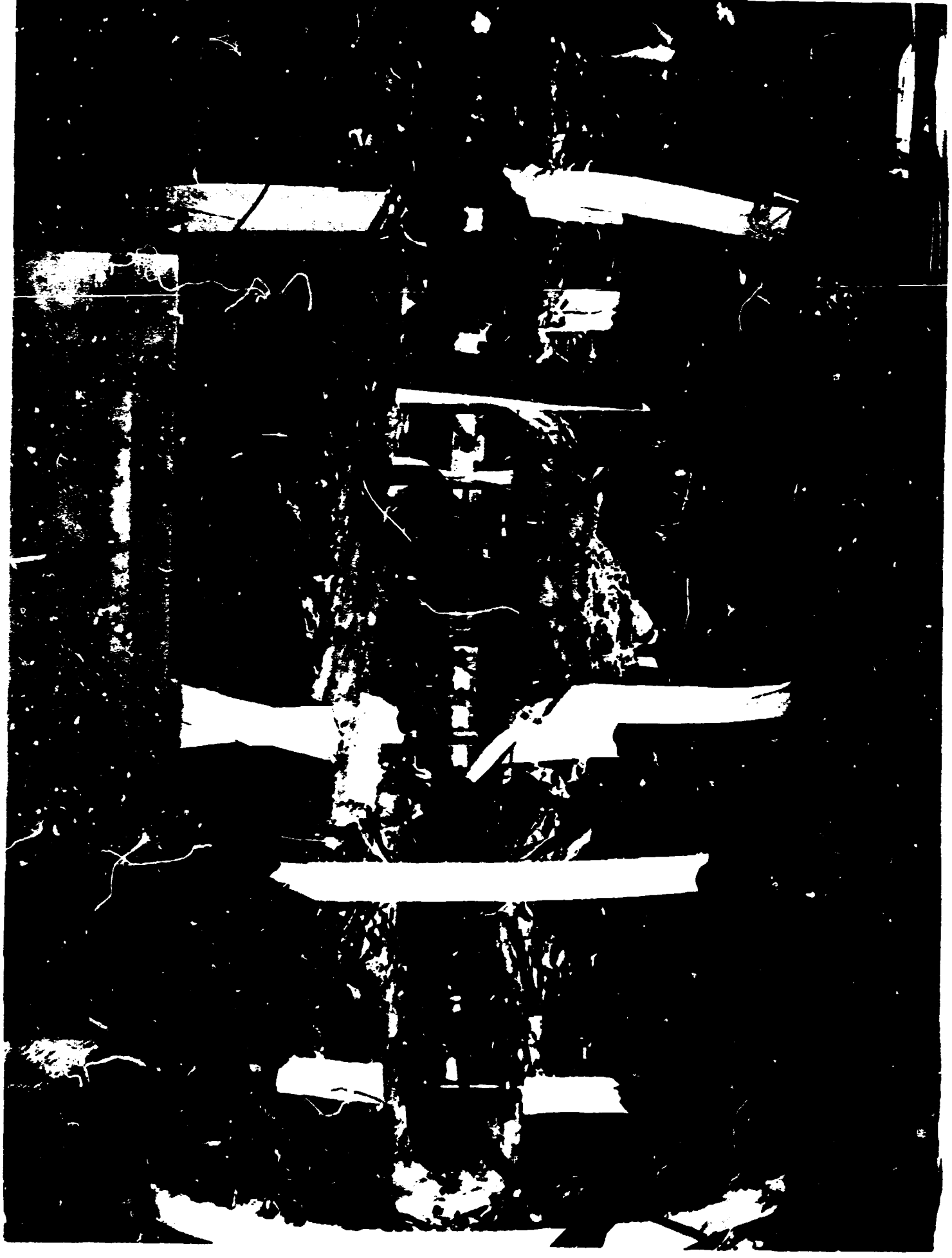

Fig. 8.1. Flaw region of vessel V-1 in test pit prior to placing crack-opening-displacement monitor on vessel.

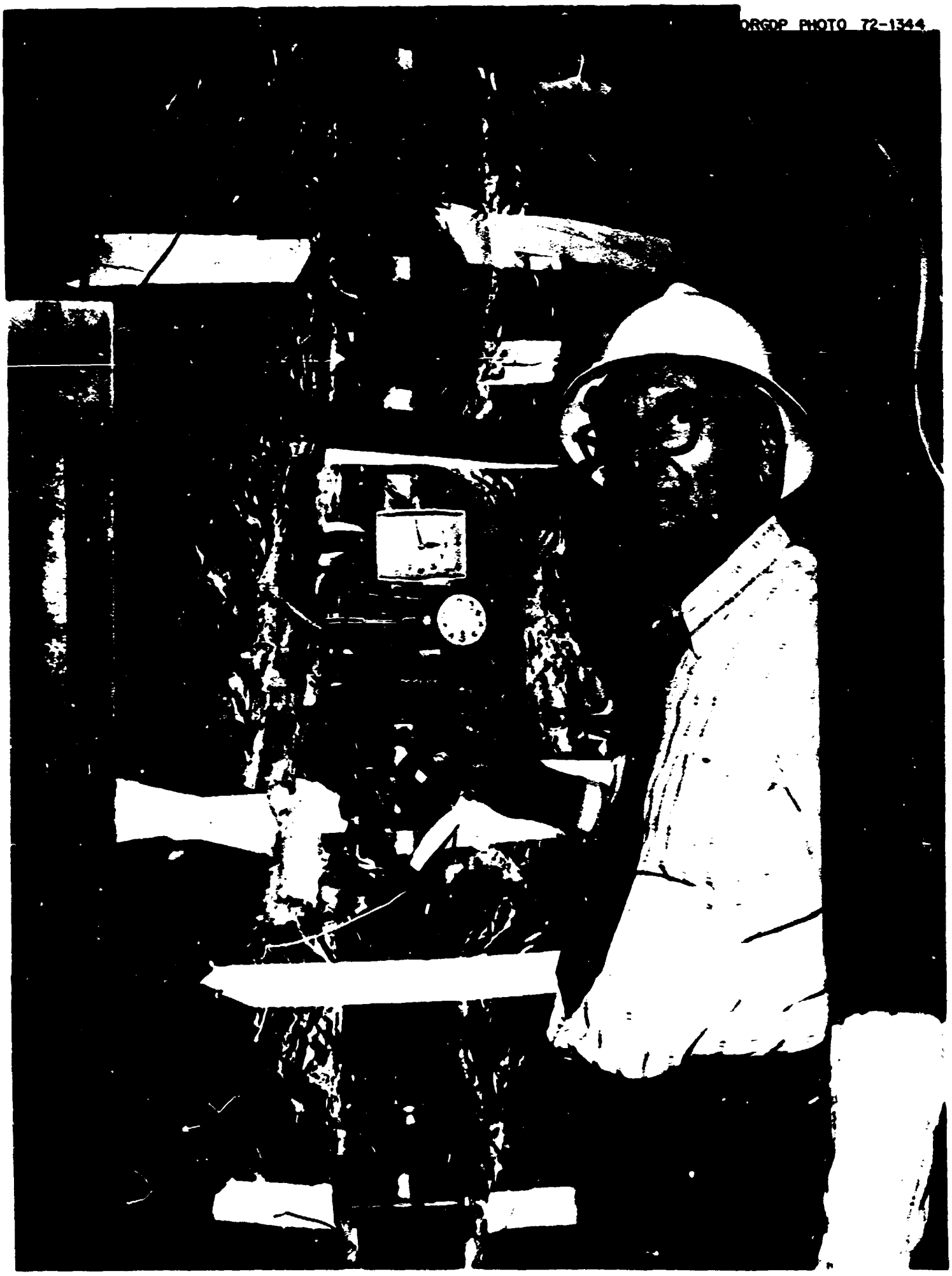

Fig. 8.2. Vessel V-1 in test pit fully instrumented.

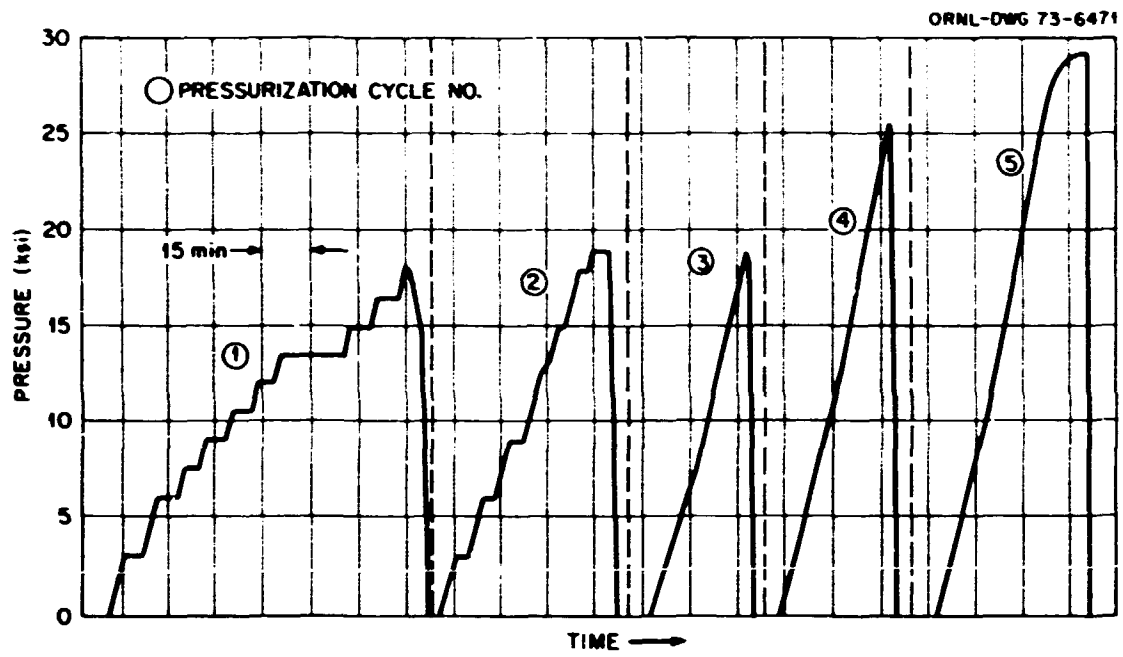

Fig. 8.3. Pressure-time history for the five pressurization cycles required to fail intermediate test vessel V-1.

autoclave by ORNL to 50,000 psi. It was thus evident that the laboratory conditions for check-out were considerably different from the service conditions (see Appendix A). It was decided to lap grind the seats for nine of the ten fittings in the vessel and increase the torque in tightening the fittings. A special torquing wrench was fabricated for this purpose. The lapping procedure of course required the cutting of all leads for each penetration.

Since time at pressure appeared to be a parameter affecting the O-ring failure, it was decided in the fourth burst attempt to eliminate the pressure holds in the test procedure and to scan the data while under pressurization. This was done (actually no pressure holds were taken during the third pressurization, but such were planned had a pressure sufficiently greater than the previous attempt been obtained), and a pressure of about 25,600 psi was obtained before leakage (see Fig. 8.3, curve 4). The leak was repaired, and on the fifth attempt, failure of the vessel was obtained at a pressure officially set at 28,800 psi (see Fig. 8.3, curve 5). In Fig. 8.3, the failure pressure is indicated as being about 28,650 psi; however, the *X-Y* plotter, which showed 28,800 psi at failure, was considered the more accurate, and this pressure was arbitrarily taken as the failure pressure. It should be noted that the rather flat top on curve 5 of Fig. 8.3 does not represent a hold period but a period (over 5 min) of near constant pressure brought about by plastic deformation occurring in the vessel, especially near the flaw, to such an extent that the pressurizer could not increase the pressure. In fact, had a pressure hold period been taken, the pressure would have dropped as observed in the model vessel tests. During the test the temperature of the vessel ranged between 134° and 138°F.

Summary of experimental data from the test of vessel V-1. During the test, it appeared that many strain gages were failing, but sufficient redundancy was available to permit continuing the test. Each time an Autoclave fitting was repaired, the gages or thermocouples through the fitting had to be cut. It is noteworthy that when the nine Autoclave fittings were removed for lapping the seats, only the gages for the one remaining fitting were operable for the remainder of the test.

Immediately after the test, it was apparent that there was a pressure-strain-time discrepancy between the pressure-strain *X-Y* plotter and the computer output. In fact, the computer output indicated that massive failure of the gages occurred at around 0.4% strain or below, in contrast to the plotter, which showed strain of around 0.9% at failure 180° from the flaw. Subsequent investigations revealed that just prior to initiating the test, a negative gage factor was placed in the computer in order to make tensile strains

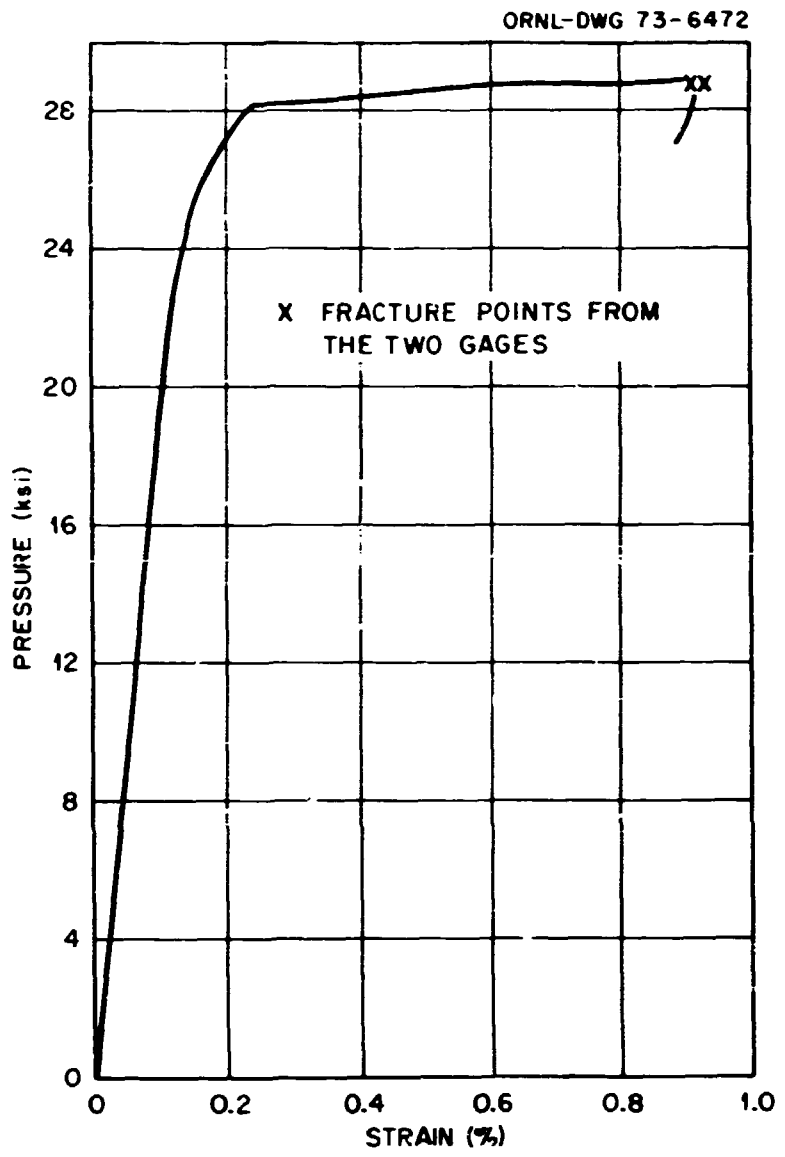

Fig. 8.4. Pressure–circumferential-strain curve for intermediate test vessel V-1 on outside surface 180° from the flaw (gages 124 and 125).

read out positive and compressive strain read out negative. However, the gage factor played a role in optimizing the computer channel limits. The results were that the maximum strain that could be accepted and printed out by the computer varied from a small strain up to around 0.4%. The initial imbalance of the gages actually determined the maximum readout. Further analysis of the raw data reveals that few gages actually failed during the test except some of the inside gages, where the waterproofing was not completely successful. Apparent failures were the manifestation of the error in introducing the negative gage factor. The *X-Y* plotter data were verified as being correct. As a result of the computer programming error, the mass of data obtained from the test during the five pressurization cycles is limited mainly to elastic behavior. These data are given in Appendix B.

The two gages plotted on the *X-Y* plotter were diametrically opposite the flaw (180° from the flaw) on the outside surface. These pressure-strain curves are the basic results from the test; that is, they represent the behavior in the region of the flaw with the flaw not present. These results are given in Fig. 8.4. The decrease in pressure at near fracture shown in this figure is a true representation of the fracture behavior. The unstable plastic deformation and tearing in the region of the flaw were such as to reduce the pressure but slow enough to record prior to rupturing the vessel.

The results from the *X-Y* plotter are compared with results from similar locations in the models in Fig. 8.5 (see Table 5.1 of Chap. 5). The prototype vessel data fall between the curve for the vessel with the flaw in the center material and the one with the flaw in surface material. Actually, the data represent the

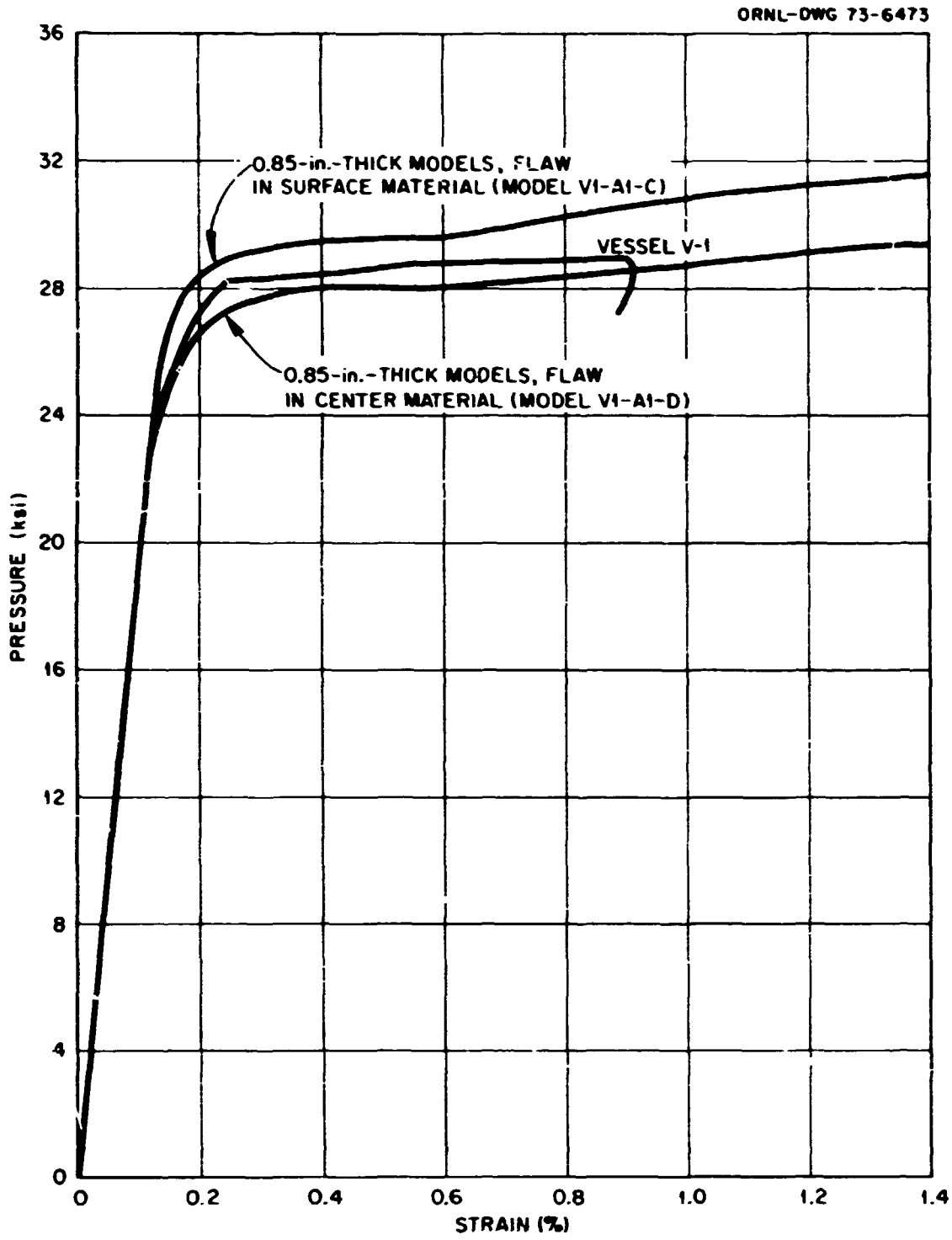

Fig. 8.5. Comparison of pressure-strain curves between vessel V-1 and the 0.85-in.-thick model vessels.

elastic-plastic behavior of the vessel irrespective of the location of the flaw and are not too surprising since the vessel surface material is continuous with the center material, which makes up most of the mass.

A comparison of data near the flaw is given in Fig. 8.6. These curves are incomplete because of the computer programming error. Similar pressure-strain behavior on the outside surface along an axial element 180° from the flaw is shown in Fig. 8.7.

The crack opening displacement was successfully monitored as a function of pressure. These results are given in Fig. 8.8. The data for the first three pressurizations were indistinguishable, indicating no plastic deformation during the test. Considerable nonlinearity was achieved during the fourth pressurization to over 25,000 psi. A very large amount of nonlinearity was observed during the final pressurization, and, in fact, the dial indicator moved too quickly to record near rupture. The photographic camera was destroyed by the vessel failure, so that some of the film was lost. The last COD recorded by the camera was 0.27 in. at a pressure of 28,500 psi. Photographs of the COD were obtained for greater COD from the television tape.

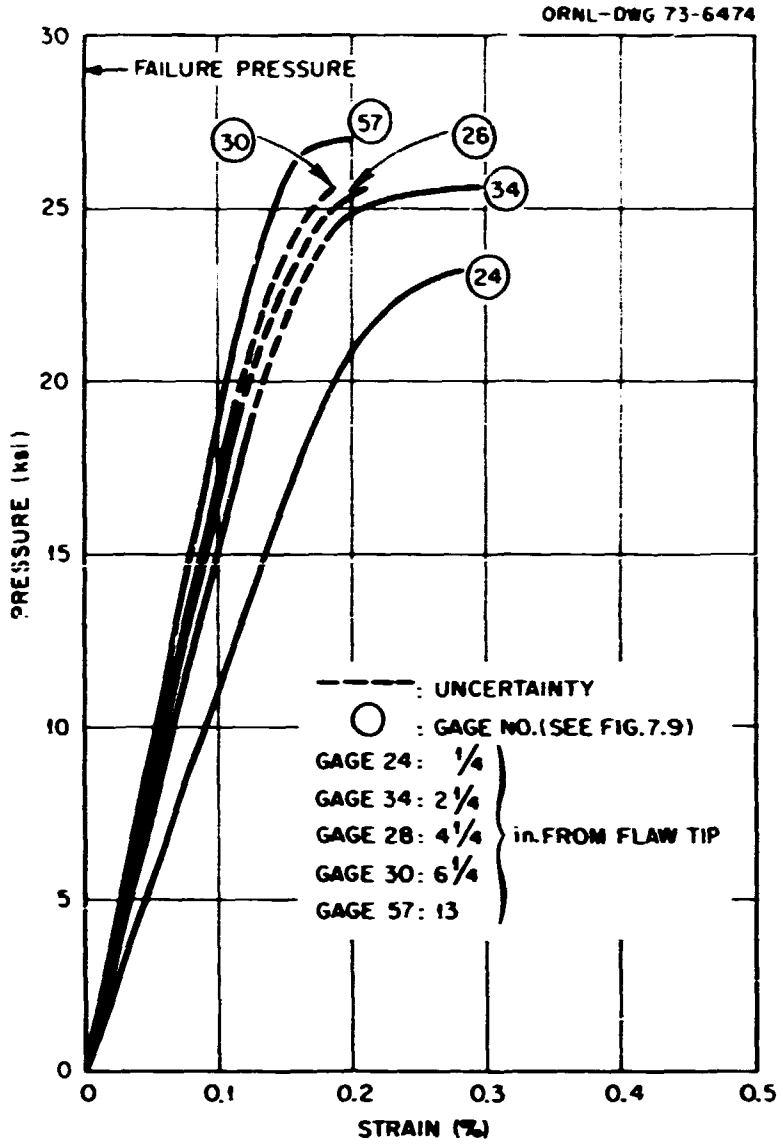

Fig. 8.6. Pressure–circumferential-strain curve in line with flaw, outside surface, intermediate test vessel V-1.

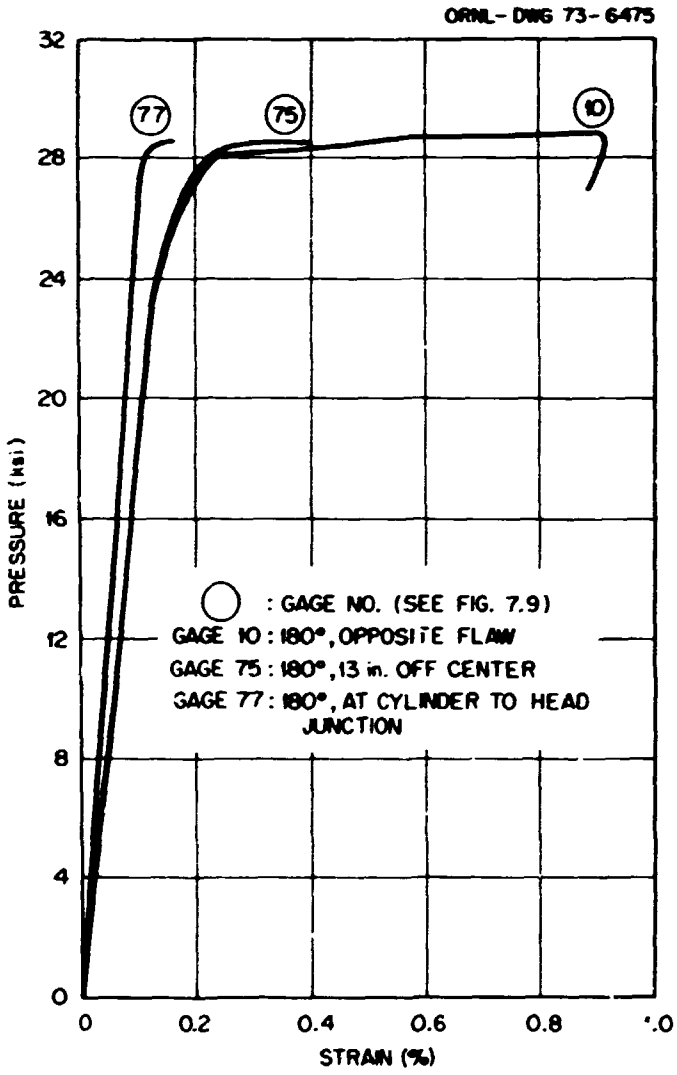

Fig. 8.7. Pressure–circumferential-strain curves along an axial element, 180° from flaw, outside surface, intermediate test vessel V-1.

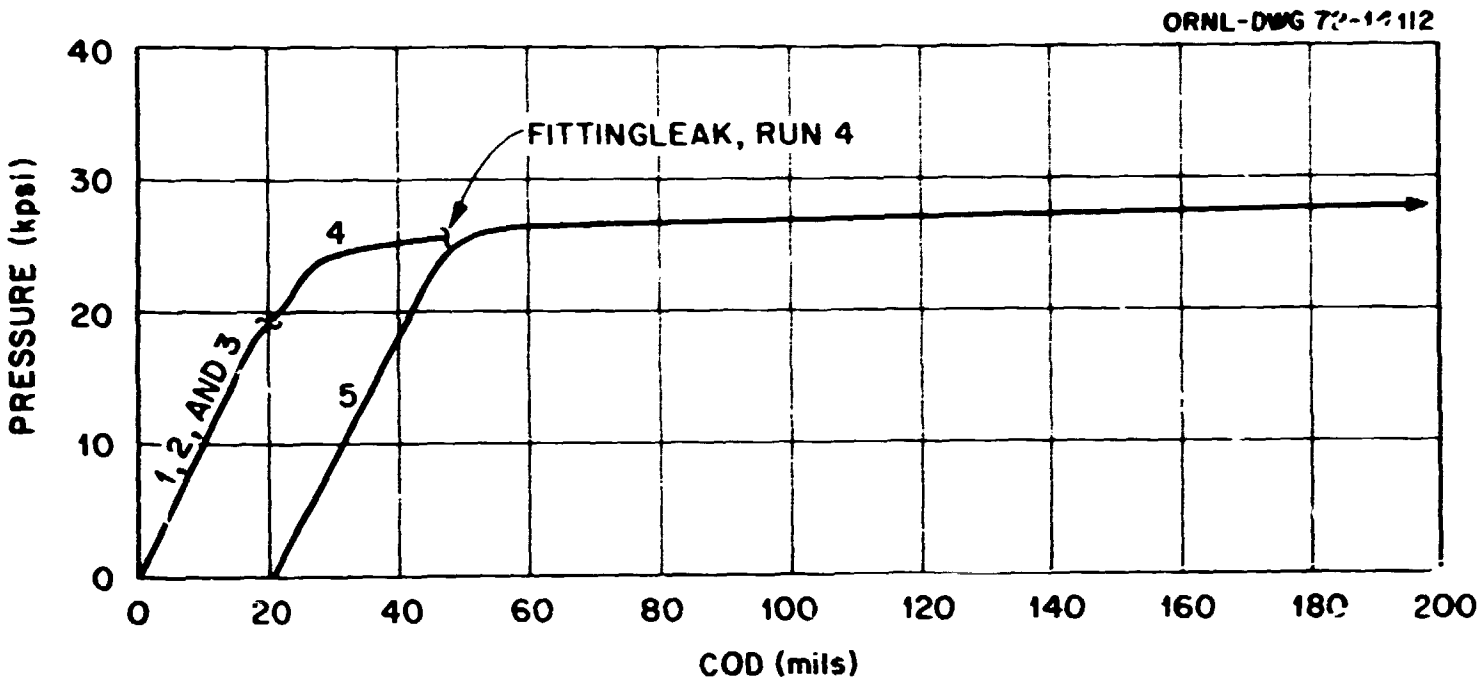

Fig. 8.8. Crack-opening-displacement measurement for vessel V-1 during the five pressurization cycles (indicated by numbers).

The last recordable television reading showed 0.77 in. at failure pressure (recorded at 28,700 psi). Fast ductile tearing initiated at this pressure, but the dial indicator needle moved too rapidly to record. An estimated COD of close to 2 in. existed just prior to rupture. The COD data are given in Table 8.1, and plots of pressure and COD vs time are shown in Fig. 8.9. It may be observed from the figure that the COD at or very near maximum pressure is between 250 and 350 mils and that, indeed, ductile tearing is taking place at the flaw under an almost constant pressure. In fact, the plasticity was so great that the pressure 5 min before burst was within 100 psi of the failure pressure. Pictures of the flawed region near failure are shown in Fig. 8.10.

Fracture mode of vessel V-1. During the test of vessel V-1 the region of the flaw was recorded on television tape. Frames near fracture are shown in Fig. 8.10. The crack opening at maximum pressure is very similar in appearance to that of the 6-in.-thick flawed tensile specimen at maximum load tested at about the same temperature.[2] In fact, it was previously noted that rupture actually occurred at a pressure less than the maximum pressure.

Views of the ruptured vessel in the test pit immediately after the test are shown in Figs. 8.11–8.13. As noted in these figures, the crack propagated after rupture in a much less ductile mode than the tearing fracture near the crack. In the down direction the crack ran all the way through the hemispherical end of the vessel and arrested in the back side. In the other direction the crack ran close to the closure head, branched near the weld, and stopped when it reached the interface between the bolted head and the vessel. During the crack propagation, shear lips slightly over 1 in. thick were formed on both the inside and the outside surfaces. A picture of the vessel removed from the test pit is shown in Fig. 8.14.

The fractured surface was metallurgically examined at ORNL under the direction of D. A. Canonico, and the results are summarized in Fig. 8.15. The inner 3 to 3¼ in. of the 6-in.-thick vessel fracture surface well away from the flaw was cleavage, as might well be expected from the obvious rapidity of the fracture. The remainder of the fracture surface was ductile tearing or dimple rupture. More extensive details of the study are given in Appendix G.

Table 8.1. Pressure vs deflection (COD) for vessel V-1 test, fifth pressurization cycle[a]

Approximate elapsed time (min)	Real time (7-1-72)	Pressure (psi)	Photo No. (on film)	Photo clock time (on film)	COD (in.)
0	12:24	0	130		0.022
5	12:29	4,000	134	6:44:17	0.024
10	12:35	9,000	139	6:51:15	0.029
15	12:39	12,000	142	6:55:16	0.034
20	12:45	16,000	146	7:01:16	0.036
25	12:49	20,000	150	7:05:05	0.041
30	12:54	24,000	154	7:11:52	0.046
35	12:59	27,000	163	7:14:14	0.106
36	1:00	27,100	164	7:14:25	0.114
38	1:02	28,250	172	7:17:04	0.229
40	1:03	28,400	174	7:17:41	0.256
42	1:03	28,500	175	7:18:06	0.270[b]
43	1:04	28,550	178[c]		0.350
43	1:07	28,600	183[c]		0.420
43	1:07	28,600	184[c]		0.440
44	1:08?	28,700	188[c]		0.550[d]
45	1:09?	28,700	190[c]		0.600
46	1:10?	28,700	193		0.720
47	1:10?	28,700	194		0.770[e]
47	1:11?	28,700			1–2[f]

[a]These data were combined from 35-mm photos and television tape pictures. Values were obtained at 1000-psi increments during the test but have been condensed to about one-fifth of the original table length.

[b]Last 35-mm photo that was salvaged.

[c]Film exposed or partially exposed when camera destroyed.

[d]From TV tape picture only.

[e]Last TV reading taken.

[f]COD needle rotating at 10 rps, estimated.

In contrast to the fracture behavior of vessel V-1, the models tested at the same temperature simply leaked (see Fig. 5.8). This difference in behavior is not unlike the behavioral difference observed for the similar large and small specimens that have been tested throughout the HSST program. For all these cases, it may be said that stored energy varies as the cube of the dimension, whereas the energy needed to form new surfaces requires less energy, perhaps varying more as the square of the dimensions.

Acoustic emission results from vessel V-1 test. The acoustic emission monitoring of the intermediate vessel tests is set up as a cooperative effort between ORNL and industry. Each series of vessels (see Chap. 1) has been assigned under contract to a specific company. ORNL pays travel and lodging, while the company assumes the remaining cost. Southwest Research Institute was awarded the contract to monitor the first series of vessels (vessels V-1 and V-2). A report discussing the results from both tests has been prepared and is summarized following the discussion of the test of vessel V-2.

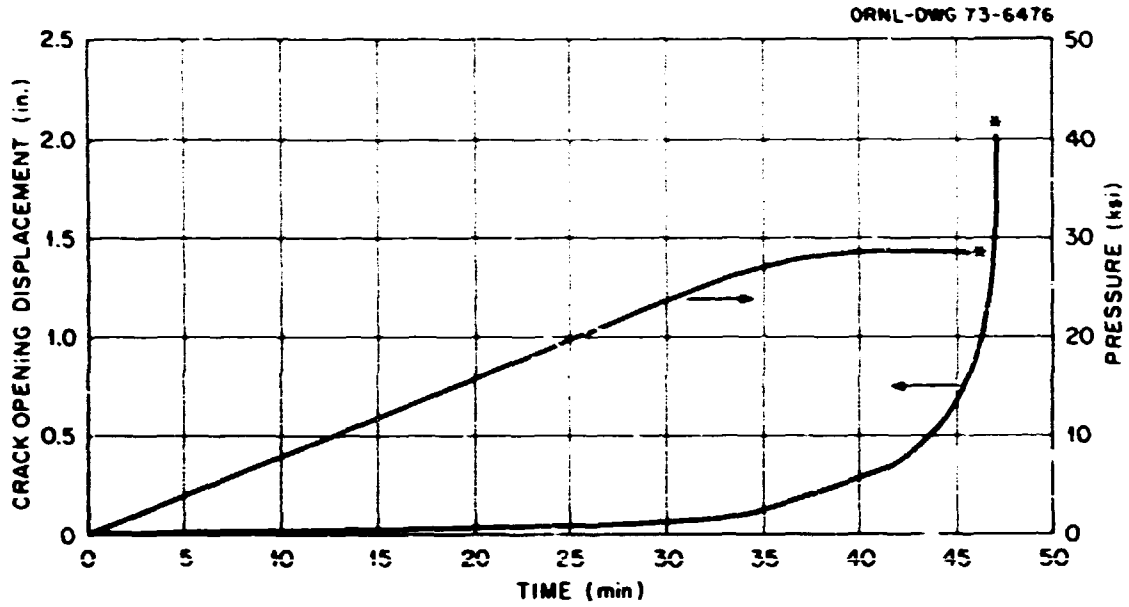

Fig. 8.9. Pressure–crack-opening-displacement–time plot for vessel V-1.

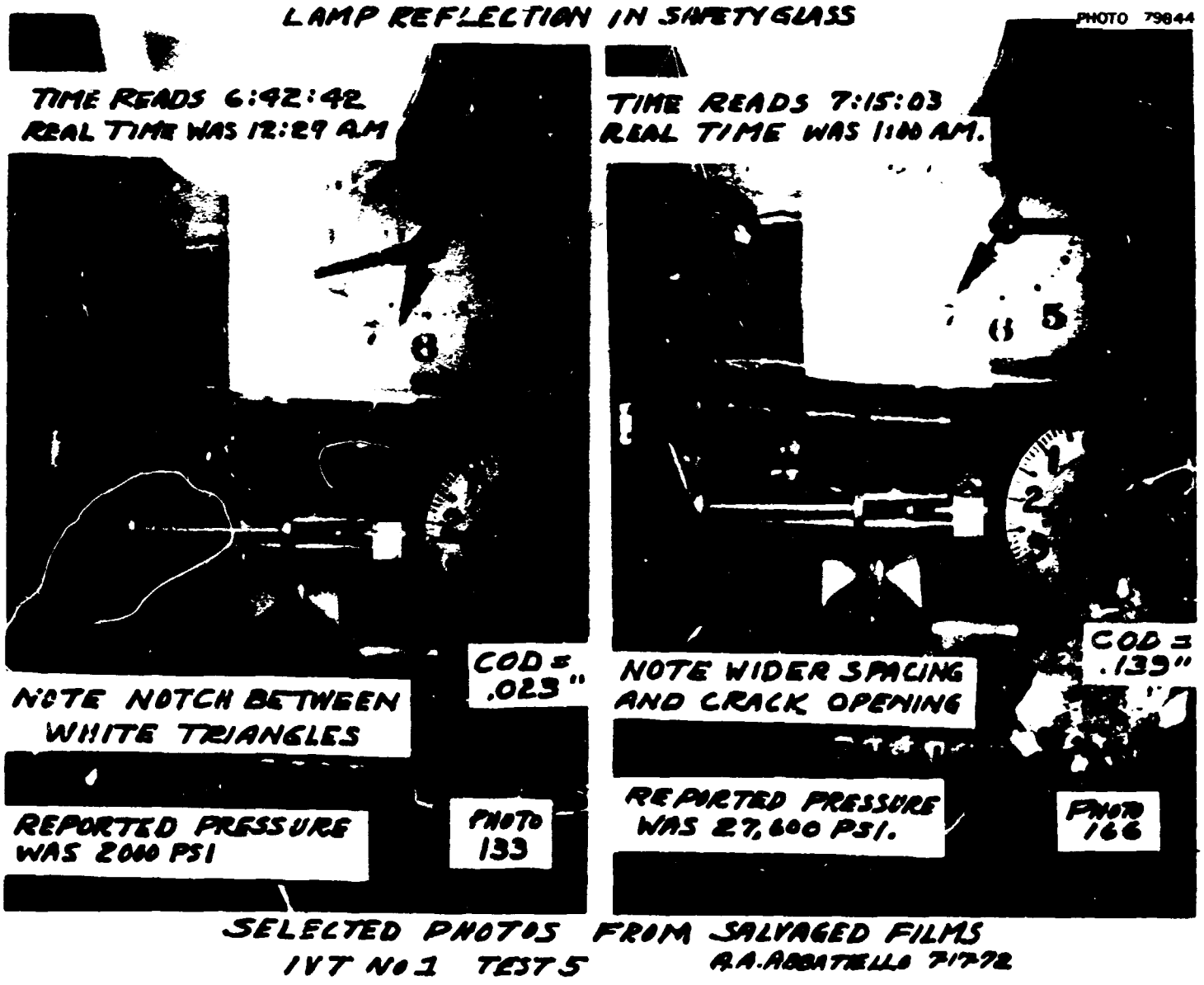

Fig. 8.10. Typical photographs of crack opening displacements made during test, intermediate test vessel V-1.

Fig. 8.11. Vessel V-1 in test pit immediately after fracture.

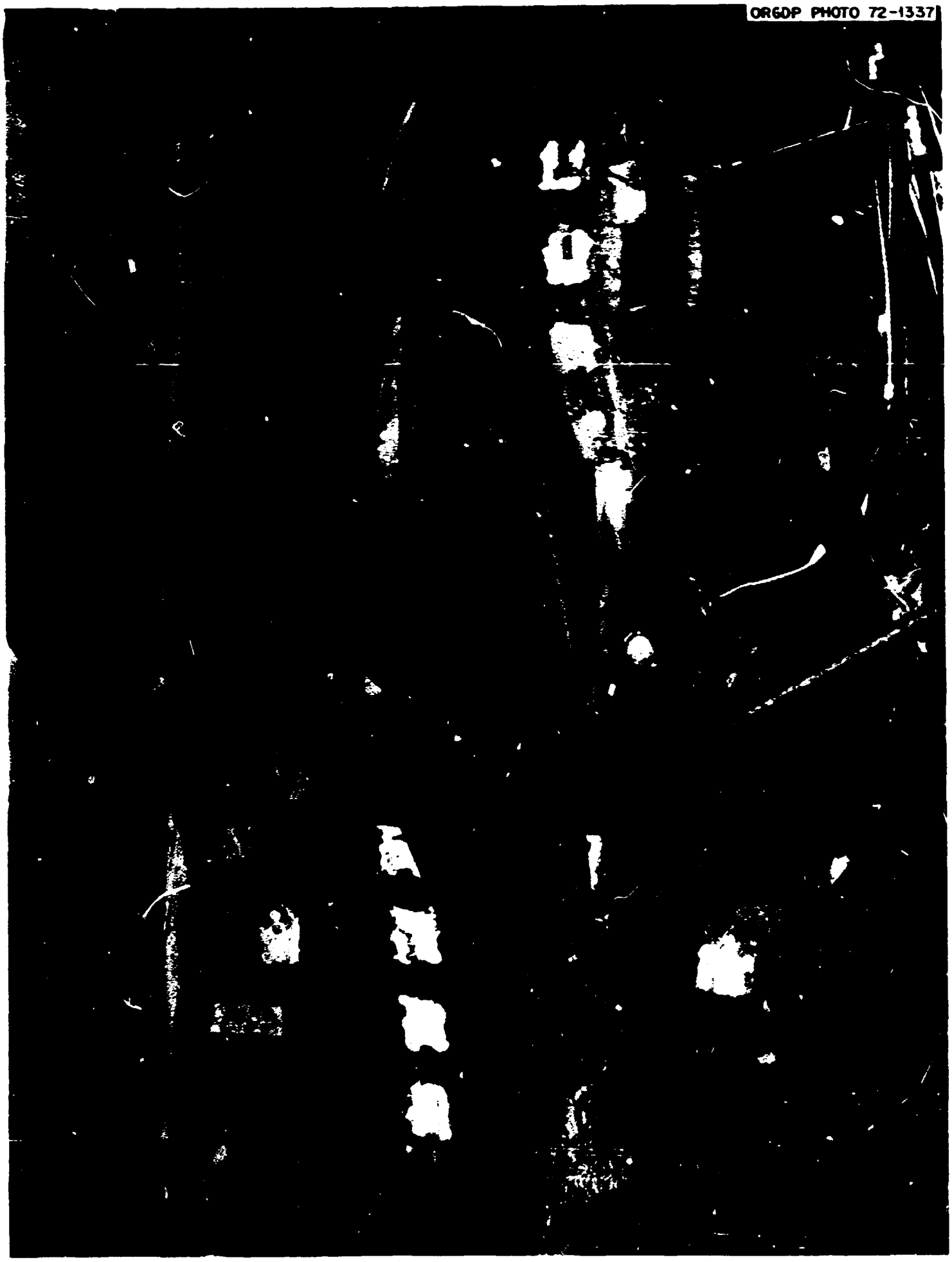

Fig. 8.12. Flawed region of vessel V-1 after fracture.

Fig. 8.13. Vessel V-1 in test pit showing size of opening in region of flaw.

Fig. 8.14. Vessel V-1 removed from test pit.

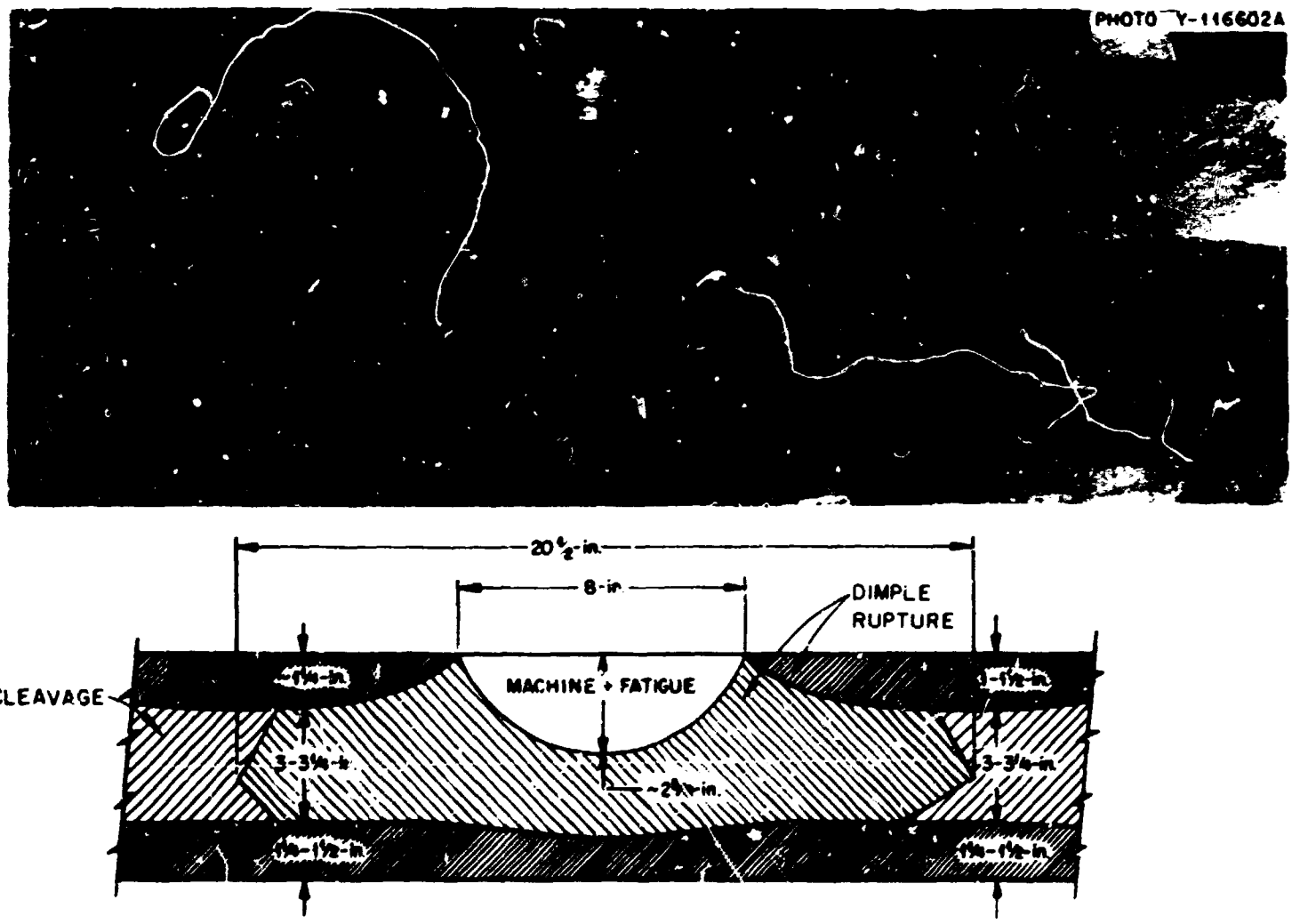

Fig. 8.15. Metallurgical description of fracture surface of vessel V-1.

Vessel V-2 Test

Intermediate test vessel V-2 was an exact duplicate of vessel V-1 insofar as possible. Since vessel V-1 was successfully tested and significant data were obtained, the test temperature for vessel V-2 was selected at 32°F, as previously discussed in Chap. 6. A photograph of vessel V-2 fully instrumented is shown in Fig. 8.16. The wood frame is part of a mirror device set up to allow the crack monitor cameras to view the vessel flaw remotely.

Test of vessel V-2. The test of vessel V-2 was initiated on September 28, 1972. The nominal test temperature was 32°F; however, some difficulty was encountered in maintaining the temperature. In fact, as the vessel was pressurized the temperature dropped as low as 22°F. Since 32°F was thought to be in the rapid toughness transition region, heating or cooling was applied to the vessel as necessary in an attempt to maintain the temperature. A temperature-time history of the test from thermocouples in the test region is given in Fig. 8.17; test pressures are also indicated on the figure.

As before, the vessel was pressurized to a predetermined pressure, and a hold period was taken for obtaining and evaluating pertinent data. During the test the pressurizer developed a leak in the seals, first on one side and then on the other, and no greater pressure could be obtained. At the termination of the first pressurization cycle, a pressure of about 24,500 psi had been reached. The seals in the pressurizer were replaced, and the test was reinitiated. The seal on one side leaked once again, but sufficient pressure was obtained to fail the vessel at a pressure of 27,900 psi. The temperature in the flaw at failure was 30°F. Pressure-time curves for both pressurization cycles are shown in Fig. 8.18.

Summary of experimental data from the test of vessel V-2. The experimental pressure-strain data obtained during the test of vessel V-2 are given in Appendix B. A plot of the outside surface circumferential strain 180° from the flaw is given in Fig. 8.19, which may be compared with Fig. 8.4. As may be seen, gross yielding through the vessel wall was just initiating.

Considerably greater strain existed in the region of the flaw. Outside surface data near the flaw are given in Fig. 8.20, which shows that a strain of 0.8% was obtained very close to the flaw. The nominal pressure-strain curve of Fig. 8.19 is almost identical with the curve from gage 57. A comparison of pressure vs circumferential strain curves 13 in. from the flaw tip (gages 57 and 103, Fig. 7.10) with a curve in the same position 180° away (gage 68) is given in Fig. 8.21. At these locations the curves are identical.

A comparison of results from various internal gages is given in Fig. 8.22. These results again show that gross yielding of the vessel was commencing with strains directly under the flaw less than the nominal strain. This observation will be discussed further in Chap. 9.

The results from the COD measurements are given in Fig. 8.23, which shows considerable nonlinearity prior to fracture. A picture of the flawed region just prior to fracture is shown in Fig. 8.24. Further discussions of the fracture are given in Chap. 9.

Fracture mode of vessel V-2. The propagation characteristics of vessel V-2 at fracture were as expected – catastrophic and complete with degrees of fragmentation. An annotated picture of the vessel in the test pit immediately after the test is shown in Fig. 8.25 (note the flaw). One large fragment is seen to have been formed. The support skirt, which was unattached to the vessel, was fractured as seen in Fig. 8.26. In general, the vessel had many cracks, indicating the near generation of additional fragments. Pictures of the vessel removed from the test pit are given in Figs. 8.27 and 8.28. Figure 8.27, also shows the fragments of the model vessel (vessel V2-A1-D, Chap. 5) tested at −55°F.

Fig. 8.16. Vessel V-2 in test pit fully instrumented.

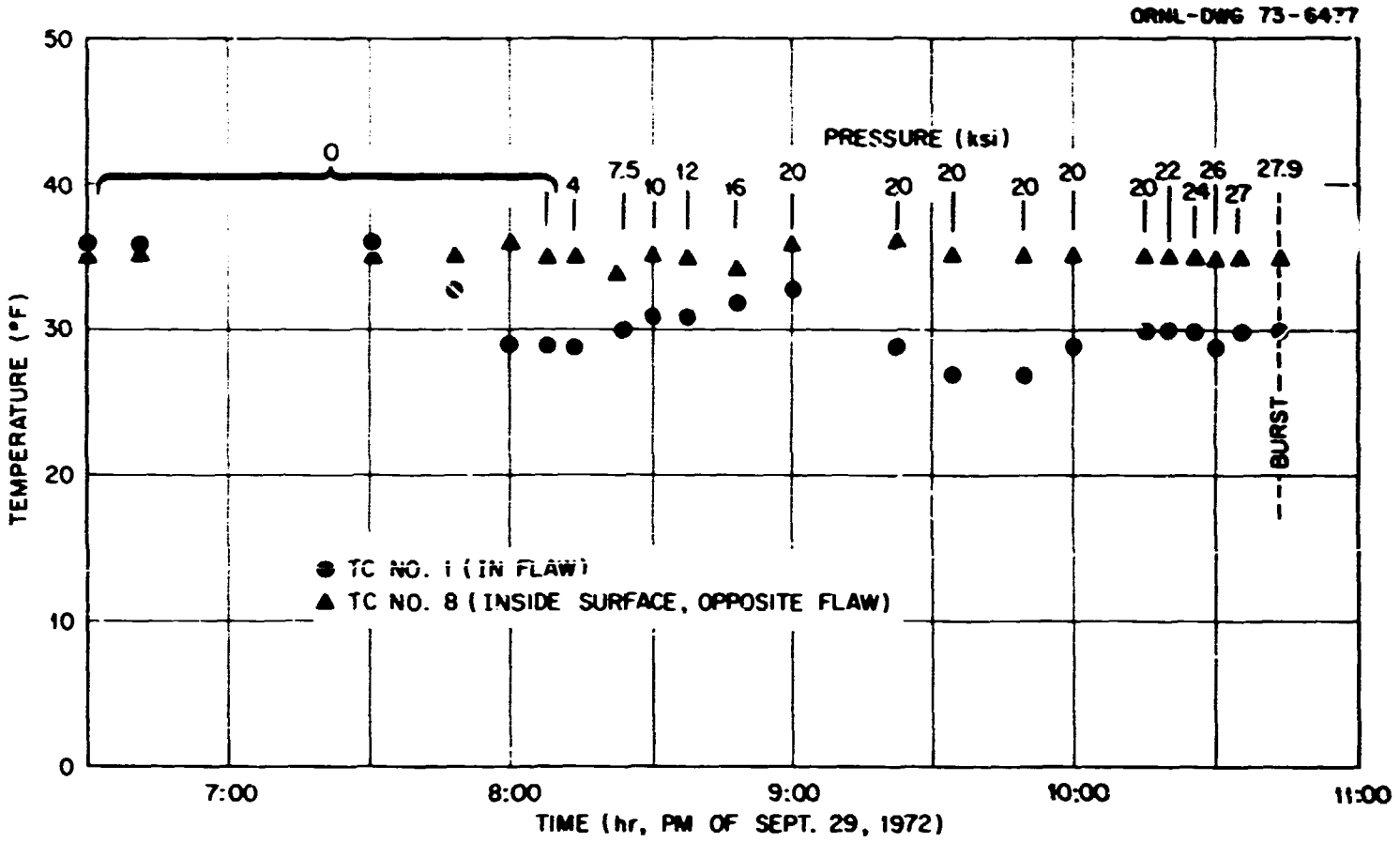

Fig. 8.17. Temperature-time-pressure record for vessel V-2 during second pressurization.

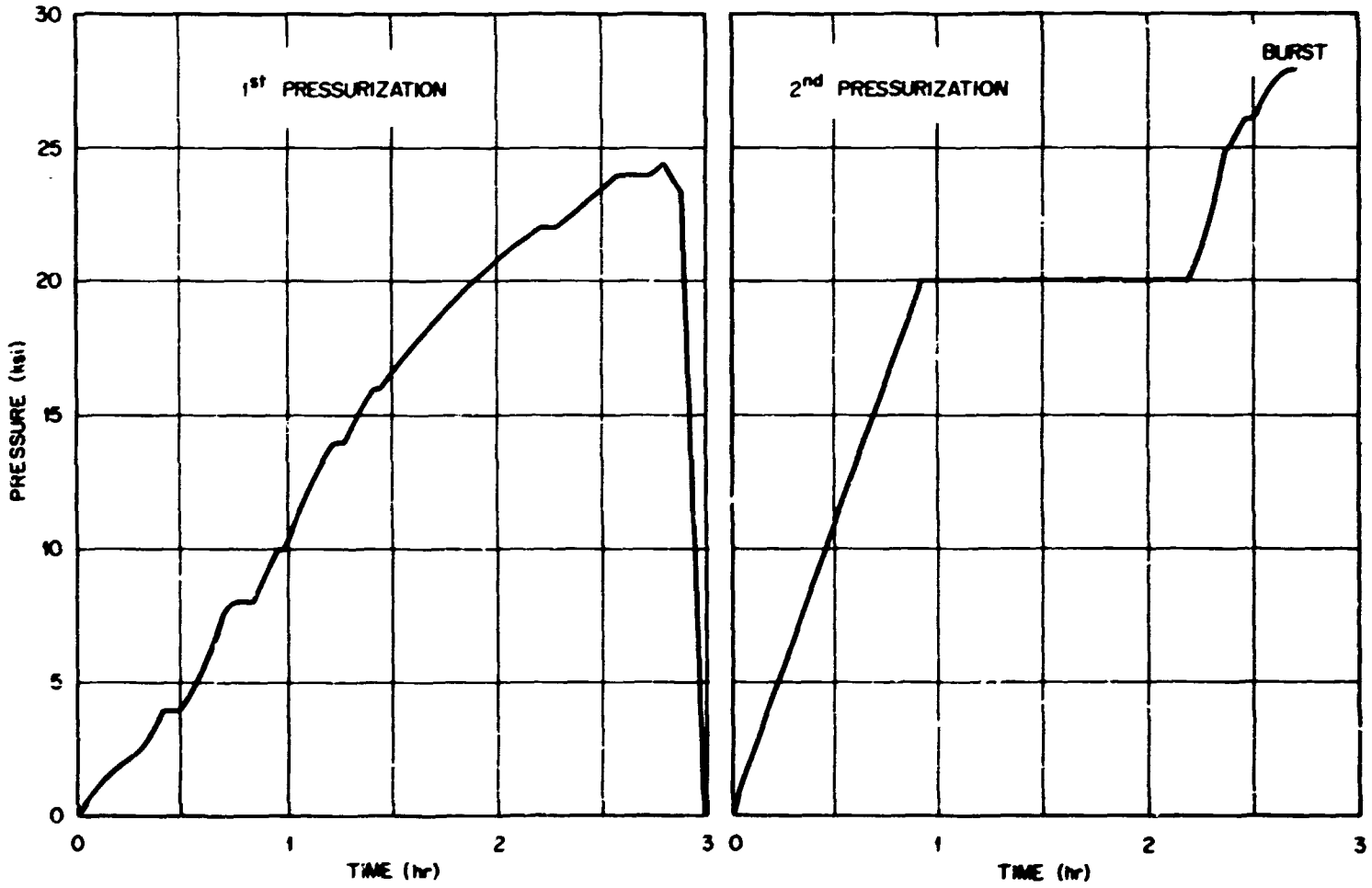

Fig. 8.18. Pressure-time curve for vessel V-2 test.

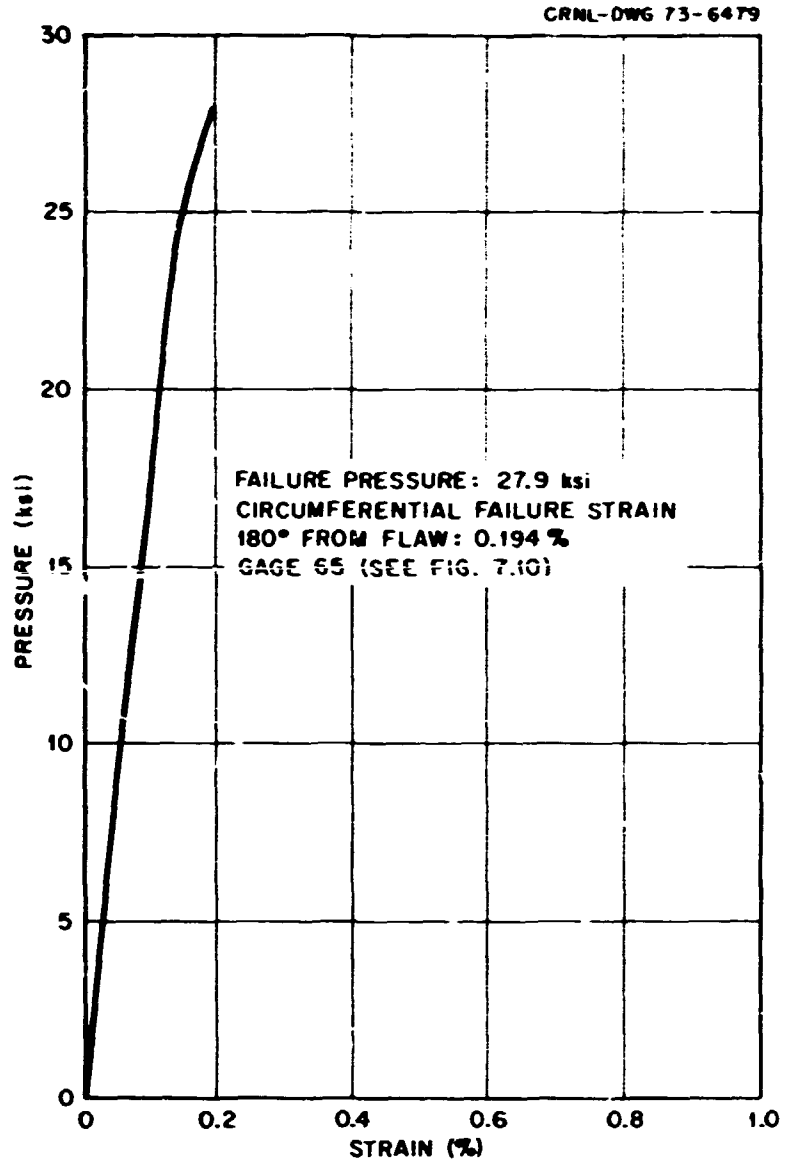

Fig. 8.19. Pressure vs outside surface circumferential strain curve 180° from flaw, intermediate test vessel V-2.

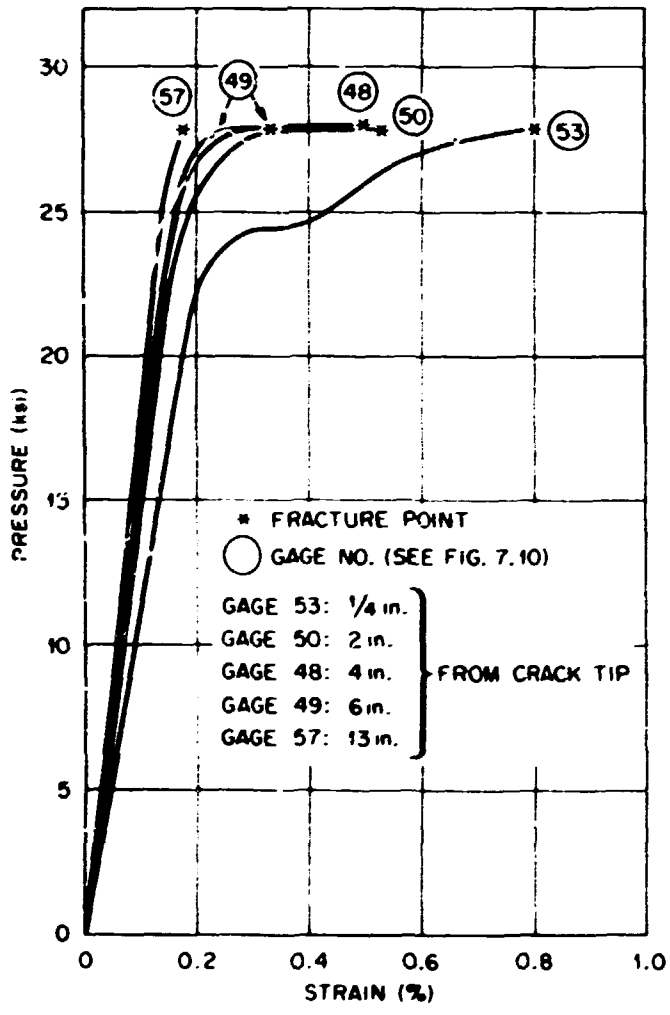

Fig. 8.20. Pressure–circumferential-strain curves in line with flaw, outside surface, intermediate test vessel V-2.

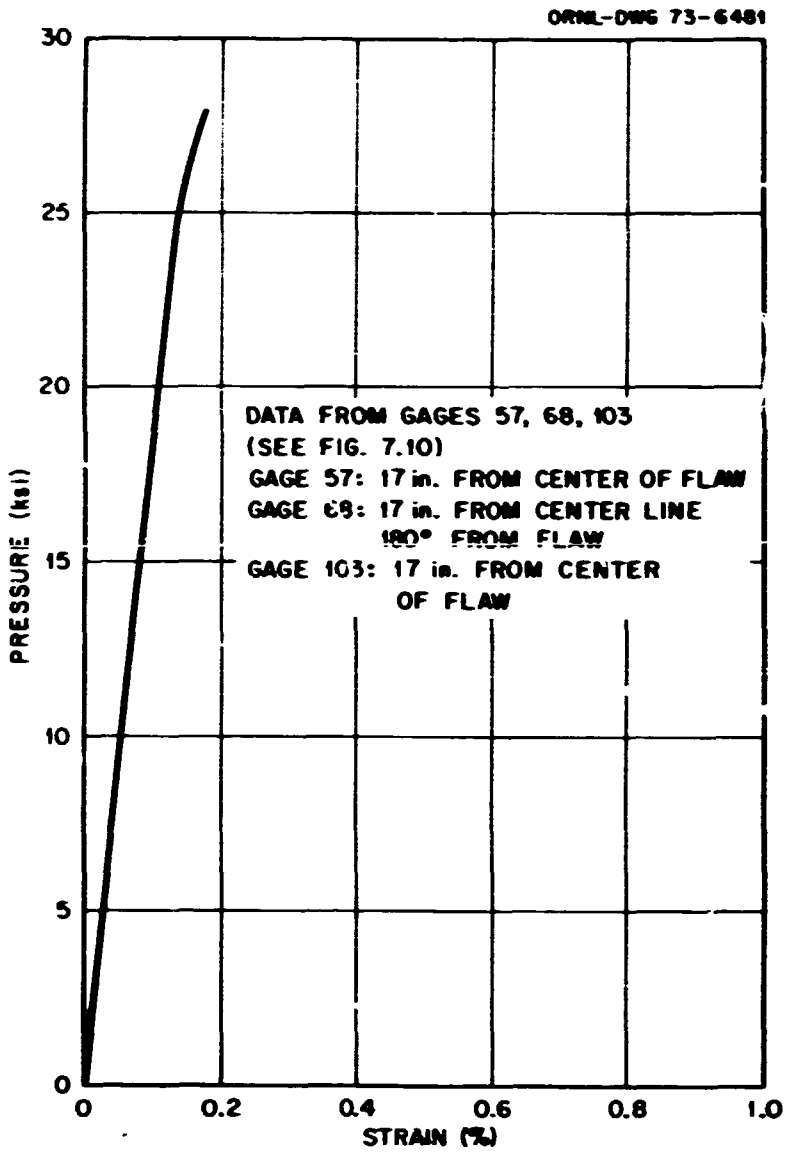

Fig. 8.21. Pressure–circumferential-strain curves from gages 17 in. from center of vessel, intermediate test vessel V-2.

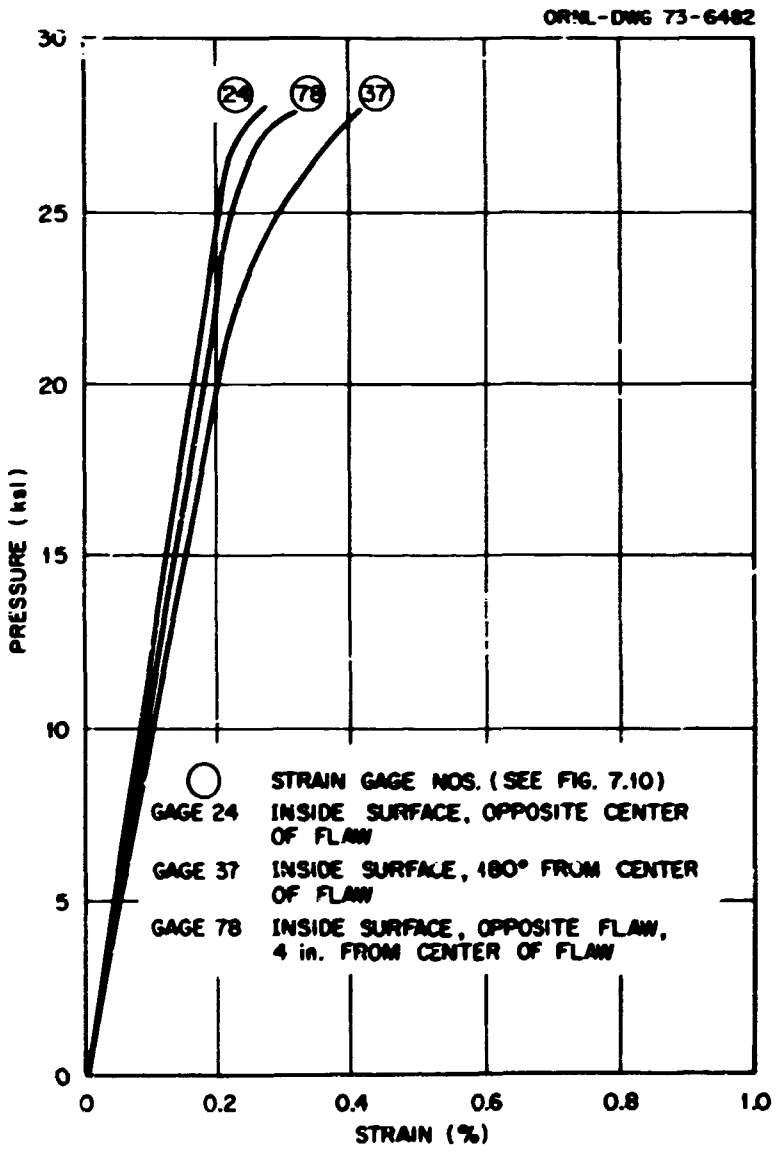

Fig. 8.22. Comparison of pressure vs circumferential inside surface strain curves in line with flaw and 180° removed, intermediate test vessel V-2.

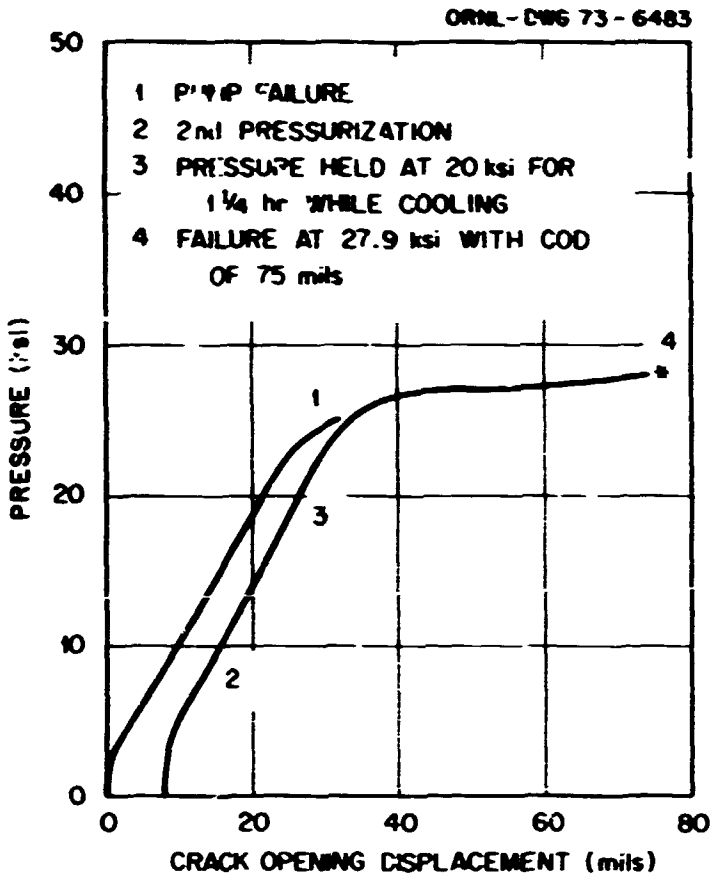

Fig. 8.23. Plot of crack opening displacement vs pressure for vessel V-2.

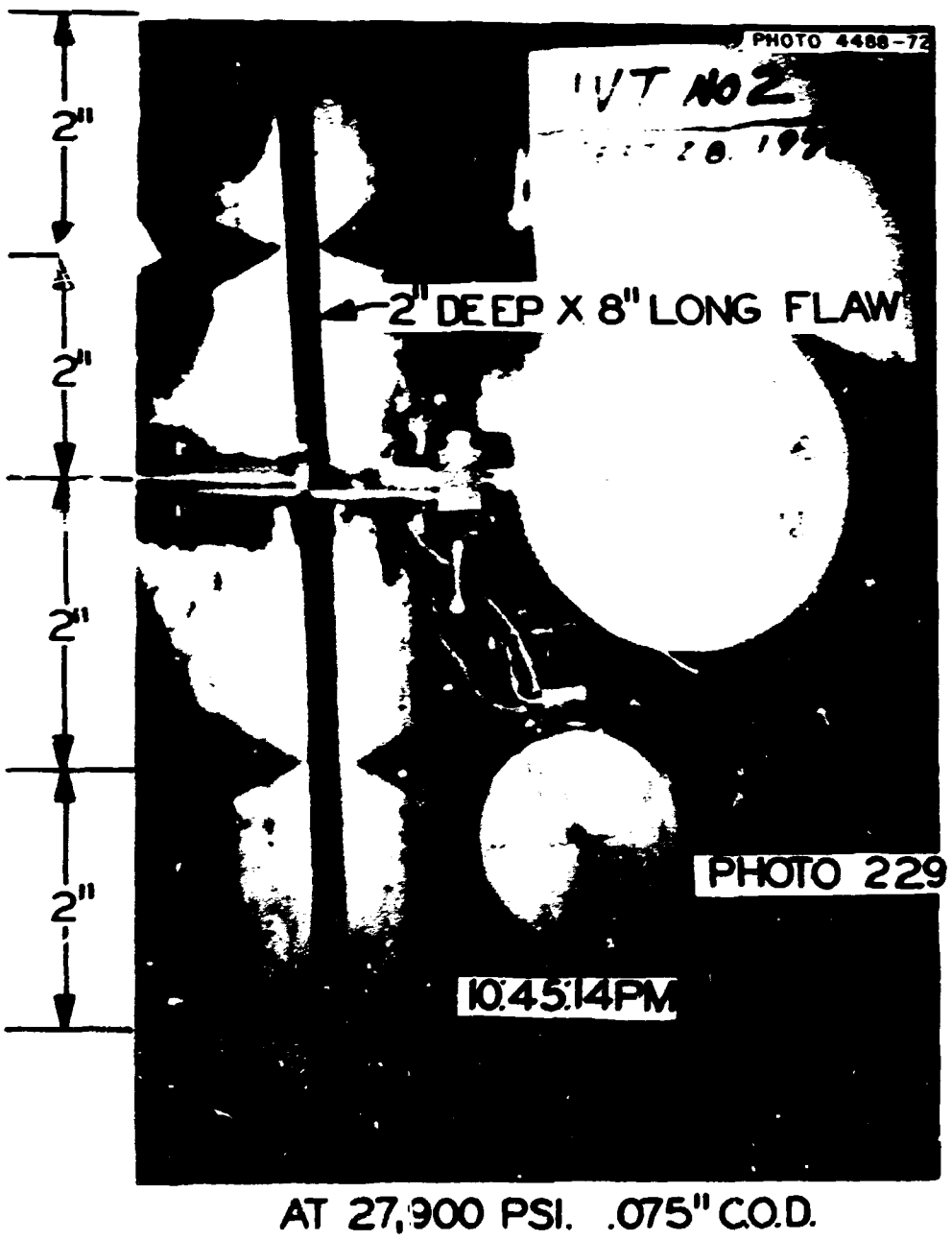

Fig. 8.24. Last photograph of flaw of vessel V-2 prior to fracture.

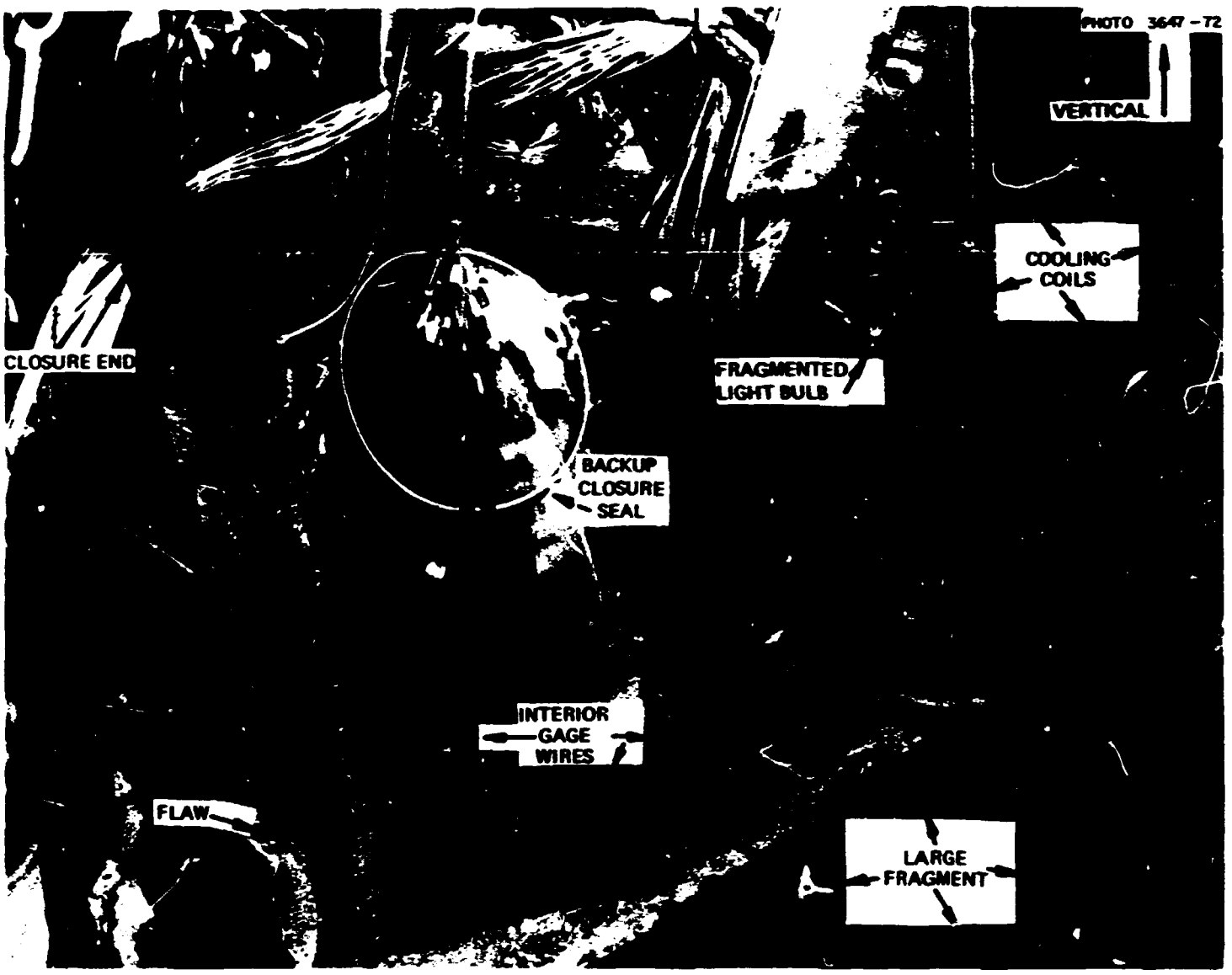

Fig. 8.25. Picture of intermediate test vessel V-2 immediately after fracture.

Fig. 8.26. Vessel V-2 in test pit immediately after fracture, showing the devastation.

Fig. 8.27. Vessel V-2 removed from the pit, showing the extensive cracking. Pieces of model vessel tested at −55°F are shown on foreground fragment.

Fig. 8.28. Closure end region of vessel V-2 after fracture, showing the extensive cracking.

Acoustic Emission Results from Vessel V-1 and V-2 Tests

As noted previously, the first series of vessels (vessels V-1 and V-2) were acoustically monitored by Southwest Research Institute. E. R. Reinhart and S. P. Ying were in charge of these efforts, and their report is summarized below.

Test preparation. After a review of the proposed ORNL test setup, a number of areas on the pressure vessel were identified as possible sources of extraneous noise which could possibly mask actual acoustic emission signals during the test. The areas of concern were (1) the vessel coolant circulation coils, (2) the metal seal in the vessel head, and (3) bolt and flange noises in the vessel head.

As shown in Fig. 8.29, the vessel coolant coils (on a full-scale mockup model) are attached directly to the vessel wall and limit access to the vessel outside surface. It was thought that as the vessel expanded under pressure and temperature, relative movement between the coolant coils and the vessel could cause extraneous noise signals. The nature and extent of this noise were unknown.

The metal pressure seal was also considered as a potential source of extraneous noise, since the seal will undergo considerable deformation as the pressure in the vessel increases. It was thought that once the seal was properly seated, the noise should be minimal, but background data were again unavailable.

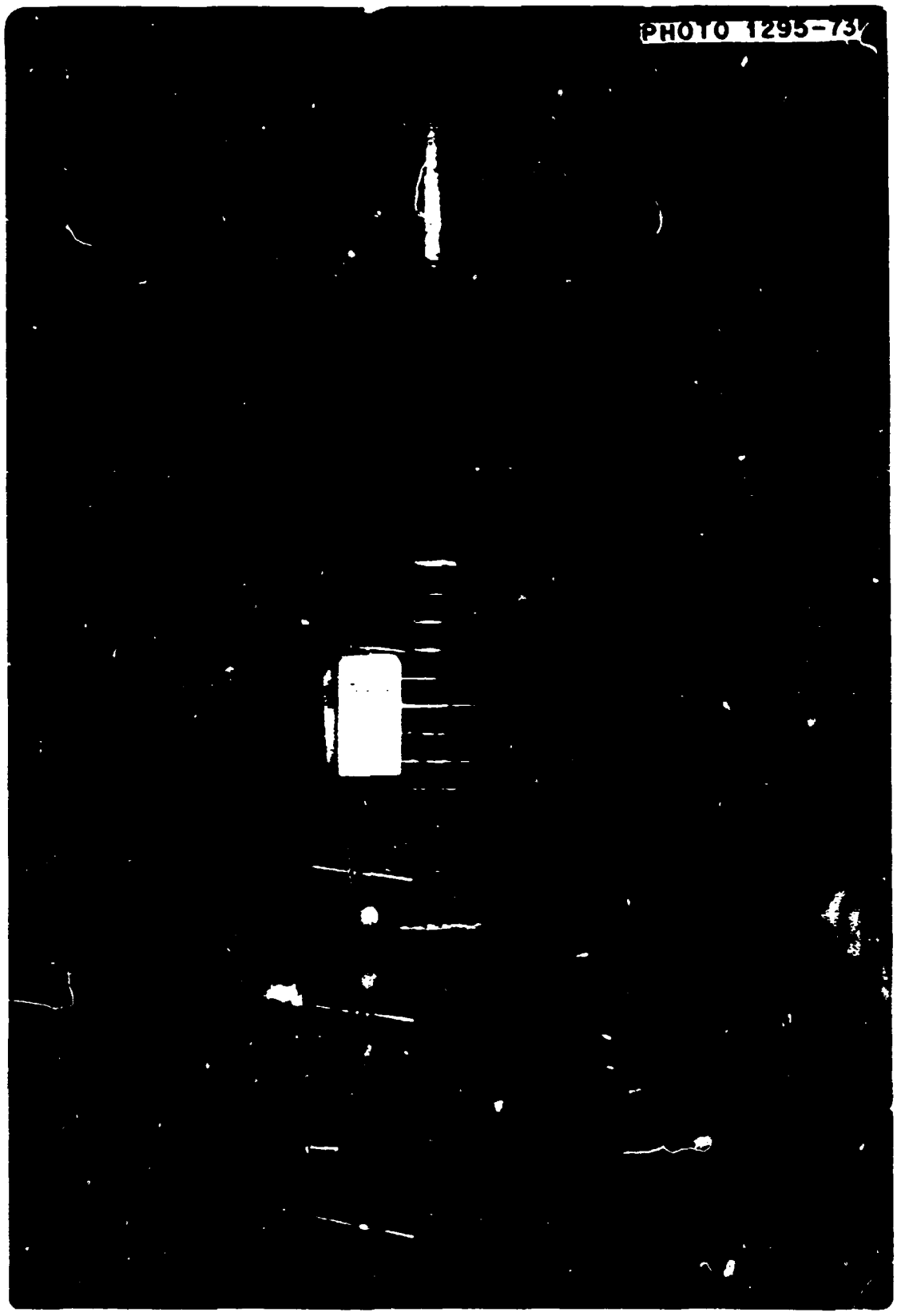

Fig. 8.29. Coolant coils mounted on vessel mockup.

The third area of potential extraneous noise was anticipated to occur in the area of the bolted head flange. Rotation of the flange, elastic elongation of the studs, and elastic movement of all the associated hardware in the head were all anticipated as possible noise sources. It should be mentioned that the majority of these mechanical noises are in the low-frequency spectrum (<80 kHz) of the acoustic emission monitoring system and are eliminated by frequency filtering. However, for the anticipated test a more refined method of data recording was warranted.

Since the primary interest of this test was to record the acoustic emission as generated in the region of the flaw, a data processing technique known as coincident detection was employed to exclude the recording

of extraneous noise. This technique employs a multiple sensor array and a coincident circuit to permit the recording of only those signals which arrive at the sensor array within a preselected time gate. All other signals are excluded. The sensor array pattern used for this technique is shown in Fig. 8.30. Sensors *L*, *G*, and *J* comprise the coincident detection sensor array. The coincidence technique functions in the following manner.

1. When sound (acoustic emission) is transmitted from the region of the flaw as a surface wave on the outside surface of the vessel, transducers *L*, *G*, and *J* will be excited at nearly the same time. For this case, the coincident circuit compares the arrival time of signals from information channels *G* and *J*; if they are within acceptable time gate limits, the coincident circuit is then open to accept data from sensor *L*, the

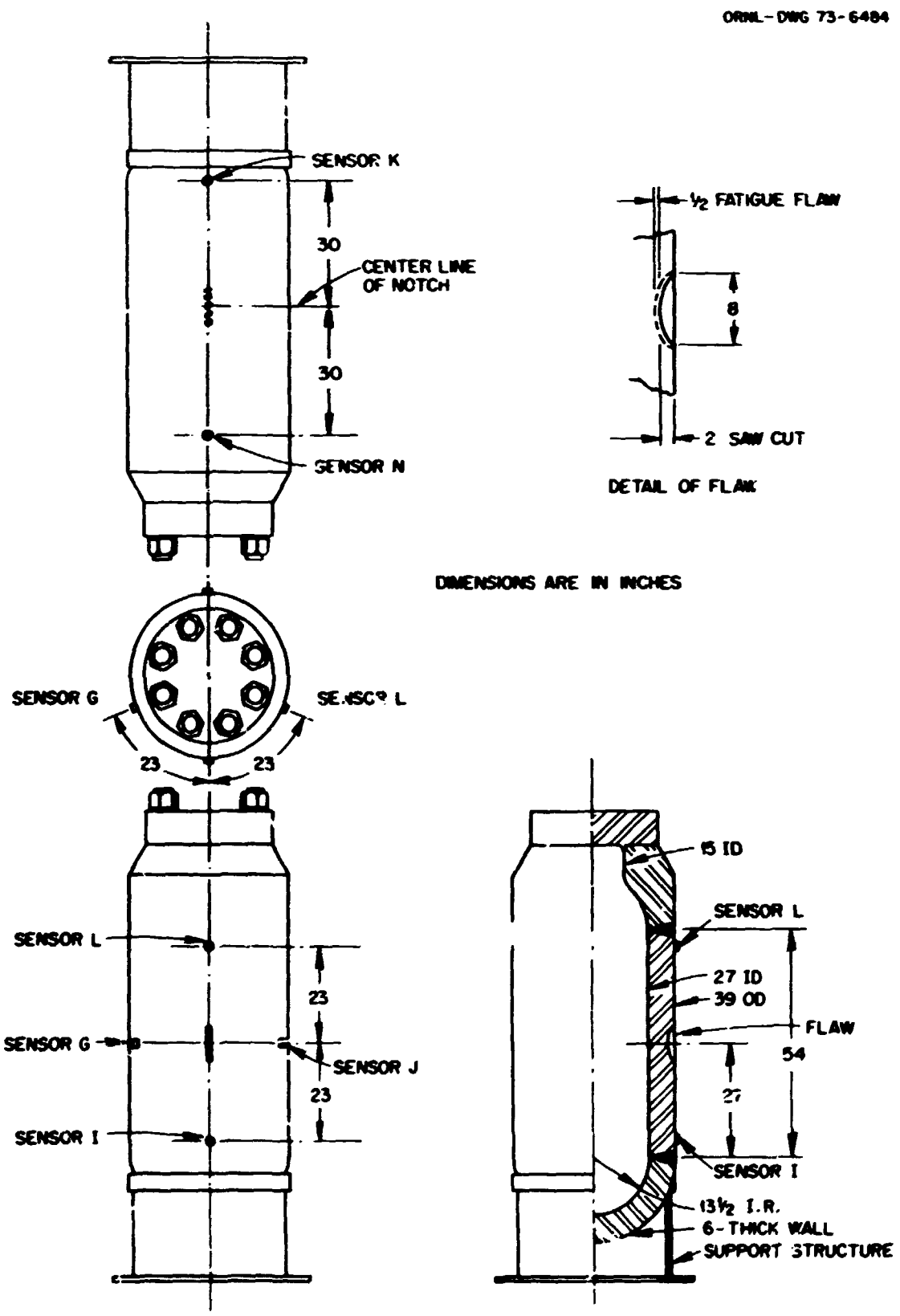

Fig. 8.30. Location of transducers on vessel.

actual data channel. This is termed two-channel coincidence. If a signal has arrived within the same time gate as the information channels, the data from this channel are accepted and recorded. This final step comprises three-channel coincidence.

2. It should be noted that two-channel coincidence could occur if sensors *G* and *J* were excited by a noise source equidistant from the sensors or by simultaneous sound transmission from either end of the vessel. For this case the data channel would not be excited in the necessary time gate, and no data would be recorded.

3. Noise sources outside the area of the flaw will usually not provide the necessary three-channel coincidence, and therefore the majority of extraneous signals are eliminated.

Noise sources outside the flaw area could also cause three-point coincidence and the recording of erroneous data if the following conditions were met: (1) the noise source was located at an area that would cause a wave front to strike sensors *G* and *J* at the same time that a noise wave front from another area strikes sensor *L;* and (2) a high-amplitude constant noise source could also be recorded, since a signal will always be in the time gate of the data channel.

These two conditions were not anticipated to occur, since any noise from the coolant coils or other areas of the vessel would probably be intermittent and have a point source location. The preliminary results of the test verified these assumptions. It also appears that the severity of the noise problem may have been overemphasized; however, the number of pressure cycles that were conducted prior to the final fracture test may have eliminated much of the anticipated mechanical noise.

Instrumentation. Typical instrumentation for monitoring acoustic emission for the test is illustrated in Figs. 8.31 and 8.32. Figures 8.33 and 8.34 show the transducers mounted on the vessel wall, Fig. 8.35 is a detailed photograph of the transducer, and Fig. 8.36 is the schematic diagram of the experiment. In general, the output from each transducer was fed into a high-input-impedance, low-noise-level preamplifier through a short coaxial cable. A second-stage amplifier was used for each channel operating in 100 to 300 kHz to achieve a gain of about 90 dB for the overall system. Since the amplifiers were designed for general purpose with a wide frequency band, bandpass filters, acting in the frequency range from 100 to 300 kHz, filtered out most mechanical and electrical noises. The signals obtained from the data channel fed into a digital counter. Only those signals significantly above electric noise level are counted as acoustic emission. The digital-to-analog converter changed the digital counts into analog signals which were applied to the *Y* axis of an *X-Y* recorder; the *X* axis was reserved for the information obtained from pressure transducer mounted in the test system. The *X-Y* recorder thereby provides an on-line graphic presentation of accumulative counts as a function of vessel pressure.

The outputs of the bandpass filters of the data channel and two information channels were also fed into a coincident circuit, recorded on magnetic tape, and displayed on the oscilloscope. Since the sensors of the data channel and the information channels were mounted at an equal distance from the precracked notch area, only the emissions from the notch area could pass through the coincident circuit and were counted in the counter at the output of the coincident gate, as previously discussed. However, the counter before the coincident circuit could count all detectable acoustic emissions from the vessel. The amplitudes as well as the durations of acoustic emission pulses were also recorded in a chart recorder through a detector and an operation amplifier. As shown in Fig. 8.36, an additional three channels with the oscilloscope were used to periodically monitor other areas of the vessel during the test.

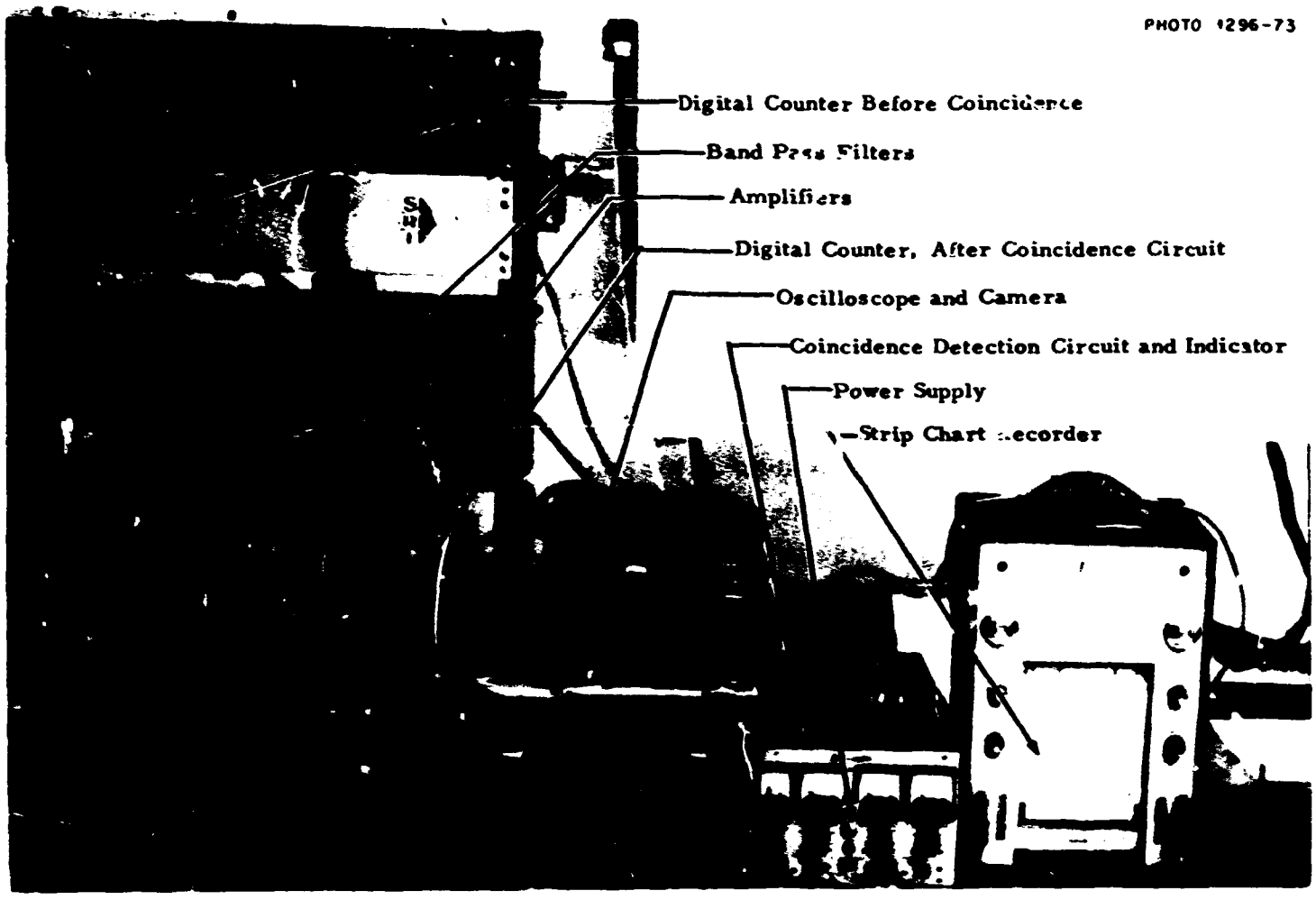

Fig. 8.31. Acoustic emission monitoring system.

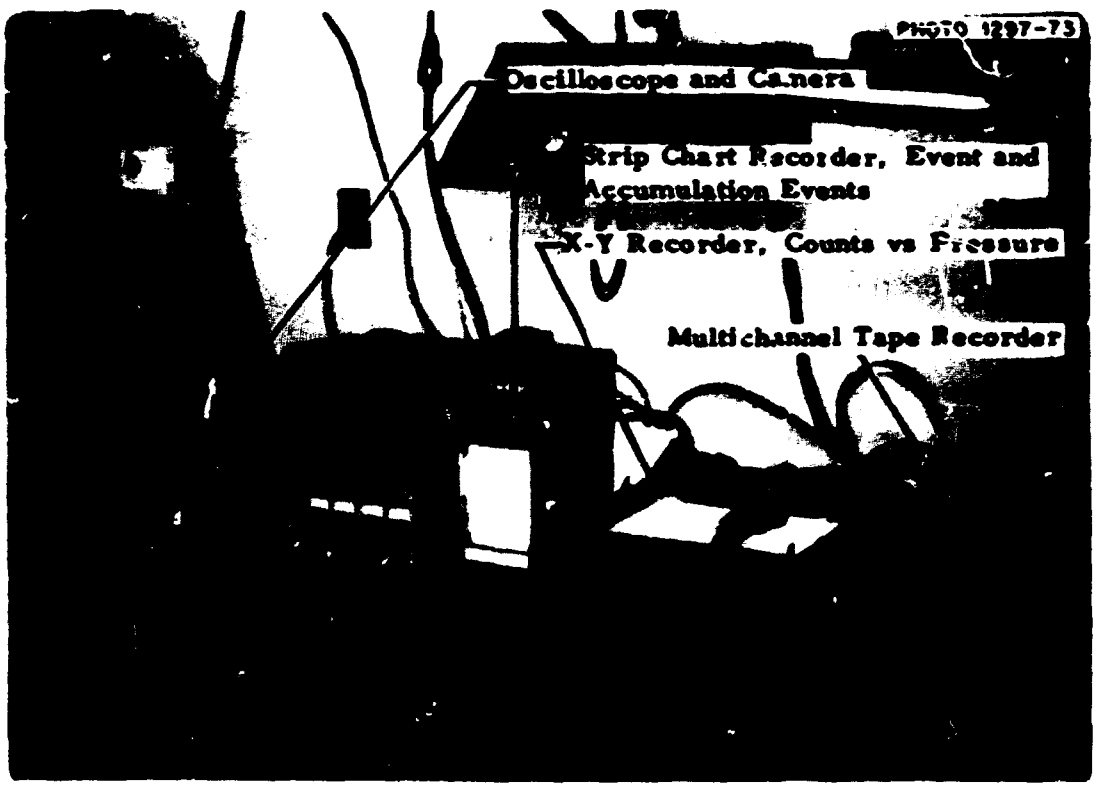

Fig. 8.32. Acoustic emission data acquisition system.

PHOTO 1298-73

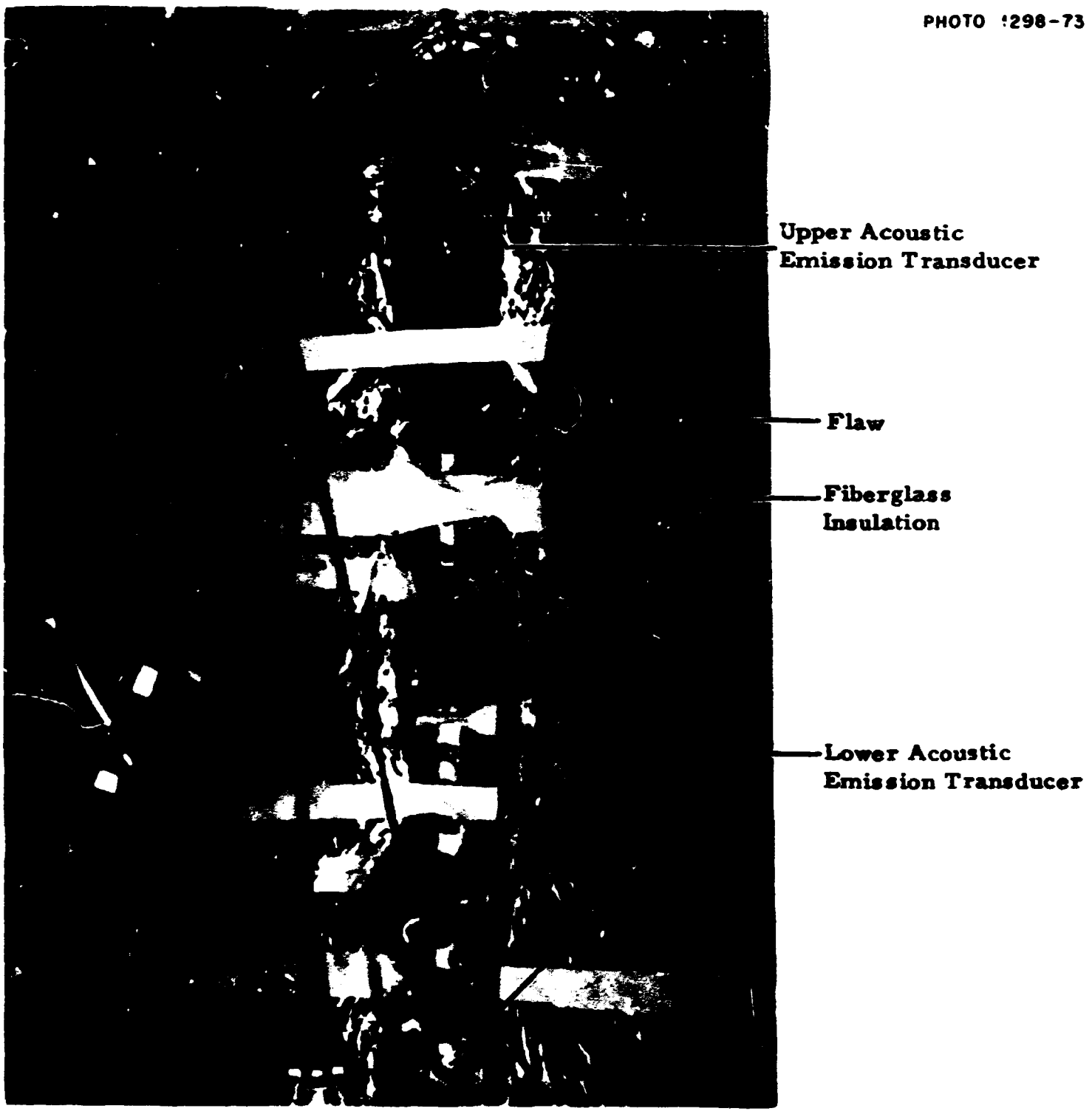

Fig. 8.33. Location of acoustic emission transducers above and below flaws.

Fig. 8.34. Acoustic emission transducer mounted below flaw.

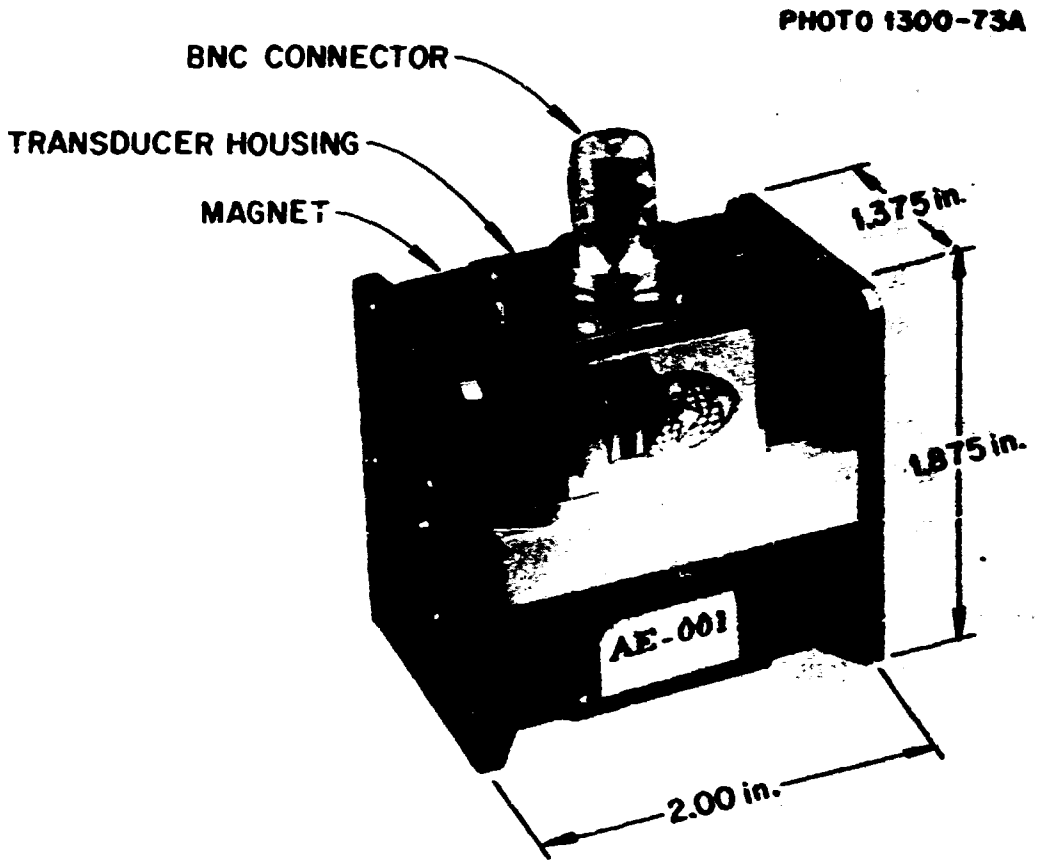

Fig. 8.35. Acoustic emission transducer.

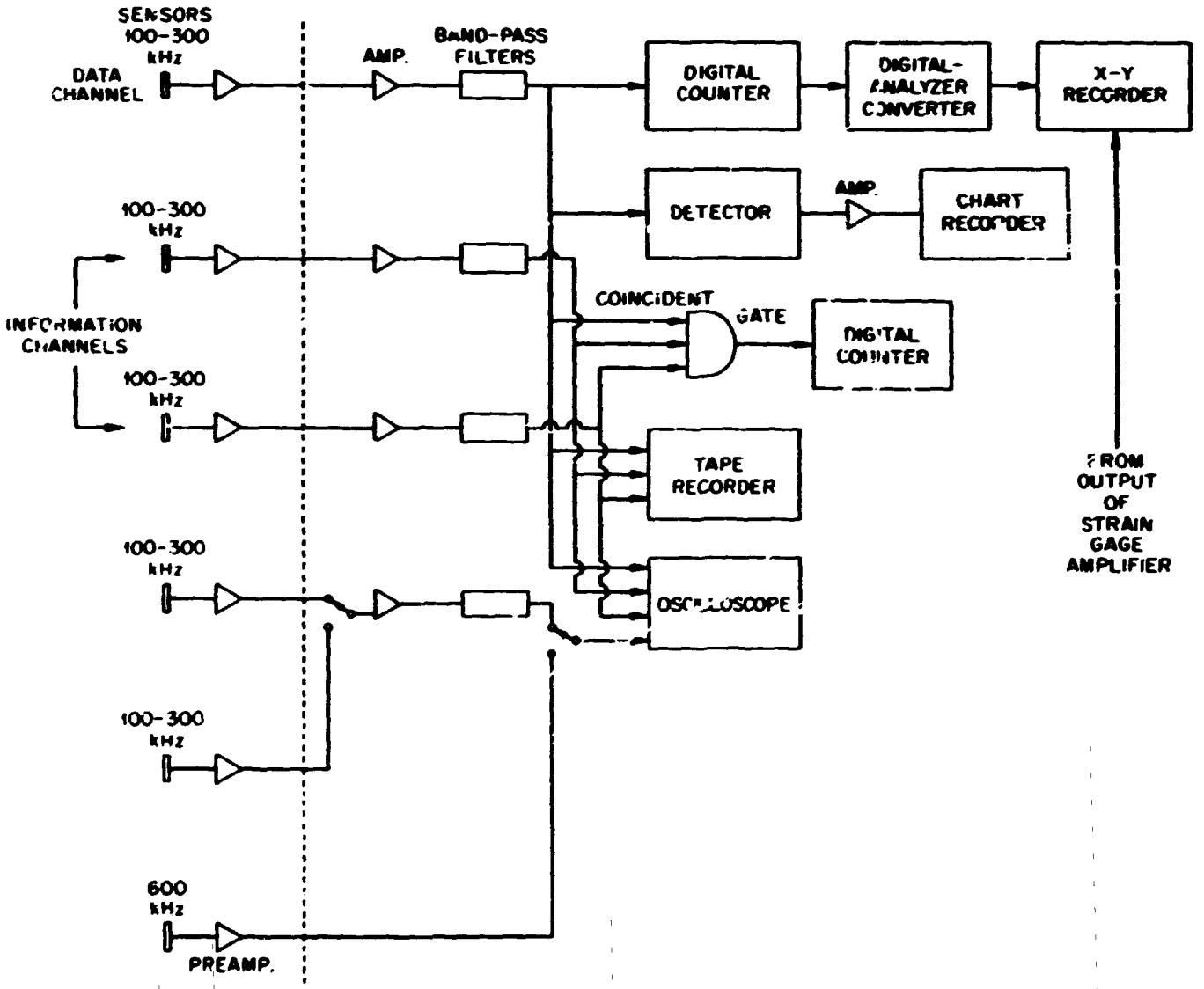

Fig. 8.36. Block diagram of acoustic emission monitoring system.

Results. Acoustic data were taken during all the pressure tests. Data presented and discussed in this report were normalized to the first loading from zero pressure to the final fracture of each test. Figures 8.37 and 8.38 show the accumulation of the emission counts obtained from the digital counters before and after the coincident circuit respectively. Since the counters counted every frequency cycle of each emission pulse and usually a pulse with a higher amplitude has a longer duration, the accumulation counts directly relate to amplitudes and durations of emission pulses as well as the number of pulses. The counts in Fig. 8.38 represent the detectable emission from the vessel of each test, and the counts in Fig. 8.37 correspond to the emission from the notch area at different test temperatures. These two sets of curves are similar in shape to those obtained from flawed specimens during the HSST tensile tests.[3] The counts increase rapidly before the yield point, there are smaller counting rates during yielding, and the counting rates increase again prior to the failure of the vessel. The counts prior to failure in Fig. 8.38 are greater than those in Fig. 8.37 because the counter for Fig. 8.37 was placed after the coincident circuit and detected bursts in a limited notch area which was smaller than the final crack area, whereas the counter for Fig. 8.38 was placed prior to the coincident gate, and the vessel failure detected all the emission from the entire fracture area of the vessel.

Figure 8.39 is a typical record of acoustic emission from the strip chart. The length of each line represents the amplitude and the duration of an individual emission pulse. The emission pulses shown in

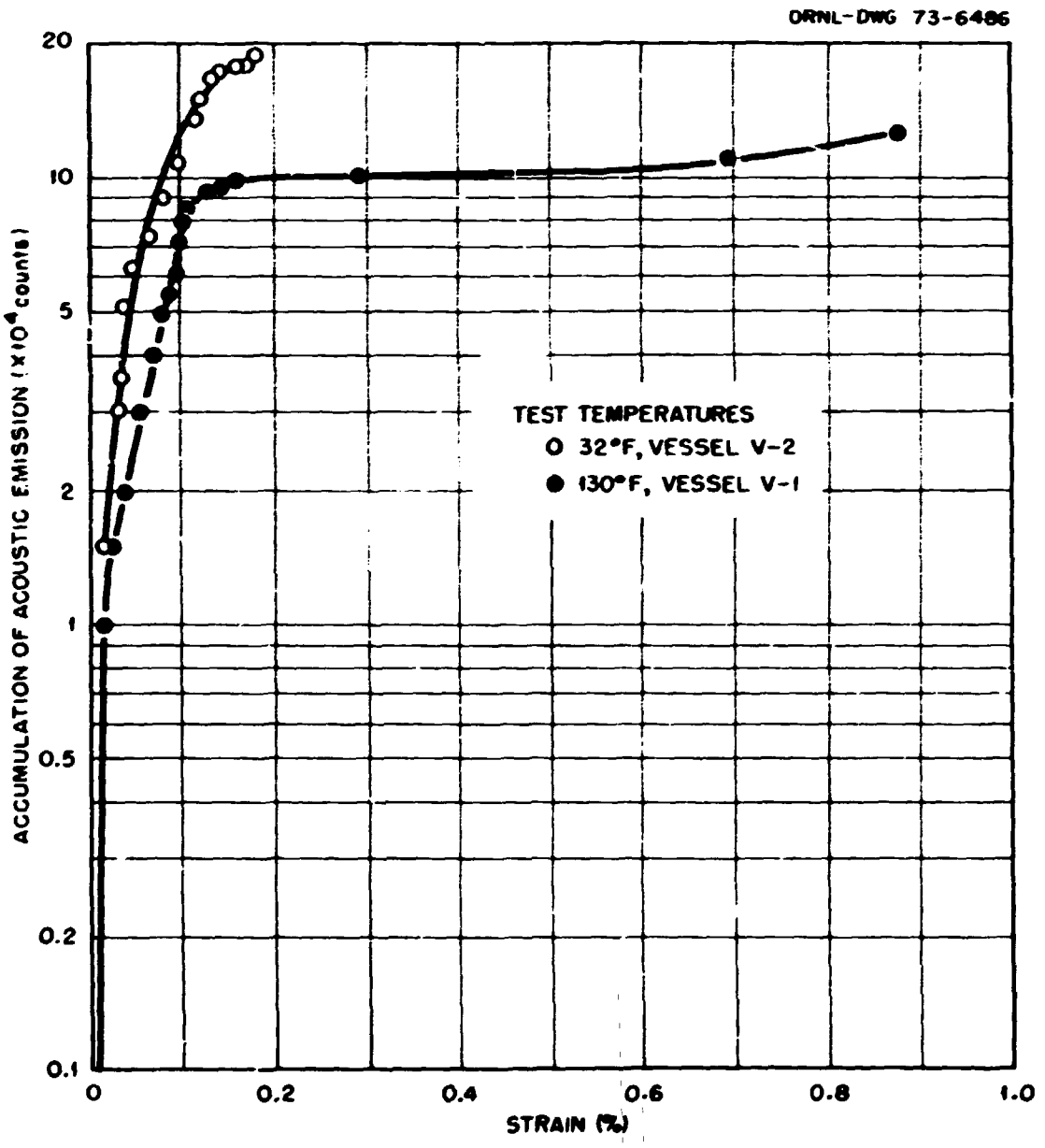

Fig. 8.37. Acoustic emission from precracked notch areas of vessels V-1 and V-2.

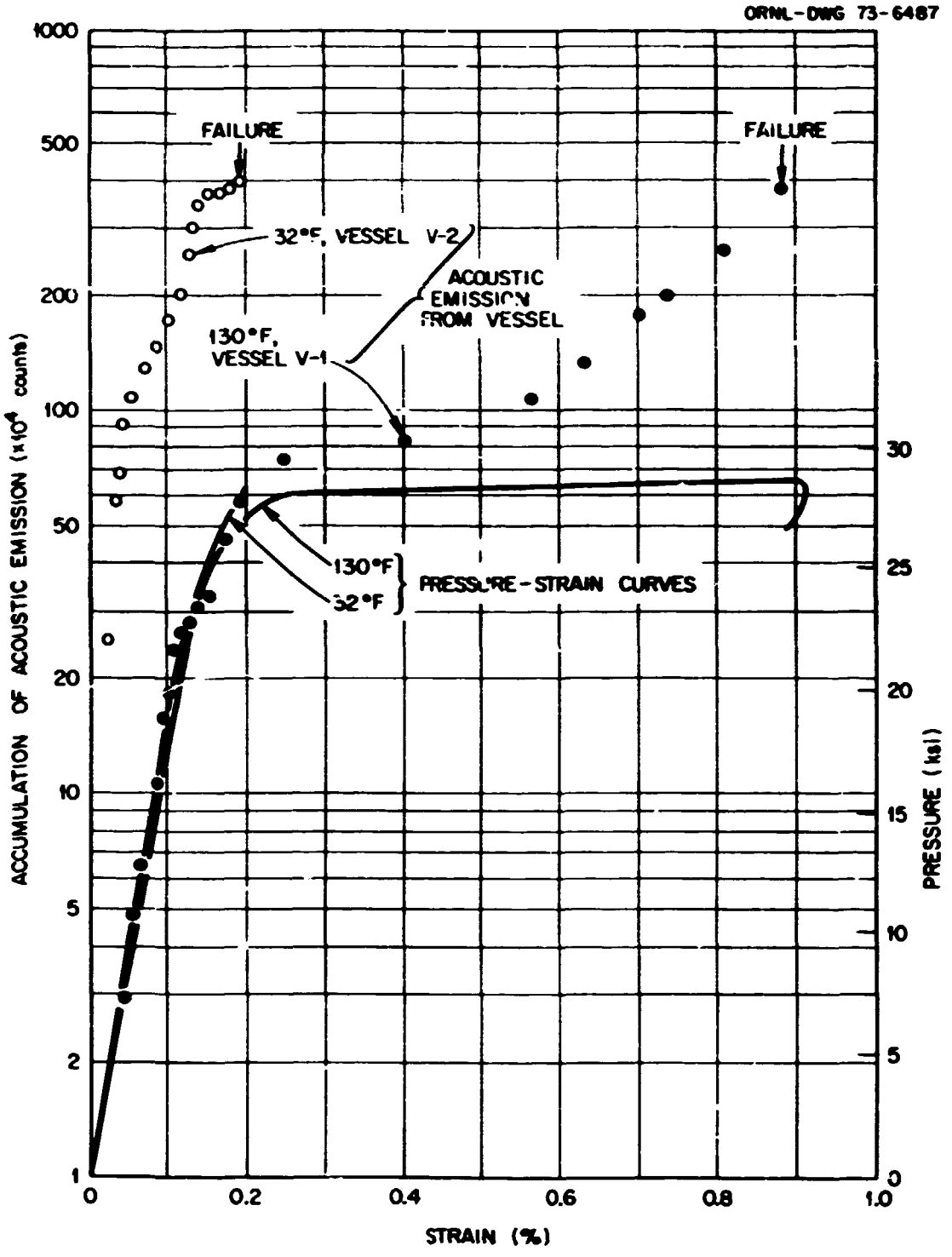

Fig. 8.38. Acoustic emission from vessel as a function of strain.

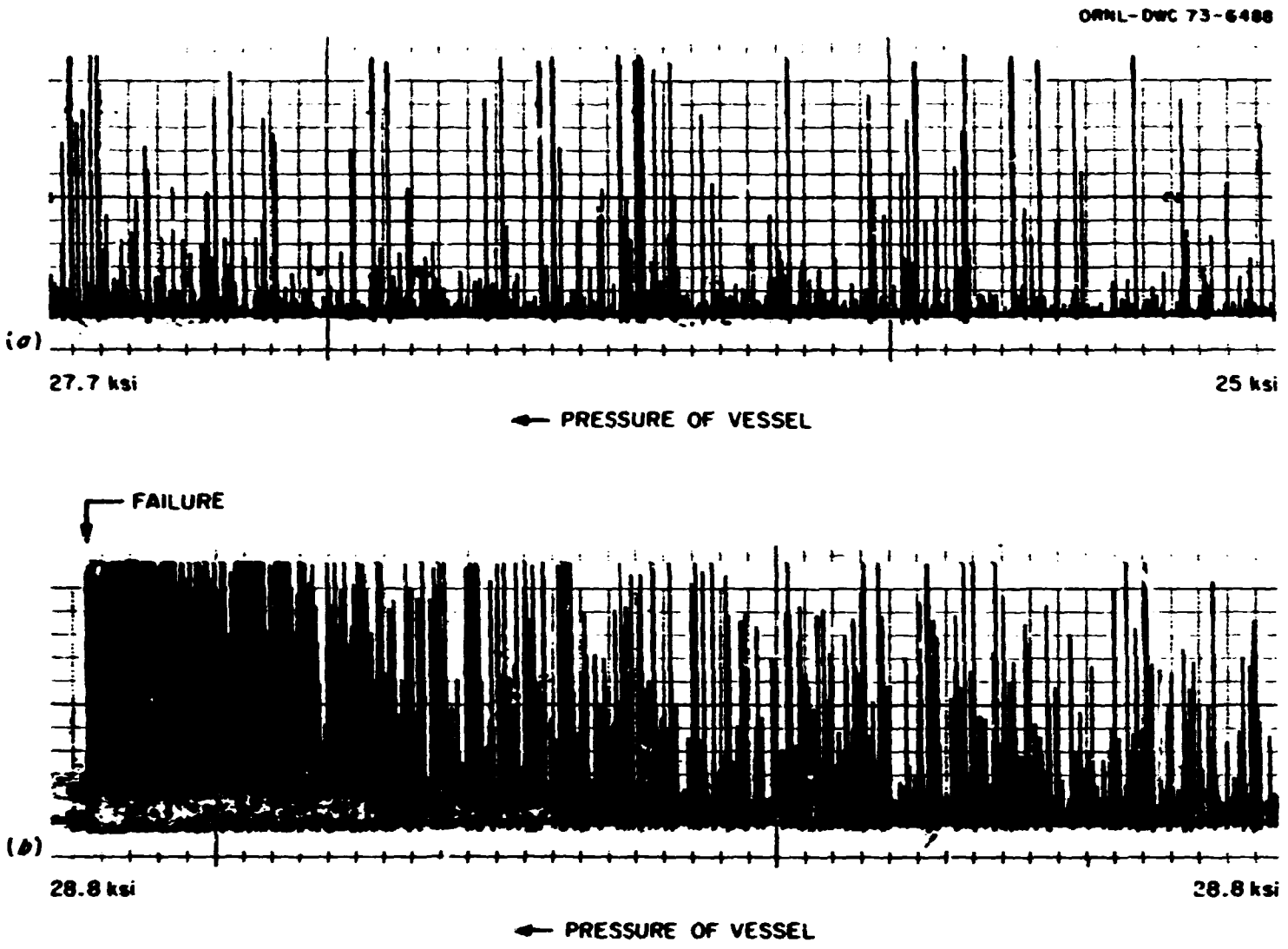

Fig. 8.39. Records of acoustic emission bursts.

Fig. 8.39 were recorded for 130°F tests at the vessel pressures from 25 to 28 ksi. Figure 8.39 is the record of acoustic emission prior to the failure for the same test. Both the amplitudes and the rate increased tremendously during this period up to failure.

References

1. S. Timoshenko and J. N. Goodier, *Theory of Elasticity*, 2d ed., pp. 58–60, McGraw-Hill, New York, 1951.
2. S. C. Grigory, *Six-Inch-Thick Flawed Tensile Tests, First Technical Summary Report, Longitudinal Specimens 1 through 7*, HSSTP-TR-18, SwRI 03-2520, Southwest Research Institute, San Antonio, Tex. (June 1972).
3. S. P. Ying and S. C. Grigory, *Tests of 6-Inch-Thick Tensile Properties, Fifth Technical Summary Report, Acoustic Emission Monitoring of One-Inch-Thick and Six-Inch-Thick Tensile Specimens*, HSSTP-TR-24, Southwest Research Institute, San Antonio, Tex. (November 1972).

9. DISCUSSION

Previous chapters of this report have presented the extensive data accumulated from mechanical properties tests, fracture toughness tests, model vessel tests, and nondestructive inspections. These data were used to formulate the test plans for intermediate pressure vessels V-1 and V-2 and provided the necessary input for a variety of analytical fracture analyses of their expected behavior. In addition, certain key observations can be made from these ancillary tests. These are briefly summarized here, followed by a detailed discussion of the experimental results of the vessel V-1 and V-2 tests and their associated analysis.

Material Investigations

An engineering method to provide a safety assessment for reactor pressure vessels must utilize materials data from which a realistic prognosis may be made. The specimens from which such data are obtained should be as small as practical (including irradiation surveillance considerations) and should be economical to test, and, insofar as possible, the test method should be one with which the technical community is familiar. Most important, the data obtained must be quantitative and, through proper validations, be demonstrated to provide adequate representation of structural behavior. One of the important efforts of the HSST program is to develop specimen types having such qualifications. For fracture initiation, two specimen types have received the most attention. The first of these is the compact tension specimen.[1] Specimens of this type have been extensively tested in thicknesses up to 12 in.[2–5] Results from these tests show that the compact tension specimen is suitable to provide fracture toughness values at temperatures up to 550°F.[3]

The second specimen type that has been extensively evaluated is the Charpy specimen, precracked and tested in either a slow-bend or a dynamic mode. This specimen, without precracking, is familiar to materials engineers throughout the world and is widely used in irradiation surveillance programs. As in the case of the compact tension specimens, the precracked Charpy data can be used to obtain adequate lower-bound fracture toughnesses; that is, the value obtained from these small specimens is less than or equal to that obtained from a larger specimen. This is exemplified by the fact that the data from precracked Charpy specimens at the test temperature (32°F) of vessel V-2 well defined the existing toughness established from larger specimens. In fact, those data very well described the sharp toughness transition temperature region to higher toughness levels.

Another example of the use of the precracked Charpy specimen data is to calculate the lowest temperature for which the ASME code would allow design pressure to be reached for a vessel with an assumed flaw size. When this was done for the intermediate pressure vessels (see Appendix E), a value of −50°F was calculated based on static toughness.

A very important observation that is common to both the compact tension and the bend specimens (more specifically the precracked Charpy specimen) is that toughness values (K_{Ic} and K_{Icd}) can be obtained which are independent of crack length within given bounds.[1] This means that for a given type of specimen, all such specimens tested may be compared on the basis of dimensional analysis[3] without regard to crack length; that is, each is a model for all the others. This characteristic plays an important role in subsequent discussions of the results of model and intermediate vessel tests.

In addition to compact tension and precracked Charpy specimen data, standard tensile, drop-weight, and Charpy impact specimen data were obtained from which toughness correlations can be made. For example, impact energy could be correlated with lower-bound toughness from the data presented in Tables 4.7–4.10. It is expected that additional correlations will be done after all the intermediate vessels have been tested.

Model Testing

Model testing has played an important role in the HSST program for at least two reasons. First, a flawed model of a structure provides the same constraint (geometry and loading conditions) at the flaw for a given normalized load as the structure, at least as long as fracture or stable crack growth has not occurred. Thus the effect of constraint is exact within the capability to model and is not dependent on conservative or arbitrary assumptions. Second, modeling offers the most economical method of comparing the behavior of different types of specimens.

As described in Chap. 5, two series of 0.85-in.-thick model pressure vessels were tested to failure as part of the test program for vessels V-1 and V-2; one series was fabricated from vessel V-1 prolongation material and the other from vessel V-2 prolongation material. Insofar as practical, an identical flaw was placed in all vessels of a given series.

In addition to the model vessels, a number of 0.85-in.-thick compact tension specimens were fabricated from the same material and appropriate data collected. To substantiate the premise that test results from compact tension specimens can be used to predict the behavior of the model vessels, some basis for comparison had to be established. Possible bases included load, strain, crack opening displacement, energy, etc.; however, to date, energy has provided the most useful basis for comparison.[3,6,7] Accordingly, the volumetric energy ratio[3] was used to calculate the behavior of the model vessels from the behavior of the compact tension specimens. To do this, it was assumed that at a selected test temperature the energy to maximum load of the compact tension specimen is equivalent to that of the pressure vessel. The energy is represented by a load-deformation curve for the structure or specimen of interest. To calculate the behavior of pressure vessels at other temperatures, the energy to maximum load of the pressure vessel, at the selected temperature, was divided by the volumetric energy ratios of the compact tension specimen at the other temperature. (Here volumetric energy ratio is defined as the energy to maximum load of the compact tension specimen tested at the selected temperature divided by the energy to maximum load of the compact tension specimen tested at the other temperature.) Where necessary, the compact tension specimen data were adjusted to compensate for small variations in flaw size.

The results of the above procedure are shown in Fig. 9.1. It should be noted that the actual curves used to prepare Fig. 9.1 were adjusted to account for the slight effect of temperature and material variations on yield properties and strain hardening. This does not significantly affect the estimates of energy as determined from the area under the curve. Of importance is the comparison of the energy (area under the curve) to maximum pressure between experiment and calculation. Based on these data, it may be concluded that, with the exception of the results at −35°F obtained from model vessel V1-A1-E, the fracture behavior of these series of vessels can be reasonably well predicted from compact tension specimen data. The −35°F point falls in the region of the yield plateau where a strain instability exists; that is, various values of strain can occur for the same load. This test, along with several others conducted in the HSST program, has shown that failure above the initial yield strain does not occur until the onset of strain hardening as measured in the gross section. Since compact tension specimens do not exhibit the yield instability, they do not reflect this behavior; thus by the volumetric energy ratio comparison the compact tension specimens indicate failure of the vessels occurring within the strain interval defining the instability. This behavior is further discussed in Appendix H.

It is important to note that the fracture behavior of the two series of model pressure vessels was well described from compact tension specimen data for all cases above yield point load. In this region it can be shown that (1) the model pressure vessels and compact tension specimens have the same transition temperature behavior based on energy to maximum load, (2) the volumetric energy ratio curve as a function of temperature is the same for the pressure vessels as for the compact tension specimens, and (3)

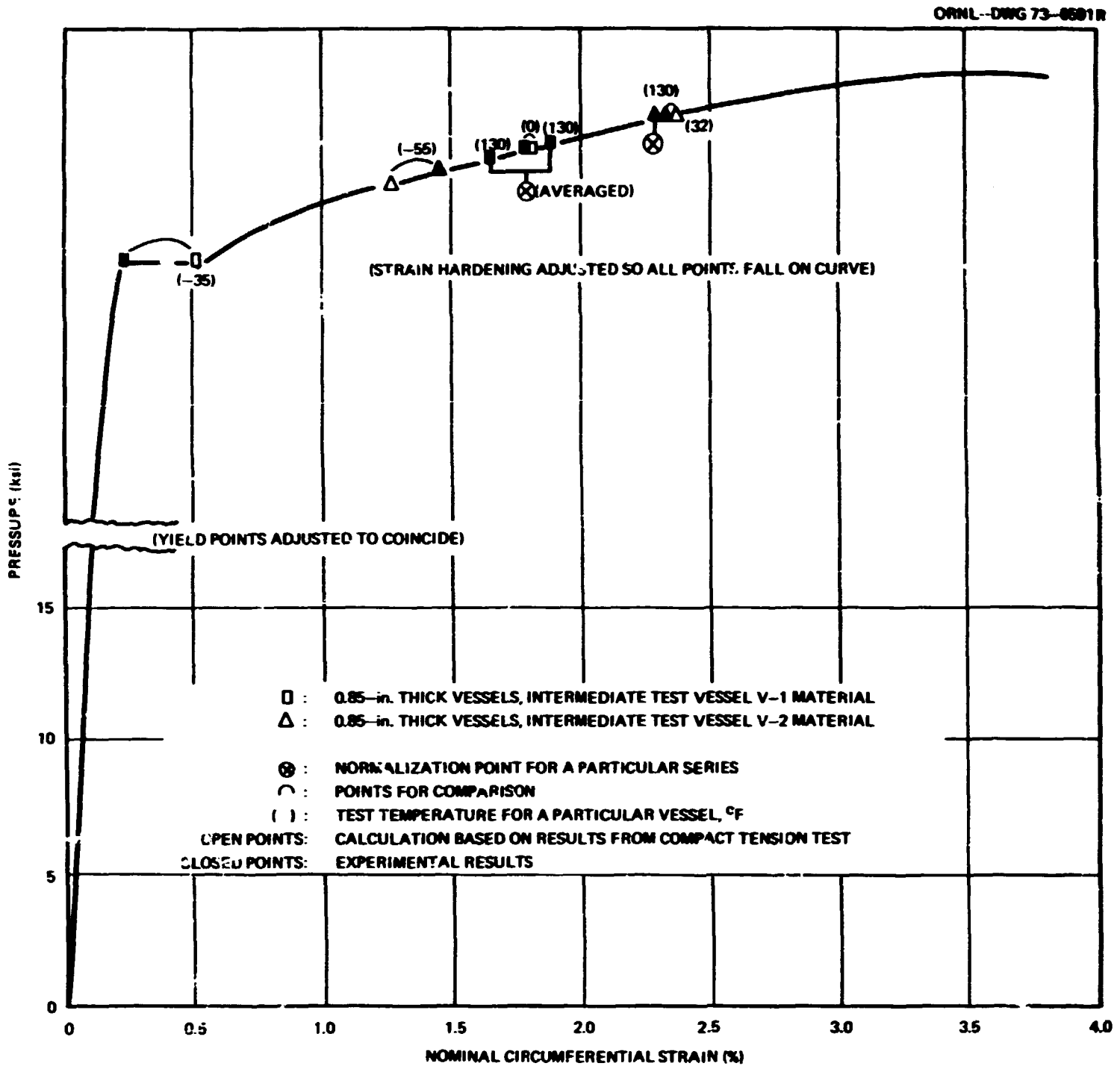

Fig. 9.1. Calculated fracture conditions in model and prototype pressure vessels, normalized to the behavior of compact tension specimens, compared with experiments.

the shape factor (geometry and loading factor)[6] from each set of pressure vessels with a specific flaw shape is independent of temperature.

Summary of Fracture Calculations for Vessels V-1 and V-2

Extensive work has been done by a number of investigators to develop analytical methods for predicting failure in flawed vessels. As part of the HSST program a number of these investigators were asked to analyze the performance of the first two intermediate pressure vessels; their calculations are summarized in Appendix C. The objectives of the various investigators making the calculations varied somewhat; some were meant to be conservative, while others attempted to be accurate with varying degrees of conservatism.

For comparison, the actual test conditions and results from vessels V-1 and V-2 are summarized in Table 9.1 and in Figs. 9.2 and 9.3, which show the circumferential strain data 180° from the flaw and crack opening displacement, respectively, plotted as a function of pressure. In the case of the strain data, it has been shown[8] that Lamé equations give almost identical results with those obtained in the elastic region.

Table 9.1. HSST program intermediate pressure vessel test conditions

Condition	Vessel V-1	Vessel V-2
Date tested	6-30-72	9-28-72
Flaw location	Cylindrical course, outside	Cylindrical course, outside
Test temperature (°F)	130	32
Fracture toughness (ksi $\sqrt{in.}$)	311	200
Failure conditions		
Pressure (ksi)	28.8	27.9
Strain (%)	0.90	0.194
Crack opening displacement at rupture (in.)	>0.88	0.075
Estimated flaw size (in.)		
Depth	2.625	2.56
Length	8.25	8.25
Actual flaw size (in.)		
Depth	2.56	2.53
Length	8.25	8.30
Energy (psi)	239	31.3

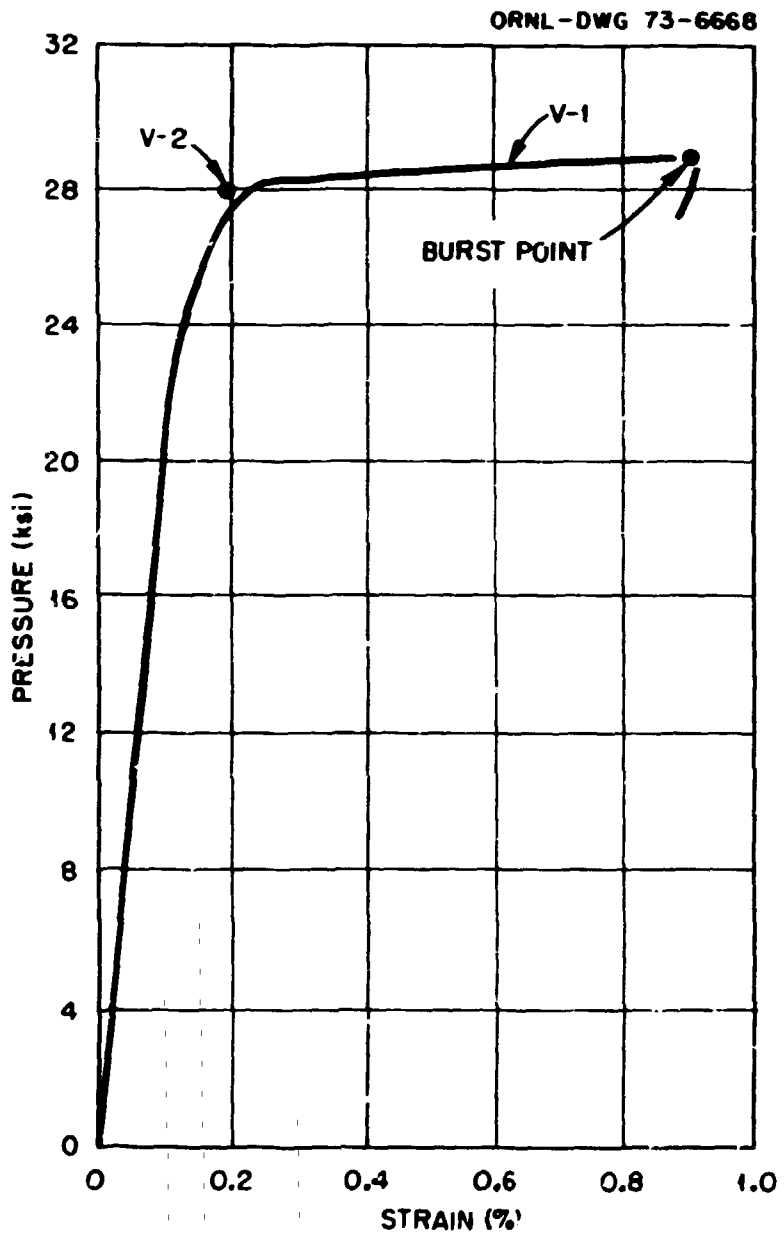

Fig. 9.2. Pressure–nominal-circumferential-strain curves 180° from the flaw for vessels V-1 and V-2.

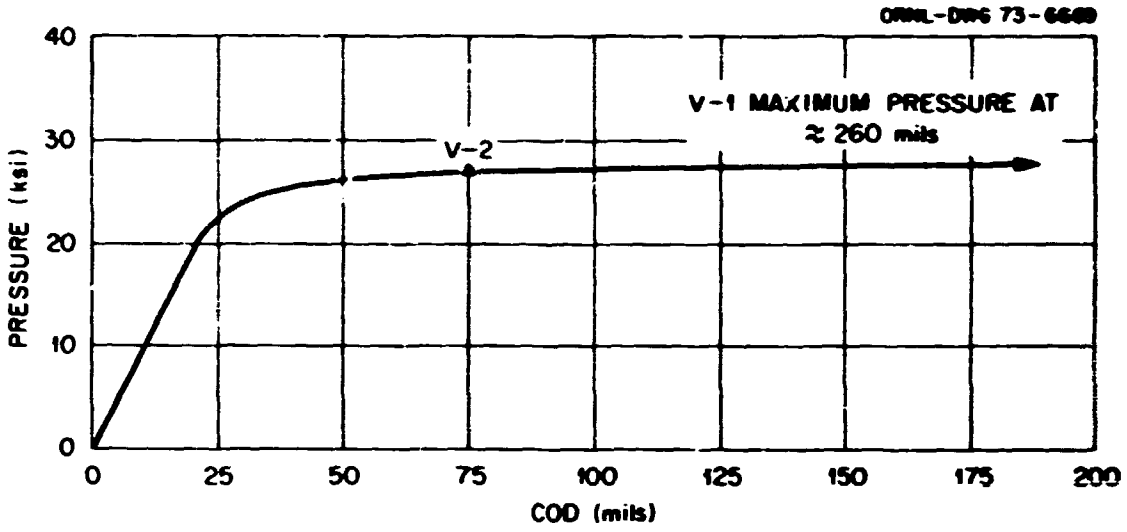

Fig. 9.3. Comparison of crack opening displacements of vessels V-1 and V-2 at maximum pressure.

It should be noted that in the analyses discussed in Appendix C, small differences between the values of some of the quantities used as input and the true values do exist. However, the effect of these differences is considered to be minor unless otherwise noted.

Analyses of vessel V-1. Vessel V-1 was tested at 130°F. The results of the 12 different fracture analyses performed for vessel V-1 are listed in Table 9.2. Note that the underlined values were calculated directly by the method of analyses indicated; other values were determined from the calculated values and estimates of the pressure-strain curve for the test vessel. For comparison, pretest estimates and posttest calculations are listed separately in Table 9.2.

The estimated values in Table 9.2 are plotted vs the corresponding measured values in Figs. 9.4–9.6. In these plots, estimates greater than the corresponding measured value fall above a 45° line of equal values, while estimates less than the corresponding measured value fall below the line. The pretest estimates are plotted as open points, and the posttest calculations are plotted as closed points. The directly calculated values are plotted as circles, and the values determined indirectly, with reference to an estimate of the pressure-strain curve, are plotted as triangles. The numbers accompanying the plotted points are the designation numbers of the methods of analysis listed in Table 9.2.

From Table 9.2 and Fig. 9.4, it can be seen that the four most accurate estimates of the failure pressure for vessel V-1 were obtained from the *J*-integral method (No. 7), the plastic instability method (No. 2), the stress concentration method (as applied by ORNL, No. 3), and the equivalent-energy method (No. 8). The *J*-integral and plastic instability methods are based on estimates of the pressure-strain curve, while the plastic instability and stress concentration methods are direct calculations of the failure pressure. No method of analysis overestimated the failure pressure for vessel V-1 by more than 10%. From Fig. 9.5, it can be seen that the most precise estimate of the failure strain for vessel V-1 was made by the inverse square root method based on strain (No. 6).

As shown in Fig. 9.6, the posttest calculation of the failure energy by the equivalent-energy method (No. 11), based on an additional model test performed after the test of vessel V-1, was considerably more accurate than the pretest estimate (No. 8). This additional model (V2-A1-B) from V-2 prolongation material had a flaw almost identical to that in vessel V-1 and gave considerably greater strains, indicating that the flaws in the first series of models were considerably more severe than those in the actual vessel (see Tables 5.1 and 5.2). The calculation based on vessel V2-A1-B data gave approximately the correct energy to maximum pressure for vessel V-1. This result is significant. Indeed, at 130°F, where significant plastic

Table 9.2. Fracture analyses for vessel V-1

Item No.	Method	Pressure (ksi)	Strain (%)	Energy (psi)	Remarks	Estimate prepared by
			Pretest estimates[a]			
1	Fracture analysis diagram				Predicts gross yield before fracture	J. G. Merkle, ORNL
2	Plastic instability	29.5			Not based on a fracture toughness	J. G. Merkle, ORNL
3	Stress concentration	28.0				J. G. Merkle, ORNL
4	Stress concentration	24.0				W. H. Irvine, UKAEA
5	Gross strain plus a bulging correction	25.0				P. N. Randall, USAEC
6	Inverse square root based on strain	30.6	0.97		Flaw not accurately modeled	R. W. Derby, ORNL
7	J-integral plus model	29.4	0.47		Based on data from models with flaws in surface material	H. T. Corten, Univ. of Illinois
8	Equivalent energy	29.6	0.48	116	Based on data from models with flaws in surface material – flaw not accurately modeled	F. J. Witt, ORNL
			Test results			
		28.8	0.92	239	Gross yield before fracture	
			Posttest calculations[a]			
9	Notch sensitivity analysis	26.3				D. Costes, CEA
10	Stress concentration	27.2				A. Quirk, UKAEA
11	Equivalent energy			237	Based on model from V-2 prolongation – flaw more accurately modeled	F. J. Witt, ORNL
12	J-integral plus model	29.4	0.44		Based on model from V-2 prolongation	J. G. Merkle, ORNL

[a]Underlined values were determined by the method indicated; other values were determined from the calculated values and an estimate of the pressure-strain curve.

deformation occurs, the volumetric energy ratio between the 0.85-in.-thick model vessel and the 6-in.-thick vessel V-1 is the same as that for the 0.85- and 6-in.-thick compact tension specimens. Thus it is demonstrated that the fracture behavior for a pressure vessel can be calculated accurately and precisely at higher temperatures, where the material is very tough, if precise parameters are available to make the calculation.

The erroneous pretest calculations using the equivalent-energy method (Nos. 8 and 11) emphasize the necessity to model accurately. More specifically, the sensitivity of fracture to flaw shape is evident. With proper model data in hand for model vessel V2-A1-B, this method quite accurately estimated the fracture energy for vessel V-1. On the other hand, when the same additional model data were used for a posttest calculation by the *J*-integral method, the result was essentially the same as the pretest estimate by this method, as indicated by Table 9.2. This turned out to be due to the fact that a correction had been made for flaw size differences in the original calculation.

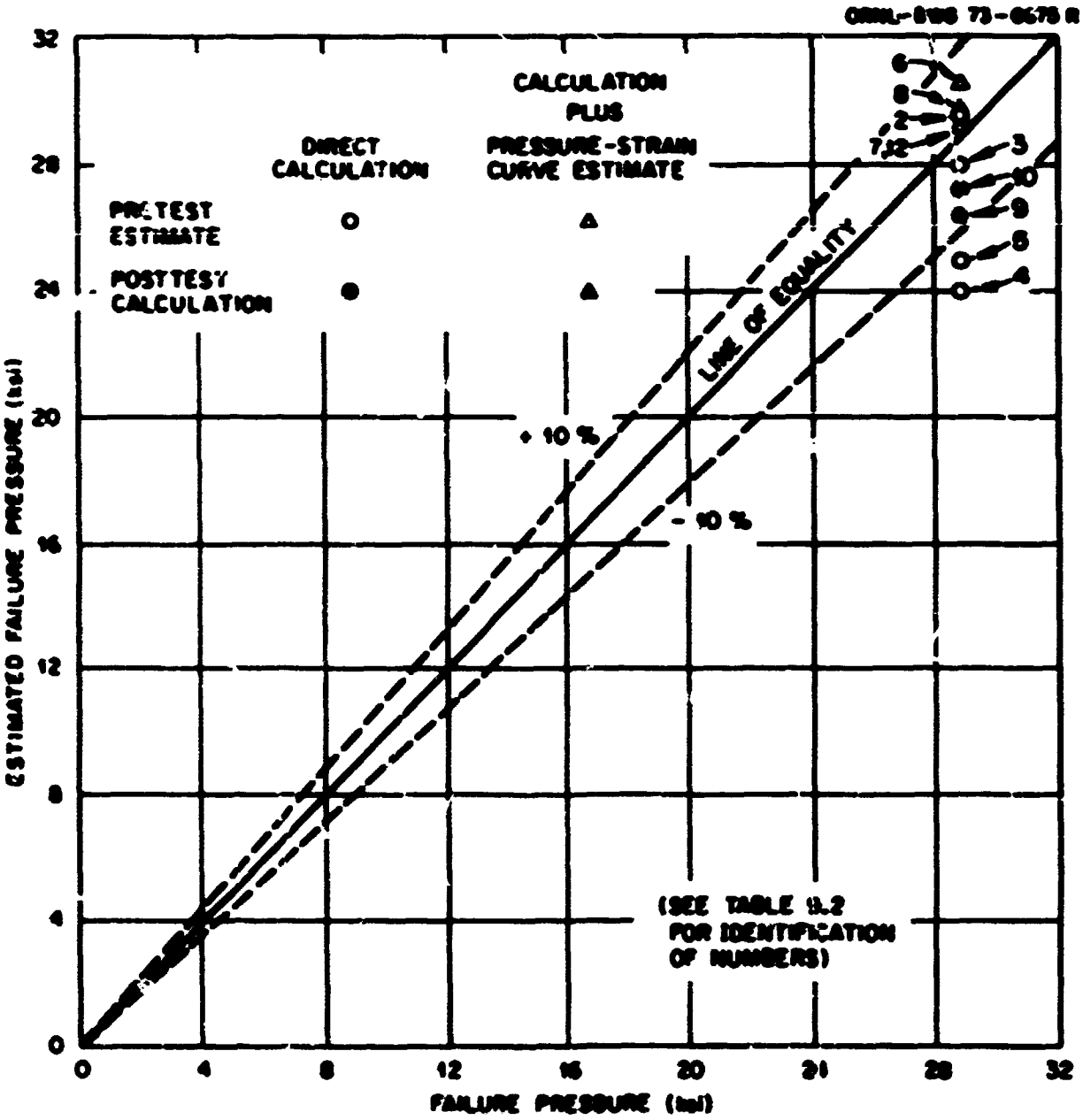

Fig. 9.4. Failure pressure estimates for vessel V-1.

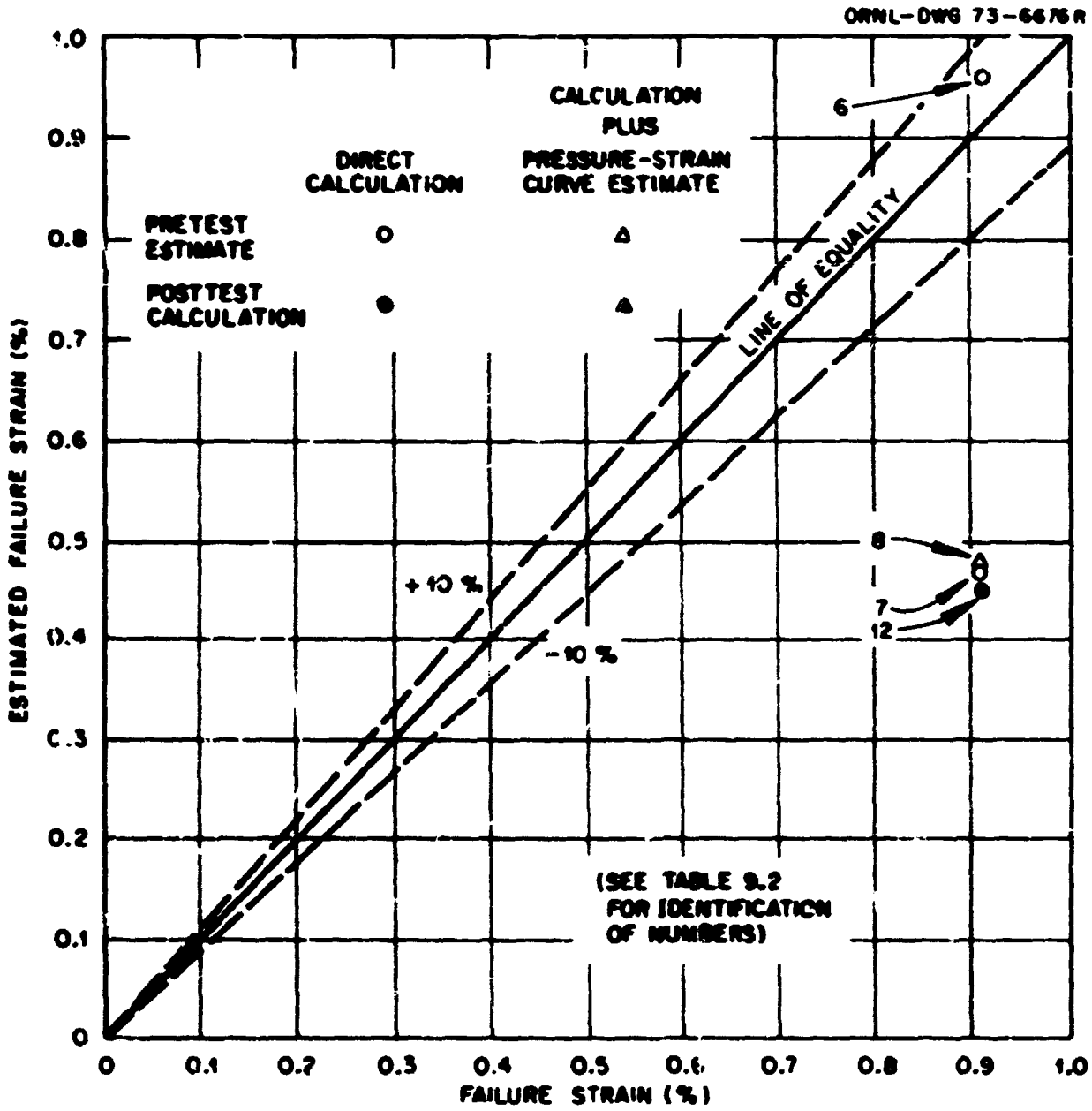

Fig. 9.5. Failure strain estimates for vessel V-1.

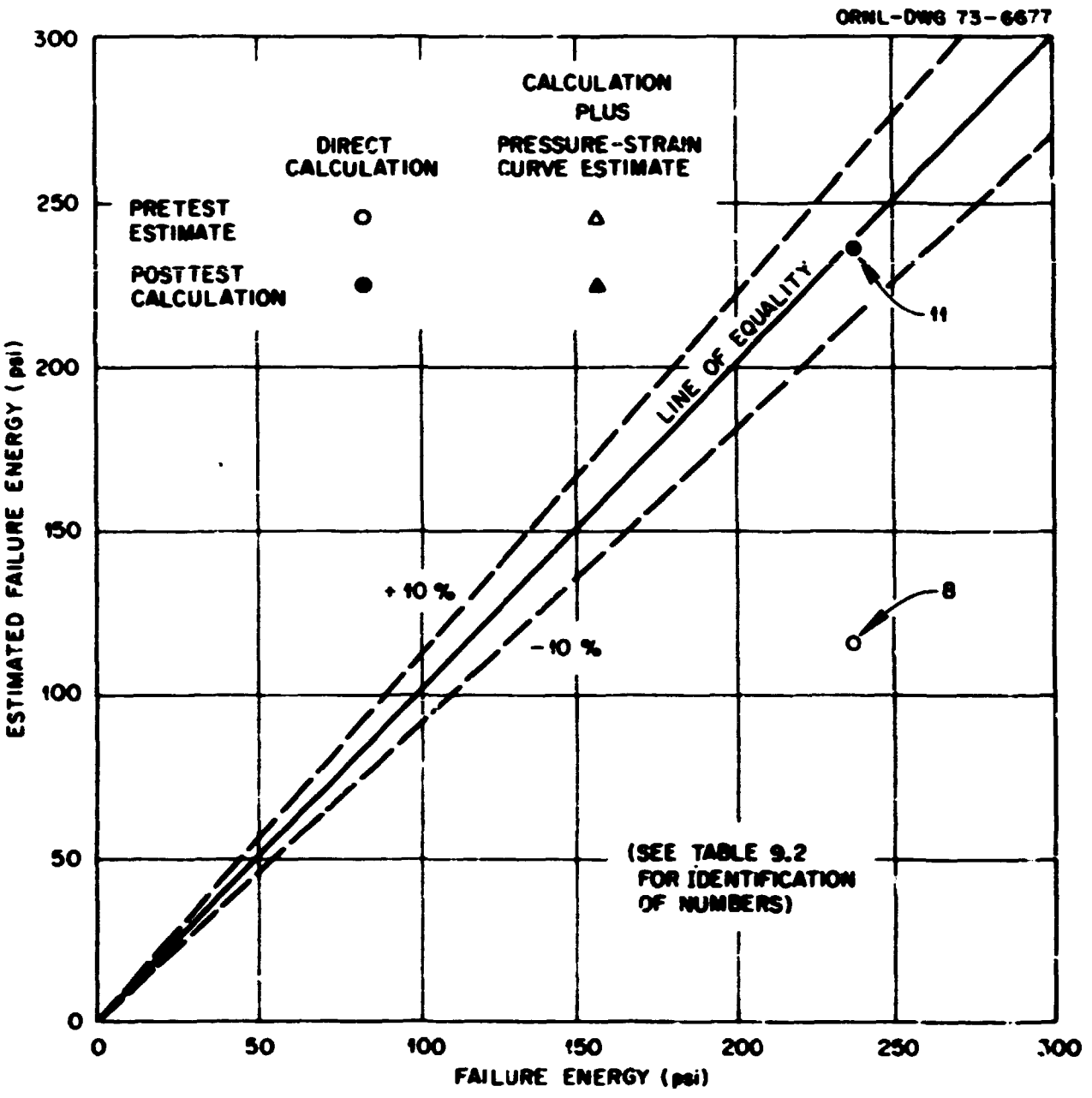

Fig. 9.6. Failure energy estimates for vessel V-1.

A first glance at the evaluation of the fracture predictions for vessel V-1 would suggest that almost without exception each investigator was successful. However, this is not the case for the type of test performed. A calculation which does not allow for large increases in nominal strains near yield pressure may not have the potential for realistic conservative or accurate estimates. A direct pressure calculation may not produce realistic values of strain. The inverse square root method based on strain, the *J*-integral method, and the equivalent-energy method have an advantage in this respect.

Analyses of vessel V-2. The results of the fracture analyses performed for vessel V-2, tested at 32°F, are listed in Table 9.3. The calculated values listed in the table are plotted vs the corresponding measured values in Figs. 9.7–9.9. The format and symbols used in Table 9.3 and Figs. 9.7–9.9 are the same as those used for Table 9.2 and Figs. 9.4–9.6.

As shown in Fig. 9.7, the most accurate pretest estimate of the failure pressure for vessel V-2 was made by the equivalent-energy method (No. 11). Again, no method overestimated the failure pressure by more than 10%. As shown in Fig. 9.8, the most accurate pretest estimate of the nominal failure strain was made

Table 9.3. Fracture analyses for vessel V-2

Item No.	Method	Pressure (ksi)	Strain (%)	Energy (psi)	Remarks	Estimate prepared by –
			Pretest estimates[a]			
1	Fracture analysis diagram	<u>24.6</u>	0.13			J. G. Merkle, ORNL
2	Stress concentration	<u>25.3</u>	0.13			J. G. Merkle, ORNL
3	Stress concentration	<u>23.0</u>				A. Quirk, UKAEA
4	Notch sensitivity analysis	<u>24.0</u>				D. Costes, CEA
5	Fracture mechanics	29.4	<u>0.21</u>		Based on strain	J. G. Merkle, ORNL
6	Martin-Marietta Corp. empirical equation	29.4	<u>0.27</u>			J. G. Merkle, ORNL
7	Fracture mechanics with β_{Ic} correction	29.4	<u>0.36</u>			J. G. Merkle, ORNL
8	Gross strain	29.4	<u>0.48</u>			J. G. Merkle, ORNL
9	Tangent modulus	29.4	<u>0.52</u>			J. G. Merkle, ORNL
10	Linear strain interpolation	29.5	<u>0.36</u>			R. W. Derby, ORNL
11	Equivalent energy	28.5	0.43	<u>99</u>		F. J. Witt, ORNL
			Test results			
		27.9	0.194	31.3		
			Posttest calculations[a]			
12	Fracture mechanics	25.0 27.0	<u>0.16</u> <u>0.19</u>		Lower bound; based on strain Upper bound; based on strain	P. C. Riccardella, Westinghouse Corp.
13	Martin-Marietta Corp. empirical equation		<u>0.21</u>		Correct strain at gross yield	J. G. Merkle, ORNL
14	Tangent modulus		<u>0.19</u>		Eliminate β_{Ic} correction	J. G. Merkle, ORNL
15	Equivalent energy	28.5	0.43	<u>99</u>	Yield plateau phenomenon demonstrated to exist – see App. H	F. J. Witt, ORNL

[a]Underlined values were determined by the method indicated; other values were determined from the calculated values and an estimate of the pressure-strain curve.

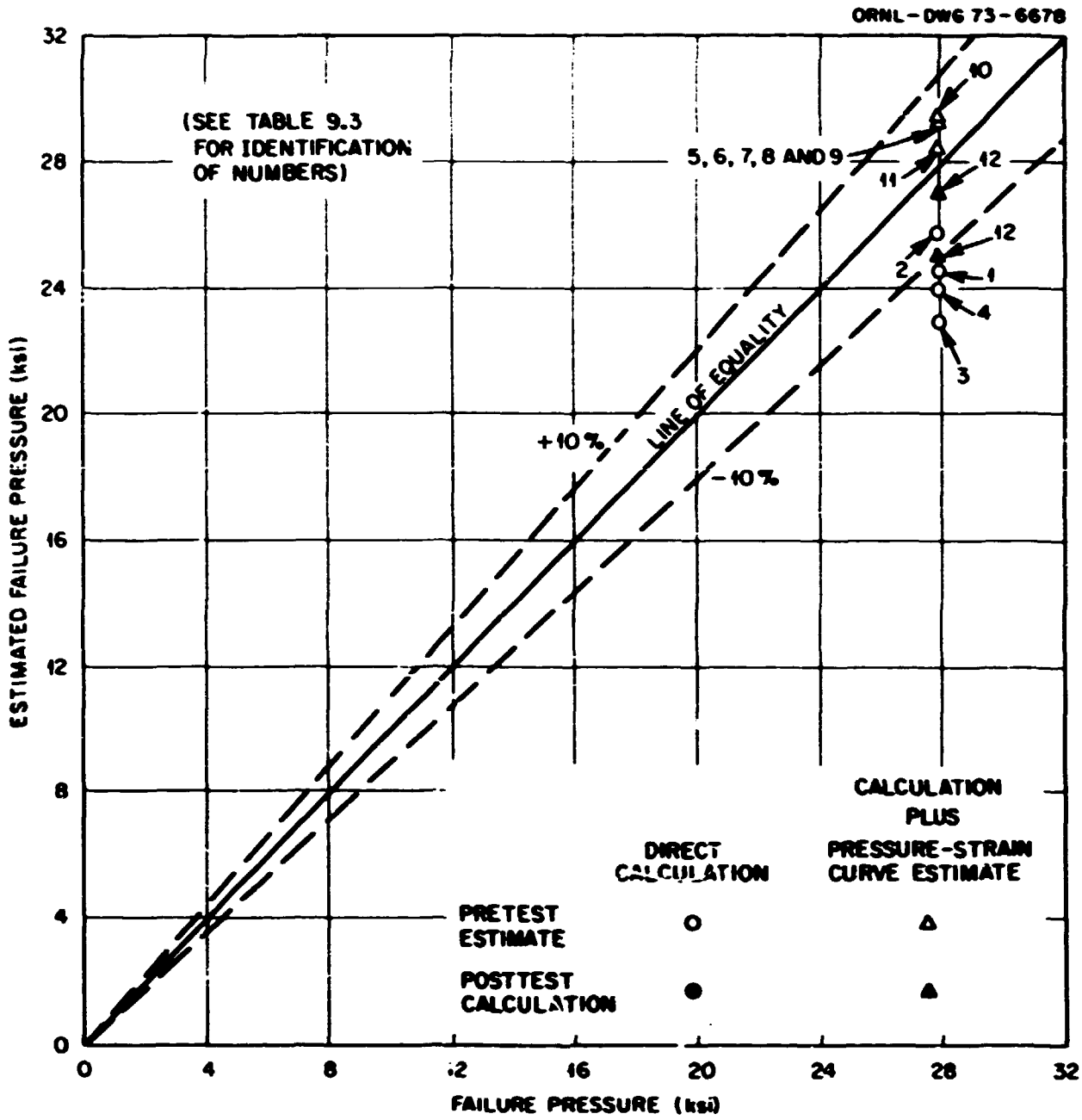

Fig. 9.7. Failure pressure estimates for vessel V-2.

by the linear elastic fracture mechanics method based on strain (No. 5). An accurate posttest calculation of the failure strain was made independently by basically the same method (No. 12). Accurate posttest calculations of the failure strain were also made by the Martin-Marietta Corporation empirical equation (No. 13) and the tangent modulus method (No. 14). Inaccuracies in estimating the pressure-strain curve caused some methods to be accurate for estimating the failure pressure or the failure strain but not for estimating both. As indicated by Fig. 9.7, the most accurate estimates of the failure pressure for vessel V-2 were all indirect estimates. Only linear elastic fracture mechanics (Nos. 5 and 12) gave accurate calculations of both failure pressure and failure strain for vessel V-2.

Figure 9.9 shows that on the basis of the comparison of the data and analysis alone, the pretest estimate of the failure energy by the equivalent-energy method (No. 11) was not accurate. However, as was the case for model vessel V1-A1-E, the V-2 failure occurred at yield load, whereas the calculation predicted a point in the yield plateau region. Therefore, all the detailed arguments set forth in Appendix H are applicable to this analysis.

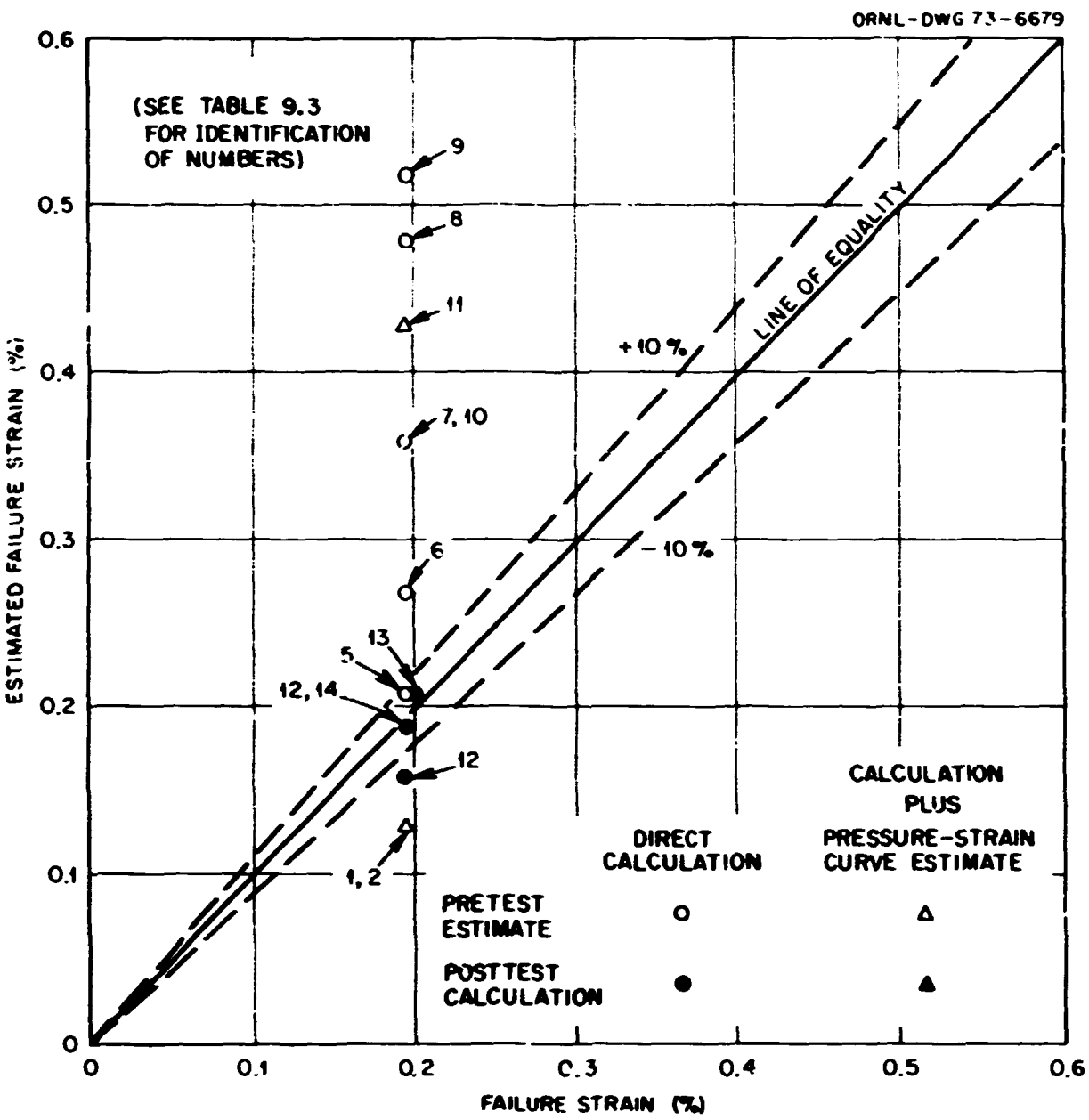

Fig. 9.8. Failure strain estimates for vessel V-2.

Metallurgical behavior of vessels V-1 and V-2. The fracture surfaces for burst of vessels V-1 and V-2 were as expected. Vessel V-1 exhibited a tough tearing dimple rupture mode of fracture until the wall ruptured, and the extensive cracking of the vessel was correctly evaluated using arrest toughness values from plate (see Appendix C).

The energy in the vessel was such that fast cleavage fracture propagated into the heads of the vessel. Similar model vessels exhibited much the same behavior, but the cracks arrested. These types of behavior are similar to those of the dynamic tear tests performed early in the HSST program on HSST plate 01.[9] The small, 1-in.-thick, specimens exhibited full ductile tearing at around 120°F, while the larger, 12-in.-thick, specimens still exhibited some cleavage at over 200°F. Since the stored energy available for propagation in the smaller vessel should well model that in the larger vessel, the crack propagation in vessel V-1 reflects a thickness or flaw size effect for this type of fracture as suggested in Appendix C. One might well surmise that at higher temperatures the crack arrest toughness increases significantly, thus suggesting the potential of crack arrest for the larger vessel. The fracture mode of vessel V-2 was flat cleavage fracture throughout.

It is significant that the total acoustic emission from the 32°F test exceeded that of the 130°F test in the region of the flaw (see Fig. 8.37), although no prior warning of fracture of the lower temperature test vessel such as a sudden burst of emission is evident based on the data presented. The total emissions detectable from throughout the two vessels were almost the same.

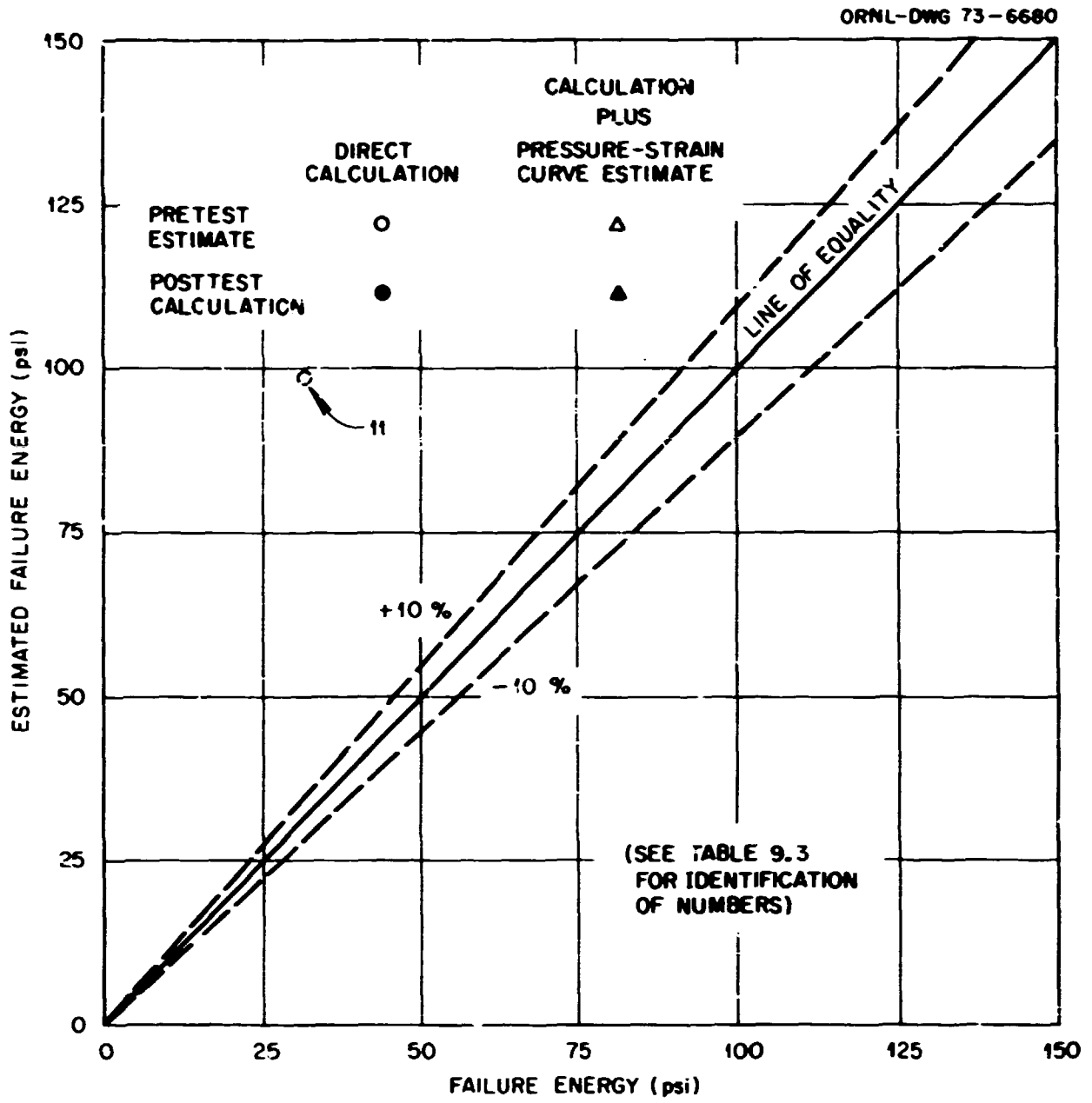

Fig. 9.9. Failure energy estimates for vessel V-2.

References

1. *1969 Book of ASTM Standards, Part 31, Physical and Mechanical Testing of Metals - Metallography, Nondestructive Testing, Fatigue, Effect of Temperature,* pp. 1099–1114, American Society for Testing and Materials, 1969.
2. W. O. Shabbits, W. H. Pryle, and E. T. Wessel, *Heavy Section Fracture Toughness Properties of A 533 Grade B Class 1 Steel Plate and Submerged Arc Weldment,* WCAP-7414, Westinghouse Electric Corporation, PWR Systems Division, Pittsburgh, Pa. (December 1969).
3. F. J. Witt and T. R. Mager, *A Procedure for Determining Bounding Values on Fracture Toughness K_{Ic} at Any Temperature,* ORNL-3894 (October 1972).
4. F. J. Witt, *HSST Program Semiannu. Progr. Rep. Feb. 29, 1972,* ORNL-4816, pp. 40–47 (October 1972).
5. J. A. Begley and J. D. Landes, *"The J-Integral as a Fracture Criterion,"* pp. 1–20 in *Fracture Toughness, Proceedings of the 1971 National Symposium on Fracture Mechanics,* Part II, ASTM STP 514, American Society for Testing and Materials, 1972.

6. F. J. Witt, *The Equivalent Energy Method for Calculating Elastic-Plastic Fracture* (to be published).

7. F. J. Witt, "Factors Influencing a Quantitative Safety Assessment of Water Reactor Pressure Vessels," *Topical Meeting on Water-Reactor Safety, March 26–28, 1973*, CONF-730304, pp. 16–38 (1973).

8. S. Timoshenko and J. N. Goodier, *Theory of Elasticity*, pp. 58–60, McGraw-Hill, New York, 1951.

9. F. J. Loss, *Dynamic Tear Test Investigations of the Fracture Toughness of Thick-Section Steel*, NRL-7056, U.S. Naval Research Laboratory, Washington, D.C. (May 14, 1970).

10. CONCLUSIONS

The tests of the first two intermediate test vessels culminated an extensive program, spanning several years, which included procurement, research and development, design, fabrication, and construction. This report summarizes the work to date in this program and is designed to be a reference document for the remaining vessel tests as well as a source of basic information and data for other investigators.

The selection of the type of vessels and test parameters for the investigations was based on recommendations from the research and regulatory bodies of the AEC, the HSST advisory committees, members of standard and code writing bodies, consultants, HSST staff, and interested individuals. The effort was undertaken with the primary objective of qualitatively demonstrating and quantitatively verifying means of assessing the margins of safety against fracture in reactor pressure vessels of water reactor nuclear power plants.

The capability of any method of analysis used to predict flawed pressure vessel behavior over a full range of temperature needs to be carefully and completely validated. Several methods have been used in the predictions of V-1 and V-2 behavior with considerable success. However, additional testing is needed to better establish the effect of flaw size, more complex stress states, limitations of methods that are applied in the transition region between elastic and elastic-plastic behavior, and crack arrest phenomena.

Those methods that utilize data obtained from models must be evaluated on the accuracy of the models that were used in the predictions. The size and shape of the flaw and the orientation of the flaw in the material from which the model was fabricated are most important. Models have played an important role in the HSST program, since the effect of constraint at the flaw for a given normalized load prior to fracture or crack growth is obtained directly; that is, the effect of constraint is determined exactly, within the capability to model, and is not dependent on complex analytical methods. Modeling also offers a more economical method for comparing the behavior of different types of specimens.

In the case of vessel V-1, it was shown that a calculation which does not explicitly allow for large increases in nominal strains near yield pressure may not have a general potential for conservative or accurate estimates.

In the case of vessel V-2, the observed failure strain at near 0.2% may not be indicative of the actual behavior of the vessel at lower temperatures. Sufficient strain occurred near the flaw so that the fracture was not a frangible fracture as defined by linear elastic fracture mechanics, and indeed considerable evidence is presented to show that the fracture pressure would not decrease with temperature in proportion to the decrease in K_{Ic} at lower test temperatures.

In summary, the following observations and conclusions can be drawn:

1. A facility has been constructed and appropriate test methods have been developed for testing flawed thick-walled pressure vessels to failure under internal hydraulic pressure. This facility has been used to successfully test the first two 6-in.-thick, 39-in.-diam intermediate pressure vessels of the HSST program.

2. Materials properties have been obtained from small specimens (e.g., precracked Charpy specimens) from which the temperature at which near frangible fracture occurs for intermediate test vessels can be identified. The ability to identify the temperatures at which nonfrangible fracture occurs has been demonstrated. In addition, the lower-bound fracture toughness testing procedure has been further validated by the toughness testing performed.

3. Vessels containing large flaws endured overloads approximately three times ASME code-allowable pressure level before failure. These vessels were tested at temperatures well below the startup and operating conditions of typical reactors, and it is reasonable to assume that similar behavior can be expected for full-scale vessels having equivalent flaws.

4. Modeling techniques have been shown to be useful to describe elastic and elastic-plastic behavior.

5. Energy to maximum load of compact tension specimens has been demonstrated to be a useful parameter from which fracture behavior of pressure vessels can be predicted over a range of temperatures when failure is expected above yield pressure. When material properties, flaw size, and operating conditions are such that vessel failure occurs at the yield point, an anomaly has been shown to exist in the energy relationships. This leads to an unconservative prediction that fracture should have occurred at a higher strain lying out on the yield plateau. Preliminary explanations for this anomaly have been developed, and additional work is planned in this area.

6. Tests showed that the crack propagation in the larger intermediate pressure vessels was more extensive than in their associated models.

7. It has been shown that acoustic emission can be used to identify large flaw locations. However, in the case of the second intermediate pressure vessel (V-2), incipient failure was not detected.

Appendix A

VERIFICATION OF STRAIN-GAGING PROCEDURES

The strain-gage instrumentation of the intermediate test vessels required additional development work. This work was primarily associated with accessibility for installation, measurement of large postyield strains, and measurement of strains in a high-pressure environment.

About half of the strain gages were installed inside the 27-in.-ID pressure vessel, accessible only through a 15-in.-diam opening. Figure A-1 shows the vessel with the technician riding on a small elevator up into the vessel, which has been mounted in a vertical position with the open end down on a special quadripod. (Fresh air is supplied continuously both for breathing and to flush away fumes from solvents and soldering.) Because of the shorter time requirement and the environmental difficulty, a concentrated effort for gage attachment was focused on qualifying the rapid-curing contact cement Eastman 910.

A second requirement that was particularly stringent was the high postyield strains that were expected prior to burst, particularly near the flaw. Consequently, practice instrumentation was done with high-elongation gages. The gages chosen were Micro Measurement EP-08-250BG-120 without options.

A third development effort involved the use of gages mounted on the inside of the vessel, where hydrostatic pressure would exceed 30,000 psi. Although investigators[1-4] had worked in such an environment, it was necessary to qualify our techniques for this service.

Related to the high pressurization was the necessity of using a nonflammable pressurizing medium. Because of insulation problems it is much easier to operate strain gages in oil than in water. On the other hand, a fine mist of oil formed in a test cell after burst would be extremely dangerous, particularly in the presence of broken lights or severed power lines. Hence it was decided to use water or some nonflammable solvent. We soon found that nonflammable liquids other than water have disadvantages: expense, toxicity, incompatibility with plastics. Thus water became the first choice despite its poor insulating characteristics.

The following discussions summarize the various areas investigated for qualifying the gaging techniques.

Surface Roughness and Large Strains

While making burst tests on models, it was found that consistently measured strains above 3% could not be obtained even though high-elongation strain gages were used in strict accordance with procedures recommended by the manufacturer. Since the gages were supposed to be accurate for 15% strain, it was suspected that there was something degrading about the cementing procedure. As a result, the ORNL staff, working at the manufacturer's plant, used various techniques to verify a satisfactory procedure. Several gages were installed using AE/15 cement, and the gage installation was tested, with failure of the cement occurring around 3 or 4%. Application of several gages did not improve the performance, but during the course of the study two important points emerged.

First, the capability of high-elongation gages had originally been checked with Armstrong C-3 cement, a material which was no longer commercially available, and the recommended procedure using AE/15 would not allow the full capabilities of the gages to be developed. Second, to use the gages successfully, it is necessary to increase the surface roughness far beyond that normally used in strain gage practice. Whereas a 200-grit finish had been recommended, we finally used a 50-grit finish.

The problem and the solution are well illustrated by a test on a small stainless steel pressure vessel. Figure A-2 shows a 6-in. thin-walled pressure vessel which has been pressurized to near burst conditions. Note the gross deformation near the corners. A dozen gages were mounted on the vessel to check attachment techniques, with the result shown in Fig. A-3. All those gages mounted on 100- and 200-grit

Fig. A-1. Inverted intermediate test vessel, showing technician ascending.

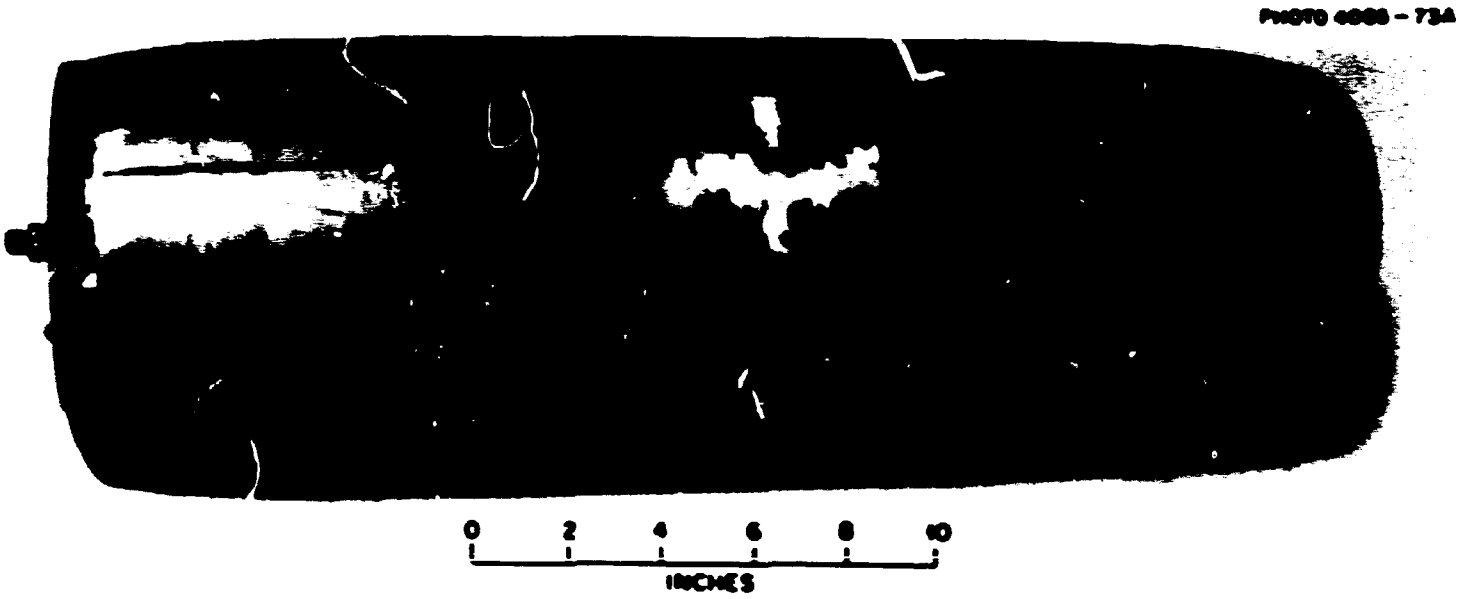

Fig. A-2. Small thin-walled vessel used to study the effect of surface roughness and gage attachment.

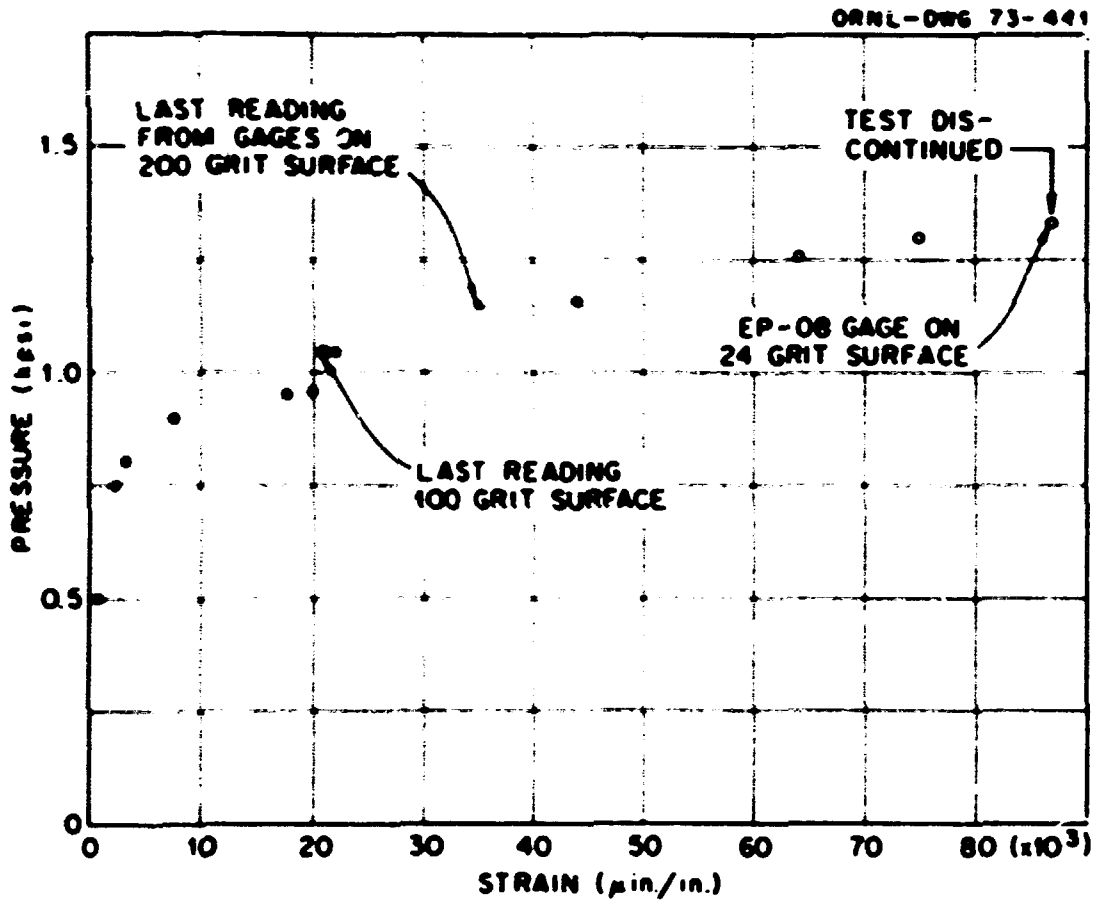

Fig. A-3. Results of study to relate surface roughness with gage attachment.

surfaces slipped off long before the end of the test. Furthermore, there appeared to be no improvement gained by using 100 instead of 200 grit. Evidently a small increase in roughness is not enough to keep the gage in place at high strains.

During the course of testing many little beams, it was found that a 36-grit finish used in conjunction with Eastman 910 cement would consistently give strains before installation failure of around 8% (see Fig. A-4). However, being able to measure large strains under atmospheric conditions did not resolve the problem associated with gaging inside the vessel.

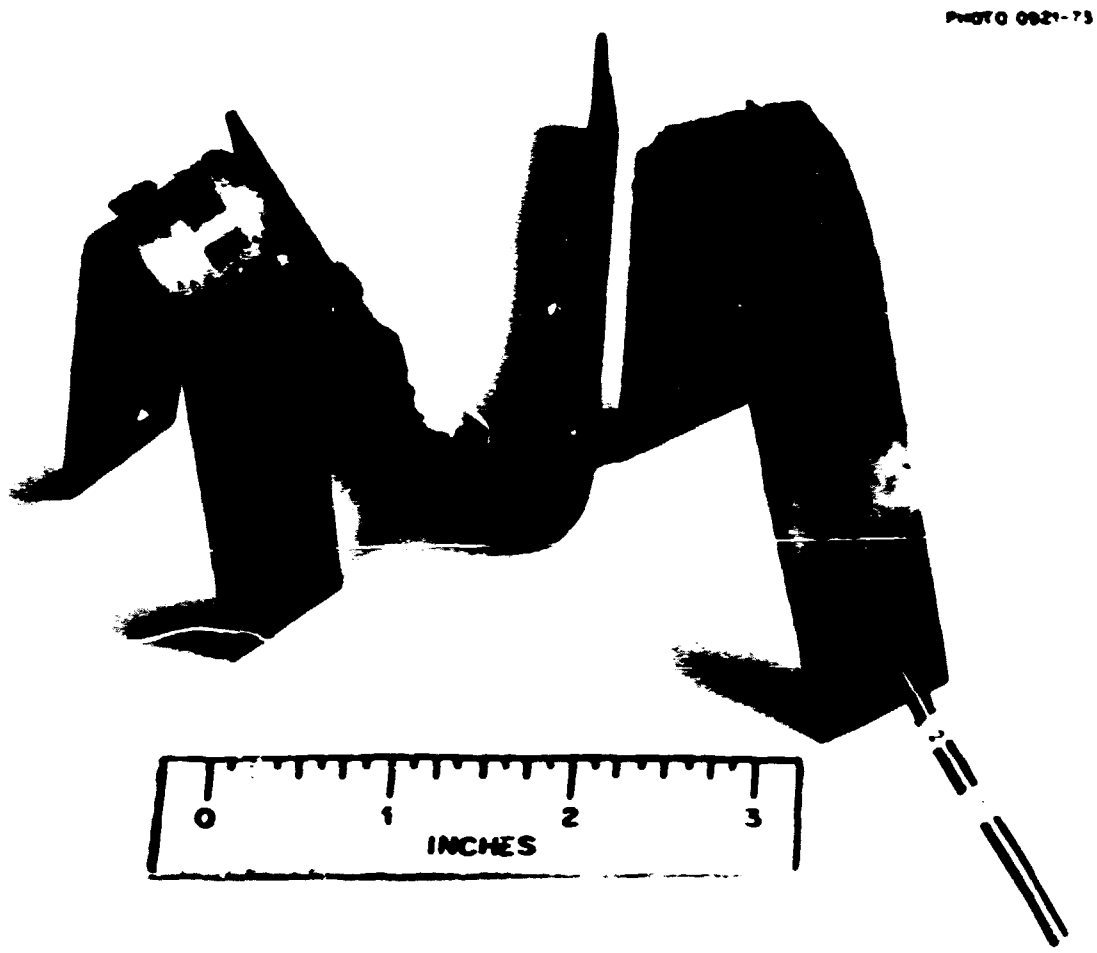

Fig. A-4. Small beams used to study the effect of surface roughness and waterproofing techniques.

Gage Factor and High Pressure

Very early in the project, attempts were made to demonstrate that the gage factor is insensitive to pressure or, at the least, varies in a regular and predictable fashion. (At this time we had not yet seen recent work of Kular.[5]) Specifically, a gage was placed on a beam, and then the beam was deflected. Next, the beam was placed in an autoclave, and the pressure was raised while changes in strain were being recorded. Objections were raised on the lack of flexibility in this concept, so a device was constructed to load and unload the beam while the pressure was applied as shown in Fig. A-5. Here we see a 6-in.-OD, 3-in.-ID autoclave mounted on a trunnion. The ropes and pulleys permitted rotation of the device from vertical to horizontal and vice versa from a remote location. The strain gages are mounted on opposite sides of the cantilever beam shown in Fig. A-6, and the beam is fixed to a cagelike assembly, which in turn is attached to the head of the vessel. Thus the whole assembly can be easily slipped into the autoclave. The basic test procedure is as follows.

First, the unpressurized autoclave is put in the vertical position, and the potentiometers are balanced to give a zero reading. Next, with pressure still at zero, the autoclave is rotated 90°, thus placing one gage in tension and the other in compression. Then the pressure is raised by a convenient amount, say 5000 psi, and a reading of strain is taken. The autoclave is then returned to the vertical *without* releasing the pressure. Again a reading is taken, but now pressure is increased before returning to the horizontal. The sequence can be seen in Fig. A-7, which also contains plots of strain as a function of pressure a would be predicted by Hooke's law for simple hydrostatic loading and also the data from an unloaded gage mounted on the steel cage. Note that the experimental data are always greater than the Hooke's law calculation. This observation

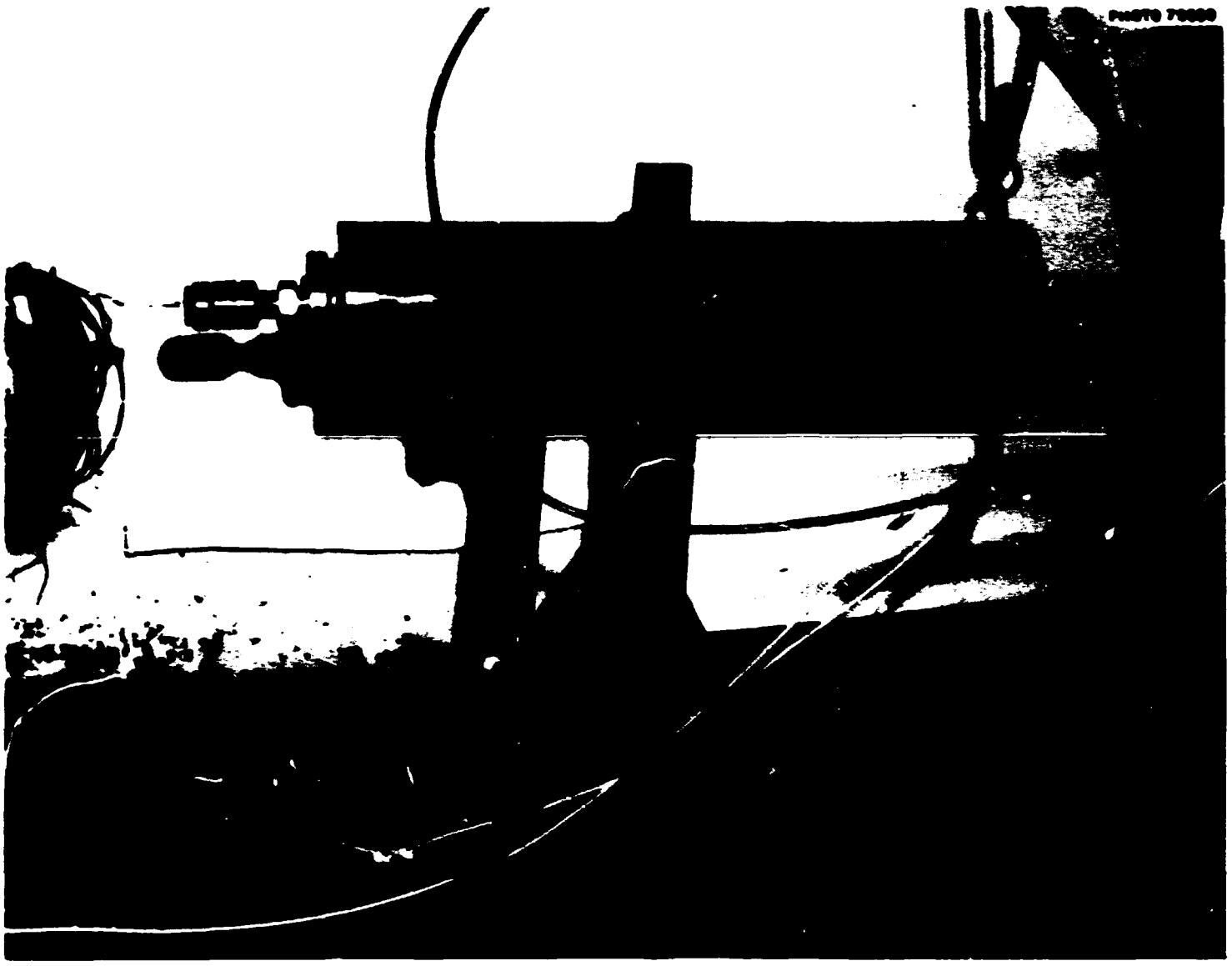

Fig. A-5. Autoclave used to investigate the effect of high pressure on strain gage readings.

PHOTO 79557

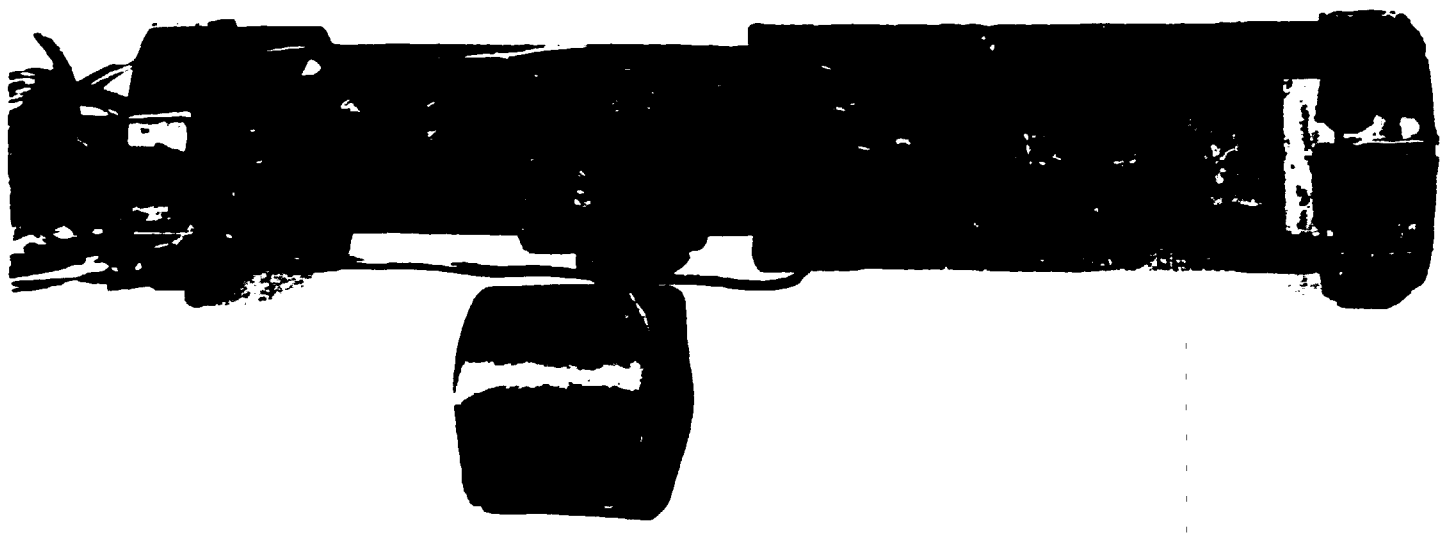

Fig. A-6. Capsule for loading beam in high-pressure environment inside autoclave.

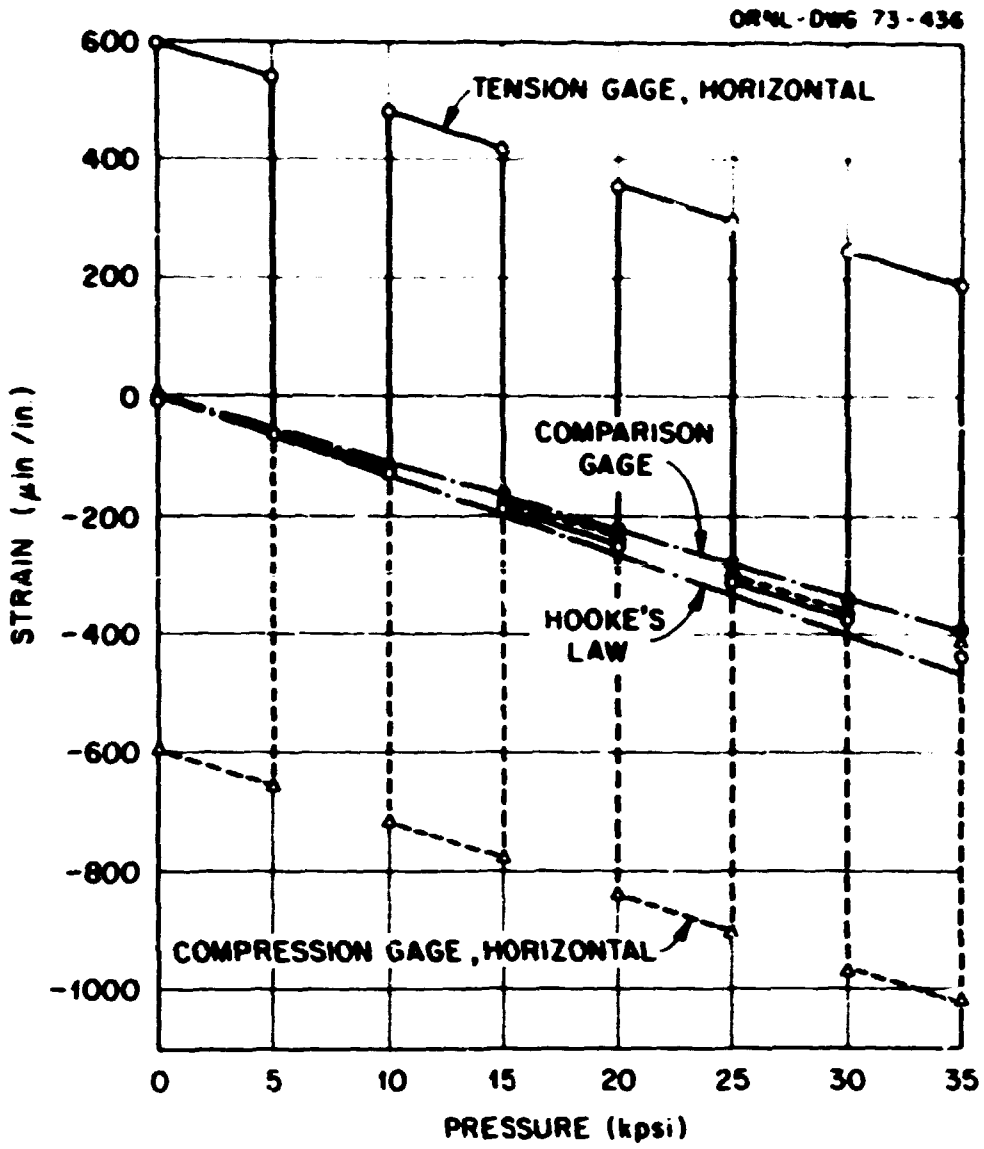

Fig. A-7. Results of investigation to assess the effect of high pressure on strain gage readings.

is in agreement with those of previous investigators, Gerdeen,[1] for example, and represents the so-called pressure effect, which is a small, but positive, apparent strain due to the squashing of the gage into the tiny protrusions of the surface. Further discussion of the usefulness of this technique for our application is given below. The significant conclusion here is that the strain generated in the beam due to the rotation of the autoclave appears to be independent of pressure. In short, gage factor appears to be very insensitive to pressure, but a small pressure effect due to other causes does exist.

Surface Roughness and High Pressure

While checking techniques using the same procedures as planned for the vessel tests, it was found that gages installed on 36-grit surfaces gave erroneous readings when subjected to high hydraulic pressure. The problem is clearly illustrated in Fig. A-8. A number of gages were cemented to a small flat plate which had four different zones of surface roughness. Thus several gages were cemented down on a 200-grit surface, some on a 100-grit surface, some on a 36-grit surface, and finally two on a chemically etched surface. As hydraulic pressure was applied, the gages on the 36-grit surface responded in a systematic but completely erroneous fashion. Instead of indicating increasingly negative strains, these gages indicated positive strains as the pressure increased. Between the other gages in the experiment there was no measurable systematic difference. The gages fell within a 15-μin./in. scatter band at 30,000 psi. The band is shown in Fig. A-8, as is the strain expected according to Hooke's law. Note that the experimental data lie above the predictions by 40 μin./in. at 30,000 psi. For the very rough 36-grit finish, however, the pressure effect is so large that the

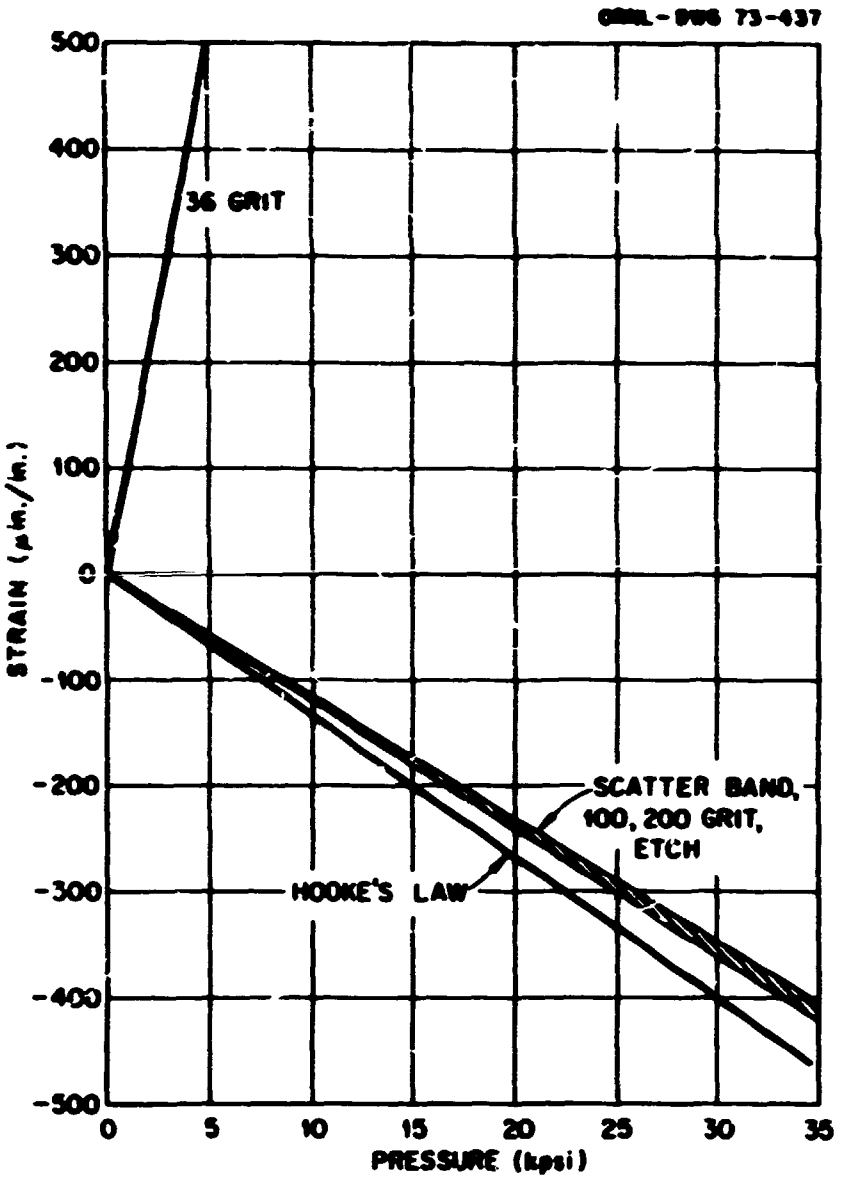

Fig. A-8. Combined effect of surface roughness and high pressure on strain gage readings.

small negative strains caused by the hydrostatic pressure are hidden. Evidently the 36-grit finish, which was desirable for high strains under atmospheric pressure, is too rough for high pressure. Hence, for gages internal to the vessel, we elected to use a 100-grit finish and hope that the pressure itself would hold them in place.

Although the procedure described above worked well at room temperature, there was still some concern that it would fail at 130°F because both the cement and the wax were approaching their temperature limits. Consequently, four beams were prepared for a submergence test. On two of the beams the gages were cemented onto a 36-grit surface and on the others onto a 100-grit surface. All four beams were submerged in a 130°F bath for five days. The beams were then removed and promptly wrapped around a mandrel while the maximum strains were being read with a digital strain indicator. The results are summarized in Table A-1.

Table A-1. Gage survival test

Five days in 130°F water, 910 cement; waterproofing: gage coat 1, rubber cement, Di-jell wax.

	No. 1	No. 2	No. 3	No. 4
Grit number	100	100	36	36
Percent strain	2.8	4.0	9.2	9.3

Waterproofing and Cementing for 130° Service

The effort here centered on finding a technique for waterproofing that could be used in water at 35,000 psi. After a number of unsuccessful attempts, we consulted the Facilities Branch of the U S. Navy Ship and Development Center (formerly David Taylor Model Basin). There it was found that strain gages had been used for years under salt water at pressures equivalent to those found at the bottom of the deepest oceans. Also, Eastman 910 was the favored cement. The important steps in the Navy procedure were the two final coatings: one of metal to rubber cement and the other of a soft wax.[6] The details of the procedure used on the vessels are:

1. After the gage has been cemented down with Eastman 910, it is coated with a thin layer of Bean's Gage Coat No. 1.
2. Next a layer of a metal-to-rubber cement made by GC Electronics (GC No. 35-2) is applied and allowed to dry overnight.
3. Finally, a layer of BLG's Di-jell wax is applied with a brush. The wax was melted for such an application, which is preferred over the more obvious approach of using a spatula because the latter may leave tiny pinholes. A beam used in these investigations is shown in Fig. A-4.

Lead-Through Devices

One of the development problems to be resolved during the preparation for the tests of the intermediate-size pressure vessels was getting the strain-gage lead wires out through the head of the vessel. Several approaches were considered, one of which was based on a paper by Gerdeen.[1]

During the course of his study of influence of high pressure on foil gages, Gerdeen found that Conax thermocouple glands could be adapted for use with strain-gage lead wires. Although only rated by the manufacturer for 10,000 psi, Gerdeen had used these devices routinely to 20,000 psi, and some of his data imply that he had at least occasionally gone over 30,000 psi. We purchased similar devices and tested them in our autoclave and found that the seals were not reliable above about 25,000 psi and therefore tried other approaches. In the end a commercially available thermocouple lead-through device was used. The device was available from Autoclave Engineering and applied a concept very similar to one invented by Bridgman over 40 years ago.[7] A photograph of the device is shown in Fig. A-9.

As is shown in Fig. A-9, the lead-through device permits only eight wires to be brought through the packing. Thus if one is using a three-wire system, all available holes will be rapidly used up. Consequently, we elected to use a commercially available $^1/_{16}$-in.-diam stainless steel sheath containing three copper wires insulated by magnesium oxide to go through the holes in the packing. This choice, in effect, tripled our strain-measuring capacity on the inside of the vessel.

The difficulties experienced with the O-rings shown in Fig. A-9 are also worth mentioning. After purchasing several Autoclave fittings, we tested them with the small autoclave described earlier. No trouble was experienced in sealing the lead wire to 40,000 psi; however, during the test of the first vessel, we had numerous leaks at 18,000 psi, as discussed later. The trouble was attributed to two causes: the finish on the metal surface of the vessel was slightly rougher than on the laboratory vessel, and the mating surface was probably not as close to being perpendicular to the axis of the hole as on the laboratory vessel. The problem was quickly solved during the actual test by polishing the mating surface and by increasing the torque to tighten the fitting. No trouble has been experienced since.

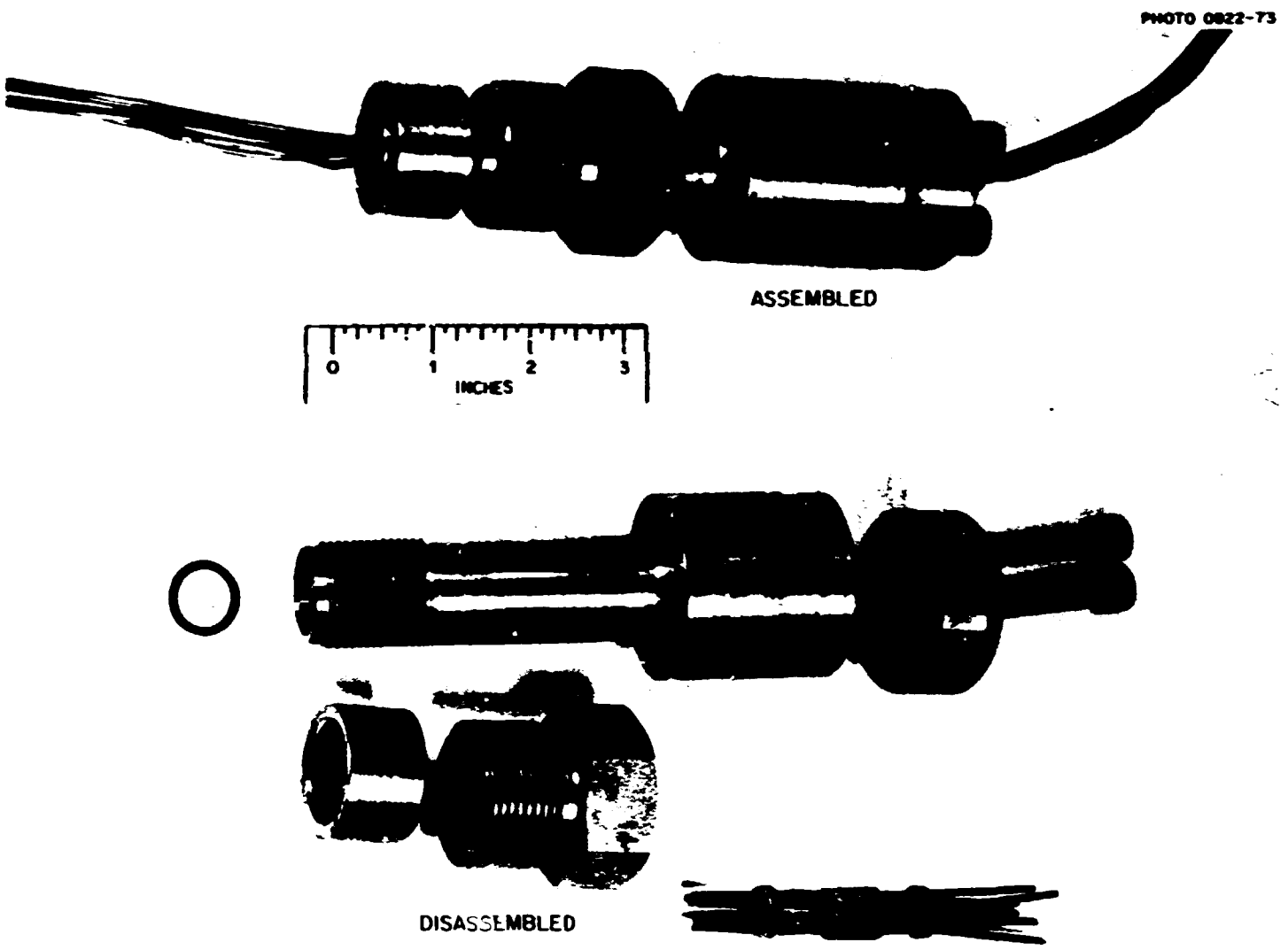

Fig. A-9. Lead-through device used for the vessel tests.

References

1. J. C. Gerdeen, "Effects of Pressure on Small Foil Strain Gages," *Exp. Mech.*, March 1963, pp. 73–80.
2. R. V. Milligan, "The Effect of Pressure on Foil Strain Gages," *Exp. Mech.*, April 1964, pp. 25–36.
3. R. V. Milligan, "The Effects of High Pressure on Foil Strain Gages on Convex and Concave Surfaces," *Exp. Mech.*, May 1965, pp. 59–64.
4. R. V. Milligan, "The Gross Hydrostatic-Pressure Effect as Related to Foil and Wire Strain Gages," *Exp. Mech.*, February 1967, pp. 67–74.
5. G. S. Kular, "Use of Foil Strain Gage at High Hydrostatic Pressure," *Exp. Mech.*, July 1972, pp. 311–316.
6. W. W. Murray, personal communication: Deep Sea Rescue Vehicle Pressure Hull Instrumentation Procedures for Strain Gage Installation, USNR&DC, Washington, D.C., 1970.
7. P. W. Bridgman, *The Physics of High Pressure*, G. Bell and Sons, London, 1931.

Appendix B

PRESSURE-STRAIN DATA FROM TESTS OF VESSELS V-1 AND V-2

Numbers in parentheses indicate second recorded stra
Gages out at beginning of test: 13, 22, 25, 29, 33, 35

Pressure (ksi)	10	11	12	14	15	16	17	18	19	20	21	23	24	26	27	28	30	31	32	34	36	38	50	52	54	55	57	5
0.12	10	15	556	15	34	14	9	13	7	1	5	12	20	11	15	7	8	13	38	13	6	9	217	7	-22	5	8	9
3.1	174	174	327	328	326	175	175	170	173	174	168	333	275	203	50	192	182	50	288	205	195	187	384	292	338	112	168	78
6.2	344	343	811	637	632	344	342	330	342	342	329	644	554	403	99	378	360	98	585	407	384	366	819	593	640	220	331	13
7.7	427	426	1195	789	781	426	425	410	425	425	409	795	691	501	124	468	447	122	730	506	477	454	1053	748	790	272	410	16
9.1	504	503	1515	933	922	504	502	485	503	501	483	937	820	593	146	553	528	143	867	599	564	536	1256	894	970	321	484	19
10.6	583	581	1829	1076	1065	583	579	561	582	578	557	971[b]	951	686	169	638	610	166	1006	693	651	619	1448	1035	1079	371	559	22
12.1	664	662	2115	1220	1206	661	656	637	662	656	633		1086	780	191	725	694	187	1149	789	739	704	1649	1183	1272	421	636	25
13.7	748	747	2364	1363	1350	743	735	715	745	736	711		1227	879	216	815	782	211	1299	888	831	790	1847	1339	1431	474	715	29
15.1	831	830	2494[b]	1508	1491	824	813	792	828	814	789		1367	975	240	903	868	234	1448	986	920	876	2051	1469	1687	525	793	32
16.7	914	914		1656	1639	907	895	872	911	895	868		1512	1674	265	994	957	258	1607	1087	1014	965	2223	1620	1874	578	872	39
18.2	998	997		1805	1787	990	978	952	994	976	946		1662	1174	292	1085	1046	283	1771	1188	1109	1055	2380	1748	2089	632	952	30
0.4	-8	-7	689	-11	22	-7	-13	-4	-7	-19	0		6	-7	11	25	3	8	21	-2	-11	-8	223	-60	160	-1	25	2
0.08	0	0	0	0	0	0	0	0	0	0	0	0	0	0	0	0	0	0	0	0	0	0	0	-1	56	0	0	0
3.1	172	172	432	321	321	172	172	166	171	172	165	328	281	203	50	190	180	48	298	204	193	183	408	327	236	112	166	49
6.1	344	343	962	637	636	342	342	330	342	343	329	645	565	405	100	380	361	98	598	409	386	367	835	647	722	221	331	13
9.1	504	503	1455	935	932	502	501	483	502	502	482	943	830	594	147	558	529	143	879	600	565	537	1236	951	1098	324	485	20
12.2	667	665	1903	1230	1229	664	663	639	665	664	638	959[b]	1101	787	195	738	701	189	1166	795	748	711	1626	1256	1252	426	641	26
15.1	825	823	1966[b]	1522	1519	822	818	790	823	821	788		1366	973	241	914	867	234	1447	984	926	880	1985	1550	1375	528	793	32
18.1	992	989		1821	1816	987	982	950	990	986	947		1647	1170	291	1098	1043	281	1748	1184	1113	1058	1980	1785	1086	636	952	39
19.1	1043	1040		1913	1911	1038	1033	998	1041	1036	996		1741	1232	307	1155	1098	296	1854	1246	1170	1112	2178	1906	1339	668	1001	41
0.2	-16	-18	342	7	5	-14	15	-14	-15	-15	-14	-6	-12	-13	0	-20	-14	-5	0	-14	-16	-16	121	-8	51	-12	-16	-1
0.1	0	0	0	0	0	0	0	0	0(1)	0	0	0	0	0		1	1	0	1	1	1	0				0	0	0
3.2	182	183	447	320	319	179(180)	171	172	183(183)	176	174	313	299	214		202	192	53	311	215	201	191				120	177	71
6.2	352	352	941	633	632	348(349)	341	334	352(352)	345	336	632	580	414		390	371	100	608	417	392	373				228	340	13
9.2	517	517	1388	936	935	513(513)	505	492	517(517)	509	494	937	853	609		573	544	148	898	614	578	549				333	498	20
12.2	678	677	1701[b]	1230	1228	673(673)	664	646	677(678)	669	647	958[b]	1120	799		751	713	193	1181	806	758	721				435	653	26
19.3	1064	1063		1926	1925	1057(1056)	1041	1014	1062(1061)	1050	1015		1770	1255		1179	1118	302	1874	1266	1190	1130				682	1023	41
18.1	1086	1005		1822	1821	999		959	1004	994	960		1670	1186		1115	1057	285	1767	1197	1125	1870				645	967	
0.3	-1	-1		5	5	-2(-2)	-9	3	0(0)	-5	0		-6	-2		-2	7	3	19	1	-1	4				-2	0	3
0.1	0	0			0	0(0)	0	0(0)	0	0	0		0	0		0	0	0	0	1	0	0				0	0	0
3.2	176	176			326	176(177)	176	169(170)	175(177)	176	170		291	210		195	186	47	309	213	198	189				111	172	71
6.2	347	346			637	345(346)	345	332(333)	344(346)	346	332		573	411		384	364	94	606	416	389	371				219	336	13
9.2	510	509			937	508(509)	507	489(489)	508(509)	508	489		843	604		566	537	142	893	611	574	546				325	493	20
12.2	670	669			1228	667(668)	665	641(642)	667(668)	667	641		1107	793		743	705	187	1174	801	753	716				428	646	26
15.1	828	826			1515	824(825)	821	792(793)	824(825)	823	792		1370	979		918	871	232	1454	989	929	884				529	798	33
18.2	1000	998			1823	995			996	992	956		1651	1184		1111	1052	281	1764	1195						638	964	
19.1	1052	1050			1913	1046				1042	1004															670	1013	
19.7	1089	1087			1979	1083																				693		
20.0	1118	1107			2014	1103				1098	1058															706	1069	
20.7	1142	1140			2071	1135				1129																726	1099	
21.2	1170	1168			2123	1162																				744	1125	
21.6	1197	1195			2175	1191																				762	1152	
22.2	1234	1231			2163	1233				1227	1188		2247													779	1183	
22.7	1281	1278			2227	1278																				798	1220	
23.1	1321	1318			2279	1317				1315	1269		2848													814	1252	
23.7	1376	1372			2329	1372																				832		
24.1	1427	1422			2369	1422				1419	1365		3391[b]													848	1331	
24.7	1492	1487			2412	1486																				865		
25.1	1544	1539			2445	1537			1561	1531	1464			2044		1855	1735	469	3221[b]	2044						876	1411	
25.6	1646	1596			2520	1637(1636)	1607	1551(1548)	1667(1665)	1627	1542			3212		2113	1888	533		2979	2098	1879				885	1478	52
0	207	204			-34	211(211)	197	181(180)	236(235)	206	173			1492		499	367	126	2496	1239	467	338				-21	106	-1
3.1	389	385			298	391(392)	378	355(355)	416(417)	387	346			1709		701	559	177	2821	1458	672	533				96	281	41
6.2	564	559			615	565(565)	551	521(522)	591(592)	560	513			1918		897	743	228	3137	1670	870	720				207	449	18
9.2	727	722			911	728(729)	712	678(678)	753(755)	722	668			2115		1081	914	272	3218[b]	1869	1056	896				309	607	17
12.2	891	885			1205	890(891)	875	834(834)	917(918)	885	824			2314		1264	1087	319		2069	1241	1071				414	763	23
15.0	1049	1043			1488	1048(1049)	1031	985(985)	1074(1075)	1042	975			2507		1442	1255	364		2263	1422	1241				514	915	30
18.2	1226	1221			1798	1223(1224)	1200	1155	1250(1251)	1214	1143			2724		1642	1442	414		2480	1622	1430				625	1084	36
20.1	1340	1335			1993	1335(1337)	1310	1261	1362(1363)	1325	1251			2864		1770	1562	446		2620	1751	1550				696	1192	41
22.2	1459	1454			2198	1453(1454)	1426	1374	1481(1483)	1442	1364			3013		1905	1689	480		2769	1888	1679				770	1304	45
24.0	1570	1565			2388	1562			1593	1551	1469			3157		2033	1808	512		2913	2017					839	1409	
25.0	1626	1597[b]			2481	1619			1649	1607	1523			3236		2099										874	1462	
25.7	1675				2555	1668																				897	1508	
26.0	1739				2634	1731			1769	1716	1615			3297[b]												902	1559	
26.6	1864				2864	1856				1832	1694															909	1712	
27.0	1991				2880[b]	1978			2038	1953	1764															918	2007	
27.4	2172					2143																						
27.6	2263					2231				2247	1906															960	3154[b]	
27.9	2435					2432			2256	2603	1984					2414[b]	3433[b]	883								1011		
28.2	2676[b]					2488				3439	2147															1145		
28.3	3137[b]					2534		1553[b]		3173[b]	2308							1303		3466[b]	3035[b]	2849[b]				1299		
28.5						2614[b](2614)[b]	2706[b]				2931															1629		
28.5											3037[b]							1746								1804		
28.6																										2065		
28.6																		2269								2117[b]		
28.6								(1548)[b]	(2253)[b]									2593										

[a] To convert microinches strain to percent strain, move decimal point four places to left.

[b] Computer output capacity exceeded; the datum may not be correct; subsequent data deleted.

Table B-1. Pressure-strain data from vessel V-1

rain at a single computer scan.

5, 37, 39, 48, 49, 51, 53, 56, 60, 61, 62, 63, 65, 67, 68, 71, 73, 74, 83, 85, 87, 88, 95, 96, 98, 99, 101, 105, 108

Strain (μin./in.)[a] from gage No. -																													
58	59	64	66	70	72	75	76	77	78	79	80	81	82	84	86	89	90	91	92	93	94	97	100	102	103	104	106
First pressurization cycle																													
		-14	115	4	23	9	-3	12	0	6	8	10	11	9	103	421	8	42	165	1	27	1	27	72	1	10	4
		339	324	52	4	171	171	108	61	62	44	44	44	45	72	320	48	12	6	1	37	91	145	24	282	169	140
5		669	609	99	51	338	339	212	120	121	88	86	87	90	-43	776	78	30	19	1	76	276	164	105	541	333	236
8		832	753	124	69	419	421	263	148	151	110	108	109	113	98	1068	86	36	14	8	96	367	178	79	649	413	293
9		991	885	146	88	495	498	311	175	178	131	127	129	133	171	1289	101	44	22	28	114	452	130	58	751	489	347
9		1143	1014	170	102	578	576	359	203	206	151	147	149	154	344	1512	118	51	36	48	133	537	121	80	852	565	402
9		1294	1097	189	114	651	655	410	229	232	170	166	169	174	298	1722	137	58	64	68	157	624	142	93	948	643	459
2		1450	1223	210	125	733	736	462	256	259	189	185	190	193	340	1932	156	64	145	88	185	713	202	94	1032	724	518
2		1604	1338	229	134	820	817	514	281	284	208	204	210	211	-442	2161	178	61	255	110	213	802	215	94	1082	802	575
4		1767	1451	254	146	896	898	567	309	312	229	225	231	233	-504	2314	194	67	318	133	234	893	220	106	1139	882	630
8		1926	1542	277	171	978	979	619	338	342	252	247	254	256	600	2484	197	73	372	157	256	986	224	115	1188	962	686
		-28	125	-16	-61	-5	-12	5	-12	-12	10	7	6	10	-173	36	21	66	199	1	6	1	181	-164	21	8	12
Second pressurization cycle																													
		0	0	1	Out	0	0	0	0	0	0	0	0	0	1	1	Out	1	4	0	0	0	24	-32	0	0	1
		343	295	53		181	169	108	61	63	44	42	43	45	-347	250		21	62	2	37	93	-242	367	184	167	118
7		682	555	106		339	340	213	122	124	89	87	88	90	726	539		41	-45	1	77	279	-363	-368	358	333	237
0		997	808	153		496	497	312	177	180	130	127	129	133	863	741		64	-17	38	114	454	389	-371	524	488	348
4		1318	1067	202		656	658	409	232	236	173	168	171	176	-863	1132		82	242[b]	80	153	634	414	-581	647	646	462
7		1627	1267	248		810	814	510	288	292	214	208	211	218	-863	1361		103		121	191	806	-417	-761	792	799	572
1		1926	1355	305		998	1020	614	389	392	257	250	254	262	-863	1598		119		165	232	988	408	851	951	959	688
1		2827	1479	289		1024	1029	644	362	368	269	262	266	275	-864	1468		125		177	243	1045	-418	-862	974	1008	721
1		0	51	4		-18	-13	-14	-7	8	-9	-9	-9	-10	-272	76		31		2	-21	2	-146	457	40	-17	-18
Third pressurization cycle																													
		-22(1)	-34(0)	0		5	1(1)	-6(3)	3	2	0	0(0)	1	0	11	2		0	2	0	1	0	-1	1	0(0)	0	1(1)
		338(338)	288(278)	48		188	185(184)	116(119)	59	55	47	45(45)	48	46	734	56		11	23	0	72	92	-619	-460	-23(-22)	178	132(133)
8		680(682)	546(548)	102		357	351(354)	224(226)	124	121	91	88(88)	91	91	-750	274		12	-227[b]	1	108	278	-644	459	-7(-5)	342	248(249)
3		1001(1003)	782(783)	149		519	514(515)	325(328)	182	180	134	130(130)	133	135	-750	559		39		37	146	458	-610	460	68(69)	502	362(363)
6		1313(1311)	995(995)	196		677	669(675)	424(426)	237	235	176	170(171)	175	178	-750	827		57		79	184	635	-569	-460	182(182)	658	474(475)
7		2054(2053)	1514(1515)	302		1057	1058(1054)	663(664)	370	371	274	266(266)	272	279	-751	1400		97		179	281	1054	-527	-361	529(522)	1031	744(743)
		1946	1439			999	998	627				252													458	975	704(703)
		4(5)	24(24)	0		8	5(6)	0(2)	-1	-7	-5	-5(-5)	4	-7	270	191		47		0	13	0	-489	460	-108(-106)	1	1(1)
Fourth pressurization cycle																													
			40(15)	30(53)		10	20(52)	7(74)	63	47		0								0	0	0				0	0(0)
			247(330)	124(116)		214	200(251)	158(262)	149	145	45	42	43	45						1	42	85				171	122(122)
8			599(572)	65(195)		255	364(449)	265(334)	234	231	89	86	85	90						0	81	272				336	239(240)
3			652(858)	131(248)		340	430(610)	217(437)	292	289	132	128	127	134						30	122	451				495	353(354)
6			1095(1084)	277(295)		712	736(768)	489(536)	349	350	173	167	167	176						72	161	625				650	464(465)
8			1304(1296)	308(339)		861	891(923)	584(633)	403	405	213	206	206	218						113	199	798				803	574(575)
			1538(1532)	368		1026		692																		970	
			1606	379		1081																				1019	
			1663	394																							
			1675	398		1143																				1075	
			1716	406		1174																				1106	
			1755	415		1203																				1133	
			1787	425		1229																				1160	
			1833	425		1258																				1193	
			1865	Out																						1232	
			1905			1331																				1266	
			1947																								
			1984			1417																				1349	
			2028																								
			2059(2045)			1509		935																		1433	
7			2108(2091)	(442)		1585	1623(1652)	956(999)	557	610	403	397	396	408						113	460	2121				1507	967(964)
Fifth pressurization cycle																													
2	-1		116(100)	46		169	207(240)	73(120)	65	105	35	37(36:	44	30						96	88	531				123	-21(-2
	-1		403(393)	99		348	384(421)	182(234)	127	167	83	83(83)	91	74						145	133	731				299	103(104)
0	9		671(651)	147		519	554(595)	294(343)	191	234	129	128(128)	137	125						192	174	923				468	234(225)
4	189		900(885)	189		681	717(755)	395(442)	245	286	171	169(169)	178	169						235	213	1104				627	33(337)
9	370		1125(1110)	229		842	882(915)	496(544)	302	345	215	211(211)	221	213						279	253	1285				785	450(451)
1	545		1331(1325)	266		995	1037(1070)	591(639)	355	401	255	251(251)	261	255						321	292	1450				938	560(561)
8	741		1572(1557)	301		1171	1210(1243)	702(749)	415	461	299	293(293)														1109	687
3	867		1720(1705)	326		1283	1322(1354)	772(819)	453	501	328	322(322)	335	331												1218	765
8	1000		1871(1857)	354		1398	1438(1470)	844(890)	492	542	358	351(352)														1332	846
			2011(1997)			1507		911				379														1437	
			2100			1580		945																		1490	
			2147																							1537	
			2165			1653		984																		1592	
			2224			1743																				1767	
			2255[b]			1829		1032																		2097	
						2002																				2756	
			(2239)[b]			2120		1095																		3639[b]	
						2416		1139																			
						2622	2194[b]	1183				961															1541
						2803																					
						2890		1321				1339															
						3285		1423																			
						3629		1498				1681															
0	4039[b]			-507		3873	(1224)[b]	1602(1651)	25	928	1606[b]	1857(1861)	1891	1724						2420	2110	4045[b]					2738[b]

2

BLANK PAGE

73, 74, 83, 85, 87, 88, 95, 96, 98, 99, 101, 105, 108

77	78	79	80	81	82	84	86	89	90	91	92	93	94	97	100	102	103	104	106	107	109	124	125
	0	6	8	10	11	9	103	421	8	42	165	1	27	1	27	72	1	10	4	5	2	13	12
8	61	62	44	44	44	45	72	320	48	12	6	1	37	91	145	24	282	169	120	57	123	174	174
2	120	121	88	86	87	90	43	776	78	30	19	1	76	276	164	105	541	333	236	110	240	343	341
3	148	151	110	108	109	113	98	1065	86	36	14	8	96	367	178	79	648	413	293	137	296	426	424
1	175	178	132	127	129	133	171	1289	101	44	22	28	114	452	130	58	751	489	347	161	352	504	50.
9	203	206	153	147	149	154	242	1512	118	51	36	48	133	537	121	80	852	565	402	186	408	583	580
0	229	232	170	166	169	174	298	1722	137	58	64	68	157	624	142	93	948	643	459	208	464	664	660
2	256	259	189	185	190	193	340	1932	156	64	145	88	185	713	282	94	1032	724	518	231	523	749	743
4	281	284	208	204	210	211	442	2161	178	61	255	110	213	882	215	94	1082	882	575	252	581	834	825
7	309	312	229	225	231	233	504	2314	194	67	318	133	234	892	220	106	1139	882	630	276	638	919	908
9	338	342	252	247	254	256	600	2484	197	73	372	157	256	906	224	115	1188	962	686	299	694	1003	992
5	-17	-12	10	-7	6	10	-173	36	21	66	199	1	6	1	181	164	21	8	12	14	15	-2	6
	0	0	0	0	0	0	1	1	Out	1	4	0	0	0	24	32	0	0	1	0	1	0	0
8	61	63	44	42	43	45	-342	350		21	62	2	37	91	-242	367	184	167	118	55	121	172	171
3	122	126	89	87	88	90	-726	539		41	45	1	77	279	-367	368	358	333	237	110	240	343	341
2	177	180	130	127	129	133	-863	861		64	-17	38	114	454	389	371	524	488	348	160	353	503	500
9	232	236	193	168	171	176	-863	1132		82	242[b]	80	153	634	414	-581	647	646	462	212	469	667	663
0	288	292	214	208	211	218	-863	1361		103		121	191	806	417	761	792	799	572	262	580	824	819
4	389	392	257	250	254	262	-863	1598		119		165	232	988	408	861	951	959	688	315	699	999	985
4	362	368	269	262	266	275	-864	1469		125		177	243	1045	418	862	974	1008	721	327	732	1042	1036
4	-7	-8	-9	-9	-9	-10	-272	-76		31		2	-21	2	-146	457	-80	17	-18	6	15	-15	-15
6(3)	3	2	0	0(0)	1	0	11	2		0	2	0	1	0	-1	-1	0(0)	0	1(1)	1	0(0)	1	1
6(139)	59	55	47	45(45)	48	46	734	56		11	23	0	72	92	-619	460	-23(-22)	176	132(133)	54	131(133)	186	182
0(226)	124	121	91	88(88)	91	91	-750	274		12	-227[b]	1	108	278	-644	459	-7(-5)	342	240(249)	109	250(251)	355	351
5(328)	182	180	134	130(130)	133	135	-750	559		39		37	146	458	-610	460	68(69)	502	362(363)	161	365(367)	520	515
0(426)	237	235	176	170(171)	175	178	-750	827		57		75	184	635	-569	460	182(182)	658	474(475)	213	479(481)	681	675
3(664)	370	371	274	266(266)	272	279	-751	1400		97		179	281	1054	-587	461	529(522)	1031	744(743)	331	752(751)	1062	1054
27				252													458	975	704(703)		711		
(2)	-1	-7	-5	-5(-5)	-4	-7	270	-191		47		0	13	0	-489	460	100(106)	1	1(1)	-2	1(0)	0	-2
(74)	63	47		0								0	0	0				0	0(0)	0	0(1)	0	0
0(262)	149	145	45	42	43	45					1	42	85					171	122(122)	56	123(125)	180	179
5(334)	234	231	89	86	85	90					0	81	272					336	239(240)	110	243(244)	351	349
7(437)	292	289	132	128	127	134					30	122	451					495	353(354)	163	359(360)	514	511
9(536)	349	350	173	167	167	176					72	161	625					650	466(465)	214	472(473)	674	670
4(633)	403	405	213	206	206	218					113	199	798					803	574(575)	264	584(585)	831	827
92																		970			707		
																		1019			742		
																		1075					
																		1106					
																		1133					
																		1160					
																		1193			859		
																		1232					
																		1266			897		
																		1349			936		
5																		1433			974		
6(999)	557	610	403	397	396	408					513	460	2121					1507	967(964)	369	996(993)	1636	1636
0(120)	65	105	35	37(36)	44	30					56	88	531					123	-21(-21)	-65	-4(-4)	205	214
2(234)	127	167	83	83(83)	91	74					115	133	731					299	103(104)	-7	122(124)	388	396
4(343)	191	234	129	128(128)	137	125					192	174	923					468	224(225)	48	244(245)	562	570
5(442)	245	286	171	169(169)	178	169					235	213	1104					627	336(337)	99	358(360)	726	732
6(544)	302	345	215	211(211)	221	213					279	253	1285					785	450(451)	152	474(476)	889	895
1(639)	355	401	255	251(251)	261	255					321	292	1460					938	560(561)	201	586(587)	1047	1051
2(749)	415	461	299	293(293)														1109	687		711		
2(819)	453	501	328	322(322)	335	331												1218	765		790		
4(890)	492	542	358	351(352)														1332	846		871		
1				379														1437			946		
5																		1490			984		
																		1537					
6																		1592			1030		
																		1767			1058		
32																		2097			1084		
																		2756			1129		
95																		3639[b]			1155		
39																					1208		
83				961															1541		1260		
																					1362		
21				1339																	1417		
23																					1521		
98				1681																	1598		
92(1651)	-25	928	1606[b]	1857(1861)	1891	1724					2420	2110	4045[b]						2738[b](2738)[b]	283	1647(1702)	2003[b]	1994[b]

3

BLANK PAGE

Table B-2. Pressure-strain data from vessel V-2 test – computer output

See Fig. 7.10 for gage location
Gages out at beginning of test: 30, 75, 107
See also Table B-3

Pressure (ksi)	Strain (μin.)[a] from gage No.														
	24	25	26	27	28	29	31	32	33	35	37	38	48	49	50
First pressurization cycle															
0	−2	−199	4	2	2	0	0	2	−10	2	2	0	0	2	2
3.8	363	1314	401	46	224	417	85	256	91	413	431	91	249	243	260
7.8	706	1742	782	99	441	804	181	504	171	802	825	177	485	479	509
11.9	1034	2008	1149	147	651	1184	272	748	248	1202	1218	260	720	712	755
16.0	1363	2146	1534	194	873	1579	363	1006	315	1609	1625	349	968	956	1016
18.0	1530	2079	1712	218	980	1766	405	1131	300	1800	1816	391	1087	1073	1140
20.0	1690	2173	1905	240	1093	1966	451	1266	341	2008	2030	438	1215	1199	1276
22.0	1831	2272	2095	268	1206	2165	494	1403	383	2218	2272	476	1339	1321	1412
23.0	1869	Out	2159	282	1270	2262	544	1500	407	2339	2367	496	1428	1400	1513
24.0	1943		2169	300	1347	2339	572	1643	Out	2554	2776	508	1544	1503	1657
24.4	1982		2177	300	1397	2326	591	1756		2677	2875	516	1631	1574	1767
Second pressurization cycle															
0	−48	Out	−97	30	44	−52	85	222	Out	240	351	2	138	105	213
0	−129		−165	4	85	135	101	339		157	373	16	150	114	225
0	−127		−163	4	5042	−133	101			159	365		150	114	
0	−131		−169	0	93	−141	97	335		155	371	16	154	118	231
3.9	244		244	44	308	292	198	562		587	810	73	412	371	497
7.9	588		631	87	522	691	294	863		992	1236	163	655	609	749
12.0	917		1002	125	730	1074	385	1115		1383	1637	250	891	842	998
16.0	1245		1373	167	943	1457	462	1371		2046	2015	337	1132	1077	1249
19.9	1566		1745	212	1157	1840	554	1622		2689	2411	423	1375	1316	1503
19.9	1562		1741	212	1165	1834	556	1618		2699	2409	421	1377	1318	1507
22.0										3207	2788		1513	1450	
22.1	1735		1941	232	1286	2052	675	1743		3235	2812	464	1521	1458	1657
24.0	1878		2118	248	1389	2235	706	1879		3684	2947	508	1641	1574	1783
25.9	2066		2310	262	1534					4237	3237		1858	1769	
25.9	2074		2302	262	1542	2451	752	2126		4263	3281	550	1874	1785	2027
27.0	2270		2415	Out	1679	2630	782	2709		4779	3721	576	2098	1994	2515
27.9	2659		2723		1860	2874	794	6113		5553	4162	643	4982	3390	5223

[a]To convert microinches strain to percent strain, move decimal point four places to left.

Table B-2 (continued)

Pressure (ksi)	Strain (μin.)[a] from gage No. 51	53	56	57	58	59	60	61	62	63	65	66	68	70	71
First pressurization cycle															
0	4	2	2	0	−2	4	2	0	0	−2	−12	6	12	−16	−34
3.8	63	343	318	215	424	412	379	438	144	221	274	270	258	108	243
7.8	124	675	649	422	828	815	797	856	288	438	436	462	398	−2	219
11.9	181	1006	945	629	1219	1199	1213	1262	428	647	686	680	661	284	669
16.0	243	1359	1239	842	1627	1599	1635	1676	574	868	943	947	909	390	903
18.0	270	1534	1387	943	1818	1789	1838	1876	645	974	1004	988	947	371	937
20.0	306	1732	1529	1051	2027	1992	2057	2089	720	1089	1114	1138	1106	460	1106
22.0	337	1949	1686	1158	2215	2189	2266	2304	795	1201	1252	1262	1217	489	1201
23.0	361	2156	1899	1219	2351	2298	2396	2323	834	1264	1317	1296	1246	497	1260
24.0	404	2617	1998	1284	2507	2408	2534	2428	868	1341	1383	1359	1310	515	1331
24.4	446	3209	2140	1319	2596	2495	2633	2517	886	1390	1385	1369	1317	481	1337
Second pressurization cycle															
0	107	1353	245	10	168	101	Out	−4	−6	47	−6	−81	−199	−79	14
0	99	1359	187	38	109	63		−81	10	65	89	113	158	103	166
0				38							146				
0	99	1365	199	43	108	65		−83	14	69	160	176	191	120	185
3.9	158	1722	548	256	552	495		373	164	296	105	396	381	201	410
7.9	219	2063	868	465	964	895		801	304	511	562	485	434	30	404
12.0	280	2402	1189	667	1357	1282		1209	442	720	830	817	791	361	826
16.0	343	2746	1548	874	1750	1671		1604	582	933	1047	1045	1004	454	1039
19.9	404	3103	1357	1081	2172	2057		2038	723	1148	759	1251	1209	533	1239
19.9	404	3107	Out	1087	2193	2053		Out	724	1150	1280	1255	1215	529	1241
22.0				1199							1282				
22.1	434	3322		1205	2695	2278			799	1274	1414	1381	1329	566	1357
24.0	467	3513		1306	2933	2465			870	1379	1511	1467	1412	590	1142
25.9				1432							1529				
25.9	611	4966		1436	3459	2773			941	1532	1641	1609	1544	629	1592
27.0	657	5844		1536	3521	3075			984	1669	1738	1655	1562	562	1627
27.9	795	8082		1745	4152	3501			1026	1846	1941	1814	1745	623	1844

[a]To convert microinches strain to percent strain, move decimal point four places to left.

Table B-2 (continued)

Pressure (ksi)	Strain (μin.)[a] from gage No.														
	72	73	74	77	78	79	97	98	99	101	102	103	104	105	106
First pressurization cycle															
0	−49	−67	−59	−61	−20	−20	0	2	0	2	0	0	0	2	0
3.8	257	251	235	668	363	49	435	385	363	53	215	213	83	412	150
7.8	93	101	91	802	310	−284	834	753	721	115	421	421	164	822	296
11.9	691	689	689	1805	1134	164	1254	1104	1053	166	622	624	245	1211	440
16.0	934	928	922	2293	1517	174	1675	1472	1399	217	832	836	327	1615	590
18.0	996	988	976	2461	1632	122	1889	1642	1586	245	932	936	365	1804	661
20.0	1144	1134	1132	2714	1843	186	2205	1827	1169	277	1039	1043	404	2009	736
22.0	1249	1243	1237	2900	1960	190	2479	2001	510	306	1144	1148	442	2181	809
23.0	1314	1296	1292	2953	2003	Out	2708	2039	3797	330	1207	1203	463	2280	848
24.0	1397	1371	1377	3028	2037		2916	2076	Out	358	1280	1268	475	2447	885
24.4	1379	1320	1306	3007	1968		Out	2110		373	1326	1308	479	2554	903
Second pressurization cycle															
0	−45	−43	−77	806	−154	Out	Out	−87	Out	57	49	18	18	136	2
0	186	164	198	802	−32		−156	43	59	30	4	104			4
0															
0	194	162	201	788	−41		160	40	63	34	4	105			6
3.9	423	389	423	1337	362		239	95	278	253	77	532			162
7.9	480	445	480	1626	561		614	130	486	460	156	941			308
12.0	857	830	850	2155	1095		966	182	687	664	235	1331			450
16.0	1083	1053	1069	2535	1450		1302	245	893	867	315	1726			594
19.9	1286	1267	1280	3359	1788		1636	290	1096	1075	394	2122			736
19.9	1296	1265	1282	3360	1784		1636	290	1098	1077	396	2122			737
22.0															
22.1	1418	1382	1405	3748	2057		1855	336	1215	1193	438	2347			822
24.0	1509	1472	1493	3900	2216		2015	363	1318	1294	477	2542			893
25.9															
25.9	1677	1636	1658	4137	2450		2207	409	1458	1424	507	2889			964
27.0	1746	1699	1707	Out	2588		2392	431	1576	1531	511	3266			998
27.9	2021	1958	1962		3218		3186	482	1705	1738	495	3828			1014

[a]To convert microinches strain to percent strain, move decimal point four places to left.

Table B-3. Pressure-strain data from vessel V-2 – switch box data

See Fig. 7.10 for gage location
See also Table B-2

Pressure (ksi)	Strain (μin.)[a] from gage No. –					
	39	52	54	55	76	100
First pressurization cycle						
0	0	0	0	0	0	0
4	380	310	220	220	210	220
8	730	610	450	420	420	430
12	1090	910	670	630	630	650
16	1440	1220	890	830	820	850
20	1790	1560	1120	1040	1050	1070
22	1960	1750	1230	1140	1140	1170
23	1990	1930	1310	1220	1210	1230
24	2010	2300	1400	1300	1270	1310
24.4	1930	2910	1470	1340	1320	1350
Second pressurization cycle						
0	−120	1270	120	100	60	90
4	70	1610	370	320	300	300
8	430	1940	600	540	510	520
12	790	2260	830	750	720	730
16	830	2590	1060	960	930	930
20	1090	2920	1280	1170	1140	1170
19.9	1130	2920	1280	1170	1140	1180
22	1260	3120	1430	1300	1270	1300
24	1410	3320	1540	1410	1380	1410
26	1580	4020	1730	1560	1520	1560
27	1820	4490	1970	1720	1670	1700
27.9	2190	6530	3510	1920	1820	1890

[a]To change microinches strain to percent strain, move decimal point four places to left.

Appendix C

CALCULATIONS OF THE FRACTURE OF VESSELS V-1 AND V-2

Introduction

One objective of the intermediate pressure vessel tests is to provide a means for determining the accuracy of the various methods of fracture analysis proposed for calculating the fracture strengths of nuclear pressure vessels in the case of hypothetical or real flaws. The intermediate test vessels are the first of their size and material type to be tested with large sharp man-made flaws and with pretest measurements of fracture toughness; therefore no similar data existed before these tests were performed.

The main purpose of this appendix is to explain how the several values of fracture pressure, strain, and/or energy for vessels V-1 and V-2 were calculated. It is not the purpose of this discussion to evaluate any of the methods of fracture analysis. Fracture calculations were made both prior to and after the tests. In the discussion that follows, the pretest calculations for each vessel are presented as a group followed by the posttest calculations. (See Appendix F for list of nomenclature.)

Pretest Fracture Strength Estimates for Vessel V-1

Pretest estimates of the fracture conditions for vessel V-1 were made by eight methods, all of which differed in varying degrees. The calculations made by each of these methods are explained in this section. A set of input data used in several of the estimates for vessel V-1 is given in Table C-1.

Table C-1. Data for fracture analyses of the HSST program intermediate test vessel V-1

Material	A508, class 2 forging steel
NDT temperature, °F	+10
Test temperature, °F	+130
Expected fatigue-sharpened flaw dimensions, in.	
Depth	2.5
Surface length	8.1
Radius of curvature	4.53
Tensile properties	
Yield stress, ksi	72
Ultimate stress, ksi	93
Elongation, %	26
Reduction in area, %	70
Strain at maximum load, %	11
Vessel dimensions, in.	
Inside radius	13.5
Wall thickness	6.0
Model vessel data	
Inside radius, in.	1.91
Wall thickness, in.	0.63
Flaw depth, in.	0.32
Flaw surface length, in.	1.4
Failure pressure at 130° F, ksi	32.2
Failure strain at $r = r_o$, %	1.68
Charpy V-notch upper-shelf impact energy, ft-lb	90

Fracture analysis diagram (analysis performed by J. G. Merkle, ORNL). The Naval Research Laboratory fracture analysis diagram,[1] modified to include the effects of section thickness, is shown in Fig. C-1. For thick sections and a flaw surface length of about 8 in., Fig. C-1 indicates that at a temperature 120°F above the nil ductility transition (NDT) temperature, stresses between the yield stress and the ultimate stress (i.e., the stress for plastic instability) will be required to produce fracture. Note that Fig. C-1 does indicate some degree of flaw size effect for thick sections at NDT + 120°F.

Plastic instability (analysis performed by J. G. Merkle, ORNL). Previous analyses have indicated that for upper shelf conditions, the gross strain tension specimens,[2] the intermediate tensile specimens tested at SwRI, and the model pressure vessels tested at ORNL have failed by the plastic instability of the net section after various assumed amounts of slow crack growth during rising load, possibly very near maximum load. In the case of the gross strain tension specimens, Randall and Merkle[2] have reported as much as a 25% increase in crack dimensions prior to maximum load.

For a pressure vessel with an external part-through surface crack, the analysis used was similar to one developed by Eiber et al.[3] Referring to Fig. C-2, failure by plastic instability was assumed to occur when the average hoop stress over a defined area adjacent to the flaw becomes equal to the hoop stress for plastic instability in an infinitely long unflawed thin-walled cylinder under internal pressure with closed ends.

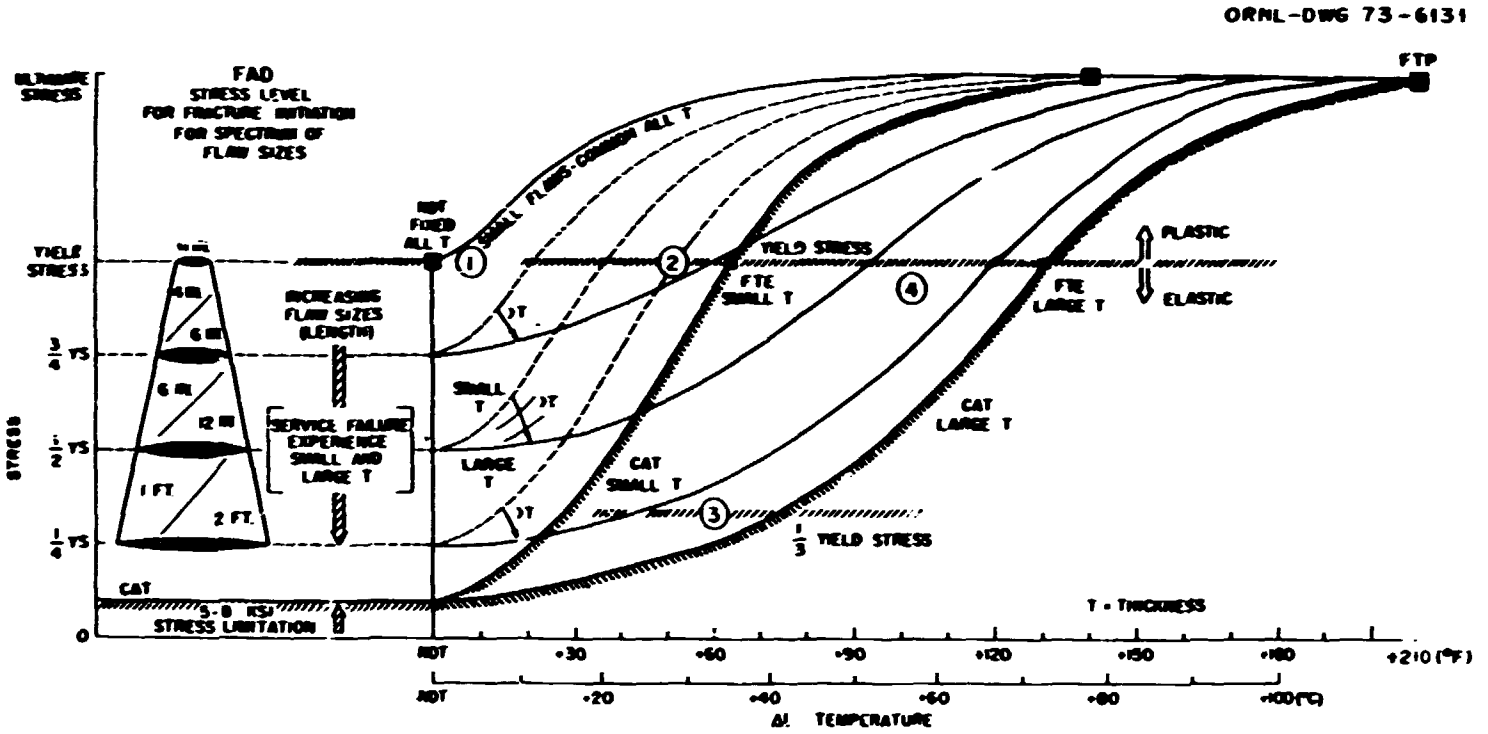

Fig. C-1. Fracture analysis diagram modified to include the effects of section size.

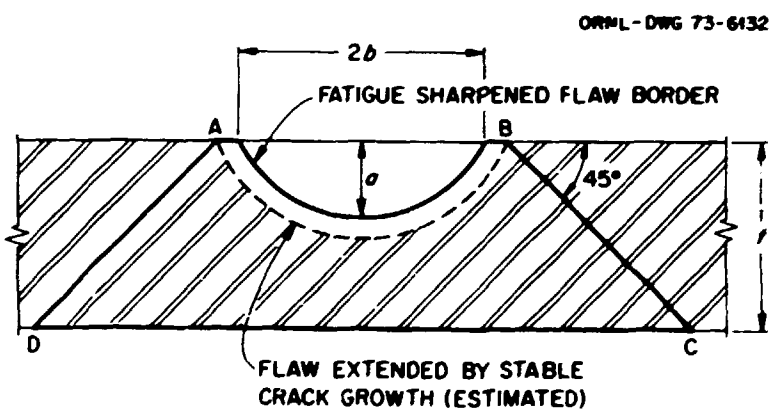

Fig. C-2. Definition of the load-bearing area for a plasti instability analysis of a surface-flawed cylinder.

Following ref. 4, the nominal hoop stress at plastic instability for an unflawed cylinder with closed ends under internal pressure can be written as

$$\sigma_\theta{}^* = q \cdot \frac{\sigma_Y + \sigma'_{ult}}{2}, \tag{1}$$

where

$$q = \frac{4/3}{\frac{e^{(H - \sqrt{3})/H}}{H} + e^{-(\sqrt{3} - 1)/H}} \tag{2}$$

and $H\sigma_Y$ is the slope of the strain-hardening branch of the stress-strain curve, assuming linear strain hardening. In Eq. (1), σ_Y is the uniaxial yield stress and σ'_{ult} is the engineering ultimate stress. The true ultimate stress is always given by

$$\sigma_{ult} = e^{\epsilon_i} \sigma'_{ult}, \tag{3}$$

where ϵ_i is the true strain at maximum load in a tension test, regardless of the shape of the stress-strain curve. Using the tensile data from Table C-1, which are for the quarter-thickness location,

$$\sigma_{ult} = (e^{0.11})(93) = 104 \text{ ksi}.$$

Then, if the strain at the onset of strain hardening is about 1.5%. $H \sim 5$, and, from Eq. (2), $q = 1.07$. Consequently, from Eq. (1),

$$\sigma_\theta{}^* = 1.07 \frac{(72 + 93)}{2} = 88.3 \text{ ksi}.$$

It was assumed that the force carried by the area $ABCD$ in Fig. C-2 would still be carried by the same area with the flaw present. Thus, if

$$A = ABCD = (2b + t)t, \tag{4}$$

then, at failure,

$$p_f \frac{r_i}{t} A = \sigma_\theta{}^* (A - A_c), \tag{5}$$

where p_f is the pressure at failure, r_i is the inside radius, t is the vessel wall thickness, and A_c is the area of the crack. From Eq. (5), it follows that

$$p_f = \frac{\sigma_\theta{}^* (1 - A_c/A)}{r_i/t}. \tag{6}$$

For these calculations, the flaw border was treated as a semiellipse, for which

$$A_c = \frac{\pi a b}{2}. \tag{7}$$

Data for the model vessel tested at 130°F are summarized in Table C-1. Using Eqs. (4) and (7) and assuming no slow crack growth, $A_c/A = 0.184$. Thus, from Eq. (6),

$$p_f = \frac{88.3\,(0.816)}{2.25} = 32.0 \text{ ksi},$$

which is very close to the observed failure pressure of 32.2 ksi.

For vessel V-1, some slow crack growth prior to maximum load was expected. Thus the expected dimensions of the fatigue-sharpened flaw (here the fatigued flaw depth was taken as 2.5 in.) were assumed to increase by 15% in order to estimate the size of the flaw at maximum load. Using Eqs. (4) and (7) and considering the estimated slow crack growth,

$$\frac{A_c}{A} = \frac{(1.15)^2\,(15.9)}{84.6} = 0.248.$$

Thus, from Eq. (6),

$$p_f = \frac{(88.3)(0.752)}{(2.25)} = 29.5 \text{ ksi}.$$

The stress concentration method (analysis performed by J. G. Merkle, ORNL). A method for estimating fracture strengths at any temperature has recently been proposed by Irvine and Quirk of the UKAEA Safeguards Division.[5-7] Their method assumes that fracture will occur when the average stress over a distance S ahead of the crack becomes equal to the ultimate tensile stress. The distance S is considered to be a material property and is calculated from the equation

$$S = 1.30\alpha \left(\frac{\text{CVN}}{\sigma_Y}\right)^{1/3}, \tag{8}$$

where α is a factor of proportionality, CVN is the Charpy V-notch impact energy (ft-lb), and σ_Y is the yield stress (ksi). From Fig. 1 in ref. 7, it can be deduced that

$$\alpha = \left(\frac{\epsilon_t}{20.5}\right)^2, \tag{9}$$

where ϵ_t is the total elongation obtained from a tension test (%). From Table C-1, $\epsilon_t = 26\%$, and, therefore, from Eq. (9), $\alpha = 1.61$. Consequently, using Eq. (8) and values from Table C-1 gives

$$S = (1.30)(1.61)\left(\frac{90}{72}\right)^{1/3} = 2.26 \text{ in.}$$

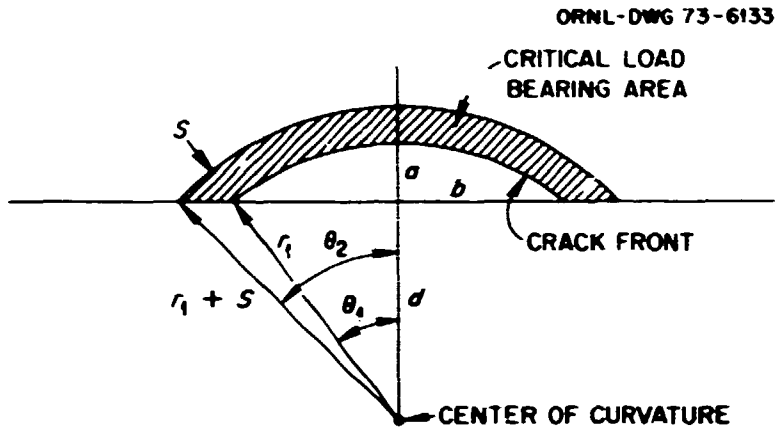

Fig. C-3. Definition of the critical load-bearing area for fracture analysis by the stress concentration method.

For a part-circular surface crack, such as the one shown in Fig. C-3, equating the nominal force acting on the flaw area plus the strip of width S, in the absence of the flaw, to the force acting on the strip of width S, adjacent to the crack, leads to

$$f_g = f_u \left\{ 1 - \left(\frac{r_1}{r_1 + S} \right)^2 \frac{\theta_1 - b\,(r_1 - a)/r_1^{\,2}}{\theta_2 - \sin\theta_2\,(r_1 - a)/(r_1 + S)} \right\}, \tag{10}$$

where

$$\theta_1 = \cos^{-1}\left(\frac{r_1 - a}{r_1} \right) \tag{11}$$

and

$$\theta_2 = \cos^{-1}\left(\frac{r_1 - a}{r_1 + S} \right). \tag{12}$$

In Eqs. (10)–(12), f_g is the average gross stress at failure, f_u is the ultimate tensile stress, and r_1 is the radius of curvature of the crack front. Using the data given in Table C-1, Eqs. (11) and (12) give $\theta_1 = 1.11$ radians and $\theta_2 = 1.27$ radians. Using $f_u = 93$ ksi, Eq. (10) then gives

$$f_g = (93)(0.677) = 63.0 \text{ ksi}.$$

The pressure corresponding to this average stress over the flaw area can be estimated by using

$$p_f = \frac{f_g}{r_i/t} = \frac{63}{2.25} = 28.0 \text{ ksi}. \tag{13}$$

The knee of the pressure-strain curve can be estimated in a consistent manner from the same equation used to calculate the code-allowable pressure, but with S_m replaced by σ_Y. Thus

$$p_Y \sim \frac{\sigma_Y}{1/(Y-1) + 1/2} = \frac{72}{2.75} = 26.2 \text{ ksi}. \tag{14}$$

Therefore, the stress concentration method, as applied to this case by ORNL, appears to indicate that gross yielding will precede fracture.

The stress concentration method (analysis submitted by W. H. Irvine, UKAEA). The UKAEA's application of this method of analysis (which they originated[5-7]) differs from the ORNL application mainly in assumptions regarding the use of the nominal stress distribution. The UKAEA assumed that the nominal stresses would still be within the elastic range at fracture, so that Eq. (1) of Appendix E would still apply. This assumption is in contrast to Eq. (13). Secondly, instead of applying the equilibrium condition to the entire area of the flaw and the surrounding strip of width S, they analyzed only the incremental element of area containing the bisector of the flaw, within a differential angle $d\theta$, measured at the center of flaw curvature. Thus no stress redistribution due to yielding was considered, as it was in the ORNL analysis.

By integration, within the angular element of area containing the flaw bisector, the following equation can be obtained for the failure pressure:

$$p_f = \frac{\frac{f_u}{2}(r_o^2/r_i^2 - 1)\left\{\left(\frac{(r_1+S)}{(r_a-S)}\right)^2 - [r_1/(r_a-S)]^2\right\}}{(N^2-1)\,[M/(r_a-S) - 1/2] - N^2 \ln N} \quad . \tag{15}$$

In Eq. (15),

$$r_a = r_o - a, \tag{16}$$

$$N = \frac{r_o}{r_a - S}\ , \tag{17}$$

and

$$M = r_1 + r_a\ . \tag{18}$$

The input data for the UKAEA estimate for vessel V-1 are as follows:

σ_Y = 70.75 ksi,

f_u = 92.6 ksi,

ϵ_t = 26.5%,

CVN = 80 ft-lb,

a = 2.6 in.,

r_1 = 5.6 in.

The calculated values, from Eqs. (9), (8), and (15) are as follows:

α = 1.65,

S = 2.25 in.,

p_f = 24.0 ksi.

This estimate predicted failure prior to the onset of gross yielding at 130°F.

Gross strain plus a bulging correction (analysis performed by P. N. Randall, USAEC). This calculation was an estimate based on the TRW gross strain data for A 533-B steel,[8] some of the HSST program intermediate tensile test data,[9] and some earlier unpublished TRW test data from 2-in.-diam surface-flawed tubes of high-strength steel. Figure C-4, taken from ref. 8, indicates that the critical gross strain for a tensile specimen containing a 2.5-in.-deep surface flaw at 130°F should not exceed 2%. This strain corresponds to an average stress roughly equal to the yield stress. The TRW tube failure data indicated that for a ratio of inside radius to thickness of 20, bulging causes about a 20% reduction in the fracture stress for a flaw oriented normal to the circumferential stress. Assuming (conservatively) that the effect of bulging is the same for a vessel with a ratio of inside radius to wall thickness of 2.25, the calculated value of the failure pressure for a yield stress of 70 ksi is

$$p_f \quad \frac{0.8\sigma_Y}{(r_i/t)} = \frac{(0.8)(70)}{(2.25)} = 24.9 \text{ ksi} . \tag{19}$$

Thus the failure pressure was estimated to be approximately 25 ksi.

Inverse square root based on strain (analysis performed by R. W. Derby, ORNL). This estimate of the behavior of the first intermediate test vessel was based on the following assumptions. First, the pressure-strain curve for a model similar to vessel V-1 (including material property variations through the thickness), except for flaw size, can be approximated by extending the pressure-strain curve for the models tested previously at 130°F, in which the flaws were located in surface material, to a strain of approximately 2.6%, as shown in Fig. C-5. The reason for extending the curve is that the strain required to cause fracture initiation was assumed to be governed by the strain tolerance of center material, while the pressure-strain curve of the remaining ligament beneath the flaw was assumed to be governed by the flow properties of surface material. Second, the gross strain at failure in a prototype is assumed to be smaller than in a model by a factor equal to the square root of the ratio of the dimensions. The idea is simply that an inverse square root law, based on strain, was assumed to be applicable for either completely ductile or completely brittle behavior. Thus the failure strain in the prototype was estimated from

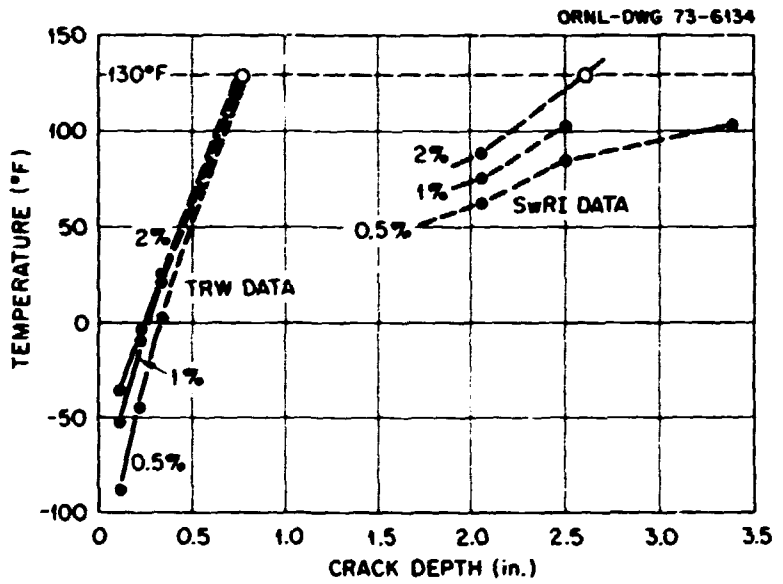

Fig. C-4. Effect of crack size on the temperature required to achieve various levels of gross strain at maximum load, for TRW and SwRI data.

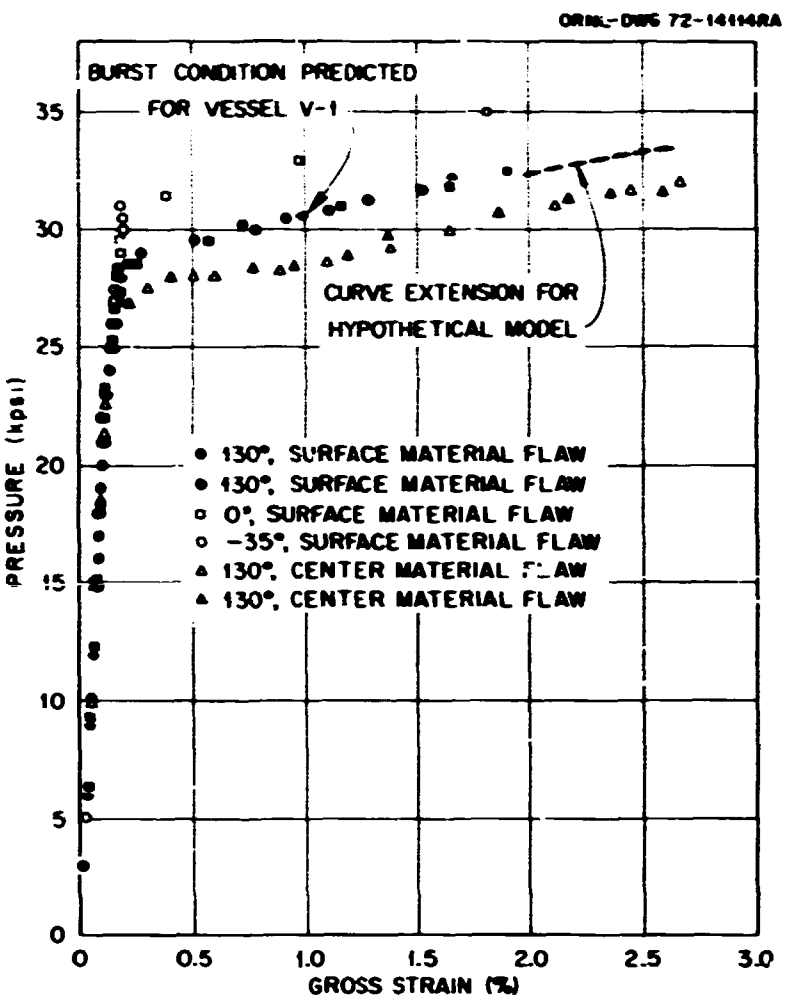

Fig. C-5. Comparison of model vessel test data with equivalent-energy prediction and test results for vessel V-1.

$$\epsilon_{fp} = \frac{\epsilon_{fm}}{\sqrt{B_p/B_m}}, \tag{20}$$

where ϵ_{fp} and ϵ_{fm} are the failure strains of the prototype and the model, respectively, and B_m and B_p are the sizes (in this case wall thicknesses) of the model and the prototype respectively. Since the prototype is 6 in. thick and the models were 0.85 in. thick, the square root of the ratio of the dimensions is 2.66. Hence the strain in the prototype at failure was estimated to be 2.6/2.66=0.97%. Reading from the higher of the two curves obtained from the models at 130°F in Fig. C-5, the failure pressure was estimated to be 30,600 psi.

***J* integral plus model** (analysis performed by H. T. Corten, University of Illinois). This estimate was based on an assumed generalization of an equation recently derived by Rice[10] for estimating the value of the *J* integral for a deep double-edge-notched tensile bar. An additional empirical coefficient was evaluated by means of model test data. Rice's expression for the *J* integral[10] for a deep double-edge-notched tensile bar is

$$J = J_{el} + \frac{1}{b}\left[\int_0^{\delta^P} P\, d\delta^P - \int_0^P \delta^P\, dP\right], \tag{21}$$

where J_{el} is identical to the elastically calculated value of K_I^2/E, based on the nominal stress, crack size, and geometry; b is the width of the uncracked ligament; P is the load per unit thickness; and δ^P is the plastic displacement of P due to the crack. The quantity in brackets is the difference between the real

plastic work and the complementary plastic work of the load P, due to the crack. For this analysis, it was assumed that an analogous expression exists for a part-through surface crack; so that, reversing the thickness and width directions, J can be estimated from

$$J = J_{el} + \frac{\beta}{b}\left[\int_0^{\delta^P} P\, d\delta^P - \int_0^P \delta^P\, dP\right], \tag{22}$$

where

$$J_{el} = \frac{1.2\sigma_Y{}^2\, \pi a}{\Phi^2 E} \tag{23}$$

In Eq. (23) the nominal stress has been estimated as the yield stress. Note that Eq. (22) ignores any bending that may be caused by the eccentricity of the load with respect to the centroid of the net section.

If the P vs δ^P curve is approximated by a straight line, beginning at a yield load P_Y, then

$$\int_0^{\delta^P} P\, d\delta^P - \int_0^P \delta^P\, dP = P_Y \delta^P . \tag{24}$$

Combining Eqs. (22) and (24) thus gives

$$J = J_{el} + \frac{\beta}{b} P_Y \delta^P . \tag{25}$$

An alternate expression is obtained by substituting the expression

$$\delta^P = \delta - \frac{P}{k} \tag{26}$$

into Eq. (22), where δ is the total displacement due to the crack and k is the elastic stiffness. The result is that

$$J = J_{el} + \frac{\beta}{b}\left[\int_0^{\delta} P\, d\delta - \int_0^P \delta\, dP\right]. \tag{27}$$

Thus the quantity in brackets in Eq. (22) also represents the same expression written in terms of the total displacement, because the elastic values of the real and the complementary energies are always equal. If P_0 is the intercept of a linear approximation to the strain-hardening branch of the P vs δ curve with the load axis, then

$$J = J_{el} + \frac{\beta}{b} P_0 (\delta - \delta_Y), \tag{28}$$

where

$$\delta_Y = \frac{P_Y}{k} . \tag{29}$$

If the following definitions are adopted:

$$P = pr_i \,, \tag{30}$$

$$\delta = \epsilon_\theta \cdot 2\pi r_m \,, \tag{31}$$

and

$$r_m = \frac{r_i + r_o}{2} \,, \tag{32}$$

then using Eqs. (30) and (31), Eq. (28) becomes

$$J = J_{el} + \frac{2\pi r_m r_i \beta p_0}{b} (\epsilon_\theta - \epsilon_{\theta Y}) \,. \tag{33}$$

At failure, Eq. (33) becomes

$$J_{ult} = J_{el} + \frac{2\pi r_m r_i \beta p_0}{b} (\epsilon_{\theta f} - \epsilon_{\theta Y}) \,, \tag{34}$$

where J_{ult} is the critical value of J and $\epsilon_{\theta f}$ is the critical circumferential strain at failure. Solving Eq. (34) for $\epsilon_{\theta f}$ gives

$$\epsilon_{\theta f} = \epsilon_{\theta Y} + \frac{b(J_{ult} - J_{el})}{2\pi r_m r_i \beta p_0} \,, \tag{35}$$

and solving the same equation for β gives

$$\beta = \frac{b(J_{ult} - J_{el})}{2\pi r_m r_i p_0 (\epsilon_{\theta f} - \epsilon_{\theta Y})} \,. \tag{36}$$

Because the models and the prototype were not exactly geometrically similar with respect to flaw size and thickness, it was decided to treat β as a function of the ratio b/B using the expression

$$\beta = (b/B)^n \,, \tag{37}$$

where B is thickness. The value of n can be obtained by rearranging Eq. (37) to read

$$n = \frac{\ln \beta}{\ln (b/B)} \,. \tag{38}$$

Values of J_{ult} were calculated from compact tension specimen load-deflection data provided by ORNL, according to the following equation, also derived by Rice:[10]

$$J_{ult} = \frac{2}{b} \int_0^\delta P \, d\delta \,, \tag{39}$$

where δ is the total displacement of the load due to the crack and P is the load per unit thickness. Data from a series of 4t CT specimens and 0.85t CT specimens of IVT-1 material were analyzed. Evidence of onset of cracking prior to final fracture was found in almost all of the P vs δ records. However, this will not be pursued further here. In this analysis, emphasis was placed on the value of J at final fracture, hereafter denoted as J_{ult}.

The series of load-deflection records were obtained from the HSST program office, and the area under the P vs δ diagram to maximum load was evaluated for each record. In Table C-2 the specimen dimensions, P_{max}, δ_{max}, and the measured area are recorded for each specimen. The measured area was adjusted for two factors. First, this area was divided by the specimen thickness B to obtain a per unit thickness number. Second, an approximate correction was made for the fact that the deflections δ were measured at the front face of each specimen instead of at the load point. For this reason, all the areas (deflections) were divided by a number close to 1.48. The values of a/W were computed, and corrections were based on an analysis supplied by Westinghouse. The minimum and maximum corrections were 1.442 and 1.496. However, the corrections for only 4 of the 19 specimens analyzed were outside the range of 1.47 to 1.49, and the average value was 1.48. While some questions surround this value, it appears that, at worst, only a small systematic error might have been introduced by this correction. The values, adjusted for thickness and deflection measurement point, are listed in Table C-2 in the column labeled $\int P\,d\delta$. A value of J_{ult} was computed from $\int P\,d\delta$ by multiplying each value by the factor $2/b$. The values of J_{ult} as a function of temperature are shown plotted in Fig. C-6. Data from the 4t CT specimens are distinguished from the 0.85t CT center data

Table C-2. Compact tension specimen data for HSST intermediate vessel prolongation of vessel V-1

Specimen	T (°F)	B (in.)	a (in.)	b (in.)	a/W	P_{max} (lb)	δ_{max} (in.)	Measured area (in.-lb)	$\int_0^{\delta} P\,d\delta$ (in.-lb/in.)	J_{ult} (in.-lb/in.^{2})
					4t CT					
VIB-6	0	4.0	4.10	3.90	0.512	148,000	0.070	5,280	880	455
VIB-2	100	3.97	4.12	3.88	0.516	232,000	0.187	28,300	4800	2470
VIB-1	120	4.0	4.33	3.67	0.541	204,000	0.180	24,000	4110	2240
VIB-5	130	4.0	4.11	3.89	0.515	227,000	0.183	27,200	4580	2350
VIB-4	130	4.0	4.27	3.73	0.535	213,000	0.190	27,800	4750	2550
VIB-3	200	4.0	4.10	3.90	0.512	228,000	0.171	25,100	4220	2160
					0.85t CT, center					
VIB-19	−50	0.852	0.88	0.82	0.518	10,250	0.04	221	175	427
VIB-14	0	0.852	0.89	0.81	0.523	11,350	0.059	593	472	1165
VIB-15	100	0.852	0.88	0.82	0.517	11,400	0.121	1,090	863	2100
VIB-17	130	0.852	0.89	0.81	0.522	10,950	0.124	1,085	862	2120
VIB-18	130	0.832	0.87	0.83	0.512	11,350	0.131	1,200	968	2330
VIB-16	200	0.853	0.88	0.82	0.518	11,000	0.122	1,060	840	2050
					0.85t CT, outside surface					
VIB-13	−100	0.85	0.958	0.742	0.563	8,400	0.037	162	132	357
VIB-12	−50	0.853	0.883	0.817	0.52	10,750	0.045	266	211	517
VIB-7	0	0.852	0.89	0.81	0.524	12,300	0.1135	1,044	833	2060
VIB-8	100	0.852	0.87	0.83	0.512	12,100	0.090	790	624	1500
VIB-10	130	0.852	0.87	0.83	0.512	11,800	0.100	900	711	1720
VIB-11	130	0.853	0.897	0.803	0.527	11,100	0.120	1,050	838	2090
VIB-9	200	0.853	0.858	0.842	0.504	11,800	0.100	885	692	1640
					0.85t CT, inside surface					
VIB-21	130	0.853	0.883	0.817	0.520	11,400	0.100	975	772	1890
VIB-20	130	0.853	0.880	0.820	0.517	11,600	0.122	1,134	900	2200

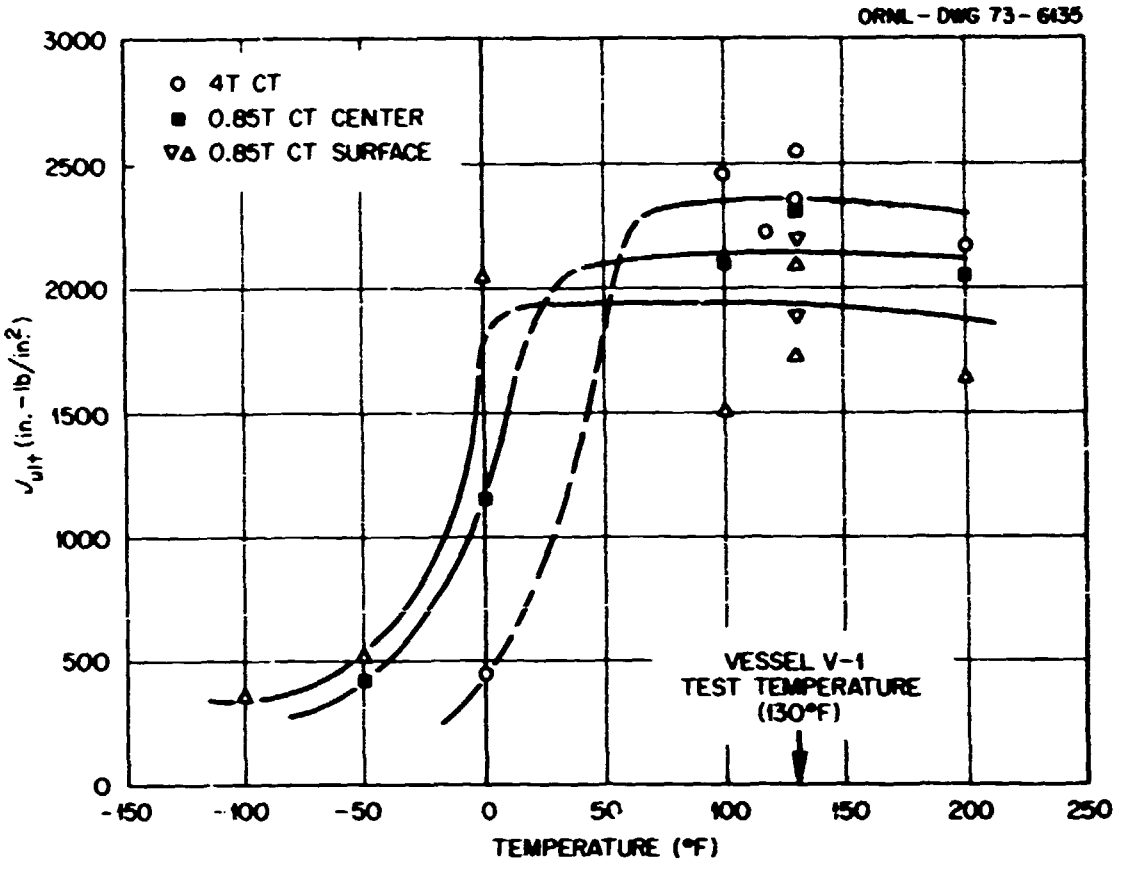

Fig. C-6. Values of J_{ult} calculated from compact tension specimen test data for vessel V-1 material.

Table C-3. Average fracture toughnesses at 130°F for vessel V-1

Specimens	Av J_{ult}[a] (in.-lb/in.^{2})	Equivalent K_{ult} (ksi $\sqrt{in.}$)
4t CT	2450	271
0.85t CT		
Center	2225	260
Outside	1855	236
Inside	2045	248

[a]Average values of two specimens for each condition.

and the 0.85t CT surface data. The low value at 0°F for the 4t specimen is consistent with the data reported in Chap. 4. As might be expected, the surface material has the highest toughness in the low-temperature range. However, the surface data showed the lowest upper-shelf toughnesses. At 130°F, the test temperature for vessel V-1, the average toughnesses corresponding to fracture were as listed in Table C-3.

Since the flaws in the models (V1-A1-F and V1-A1-C) used to evaluate the empirical coefficient β were located in outside surface material and the walls of these model vessels were 0.85 in. thick, J_{ult} for these models was taken as 1850 in.-lb/in.^{2}, based on the average 0.85t CT value for outside surface material listed in Table C-3. (Due to minor errors, this value differs from the value of 1855 in.-lb/in.^{2} listed in Table C-3, which should have been 1905 in.-lb/in.^{2}.) The value of J_{ult} for vessel V-1 was taken as 2350 in.-lb/in.^{2}, which also differs from the 4t CT value listed in Table C-3 for unspecified reasons.

The values of the quantities used for analyzing the model vessel test data and for estimating the failure strain of vessel V-1 are listed in Table C-4. For the models the value of $a/2c$ was an assumed value (the actual value was about 0.168). The value of Φ^2 was obtained from a graph of Φ^2 vs $a/2c$ (see, for instance,

Table C-4. Values used for *J*-integral analysis of vessel V-1

Quantity	0.85-in vessel	Vessel V-1
	Dimensions	
r_o, in.	2.76	19.5
r_i, in.	1.91	13.5
r_m, in.	2.34	16.5
B, in.	0.85	6.0
a, in.	0.32	2.6
b, in.	0.535	3.4
$2c$, in.		8.25
	Properties	
σ_Y, ksi	70	70
E, psi	3×10^7	3×10^7
J_{ult}, in.-lb/in.^{2}	1850	2350
J_{el}, in.-lb/in.^{2}	100	965
p_Y, ksi	29.0	
σ_0, ksi	28.5	28.5
$\epsilon_{\theta Y}$, in./in.	0.0019	0.0019
$\epsilon_{\theta f}$, in./in.	0.0174	Calc.
	Parameters	
β	0.0757	0.044
$a/2c$	0.374	0.315
Φ^2	1.875	1.65
n	5.51	5.51

ref. 11);* J_{el} was calculated from Eq. (23), and β was calculated from Eq. (36). The value of n was then calculated from Eq. (38). For vessel V-1, the values of Φ^2 and J_{el} were determined by the same procedure. The value of β was then calculated from Eq. (37). The estimated fracture strain for vessel V-1 was then calculated from Eq. (35) as follows:

$$\epsilon_{\theta f} = 0.0019 + \frac{(3.4)(2350 - 965)}{(2)(\pi)(16.5)(13.5)(0.044)(28{,}500)}$$

$$= 0.0019 + 0.0027 = 0.0046 = 0.46\% .$$

Since the estimated failure strain is within the range of the tensile yield point elongation, the failure pressure was estimated as the fully plastic (gross yield) pressure. This pressure was calculated by using the strain energy of distortion (also called the Von Mises yield criterion),

$$2\sigma_Y^2 = (\sigma_1 - \sigma_2)^2 + (\sigma_2 - \sigma_3)^2 + (\sigma_3 - \sigma_1)^2 , \tag{40}$$

and the average stresses through the vessel wall, which were taken as

$$\sigma_1 = \sigma_\theta = p\frac{r_i}{B} = 2.25p , \tag{41}$$

$$\sigma_2 = \sigma_z = \frac{p}{(r_o/r_i)^2 - 1} = 0.92p , \tag{42}$$

*Contrary to the nomenclature, $2c$ is used here to denote the length of a surface flaw to avoid confusion with b, the ligament width.

and

$$\sigma_3 = \sigma_r = -\frac{1}{2}p \,. \tag{43}$$

Substituting Eqs. (41), (42), and (43) into Eq. (40) and solving for p gives for vessel V-1,

$$p_{GY} = 0.42\sigma_Y \,. \tag{44}$$

For σ_Y = 70 ksi, p_{GY} = 29.4 ksi, which was therefore estimated to be the failure pressure for vessel V-1.

The equivalent-energy method (analysis performed by F. J. Witt, ORNL). The basic equation of the equivalent-energy method[13] can be written in the form

$$K_{Icd} = C\sigma_d \sqrt{\pi a_d} \,, \tag{45}$$

where C is a dimensionless shape and restraint factor determined by either model testing or elastic analysis, σ_d is a pseudoelastic stress at fracture for a specimen of size d, and a_d is the flaw size in a specimen of thickness d. The pseudoelastic stress σ_d defines a point on the extended initial tangent to the gross stress vs gross strain curve, the area under which is assumed to be the same as the area under the actual gross stress vs gross strain curve at maximum load. The shape and restraint factor C for surface flaws in pressure vessels is presently being determined by model testing. The value of C does not always agree exactly with the value of the calculated elastic shape factor C, based on linear elastic analysis.

The value of the fracture toughness parameter K_{Icd} is determined from compact tension specimen data:[13,14]

$$K_{Icd} = \frac{P_d^* f(a/W)}{B\sqrt{W}}, \quad d = B \,, \tag{46}$$

where P_d^* defines a point on the extended initial tangent to the load-deflection curve of a specimen of size d, the area under which equals the area under the actual load-deflection curve at the point of maximum load. The other factors in Eq. (46) have the same meaning as for a conventional linear elastic calculation[15] of K_{Ic}. Values of K_{Icd} obtained from specimens taken from a prolongation of the cylindrical region of vessel V-1 are listed in Table C-5.

Table C-5. Summary of lower-bound toughness K_{Icd} values for V-1 material obtained from compact tension specimens, circumferential orientation

Test temperature (°F)	K_{Icd} (ksi $\sqrt{\text{in.}}$)			
	d = 0.85, center	d = 0.85, outer surface[a]	d = 0.85, inner surface[a]	d = 4, center
−100		113		
−50	103	112		
0	142	214		136
100	225	192.5		292
120				285
130	228, 237	219, 202	215, 230	295, 305
200	213	209		280

[a]Surface of specimens is $^3/_{16}$ in. from surface of prolongation.

A value of K_{Icd} for $d = 6$ was obtained by calculating the volumetric energy ratio $s_{m,p}$, $m = 0.85$, $p = 4$, from the formula

$$K_{Icp} = K_{Icm}\sqrt{\frac{p/m}{s_{m,p}}} \tag{47}$$

and then extrapolating the assumed linear plot of volumetric energy ratio vs thickness to a thickness of 6 in.

The value of the shape and restraint factor C that was used in the estimate for vessel V-1 was determined from a modification of the data obtained from the 0.85-in.-thick models V1-A1-F and V1-A1-C, which are shown plotted in Fig. C-5 as well as in Fig. 5.7. Rearranging Eq. (45) and using the pressure to represent the nominal stress gives

$$C = \frac{K_{Icd}}{\sigma_d\sqrt{\pi a_d}}. \tag{48}$$

For model vessels with 0.85-in.-thick walls and flaws in originally outside surface material, Table C-5 gives an average value of K_{Icd} = 210 ksi $\sqrt{\text{in.}}$. For these two models a_d = 0.32 in., and based on Fig. C-5, the average value of σ_d is about 142 ksi. Based on other model data the effect on C of increasing the value of a/B from 0.377 (the ratio for the models) to 0.437 (the estimated ratio for the prototype) is to increase the value by 9%. Thus, with this modification, the value of C used for the analysis of vessel V-1 was calculated from Eq. (48) to be

$$C = \frac{210}{142\sqrt{0.32\pi}}(1.09) = 1.60\,.$$

Using the average values of K_{Icd} at 130°F, from Table C-5, for d = 0.85 in. and d = 4.0 in.,

$$s_{0.85,\,4} = 2.81\,,$$

which in turn gives

$$s_{0.85,\,6} = 4.0\,.$$

K_{Ic6} was then determined as

$$K_{Ic6} = 232\sqrt{\frac{6.0}{(0.85)(4.0)}} = 311 \text{ ksi}\sqrt{\text{in.}}\,.$$

The fracture estimate for vessel V-1 was obtained from Eq. (45) with K_{Ic6} = 311 ksi $\sqrt{\text{in.}}$, $C = 1.60$, and a_6 = 2.625 in. This gave

$$\sigma_p = \frac{311}{1.60\sqrt{2.625\pi}} = 68 \text{ ksi}\,.$$

Estimating the initial slope of the pressure vs outside circumferential strain curve as

$$E' = \frac{2 \times 10^4}{1 \times 10^{-3}} = 2 \times 10^7 \text{ psi},$$

the energy at maximum load was calculated to be

$$E_6 = \frac{(\sigma_p)^2}{2E'} = \frac{(6.8 \times 10^4)^2}{4 \times 10^7} = 116 \text{ in.-lb/in.}^3 .$$

The point on the pressure-strain curve in Fig. C-5 for models V1-A1-F and V1-A1-C at which the energy equals this value has the coordinates p_f = 29.6 ksi and $\epsilon_{\theta f}$ = 0.46%.

Crack Arrest Estimate for Vessel V-1

The pretest analyses of vessel V-1 included one quantitative estimate concerning crack arrest. This estimate, which is quoted below, was correct.

The NDT temperature of the vessel forging steel is the same as that of the A 533-B plate, namely, +10°F. Therefore, it will be assumed that the crack arrest toughness vs temperature curve for the two materials is the same. Figure C-7 shows Materials Research Laboratory crack arrest toughness data for A 533-B steel.[16] As shown in the figure, the value of K_{Ia} at 130°F is estimated to be 110 ksi $\sqrt{\text{in.}}$.

Whether or not crack arrest can occur in the test vessels depends upon whether fast fracture ever initiates and on the rate of decrease of pressure with crack extension following crack penetration through the wall thickness. If fast fracture initiates in sound material and a dropoff in K_I does not occur, then crack arrest cannot occur. Discounting a dropoff in load, it is instructive to calculate the value of K_{Ia} required to arrest a through crack of length equal to double the vessel wall thickness at yield stress loading. For a thickness of 1.0 in., the required value[17] of K_{Ia}/σ_Y is 1.3, or K_{Ia} = 93.5 ksi $\sqrt{\text{in.}}$. Note that this is less than the estimated value of 110 ksi $\sqrt{\text{in.}}$ at 130°F, and fast fracture did not occur in the 0.85-in.-thick model vessels tested at 130°F. For a thickness of 6 in., the required value[17] of K_{Ia}/σ_Y is 3.1, or K_{Ia} = 223 ksi $\sqrt{\text{in.}}$, which is greater than the estimated value of 110 ksi $\sqrt{\text{in.}}$. Thus, if fast fracture initiates in the first intermediate test vessel, propagation to the ends of the vessel is likely.

Posttest Fracture Strength Calculations for Vessel V-1

Notch sensitivity analysis (analysis performed by D. Costes, CEN). This method of calculation is described in a paper published in the *Proceedings of the First International Conference on Structural Mechanics in Reactor Technology*.[18] The calculated failure pressure was 26 ksi.

The stress concentration method (analysis submitted by A. Quirk, UKAEA). This calculation used a revised set of input values. The original and revised input values are as follows:

	Original	Revised
σ_Y, ksi	70.75	72.0
f_u, ksi	92.6	93.0
ϵ_u, %	26.5	28.5
CVN, ft-lb	80	90
a, in.	2.6	2.5
r_t, in.	5.6	4.53

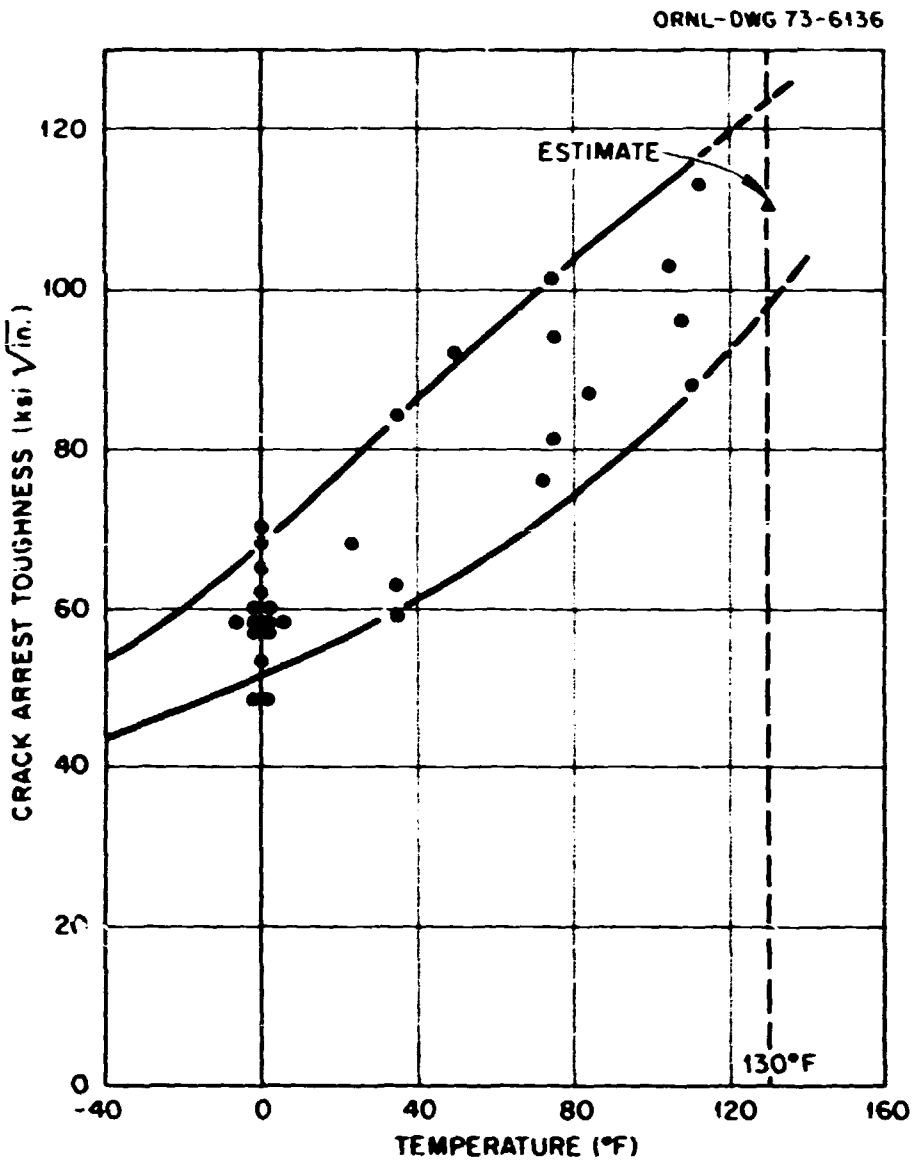

Fig. C-7. Crack arrest toughness as a function of tem perature for A533, grade B, class 1 steel. Data from tests where crack front remained within 0.10 in. of the minimum thickness section of the test specimen.

The revised elongation value is based on a gage length equal to $4\sqrt{A}$, where A is tensile specimen cross-sectional area. This adjustment is explained in more detail in the discussion to follow of the UKAEA's pretest estimate by the same method for vessel V-2.

The original and revised calculated values, using the same procedure as for the pretest estimate, are as follows:

	Original	Revised
α	1.65	1.93
S, in.	2.25	2.7
p_f, ksi	24.0	27.2

The equivalent-energy method (analysis performed by F. J. Witt, ORNL). Because the pretest calculation underestimated the energy to maximum load and the flaws in the models from which the shape and restraint factor C was calculated had surface lengths exceeding, and depths less than, those corresponding to geometric similitude with vessel V-1, another model test was performed. This model, designated V2-A1-B, was fabricated from the prolongation of the cylindrical region of vessel V-2 and had its flaw in outside surface material. The pressure-strain curves obtained from this model are shown in Fig. C-8.

The crack depth was 0.36 in. The actual flaw depth in vessel V-1 was 2.56 in., thus giving a flaw depth ratio of 7.10, compared with a wall thickness ratio of 7.07. By Eq. (48),

$$C = \frac{198}{164.4\sqrt{0.36\pi}} = 1.132 .$$

Substituting into Eq. (45) gave E_6 = 237 psi.

J integral plus model (analysis performed by J. G. Merkle, ORNL). Since the pretest estimates made by the J integral plus model and the equivalent-energy methods were nearly identical, but low in strain, and the use of additional model test data improved the equivalent-energy calculation, it was of interest to determine if these same additional model test data would also improve the J integral plus model calculation. Somewhat unexpectedly, the use of the additional data did not significantly change the J integral plus model estimate because the flaw geometry differences involved had already been accounted for in the original estimate.

The posttest and pretest calculation procedures were identical. In the following discussion, numerical values not specifically mentioned are the same as those listed in Table C-4 for the pretest calculations. From a bilinear approximation to the pressure-strain curves for model V2-A1-B shown in Fig. C-8, the following values were determined:

p_o = 28.2 ksi,

$\epsilon_{\theta Y}$ = 0.15%,

$\epsilon_{\theta f}$ = 2.30%.

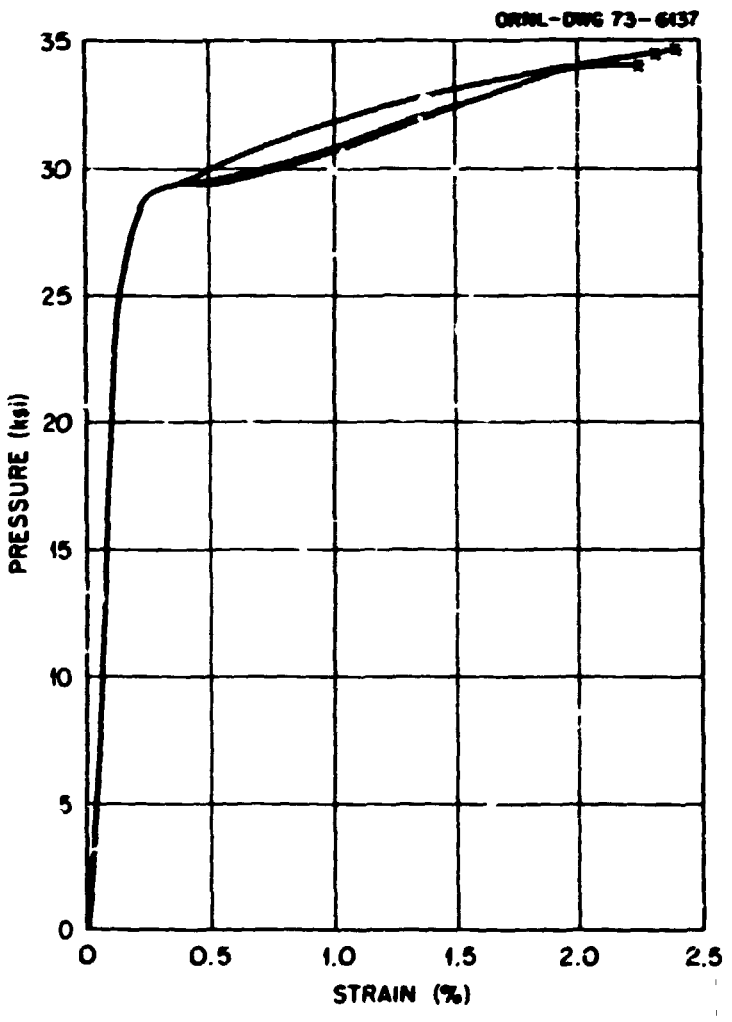

Fig. C-8. Pressure–circumferential-strain curves, 180° from flaw, for model vessel V2-A1-B, tested at 130°F (flaw in surface material).

The flaw dimensions for model V2-A1-B were a = 0.36 in. and $2c$ = 1.15 in. The values of K_{Icd} for the pre- and posttest models were slightly different. Therefore, J_{ult} for model V2-Al-B was adjusted for this difference by the calculation

$$J_{ult} = \left(\frac{198}{210}\right)^2 (1850) = 1645 \text{ in.-lb/in.}^2.$$

For the model V2-A1-B, Φ^2 = 1.67 and, from Eq. (23), J_{el} = 933 in.-lb/in.^{2}. Then, from Eq. (36), β = 0.0435, which is very close to the value originally used for the pretest estimate for vessel V-1, as shown in Table C-4. Using Eq. (38), n = 5.69, which completes the model calculations.

The actual dimensions of the flaw in vessel V-1 were a = 2.56 in. and $2c$ = 8.25 in. For this flaw, Φ^2 = 1.67 (the same as for model V2-A1-B) and, from Eq. (36), J_{el} = 946 in.-lb/in.^{2}. From Eq. (37), β = 0.0425, which is not much different from the pretest estimate. The value of J_{ult} for vessel V-1 is unchanged from the pretest estimate, 2350 in.-lb/in.^{2}. Thus, using $\epsilon_{\theta Y}$ = 0.15%, Eq. (35) gives an estimated failure strain of 0.44%, which is nearly the same as the pretest estimate. The estimated failure pressure is unchanged, 29.4 ksi.

Pretest Fracture Strength Calculations for Vessel V-2

Pretest estimates of the fracture conditions for vessel V-2 were made by 11 different or partially different methods. The calculations made by each of these methods are explained in this section. The main features of several of these methods are given in Table C-6, which provides a basic frame of reference for comparing different methods of fracture analysis. A set of input data used in several of the estimates for vessel V-2 is given in Table C-7.

Several of the estimates to be described below also made use of the same elastic–ideally plastic estimate of the pressure vs outside circumferential strain curve. This estimate was made as follows. In the elastic range, the relation between outside circumferential strain and internal pressure is given by

$$\epsilon_{\theta o} = \frac{p}{\frac{E(Y^2-1)}{(2-\nu)}}, \tag{49}$$

where $\epsilon_{\theta o}$ is the circumferential strain on the outside surface, p is the internal pressure, E is the elastic modulus, ν is Poisson's ratio, and Y is given by

$$Y = \frac{r_o}{r_i}. \tag{50}$$

In Eq. (50), r_o and r_i are the outer and the inner radii of the vessel respectively. Since r_o = 19.5 in. and r_i = 13.5 in., Eq. (50) gives Y = 1.444. Then using $E = 3 \times 10^4$ ksi and ν = 0.3, Eq. (49) gives

$$\epsilon_{\theta o} = \frac{p}{191.5}, \tag{51}$$

where p is in ksi and $\epsilon_{\theta o}$ is in percent.

In several of the failure analyses for vessel V-1 (see Table C-1) the tensile yield stress at the quarter-thickness location, at 130°F, was taken as 72 ksi. A reasonable estimate of the increase in the yield

Table C-6. Proposed methods of fracture analysis

Elements of the method	Empirical methods			Analytical or semianalytical methods				
	Fracture analysis diagram	Gross Strain	Equivalent energy (model)	Elastic fracture mechanics	J integral	Stress concentration	Equivalent energy (K_{Icd})	Tangent modulus
Crack tip fracture criterion				$K_I = K_{Ic}$	$J_I = J_{Ic}$	$S = 1.31\,\alpha\left(\frac{\phi}{f_Y}\right)^{1/3}$	K_{Icd}	$\epsilon_f\sqrt{\rho} = \text{const} \times K_c$
Critical load condition	Stress and flaw size (graphical)	Strain, flaw size, and thickness (graphical)	Energy: $E_p = \frac{E_m}{\epsilon_{m,p}}$	$K_{Ic} = C\sigma_f\sqrt{\pi a}$	$J_{Ic} = \int_{\Gamma_t} W\,dy$	(For SEN) $f_R = \frac{F}{(l/S)+1}$	$K_{Icd} = C\sigma_f^n\sqrt{\pi a_d}$	$\epsilon_f\sqrt{\rho} = 2C\sqrt{a}\int_0^{\lambda_f}\left(\frac{E_g}{E_n}\right)^{1/2} d\lambda$
Size effect condition				$\sigma_f = \frac{1}{\sqrt{a}}$	Numerical	Depends on flaw size, l	K_{Icd} determined directly or $K_{Icd} = K_{Icm}\sqrt{\frac{d/m}{\epsilon_{m,d}}}$	Flaw size a, and E_g/E_n
Partial restraint condition	Thickness (graphical)		$\epsilon_{m,p}$ depends on thickness (graphical)	$\left(\frac{K_c}{K_{Ic}}\right)^2 = 1 + 1.4\,\beta_{Ic}{}^2$				$\left(\frac{K_c}{K_{Ic}}\right)^2 = 1 + 1.4\,\beta_{Ic}{}^2$
Loading and geometry effect condition		Strain gradient (graphical)	E_m from model; no effect on $\epsilon_{m,p}$	C	Numerical	Equilibrium stress model	C	C and $E_g = \left(\frac{da}{de}\right)_{av}$
Stable crack growth condition		25% stable crack growth (upper shelf)						Estimate from test data

Table C-7. Values used for fracture analyses of the HSST program intermediate test vessel V-2

Material	A 508, class 2 forging steel
NDT temperature, °F	+10
Test temperature, °F	+32
Expected fatigue-sharpened flaw dimensions, in.	
Depth	2.5
Surface length	8.1
Radius of curvature	4.53
Tensile properties	
Yield stress, ksi	75
Ultimate stress, ksi	97
Total elongation, %	22.2
Vessel dimensions, in.	
Inside radius	13.5
Wall thickness	6.0
Charpy V-notch impact energy, ft-lb	42
Fracture toughness, K_{Ic},[a] ksi $\sqrt{\text{in.}}$	184

[a]Not valid.

stress due to a decrease in the temperature from 130 to 32°F is 3 ksi. Therefore the value of the yield stress used in several of the following calculations was 75 ksi.

The pressure vs outside circumferential strain curve for vessel V-1 underwent a sudden decrease in slope at a strain exactly equal to the uniaxial yield strain of 0.24% (see Fig. C-14). The pressure at this strain was 28.2 ksi. The corresponding pressure for vessel V-2, which will be called the gross yield pressure, was estimated simply as

$$p_{GY} = \frac{75}{72}(28.2) = 29.4 \text{ ksi} . \qquad (52)$$

This pressure was considered to be a sufficiently close estimate of the failure pressure if failure occurred after gross yielding. A bilinear estimate of the pressure vs outside circumferential strain curve for vessel V-2 is shown in Fig. C-9.

Fracture analysis diagram (analysis performed by J. G. Merkle, ORNL). Referring to Fig. C-1, the fracture-analysis diagram for thick sections indicates that an 8-in.-long flaw can cause fracture at a stress about equal to five-eighths of the yield stress at a temperature 22°F above the NDT temperature. Whether the fracture analysis diagram represents static or dynamic conditions in this case was not certain, but a conservative interpretation was that fracture prior to the onset of gross yielding was predicted. It should be noted that the A508, class 2 forging steel in the cylindrical region of vessel V-2 was considerably tougher against static initiation near the NDT temperature than the A533, grade B, class 1 steel plate tested previously under the HSST program.

Referring to Fig. C-3, it can be seen that a reasonable estimate of the ratio of the average nominal stress in the region of the flaw to the internal pressure in the vessel is 1.9. Thus the estimated failure pressure was calculated as

$$p_f = \frac{5/8\,\sigma_Y}{1.9} = 24.6 \text{ ksi} ,$$

which corresponds to an outside circumferential strain of about 0.13%.

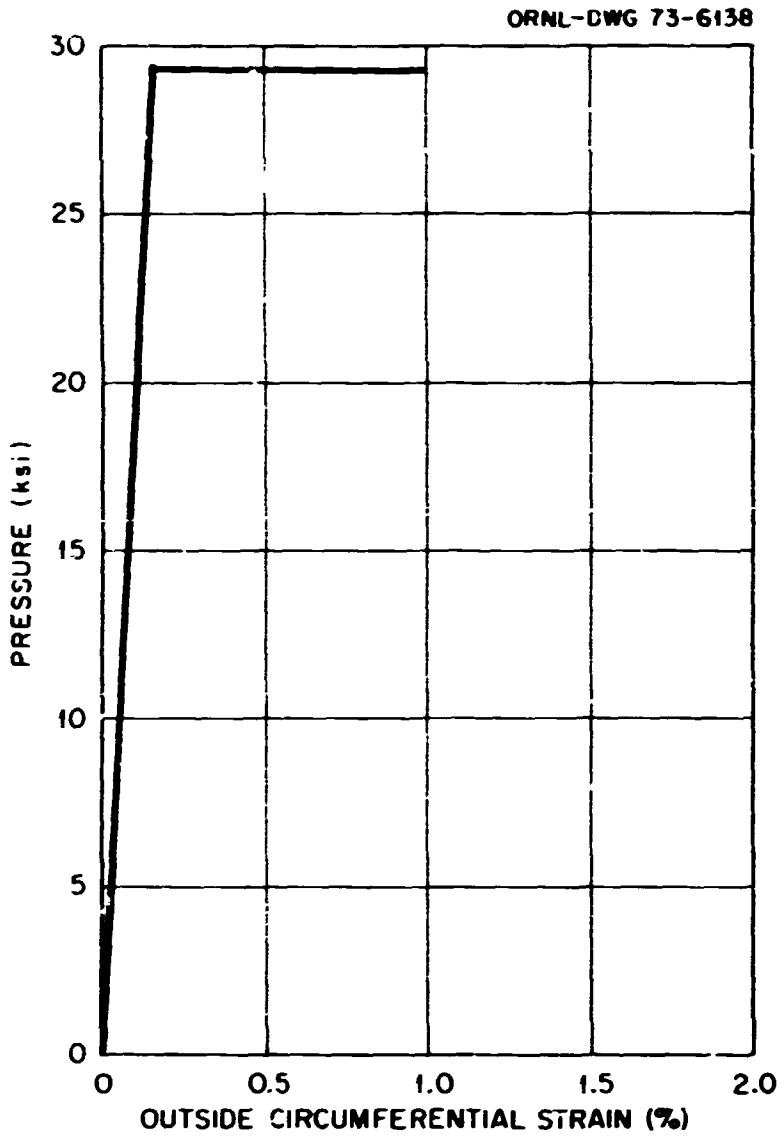

Fig. C-9. Bilinear estimate of pressure-strain curve for vessel V-2 up to 1% outside circumferential strain.

The stress concentration method (analysis performed by J. G. Merkle, ORNL). The computing procedure for this method was the same as it was for vessel V-1. From Table C-7, the input data for vessel V-2 are as follows:

σ_Y = 75 ksi,

f_u = 97 ksi,

ϵ_t = 22.2%,

CVN = 42 ft-lb,

a = 2.5 in.,

r_i = 4.53 in.

The calculated values from Eqs. (9), (8), and (10) are as follows:

α = 1.175,

S = 1.26 in.,

f_g = 49.1 ksi.

The predicted gross stress at failure in the region of the flaw, 49.1 ksi, is 66% of the yield stress, very close to that predicted by the fracture analysis diagram. In the elastic range, the pressure is related to the gross stress in the region of the flaw by the same relationship used for the fracture analysis diagram,

namely,

$$p = \frac{f_g}{1.9}. \tag{53}$$

Equation (53) gives a failure pressure of 25.8 ksi, which is less than the gross yield pressure. Thus the stress concentration method, as applied by ORNL to this case, predicts failure prior to the onset of gross yielding, at 32°F. The outside circumferential strain corresponding to the estimated failure pressure is approximately 0.13%.

The stress concentration method (analysis submitted by A. Quirk, UKAEA). Although the equation used by the UKAEA to estimate the failure pressure of vessel V-2 was rederived, it can be shown that the result is identical to Eq. (15), which was used for vessel V-1. As in the posttest calculation for vessel V-1, an adjustment was made to the total tensile elongation value supplied by ORNL. The purpose of this adjustment was to convert the reference gage length of the elongation value from that used experimentally by ORNL to a gage length equal to $4\sqrt{A}$, where A is the tensile specimen original cross-sectional area. The latter gage length was used originally by the UKAEA in developing the stress concentration method. The gage length adjustment appears to be based on the equation

$$\epsilon_{t2} = \ln\left[1 + \frac{L_{01}}{L_{02}}(e^{\epsilon_{t1}} - 1) - \left(\frac{L_{01}}{L_{02}} - 1\right)(e^{\epsilon_i} - 1)\right], \tag{54}$$

where L_{01} and L_{02} are the first and second gage lengths respectively, ϵ_{t1} and ϵ_{t2} are the first and second values of the total elongation respectively, and ϵ_i is the engineering strain at necking in a tension test. Equation (50), which can be derived in a straightforward manner, is based on the logarithmic definition of total strain. For the 0.505-in.-diam tensile specimens tested by ORNL, L_{01} is 2.25 in. and L_{02} = 1.79 in. Using ϵ_i = 0.10 and ϵ_{t1} = 0.24 (note that this value differs from the value used in ORNL's analysis), Eq. (54) gives ϵ_{t2} = 0.265, which agrees with the value used by the UKAEA for their analysis of vessel V-2.

The input data for the UKAEA estimate for vessel V-2 are as follows:

σ_Y = 72 ksi,

f_u = 96 ksi,

ϵ_t = 26.5%,

CVN = 40 ft-lb,

a = 2.625 in.,

r_1 = 4.53 in.

The calculated values from Eqs. (9), (8), and (15) are as follows:

α = 1.65,

S = 1.775 in.,

p_f = 23 ksi.

This estimate predicted failure prior to the onset of gross yielding at 32°F.

Notch sensitivity analysis (analysis performed by D. Costes, CEA). This calculation was based on ref. 18. The estimated failure pressure was 24.0 ksi.

Fracture mechanics (analysis performed by J. G. Merkle, ORNL). A first estimate of the value of K_{Ic} at 32°F for the A508, class 2 forging steel in the cylindrical region of vessel V-2 was made from the data obtained previously for vessel V-1. Scaling from the 4t CT curve in Fig. C-6, the value of J_{ult} at 32°F is

1050 in.-lb/in.^{2}. From the equation

$$K_{Ic} = \sqrt{EJ_{ult}}\,, \tag{55}$$

the calculated value of K_{Ic} is 178 ksi $\sqrt{\text{in.}}$. A second estimate was made from additional 4t CT data obtained for vessel V-2, which are shown plotted in Fig. C-10. Scaling from the curve in Fig. C-10, the estimated value of K_{Ic4} at 32°F is 190 ksi $\sqrt{\text{in.}}$. Since the two estimated values are only 7% different, their average value, 184 ksi $\sqrt{\text{in.}}$, was considered to be a good estimate of K_{Ic} at 32°F.

The flaw dimensions used in this analysis are those which define a part-circular surface crack with a fatigue-sharpened depth of 2.5 in. and a total surface length of 8.1 in. The value of the elastic shape factor for this flaw, as given by Eq. (8) of Appendix E, is 0.863. In the fracture mechanics analyses to follow, the value used was 0.9 unless otherwise stated. This value considers, at least implicitly, the effect of the plastic zone size and the back face free surface effect. Thus, referring to Eqs. (8) and (10) of Appendix E, the adjusted expressions for K_I are

$$K_I = 0.9\sigma_s\sqrt{\pi a}\,, \tag{56}$$

where σ_s is the outside circumferential stress, or

$$K_I = 1.66\,p\sqrt{\pi a}\,, \tag{57}$$

where p is the internal pressure.

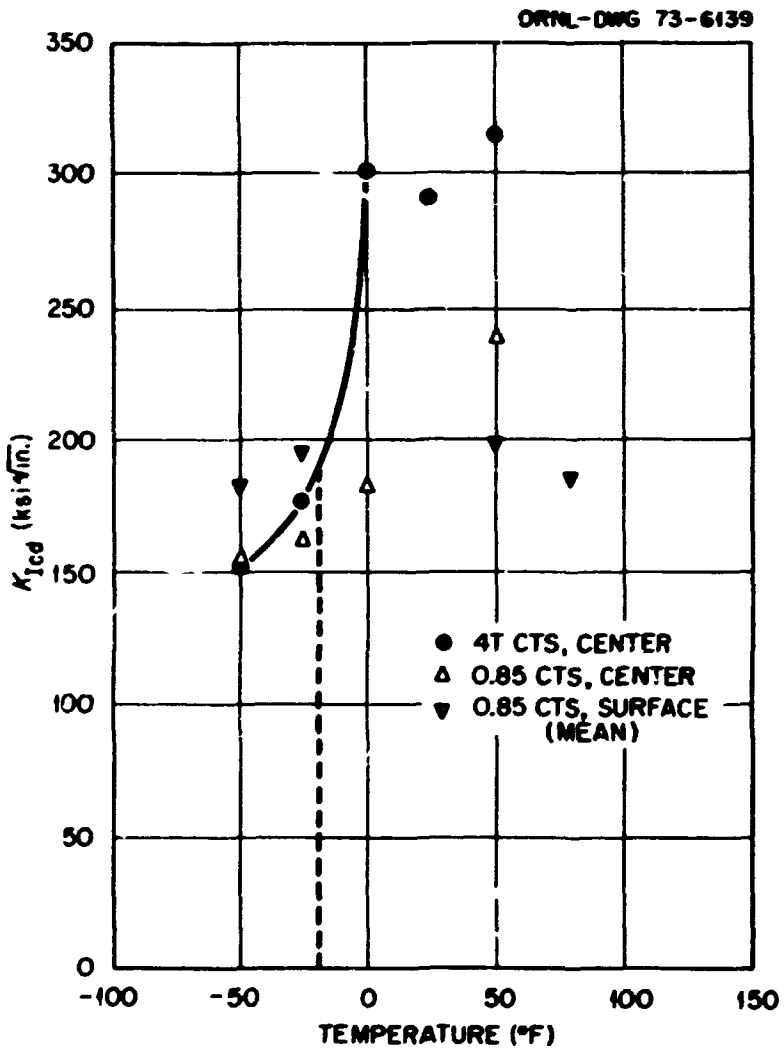

Fig. C-16. Summary of lower-bound fracture toughness data obtained from the prolongation of vessel V-2.

Before making a fracture mechanics calculation, it was considered instructive to investigate whether or not fracture was likely to occur under fully plane strain conditions. This was done by calculating the flaw size and the thickness required for fully plane strain fracture, according to the ASTM E-24 validity criterion, which is

$$a \,\&\, B \geq 2.5 \left(\frac{K_{Ic}}{\sigma_Y}\right)^2 . \tag{58}$$

Using K_{Ic} = 184 ksi $\sqrt{\text{in.}}$ and σ_Y = 75 ksi, the ratio K_{Ic}/σ_Y is 2.45, and the required value of both a and B is 15 in. Since the actual flaw size and thickness were both considerably less than this value, fully plane strain fracture was not expected. Thus a calculation based on the assumption of plane strain conditions was expected to be conservative, if properly interpreted.

Assuming plane strain conditions, a failure pressure was calculated by rearranging Eq. (57) to read

$$p_f^* = \frac{K_{Ic}}{1.66\sqrt{\pi a}}, \tag{59}$$

where p_f^* is the failure pressure calculated by linear elastic analysis. Using K_{Ic} = 184 ksi $\sqrt{\text{in.}}$ and a = 2.5 in., the calculated value of p_f^* is 39.6 ksi, well above the gross yield pressure of 29.4 ksi. Thus failure was expected to occur after the onset of gross yielding, at a pressure equal to or only slightly greater than 29.4 ksi. The strain at failure was calculated (it was assumed conservatively) from Eq. (51). Using the calculated value of p_f^*, the calculated value of strain at failure is 0.207%. This was expected to be an underestimate of the strain at failure.

The Martin-Marietta Corporation empirical equation (analysis performed by J. G. Merkle, ORNL). Recognizing that the occurrence of yielding in the region of a crack causes a reduction in constraint near the crack tip, Loechel and Lubahn[19] proposed an empirical equation for estimating strain tolerance that increases the elastically calculated value by a factor that depends on the nominal plastic strain that is expected to occur near the crack at fracture. This multiplying factor has a value of 1.0 in the elastic range and a value greater than 1.0 if plastic strain exists at fracture. For the case of failure at the gross yield load, this equation can be written in general form as[20]

$$\lambda_f = \epsilon^* \frac{1 - \epsilon_Y/\epsilon_\infty^*}{1 - \epsilon^*/\epsilon_\infty^*}, \tag{60}$$

where λ_f is the total strain at failure, ϵ^* is the elastically calculated strain at failure, ϵ_Y is the gross yield strain, and ϵ_∞^* is a characteristic strain of the material. From Eq. (51) the gross yield strain is 0.154% (this is the strain at the knee of the curve in Fig. C-9). From ref. 20, the value of ϵ_∞^* for A533, grade B, class 1 steel is 0.37%, and this value was used for vessel V-2. From the preceding linear elastic fracture mechanics calculation, the value of ϵ^* is 0.207%. Substituting all the above values into Eq. (88) gives a value of λ_f equal to 0.274%. This value was also considered to be an underestimate of the fracture strain that would occur in vessel V-2, due partly to the fact that Eq. (60) was developed from bending test data, in which the effect of the strain gradient is to maintain a higher degree of restraint in the transition region than would exist in a specimen under reverse strain gradient or tension at the same surface strain.[8]

Fracture mechanics with β_{Ic} correction (analysis performed by J. G. Merkle, ORNL). A still less conservative estimate of the strain at failure was made by estimating an increase in the effective fracture

toughness due to specimen dimensions insufficient for full restraint. Irwin's equation for making this estimate is[21]

$$\frac{K_c}{K_{Ic}} = \sqrt{1 + 1.4\beta_{Ic}{}^2}\,, \tag{61}$$

where

$$\beta_{Ic} = \frac{(K_{Ic}/\sigma_Y)^2}{B}. \tag{62}$$

Equations (61) and (62) were based mainly on data from specimens containing through-thickness cracks. However, for specimens containing part-through surface cracks, a modified definition of β_{Ic} seemed appropriate. In a through-cracked specimen, the distance from the point of greatest restraint on the crack tip to the nearest free surface, not including the crack surface, is $B/2$. In a surface-cracked specimen, the corresponding distance is a, unless the crack depth exceeds half the thickness. Thus it seemed appropriate to replace B with $2a$ in Eq. (62), so that the definition of β_{Ic} used for this analysis was

$$\beta_{Ic} = \frac{(K_{Ic}/\sigma_Y)^2}{2a}. \tag{63}$$

Since K_{Ic}/σ_Y = 2.45 and a = 2.5 in., Eq. (63) gives β_{Ic} = 1.2. Equation (61) then gives K_c/K_{Ic} = 1.74. Multiplying the elastically calculated value of fracture strain, 0.207%, by 1.74 gives a less conservative estimate of the outside circumferential strain at fracture, which is 0.36%.

Gross strain (analysis performed by J. G. Merkle, ORNL). The gross strain approach is, at present, a direct experimental approach to the problem of estimating the strain at which fracture will occur, due to a flaw of given size and shape, under specified conditions.[2] To apply this approach, it is necessary to have experimental data for the flaw size and temperature of interest. The intermediate tensile tests performed under the sponsorship of the HSST program at the Southwest Research Institute meet this requirement with respect to flaw size. However, because the vessel forging material appears to have a greater static fracture toughness at a given temperature below the upper shelf than the plate material from which the intermediate tensile test specimens were made, it is necessary to determine the test temperature of an intermediate tensile specimen at which the fracture toughness was the same as that of the vessel forging steel at 32°F. It has been found that the fracture toughness of the A 533-B plate material used for the intermediate tensile specimens can be estimated from the equation[17]

$$\frac{K_{Ic}}{\sigma_Y} = \frac{A_T}{T_\infty - T}\,, \tag{64}$$

where A_T is a material constant, T_∞ is a characteristic temperature of the material, and T is the test temperature. Using T_∞ = 125°F and A_T = 125 in.$^{1/2}$·°F, the temperature at which the value of K_{Ic}/σ_Y becomes equal to 2.45 is 74°F. An intermediate tensile specimen (No. 5) was tested at 75°F.[9] This specimen had a flaw depth at maximum load of 2.53 in. The strain across the net section was measured by two displacement gages, one on each side of the specimen, as shown in Fig. C-11. As shown in Fig. C-12,

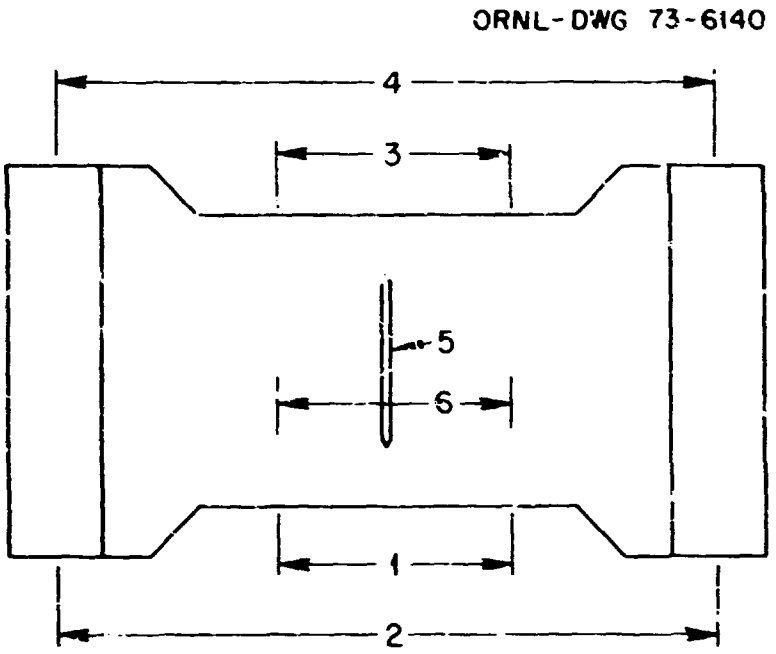

Fig. C-11. Clip gage locations and numbers for intermediate tensile specimens.

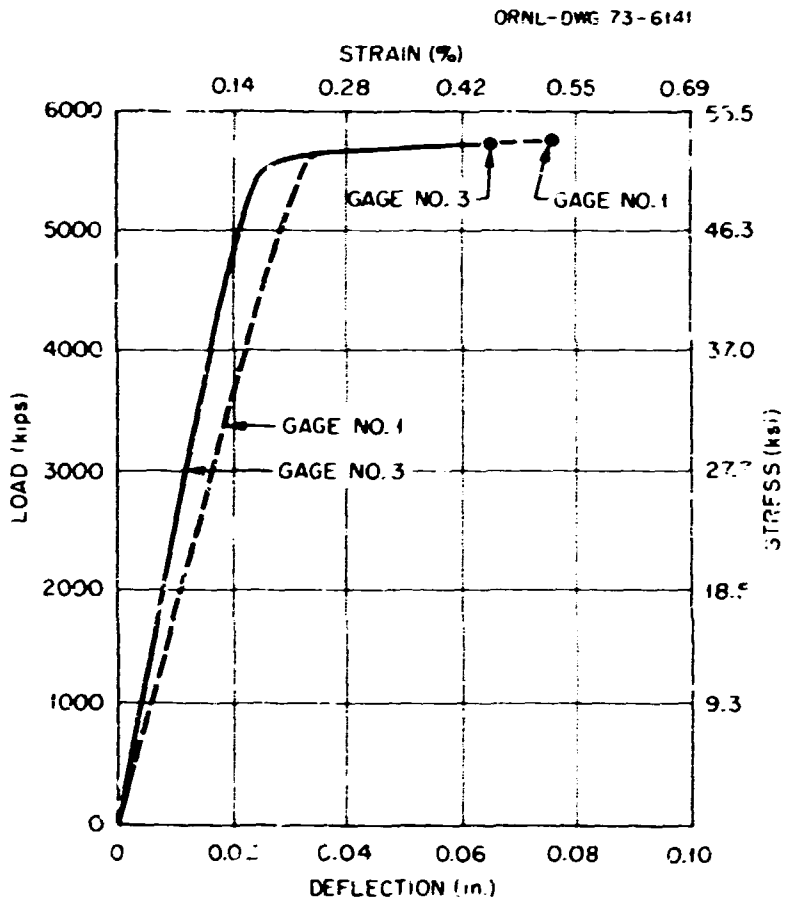

Fig. C-12. Data from clip gages 1 and 3, for intermediate tensile specimen 5, tested at 75°F.

gage 1 indicated a strain of 0.521% at maximum load, and gage 3 indicated a strain of 0.442% at maximum load. The average of these two strains is 0.48%, and this strain was considered to be a good estimate of the outside circumferential strain at failure in vessel V-2.

The tangent modulus method (analysis performed by J. G. Merkle, ORNL). The tangent modulus method is an incremental elastic-plastic method of fracture analysis that is still under development. The method is a direct extension of linear elastic fracture mechanics, and it uses a fracture criterion based on the value of K_{Ic}. The crack tip stress and strain are assumed to be related according to an equation derived by Neuber, namely,

$$K_\sigma K_\epsilon = K_f^2 \,, \tag{65}$$

where K_σ and K_ϵ are the actual stress and strain concentration factors, respectively, and K_t is the theoretical elastic stress concentration factor. The innovation in the analysis is that K_σ and K_ϵ are written in incremental form, so that

$$K_\sigma = \frac{d\sigma}{dS} \tag{66}$$

and

$$K_\epsilon = \frac{d\epsilon}{d\lambda}, \tag{67}$$

where σ and S are the notch tip and the nominal stresses respectively, and ϵ and λ are the notch tip and the nominal strains respectively. The combination of Eqs. (65), (66), and (67) leads to the following differential equation:

$$d\epsilon = K_t \sqrt{\frac{E_g}{E_n}}\, d\lambda\,. \tag{68}$$

in which E_n and E_g are the tangent moduli at the notch tip and in the gross section respectively. Equation (68) is known as the tangent modulus equation. Using the expression

$$K_t = 2C\sqrt{\frac{a}{\rho}}, \tag{69}$$

in which C is the fracture mechanics shape factor, a is crack depth, and ρ is the crack tip root radius, Eq. (68) can be rewritten to read

$$d\epsilon\sqrt{\rho} = 2C\sqrt{a}\sqrt{\frac{E_g}{E_n}}\, d\lambda\,. \tag{70}$$

Integrating Eq. (70) produces values of the quantity $\epsilon_f\sqrt{\rho}$, in which ϵ_f is the crack tip strain at fracture. The quantity $\epsilon_f\sqrt{\rho}$ is called the notch ductility factor. Its value is directly proportional to the value of K_{Ic}, and thus it can be used as a failure criterion.

Calculations based on the tangent modulus method had been made previously for the first series of longitudinal intermediate tensile specimens. It was found necessary to use an estimate of the flaw size at the onset of instability, as measured either from the specimen itself or from a photograph of the specimen, in order to calculate a fracture load close to the measured fracture load. As yet we have no way of calculating, theoretically or empirically, how much stable crack extension will occur prior to the onset of unstable fracture. Figure C-13 shows the comparison between calculation and experiment. The agreement is good in all cases. Especially noticeable is the fact that all the specimens tested at +100°F can be distinguished from each other on the basis of flaw size alone. Note in Fig. C-13 that the depth of the flaw in specimen 4 at maximum load appears to have been between 2.25 and 2.80 in., instead of the posttest estimate of 3.45 in., concerning which there is some doubt.[9] Further elaboration on the details of this method is not warranted here, but a more complete description of the method will follow if it proves to be accurate for the analysis of the intermediate vessels.

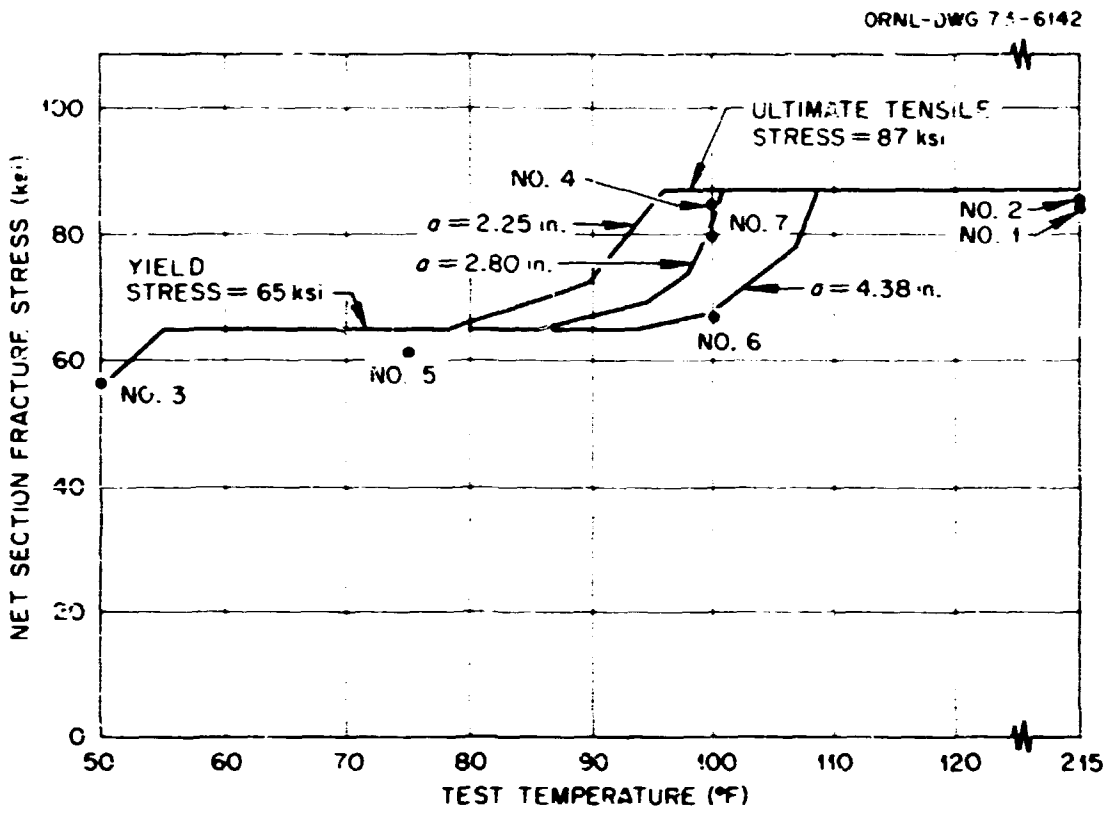

Fig. C-13. Comparison of longitudinal intermediate tensile specimen fracture stress data with fracture stress estimates made by the tangent modulus method.

A fracture strain calculation by the tangent modulus method was made for intermediate tensile specimen 5, which was considered to be an adequate gross strain model of vessel V-2, as discussed previously. The flaw depth used was 2.80 in., thus considering some stable crack growth, and the value of the elastic shape factor C was taken as 0.95. The calculated value of the net section strain at fracture is 0.521%, which, as shown in Fig. C-12, is the same as the value indicated by gage 1 on the specimen.

Linear strain interpolation (analysis performed by R. W. Derby, ORNL). This prediction was based on the assumption that for the material and flaw size given, the failure strain varies linearly with temperature over the range of strain between 0.20 and 0.92%. Assuming that the lower value of strain occurs at 4°F and the upper value occurs at 130°F, the estimated failure strain can be calculated as

$$\epsilon_{\theta f} = 0.20 + \frac{(32 - 4)}{(130 - 4)}(0.92 - 0.20) = 0.36\% .$$

The failure pressure was estimated from model test data (see, for instance, Fig. C-8) as 29.5 ksi.

The equivalent-energy method (analysis performed by F. J. Witt, ORNL). This estimate was made without recourse to a shape and restraint factor by applying a volumetric energy ratio due to a change in temperature to the value of the energy to maximum load measured in vessel V-1. A 4t compact tension specimen was tested at 32°F, the test temperature for vessel V-2, giving a value of K_{Ic4} equal to 200 ksi $\sqrt{\text{in.}}$. This value was assumed to be equal to K_{Ic6}. The volumetric energy ratio due to a decrease in temperature from 130 to 32°F was calculated from Eq. (47) to be

$$s_{130,32} = \left(\frac{K_{Ic6}\ @\ 130°F}{K_{Ic6}\ @\ 32°F}\right)^2 = \left(\frac{311}{200}\right)^2 = 2.42 .$$

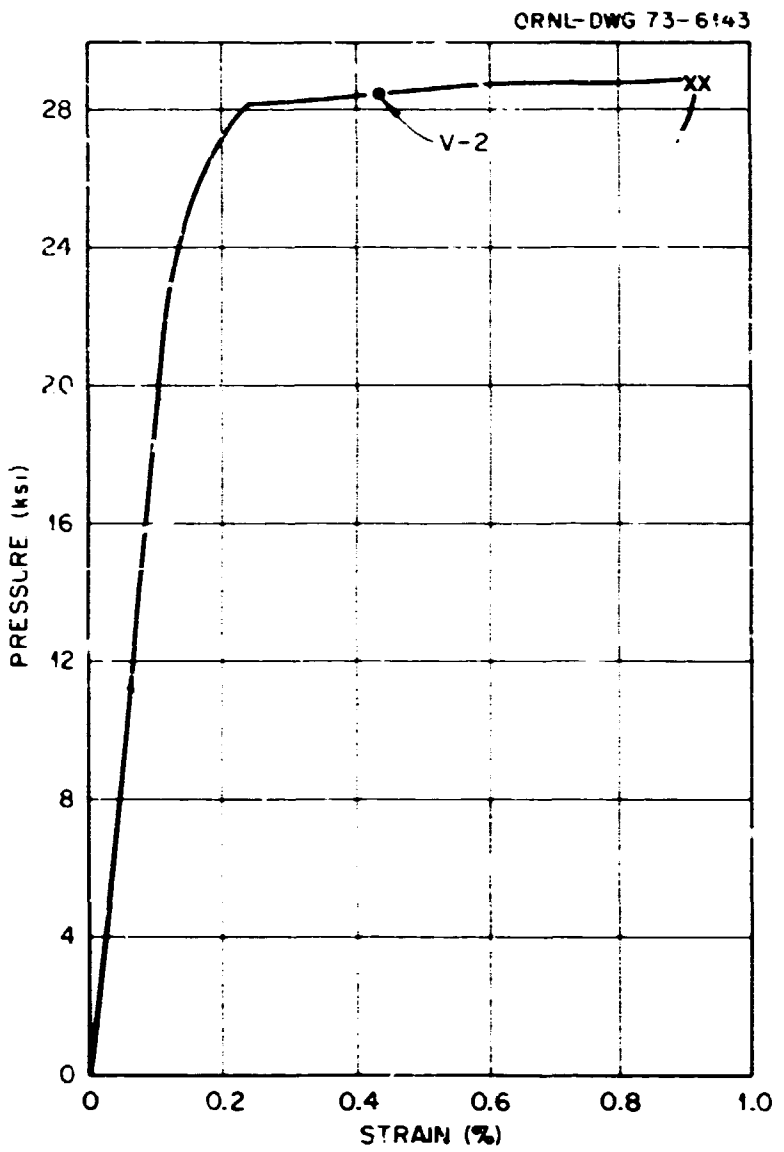

Fig. C-14. Pressure vs outside circumferential strain curve for vessel V-1, 180° from the flaw, showing the predicted failure point for vessel V-2 by the equivalent-energy method.

Assuming that the volumetric energy ratio for compact tension specimens and for pressure vessels is the same, the energy to maximum load in vessel V-2 was estimated to be

$$E_6 \text{ @ } 32°\text{F} = \frac{E_6 \text{ @ } 130°\text{F}}{r_{130,32}} = \frac{239}{2.42} = 99 \text{ in.-lb/in.}^3 .$$

The pressure and strain at failure were estimated from the pressure-strain curve for vessel V-1, shown in Fig. C-14, by finding the point on the curve up to which the area under the curve equals 99 in.-lb/in.^{3}. This point, shown in Fig. C-14, identifies a pressure of 28.5 ksi and a strain of 0.43%.

A check on this estimate of energy to maximum load was made by means of a shape and restraint factor calculated from the test data from model V2-A1-F, which was tested at 32°F (see Fig. C-15). Using Eq. (48),

$$C = \frac{194}{170\sqrt{0.345\pi}} = 1.10 .$$

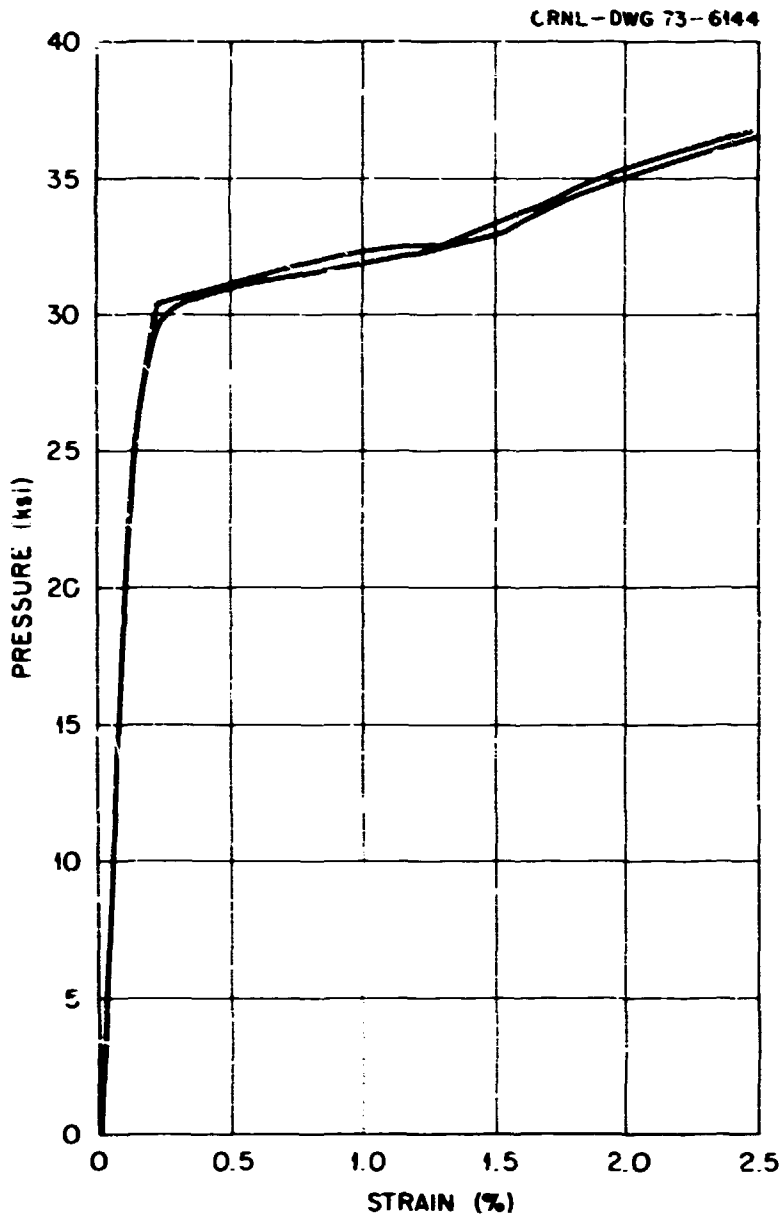

Fig. C-15. Pressure vs outside circumferential strain curves, 180° from flaw, for model vessel V2-A1-F, tested at 32°F (flaw in surface material).

For vessel V-2, the flaw depth was estimated to be 2.56 in., so that Eq. (45) gives

$$\sigma_6 = \frac{200}{1.10\sqrt{2.56\pi}} = 64.2 \text{ ksi} .$$

The energy at maximum load was calculated as follows:

$$E_6 = \frac{\sigma_6^2}{2E'} = \frac{(6.42 \times 10^4)^2}{(4 \times 10^7)} = 102 \text{ in.-lb/in.}^3 .$$

Note that the value of E' used in the latter calculation, 2×10^7 psi, does not agree exactly with the ratio $p_Y/\epsilon_{\theta Y}$ for model V2-A1-F, which was 1.80×10^7 psi.

Crack Arrest Estimate for Vessel V-2

Since the NDT temperature of the vessel forging steel is the same as that of A 533-B plate, namely, +10°F, it was considered probable that the two materials have nearly the same crack arrest toughnesses as a

function of temperature. Referring to Fig. C-7, it can be seen that the value of the crack arrest toughness, K_{Ia}, at 32°F is about 70 ksi $\sqrt{\text{in.}}$. This value is less than half the estimated value of the static fracture toughness and considerably less than the value of K_{Ia} at 130°F. Therefore, crack propagation following initiation was considered to be a certainty, and the formation of one or more fragments during propagation was even considered possible. Both predictions were correct.

Posttest Fracture Strength Calculations for Vessel V-2

Fracture mechanics (analysis performed by P. Riccardella, Westinghouse, PWR Division). This analysis is, in principle, the same as the pretest fracture mechanics analysis for vessel V-2. The two analyses differ only with respect to the particular methods used for estimating the elastic shape factor, for defining the nominal stress, and for approximating the nonlinear part of the pressure-strain curve. The flaw was analyzed as a part-through semielliptical surface flaw, and the stress was assumed to vary linearly through the wall thickness. For this case, the crack tip stress intensity factor can be estimated[11] from the equation

$$K_I = \sigma_m M_m \sqrt{\pi} \sqrt{\frac{a}{Q}} + \sigma_b M_b \sqrt{\pi} \sqrt{\frac{a}{Q}}, \tag{71}$$

where σ_m is the membrane component of the stress field, σ_b is the bending component of the stress field, Q is a parameter that accounts for both the flaw shape and the plastic zone size correction, M_m is the membrane correction factor, the value of which can be determined from Fig. C-16, and M_b is the bending correction factor, the value of which can be determined from Fig. C-17. The value of Q was calculated

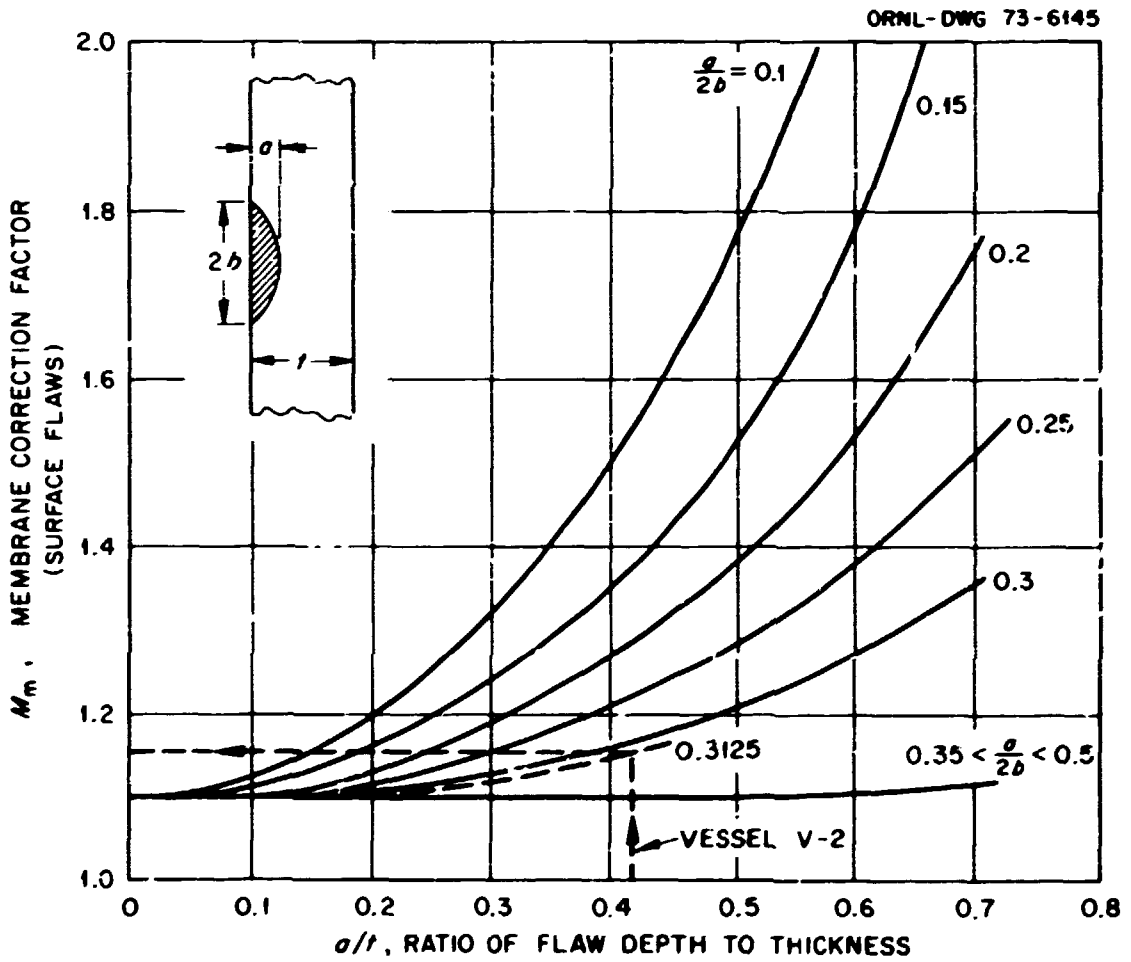

Fig. C-16. Membrane correction factor for surface flaws.

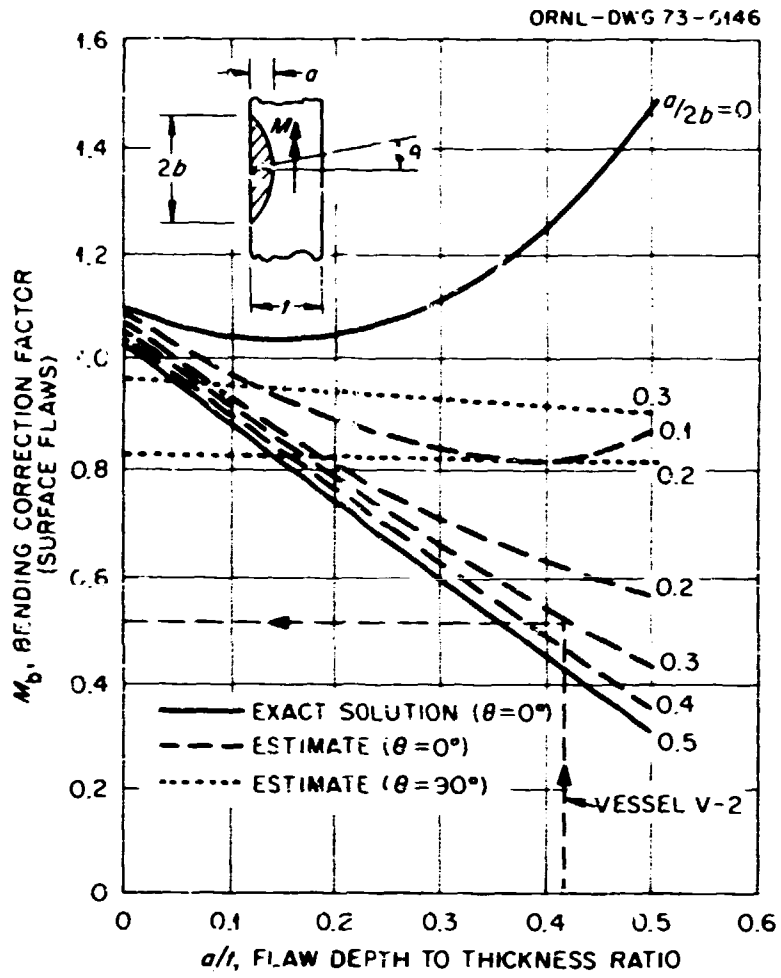

Fig. C-17. Bending correction factor for surface flaws.

from the equation

$$Q = \Phi^2 - 0.212\left(\frac{\sigma_m}{\sigma_Y}\right)^2 . \tag{72}$$

The value of Φ^2 can be calculated from the equation[11]

$$\Phi^2 = 1 + 4.593\left(\frac{a}{2b}\right)^{1.65} , \tag{73}$$

where a is the crack depth and $2b$ is the surface length of the crack. The membrane stress was calculated from

$$\sigma_m = \frac{pr_i}{t} = 2.25p , \tag{74}$$

and the bending stress at the outside surface was calculated from

$$\sigma_b = -0.5p . \tag{75}$$

The latter equation is justified by the fact that the difference between the circumferential stresses at the inside surface and at the outside surface, in the elastic range, is always numerically equal to the internal pressure.

For vessel V 2, the flaw dimensions were assumed to be a = 2.5 in. and $2b$ = 8.0 in. Thus, $a/2b$ = 0.3125 and a/t = 0.4167. Thus from Fig. C-16, M_{bt} = 1.15, and from Fig. C-17, M_b = 0.52. Substituting these values into Eq. (71) gives

$$\frac{K_I}{p} = \frac{6.52}{\sqrt{Q}}. \tag{76}$$

Equation (76) holds only in the linear range of the pressure-strain curve. However, it was assumed that up to gross yield, p could be replaced by p^* in Eq. (76), thus giving

$$\frac{K_I}{p^*} = \frac{6.52}{\sqrt{Q}}, \tag{77}$$

where, following Eq. (51),

$$p^* = 192\epsilon_{\theta o}, \tag{78}$$

and $\epsilon_{\theta o}$ is the actual outside surface circumferential strain.

The pressure for initial yielding at the inside surface was calculated from the Von Mises yield criterion, Eq. (40). For a thick-walled cylinder with closed ends under internal pressure, the initial yield pressure p_Y is given by

$$p_Y = \frac{Y^2 - 1}{Y^2}\left(\frac{\sigma_Y}{\sqrt{3}}\right), \tag{79}$$

where Y is defined by Eq. (50). Assuming a yield stress of 67 ksi and using Y = 1.444, Eq. (79) gives

$$p_Y = (0.3)(67) = 20.1 \text{ ksi}.$$

From Eq (78), the strain at initial yielding is 0.104%.

The condition for gross yielding was assumed to be

$$\sigma_Y (A - A_c) = p_{GY}\frac{r_i}{t}A \tag{80}$$

where A and A_c are the gross area and the crack area respectively. Thus,

$$p_{GY} = \left(1 - \frac{A}{A_c}\right)\frac{\sigma_Y}{r_i/t}. \tag{81}$$

The gross area was calculated from

$$A = lt = (68)(6) = 408 \text{ in.}^2, \tag{82}$$

and the crack area was calculated from

$$A_c = \frac{\pi ab}{2} = \frac{\pi(2.5)(4.0)}{2} = 15.7 \text{ in.}^2 . \tag{83}$$

Referring to Fig. 2.1, the length dimension l in Eq. (82) is seen to be the sum of the length of the cylindrical section plus the inside radius of the bottom head, taken to the nearest inch. Substituting the values from Eqs. (82) and (83) into Eq. (81) gives

$$p_{GY} = (0.427)(67) = 28.6 \text{ ksi.}$$

The strain at gross yielding was estimated, by inspection, from the uniaxial stress-strain curve shown in Fig. C-18. The strain at which the yield point elongation at the lower yield stress level begins is approximately 0.25%. This strain was estimated to be the outside circumferential strain at the onset of gross yielding in the vessel.

The foregoing equations were used to calculate the values listed in Table C-8. The term p was replaced by p^* for calculating the values of σ_m, K_I, and $\epsilon_{\theta O}$. The values listed in Table C-8 were then used to plot the two curves shown in Fig. C-19. The lower curve in Fig. C-19 is a curve of K_I vs $\epsilon_{\theta O}$; the upper curve is a plot of real pressure p vs $\epsilon_{\theta O}$. The upper curve was constructed by plotting the two points for initial yielding and gross yielding, as estimated previously, and then drawing a straight line down to the origin

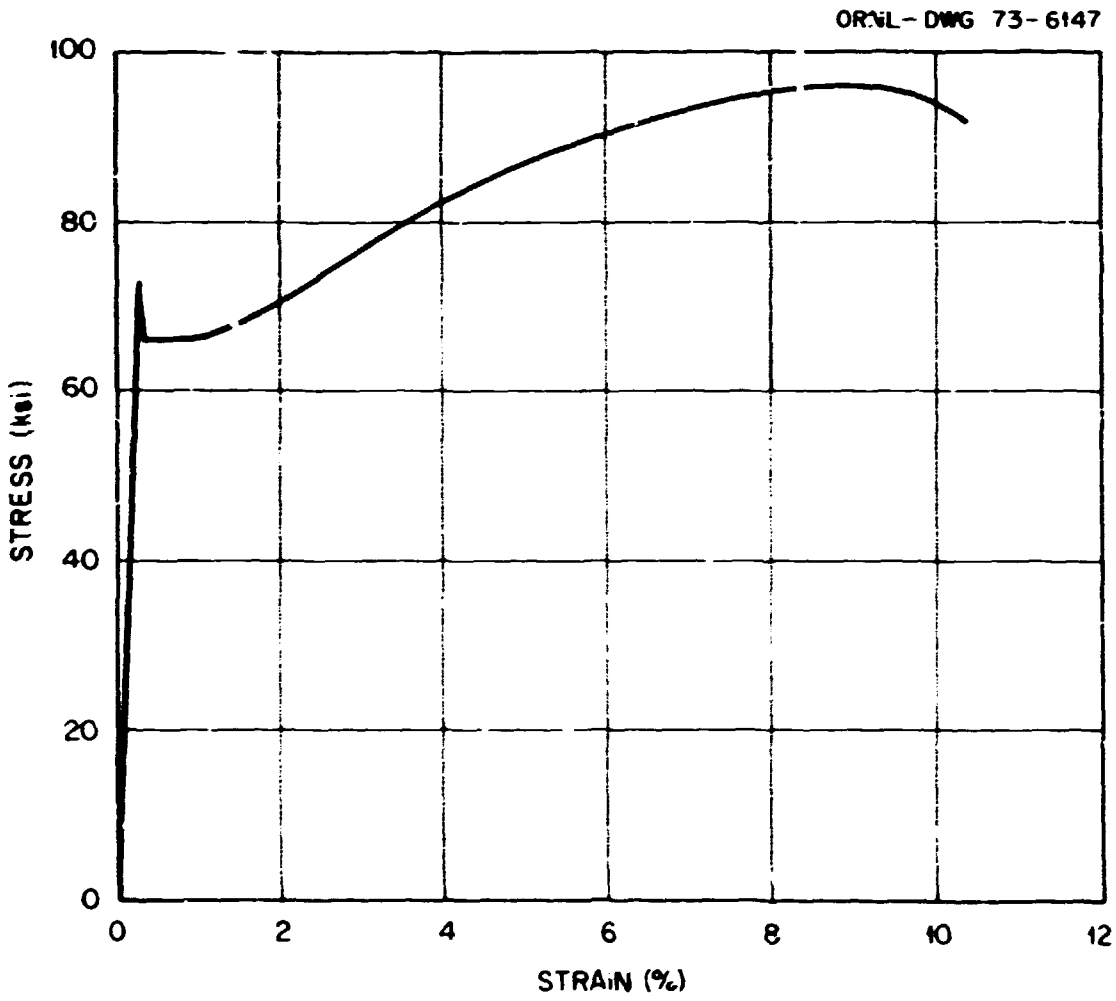

Fig. C-18. Tensile stress vs strain curve for vessel V-1 material.

Table C-8. Quantities calculated for vessel V-2 by the Westinghouse fracture mechanics analysis

p^* (ksi)	σ_m (ksi), Eq. (74)	Q, Eq. (72)	K_I (ksi $\sqrt{\text{in.}}$), Eq. (77)	$\epsilon_{\theta o}$ (%), Eq. (78)
10	22.5	1.7	50.1	0.052
20	45.0	1.6	103	0.104
30	67.5	1.5	160	0.156
40	90.0	1.5	213	0.208

from the initial yield point, a horizontal line to the right from the gross yield point, and a curved line by eye between the initial and the gross yield points.

Fracture toughness data from compact tension specimens of the actual pressure vessel material indicated that at the vessel test temperature (32°F), K_{Ic} ranged from 160 to 200 ksi $\sqrt{\text{in.}}$. Using the lower curve in Fig. C-19, this fracture toughness range was used to estimate a failure strain range. The failure strain range was then transferred to the upper curve in Fig. C-19 to estimate the range of real pressure at failure. The predicted ranges of pressure and strain at failure are listed in Table C-9.

Equivalent-energy method (analysis performed by F. J. Witt, ORNL). As discussed in Chaps. 5 and 8, the potential of a yield point effect was investigated in the model vessel tests. Essentially it was not recognized prior to the test that the model vessels would exhibit behavior similar to that of gross strain

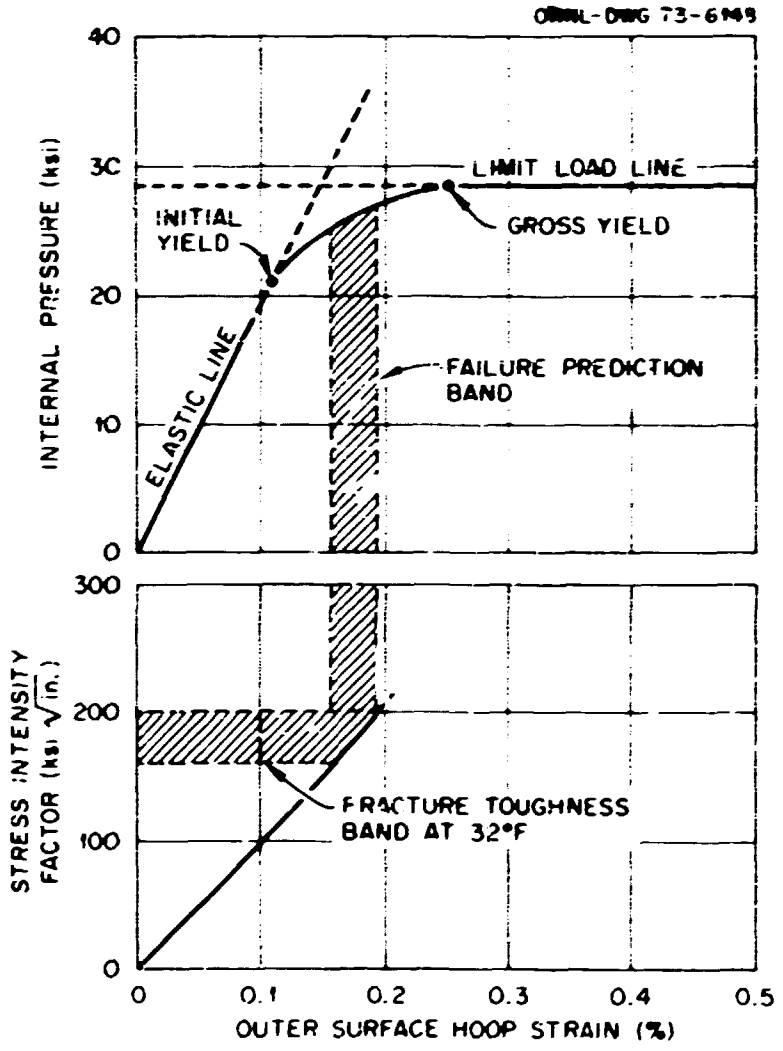

Fig. C-19. Predicted failure conditions for vessel V-2 by linear elastic fracture mechanics, modified for small nominal plastic strains.

Table C-9. Failure predictions by Westinghouse, vessel V-2

	Lower bound	Upper bound
Failure pressure, psi	25,000	27,000
Outer surface hoop strain at failure, %	0.16	0.19

specimens. In fact, only two such failures in pressure vessels had been obtained prior to the test of vessel V-2. Subsequently a model vessel was tested with special care to obtain as much strain as possible at the gross yield pressure. The results are shown in Fig. C-20. It may therefore be logically argued that, within the scatter band of toughness data, vessel V-2 did indeed exhibit the behavior calculated by the equivalent-energy method. More specifically, it is very doubtful that the vessel at failure would follow the decrease in toughness below 32°F. Most likely it would fail at the same pressure at perhaps as much as 50° below the test pressure. (See Appendix H for additional discussion.)

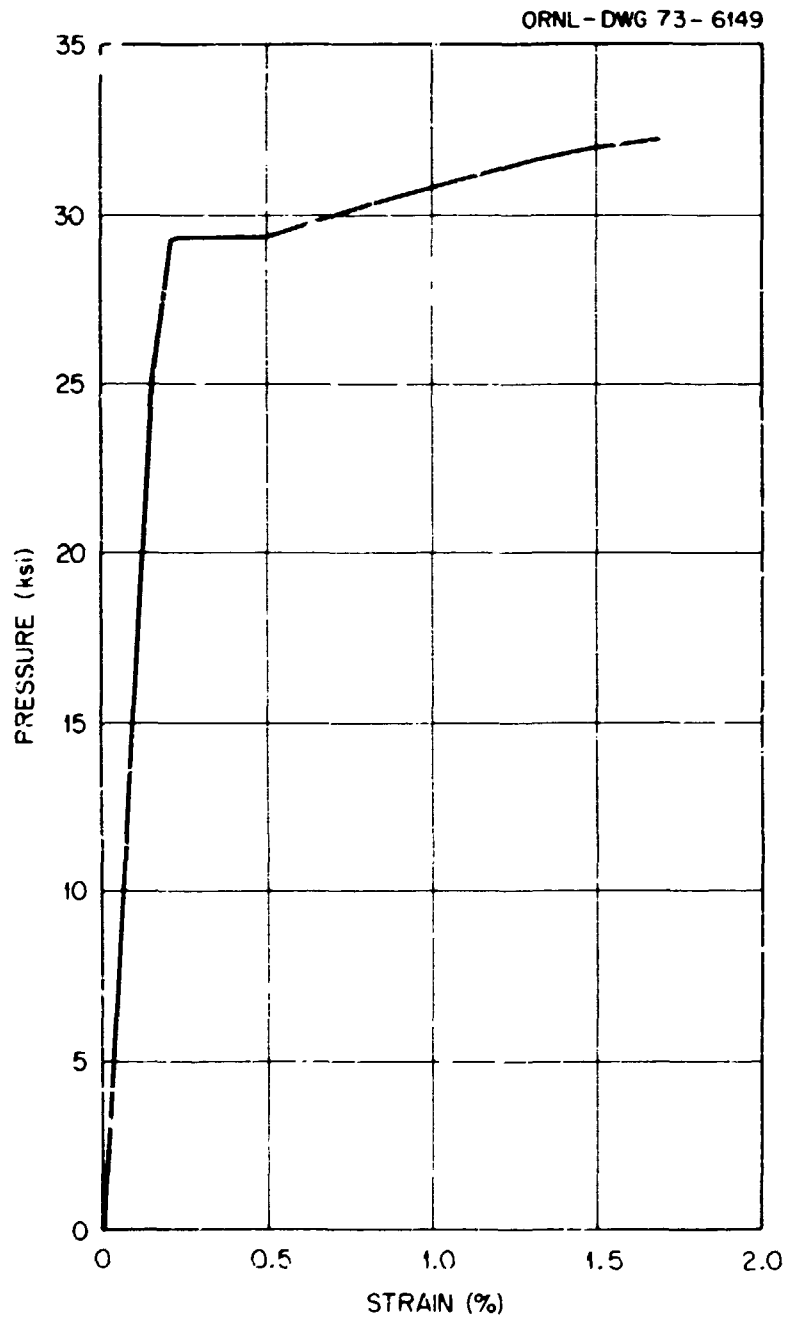

Fig. C-20. Pressure–circumferential-strain curve 180° from flaw for model vessel tested with emphasis on discerning the yield plateau (model vessel V2-A1-E).

The Martin-Marietta Corporation empirical equation (analysis performed by J. G. Merkle, ORNL). The sole reason why this prediction is different from that of the first fracture mechanics analysis was that the assumed gross yield strain of 0.154% was less than the elastically calculated fracture strain of 0.21%. However, an analytical elastic-plastic analysis of the vessel wall performed since the test indicates that the actual outside circumferential strain at the gross yield pressure is 0.22%. Therefore, the Martin-Marietta Corporation empirical equation should also have agreed with the linear elastic fracture mechanics analysis.

The tangent modulus method (analysis performed by J. G. Merkle, ORNL). The flaw in vessel V-2 was subject to nearly a plane strain condition, due to the effect of axial stress in the vessel wall, and the fracture strain estimates based on a ratio K_c/K_{Ic} greater than unity were unconservative. Therefore the β_{Ic} correction, which was used to estimate the ratio K_c/K_{Ic} in both the second fracture mechanics calculation and the tangent modulus analysis, was suspected of not properly considering the effects of biaxiality for a surface flaw. Note, however, that the tangent modulus analysis, using the β_{Ic} correction, did agree with the intermediate tensile test data for specimen 5. Apparently, by this analysis, tensile specimens do not adequately model pressure vessels because of a difference in the transverse restraint conditions. Noting this difference, then the gross strain estimate for vessel V-2 was eliminated. Removing the β_{Ic} correction from the tangent modulus analysis produces a fracture strain estimate of 0.19%, with no adjustment for differences in yield stress between the plate and the forging material. Removing the β_{Ic} correction from the second fracture mechanics analysis also makes it the same as the first fracture mechanics analysis.

References

1. W. S. Pellini, *Evolution of Engineering Principles for Fracture-Safe Design of Steel Structures,* NRL-6957, U.S. Naval Research Laboratory, Washington, D.C. (Sept. 23, 1969).
2. P. N. Randall and J. G. Merkle, "Gross Strain Crack Tolerance of Steels," *Nucl. Eng. Des.* **17**(1), 46–63 (1971).
3. R. J. Eiber, W. A. Maxey, and T. J. Atterbury, "Experimental Study of Fracture Behavior in Reactor Coolant Piping," pp. 232–249 in *The Technology of Pressure-Retaining Steel Components,* AIMME, 1970.
4. C. J. Costantino, M. A. Salmon, and N. A. Weil, "Effect of End Conditions on the Burst Strength of Finite Cylinders," *J. Appl. Mech.*, March 1964, pp. 97–104.
5. W. H. Irvine and A. Quirk, *A Stress Concentration Approach to Fracture Mechanics,* AHSB (S)R. 190, UKAEA, Risley, United Kingdom (November 1970).
6. W. H. Irvine and A. Quirk, *The Application of the Stress Concentration Theory of Fracture Mechanics to the Assessment of the Fast Fracture Characteristics of Thick-Walled Nuclear Reactor Pressure Vessels,* SRD R3, UKAEA Safety and Reliability Directorate, UKAEA, Risley (August 1971).
7. W. H. Irvine, "A Comparative Analysis of Fracture Data for Ten Rotor Steels," report presented at the May 15–16, 1972, meeting of the CREST Experts Group on Material and Mechanical Problems Related to the Safety Aspects of Steel Components in Nuclear Plants, May 1972.
8. P. N. Randall, *Effects of Strain Gradients on the Gross Strain Crack Tolerance of A 533-B Steel,* HSSTP-TR-19, TRW Systems Group, Redondo Beach, Calif. (June 15, 1972).
9. S. C. Grigory, *Tests of 6-in.-Thick Flawed Tensile Specimens, First Technical Summary Report; Longitudinal Specimens Numbers 1 through 7,* HSSTP-TR-18, Southwest Research Institute, San Antonio, Tex. (June 1972).
10. J. R. Rice, P. C. Paris, and J. G. Merkle, "Some Further Results of *J*-Integral Analyses and Estimates," presented at the Sixth National Symposium on Fracture Mechanics, Philadelphia, Pa., Aug. 28–30, 1972.

11. J. G. Merkle, *A Review of Some of the Existing Stress Intensity Factor Solutions for Part-Through Surface Cracks*, ORNL-TM-3983 (January 1973).

12. F. J. Witt, *The Equivalent-Energy Method for Calculating Elastic-Plastic Fracture* (to be published).

13. F. J. Witt and T. R. Mager, "Fracture Toughness K_{Icd} Values at Temperatures up to 550°F for ASTM A 533 Grade B, Class 1 Steel," *Nucl. Eng. Des.* **17**, 91–102 (1971).

14. F. J. Witt and T. R. Mager, *A Procedure for Determining Bounding Values on Fracture Toughness K_{Ic} at Any Temperature*, ORNL-TM-3894 (October 1972).

15. *1969 Book of ASTM Standards*, Part 31, American Society for Testing and Materials, pp. 1099–1114, May 1969.

16. E. J. Ripling and P. B. Crosley, "Crack Arrest Studies," paper 10, HSST Program Information Meeting, Oak Ridge National Laboratory, Oak Ridge, Tenn., Apr. 25–26, 1972.

17. J. G. Merkle, "Fracture Safety Analysis Concepts for Nuclear Pressure Vessels, Considering the Effects of Irradiation," *J. Basic Eng.* **93**(2), 265–273 (1971).

18. D. Costes and A. Dore, "Rupture des Recipients de Pression Fissures," paper G6/5, *Proceedings of the First International Conference on Structural Mechanics in Reactor Technology*, vol. 4, Part G, pp. 440–467, 1972.

19. L. W. Loechel, *The Effect of Testing Variables on the Transition Temperature in Steel*, MCR-69-189 (also HSSTP-TR-2), Martin Marietta Corp. (Nov. 20, 1969).

20. J. G. Merkle, L. F. Kooistra, and R. W. Derby, *Interpretations of the Drop Weight Test in Terms of Strain Tolerance (Gross Strain) and Fracture Mechanics*, ORNL-TM-3247 (June 1971).

21. G. R. Irwin et al., *Basic Aspects of Crack Growth and Fracture*, NRL-6598, U.S. Naval Research Laboratory, Washington, D.C. (Nov. 21, 1967).

Appendix D

PRESSURE-STRAIN DATA FROM THE MODEL VESSEL TESTS

Table 5-1. Pressure-strain data from model vessel V1-A1-A
(vessel V-1 prolongation)

See Fig. 5.4 for gage locations
Test temperature: 130°F
Flaw size: length, 1.4 in., depth, 0.32 in.
Flaw location: center material

Pressure (psi)	Pressure drop[a] (psi)	Strain (μin.)[b] at gage No.								
		1	2	11	12A	12B	13A	13B	13C	15
0		3	0	-3	3	1	3	0	3	0
3,000		190	50	130	150	180	150	170	150	170
6,000		370	90	260	290	310	290	300	280	300
9,000		630	140	430	470	510	480	500	480	500
12,000		840	180	570	630	660	630	650	630	650
15,000		1,060	220	710	790	810	790	810	790	810
18,000		1,300	270	860	950	970	950	980	950	980
21,000		1,620	320	990	1,110	1,140	1,120	1,140	1,110	1,130
23,000		2,250	440	1,090	1,260	1,240	1,280	1,290	1,250	1,270
25,000		4,640	500	1,210	1,480	1,480	1,510	1,540	1,470	1,490
26,000		8,700	570	1,280	1,610	1,580	1,680	1,720	1,640	1,670
27,000	250	16,000	920	1,350	1,770	1,610	1,950	2,170	2,140	1,960
27,500	250	19,740	1,250	1,410	1,840	1,770	2,260	2,780	2,760	2,320
28,000	300	22,900	1,630	1,560	1,840	1,840	2,840	3,990	4,290	3,740
28,400	450	26,250	2,140	2,180	2,160	1,880	6,240	7,580	8,310	7,050
28,500	400	27,410	2,550	3,810	2,780	1,960	8,140	9,410	9,840	8,600
29,000	500	31,140	3,220	6,920	5,310	2,830	10,830	11,960	11,800	10,830
29,750	550	37,660	4,120	9,070	8,210	6,610	13,650	13,640	14,450	13,430
30,750	550	50,250	5,520	11,850	12,070	11,670	17,590	18,620	18,270	17,200
31,400	500	67,350	6,910	13,770	14,860	14,780	20,220	21,710	21,240	20,130
31,750	550	121,170	8,040	14,820	16,510	16,540	22,430	23,620	23,080	21,940
32,200	700	117,510	9,850	15,430	18,060	18,180	24,150	25,400	24,800	23,640
31,750	850	114,150	11,970	14,550	18,340	18,460	24,690	25,970	25,320	24,160
31,500								26,100		

[a]If plastic deformation occurs after a pressure is achieved, the pressure reduces by the amount listed; such information was not always recorded.

[b]To convert microinches strain to percent strain, move decimal point four places to left.

BLANK PAGE

Table D-2. Pressure-strain data from model vessel V-1 A1-B
(vessel V-1 prolongation)

See Fig. 5.4 for gage locations
Test temperature: 0°F
Flaw size: length, 1.4 in.; depth, 0.32 in.
Flaw location: near surface material

Pressure (psi)	Strain (μin.)[a] at gage No. -								
	1	2	11	12A	12B	13A	13B	13C	15
0	2	3	7	5	-2	0	0	7	6
15,000	917	218	652	756	745	753	755	758	756
22,000	1,400	326	945	1,120	1,114	1,122	1,118	1,120	1,124
0	57	-2	-35	-4	-15	-13	-9	-12	-14
15,000							751		
22,000	1,406	327	939	1,114	1,104	1,116	1,120	1,128	1,126
27,000	2,610	601	1,204	1,570	1,558	1,532	1,526	1,560	1,516
28,000	3,750	668	1,276	1,728	1,708	1,666	1,648	1,714	1,640
29,000	5,500	632	1,326	1,984	1,916	1,810	1,778	1,872	1,770
29,500	12,900	1160	1,120	5,390	9,590	1,810	1,850	1,880	1,820
31,500	20,500	2430	2,210	13,800	11,300	6,090	3,850	4,890	3,580
33,000	27,500	3450	6,490	18,800	12,800	11,600	9,630	10,900	8,670
35,000	70,000	7440	11,100	28,800	26,200	19,100	18,100	17,100	16,400
34,500			5,240				18,600		

[a]To convert microinches strain to percent strain, move decimal point four places to left.

Table D-3. Pressure-strain data from model vessel V1-A1-C (vessel V-1 prolongation)

See Fig. 5.4 for gage locations
Test temperature: 130°F
Flaw size: length, 1.4 in.; depth, 0.32 in.
Flaw location: near surface material

Pressure (psi)	Pressure drop[a] (psi)	Strain (μin.)[b] at gage No. –								
		1	2	11	12A	12B	13A	13B	13C	15
0		10	−3	−3	−6	5	−6	−7	−2	−1
1,500		109	25	72	86	85	81	82	85	90
3,000		220	47	140	160	160	168	164	168	171
4,500		316	62	201	235	234	237	234	240	248
6,000		431	88	270	315	317	323	320	325	333
7,500		533	107	337	397	394	400	399	403	410
9,000		646	128	406	474	474	484	482	485	490
0		26	−8	−19	−13	−8	−12	−6	−5	−2
1,500		126	14	46	66	68	68	64	75	75
3,000		239	39	125	156	156	156	152	161	162
4,500		333	58	190	230	227	235	230	234	241
6,000		436	84	258	306	309	316	315	316	322
7,500		541	101	332	388	389	398	396	396	400
9,000		646	126	406	472	473	485	478	485	489
10,000		715	137	450	523	526	536	531	537	541
11,000		785	148	490	572	573	585	580	585	592
12,000		849	160	530	618	623	634	633	634	638
13,000		924	178	580	687	680	688	684	689	693
14,000		993	188	618	731	725	739	733	740	743
15,000		1,070	206	662	788	787	792	788	792	801
0		39	−22	−47	−36	−17	−30	−29	−22	−21
3,000		250	21	99	132	139	141	141	143	148
6,000		446	63	230	276	292	292	290	295	305
9,000		659	108	376	452	457	462	460	463	470
12,000		873	153	521	620	620	633	627	631	635
15,000		993	196	650	770	770	783	780	782	785
16,000		1,140	209	697	825	820	834	833	833	838
17,000		1,206	221	736	875	869	867	882	887	890
18,000		1,292	238	781	930	930	945	938	947	950
19,000		1,364	247	818	973	976	995	988	994	994
20,000		1,452	266	860	1,040	1,032	1,050	1,048	1,048	1,050
21,000		1,564	285	900	1,096	1,096	1,106	1,104	1,108	1,108
22,000		1,720	314	957	1,174	1,176	1,174	1,174	1,190	1,190
23,000		1,936	352	1,014	1,248	1,256	1,242	1,254	1,268	1,262
24,000		2,360	442	1,150	1,410	1,410	1,330	1,350	1,390	1,308
25,000		3,290	623	1,150	1,590	1,585	1,470	1,510	1,570	1,510
26,000	200	5,330	586	1,240	1,730	1,780	1,610	1,630	1,660	1,610
27,000	200	9,460	736	1,270	2,450	2,410	1,750	1,750	1,800	1,750
28,000	400	18,200	1,520	1,120	6,000	5,170	1,830	1,830	1,840	1,810
29,000	500	26,600	3,370	2,480	12,700	12,800	3,640	2,700	1,960	2,610
29,600	500	29,700	4,190	4,630	14,800	14,700	5,840	4,960	3,620	4,590
30,200	600	33,700	4,780	5,940	16,700	16,700	7,710	7,050	5,860	6,430
30,500	500	37,800	5,330	6,980	18,200	18,300	9,530	9,040	7,940	8,180
30,800	500	43,500	6,020	7,950	19,900	20,100	11,400	11,010	9,900	10,000
31,300	500	53,000	7,060	9,050	22,300	22,400	13,300	12,700	11,800	11,700
31,750	450	76,600	9,130	10,360	25,300	25,500	15,700	15,300	14,400	14,000
32,200	700	99,600	13,000	10,100	27,300	27,600	17,100	16,600	15,800	15,300
32,000										

[a] If plastic deformation occurs after a pressure is achieved, the pressure reduces by the amount listed; such information was not always recorded.

[b] To convert microinches strain to percent strain, move decimal point four places to left.

Table D-4. Pressure-strain data from model vessel V1-A1-D (vessel V-1 prolongation)

See Fig. 5.4 for gage locations
Test temperature: 130° F
Flaw size: length, 1.4 in.; depth, 0.33 in.
Flaw location: center material

Pressure (psi)	Pressure drop[a] (psi)	Strain (μin.)[b] at gage No. –								
		1	2	11	12A	12B	13A	13B	13C	15
0		−3	5	6	3	6	6	5	5	4
3,000		198	63	157	167	178	175	175	173	177
6,000		392	106	298	329	335	333	333	328	334
9,000		613	155	454	499	509	508	507	503	511
12,000		799	196	583	642	660	662	662	654	664
15,000		984	242	721	800	813	814	816	807	819
0		38	9	−10	−5	12	7	4	2	8
5,000		359	88	241	266	278	277	275	276	280
10,000		682	170	486	549	546	553	554	546	554
15,000		991	242	723	788	828	813	815	804	817
21,000		1,472	332	993	1,128	1,146	1,138	1,141	1,130	1,152
22,500		1,746	367	1,060	1,226	1,250	1,232	1,284	1,232	1.248
27,500		17,400	1,076	1,560	1,780	1,808	2,540	3,300	2,580	3.430
28,000	250	20,000	1,480	1,770	1,900	1,930	4,280	5,700	4,540	6,170
28,250		21,000	1,770	2,830	1,970	1,890	5,810	8,760	7,320	8,510
28,600	350	23,200	2,230	5,590	2,410	1,980	9,330	10,700	10,300	10,300
29,250	450	27,800	2,970	8,400	4,490	3,190	13,000	13,700	13,200	12,700
29,900		33,300	3,760	11,100	7,600	7,680	15,500	16,400	15,800	15,200
31,000	400	47,400	5,490	14,400	13,000	13,200	20,200	21,000	20,300	19,700
31,700	300	65,900	7,320	15,800	15,300	17,100	23,100	24,400	23,300	22,800
32,000	500	99,500	10,700	16,100	17,000	19,100	25,100	26,600	25,400	24.900
32,300								26,600		

[a]If plastic deformation occurs after a pressure is achieved, the pressure reduces by the amount listed; such information was not always recorded.
[b]To convert microinches strain to percent strain, move decimal point four places to left.

Table D-5. Pressure-strain data from model vessel V1-A1-E (vessel V-1 prolongation)

See Fig. 5.4 for gage locations
Test temperature: −35° F
Flaw size: length, 1.4 in.; depth, 0.31 in.
Flaw location: near surface material

Pressure (psi)	Strain (μin.)[a] at gage No. –								
	1	2	11	12A	12B	13A	13B	13C	15
0	0	0	0	0	0	0	0	0	0
5,000	290	50	220	250	240	250	260	260	230
10,000	590	130	460	490	490	500	510	520	490
15,000	900	200	690	750	750	750	770	780	740
18,000	1,100	250	330	910	910	920	930	930	900
21,000	1,300	300	970	1080	1060	1080	1100	1100	1060
23,000	1,480	330	1060	1190	1180	1190	1210	1210	1170
25,000	1,840	410	1170	1340	1330	1330	1360	1260	1310
26,000	2,150	500	1250	1450	1450	1430	1460	1460	1420
27,500	3,220	600	1350	1640	1660	1580	1620	1610	1560
29,500	8,790	710	1490	2250	2380	1840	1880	1830	1810
30,000	12,100	840	1500	3240	2870	1920	1950	1860	1880
30,500	16,840	1290	1480	5750	4030	1930	1930	1810	1900
31,000	20,500	2080	2200	9950	9060	1870	1820		

[a]To convert microinches strain to percent strain, move decimal point four places to left.

Table D-6. Pressure-strain data from model vessel V1-A1-F (vessel V-1 prolongation)

See Fig. 5.4 for gage locations
Test temperature: 130°F
Flaw size: length, 1.4 in.; depth, 0.32 in.
Flaw location: near surface material

Pressure (psi)	Pressure drop[a] (psi)	Strain (μin.)[b] at gage No. –								
		1	2	11	12A	12B	13A	13B	13C	15
0		0	0	0	0	0	0	0	0	0
3,000		200	60	160	150	170	170	170	150	150
6,000		380	100	290	300	320	320	330	330	310
9,000		590	150	440	460	490	490	500	500	480
12,000		800	200	600	630	650	650	660	660	640
15,000		990	240	720	770	800	800	810	800	790
18,000		1,200	290	860	930	960	960	970	970	950
21,000		1,470	340	1,020	1,100	1,140	1,150	1,150	1,140	1,130
23,000		1,800	390	1,130	1,250	1,290	1,300	1,300	1,290	1,270
25,000	100	2,790	640	1,250	1,480	1,530	1,510	1,510	1,490	1,480
26,000	100	4,640	610	1,330	1,690	1,720	1,640	1,650	1,650	1,630
27,000	200	7,600	740	1,410	2,000	2,000	1,770	1,790	1,800	1,760
27,500	200	10,300	860	1,420	2,570	2,430	1,840	1,830	1,870	1,820
28,000	400	13,840	1,040	1,390	3,520	3,200	1,860	1,830	1,900	1,800
28,500	500	18,410	1,520	1,320	6,340	6,850	2,000	2,150	2,420	1,910
28,500	400	19,330	1,720	1,490	8,320	8,510	2,160	2,440	2,840	2,150
29,500	500	24,670	2,840	5,030	13,480	13,400	5,880	5,710	6,890	5,030
30,000	550	27,020	3,320	6,960	15,050	15,040	8,020	7,680	8,690	6,750
31,000	550	34,990	7,560	10,100	18,990	18,980	11,850	11,500	12,250	10,280
31,800	490	55,470	7,230	13,620	24,820	24,800	16,740	16,430	17,020	14,990
32,500	1100	111,700	12,500	13,920	28,440	28,360	19,300	19,000	19,550	17,450
32,000								19,000		

[a]If plastic deformation occurs after a pressure is achieved, the pressure reduces by the amount listed; such information was not always recorded.

[b]To convert microinches strain to percent strain, move decimal point four places to left.

Table D-7. Pressure-strain data from model vessel V2-A1-A (vessel V-2 prolongation)

See Fig. 5.10 for gage locations
Test temperature: 32°F
Flaw size: length, 1.15 in.; depth, 0.35 in.
Flaw location: center material

Pressure (psi)	Strain (μin.)[a] at gage No. –						
	1	2	3	4	5	6	7
0	30	30	40	40	40	40	30
10,000	670	540	580	580	580	590	580
20,000	1,300	1,010	1,090	1,090	1,090	1,100	1,090
25,000	1,920	1,250	1,390	1,380	1,400	1,420	1,410
27,000	3,030	1,400	1,560	1,580	1,600	1,610	1,610
29,000	11,210	1,650	1,810	1,960	2,210	2,530	1,910
31,000	20,060	3,380	1,940	4,090	6,190	7,750	2,250
31,500	22,420	7,790	1,940	9,340	10,520	11,240	5,510
32,500	27,400	10,870	2,440	12,870	13,820	14,330	9,260
32,500	32,990	13,260	6,220	15,640	16,620	17,180	11,920
33,000	39,070	15,350	10,950	18,120	19,140	19,830	14,360
34,000	43,970	16,670	13,170	19,750	20,830	21,620	16,020
34,500	51,360	18,370	15,720	21,910	23,070	24,040	18,170
35,000	59,490	19,550	17,500	23,560	24,770	25,830	19,730
35,000	Out	20,900	19,850	25,850	27,180	28,450	21,990
35,500					27,940		

[a]To convert microinches strain to percent strain, move decimal point four places to left.

Table D-8. Pressure-strain data from model vessel V2-A1-B
(vessel V-2 prolongation)

See Fig. 5.10 for gage locations
Test temperature: 130°F
Flaw size: length, 1.14 *in.*; depth, 0.36 *in.*
Flaw location: near surface material

Pressure (psi)	Pressure drop[a] (psi)	Strain (μin.)[b] at gage No. –																		
		1	2	3	4	5	6	7	8	9	10	11[c]	12	13	14	15	16	17	18	19
0		30	20	20	20	20	20	30	20	20	Out	30	30	30	20	20	20	20	20	10
5,000		320	270	290	290	290	290	290	300	290		370	290	240	290	270	220	280	270	210
10,000		610	510	550	560	550	550	550	570	550		710	550	450	550	530	420	540	520	400
15,000		880	750	810	820	820	820	810	850	810		1,070	820	650	810	780	620	810	760	590
20,000		1,170	1,000	1,090	1,100	1,100	1090	1,090	1,140	1,100		1,470	1,100	880	1,100	1,070	840	1,100	1,050	810
23,000		1,380	1,160	1,270	1,290	1,290	1280	1,260	1,340	1,250		1,790	1,260	990	1,270	1,210	940	1,260	1,200	920
25,250		1,610	1,310	1,480	1,500	1,500	Out	1,440	1,580	1,410		2,290	1,410	1100	1,460	1,360	1040	1,450	1,340	1020
26,200		1,770	1,410	1,620	1,620	1,640		1,590	1,750	1,510		2,630	1,510	1140	1,570	1,460	1090	1,570	1,430	1070
27,700		2,350	1,570	2,760	1,880	1,930		2,550	2,350	1,720		4,710	1,720	1230	1,810	1,650	1200	1,800	1,620	1150
28,100		3,370	1,590	4,710	2,010	2,160		4,110	3,440	1,890		7,250	1,930	1280	2,000	1,810	1270	1,940	1,760	1210
29,200		6,440	1,520	8,680	3,400	3,710		8,020	6,860	2,980		14,810	3,330	1530	3,830	2,900	1660	3,470	2,580	1600
29,500		9,870	1,620	10,790	6,480	6,660		10,090	9,520	3,990		19,250	4,190	1790	5,500	3,830	1870	4,720	3,320	1790
30,200		11,480	2,190	12,250	8,100	8,380		11,610	11,330	5,090		22,840	4,930	2110	6,880	4,600	2090	6,020	4,030	2000
31,000		12,980	4,180	14,240	9,980	10,400		13,610	12,920	6,230		26,590	5,620	2590	8,540	5,520	2360	7,640	4,950	2340
31,600		15,600	8,320	17,600	13,020	13,610		16,920	15,800	8,040		33,480	6,710	3300	11,220	7,140	2940	10,290	6,570	3030
32,400	400	18,150	10,120	19,840	14,970	15,650		19,120	18,340	9,600		Out	7,810	3780	12,970	8,360	3390	11,980	7,720	3490
33,000	700	20,590	11,460	21,720	16,570	17,320		21,010	20,860	11,180			9,020	4250	14,450	9,330	3800	13,410	8,750	3900
33,200	500	22,090	12,140	22,710	17,410	18,180		21,910	22,120	11,990			9,640	4480	15,140	9,830	4020	14,070	9,240	4100
33,500	600	24,050	12,870	23,930	18,410	19,220		23,130	24,040	13,190			10,570	4820	16,060	10,490	4310	14,950	9,900	4360
33,900		26,280	13,530	25,170	19,410	20,250		24,320	26,140	14,450			11,560	5160	16,950	11,130	4600	15,810	10,530	4620
34,200	900	31,170	14,680	27,570	21,290	22,170		26,660	30,770	17,070			13,560	5880	18,630	12,520	5140	17,410	11,700	5110
34,100	700	35,010	15,120	28,860	22,270	23,180		27,880	34,430	18,930			15,090	6400	19,490	12,960	5440	18,230	12,310	5350
34,700						23,940														

[a]If plastic deformation occurs after a pressure is achieved, the pressure reduces by the amount listed; such information was not always recorded.
[b]To convert microinches strain to percent strain, move decimal point four places to left.
[c]Possible loose gage.

Table D-9. Pressure-strain data from model vessel V2-A1-D (vessel V-2 prolongation)

See Fig. 5.10 for gage locations
Test temperature: −55°F
Flaw size: length, 1.15 in.; depth, 0.36 in.
Flaw location: near surface material

Pressure (psi)	Strain (μin.)[a] at gage No. –						
	1	2	3	4	5	6	7
0	0	20	0	20	0	0	0
5,000	350	250	260	260	230	240	250
10,000	730	490	520	520	490	500	500
15,000	1,060	710	750	760	740	720	720
20,400	1,550	960	1,030	1,040	950	960	960
24,000	1,870	1130	1,280	1,230	1,210	1,130	1,160
26,000	2,250	1250	1,460	1,390	1,370	1,320	1,310
28,000	2,880	1380	1,630	1,560	1,550	1,500	1,490
28,500				1,650	1,630	1,580	
29,000				1,690	1,670	1,620	
29,300	4,010	1510	1,870	1,760	1,730	1,690	1,690
30,000				1,870	1,830	1,780	
30,200				1,960	1,910	1,860	
31,000	6,240	1650	2,530	2,110	2,040	2,000	2,380
31,500				2,240	2,220	2,150	
32,000				2,490	2,530	2,500	
32,500				3,020	3,090	3,490	
32,000	13,720	1600	6,430	3,350	3,780	4,300	6,550
32,500				3,700	4,300	4,980	
32,500	17,350	1630	8,570	5,510	6,350	6,590	9,060
33,000	19,450	1690	9,860	7,090	7,810	7,960	9,950
33,400	23,350	2510	11,880	9,260	9,810	9,560	11,610
33,300	26,220	4220	13,640	10,960	11,430	11,100	13,260
34,300	20,900	6580	15,250	12,430	12,880	12,470	14,770
33,600	Out	7090	15,540	12,660	13,100	12,670	14,410
34,500		8520	16,690	13,740	14,190	13,730	14,960
34,700					14,340		

[a]To convert microinches strain to percent strain, move decimal point four places to left.

Table D-10. Pressure-strain data from model vessel V2-A1-F (vessel V-2 prolongation)

See Fig. 5.10 for gage locations
Test temperature: 32°F
Flaw size: length, 1.14 in.; depth, 0.36 in.
Flaw location: near surface material

Pressure (psi)	Strain (μin.)[a] at gage No. –						
	1	2	3	4	5	6	7
0	20	20	0	0	10	10	0
12,500	970	630	670	680	680	670	670
25,000	2,150	1,230	1,390	1,360	1,390	1,340	1,360
27,500	2,840	1,410	1,670	1,610	1,640	1,650	1,620
29,000	4,810	1,580	2,020	1,870	1,890	1,960	2,460
30,500	10,810	1,580	5,160	2,190	2,270	3,330	7,820
31,000	15,170	1,620	8,350	4,560	4,440	6,050	10,460
32,000	20,880	2,370	10,770	7,370	7,290	8,620	12,120
32,000	27,870	5,150	13,160	9,700	9,690	10,830	14,250
33,000	32,720	7,760	14,900	11,360	11,350	12,470	15,920
33,000	Out	9,940	17,080	13,470	13,470	14,590	18,100
33,500		11,530	19,080	15,360	15,350	16,410	20,080
34,000		12,150	19,950	16,170	16,170	17,360	20,960
34,500		12,880	20,960	17,110	17,100	18,340	21,980
35,000		13,630	22,130	18,170	18,160	19,450	23,130
35,500		14,700	24,560	19,720	19,710	21,090	24,910
35,500		15,730	Out	21,380	21,350	22,810	26,820
36,000		16,370		22,500	22,490	24,030	28,200
36,000		16,770		23,430	23,410	25,020	29,330
36,500					24,860		

[a] To convert microinches strain to percent strain, move decimal point four places to left.

Appendix E

CALCULATION OF TEMPERATURES FOR DEMONSTRATING THE NONFAILURE OF THE HSST PROGRAM INTERMEDIATE TEST VESSELS

In March 1972, the HSST Program Review Committee suggested that the testing plan for each intermediate test vessel should include a demonstration of nonfailure, under the maximum pressure permitted by the new fracture control provisions of Section III of the ASME Pressure Vessel Code,[1] at temperatures to be selected. Conditions in the vessel tests are not actually as severe as those assumed in the new Code provisions, because the vessel tests are static initiation tests instead of crack arrest tests. Thus, two temperatures were calculated. The first is a temperature based on an underestimate of the static initiation fracture toughness of the vessel forging steel, and the second is a temperature based on the ASME Code lower-bound reference toughness curve, which is a lower bound to the existing crack arrest toughness data for A 533-B steel.[2] The fact that the drop-weight NDT temperatures of the vessel forging steel and of A 533-B plate are the same indicates that the crack arrest properties of the two materials are probably similar.

The procedure for making these calculations was to first determine the Code-allowable pressure for the vessel without a flaw and then to determine the lowest temperature at which this pressure could be applied if the reference flaw was of the size intended for the tests of vessels V-1 and V-2.

Stress Analysis of the Cylindrical Region

In the cylindrical region of vessels V-1 and V-2, halfway between the ends, the state of stress under internal pressure in the elastic range is virtually the same as for an infinitely long thick-walled hollow cylinder with closed ends. This fact has been verified by comparing the analytical thick-walled hollow cylinder solution with a finite-element analysis of the vessel.[3] Thus the equation for the circumferential

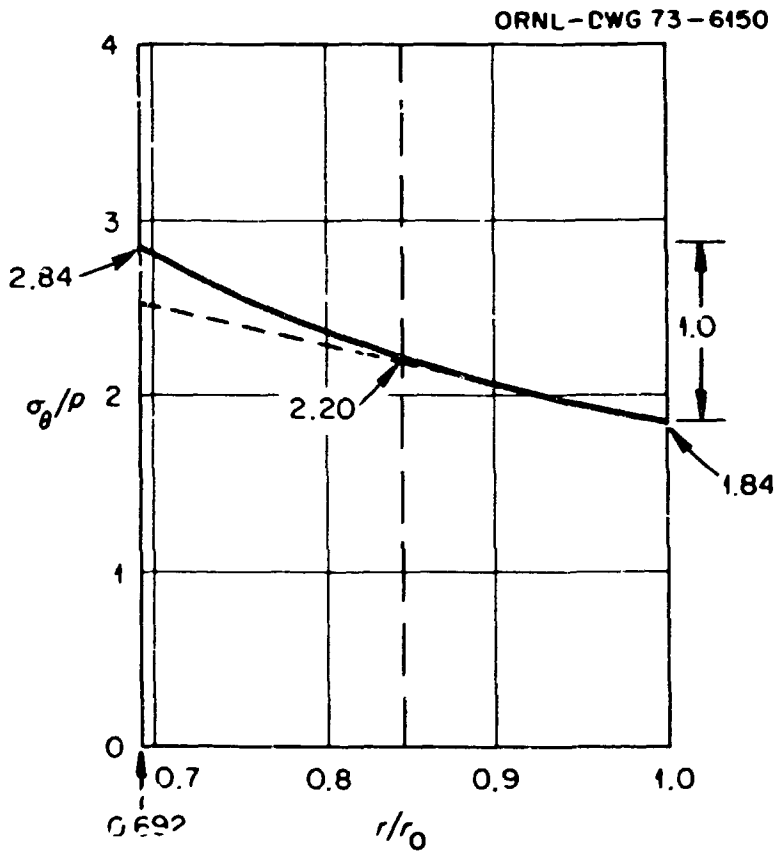

Fig. E-1. Circumferential stress distribution in the cylindrical region of vessels V-1 and V-2.

stress is

$$\sigma_\theta = p\frac{(r_O/r)^2 + 1}{(r_O/r_i)^2 - 1}, \tag{1}$$

where r_i, r_O, and r are the inside, outside, and general radii, respectively, and p is the internal pressure. Equation (1) is shown plotted in Fig. E-1, which also shows a linear estimate of the elastic stress distribution in the outer half of the vessel wall for use in estimating the elastic stress intensity factor. The outside diameter of the vessel is 39 in., and the wall thickness is 6 in.

Code-Allowable Pressure

The Code-allowable pressure for a cylindrical vessel is determined by the general primary membrane stress intensity, which is defined by[4]

$$S = \frac{pR}{t} + \frac{p}{2}, \tag{2}$$

where

$$R = r_i \tag{3}$$

and

$$t = r_O - r_i\,. \tag{4}$$

Thus, setting $S = S_m$, the allowable primary membrane stress intensity gives

$$p_{all} = \frac{S_m}{1/(Y-1) + 1/2}, \tag{5}$$

where

$$Y = \frac{r_O}{r_i}. \tag{6}$$

For the intermediate vessels, S_m = 26,700 psi[5] and $Y = 1^4/_9$; so that p_{all} = 9710 psi. Note that for the 3-in.-diam model vessels tested earlier,[6,7] $Y = 1^3/_7$ and p_{all} = 9430 psi.

Elastic Stress Intensity Factor

Vessels V-1 and V-2 each contained a part-through surface flaw, projecting inward from the outside surface, normal to the circumferential direction, in the test area of the vessel, as defined in Fig. 2.1. Each flaw was machined as a part-circular notch having a depth of 2 in., a surface length of 8 in., and a radius of curvature of 5 in., as shown in Fig. E-2. After fatigue sharpening by cyclically pressurizing the notch

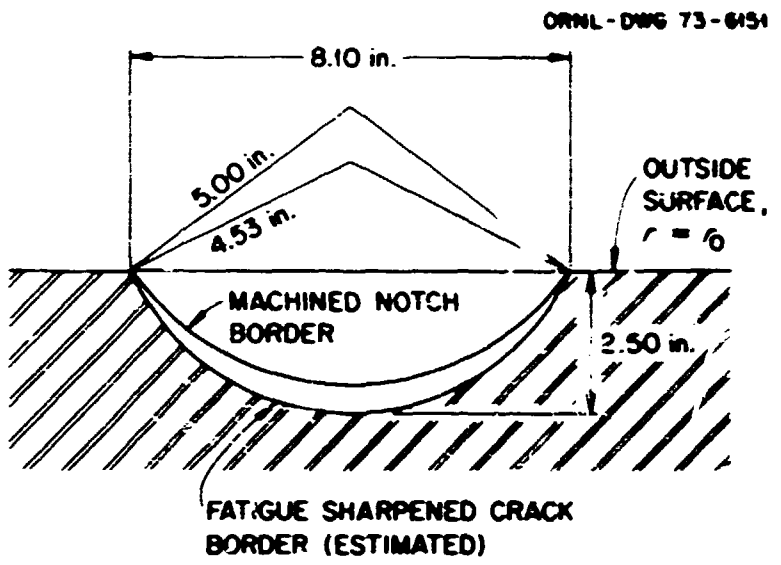

Fig. E-2. Flaw geometry used for stress intensity factor analysis of vessels V-1 and V-2.

Table E-1. Values used for calculating the value of K_I for vessels V-1 and V-2

Quantity	Value	Source
$\psi_0(\theta)$	0.904	Refs. 11 and 12
$\psi_1(\theta)$	0.760	Refs. 11 and 12
σ_0/σ_s	1.194	Fig. E-1
$(r_1 - a)/c$	0.677	
r_1/c	1.51	

cavity,[8-10] it was estimated that the flaw depth would be 2.5 in., the surface length would be 8.10 in., and the radius of curvature would be 4.53 in., also as shown in Fig. E-2.

Numerical solutions for the stress intensity factor for a part-circular surface crack in a plate have been obtained by Smith and Alavi.[11] For a linearly varying stress field, the value of K_I is given by[12]

$$K_I = \frac{2}{\pi}\sqrt{\frac{r_1}{a}}\sqrt{\pi a}\,\sigma_s\left\{\left[1-\left(\frac{\sigma_0}{\sigma_s}-1\right)\frac{r_1-a}{c}\right]\psi_0(\theta)+\left(\frac{\sigma_0}{\sigma_s}-1\right)\frac{r_1}{c}\,\psi_1(\theta)\right\}. \tag{7}$$

where r_1 is the radius of curvature of the crack front, a is the crack depth, c is half the plate thickness, and σ_s and σ_0 are the front surface and the midthickness stresses respectively. The functions $\psi_0(\theta)$ and $\psi_1(\theta)$ determine the variation of K_I around the perimeter of the flaw. For the flaw geometry shown in Fig. E-2, the maximum value of K_I occurs at the deepest point of the flaw. Table E-1 lists the values of the nondimensional terms in Eq. (7) for vessels V-1 and V-2. Using the values given in Table E-1, Eq. (7) reduces to

$$K_I = 0.863\sigma_s\sqrt{\pi a}\,. \tag{8}$$

From Fig. E-1,

$$\sigma_s = 1.84p, \tag{9}$$

so that

$$K_I = 1.59p\sqrt{\pi a}. \tag{10}$$

For $p = 2710$ psi and $a = 2.5$ in., $K_I = 43.2$ ksi $\sqrt{\text{in.}}$

Fracture Toughness

These calculations were made prior to the test of vessel V-1 using the static fracture toughness data obtained from precracked Charpy specimens of vessel V-1 material, shown plotted in Fig. 4.13. These data may be used directly; however, it was assumed that the static fracture toughness as a function of temperature could be represented by the equation[13]

$$\frac{K_{Ic}}{\sigma_Y} = \frac{A_T}{T_{-} \quad T} \tag{11}$$

Equation (11) can be rearranged to give

$$T = T_{-} \quad A_T \frac{\sigma_Y}{K_{Ic}}. \tag{12}$$

From data on A 533-B steel, it was assumed that $A_T = 135°F\sqrt{\text{in.}}$. From the vessel V-1 precracked Charpy data shown plotted in Fig. 4.13, it was assumed that $T_{-} = +50°F$, and from Fig. 4.4 it was conservatively assumed that $\sigma_Y = 65$ ksi. Equation (12) thus becomes

$$T = 50 \quad 135\frac{65}{K_{Ic}} \tag{13}$$

The lower-bound crack arrest fracture toughness was estimated from Fig. E-3, which was taken from refs. 1 and 2. The NDT temperature for the A 508-2 forging steel in the midthickness region is $+10°F$ (see Table 4.3). The equation for the fracture toughness curve in Fig. E-3 is

$$K_{IR} = 26.8 + 1.22\exp\{0.0145[(T \quad RT_{NDT}) + 160]\}. \tag{14}$$

Equation (14) can be rearranged to give

$$T \quad RT_{NDT} = 69\ln\left(\frac{K_{IR}}{1.22} \quad 22.0\right) \quad 160 \tag{15}$$

The minimum temperatures for full pressurization, as governed by static initiation and crack arrest conditions, were determined from Eqs. (13) and (15), respectively, for specified values of K_{Ic}.

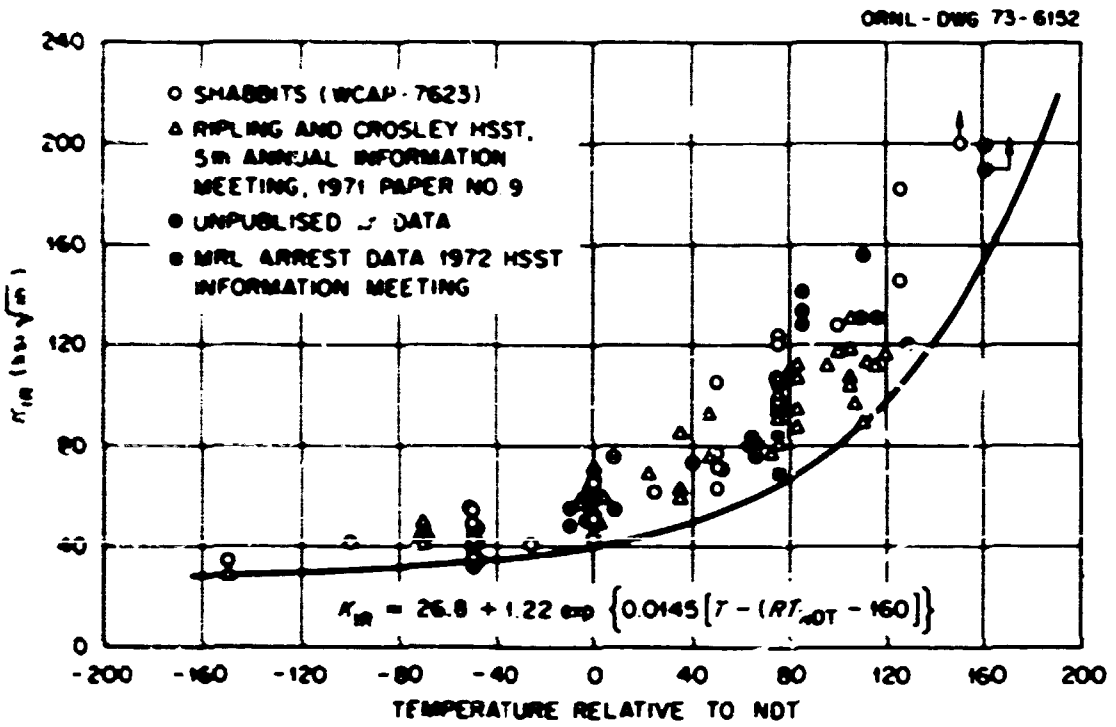

Fig. E-3. PVRC-ASME reference fracture toughness curve, based on dynamic crack initiation and crack arrest fracture toughness data for A533, grade B, class 1 steel.

Minimum Temperatures for Full Pressurization

At design pressure, 9710 psi, the value of K_I is 43.2 ksi $\sqrt{\text{in.}}$. Using a safety factor[1] of 2.0, the value of K_{Ic} must be equal to or greater than 86.4 ksi $\sqrt{\text{in.}}$. Using Eq. (13) or Fig. 4.13 directly for static initiation conditions gives a value for T of about −50°F. Using Eq. (15) or the K_{Ia} curve in Fig. E-3 directly for crack arrest conditions and $RT_{NDT} = +10$°F gives a value for T of about 120°F.

For hydrotesting,[1] the pressure is 1.25 times design pressure, but the safety factor is 1.5. Thus the minimum value of K_{Ic} is 1⅞ times 43.2 ksi $\sqrt{\text{in.}}$ = 81.0 ksi $\sqrt{\text{in.}}$, which is not much different from the previously determined value for operating conditions.

References

1. Section III, ASME Boiler and Pressure Vessel Code, Summer 1972 Addenda.
2. W. D. Doty et al., *Recommendations of PVRC – Toughness Requirements for Ferritic Materials*, Welding Research Council Bulletin No. 175, August 1972.
3. *HSST Intermediate Vessel Closure Analysis*, Report No. E-1253(b) (also HSSTP-TM-3), Teledyne Materials Research Company, Waltham, Mass. (Mar. 25, 1970).
4. Section III, ASME Boiler and Pressure Vessel Code, 1971, paragraph A-2221, p. 548.
5. Ibid., Table 1-1.1, p. 392.
6. R. W. Derby, "Preliminary Results of Steel Model Tests," paper 25, 5th Annual Information Meeting, Heavy-Section Steel Technology Program, Oak Ridge National Laboratory, Oak Ridge, Tenn., Mar. 25–26, 1971.
7. R. W. Derby, "Fracture Studies of Model Pressure Vessels Made from Nuclear Grade Steel," First International Conference on Structural Mechanics in Reactor Technology, Berlin, Sept. 20–24, 1971.
8. J. G. Merkle, "An Analytical Basis for Notch Sharpening by Fatigue," paper 19, 5th Annual Information Meeting, Heavy-Section Steel Technology Program, Oak Ridge National Laboratory, Oak Ridge, Tenn., Mar. 25–26, 1971.
9. A. A. Abbatiello and R. W. Derby, *Notch Sharpening in a Large Tensile Specimen by Local Fatigue*, ORNL-TM-3925 (November 1972).

10. R. W. Derby et al., panel discussion, "First Intermediate Pressure Vessel Test," paper 19, HSST Program Information Meeting, Oak Ridge National Laboratory, Oak Ridge, Tenn., Apr. 25–26, 1972.

11. F. W. Smith and M. J. Alavi, "Stress-Intensity Factors for a Part-Circular Surface Flaw," pp. 793–800 in part II, *Proceedings of the First International Conference on Pressure Vessel Technology, Delft, Netherlands*, ASME, 1969.

12. J. G. Merkle, *A Review of Some of the Existing Stress Intensity Factor Solutions for Part-Through Surface Cracks*, ORNL-TM-3983 (January 1973).

13. J. G. Merkle, "Fracture Safety Analysis Concepts for Nuclear Pressure Vessels, Considering the Effects of Irradiation," *J. Basic Eng.* 93(2), 265–73 (1973).

Appendix F

NOMENCLATURE FOR APPENDIXES C AND E

A	Cross-sectional area, in.^{2}
A_c	Crack area, in.^{2}
A_T	Material parameter, °F $\sqrt{\text{in.}}$
a	Crack depth, in.
a_d	Crack depth in a specimen of size d, in.
B	Thickness, in.
B_d	Thickness of a specimen of size d, in.
b	Half the surface length of a part-through surface flaw, in.
b	Ligament width, in.
C	Fracture mechanics shape factor, dimensionless
CVN	Charpy V-notch impact energy, ft-lb
c	Half the thickness of a plate, in.
c_o	Empirical coefficient, in.$^{-1}$
d	Size, usually thickness, in.
E	Modulus of elasticity, ksi
E'	Initial slope of a pressure vs strain curve, ksi
E_d	A defined energy per unit volume, up to maximum load, in a specimen of size d, psi
E_g	Tangent modulus away from the notch tip, ksi
E_n	Tangent modulus at the notch tip, ksi
f_g	Gross stress, ksi
f_u	Ultimate tensile strength, ksi
$f(a/W)$	Fracture mechanics shape factor for the compact tension specimen, dimensionless
H	Strain-hardening coefficient for linear strain hardening, dimensionless
J	J integral, in.-lb /in.^{2}
J_{el}	Elastic portion of the J integral, in.-lb /in.^{2}
J_{ult}	Value of the J integral at fracture, in.-lb /in.^{2}
K_I	Elastic crack tip stress intensity factor, ksi $\sqrt{\text{in.}}$
K_{Ia}	Value of K_I at crack arrest, ksi $\sqrt{\text{in.}}$
K_{Ic}	Critical value of K_I for fracture initiation under static plane strain conditions, ksi $\sqrt{\text{in.}}$
K_{Icd}	Estimate of K_{Ic} made by the equivalent-energy method for a specimen of size d, ksi $\sqrt{\text{in.}}$
K_{IR}	Reference value of the fracture toughness, ksi $\sqrt{\text{in.}}$
K_t	Theoretical elastic stress concentration factor, dimensionless
K_ϵ	Actual strain concentration factor, dimensionless
K_σ	Actual stress concentration factor, dimensionless
k	Initial slope of a load per unit thickness vs deflection curve, lb/in.^{2}
L_{o1}, L_{o2}	First and second gage lengths for a tensile specimen, in.

l	Length of a rectangular area subject to load, in.
M	Distance from the center of curvature of an external part-circular surface crack to the axis of a pressure vessel, in.
M_b	Elastic K_I magnification factor for bending stress, dimensionless
M_m	Elastic K_I magnification factor for membrane stress, dimensionless
N	Geometry parameter defined by Eq. (17) of Appendix C, dimensionless
n	Empirical exponent, dimensionless
P	Load per unit thickness, lb/in.
P_a^*	Pseudoelastic load on a compact tension specimen of size d at fracture, kips
P_e	Intercept of the strain-hardening branch of a bilinear load per unit thickness vs displacement curve with the load axis, lb/in.
P_Y	Yield load per unit thickness, lb/in.
p	Pressure, ksi
p^*	Pseudoelastic pressure, ksi
p_{all}	Code-allowable pressure, ksi
p_f	Failure pressure, ksi
p_f^*	Pseudoelastic failure pressure, ksi
p_{GY}	Gross yield pressure, ksi
p_e	Intercept of the strain-hardening branch of a bilinear pressure vs strain curve with the pressure axis, ksi
p_Y	Yield pressure, ksi
Q	Flaw shape and plastic zone size parameter, dimensionless
q	Burst stress coefficient, dimensionless
R	Inside radius, in.
RT_{NDT}	Reference value of the transition temperature, °F
r	Radial distance, in.
r_a	Radial distance to the deepest point of an external part-through surface flaw, in.
r_i	Inside radius, in.
r_m	Mean radius, in.
r_o	Outside radius, in.
r_t	Radius of curvature of a part-circular surface crack, in.
S	Stress intensity ($S = \sigma_1 - \sigma_3$), ksi
S	Critical distance ahead of a crack tip over which the average stress is assumed to equal the ultimate tensile strength at fracture, in.
S	Nominal stress in the region of a flaw, ksi
S_m	Allowable primary membrane stress intensity, ksi
$s_{m,p}$	Size effect, also called the volumetric energy ratio, between a model of size m and a prototype of size p, dimensionless
T	Temperature, °F
T_o	Characteristic temperature of a material, °F

t	Thickness, in.
W	Width, in.
Y	Ratio r_o/r, dimensionless
α	Empirical ductility parameter, in./(ft-lb/ksi)$^{2/3}$
β	Empirical coefficient in the expression for J for a part-through surface crack in the wall of a pressure vessel, dimensionless
β_{1c}	Parameter proportional to the ratio of the plastic zone size to the thickness in plane strain, dimensionless
δ	Displacement, in.
δ_Y	Displacement at initial yield, in.
δ^p	Plastic displacement, in.
ϵ	Strain, in./in.
ϵ_f	Strain at failure, in./in.
$\epsilon_{fm}, \epsilon_{fp}$	Failure strains in a model and in a prototype, respectively, in./in.
ϵ_i	True strain at maximum load in a tension test, in./in.
ϵ_Y	Tensile yield strain, in./in.
ϵ_t	Total elongation in a tension test, in./in.
$\epsilon_{t1}, \epsilon_{t2}$	Total elongation in a tension test over the first and second gage lengths, respectively, in./in.
ϵ_θ	Circumferential strain, in./in.
$\epsilon_{\theta f}$	Circumferential strain at failure, in./in.
$\epsilon_{\theta o}$	Circumferential strain on the outside surface of a cylinder, in./in.
$\epsilon_{\theta Y}$	Circumferential strain at yield, in./in.
ϵ^*	Elastically calculated fracture strain, in./in.
ϵ_-^*	Characteristic strain of a material, in./in.
θ_1, θ_2	Angles, radians
λ	Total strain, in./in.
λ_f	Total strain at failure, in./in.
ν	Poisson's ratio, dimensionless
ρ	Root radius of a notch, in.
σ	Stress at the root of a notch, ksi
σ_b	Bending stress, ksi
σ_d	Pseudoelastic failure stress in a specimen of size d, ksi
σ_m	Membrane stress, ksi
σ_0	Stress at midthickness, ksi
σ_s	Surface stress, ksi
σ_{ult}	True ultimate tensile stress, ksi
σ'_{ult}	Nominal ultimate tensile stress, ksi
σ_Y	Tensile yield stress, ksi
$\sigma_1, \sigma_2, \sigma_3$	Major, intermediate, and minor principal stress, respectively, ksi
$\sigma_\theta, \sigma_r, \sigma_z$	Circumferential, radial, and axial normal stresses, respectively, ksi

$\sigma_\theta{}^*$	Circumferential stress at plastic instability for a thin-walled cylinder under internal pressure, ksi
Φ	Elliptical integral, dimensionless
$\Psi_0(\theta), \Psi_1(\theta)$	Functions describing the variation of K_I around the perimeter of a part-circular surface crack due to the uniform and the linearly varying portions of the total nominal stress acting over the crack area, respectively, dimensionless

Appendix G

FRACTOGRAPHIC STUDY OF FRACTURE SURFACE OF VESSEL V-1

Initially, attempts were made to extract fracture surface replicas without disturbing the failed vessel. However, the rough texture of the fracture did not allow this nondestructive approach; so oxyacetylene burning and saw cutting were used for obtaining samples. The flame cut was made approximately 8 in. away from the fracture surface. This distance is more than ample to assure that the flame-cutting operation would have no detrimental effect. A photograph of the fracture surface to be examined is shown in Fig. G-1, which shows the original man-made flaw quite clearly. The circumferential weld that joined the bottom hemihead to the cylindrical test section is easily seen at the left side of the photograph. (It is located at the change in contour.) The circumferential weld at the upper end of the cylindrical test section is not evident; however, it is also located at the geometric change in section size at the right side of the photograph. After obtaining samples by sawing, a scanning electron microscope was used in the investigation.

Several regions of the fracture surface shown in Fig. G-1 were studied. One is located in the transition piece; others are located in the cylindrical test section and the hemihead.

Figure G-2 shows the results of the study of the region just adjacent to the man-made flaw. Two areas within this region were studied. (The corner of the flaw can be seen.) From the appearance of the fracture surface, we concluded that this region exhibited a dimpled mode of failure.

A region just under the steel rope shown in Fig. G-1 was also investigated. This location exhibits a change in appearance and color. The dark "ductile" coloration seems to terminate in a vee. Chevron lines, lighter in color, appear to originate from its apex. This is usually indicative of an initiation site for fracture propagation. Figure G-3 contains the results of the fractography study of this region. Two areas were studied. The first is located close to the center of the fracture surface and was within an area that was similar (visually) to the regions shown in Fig. G-2. It has a fracture appearance nearly identical to those previously discussed. The second area studied was from outside the V-shaped area and in the lighter (shinier) area. The fracture surface of this area is unlike that of Fig. G-2. This area exhibits a fracture surface identical to that seen in a low-energy (cleavage) failure.

Fig. G-1. Photograph of fracture surface from intermediate test vessel V-1.

Additional regions were studied, which included regions approximately 3 in. from the circumferential welds in the top transition piece and the bottom hemihead. Both exhibited cleavage fracture. Regions in the cylindrical test section approximately 3 in. from the two circumferential welds were also found to exhibit cleavage fracture appearances.

In summary, the fractography study revealed that the region around the man-made flaw exhibited a fracture appearance that is indicative of tough behavior (dimpled). This mode of failure continues for some distance in either direction away from the man-made flaw to a point where it undergoes a transition from dimple to cleavage. This cleavaged fracture continues and is found both in the bottom hemihead and in the top transition piece.

PHOTO 4213-73

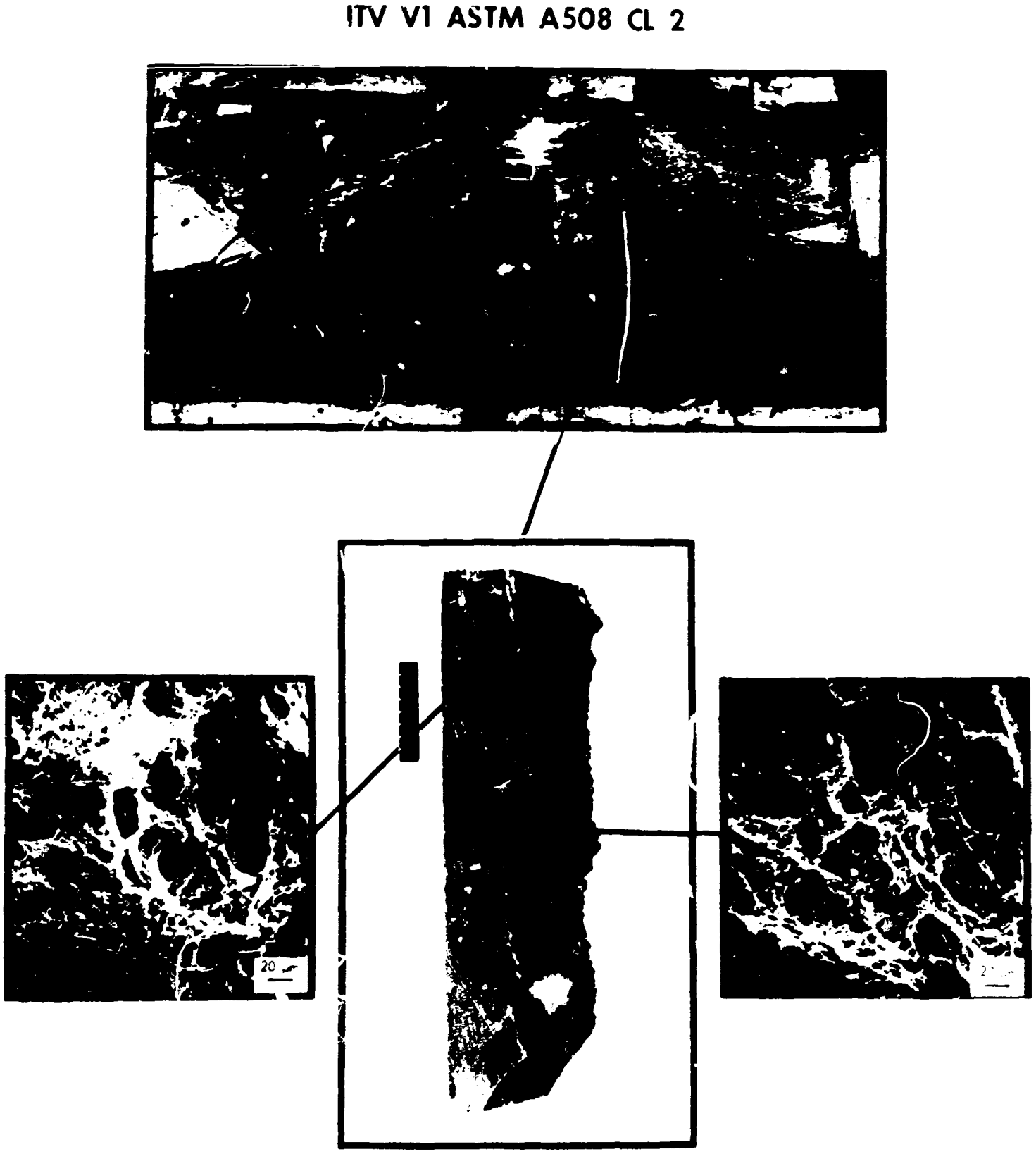

Fig. G-2. Results of scanning electron microscopy study of fracture surface near the machined flaw. The two areas shown illustrate dimple mode of failure.

PHOTO 4212-73

ITV V1 ASTM A508 Cl 2

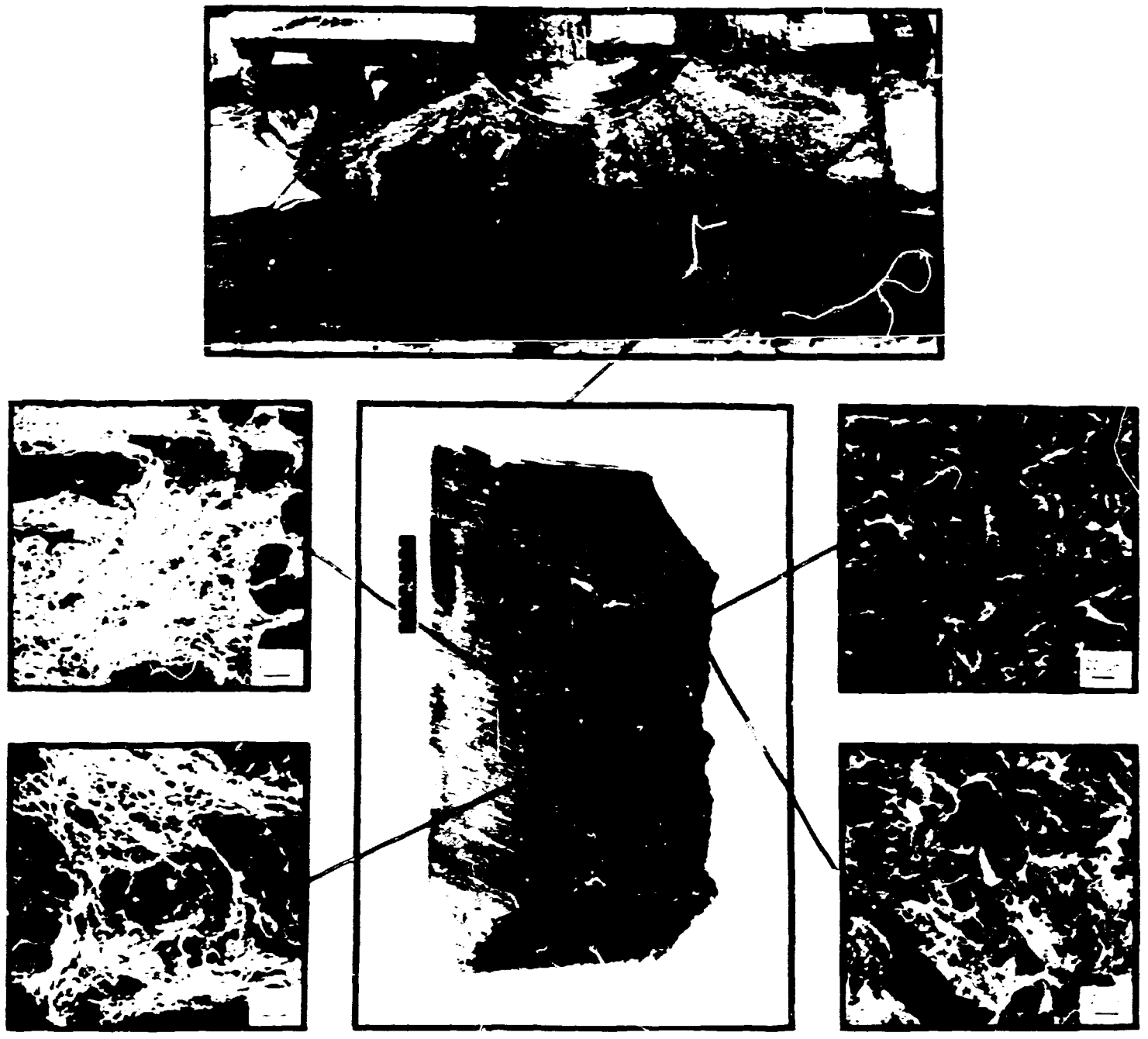

Fig. G-3. Results of scanning electron microscopy study of region where failure mode changed from dimple to cleavage. Photomicrographs on the left are dimples; photomicrographs at the right show the cleavage mode of failure.

Appendix H

FRACTURE BEHAVIOR OF MODEL VESSEL V1-A1-E AND INTERMEDIATE TEST VESSEL V-2

Model vessel V1-A1-E and intermediate test vessel V-2 exhibited common fracture characteristics in that significant strains were present near the flaws at fracture pressure, while the nominal outside surface circumferential strains were near the initial yield strain. The calculations of energy to fracture for the pressure–outside surface circumferential strain curve, based on the behavior of compact tension specimens, were unconservative for both cases. This appendix discusses the significance of the large strains measured near the crack tip and relevant conclusions pertaining to the fracture of the two vessels.

General Fracture Behavior of Structures Exhibiting a Yield Plateau

For this discussion we first consider Fig. H-1, showing the nominal pressure–outside surface circumferential strain curve (gage 13B, Fig. 5.4) 180° from the flaw in vessel V1-A1-E (Table 5.1 and Appendix D) in comparison with the pressure–circumferential strain curve ¼ in. from the crack tip (gage 1). Based on nominal strain alone, a frangible or near-frangible result for the vessel might be postulated. With this postulation might follow the inference that linear elastic fracture mechanics is applicable to this situation, which in turn implies that the fracture pressure is linearly related to the fracture toughness of the material, at least at −35°F and for all temperatures below, as given in Fig. 4.13.

To examine fully the question of whether linear elastic fracture mechanics is applicable to the results of model vessel V1-A1-E, we shall first refer to tests of other types of specimens. The example of structures other than pressure vessels most applicable to this situation goes back to one of the earlier investigations sponsored by the HSST program.[1] Randall's results, depicted in Fig. H-2, show that the gross strain (gross section strain to fracture) for the center flawed tensile specimen is a constant 0.2% (yield strain), at least from −50 to +20°F. Over this range of temperature the fracture toughness probably varies by at least 50%, but fracture continues to occur at 0.2%. The material tested by Randall (HSST plate 01) exhibits about the same yield plateau behavior as depicted in Fig. 4.3, which is also typical for vessel V-2 material. In terms of a comparison with compact tension specimens the results given in Fig. H-3 are obtained.[2] Specifically, compact tension specimens do not exhibit the yield point instability; therefore when these results are compared with results of specimens that do, using a high temperature as a basis for normalization, the compact tension specimens appear to give unconservative results. However, this is not necessarily the case if one is concerned with fracture either at, or significantly below, the yield point instability. The compact tension specimen behavior indicates fracture points falling along the yield plateau, hence giving the correct load if not the correct strain. Since gross strain specimens were not tested below −50°F, it cannot be directly inferred that these specimens still fail at yield even though the compact tension specimens indicate such behavior. However, a series of 1-in.-thick pressure vessels have been tested with the results given in Fig. H-4. As may be observed, the results of a vessel tested at 200°F with over 2.5% circumferential strain, combined with those of compact tension specimens, accurately defined the failure strain of a vessel tested at −75°F as about 0.2%.[3] Similarly, results from a 1-in.-thick compact tension specimen combined with results from a 1-in.-thick flawed tensile specimen, each tested at 200°F, and the fracture toughness of the material at −40°F led to the prediction of the failure load of a similar 6-in.-thick tensile specimen (see ref. 4, specimen 15) to be between 3.0 and 3.6 million pounds.[5] Actual failure occurred at 3.4 million pounds (about half the yield strain). These last two results demonstrate that failure significantly below yield does not occur until such a low temperature is reached that the volumetric energy ratio of the compact tension specimen,

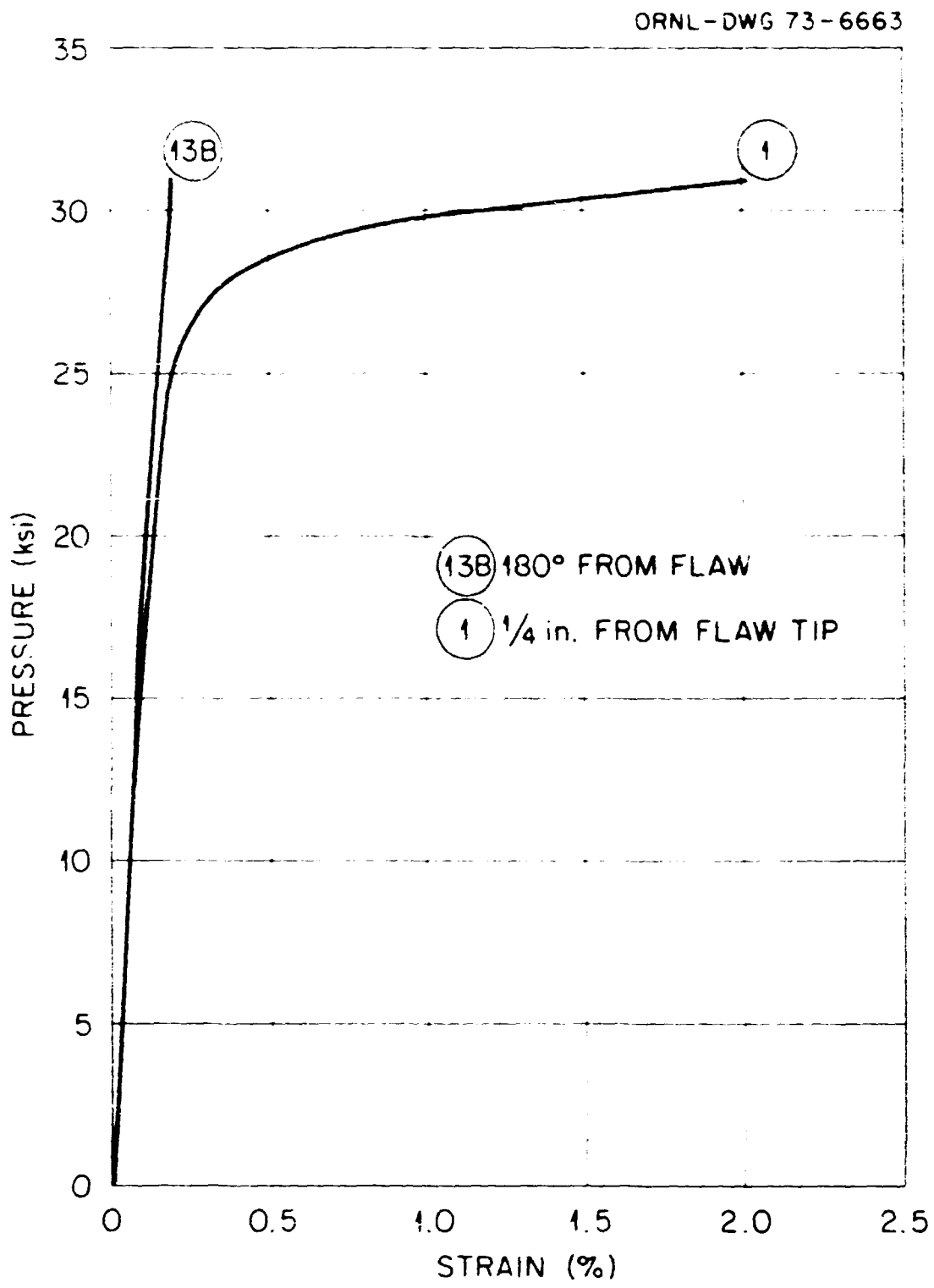

Fig. H-1. Pressure–circumferential strain curves for vessel V1-A1-E tested at −35° F.

when applied to higher temperature results of the specimen in question, produces such a result. That the pressure vessels fabricated from the steel in question exhibit a yield point instability is shown in Fig. 5.12 (vessel V2-A1-D), Fig. 8.4, and more precisely in Fig. C-20.

Essentially then we have established the correspondence as sketched in Fig. H-5, where the energies to maximum load are normalized at a high temperature (point A). Both specimens exhibit the same volumetric energy ratio to point B; at a temperature slightly higher than that at point B, specimen 2 fails at a load slightly higher than yield load. In terms of strain it experiences the yield point instability and exhibits some strain hardening at failure. At point B, however, specimen 2 fails at yield load, does not experience the yield point instability, and fails at yield strain; hence the discontinuity with the volumetric energy ratio for specimen 2 jumping to B'. At point C the energy ratios coincide again and continue to coincide for all lower temperatures.

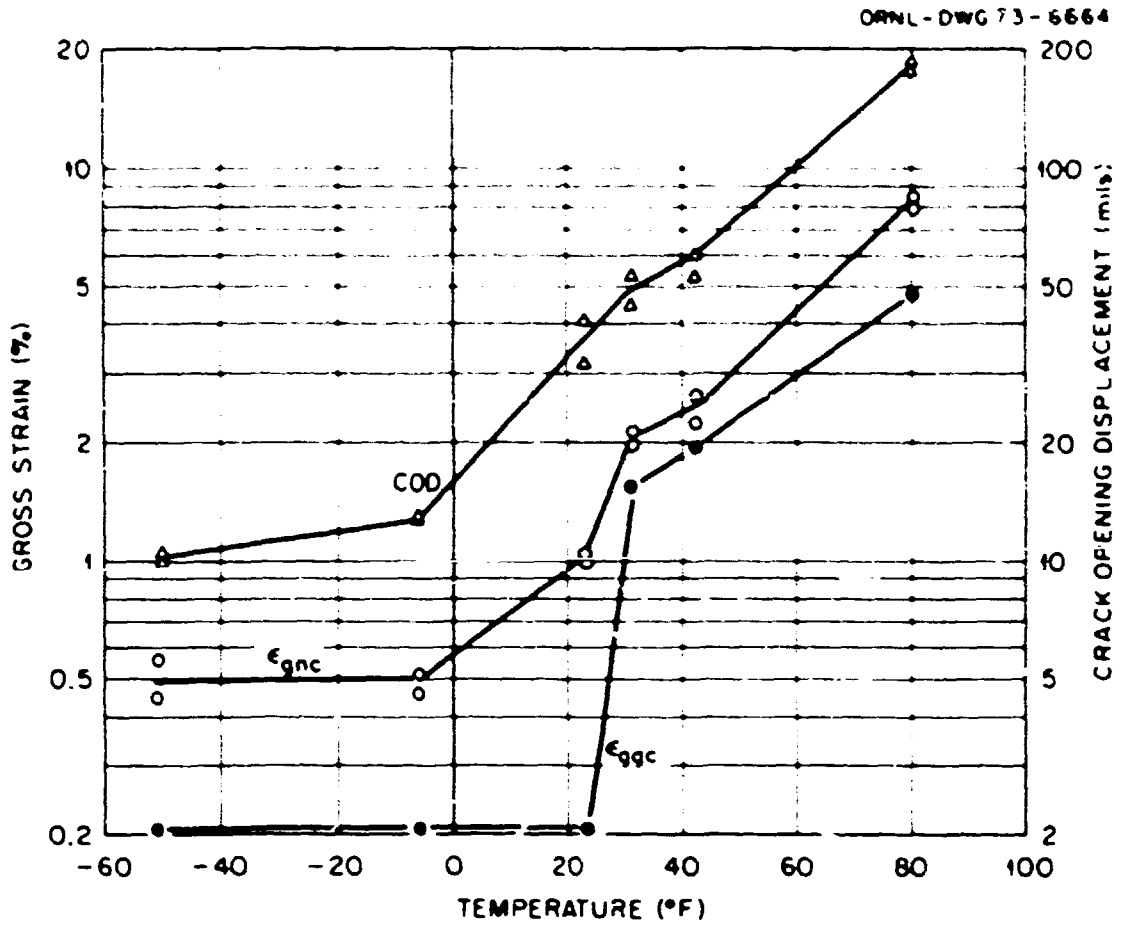

Fig. H-2. Effect of temperature on critical displacements in 4.00- by 1.08-in. specimens containing 0.38-in.-deep, 1.40-in.-long cracks. Fig. 30 of ref. 1.

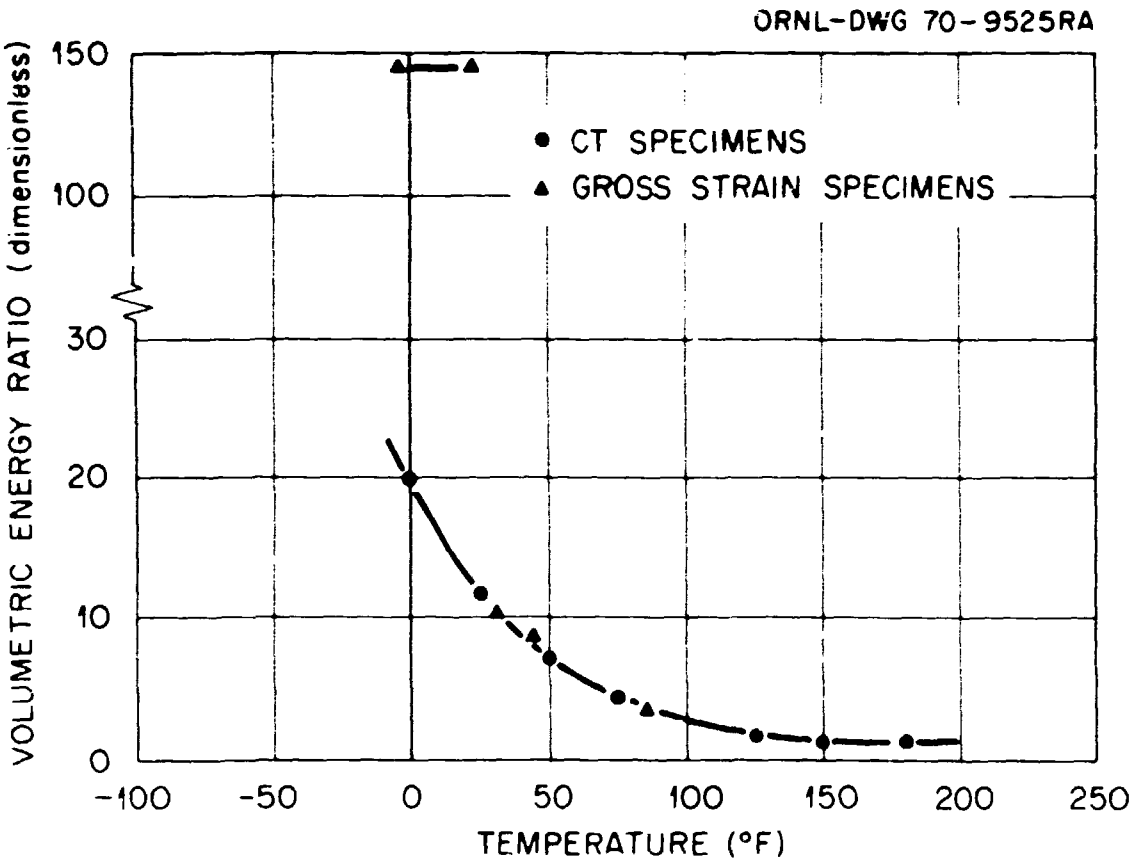

Fig. H-3. Comparison of volumetric energy ratios between compact tension specimens and gross strain specimens, emphasizing the fracture behavior at yield strain. Specimens are nominally 1 in. thick.

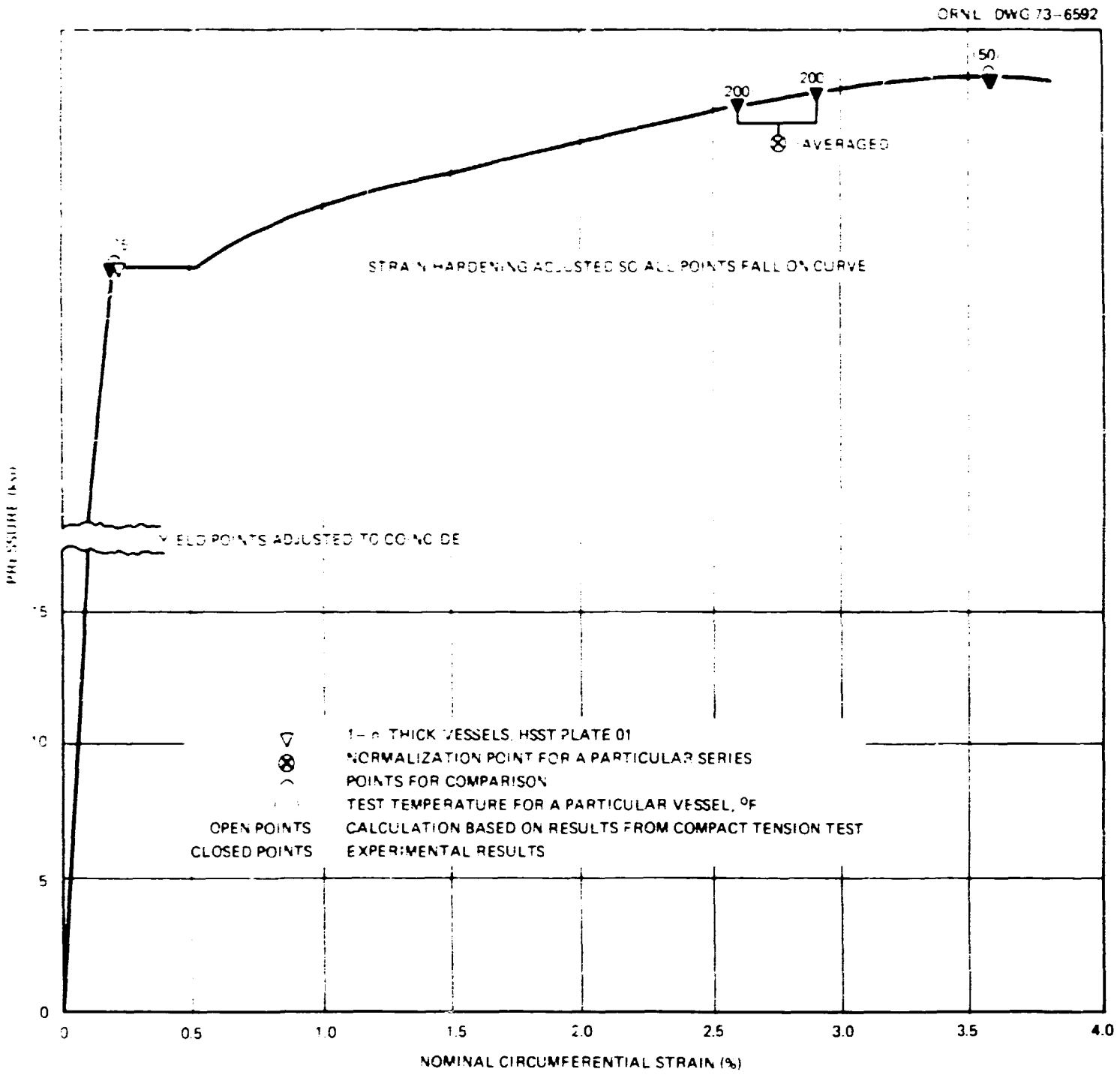

Fig. H-4. Calculated fracture conditions in 1-in.-thick pressure vessels, normalized to the behavior of compact tension specimens, compared with experiments.

Both model vessel V1-A1-E and intermediate test vessel V-2 failed near nominal yield strain, while the behavior premised on the compact tension specimens indicated fracture well along on the yield plateau. To further determine the actual behavior of the two vessels, load-strain behavior near the flaw is examined, where the yield plateau instability probably does not exist.

Fracture of Model Vessel V1-A1-E

We shall now examine in more detail the behavior in the model pressure vessels in question 180° from the flaw in conjunction with behavior near the flaw with specific reference to the yield point instability. The test most definitive for this discussion is that of a 1-in.-thick model of the intermediate vessels fabricated from a 12-in.-thick plate (HSST plate 01),[3] designated model 01-HW. This vessel had a flaw similar to that of the V-1 material models and was tested at 50°F (see Fig. H-4). Figure H-6 is a plot of the

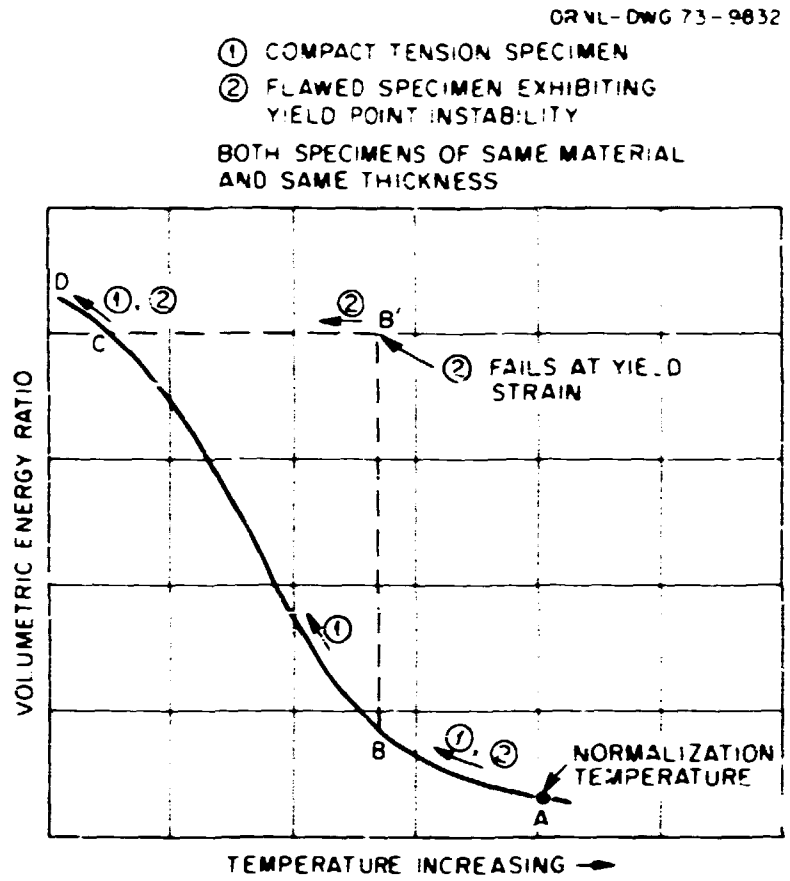

Fig. H-5. Volumetric energy ratios of compact tension specimens compared with that of flawed specimens exhibiting a yield point instability in the region of the flaw when unflawed.

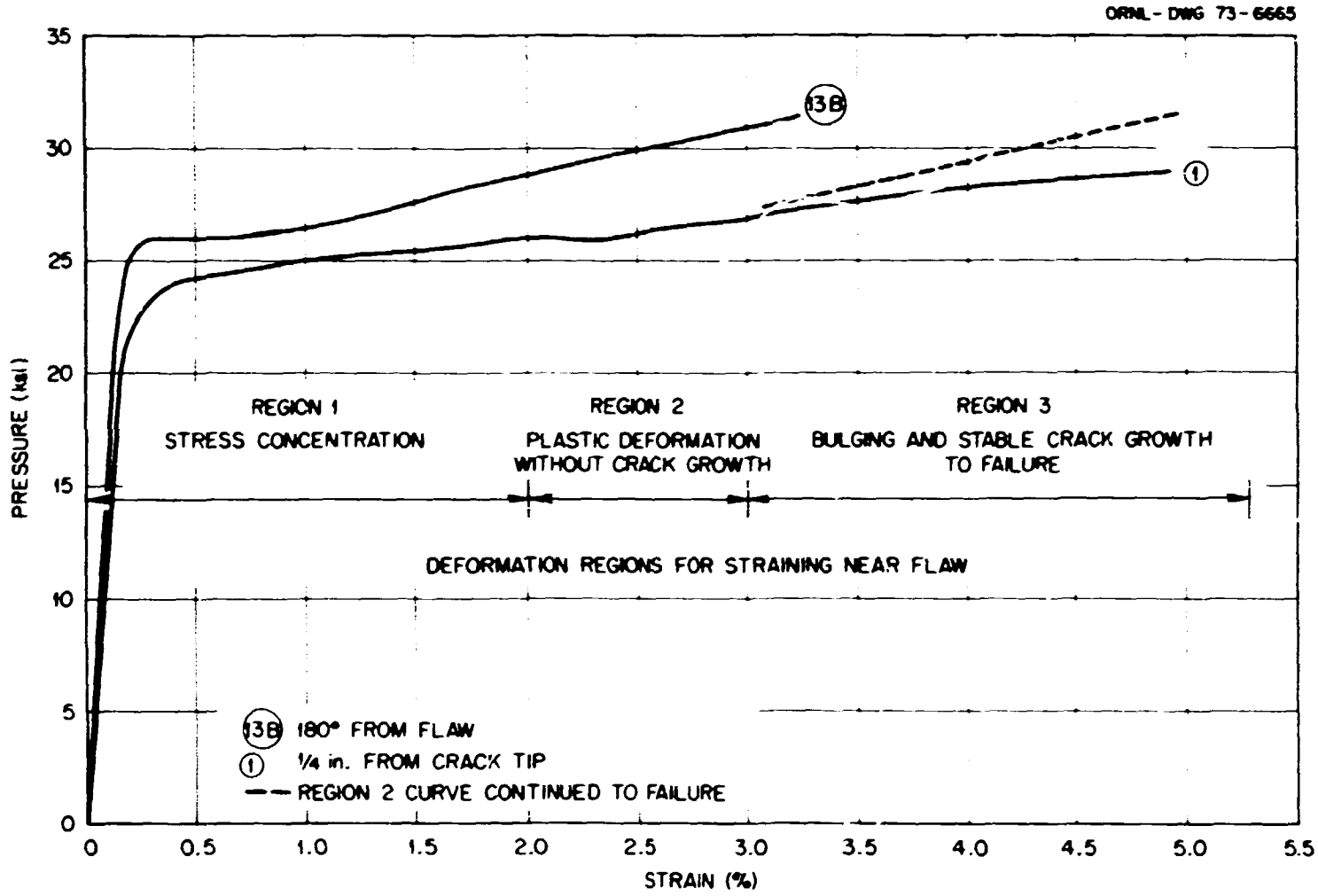

Fig. H-6. Pressure–circumferential strain curves for a 1-in.-thick pressure vessel tested at 50°F.

pressure-strain curves 180° from the flaw and ¼ in. from the crack tip (see Fig. 5.4, gages 13B and 1 respectively). In this test the yield point instability is well defined; however, most noteworthy for this discussion is the behavior near the flaw. As the nominal circumferential strain increases from around 0.3% to around 0.6% at 26,000 psi, the strain near the crack tip increases about the same amount. In fact, from 26,000 to 27,000 psi, these two strains increase by the same amount (over 0.6%). At higher pressure the strain near the crack tip increases rapidly, indicating local bulging and stable crack growth. At 29,000 psi the strain from gage 1 began to decrease, suggesting either gage failure or release of strain due to stable crack growth.

The above results define three regions of behavior near the flaw: (1) straining due to the stress concentration near the crack, (2) plastic deforming typical of the same region unflawed, and (3) bulging accompanied by stable crack growth. These regions are indicated in Fig. H-6. Without crack growth or bulging, plastic deformation similar to that of region 2 would be expected to continue; that is, the curve in region 2 would remain parallel to the nominal strain curve, as indicated in Fig. H-6 by the dashed line.

The behavior of model vessel V1-A1-E, tested at −35°F, will now be further explored, based on the results from vessel V1-A1-C, tested at 130°F. This choice is arbitrary since results from vessel V1-A1-B or V1-A1-F could be used where data are available. Figure H-7, in a plot of the nominal pressure–circumferential strain curve (gage 13B, Fig. 5.4) 180° from the flaw in vessel V1-A1-C (see Table 5.1 and Appendix D) and the curve ¼ in. from the crack tip (gage 1). The pressure increments were not taken to well define the yield point instability, but the yield plateau starts at about 29,000 psi (the beginning of region 2 as defined above). Region 3 starts at slightly less than 30,000 psi. As in Fig. H-6, the dashed line represents the continuation of region 2 to failure pressure.

The curves near the flaw from Figs. H-1 and H-7 are compared in Fig. H-8. The difference in yield pressure is probably due mostly to the 165° difference in test temperature. The same procedures used to obtain Fig. 9.1 will now be applied. The volumetric energy ratio for the near-surface material of vessel V-1 material is determined from the data in Table 4.7 and Fig. 4.12. At −35°F, the interpolated lower-bound toughness for surface material from 0.85-in.-thick compact tension specimens is taken as 135 ksi $\sqrt{\text{in.}}$; at 130°F the average value is 210.5 ksi $\sqrt{\text{in.}}$. From these values the volumetric energy ratio from 130 to −35°F is 2.44 [i.e., $(210/135)^2$]. In Fig. H-8, the area to point A divided into the area to point B is 2.1, while the area to point A divided into the area to point C is 5.3. In other words, if data near the flaw, which reflect the actual local bulging and crack growth, had been used, the predicted area under the curve for vessel V1-A1-E would have been high by a factor of over 2. On the other hand, using the plastic deformation extended curve for the vessel, the result is accurate within 15%. Similar results would have been found for vessel V1-A1-B or V1-A1-F.

The above calculations using actual data near a flaw where stable crack growth occurs prior to maximum pressure well illustrate why the nominal strain is used in making the comparison with compact tension specimens. The compact tension specimen exhibits little or no crack growth prior to maximum load for the materials being investigated; thus displacements reflect only the stress concentration behavior (region 1) and plastic deformation behavior (region 2). This is also a basic reason for emphasizing the compact tension specimen tests in the material investigations discussed in Chapter 4.

From the above discussion, it is concluded, assuming no local bulging or crack growth prior to fracture and accounting for this in the near-flaw behavior, that a correct fracture assessment may be obtained for cases where the nominal strain is near yield.

Figure H-2 generally shows that varying the temperature at which failure occurs at a nominal yield load does not degrade the failure conditions over the temperature range investigated. This implies that the increase in yield strength with the lowering temperature compensates for the decreasing toughness of the

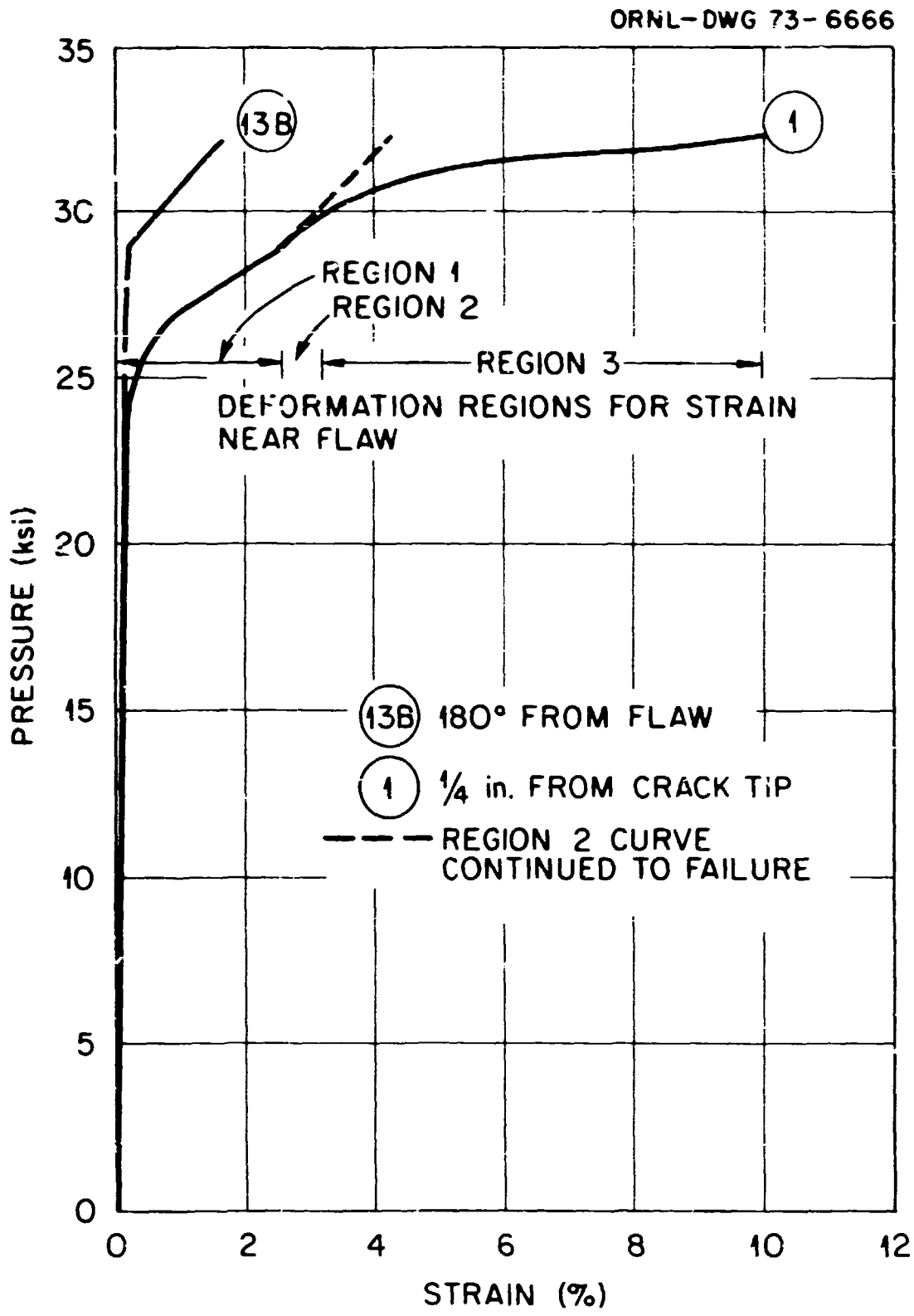

Fig. H-7. Pressure–circumferential strain curves for 0.85-in.-thick model vessel V1-A1-C tested at 130°F.

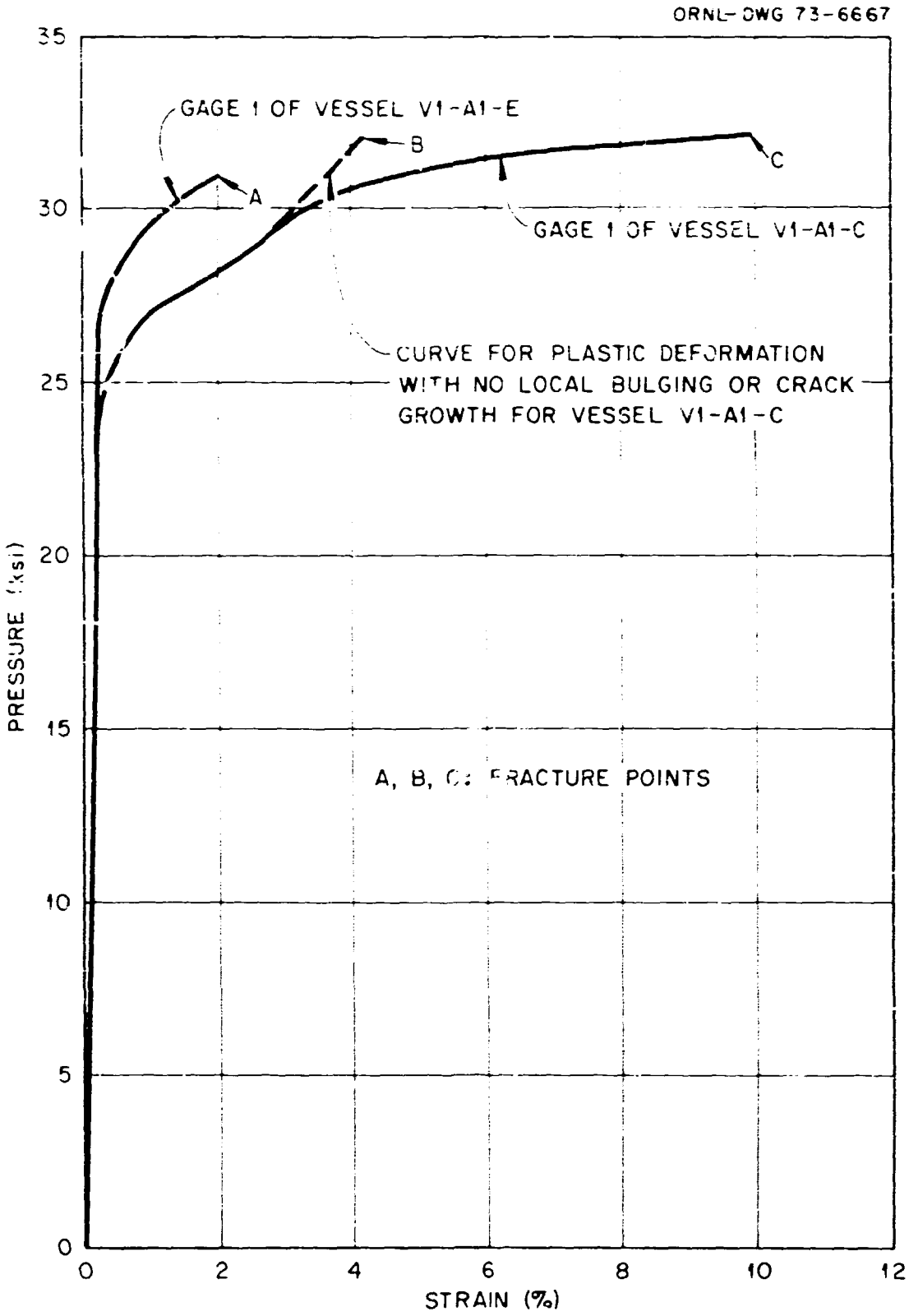

Fig. H-8. Comparison of pressure–circumferential strain curves obtained $^1/_4$ in. from crack tip for model vessels V1-A1-E tested at −35° F and V1-A1-C tested at 130° F (with region 2 defined).

specimen over the range of temperature. On the other hand, if thickness is the varying fracture parameter at a given temperature, the nominal load and strain at failure would decrease. For instance, if a 6-in.-thick prototype of model vessel V1-A1-E with the same flaw shape and size scaled by the scaling factor of 7.06 were tested at −35°F, fracture would be expected to occur at a pressure of about 26,000 psi. (Note: The flaws in vessels V-1 and V-2 were not modeled in vessel V1-A1-E; see Table 5.1 and Fig. 5.9.) This is premised on the fact that the volumetric energy ratio at −35°F between compact tension specimens 0.85 and 6 in. thick is the ratio of the dimensions, 7.06 in this case. Thus at −35°F, a near-frangible behavior would occur in the prototype vessel.

Fracture of Intermediate Test Vessel V-2

The examination of the fracture behavior of intermediate test vessel V-2 will follow the same steps as for model vessel V1-A1-E.

As shown in Fig. 8.20, a strain of over 0.8% was measured near the flaw in vessel V-2. In this region the material is obviously yielding very rapidly with pressure; however, at 13 in. from the crack tip, no yielding has occurred. Likewise, inside the vessel opposite the flaw (see Fig. 8.22), the strain is actually less at the thinnest section and increases as the point opposite the crack tip is approached. Thus significant straining is

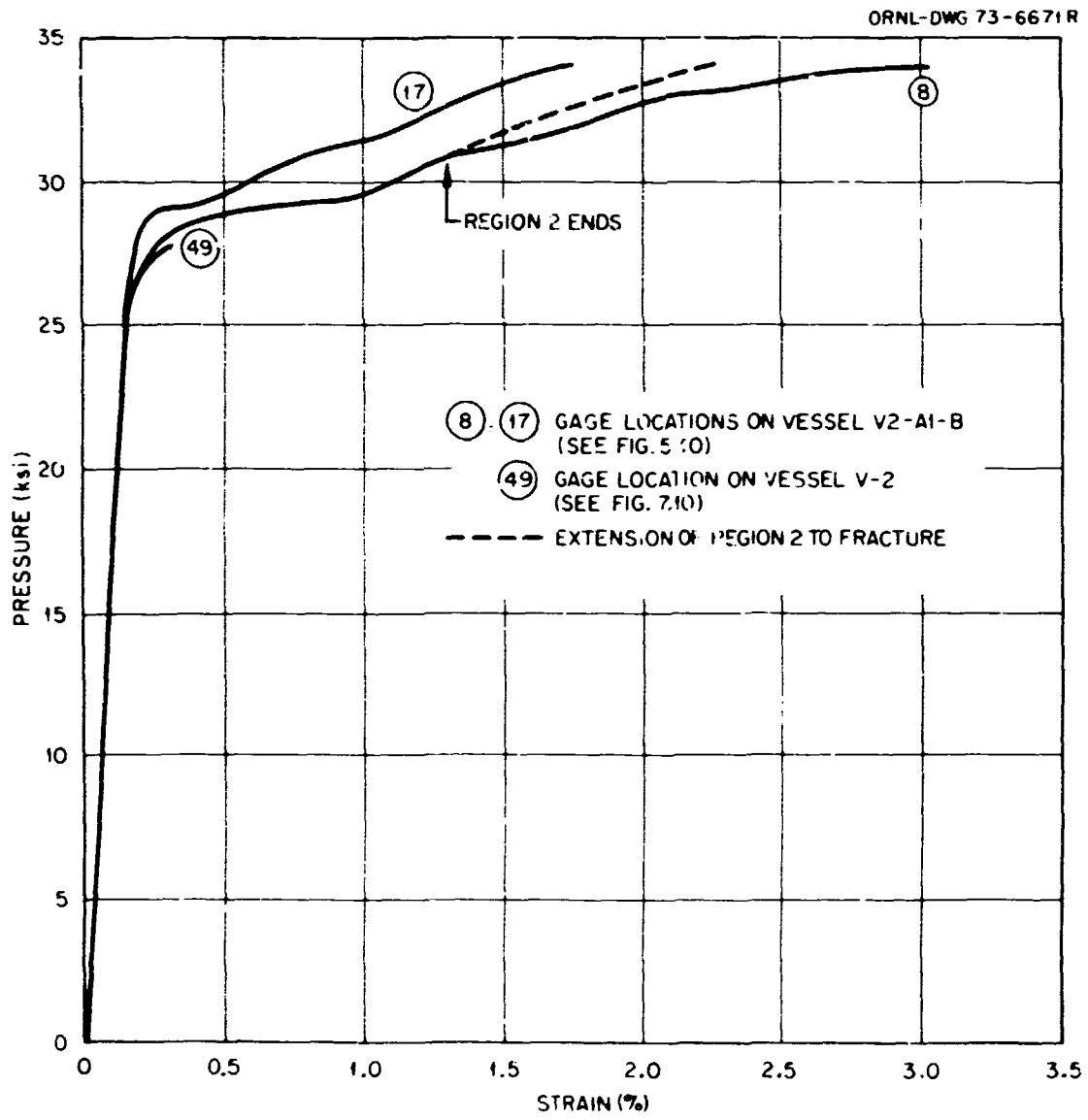

Fig. H-9. Comparison of pressure–circumferential strain curves at gage locations 8 and 17 on vessel V2-A1-B with gage location 49 on vessel V-2.

apparently limited to the close confines of the flaw. The significance of these strains to the fracturing process is examined below.

Since strain data close to the flaw were not obtained near the burst pressure of vessel V-1, model V2-A1-B (Table 5.2 and Appendix D) will be used for examining the significance of the strains near the flaw at the burst of vessel V-2. On this model, gage 1 (Fig. 5.10) coincides in location roughly with gage 50 of vessel V-2 (Fig. 7.10), while gage 8 coincides quite well with gage 49 (6 in. from crack tip). Comparisons of the pressure-strain behavior at these two locations on the model with similar locations 180° away are given in Figs. H-9 and H-10, along with results from gages 49 and 50 of vessel V-2. The region 3 portions of the curves, as discussed above, are identifiable from these curves, and the dashed lines represent the region 2 extension to fracture.

The energy ratio between the model tested at 130°F and vessel V-2 will now be established. As indicated in the discussion above and in the discussions of the equivalent-energy method in Appendix C, an average energy ratio of 4 was established between the model and the prototype for the 130°F test, following Eq. (47) in Appendix C. For an average K_{Ic6} of 311 ksi $\sqrt{\text{in.}}$ at 130°F and 160 to 200 ksi $\sqrt{\text{in.}}$ at 32°F, an energy ratio of from 2.42 to 3.84 is established. The product of the energy ratios of these numbers will give the volumetric energy ratio between the model tested at 130°F and vessel V-2. This product is between 9.68 and 15.36. Figure H-11 is a plot of the results from gages 49 and 50 together with estimates for the fracture conditions based on the model behavior. The calculation for gage 49 location is

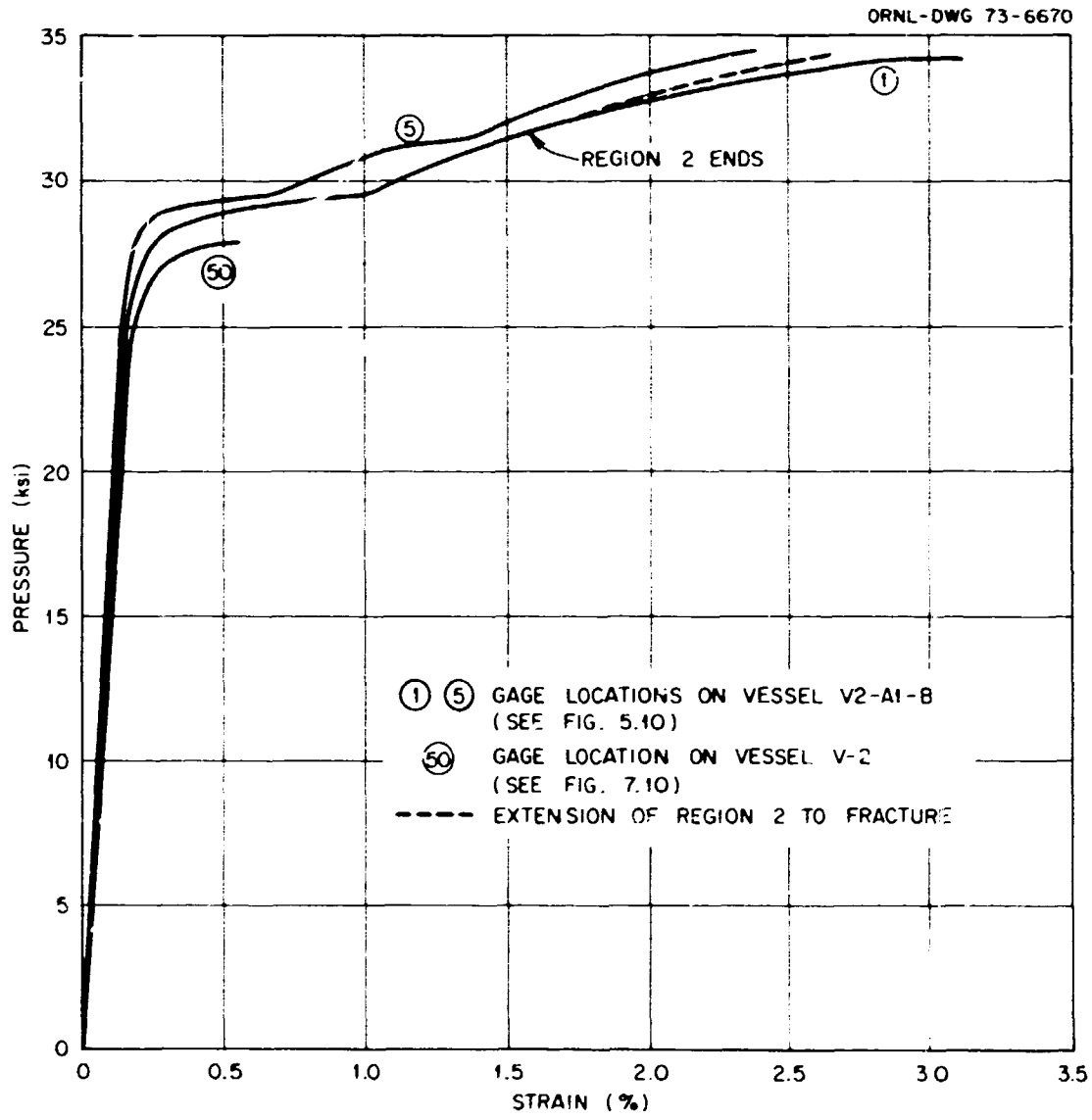

Fig. H-10. Comparison of pressure–circumferential strain curves at gage locations 1 and 5 on model vessel V2-A1-B with gage location 50 on vessel V-2.

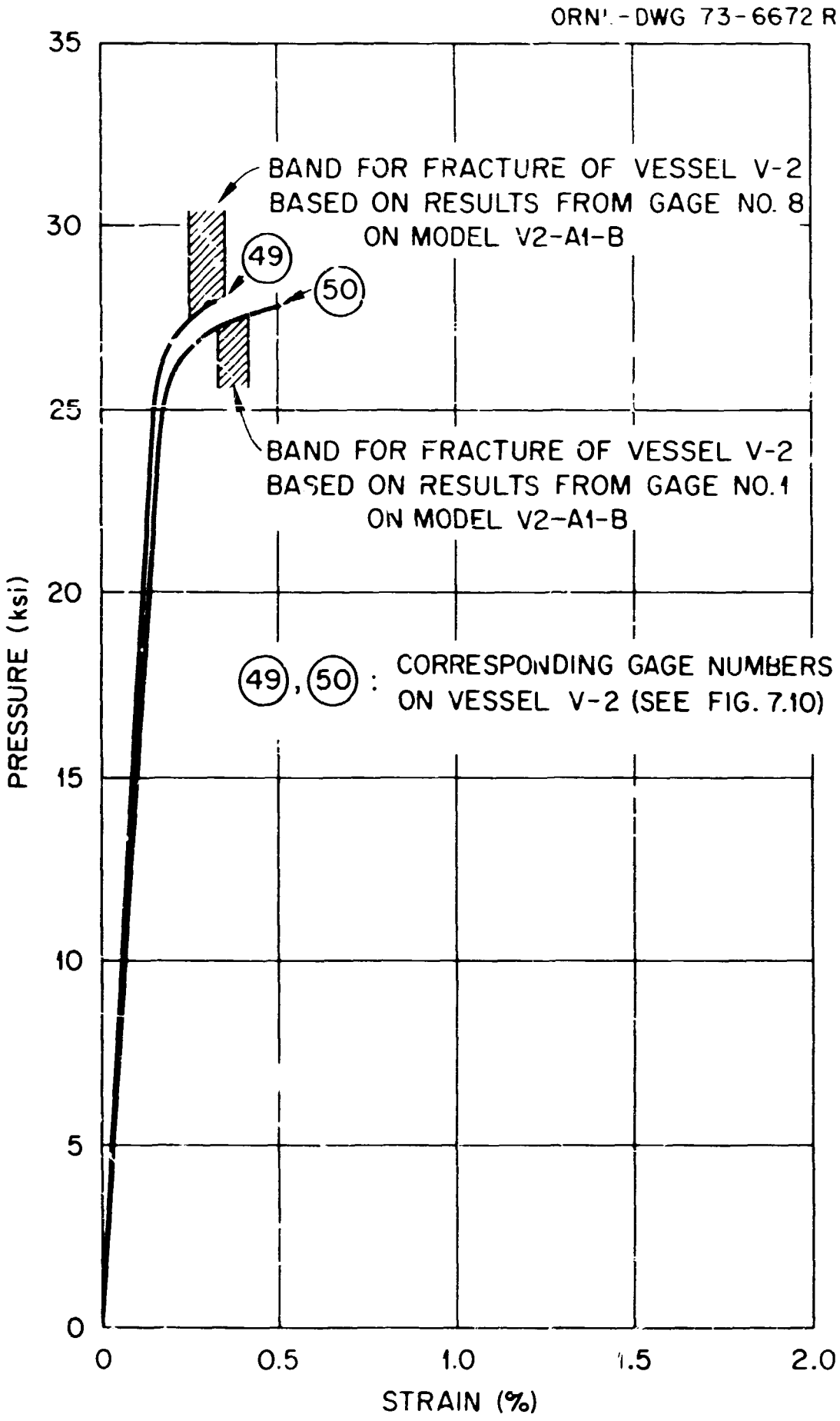

Fig. H-11. Estimates of fracture of vessel V-2 based on behavior of strains in model V2-A1-B near the flaw.

quite accurate, while less accuracy is obtained for the gage 50 location. In general, it may be concluded that the fracture conditions defined here may be applied to similar models.

The question of the frangibility of the vessel V-2 test may now be explored. More specifically, it may be asked if linear elastic fracture mechanics is applicable to the analysis; that is, whether fracture pressure reduces inversely as the square root of the flaw size and directly with fracture toughness. The results from gage 49 of vessel V-2 (Fig. 8.20) will be used. At 32°F, we shall take an average fracture toughness of 180 ksi $\sqrt{\text{in.}}$ (Fig. 4.13). The fracture behavior at 32°F of vessels geometrically similar to vessel V-2 (including scaling up the flaw) in greater thicknesses may now be estimated using linear elastic fracture mechanics based on a fracture pressure of 27,900 psi for vessel V-2. The fracture behavior based on gage 49 (Fig. H-11) may be calculated by simply dividing by the scale factor. These two results are plotted in Fig. H-12. Based on the above discussion, it may be concluded that linear elastic fracture mechanics was not applicable

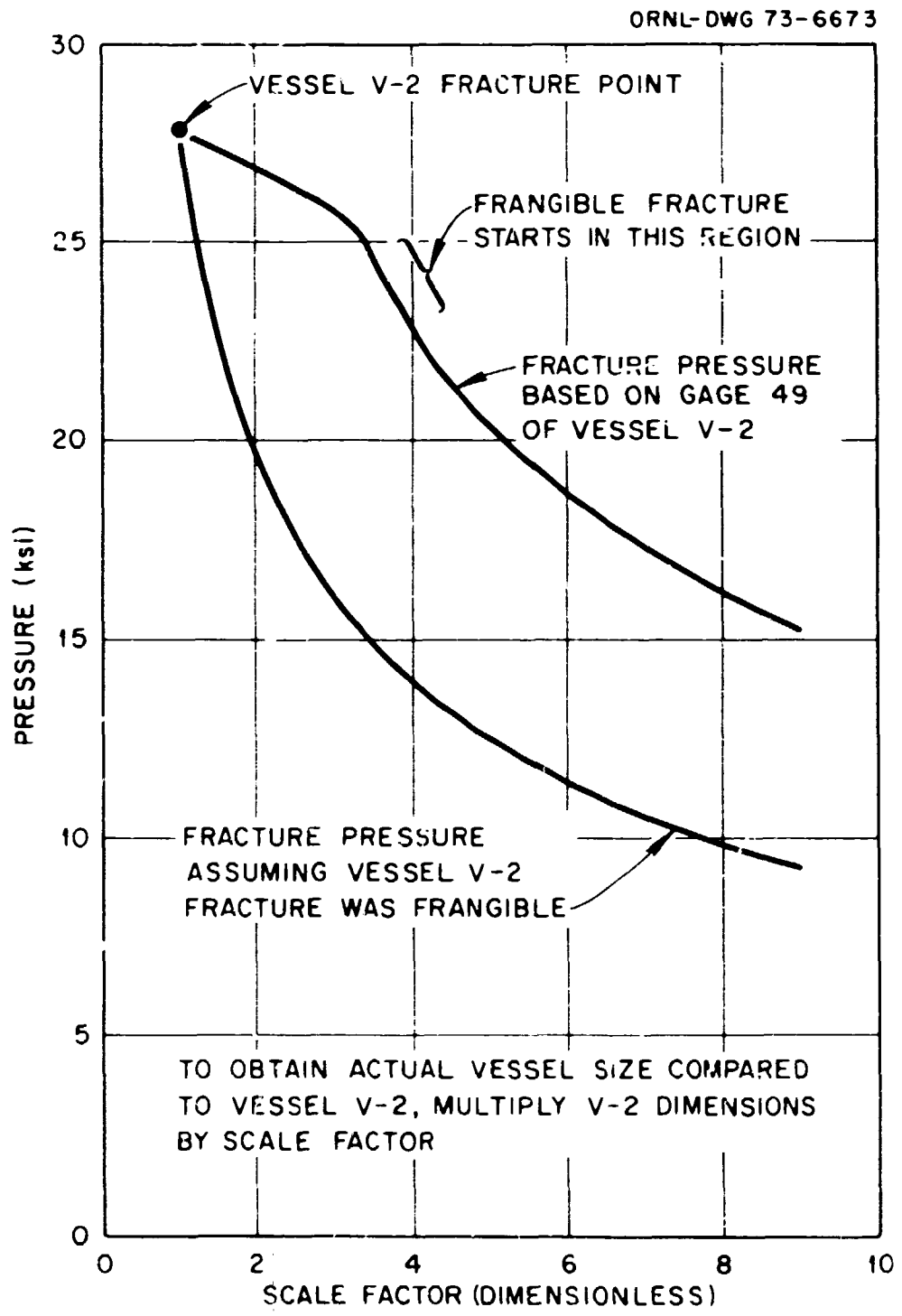

Fig. H-12. Comparison of the fracture pressure of vessel V-2 with fracture pressures on larger similar vessels tested at 32°F.

at 32°F; that is, the fracture pressure initially would not increase inversely as the square root of the flaw size.

From the average toughness data of Fig. 4.13, the fracture pressures at lower temperatures of vessel V-2, based on gage 49 results as well as those based on the assumption of frangible behavior are plotted in Fig. H-13. Again, based on the above discussion, frangible fracture is seen to occur in vessel V-2 at around

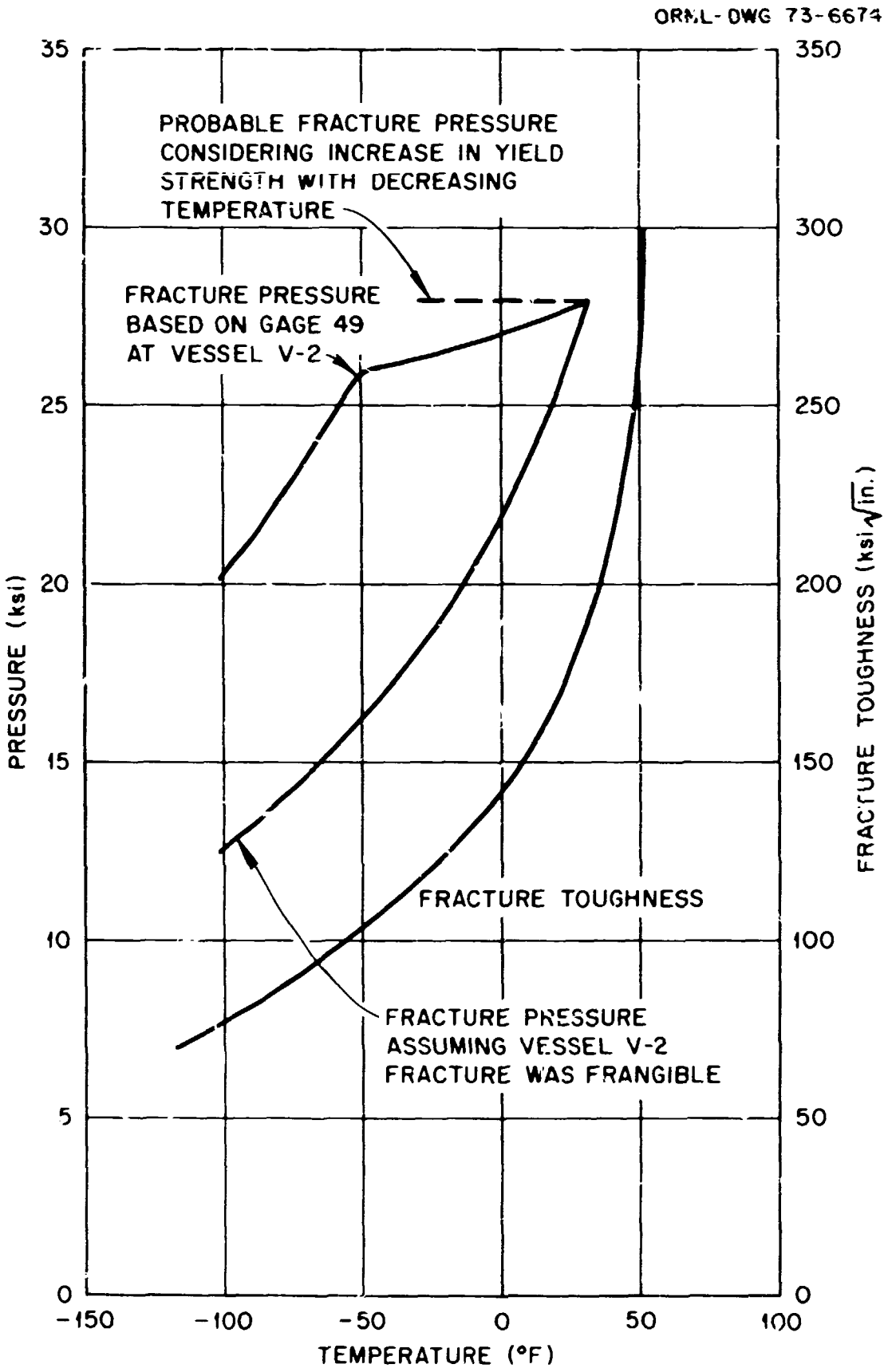

Fig. H-13. Comparison of the fracture pressures of vessel V-2 with fracture pressures had vessel V-2 been tested at lower temperatures.

-50°F. Since the yield strength increases with decreasing temperature, the fracture pressure would probably remain more or less constant, at least until near frangible fracture.

Last to be discussed of the relative fracture behavior between vessels V-1 and V-2 will be the crack opening displacements. These results are compared in Fig. 9.3. It should be recalled that for vessel V-1 the pressurization near failure was continuous. Experience with the model vessels has well demonstrated that near-failure conditions actually can be made to occur by regaining a pressure (the pressure drops due to deformation) and allowing the vessel to strain more (bulge) in the region of the flaw as the pressure again is reduced due to the local bulging. Of course stable crack growth is occurring all the while. The same behavior could have been expected for vessel V-1 if the original test plan had been followed (see Chapter 8).

While it is difficult to assess accurately when near-unstable crack growth initiated for vessel V-1, a reasonable choice can be made from Fig. 8.9 (see also Table 8.1), from which one may conclude that such growth initiates between crack opening displacements of 0.2 and 0.35 in. For instance, for a crack opening displacement of 0.256 in. (Table 8.1) the pressure is within 300 psi (about 1%) of failure pressure. In Fig. 9.2, the energy ratio of vessel V-2, based on a crack opening displacement of 0.256 in. for vessel V-1, is 4.15. This compares fairly well with the scatter band of values from 2.5 to 4.15 obtained from compact tension specimens.

Conclusions

Several aspects of the fracture behavior of vessel V-2 and model vessel V1-A1-E have been discussed in this appendix. Each discussion indicates that neither vessel failed in a frangible mode for which linear elastic fracture mechanics is directly applicable. While any one discussion taken individually may not be a completely satisfactory argument, the overall results presented serve to demonstrate that vessel V-2 did not exhibit frangible fracture at initiation and that the low nominal strain is no more than a manifestation of the yield point instability type of fracture behavior as seen throughout the fracture investigations of the HSST program.

References

1. P. N. Randall, *Gross Strain Measure of Fracture Toughness of Steels*, HSSTP-TR-3, TRW Systems Group, Redondo Beach, Calif. (Nov. 1, 1969).
2. F. J. Witt, *The Equivalent Energy Method for Calculating Elastic-Plastic Fracture* (to be published).
3. F. J. Witt, "Factors Influencing a Quantitative Safety Assessment of Water Reactor Pressure Vessels," *Topical Meeting on Water-Reactor Safety, Mar. 26–28, 1973*, CONF-730304, USAEC Technical Information Center, pp. 16–38, (1973).
4. S. C. Grigory, *Tests of Six-Inch-Thick Flawed Tensile Specimens, Third Technical Summary Report, Longitudinal Specimens Numbers 14 through 16, Unflawed Specimen Number 17*, HSSTP-TR-22, Southwest Research Institute, San Antonio, Tex. (October 1972).
5. Personal communication, F.J. Witt, Oak Ridge National Laboratory, to be published.

☆U.S. GOVERNMENT PRINTING OFFICE: 1973-747-302/113